2011-08-04

Ferritin Diversity: Mechanistic Studies, Disease Implications, and Materials Chemistry

Robert Joseph Hilton
Brigham Young University - Provo

Ferritin Diversity: Mechanistic Studies, Disease Implications, and Materials Chemistry

Robert J. Hilton

A dissertation submitted to the faculty of
Brigham Young University
in partial fulfillment of the requirements for the degree of

Doctor of Philosophy

Richard K. Watt, Chair
Steven W. Graves
Roger G. Harrison
Barry M. Willardson
Dixon J. Woodbury

Department of Chemistry and Biochemistry

Brigham Young University

December 2011

ABSTRACT

Ferritin Diversity: Mechanistic Studies, Disease Implications, and Materials Chemistry

Robert J. Hilton
Department of Chemistry and Biochemistry
Doctor of Philosophy

The study of ferritin includes a rich history of discoveries and scientific progress. Initially, the composition of ferritin was determined. Soon, it was shown that ferritin is a spherical, hollow protein. Eventually, over several decades of research, the structure and some function of this interesting protein was elucidated. However, the ferritin field was not completely satisfied. Today, for example, researchers are interested in refining the details of ferritin function, in discovering the role of ferritin in a variety of diseases, and in using ferritin for materials chemistry applications. The work presented in this dissertation highlights the progress that we have made in each of these three areas:

1)   Mechanistic studies: The buffer used during horse spleen ferritin iron loading significantly influences the mineralization process and the quantity of iron deposited in ferritin. The ferrihydrite core of ferritin is crystalline and ordered when iron is loaded into ferritin in the presence of imidazole buffer. On the other hand, when iron is loaded into ferritin in the presence of MOPS buffer, the ferrihydrite core is less crystalline and less ordered, and a smaller amount of total iron is loaded in ferritin. We also show that iron can be released from the ferritin core in a non-reductive manner. The rate of Fe^{3+} release from horse spleen ferritin was measured using the Fe^{3+}-specific chelator desferoxamine. We show that iron release occurs by three kinetic events.

2)   Disease studies: In order to better understand iron disruption during disease states, we performed in vitro assays that mimicked chronic kidney disease. We tested the hypothesis that elevated levels of serum phosphate interrupted normal iron binding by transferrin and ferritin. Results show that phosphate competes for iron, forming an iron(III)-phosphate complex that is inaccessible to either transferrin or ferritin. Ferritin samples separated from the iron(III)-phosphate complex shows that as the phosphate concentration increases, iron loading into ferritin decreases.

3)   Materials chemistry studies: Anion sequestration during ferritin core reduction was studied. When the core of horse spleen ferritin is fully reduced using formamidine sulfinic acid, a variety of anions, including halides and oxoanions, cross the protein shell and enter the ferritin interior. Efforts have been made to use ferritin to control the concentration of anions for reactions. In addition, the native ferrihydrite mineral core of ferritin is a semi-conductor capable of catalyzing oxidation/reduction reactions. Light can photo-reduce $AuCl_4^-$ to form gold nanoparticles (AuNPs) with ferritin as a photocatalyst. The mechanism of AuNP formation using ferritin as a photocatalyst was examined. From this work, we propose that the ferrihydrite core of ferritin photo-reduces; the mineral core dissolves into a soluble iron(II) mineral. The iron(II) then re-oxidizes, and a new mineral forms that appears to be the new photocatalyst, as the lag phase is significantly decreased with this new mineral form of ferritin.

Keywords: ferritin, chronic kidney disease, nanocage, anion, gold nanoparticles, photochemistry

ACKNOWLEDGEMENTS

TABLE OF CONTENTS

LIST OF TABLES

LIST OF FIGURES

LIST OF SCHEMES

ABBREVIATIONS

AA – atomic absorption spectroscopy

AFM – atomic force microscopy

AgNP – silver nanoparticle

AMPSO – 3-((1,1-Dimethyl-2-hydroxyethyl)amino)-2-hydroxypropanesulfonic acid

AuNP – gold nanoparticle

Bipy – 2,2'-bipyridine

BSA – bovine serum albumin

CKD – chronic kidney disease

DES – desferoxamine

DMT – divalent metal transporter

EDTA – ethylenediaminetetraacetic acid

EDX – energy-dispersive X-ray spectroscopy

EPPS – 3-[4-(2-hydroxyethyl)-1-piperazinyl]propanesulfonic acid

EPR – electron paramagnetic resonance spectroscopy

FeDES – iron(III)-desferoxamine complex

FSA – formamidine sulfinic acid

HEPES – 4-(2-hydroxyethyl)-1-piperazineethanesulfonic acid

HFE – human hemochromatosis protein

HoSF – horse spleen ferritin

IC – ion chromatography

ICP-OES – inductively coupled plasma optical emission spectroscopy

ISE – ion selective electrodes

JCPDS – Joint Committee on Powder Diffraction Standards

(k)Da – (kilo)Dalton

MES – 2-(N-morpholino)ethanesulfonic acid

MOPS – 3-(N-morpholino)propanesulfonic acid

NMR – nuclear magnetic resonance

NTA – nitrilotriacetic acid

NTBI – non-transferrin bound iron

PDB – protein database

PIPES – piperazine-N,N'-bis(2-ethanesulfonic acid)

rHuHF – recombinant human heavy chain ferritin

rHuLF – recombinant human light chain ferritin

RMSD – root mean square deviation

ROS – reactive oxygen species

SPD – surface photo deposition

SPR – surface plasmon resonance

(S)TEM – (scanning) transmission electron microscopy

TES – 2-[[1,3-dihydroxy-2-(hydroxymethyl)propan-2-yl]amino]ethanesulfonic acid

Tris – tris(hydroxymethyl)aminomethane

TSAT – transferrin saturation

XRD – X-ray powder diffraction

CHAPTER 1: INTRODUCTION TO FERRITIN

Iron is the most abundant element in the earth as a whole. It is the fourth most abundant element in the earth's crust, and the second most abundant metal, after aluminum. Iron is most commonly found in the +2 and +3 oxidation states (ferrous and ferric, respectively). Living organisms take advantage of iron not only because of its abundance, but also because of the useful redox chemistry that is characteristic of iron. The ability of iron to cycle from the ferric to the ferrous oxidation state makes iron a key element for a number of necessary processes within the cell. Unfortunately, this same useful property makes iron a toxic substance to cells through the generation of reactive oxygen species (ROS), which damage proteins, lipids, and DNA. In addition, ferrous iron is not easily obtained from our oxygen abundant environment because ferrous iron is reactive to oxygen, forming the highly inaccessible and insoluble ferric iron. Thus, organisms evolved to develop sophisticated methods of acquiring iron. In addition to evolving methods of iron acquisition, organisms have also established complex systems of iron transport and storage in order to protect against ROS. The main player in the storage of iron is the protein ferritin.

Ferritin was first described in 1937 by Victor Laufberger,[1] and since that time thousands of publications concerning both the structure and function of ferritin have been published. Although much is known concerning ferritin, certain aspects of ferritin remain uncertain. For example, the structure of ferritin is well established, and this has yielded important information concerning the uptake and storage of iron. On the other hand, the mechanism of iron release, the role ferritin plays in diseased states, and the extent of applications using ferritin in materials chemistry have only recently been investigated, and many questions are still left to be answered.

The general biological function of ferritin is iron storage and release during times of iron abundance or scarcity, respectively. Because protein function relies heavily on structure, a discussion on the structure of ferritin will be presented.

Ferritin is an approximate 20 kDa polypeptide of 182 amino acids. Twenty-four subunits come together to form a hollow, octahedral sphere or nanocage of 450 kDa. Theoretically, 4,500 iron atoms are capable of being stored within this nanocage (volume = 2.68×10^{-22} L), although in biology, this number is generally closer to 2,000 iron atoms per ferritin. Iron loading into ferritin occurs when iron is oxidized from ferrous to ferric iron in the presence of oxygen.

Single Ferritin Subunit Structure

A single ferritin polypeptide chain folds into an all α-helical domain comprised of five α-helices (Figure 1–1). Four helices, helices A, B, C, and D, arrange to form a four-helix bundle, with up-down-down-up topology. The loop connecting helix B with helix C (loop BC) back tracks the entire length of the protein, giving the down-down orientation of helices B and C. Helices A, B, and C are made up of 28 amino acids each and form 43 Å long α-helices. Helix D is comprised of 32 amino acids and is 52 Å in length. The fifth helix, helix E, caps one end of the four-helix bundle. It is made of 10 amino acids and is 16 Å in length. The four-helix bundle motif provides considerable stability to the ferritin subunit. Similar to other four-helix bundle motifs, most of the core of the bundle is composed of hydrophobic residues (~70% hydrophobic). A strong ionic interaction from Arg77 of helix B to Asp127 of helix D also provides stability and possible gated action.[2] The short helix E is stabilized next to helix B and D due to the ionic interaction of Asn51 of helix B interacting with Asp172 of helix E. Loop BC is stabilized next to the four-helix bundle due largely to a disulfide bond between Cys90 on loop BC and Cys102 on helix C.
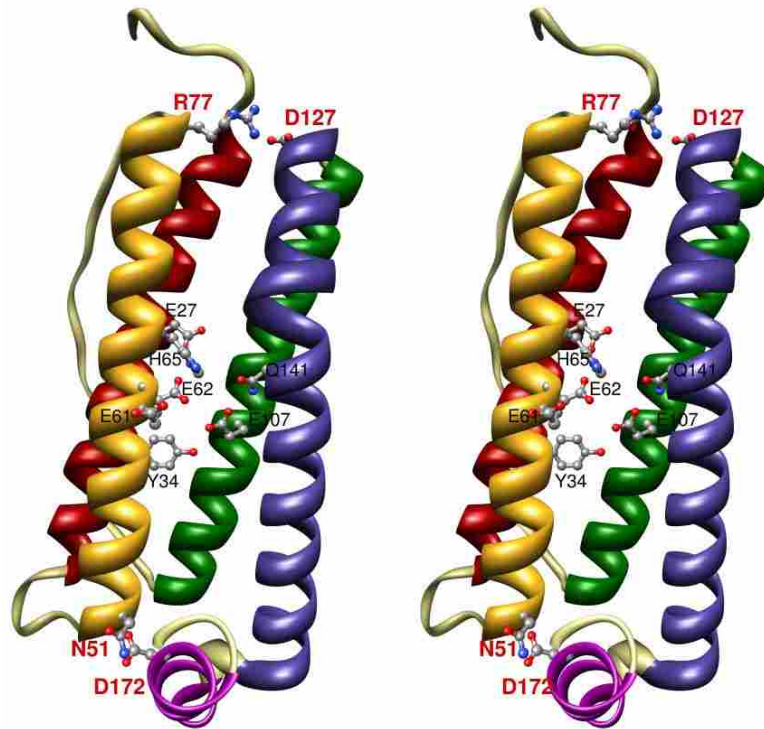
Figure 1-1. Stereo diagram of human heavy ferritin subunit. The single subunit (PDB code 2FHA[3]) folds into a four-helix bundle, with a fifth, smaller helix packed on one end. Helix A is **red**, Helix B is **gold**, Helix C is **green**, Helix D is **blue**, and Helix E is **magenta**. Loops connecting the helices are in tan. The four helix bundle is brought together by a strong hydrophobic core. An ionic lock consisting of negatively charged D127 from Helix D and positively charged R77 from Helix B to further stabilize the bundle, shown here in ball and stick form (labeled in red). A similar interaction takes place between N51 and D172 to stabilize Helix E next to the bundle, also shown (labeled in red). The residues that make up the ferroxidase center (labeled black) are also shown here in ball and stick form. These residues bind and oxidize iron for iron deposition into ferritin. This is an inside looking out perspective of ferritin. Molecular graphics images were produced using the UCSF Chimera package from the Resource for Biocomputing, Visualization, and Informatics at the University of California, San Francisco (supported by NIH P41 RR-01081).[4]

Nanocage Structure

When 24 subunits come together, an octahedral protein shell is formed. The quaternary structure of ferritin is referred to as a nanocage, and is a spectacular display of nature's

symmetry. This nanocage is 12 nm in exterior diameter with an 8-nm interior diameter. The interface of four subunits forms a 4-fold axis, for a total of three 4-fold axes throughout the nanocage (Figure 1–2A). The 4-fold axis forms a channel that is ~2 Å in diameter and is packed with hydrophobic residues. Two residues (Leu165 and Ile169) from each of the four subunits contribute to this hydrophobic channel, for a total of eight hydrophobic residues. The nanocage also has four 3-fold axes. The 3-fold axis is formed at the interface of three subunits (Figure 1–2B). This interface forms an approximate 4 Å channel that is lined with six negatively charged amino acids. Each subunit contributes both Asp131 and Glu134 to the channel, creating a negatively charged environment. Finally, ferritin also has six 2-fold axes at the interface of two subunits. This interface is lined with helices A and B, as well as the BC loop. This dimer interaction is lined with hydrophobic residues and contains salt bridges, providing a large area of inter-subunit stability. Overall, the nanocage is extremely stable, and remains intact up to 70 ºC and over pH extremes of 3–10.[5-7] At pH less than 3, the 24 subunits will dissociate, but reversibly reassemble at pH greater than 3. A pH less than 2 will cause irreversible denaturation of the single subunits. The robust nature of ferritin ensures its function in a variety of organisms living in diverse environments.
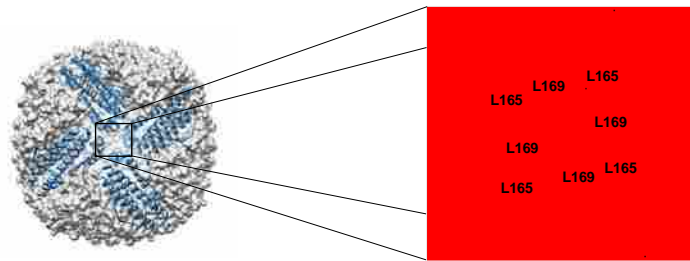
A. Hydrophobic Four-fold Axis
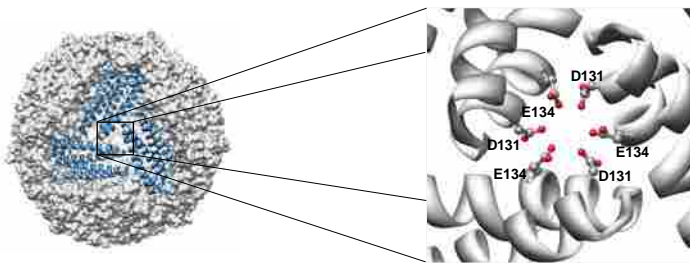
B. Negatively charged Three-fold Axis
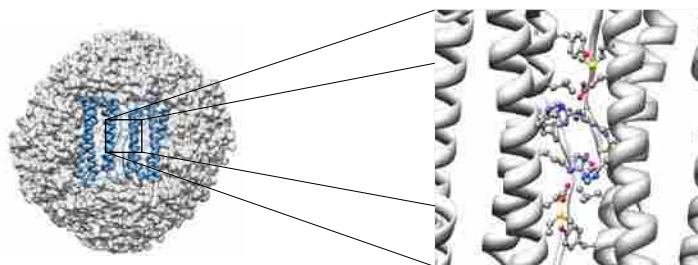
C. Two-fold Axis

Figure 1-2. Packing interactions between subunits of ferritin quaternary structure (PDB code 2FHA[3]). Ferritin has three 4-fold axes (A), four 3-fold axes (B), and six 2-fold axes (C) of symmetry. An expanded view of each image is shown on the right, with important residues displayed. The 4-fold axis is characterized by hydrophobic residues. The 3-fold axis is characterized by negatively charged residues. The 2-fold axis contains no distinct character in residue composition. Figure adapted from Bou-Abdallah et al.[8] Molecular graphics images were produced using the UCSF Chimera package from the Resource for Biocomputing, Visualization, and Informatics at the University of California, San Francisco (supported by NIH P41 RR-01081).[4]

The Role of H and L Chain Ferritin

Two isoforms of ferritin are common among vertebrates; the heavy chain (H ferritin) and the light chain (L ferritin). The genes for the H and L ferritin proteins for humans are encoded on separate chromosomes[9] (11 and 19, respectively) and consist of 182 and 174 amino acids, respectively.[10, 11] H and L ferritins share 55% amino acid sequence identity and are structurally homologous (RMSD = 0.461 Å),[12] but despite their similarity, they have distinct roles.[13] H chain ferritin contains a ferroxidase center (Figure 1–1), a group of amino acids that is capable of rapidly oxidizing ferrous iron to ferric iron. The ferroxidase center is made up of residues Glu27, Glu61, Glu62, His65, and Glu107. Several studies have investigated the role that these residues play, and mutation of these residues leads to a loss of ferroxidase activity by the H chain ferritin.[14-16]

L chain ferritin lacks the ferroxidase residues but does contain residues that act as nucleation sites for iron binding upon iron entry into ferritin. Specifically, Glu53, Glu56, and Glu57 have been shown to be the nucleation sites within L chain ferritin.[17] Thus, whereas the H ferritin is important for iron incorporation and oxidation, the L chain is important for iron mineralization. The proper mineralization allows for greater iron incorporation over longer periods of time. This notion is further supported by the observation that in various tissue types, the ratio of H ferritin to L ferritin varies.[11, 18, 19] For example, heart and brain ferritin is composed of 90% H and 10% L ferritin, presumably because of the need to quickly oxidize and incorporate any free iron into ferritin.[20] On the other hand, liver and spleen ferritin is predominantly L chain, presumably for the long-term storage of iron (Figure 1–3).
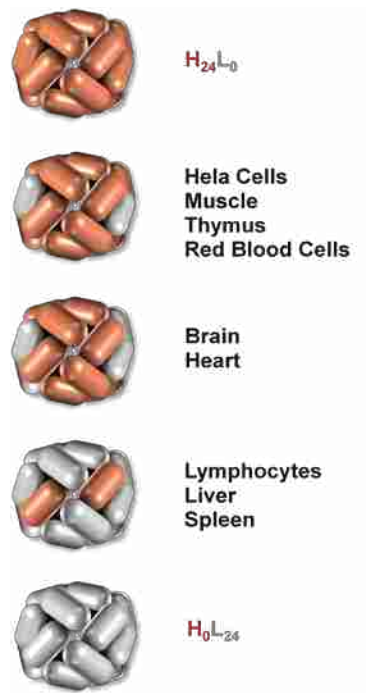
Figure 1-3. The ratio of H to L chain ferritin varies across tissue types**.** The varied ratios of ferritin isoforms confers slightly varied abilities with each type. The predominantly H chain ferritins, such as heart or brain, are able to quickly oxidize and store ferritin in these types of high iron metabolism tissue types. In the liver and spleen, the long term storage of iron is the main focus, and so ferritin is made up predominantly of the L chain isoform.

Work in our laboratory where we expressed and purified recombinant human heavy or recombinant human light chain ferritin also supports the roles that these isoforms have. Homopolymers of H chain ferritin quickly oxidize and incorporate iron into the core (Figure 1–4). However, only about 500 iron atoms accumulate into ferritin before the protein begins to precipitate. This likely is due to the formation of a quickly formed, disorganized iron core, which in turn limits the amount of iron that effectively incorporates into H ferritin. On the other hand, homopolymers of L chain ferritin slowly incorporate iron into the core (at the same rate of iron oxidation in buffer). However, L chain ferritin is capable of storing over 2,000 irons per ferritin in an ordered iron core. Heteropolymers of H and L chain ferritin are able to both quickly incorporate iron and store larger amounts of iron.
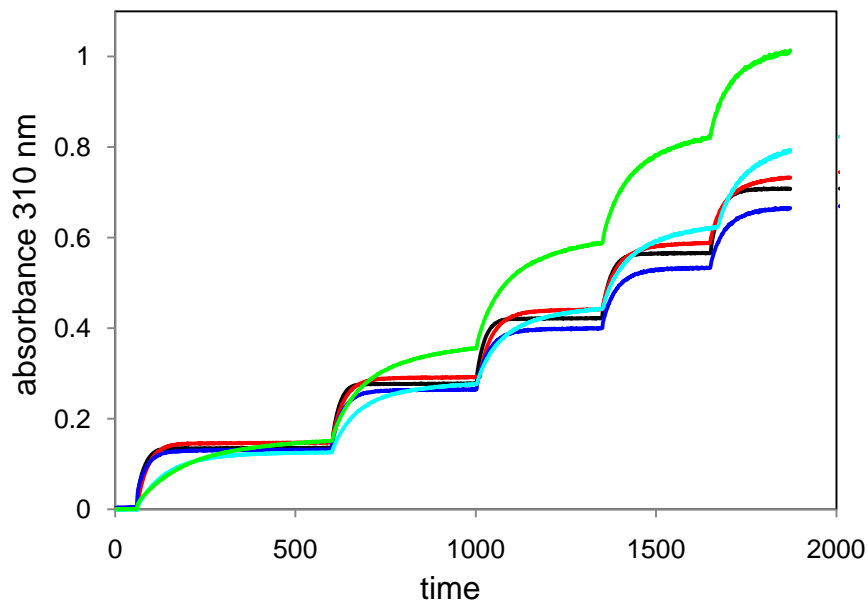
Figure 1-4. Kinetic loading of iron into H or L chain homo- and heteropolymers of ferritin. A loading of 100 irons/ferritin was performed five times and monitored spectrophotometrically at 310 nm using an Agilent 8453 diode array spectrophotometer. The curves are as follows; the **black** is all H, the **red** curve is 90% H, the **blue** curve is 50% H, the **cyan** curve is 10% H, and the **green** curve is all L. The final absorbance is higher for L chain homopolymer, indicating that the greatest amount of iron is incorporated into this sample.

Mechanism of Ferritin Function

By understanding the structure of ferritin, a significant amount of information concerning the function of ferritin has been derived. For example, several possible routes of iron entry exist in the ferritin protein. The ionic diameter of iron is 1.64 Å, so any possible routes of entry would need to accommodate this size. The six 4-fold channels, although of appropriate diameter (~2Å), are hydrophobic, and so are not amenable to iron entry. On the other hand, the eight 3-fold channels are prime candidates because they are lined with six negatively charged aspartate and glutamate residues, which can act as a funnel for positively charged iron ions to flow into ferritin (Figure 1–2B). Furthermore, the channel size of ~4 Å would easily accommodate an ion the size of iron. It is now generally accepted that iron enters ferritin at these 3-fold channels.[8, 21-25]

Once iron enters ferritin, it must be oxidized from the ferrous form to the ferric form. In order to accomplish this feat, H chain ferritin contains a ferroxidase center. The ferroxidase center is located in the middle of the four helix bundle, and is made up of negatively charged residues, as described previously. These negatively charged residues are thought to coordinate iron upon entry, thus allowing nearby residues to quickly oxidize Fe(II) to Fe(III). It is this oxidation process that allows iron to mineralize within ferritin in a non-toxic form. The mineral that forms is a nano-phase ferrihydrite mineral.

As important as iron uptake and storage is, it is equally important for the organism to be able to reclaim iron from these storage sites during times of iron scarcity. Despite the clues for iron entry, there exist no clear structural clues as to how iron is released. In vitro, iron is released in a two-step process. First, the Fe(III) is reduced with a reducing agent, often sodium hydrosulfite. Next, the iron is chelated with a strong Fe(II) chelator, often 2,2'-bipyridine. Because these are not physiological species, a different mechanism for in vivo retrieval of iron must exist. Several studies have shown that ferritin is directed to the lysosome for degradation.[26, 27] The degradation of ferritin results in a release of iron, which is then subsequently taken up for other uses. Other researchers suggest that physiologically relevant small molecules are capable of chelating iron from ferritin in order for the cell to obtain necessary iron.[28-30] Likely, both of these processes are taking place.

The first portion of this dissertation will address these mechanistic questions. In Chapter 2, the study of iron core formation will be addressed. Specifically, we investigate the mineral core formation of ferritin and show that it can be controlled, depending on environmental factors. Chapter 3 discusses progress we have made in our laboratory to understand the release of iron from ferritin. We investigate the non-reductive release of iron from ferritin, and show that iron

can be retrieved from ferritin without destroying the protein itself. The release of iron also tends to depend greatly upon the environmental conditions.

Disease

An interesting observation in our mechanistic studies showed that when we load iron into ferritin in the presence of phosphate, we observe an accelerated oxidation of iron. Initially, we also thought that this meant an increased deposition of iron into ferritin. However, following the appropriate purification and analysis, we determined that much of the iron was not actually going into ferritin. This led us to investigate circumstances where phosphate concentrations would be increased in vivo. Thus, our mechanistic studies led to studies of ferritin involvement in disease.

The role of ferritin in disease has only recently been considered due to several recent discoveries that link iron dysregulation to each of several diseases.[31] For example, patients with Alzheimer's disease,[32, 33] Parkinson's disease,[34] diabetes,[35] age-related macular degeneration,[36-40] chronic kidney disease,[41-43] heart disease,[44] and many others[45-47] all have a disruption in iron metabolism and can be linked to ferritin. This is perhaps not too surprising because of the central role iron plays in cellular metabolism for organisms. Indeed, any deviation from normal iron regulation, no matter to which extreme, leads to serious problems for the organism. Thus, cellular iron metabolism is tightly regulated. Several key proteins play a role in the regulation of iron. In Figure 1–5, pathway A diagrams how iron is incorporated into the cell. Transferrin binds up to two ferric iron atoms and then holotransferrin binds to the transferrin receptor. Holotransferrin and its receptor are endocytosed together and the iron is released in the endosome. Pathway B diagrams the uptake of iron by ferritin and iron release from the cell. Holoferritin releases its iron by one of several possibilities (as discussed above), and iron is exported through ferroportin, where ceruloplasmin or hephaestin oxidizes the iron for transferrin

uptake. Pathway C highlights how iron release through ferroportin is blocked by hepcidin. The mode of action for hepcidin inhibition is for hepcidin to bind to ferroportin causing its endocytosis and degradation. Pathway D shows how iron intake is blocked by HFE. Together, this brief picture of cellular iron metabolism underscores the complexity of iron regulation within the cell. Variations in these processes lead to diseased states.
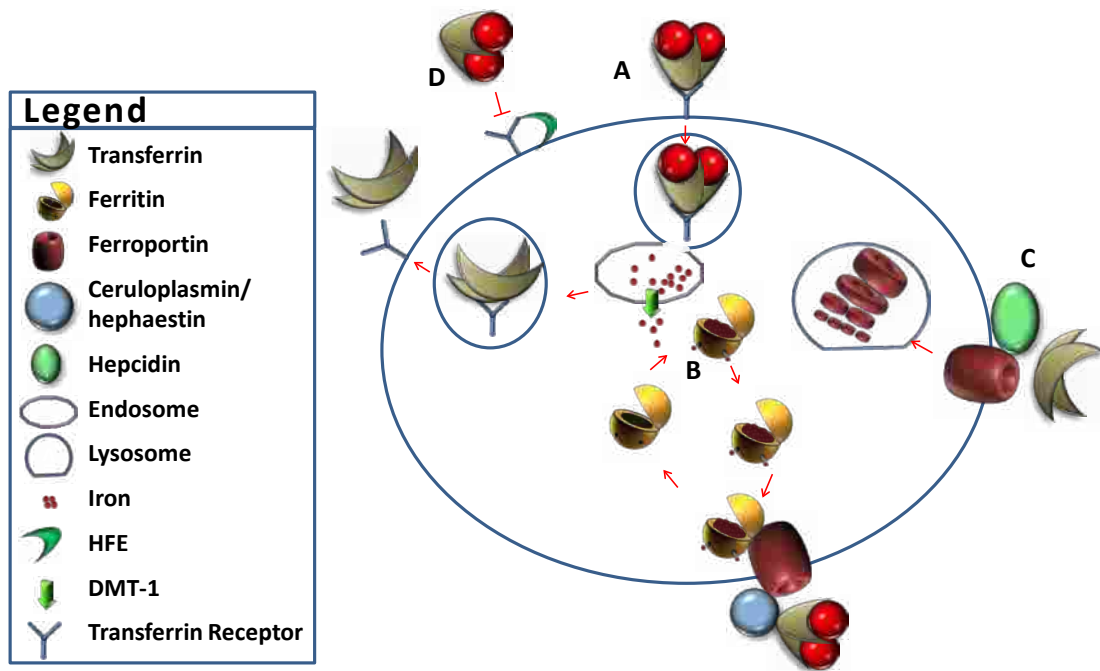
Figure 1-5. Pathway of iron transport in the cell**.** (A) Pathway for iron entry. Holotransferrin binds to transferrin receptor. This complex is endocytosed into the cell in clathrin coated pits. The transferrin with its receptor binds to an endosome, where the low pH allows for iron release. Apo-transferrin and receptor are then exported back to the cell membrane. (B) Pathway for iron storage and release. Iron is reduced in the endosome by ferric reductase and sent to the cytosol by DMT-1. Ferritin sequesters iron during iron excess. During iron deficiency, ferritin releases its iron to ferroportin. Ferroportin transfers iron to transferrin, mediated by ceruloplasmin. (C) During inflammation, hepcidin binds to ferroportin causing its endocytosis and degradation within the lysosome, thus limiting iron export. (D) HFE regulates the amount of transferrin that is endocytosed.

11

Understanding the fundamental principles of iron loading into ferritin, how ferritin interacts with other proteins, and how small molecules that are present in vivo affect ferritin function can lead to useful and interesting data concerning the role ferritin plays in a number of diseases. Chapters 4 and 5 of this work highlight the discovery that phosphate competes with ferritin for iron. Phosphate binds iron and forms an insoluble iron-phosphate complex. These data and the results discussed in these chapters provide some answers about the symptoms that patients with chronic kidney disease are experiencing. Additional work in our lab shows that other small molecules may be involved in altering the ability of ferritin to function properly. Although these studies will not be discussed in great detail in this work, the principle that small molecules can change ferritin function is noteworthy.

Ferritin in Materials Chemistry

Ferritin has recently garnered significant attention for its use in materials chemistry. Ferritin is useful in this application because it is a biological nanocage — a spherical protein with a hollow interior that can act as a template for material growth. The added benefit is that Nature perfected this nanocage, and with some slight modifications, scientists can tune the protein for specific uses. Applications include, but are not limited to, nanoparticle synthesis,[48-50] biomedical imaging,[51] drug delivery,[52] and as a foundation for carbon nanotube growth.[53, 54]

Chapters 6, 7, and 8 delve into the important discoveries of materials synthesis that have been made in this lab. Ferritin is a dynamic tool for making novel materials because it is a nanocage that has an interior environment separated from the exterior. This is helpful in the synthesis of nanoparticles that would otherwise be difficult to form. In Chapter 6, we show that we are able to incorporate anions into ferritin in a controlled and reversible manner. The incorporation of anions using the method described in Chapter 6 is efficient for a large number of

anions that we tried. Our synthetic method is general enough that it can be applied to a wide range of anions for a variety of applications.

In Chapters 7 and 8, we show the ability of ferritin as a photocatalyst for directing gold nanoparticle synthesis. This system can be used for a variety of metals and applications, and these will be discussed in greater detail in these chapters.

Conclusion

Over many decades, meticulous study of ferritin has slowly yielded information both structurally and functionally. The structure of ferritin is clear. It consists of 24 subunits arranged in an octahedral sphere, with a volume capable of holding 4,500 iron atoms. Iron entry into ferritin was recently shown to take place through a two-step process, where iron first enters the 3-fold channels.[8] Next, iron traverses the 4-helix bundle to the ferroxidase center. Upon binding at the ferroxidase center, ferrous iron is oxidized to ferric iron, and deposited into the interior of ferritin. How ions other than iron traverse ferritin is not yet certain, but has been made more clear with the results of the research contained in this work. Ferritin, it appears, may not be the rock-solid, static protein that many scientists imagined it to be. Indeed, this work shows that ferritin is a dynamic and active protein. An overall evaluation and summary of this work is presented in Chapter 9.

References

1.   Laufberger, V. Sur la Cristallisation de la Ferritine. *Bull Soc Chim Biol* **1937,** *19*, 1575–1582.

2.   Liu, X.; Jin, W.; Theil, E. C. Opening Protein Pores with Chaotropes Enhances Fe Reduction and Chelation of Fe from the Ferritin Biomineral. *PNAS* **2003,** *100* (7), 3653–3658.

3.   Hempstead, P. D.; Yewdall, S. J.; Fernie, A. R.; Lawson, D. M.; Artymiuk, P. J.; Rice, D. W.; Ford, G. C.; Harrison, P. M. Comparison of the Three-Dimensional Structures of Recombinant Human H and Horse L Ferritins at High Resolution. *J Mol Biol* **1997,** *268* (2), 424–448.

4.   Pettersen, E. F.; Goddard, T. D.; Huang, C. C.; Couch, G. S.; Greenblatt, D. M.; Meng, E. C.; Ferrin, T. E. UCSF Chimera - A Visualization System for Exploratory Research and Analysis. *J Comput Chem* **2004,** *25* (13), 1605–1612.

5.   Santambrogio, P.; Levi, S.; Arosio, P.; Palagi, L.; Vecchio, G.; Lawson, D. M.; Yewdall, S. J.; Artymiuk, P. J.; Harrison, P. M.; Jappelli, R.; Cesareni, G. Evidence that a Salt Bridge in the Light Chain Contributes to the Physical Stability Difference Between Heavy and Light Human Ferritins. *J Biol Chem* **1992,** *267* (20), 14077–14083.

6.   Santambrogio, P.; Levi, S.; Cozzi, A.; Rovida, E.; Albertini, A.; Arosio, P. Production and Characterization of Recombinant Heteropolymers of Human Ferritin H and L Chains. *J Biol Chem* **1993,** *268* (17), 12744–12748.

7.   Kim, M.; Rho, Y.; Jin, K. S.; Ahn, B.; ; Kim, H.; Ree, M. pH-Dependent Structures of Ferritin and Apoferritin in Solution: Disassembly and Reassembly. *Biomacromolecules* **2011,** *12*, 1629–1640.

8.   Bou-Abdallah, F.; Zhao, G.; Biasiotto, G.; Poli, M.; Arosio, P.; Chasteen, N. Facilitated Diffusion of Iron(II) and Dioxygen Substrates into Human H-Chain Ferritin. A Fluorescence and Absorbance Study Employing the Ferroxidase Center Substitution Y34W. *JACS* **2008,** *130*, 17801–17811.

9.   Caskey, J. H.; Jones, C.; Miller, Y. E.; Seligman, P. A. Human Ferritin Gene is Assigned to Chromosome 19. *PNAS* **1983,** *80* (2), 482–486.

10.   Andrews, S.; Harrison, P.; Yewdall, S.; Arosio, P.; Levi, S.; Bottke, W.; Briat, J.; Laulhère, J.; Lobreaux, S. Structure, Function, and Evolution of Ferritins. *J Inorg Biochem* **1992,** *47*, 161–174.

11.   Dedman, D. J.; Treffry, A.; Candy, J. M.; Taylor, G. A.; Morris, C. M.; Bloxham, C. A.; Perry, R. H.; Edwardson, J.; Harrison, P. Iron and Aluminium in Relation to Brain Ferritin in Normal Individuals and Alzheimer's-Disease and Chronic Renal-Dialysis Patients. *Biochem J* **1992,** *287*, 509–514.

12.   Watt, R. K.; Hilton, R. J.; Graff, D. M. Oxido-Reduction is not the Only Mechanism Allowing Ions to Traverse the Ferritin Protein Shell. *BBA* **2010,** *1800* (8), 745–759.

13.   Arosio, P.; Levi, S. Ferritin, Iron Homeostasis, and Oxidative Damage. *Free Rad Biol Med* **2002,** *33*, 457–463.

14.   Wade, V. J.; Levi, S.; Arosio, P.; Treffry, A.; Harrison, P. M.; Mann, S. Influence of Site-Directed Modifications on the Formation of Iron Cores in Ferritin. *J Mol Biol* **1991,** *221* (4), 1443–1452.

15.   Levi, S.; Corsi, B.; Rovida, E.; Cozzi, A.; Santambrogio, P.; Albertini, A.; Arosio, P. Construction of a Ferroxidase Center in Human Ferritin L-Chain. *J Biol Chem* **1994,** *269*, 30334–30339.

16.   Levi, S.; Santambrogio, P.; Albertini, A.; Arosio, P. Human Ferritin H-Chains can be Obtained in Nonassembled Stable Forms Which Have Ferroxidase Activity. *Febs Letters* **1993,** *336* (2), 309–312.

17.   Crichton, R. R.; Herbas, A.; Chavez-Alba, O.; Roland, F. Identification of Catalytic Residues Involved in Iron Uptake by L-Chain Ferritins. *J Biol Inorg Chem* **1996,** *1* (6), 567–574.

18.   Wagstaff, M.; Worwood, M.; Jacobs, A. Properties of Human Tissue Isoferritins. *Biochem J* **1978,** *173* (3), 969–977.

19.   Connor, J. R.; Boeshore, K. L.; Benkovic, S. A.; Menzies, S. L. Isoforms of Ferritin have a Specific Cellular Distribution in the Brain. *J Neurosci Res* **1994,** *37* (4), 461–465.

20.   Zhao, G.; Su, M.; Chasteen, N. D. [mu]-1,2-Peroxo Diferric Complex Formation in Horse Spleen Ferritin. A Mixed H/L-Subunit Heteropolymer. *J Mol Biol* **2005,** *352* (2), 467–477.

21.   Bou-Abdallah, F. The Iron Redox and Hydrolysis Chemistry of the Ferritins. *BBA* **2010,** *1800*, 719–731.

22.   Theil, E. C.; Takagi, H.; Small, G. W.; He, L.; Tipton, A. R.; Danger, D. The Ferritin Iron Entry and Exit Problem. *Inorgan Chim Acta* **2000,** *297* (1–2), 242–251.

23.   Bou-Abdallah, F.; Arosio, P.; Levi, S.; Janus-Chandler, C.; Chasteen, N. D. Defining Metal Ion Inhibitor Interactions with Recombinant Human H- and L-Chain Ferritins and Site-Directed Variants: An Isothermal Titration Calorimetry Study. *J Biol Inorg Chem* **2003,** *8* (4), 489–497.

24.   Bauminger, E. R.; Harrison, P. M. Ferritin, the Path of Iron into the Core, as Seen by Mossbauer Spectroscopy. *Hyperfine Interact* **2003,** *151* (1), 3–19.

25.   Treffry, A.; Bauminger, E. R.; Hechel, D.; Hodson, N. W.; Nowik, I.; Yewdall, S. J.; Harrison, P. M. Defining the Roles of the Threefold Channels in Iron Uptake, Iron Oxidation and Iron-Core Formation in Ferritin - A Study Aided by Site-Directed Mutagenesis. *Biochem J* **1993,** *296*, 721–728.

26.   Radisky, D. C.; Kaplan, J. Iron in Cytosolic Ferritin can be Recycled Through Lysosomal Degradation in Human Fibroblasts. *Biochem J* **1998,** *336*, 201–205.

27.   Kidane, T. Z.; Sauble, E.; Linder, M. C. Release of Iron from Ferritin Requires Lysosomal Activity. *Am J Physiol* **2006,** *291* (3), C445–C455.

28.   Cassanelli, S.; Moulis, J.-M. Sulfide is an Efficient Iron Releasing Agent for Mammalian Ferritins. *BBA* **2001,** *1547* (1), 174–182.

29.   Liu, X. S.; Patterson, L. D.; Miller, M. J.; Theil, E. C. Peptides Selected for the Protein Nanocage Pores Change the Rate of Iron Recovery from the Ferritin Mineral. *J Biol Chem* **2007,** *282*, 31821–31825.

30.   De Domenico, I.; Ward, D. M.; Kaplan, J. Specific Iron Chelators Determine the Route of Ferritin Degradation. *Blood* **2009,** *114* (20), 4546–4551.

31.   Watt, R. K. The Many Faces of the Octahedral Ferritin Protein. *Biometals* **2011,** *24* (3), 489–500.

32.   Lavados, M.; Guillon, M.; Mujica, M. C.; Rojo, L. E.; Fuentes, P.; Maccioni, R. B. Mild Cognitive Impairment and Alzheimer Patients Display Different Levels of Redox-Active CSF Iron. *J Alzheimers Dis* **2008,** *13* (2), 225–232.

33.   Gerlach, M.; Ben-Shachar, D.; Riederer, P.; Youdim, M. B. Altered Brain Metabolism of Iron as a Cause of Neurodegenerative Diseases? *J Neurochem* **1994,** *63* (3), 793–807.

34.   Kaur, D.; Rajagopalan, S.; Andersen, J. K. Chronic Expression of H-Ferritin in Dopaminergic Midbrain Neurons Results in an Age-Related Expansion of the Labile Iron Pool and Subsequent Neurodegeneration: Implications for Parkinson's Disease. *Brain Res* **2009,** *1297*, 17–22.

35.   Jehn, M. L.; Guallar, E.; Clark, J. M.; Couper, D.; Duncan, B. B.; Ballantyne, C. M.; Hoogeveen, R. C.; Harris, Z. L.; Pankow, J. S. A Prospective Study of Plasma Ferritin Level and Incident Diabetes: The Atherosclerosis Risk in Communities (ARIC) Study. *Am J Epidemiol* **2007,** *165* (9), 1047–1054.

36.   Loh, A.; Hadziahmetovic, M.; Dunaief, J. L. Iron Homeostasis and Eye Disease. *BBA* **2009,** *1790* (7), 637–649.

37.   Goralska, M.; Ferrell, J.; Harned, J.; Lall, M.; Nagar, S.; Fleisher, L. N.; McGahan, M. C. Iron Metabolism in the Eye: A Review. *Exp Eye Res* **2009,** *88* (2), 204–215.

38. Deleon, E.; Lederman, M.; Berenstein, E.; Meir, T.; Chevion, M.; Chowers, I. Alteration in Iron Metabolism During Retinal Degeneration in rd10 Mouse. *Invest Ophthal Vis Sci* **2009,** *50*, 1360–1365.

39. Wong, R. W.; Richa, D. C.; Hahn, P.; Green, W. R.; Dunaief, J. L. Iron Toxicity as a Potential Factor in AMD. *Retina* **2007,** *27* (8), 997–1003.

40. Dunaief, J. L. Iron Induced Oxidative Damage as a Potential Factor in Age-Related Macular Degeneration: The Cogan Lecture. *Invest Ophthalmol Vis Sci* **2006,** *47* (11), 4660–4664.

41. Zarjou, A.; Jeney, V.; Arosio, P.; Poli, M.; Antal-Szalmas, P.; Agarwal, A.; Balla, G.; Balla, J. Ferritin Prevents Calcification and Osteoblastic Differentiation of Vascular Smooth Muscle Cells. *J Am Soc Nephrol* **2009,** *20* (6), 1254–1263.

42. Kalantar-Zadeh, K.; Lee, G. H. The Fascinating but Deceptive Ferritin: To Measure it or not to Measure it in Chronic Kidney Disease? *Clin J Am Soc Nephrol* **2006,** *1 Suppl 1*, S9–18.

43. Nakanishi, T.; Kuragano, T.; Nanami, M.; Otaki, Y.; Nonoguchi, H.; Hasuike, Y. Importance of Ferritin for Optimizing Anemia Therapy in Chronic Kidney Disease. *Am J Nephrol* **2010,** *32*, 439–446.

44. Cantor, E. J.; Mancini, E. V.; Seth, R.; Yao, X. H.; Netticadan, T. Oxidative Stress and Heart Disease: Cardiac Dysfunction, Nutrition, and Gene Therapy. *Curr Hypertens Rep* **2003,** *5* (3), 215–220.

45. Bennett, T. D.; Hayward, K. N.; Farris, R. W.; Ringold, S.; Wallace, C. A.; Brogan, T. V. Very High Serum Ferritin Levels are Associated with Increased Mortality and Critical Care in Pediatric Patients. *Pediatr Crit Care Med* **2011,** *in press*.

46. Yonal, O.; Akyuz, F.; Demir, K.; Ciftci, S.; Keskin, F.; Pinarbasi, B.; Uyanikoglu, A.; Issever, H.; Ozdil, S.; Boztas, G.; Besisik, F.; Kaymakoglu, S.; Cakaloglu, Y.; Mungan, Z.; Okten, A. Decreased Prohepcidin Levels in Patients with HBV-Related Liver Disease: Relation with Ferritin Levels. *Dig Dis Sci* **2010,** *55* (12), 3548–3551.

47. Alsultan, A. I.; Seif, M. A.; Amin, T. T.; Naboli, M.; Alsuliman, A. M. Relationship Between Oxidative Stress, Ferritin and Insulin Resistance in Sickle Cell Disease. *Eur Rev Med Pharmacol Sci* **2010,** *14* (6), 527–538.

48.   Kasyutich, O.; Ilari, A.; Fiorillo, A.; Tatchev, D.; Hoell, A.; Ceci, P. Silver Ion Incorporation and Nanoparticle Formation inside the Cavity of Pyrococcus furiosus Ferritin: Structural and Size-Distribution Analyses. *JACS* **2010,** *132* (10), 3621–3627.

49.   Ensign, D.; Young, M.; Douglas, T. Photocatalytic Synthesis of Copper Colloids from Cu(II) by the Ferrihydrite Core of Ferritin. *Inorg Chem* **2004,** *43* (11), 3441–3446.

50.   Butts, C. A.; Swift, J.; Kang, S. G.; Di Costanzo, L.; Christianson, D. W.; Saven, J. G.; Dmochowski, I. J. Directing Noble Metal Ion Chemistry within a Designed Ferritin Protein. *Biochemistry* **2008,** *47* (48), 12729–12739.

51.   Valero, E.; Tambalo, S.; Marzola, P.; Ortega-Munoz, M.; Lopez-Jaramillo, F. J.; Santoyo-Gonzalez, F.; Lopez, J. D.; Delgado, J. J.; Calvino, J. J.; Cuesta, R.; Dominguez-Vera, J. M.; Galvez, N. Magnetic Nanoparticles-Templated Assembly of Protein Subunits: A New Platform for Carbohydrate-Based MRI Nanoprobes. *JACS* **2011,** *133* (13), 4889–4895.

52.   Ma-Ham, A. H.; Wu, H.; Wang, J.; Kang, X. H.; Zhang, Y. Y.; Lin, Y. H. Apoferritin-Based Nanomedicine Platform for Drug Delivery: Equilibrium Binding Study of Daunomycin with DNA. *J Mater Chem* **2011,** *21* (24), 8700–8708.

53.   Bhaviripudi, S.; Mile, E.; Steiner, S. A.; Zare, A. T.; Belcher, A. M.; Kong, J. CVD Synthesis of Single-Walled Carbon Nanotubes from Gold Nanoparticle Catalysts. *JACS* **2007,** *129*, 1516–1517.

54.   Park, J.; Yoon, J.; Kang, S. J.; Kim, G. T.; Ha, J. S. High Yield Production of Semiconducting p-type Single-Walled Carbon Nanotube Thin-Film Transistors on a Flexible Polyimide Substrate by Tuning the Density of Ferritin Catalysts. *Carbon* **2011,** *49* (7), 2492–2498.

CHAPTER 2: CRYSTALLINE FERRIHYDRITE FORMATION IN FERRITIN

Abstract

The buffer used during horse spleen ferritin iron loading significantly influences the mineralization process and the quantity of iron deposited in ferritin. Ferritin iron loading in imidazole ($C_3H_4N_2$) buffer shows a rapid hyperbolic curve in contrast to iron loading in 3-(N-morpholino)propanesulfonic acid (MOPS) buffer, which displays a slower sigmoidal curve. Ferritin iron loading in an equimolar mixture of imidazole and MOPS produces an iron-loading curve that is intermediate between the imidazole and MOPS curves, indicating that one buffer did not dominate the reaction mechanism. The UV-Visible spectrum of the ferritin mineral has a higher absorbance from 250–450 nm when prepared in imidazole than when prepared in MOPS. These results suggest that different mineral phases form in ferritin by different loading mechanisms in imidazole and MOPS buffered reactions. Samples of 1,500 Fe/ferritin were prepared in MOPS or imidazole buffer and were analyzed for crystallinity using the electron diffraction capabilities of the electron microscope. The iron cores formed in imidazole showed significantly more crystallinity than those prepared in MOPS. X-ray powder diffraction studies showed that small cores (~500 Fe/ferritin) prepared in MOPS or imidazole possess a 2-line ferrihydrite spectrum. As the core size increases, the mineral phase begins to change from 2-line to 6-line ferrihydrite, with the imidazole sample favoring the 6-line ferrihydrite phase. Taken together, these data suggest that the iron deposition mechanism in ferritin can be controlled by properties of the buffer, with samples prepared in imidazole forming a more crystalline mineral than samples prepared in MOPS.

Introduction

Ferritin is composed of 24 subunits that self-assemble into a spherical protein cage with an outer diameter of 12 nm and an interior cavity diameter of 8 nm.[1] Molecules enter and leave ferritin through channels of 4 Å in diameter, eight of which are hydrophilic and six of which are hydrophobic. The iron atoms form a ferric oxyhydroxide core in the center of the ferritin cavity that most resembles ferrihydrite.[2-4] The solid iron core can be removed through chemical reduction followed by chelation and dialysis.[5, 6]

Ferritin can theoretically sequester 4,500 iron atoms, but in nature the average is closer to 2,000. It has been proposed that oxidative damage to apoferritin results in the termination of core formation and presents a serious problem when trying to maximize the number of iron atoms loaded into the protein.[1, 7] In the natural process of core formation, Fe^{2+} is oxidized at the ferroxidase center or oxidized on the mineral core surface where it crystallizes in the central cavity.[8] If the Fe^{2+} is oxidized at other protein sites, hydroxyl radicals are produced through the well-known Fenton chemistry ($Fe^{2+} + H_2O_2 \rightarrow Fe^{3+} + OH\cdot + OH^-$). The production of these radicals damages the ferritin protein and inhibits iron core formation.[9] An alternative hypothesis for the much lower iron loading in vitro may simply be based on solubility arguments. At physiological pH, Fe^{2+} and Fe^{3+} interact with hydroxide ions and precipitate.

Previous studies showed that buffers could greatly affect iron uptake in ferritin during in vitro iron loading.[10, 11] Salt concentrations can also influence the rate of iron loading into ferritin. Studies by Cutler et al. concluded that in general, cations slow the rate of iron loading into ferritin by competing with Fe^{2+} for negatively charged amino acids near the 3-fold channels.[12] On the other hand, some anions, such as halides and sulfate, had no effect. However, other anions, such as phosphate and its tetrahedral oxoanion analogs have been shown to stimulate the

rate of iron loading into ferritin and produce a different mineral phase with the oxoanions incorporated into the mineral.[7, 13-15]

Iron loading into ferritin has been studied extensively, and the mechanism of iron entry is well characterized.[16-18] In addition, the mineralization and characterization of the ferrihydrite core of ferritin is also well characterized.[4, 19, 20] Nevertheless, we recently observed that various forms of ferrihydrite are capable of forming inside ferritin depending on the environmental conditions. This chapter examines the effects of buffers on iron loading in ferritin with the goal of maximizing the amount of iron that can be loaded into ferritin. We reasoned that maximal iron loading into ferritin might be enhanced by using buffers that stabilized Fe^{2+} in solution by slowing oxidation, minimizing the formation of radicals that might damage ferritin, and minimizing side reactions that lead to precipitation of $Fe(OH)_3$ (s) outside ferritin. Ferritin iron-loading reactions were performed in imidazole ($C_3H_4N_2$) buffer, which coordinates Fe^{2+} and its oxidation product Fe^{3+}. These reactions were compared to iron loading reactions performed in 3-(N-morpholino)propanesulfonic acid (MOPS) buffer, a Good's buffer that is commonly used for iron loading reactions with ferritin. MOPS buffer coordinates to Fe^{2+} poorly, if at all. We observed that the iron loading kinetics were very different in imidazole than in MOPS. This suggests that imidazole loads ferritin by a different mechanism than MOPS. This different iron loading mechanism that we observed when using imidazole allows iron loading to a greater extent under the conditions used in this work and produces a mineral phase with different mineral properties than the core formed using MOPS buffer.

Materials and Methods

Materials. All aqueous solutions in this study were made using Milli-Q water having a resistance of 18 MΩ. Chemical reagents were obtained commercially and used without further purification. Horse spleen ferritin (HoSF) was acquired from Sigma-Aldrich in a 0.15 M NaCl solution. Thioglycolic acid was also purchased from Sigma-Aldrich as a 98% solution, and MOPS buffer was purchased from Fisher Bioreagents with purity greater than 97%. All other reagents had a purity of at least 97%.

Preparation of apoferritin. Native HoSF obtained from Sigma-Aldrich was treated according to established methods to make apoferritin.[21] As obtained, HoSF in saline solution was dialyzed for 24 hours against 1% thioglycolic acid and 0.25 M sodium acetate ($NaC_2H_3O_2$) at 4 °C. This process was repeated with an addition of 100 mg/L of 2,2'-bipyridyl, which chelates Fe^{2+} forming the red $[Fe(2,2'\text{-bipyridyl})_3]^{2+}$ complex. The HoSF was then dialyzed twice with 5 g/L sodium bicarbonate ($NaHCO_3$) at 4 °C. The apoferritin solution was then dialyzed several times with H_2O at 4 °C to remove ionic species from the solution. Dialysis with H_2O was terminated when Na, S, C, Cl, and Fe ions could not be detected in the water outside the dialysis tubing. The Na was analyzed by atomic absorption spectroscopy (AA), whereas S, C, and Fe were analyzed using inductively coupled plasma optical emission spectroscopy (ICP-OES), and the Cl was quantified using ion chromatography (IC).

Kinetics of iron core formation in MOPS and imidazole buffers. Kinetic studies of iron loading in ferritin were carried out on an Agilent 8453 UV-Visible spectrophotometer. Imidazole and MOPS solutions (0.05 M) were prepared and the pH was adjusted to 7.5 by the addition of NaOH for MOPS and HNO_3 for imidazole. A 0.010 M Fe^{2+} solution was prepared by dissolving

Fe(NH$_4$)$_2$(SO$_4$)$_2$·6H$_2$O in a 1 x 10^{-3} M HCl solution. Iron loading reactions were carried out in a cuvette by adding apoferritin (0.3 μM) and a Teflon stir bar into 2.0 mL of the indicated buffer. The spectrophotometer was zeroed on the buffer prior to the addition of ferritin. The reaction was initiated by the addition of 25 μL of 0.010 M Fe^{2+} (~400 Fe^{2+}/ferritin) and the absorbance at 310 nm was measured over time to monitor ferritin iron mineralization. The beginning of each time trace shows a lag phase, which is the background absorbance prior to the addition of Fe^{2+}. The absorbance measurements were continued until the reaction reached a plateau, and in some instances multiple additions of Fe^{2+} were added to the same solution.

Transmission electron microscopy (TEM). Samples were prepared by adding 1.0 mL apoferritin (5.4 mg/mL) into 10 mL 0.050 M MOPS, 0.1 M NaCl pH 7.5 or 0.050 M imidazole buffer, 0.1 M NaCl pH 7.5. The samples were stirred in air and 0.60 mL of 0.010 M Fe(NH$_4$)$_2$(SO$_4$)$_2$·6H$_2$O was added to deliver 500 Fe/ferritin. The sample was stirred for 30 minutes in air to allow the Fe^{2+} to oxidize. Two additional aliquots of Fe^{2+} were added following the identical procedure to reach an iron core of 1,500 iron atoms/ferritin. The samples were centrifuged to remove any unbound iron or precipitated protein and an iron and protein analysis was performed to confirm the samples contained 1,500 Fe/ferritin. The samples were deposited on charged grids (lacey carbon fiber, 400 mesh copper grids, Ted Pella, Inc.). Following 30 to 60 seconds on the grid, the solution was wicked off of the grid, and the grid was rinsed in water to remove salts or buffers. The grid was then dried. The grids were analyzed using a FEI Tecnai F30 TEM (FEI Company, the Netherlands), operating at 140 keV.

Preparation and characterization of reconstituted ferritin mineral cores in imidazole and MOPS. Ferritin was reconstituted in the presence of imidazole or MOPS buffer by adding apoferritin to the imidazole or MOPS buffer followed by slowly titrating with a 0.010 M Fe^{2+}

solution at room temperature under constant stirring. Various imidazole and MOPS concentrations were tested and reactions were performed in the presence and absence of various concentrations of NaCl. Some samples were loaded with iron by slowly adding Fe^{2+} from a peristaltic pump that delivered a very dilute Fe^{2+} concentration at a very slow delivery speed. The pH of the solutions was monitored and maintained at 7.5 by the addition of NaOH (aq). As the titration progressed, the solution turned to a dark brownish-red. When the solution began to appear cloudy, the addition of iron was stopped and the sample was centrifuged to remove any solid material. The ferritin solution was then transferred to a dialysis bag and dialyzed at 4 $^\circ$C with repeated changes of water to remove all salts and impurities. The water removed from each round of dialysis was analyzed for S, Na, C, and Cl ions. Once the levels of these species were below detection limits (using the methods described above), the dialysis was stopped. Samples used for X-ray powder diffraction (XRD) were lyophilized. The crystallinity of the ferritin cores were characterized by XRD using a Scintag Diffractometer (Cu-Kα radiation, $\lambda = 1.54176$ nm) at a scanning rate of 0.1 2$\theta$$^.$min^{-1} and a power of 15 kW over the range 5 to 80°. The XRD data for the ferritin samples were smoothed using a boxcar calculation of 25 points on either side of a given point. Although the signal intensity is slightly decreased as a result of the smoothing, the noise in the spectrum is dramatically reduced and the XRD reflections are much more evident.

Results

        Kinetic traces of iron loading in the presence of MOPS and imidazole. Because iron mineralization in ferritin corresponds with a strong absorbance at 310 nm, the absorbance change at this wavelength versus time was measured.[11] The reactions were performed in both MOPS and imidazole to compare the iron loading kinetics for each buffer (Figure 2–1). The MOPS reaction is characterized by a sigmoidal shape, which was described previously as the result of two different iron-loading reactions.[22] The first reaction occurs when no iron is present in ferritin and Fe^{2+} is oxidized at the ferritin ferroxidase center. As a core begins to form inside ferritin, Fe^{2+} is oxidized on the surface of the growing mineral. As the surface area of the core increases, the rate of iron oxidation increases, and the sigmoidal shape is a result of these two reactions. In contrast, the curve for the imidazole reaction is hyperbolic. This behavior suggests that the mechanism of iron loading in imidazole is different than the MOPS reaction, although the mechanism has yet to be characterized. The final absorbance of the imidazole sample was higher than that of the MOPS sample, also suggesting that the mineral phase of iron formed in ferritin when using imidazole is different than that formed when using MOPS because it has a higher extinction coefficient.
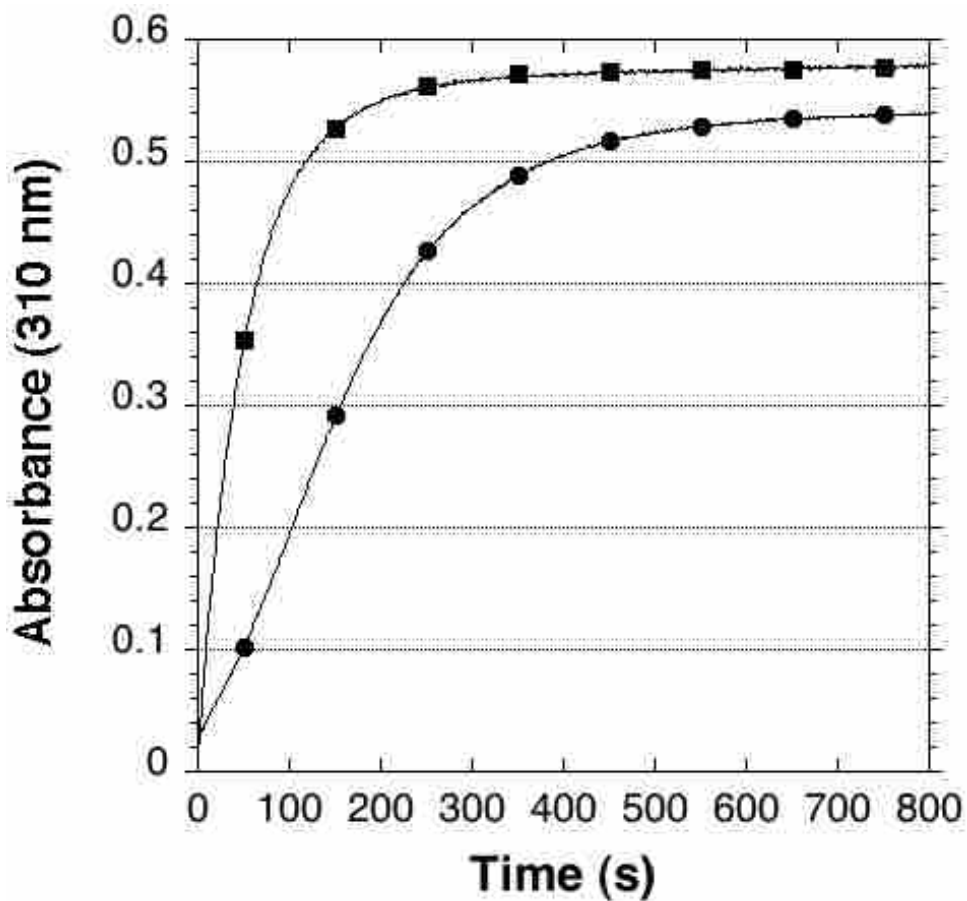
Figure 2-1. Kinetics of iron loading into ferritin in MOPS (●) or imidazole buffer (■). The absorbance at 310 nm versus time was monitored to follow iron core formation. The reaction was initiated by adding 50 μL of 0.010 M Fe^{2+} to 0.3 μM apoferritin for a ratio of 800 Fe/ferritin. Each buffer was 0.050 M at pH 7.5. The reaction was continuously stirred with a magnetic stirrer.

The effects of combining buffers. The observation that ferritin in imidazole appeared to load iron by a different mechanism than ferritin in MOPS led us to test an equal mixture of the two buffers to determine if one of them was dominant in controlling the reaction mechanism and the resulting iron mineral that formed. Figure 2–2 shows kinetic traces of iron loading in ferritin for solutions of 0.050 M MOPS, 0.050 M imidazole, or an equal mixture of 0.025 M MOPS and 0.025 M imidazole. The equimolar mixture of MOPS and imidazole produces an iron-loading curve that is intermediate between that of the individual buffers. As additional iron is added, the

26

curves begin to approach the same kinetic rates, suggesting that oxidation of iron on the core surface begins to be the dominant mechanism for iron deposition into ferritin.
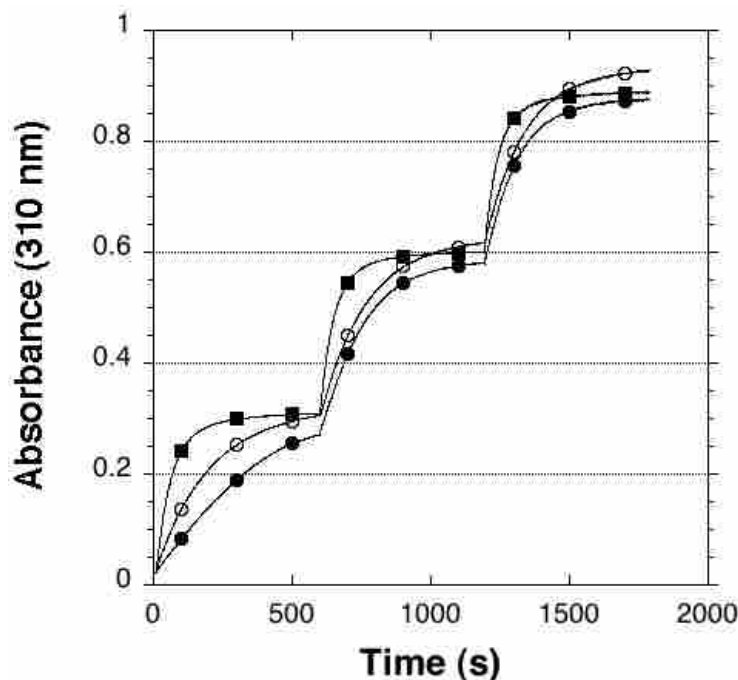
Figure 2-2. Comparison of iron loading kinetics in MOPS, imidazole, and an equimolar mixture of MOPS/imidazole. Kinetic traces of Fe^{2+} (25 μL 0.010 M Fe^{2+}) added to ferritin (0.3 μM). The different reactions are done in: (■) 0.050 M imidazole buffer pH 7.5, (●) 0.050 M MOPS buffer pH 7.5, and (○) 0.025 M MOPS/0.025 M imidazole mixture pH 7.5. 400 Fe^{2+} were added in each addition for 1,200 Fe/ferritin at the end of the reaction. The sizes of the symbols were chosen to represent the maximum error bars between duplicate samples prepared for each run.

One explanation for the higher final absorbance of the imidazole sample after the first addition of iron (Figure 2–1) is that a different mineral phase forms with a higher extinction coefficient than the mineral formed using MOPS. Figure 2–3 shows spectra of ferritin samples of identical protein concentration (1.0 μM) that were treated with identical concentrations of iron (200 μM) and stirred in air for 30 minutes. No obvious distinguishing features are apparent in either of the curves except for the small peak at 280 nm attributed to the protein absorbance, yet

a comparison of the two curves shows that the imidazole sample has a more intense absorbance from 250–450 nm and therefore has different properties in the mineral core.
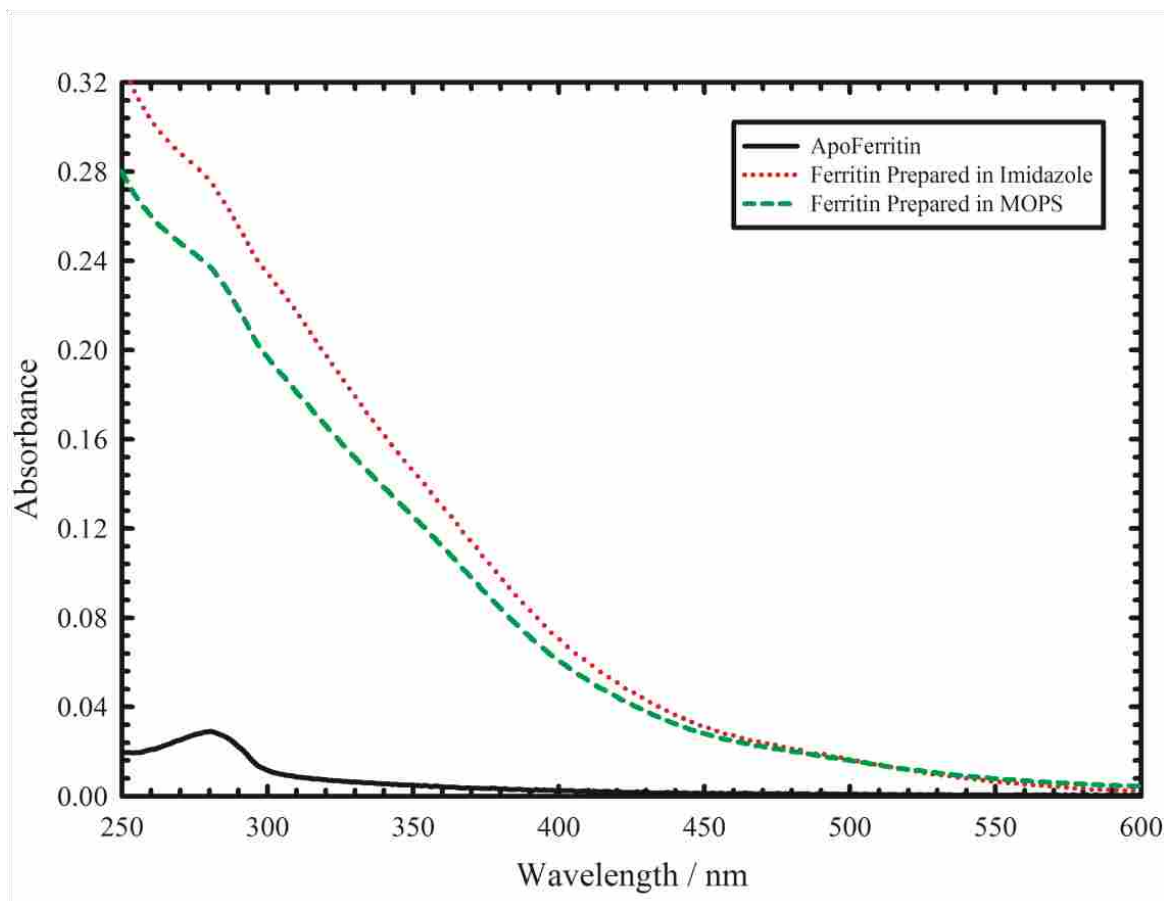
Figure 2-3. Spectra of ferritin samples prepared in MOPS or imidazole buffer. Curves are: (**black**) apoferritin, (**red**) 200 Fe/ferritin loaded in 0.050 M imidazole buffer, pH 7.5, and (**green**) 200 Fe/ferritin loaded in 0.050 M MOPS buffer, pH 7.5.

The difference in absorbance intensities between the imidazole and MOPS samples is due to the iron distribution within ferritin. A diffuse organization of iron atoms lining the protein exhibits a different extinction coefficient than iron atoms clustered in an ordered mineral phase.[23, 24] In contrast to the disperse ions lining the protein interior, other studies have shown that the iron mineral core forms in discrete clusters initiated from the nucleation sites on the

interior of ferritin. The crystallinity and number of these individual sites may influence the absorbance maxima of the mineral formed inside ferritin.[20, 25]

Because no precipitation was observed during iron loading in our studies, it is assumed that all of the iron is bound to ferritin in both reactions. The different buffers may influence the distribution of iron between the mineral core, the ferroxidase center, the channels, and the outside surface of ferritin. Thus, the higher absorbance that is observed in the imidazole buffer may be from strong iron oxygen interactions associated with an organized and ordered iron mineral core. On the other hand, the lower absorbance observed in the MOPS sample may correspond to iron bound to the surface, the channels, the ferroxidase centers, and the pathway to the nucleation site, with a smaller, less organized mineral phase. We used additional analyses to determine whether the imidazole prepared samples were more crystalline than the MOPS prepared samples.

Iron loading of ferritin. A variety of methods were used to maximize loading of iron into ferritin in order to obtain high signals for crystallinity analyses. Ferritin samples were prepared by either trying to completely pack the ferritin interior (iron additions ceased when the sample became cloudy due to iron or protein precipitation) or by a targeted loading, where iron was added to reach a targeted goal such as 2,000 or 3,000 Fe/ferritin, even if the solution became cloudy. Iron was added in doses such as 500 Fe/ferritin, 200 Fe/ferritin, or 100 Fe/ferritin and iron was allowed to accumulate inside ferritin before the next addition of the same amount of iron was given to the sample (generally 20 minutes between additions of iron). Another approach was to load iron slowly by adding Fe^{2+} from a peristaltic pump that delivered dilute Fe^{2+} at a very slow delivery speed. The pH of all the solutions was monitored and maintained at 7.5 by the addition of NaOH (aq).

Qualitatively, higher buffer concentrations improved ferritin iron loadings by maintaining a constant pH. The presence of NaCl favored core growth in both buffers. The addition of iron after the solution appeared cloudy caused further protein precipitation and did not lead to improved iron loading into ferritin. We observed that the lower doses of iron/ferritin were more favorable for reaching higher iron loadings of ferritin, presumably because excess iron initiated more radicals that caused damage to the ferritin protein. The peristaltic pump method, allowing a very slow exposure of Fe^{2+} to ferritin, produced the samples with the highest loaded mineral cores.

Structural characterization of the iron core. To test the hypothesis that MOPS and imidazole form minerals with different properties, the ferritin cores were studied using transmission electron microscopy (TEM). Ferritin samples containing 1,500 Fe/ferritin were prepared in either MOPS or imidazole buffer and placed on EM grids. Iron analysis and protein analysis demonstrated that each sample contained 1,500 Fe/ferritin and that the samples contained the same amount of protein. The results of the TEM analysis are shown in Figure 2–4. The ferritin samples appear similar in size and density and are dispersed on the EM grid in similar densities. However, the crystallinity of the two samples was very different when studied by electron diffraction. The MOPS sample (Figure 2–4C) diffracted poorly, suggesting an amorphous mineral composition. In contrast, the imidazole sample (Figure 2–4D) had a strong diffraction pattern, indicative of a crystalline mineral phase.
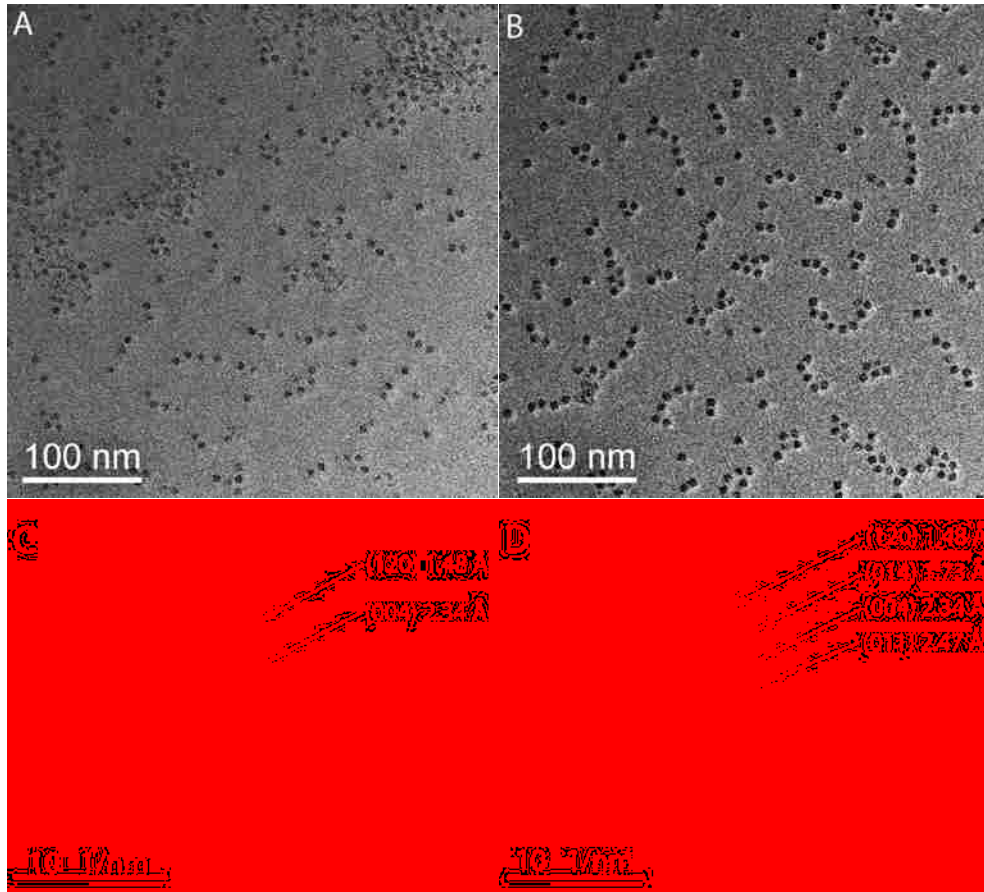
Figure 2-4. Electron micrographs of ferritin samples prepared in MOPS or imidazole buffers. Ferritin samples were prepared with 1,500 Fe/ferritin in A) MOPS or B) imidazole and analyzed by EM to visualize the ferritin particles. The grids were not stained in order to obtain clear diffraction patterns of the iron cores. Iron minerals of approximately 8 nm diameters were observed in both samples. The distribution of ferritin was similar on both grids. Using the electron diffraction capabilities of the TEM, the samples were analyzed for crystallinity. Both samples showed electron diffraction and crystallinity but the sample prepared in C) MOPS showed less electron diffraction compared to the sample prepared in D) imidazole, which had a more crystalline mineral phase within the ferritin protein. The d-spacings of the rings are shown for each sample and these data correspond to d-spacings for ferrihydrite. The numbers in parentheses show the planes of the lattice fringes. The grids were analyzed using a FEI Tecnai F30 TEM (FEI Company, the Netherlands), operating at 140 keV.

The TEM studies also revealed that the crystallinity of the iron core increased over time (data not shown). If the samples that were prepared in either the MOPS or imidazole buffers were allowed to incubate for a period of many days, and then placed on an electron microscope grid, the electron diffraction patterns of these samples showed much higher patterns of crystallinity, suggesting that as the iron core ages, the core becomes more ordered and crystalline. Thus, in order to distinguish between the immediate effects of the buffers on iron loading and core formation inside ferritin, the samples needed to be prepared fresh and analyzed immediately. For a more comprehensive study of the aging effect of the iron core, please refer to Chapter 3 of this work.

Ferrihydrite is the mineral generally reported to form in ferritin. To further characterize these ferritin samples, the ferritin was lyophilized and analyzed by XRD to determine whether the crystalline mineral phase that formed in imidazole buffer was a mineral other than ferrihydrite. An XRD spectrum in the range 5 to 80° for a lyophilized sample of apoferritin (control sample) is shown in Figure 2–5. Two reflections are observed at 2θ values of 9.72°, and 19.80°. After the second peak, the spectrum decays with no other features.
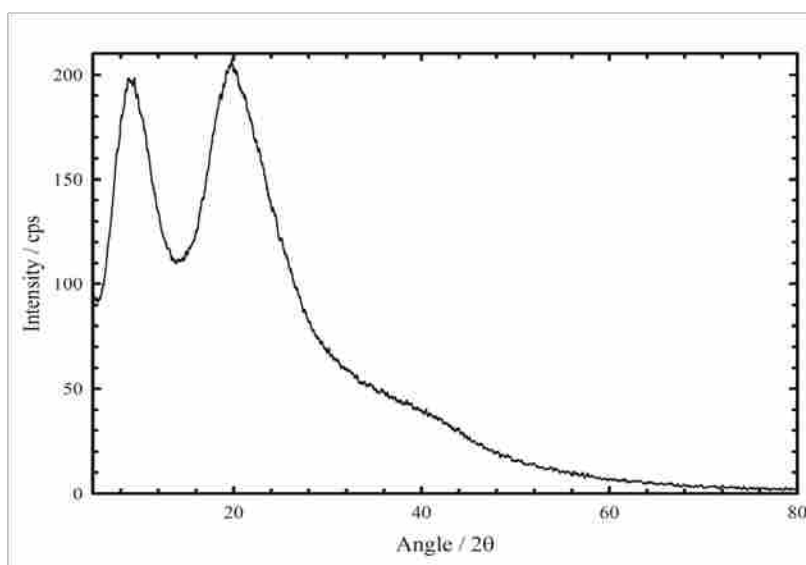
Figure 2-5. XRD spectrum of lyophilized apoferritin powder.

Ferrihydrite is known to exist as the 2-line polymorph in small particles and shift to the 6-line structure as the particle grows and becomes more ordered.[26] To determine if a similar process occurred in ferritin, samples were prepared with a target of 500 Fe/ferritin to compare the XRD spectra of ferritin of low iron contents. Figure 2–6 shows the XRD patterns for a ferritin sample prepared with 500 Fe/ferritin in imidazole and MOPS buffers. These patterns are almost identical and mainly resemble the pattern for apoferritin. However, focusing on the region where the 2-line ferrihydrite sample is observed, a reflection at 63˚ for 2-line ferrihydrite is visible and a shoulder around 35˚ is observed. This indicates that low iron loading into ferritin in both MOPS and imidazole produces a 2-line ferrihydrite mineral phase.
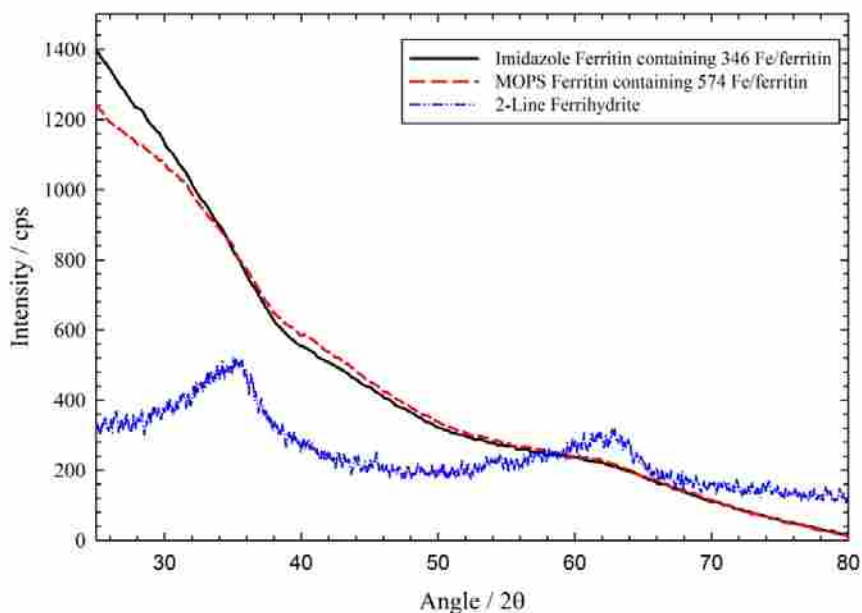
Figure 2-6. XRD spectra of 500 Fe/ferritin samples reconstituted in MOPS or imidazole. Imidazole is shown in **black** and MOPS is shown in **red**. A control of 2-line ferrihydrite (**blue**) is shown with peaks at 35° and 63°. In both the MOPS and imidazole samples, an absorption peak is observed at 63° and a shoulder is observed at 35°.

Figure 2–7 shows the XRD spectrum from two samples, one loaded in MOPS (~2,000 Fe/ferritin) and one loaded in imidazole (~3,300 Fe/ferritin). These samples represent the

33

maximum iron loading that we could achieve using these respective buffers. Figure 2–7 also shows the reference peaks for the reflections of 6-line ferrihydrite found in JCPDS card 00-029-0712 and the spectrum for a 2-line ferrihydrite standard.[27] The MOPS sample shows an overall lower intensity and a character that mostly corresponds to 2-line ferrihydrite. There is a small indication of reflections at 46° and 53° that suggests that cores of this size have some 6-line character. These reflections are seen with much more intensity in the spectrum of the imidazole sample that has a much larger core. As indicated by the arrows in this figure, there are two prominent features, which are not observed in the spectrum of the MOPS sample. First is an additional peak at 41˚, and the second is the bifurcation of the peak centered at 62˚. Both of these features indicate a greater 6-line character than that observed in the spectrum of the MOPS sample.
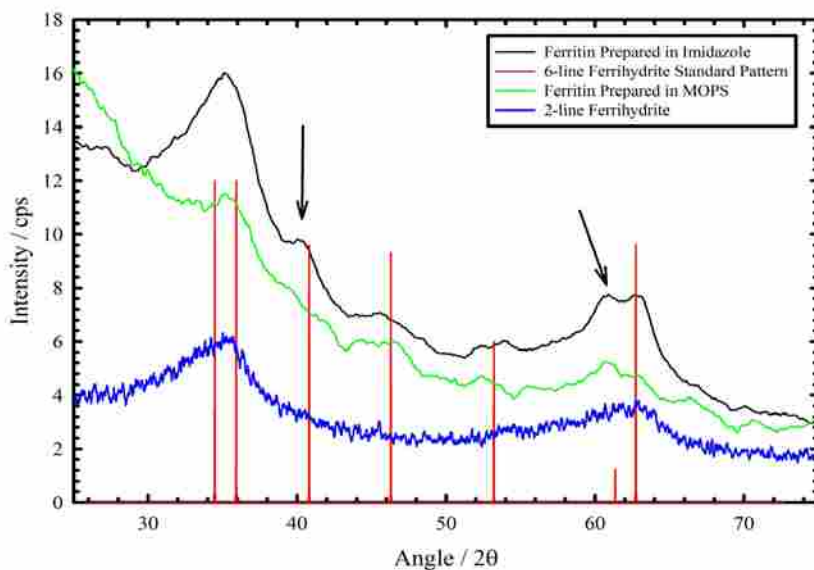
Figure 2-7. XRD spectrum of maximally loaded ferritin samples reconstituted in MOPS and imidazole. The **red** lines represent the standard pattern for 6-line ferrihydrite. The **blue** trace represents a 2-line ferrihydrite standard. The **green** line represents ferritin loaded in MOPS with ~2,000 Fe/ferritin. The **black** line represents ferritin loaded in imidazole (3,300 Fe/ferritin). The data suggest that as the iron cores of ferritin become larger, there is a transition from 2-line ferrihydrite to 6-line ferrihydrite.

The evidence provided in this figure suggests that while both buffers direct the formation of ferrihydrite, the higher iron loading allowed by imidazole allows imidazole ferritin to form larger particles that are capable of producing the 6-line ferrihydrite product inside ferritin. The fact that imidazole produces a more crystalline core (Figure 2–4) may also contribute to the 6-line spectrum because 6-line ferrihydrite is more ordered than 2-line ferrihydrite. At present, it is unclear if the more ordered core observed in the imidazole samples leads to the production of the 6-line ferrihydrite mineral or if the increased core size is simply large enough to cross the threshold that transitions the mineral from 2-line to 6-line ferrihydrite. The reason that MOPS cannot achieve the higher iron content achieved by imidazole is also puzzling. Does imidazole influence the stability of ferritin by preventing the formation of radicals and favor more extensive iron loading, or does the more ordered mineral allow more efficient iron mineralization inside ferritin? This work is ongoing in our laboratory in order to explore these possibilities.

Discussion

The results of this study indicate that the efficiency of iron core formation inside ferritin varies depending on which molecules are in the environment. Imidazole is a molecule that is able to bind iron to a higher degree than MOPS. Although both buffer types are able to maintain a physiological pH during iron loading, imidazole may be a more effective buffer because it is able to bind iron, thus assisting ferritin in the uptake of iron. In addition to allowing greater iron uptake, imidazole also tends to favor a more ordered and crystalline formation of iron inside ferritin. Thus, the mechanism of iron uptake is directly influenced by the environment surrounding ferritin. Ongoing studies in our laboratory are designed to determine the interaction between ferritin and imidazole and between imidazole and iron so that the mechanism of iron loading can be directly determined.

In the body, ferritin is most effective when it can quickly and efficiently incorporate and store iron, thus mitigating the harmful effects of reactive oxygen species (ROS). There may be physiologically relevant molecules or peptides that are able to act in a manner similar to imidazole by cooperating with ferritin for enhanced iron oxidation and uptake. Future studies can be designed to load iron into ferritin in the presence of these physiologically relevant molecules and peptides to determine their efficacy in this role. Continued efforts in this area will contribute to the growing understanding of the mechanism of iron loading into ferritin.

This work was published in part in the Journal of Inorganic Biochemistry.[28]

References

1.   Arosio, P.; Ingrassia, R.; Cavadini, P. Ferritins: A Family of Molecules for Iron Storage, Antioxidation and More. *BBA* **2009,** *1790* (7), 589–599.

2.   Allen, M.; Douglas, T.; Nest, D.; Schoonen, M.; Strongin, D. Charge Development on Ferritin: An Electrokinetic Study of a Protein Containing a Ferrihydrite Nanoparticle. *ACS Symposium Series* **2005,** *890*, 226–229.

3.   Gorham, N. T.; Pierre, T. G. S.; Chua-Anusorn, W.; Parkinson, G. M. Magnetic Energy-Barrier Distributions for Ferrihydrite Nanoparticles Formed by Reconstituting Ferritin. *J Appl Phys* **2008,** *103* (5), 1–5.

4.   Kim, S.-W.; Seo, H.-Y.; Lee, Y.-B.; Park, Y. S.; Kim, K.-S. Crystal Structure of Ferrihydrite Nanoparticles Synthesized in Ferritin. *Bull Korean Chem Soc* **2008,** *29* (10), 1969–1972.

5.   Joo, M. S.; Tourillon, G.; Sayers, D. E.; Theil, E. C. Rapid Reduction of Iron in Horse Spleen Ferritin by Thioglycolic Acid Measured by Dispersive X-ray Absorption Spectroscopy. *Biol Met* **1990,** *3* (3-4), 171–175.

6.   Granick, S.; Michaelis, L. Ferritin and Apoferritin. *Science* **1942,** *95* (2469), 439–440.

7.   Orino, K.; Kamura, S.; Natsuhori, M.; Yamamoto, S.; Watanabe, K. Two Pathways of Iron Uptake in Bovine Spleen Apoferritin Dependent on Iron Concentration. *Biometals* **2002,** *15* (1), 59–63.

8.   Xu, B.; Chasteen, N. D. Iron Oxidation Chemistry in Ferritin. Increasing Iron/Oxygen Stoichiometry During Core Formation. *J Biol Chem* **1991,** *266* (30), 19965–19970.

9.   Linder, M. C.; Kakavandi, H. R.; Miller, P.; Wirth, P. L.; Nagel, G. M. Dissociation of Ferritins. *Arch Biochem Biophys* **1989,** *269* (2), 485–496.

10.   Yang, X.; Chasteen, N. D. Ferroxidase Activity of Ferritin: Effects of pH, Buffer and Fe(II) and Fe(III) Concentrations on Fe(II) Autoxidation and Ferrooxidation. *Biochem J* **1999,** *338* (3), 615–618.

11.   Paques, E. P.; Paques, A.; Crichton, R. R. A Study of the Mechanism of Ferritin Formation. The Effect of pH, Ionic Strength and Temperature, Inhibition by Imidazole and Kinetic Analysis. *Eur J Biochem* **1980,** *107* (2), 447–453.

12.   Cutler, C.; Bravo, A.; Ray, A. D.; Watt, R. K. Iron Loading into Ferritin can be Stimulated or Inhibited by the Presence of Cations and Anions: A Specific Role for Phosphate. *J Inorg Biochem* **2005,** *99* (12), 2270–2275.

13.   Cheng, Y. G.; Chasteen, N. D. Role of Phosphate in Initial Iron Deposition in Apoferritin. *Biochemistry* **1991,** *30* (11), 2947–2953.

14.   Aitken-Rogers, H.; Singleton, C.; Lewin, A.; Taylor-Gee, A.; Moore, G. R.; Le Brun, N. E. Effect of Phosphate on Bacterioferritin-Catalysed Iron(II) Oxidation. *J Biol Inorg Chem* **2004,** *9* (2), 161–170.

15.   Polanams, J.; Ray, A. D.; Watt, R. K. Nanophase Iron Phosphate, Iron Arsenate, Iron Vanadate, and Iron Molybdate Minerals Synthesized Within the Protein Cage of Ferritin. *Inorg Chem* **2005,** *44* (9), 3203–3209.

16.   Bou-Abdallah, F.; Zhao, G. R.; Biasiotto, G.; Poli, M.; Arosio, P.; Chasteen, N. D. Facilitated Diffusion of Iron(II) and Dioxygen Substrates into Human H-Chain Ferritin. A Fluorescence and Absorbance Study Employing the Ferroxidase Center Substitution Y34W. *JACS* **2008,** *130* (52), 17801–17811.

17.   Levi, S.; Corsi, B.; Rovida, E.; Cozzi, A.; Santambrogio, P.; Albertini, A.; Arosio, P. Construction of a Ferroxidase Center in Human Ferritin L-Chain. *J Biol Chem* **1994,** *269* (48), 30334–30339.

18.   Liu, X. S.; Patterson, L. D.; Miller, M. J.; Theil, E. C. Peptides Selected for the Protein Nanocage Pores Change the Rate of Iron Recovery from the Ferritin Mineral. *J Biol Chem* **2007,** *282* (44), 31821–31825.

19.   Kim, M.; Rho, Y.; Jin, K. S.; Ahn, B.; Jung, S.; Kim, H.; Ree, M. pH-Dependent Structures of Ferritin and Apoferritin in Solution: Disassembly and Reassembly. *Biomacromolecules* **2011**, in press.

20.   Pan, Y. H.; Sader, K.; Powell, J. J.; Bleloch, A.; Gass, M.; Trinick, J.; Warley, A.; Li, A.; Brydson, R.; Brown, A. 3D Morphology of the Human Hepatic Ferritin Mineral Core: New Evidence for a Subunit Structure Revealed by Single Particle Analysis of HAADF-STEM Images. *J Struct Biol* **2009,** *166* (1), 22–31.

21.   Treffry, A.; Harrison, P. M. Incorporation and Release of Inorganic-Phosphate in Horse Spleen Ferritin. *Biochem J* **1978,** *171* (2), 313–320.

22.   Hanna, P. M.; Chen, Y.; Chasteen, N. D. Initial Iron Oxidation in Horse Spleen Apoferritin. Characterization of a Mixed-Valence Iron(II)-Iron(III) Complex. *J Biol Chem* **1991,** *266* (2), 886–893.

23.   Tosha, T.; Ng, H. L.; Bhattasali, O.; Alber, T.; Theil, E. C. Moving Metal Ions through Ferritin-Protein Nanocages from Three-Fold Pores to Catalytic Sites. *JACS* **2010,** *132* (41), 14562–14569.

24.   Turano, P.; Lalli, D.; Felli, I. C.; Theil, E. C.; Bertini, I. NMR Reveals Pathway for Ferric Mineral Precursors to the Central Cavity of Ferritin. *PNAS* **2010,** *107* (2), 545–550.

25.   Massover, W. H. Ultrastructure of Ferritin and Apoferritin. *Micron* **1993,** *24* (4), 389–437.

26.   Carta, D.; Casula, M. F.; Corrias, A.; Falqui, A.; Navarra, G.; Pinna, G. Structural and Magnetic Characterization of Synthetic Ferrihydrite Nanoparticles. *Mater Chem Phys* **2009,** *113* (1), 349–355.

27.   Drits, V. A.; Sakharov, B. A.; Salyn, A. L.; Manceau, A. Structural Model for Ferrihydrite. *Clay Miner* **1993,** *28* (2), 185–207.

28.   Snow, C. L.; Martineau, L. N.; Hilton, R. J.; Brown, S.; Farrer, J.; Boerio-Goates, J.; Woodfield, B. F.; Watt, R. K. Ferritin Iron Mineralization Proceeds by Different Mechanisms in MOPS and Imidazole Buffers. *J Inorg Biochem* **2011,** *105* (7), 972–977.

CHAPTER 3: FERRIC IRON RELEASE FROM FERRITIN USING DESFEROXAMINE

Abstract

The rate of Fe^{3+} release from horse spleen ferritin (HoSF) was measured using the Fe^{3+}-specific chelator desferoxamine (DES). The reaction consists of two kinetic phases. The first is a rapid non-linear reaction followed by a slower linear reaction. The overall two-phase reaction was resolved into three kinetic events: 1) a rapid first-order reaction (k_1); 2) a second slower first-order reaction (k_2); and 3) a zero-order slow reaction (k_3). The zero-order reaction was independent of DES concentration. The two first-order reactions had a near zero-order dependence on DES concentration and were independent of pH from 6.8 to 8.2. The two first-order reactions accounted for 6–9 rapidly reacting Fe^{3+} ions. Activation energies of 10.5 ± 0.8, 13.5 ± 2.0, and 62.4 ± 2.1 kJ/mol were calculated for the kinetic events associated with k_1, k_2, and k_3, respectively. Iron release occurs by: 1) a slow zero-order rate-limiting reaction governed by k_3 and corresponding to the dissociation of Fe^{3+} ions from the FeOOH core that bind to an Fe^{3+} binding site designated as Site 1 (proposed to be within the 3-fold channel); 2) transfer of Fe^{3+} from Site 1 to Site 2 (a second binding site in the 3-fold channel) (k_2); and 3) rapid iron loss from Site 2 to DES (k_1). Several factors affect the rate of Fe^{3+} release from ferritin, including the size of the iron core, the age of the iron core, and the presence of small molecules present in the ferritin environment.

Introduction

In the previous chapter, the deposition and storage of iron in ferritin was shown to be enhanced depending upon the presence of environmental stimuli. In this chapter, the release of ferric iron is discussed. The ability of ferritins to dynamically control iron location and availability within an organism is determined by two distinct biochemical redox reactions. The

first is the binding and oxidation of free Fe^{2+} with subsequent deposition as FeOOH within the hollow ferritin interior during periods of abundant cellular iron (see Chapter 2).[1] This iron deposition process not only stores iron within the hollow interior for later metabolic uses but also decreases the likelihood of cellular damage arising from the formation of oxygen radicals.[2] The second redox process is the reductive release of Fe^{2+} from the FeOOH mineral core stored within the ferritin interior.[3-7] Both of these processes are readily conducted in vitro using various types of ferritins ranging from native animal and bacterial ferritins to a variety of recombinant ferritins.[8-12]

The reactions conducted by native animal ferritins are of particular interest because in contrast to the bacterial ferritins that only have one subunit type,[13] the animal ferritins are heteropolymers consisting of two different subunit types, heavy (H) and light (L).[14] The presence of H and L subunits in animal ferritins suggests specialized roles for each of these subunits. For a detailed overview comparing the subunit types, see Chapter 1. Although extensive studies of iron deposition within various ferritin types have been conducted,[10-12, 15-19] the complete loading process remains poorly understood because it is difficult to separately study the redox reactions from the non-redox processes of migration and hydrolysis of Fe^{3+} to form the mineral core.

Initial iron loading requires the ferroxidase center to catalyze the oxidation of Fe^{2+} to Fe^{3+} followed by migration of the Fe^{3+} to the interior of ferritin for nucleation and mineralization. Once a mineral core begins to form, Fe^{2+} can pass through the 3-fold channels and oxidize on the mineral core surface without passing through the ferroxidase center.[11] Electrostatic potential calculations for divalent metals entering the ferritin 3-fold channel showed that there are two divalent metal binding sites in each 3-fold channel.[20] From these calculations, there are two

potential metal ion-binding sites in each of the 3-fold channels of ferritin. A model showing

these channel binding sites is represented in Figure 3–1.
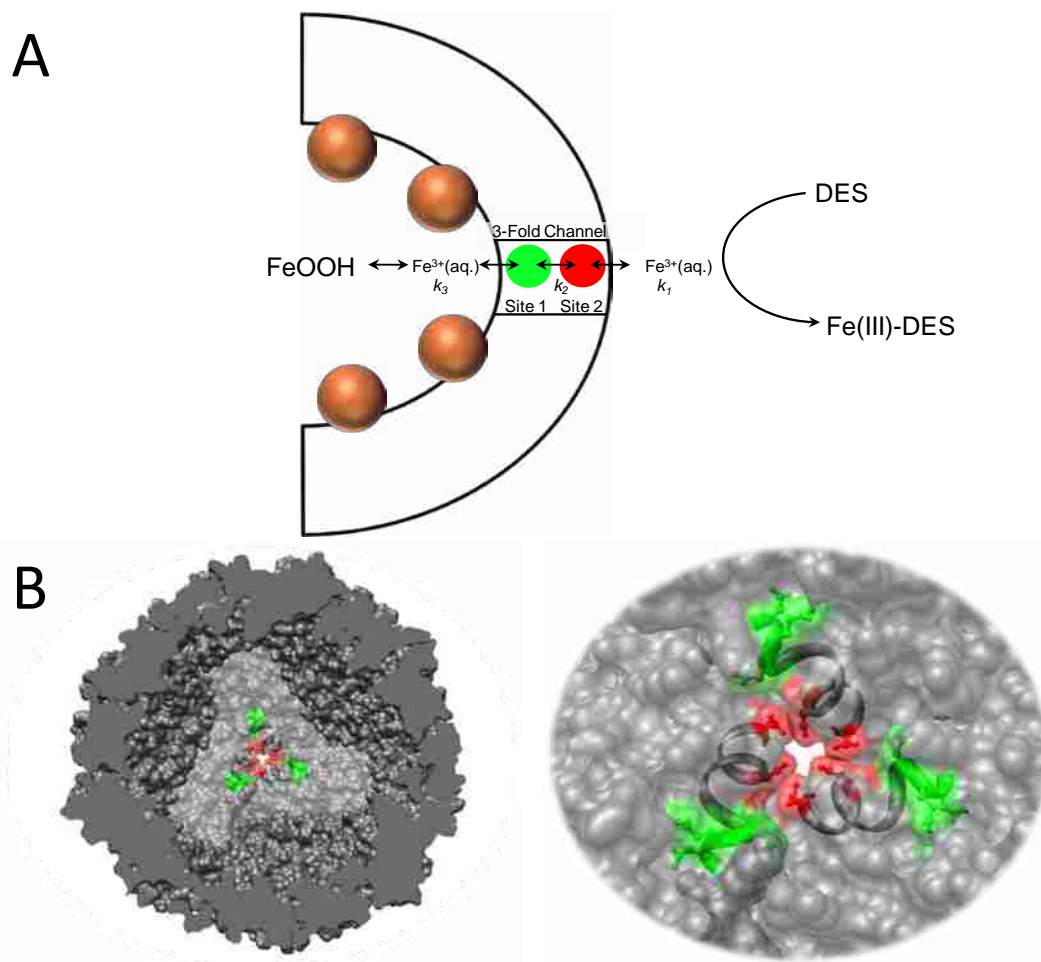
Figure 3-1. Channel binding sites. A) Schematic representation for the release of Fe^{3+} from ferritin by DES chelation. DES rapidly chelates Fe^{3+} bound in **Site 1** and **Site 2** of the 3-fold channels, represented by k_1 and k_2. Once the channel-bound Fe^{3+} has been removed, iron release is dependent on the rate-limiting step, which is the equilibrium of Fe^{3+} dissociating from the iron mineral core (orange spheres) inside ferritin, represented by k_3. B) Left, space filling model that highlights the residues that act as **Site 1** (Asp-139, Glu-140, and Glu-141) and **Site 2** (Asp-131 and Glu-134) metal binding sites, with a magnified view on the right.

Previously, Zhang et al. attempted to separate the non-redox reactions from the redox reactions.[21] They investigated the rates of Fe^{3+} and Fe^{2+} transfer into horse spleen ferritin (HoSF)

interior by trapping ferrocyanide or ferricyanide inside ferritin. As Fe^{3+} or Fe^{2+} traversed the protein shell and entered the ferritin interior, a color change was observed based upon the formation of Prussian blue. The rate of Fe^{3+} entering ferritin was also measured by trapping the Fe^{3+}-specific chelator desferoxamine (DES, shown below) inside ferritin by pH disassembly of ferritin followed by reassembly of ferritin in the presence of DES. These studies showed that Fe^{3+} entered ferritin at a rate nearly twice that of Fe^{2+} with rate constants of 0.4 sec^{-1} for Fe^{2+} and 0.76 sec^{-1} for Fe^{3+}.[21] Unfortunately, attempts to measure the rate of transfer of these two iron species out of the HoSF interior were not successful.
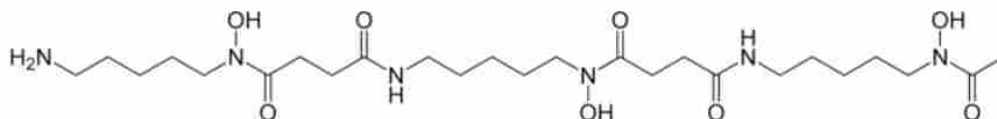
In a recent study, the non-redox release of Fe^{3+} from the mineral core of HoSF was studied by using the small iron chelating agents, aceto- and benzo-hydroxamic acids.[22] The results suggested that these small chelators entered the ferritin interior and directly removed iron from the mineral core. In contrast, in this work we examined the non-redox release of Fe^{3+} from the mineral core in HoSF using DES. DES is larger than aceto- and benzo-hydroxamic acids and is restricted from entering the ferritin interior. As a consequence, iron must transfer through the protein shell to DES at the ferritin exterior.[23] During redox mediated iron release, Fe^{2+} is the dominant form of iron transferred through the ferritin protein shell to the external chelating reagents. Here we describe the reactions for Fe^{3+} release from native HoSF using DES chelation and identify several steps involved in the Fe^{3+} export system. We also investigate the role of small molecules in the release of Fe^{3+} from ferritin. From these reactions, we propose an overall mechanism for iron transport from the mineral core through binding sites within the 3-fold channels to the chelator on the exterior of ferritin.

Materials and Methods

Materials. HoSF containing 2,050 iron atoms and 375 phosphate groups was obtained from Sigma. Stock HoSF solutions at 0.5 and 7.0 mg/mL (1.1 and 15.6 μM) were prepared in 0.025 M N-tris(hydroxymethyl)methyl-2-aminoethanesulfonic acid (TES), 0.05 M NaCl at pH values of 6.8, 7.5, and 8.2. Medicinal grade DES was obtained from Ciba-Geigy Limited, Basel, Switzerland and stock solutions were prepared in 0.025 M TES at pH values of 6.8, 7.5 and 8.2. Aceto- and benzo-hydroxamic acids were purchased from Sigma. A molar absorptivity of 2,865 $M^{-1}cm^{-1}$ at 430 nm for FeDES was used to quantitate iron release from HoSF. Ferritin samples were incubated with ethylenediaminetetraacetic acid (EDTA) and passed down a Sephadex G-25 column to remove adventitiously bound iron. Iron-release reactions were compared with samples treated with or without EDTA and no differences were observed between these samples.

Recombinant human heavy ferritin (rHuHF) from the pET12b HF plasmid and recombinant human light ferritin (rHuLF) from the pDS20pTrp LF plasmid were generously provided by Paulo Santambrogio.[24] These plasmids were placed into a BL21-DE3 *E. coli* strain. The rHuHF was grown in LB medium for eight hours at 37 °C in a New Brunswick Scientific Bioflo 110 Fermentor/Bioreactor. The rHuLF was grown under the Trp promoter in minimal media M9 broth under similar conditions. Both were purified identically. The bacterial cells were lysed using sonication and the cellular debris was removed by centrifugation. The crude extract was heated to 75 °C for 10 minutes, and the denatured protein was removed with centrifugation. The supernatant was run over a Superdex[TM] 200 10/300 GL size-exclusion column using a GE Healthcare ÄKTApurifier FPLC. H and L ferritin samples were prepared in the apo-form and analyzed for protein and iron content.

Ferritin reconstitution. HoSF, rHuHF, and rHuLF were reconstituted in TES buffer, pH 7.5 to target-sized cores. Samples were then treated with DES either immediately, following overnight incubation, or following a ten-day incubation.

Stopped-flow measurements. A DX.17MV Sequential Stopped flow Spectrofluorimeter from Applied Photophysics with optical path lengths of 10.0 and 2.0 mm was used for the acquisition of stopped-flow kinetic data. The stopped-flow instrument was connected to a variable-temperature circulator water bath that controlled the temperature of the optical cell and the sample syringes to $\pm$ 0.10 ^{o}C. Kinetic traces were typically obtained by mixing ~0.01 M DES with 1.0–5.0 µM native holo HoSF (DES/HoSF ~ 2,000, DES/Fe ~ 1.0) at 5 ^{o}C intervals using computer programmed temperature variation from 10–50 ^{o}C. Multiple kinetic reactions were recorded and averaged at each temperature to correct for random error. When the reaction sequence was finished at 50 ^{o}C, the temperature was returned to 20 ^{o}C for the final reaction. This final 20 ^{o}C reaction was compared with the 20 ^{o}C reaction measured during the initial 10–50 ^{o}C temperature sequence to be certain that no modification of the protein occurred while at 50 ^{o}C. Stopped-flow curves were analyzed using a user-derived equation consisting of two exponential terms and a linear zero-order term.

The reaction of DES with native holo HoSF produced a two-phase kinetic curve, which indicated a rapid nonlinear release of iron lasting ~500 s followed by a slower nearly linear release of iron. Another set of stopped-flow measurements were conducted after holo HoSF was first equilibrated with DES for >500 s to eliminate the rapid kinetic phase. For this sequence of reactions, 1.0 mL of ~5.0 µM holo HoSF was reacted with a 100-fold excess of DES for 500 s to remove the rapidly reacting iron atoms and the reacted holo HoSF was separated from unreacted DES and FeDES on a 1.0 x 10 cm Sephadex G-25 column equilibrated in 0.025 M TES, 0.05 M

NaCl, pH 7.5. This DES-free HoSF was then loaded into the stopped-flow instrument ~1–2 h later and reacted with a second portion of DES as outlined above to determine if the rapidly reacting iron atoms had been restored.

UV-visible spectrophotometry. An Agilent 8453 UV-Visible spectrophotometer was used to measure the kinetic data for the formation of the FeDES complex ($\varepsilon_{430} = 2,865$ M^{-1} cm^{-1}). A 5 μM ferritin solution in 25 mM TES, 50 mM NaCl, pH 7.5 was stirred and monitored. During the iron loading experiments, injections of 10 mM ferrous ammonium sulfate in 1 mM HCl stock solution was added in the appropriate amounts to create the target core sizes, and the absorbance at 330 nm was monitored. For iron chelation, a final concentration of 10 mM DES was added and the absorbance at 430 nm was monitored.

Electron paramagnetic resonance (EPR) measurements. HoSF was reacted with DES until the fast reaction was complete and the zero-order reaction was well established. The reaction mixture was cooled and passed through a Sephadex G-25 column equilibrated at 4 ^{o}C to separate holo HoSF from FeDES and unreacted DES. A portion of the separated HoSF at 4 ^{o}C was then placed in an EPR tube and frozen in liquid nitrogen. A second portion was placed in an identical EPR tube and equilibrated at 30 ^{o}C for 1.0 hr, to allow repopulation of the rapidly reacting sites from the FeOOH mineral core, and then frozen in liquid nitrogen. The EPR spectra of these samples were collected at a temperature of 4 K on a Bruker EMX spectrometer with the following settings: power = 1.997 mW, modulation frequency 100 = kHz, and modulation amplitude = 9.99 G.

Results

Figure 3–2 shows the rate of FeDES formation at 25 ^{o}C. Equation 1 represents the reaction of holo HoSF with a ten-fold excess of H$_4$DES (H$_4$DES/HoSF) at pH 7.5.
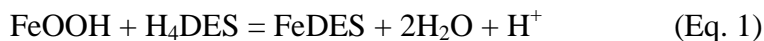
$$FeOOH + H_4DES = FeDES + 2H_2O + H^+ \qquad (Eq. \ 1)$$

FeOOH represents the native mineral core sequestered within the hollow interior of HoSF and H_4DES is the protonated form of DES occurring at pH 7.5 prior to Fe^{3+} chelation. The reaction was monitored at 430 nm, where FeDES has a maximum absorbance. Fitting analysis of this iron release curve shows two distinct kinetic phases for the formation of FeDES. The first is a non-linear reaction occurring from about 0–500 s followed by a slower, nearly linear reaction occurring from about 500 s until the reaction was terminated at 1,000 s. The shape of the curve is typical of "burst" kinetics, indicating that intermediates were quickly lost but the reaction slowly attains a steady state replenishment of these intermediates. The analysis of each of these distinct kinetic regions provides information about the movement of iron from the mineral core through the protein shell to the DES chelator.
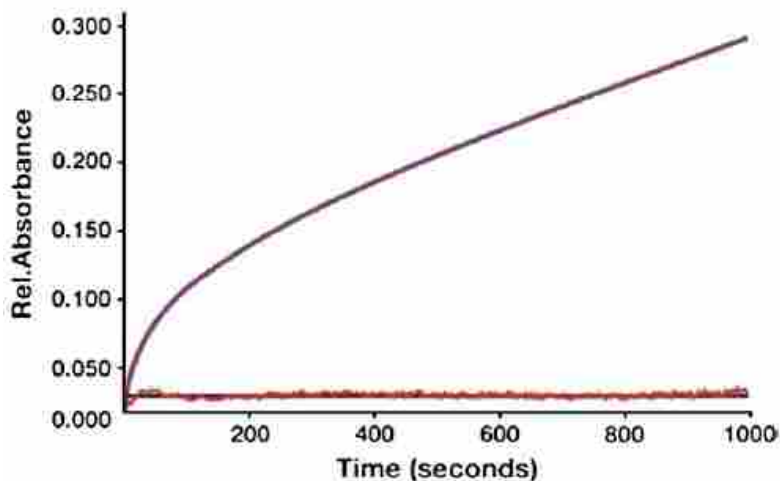
Figure 3-2. The release of Fe^{3+} from the HoSF mineral core using DES chelation. The change of absorbance at 430 nm during the release of Fe^{3+} from HoSF was monitored by stopped-flow spectrophotometry (solid blue line). The fit to the experimental data using Equation 2 is shown as the red dashed line that overlays the blue line. The solid red line is the deviation of the fit from the experimental measurement. The relative standard deviation is less than 1% for each rate constant and the variance of the overall fit is less than 10^{-6} for all 4,000 data points. Only a slight deviation is observed during the first 10 seconds of the reaction for which Equation 2 was unable to account. The kinetic traces were obtained by mixing 0.01 M DES with 5.0 μM native holo HoSF (2,050 Fe/ferritin) in the following ratios (DES/HoSF = 2000, DES/Fe = 1.0) in TES buffer, pH 7.5 at 25 °C.

47

The overall reaction sequence is given by Equation 2 and consists of two sequential first-order iron-release reactions followed by a zero-order iron-release reaction.

$$\text{rate} = ae^{-k_1t} + be^{-k_2t} + k_3t + c \qquad \text{(Eq. 2)}$$

The rate constants, k_1 (6.2×10^{-2} s^{-1}) and k_2 (5.7×10^{-3} s^{-1}) are first-order rate constants in HoSF accounting for the rapid release ("burst") of iron, k_3 is a zero-order rate constant, t is time in seconds and a, b, and c are representative amplitudes ($a = 4.4 \times 10^{-2}$, $b = 6.6 \times 10^{-2}$, and $c = 0.13$) associated with k_1, k_2, and k_3, respectively. Equation 2 gives good fits to the absorbance vs. time data, as seen by the calculated residuals shown in Figure 3–2.

The linear rate for iron chelation was truncated for convenience of presentation after 1,000 s in Figure 3–2 but remains linear for much longer time intervals (days). This linear portion suggests a zero-order reaction for Fe^{3+} release. The zero order rate constant for k_3 was determined to be 1.6×10^{-4} M s^{-1}. To more fully describe the rate law for this linear iron-release process, identical reactions were conducted with a 10-, 50-, and a 100-fold excess of DES under identical conditions. In all cases, linear curves were obtained with k_3 values nearly identical to that in Figure 3–2, suggesting that the reaction was independent of DES concentration. The DES independence of k_3 suggests that iron release from the HoSF core is the rate-limiting step and corresponds to Equation 3.

$$\text{Fe(OOH)} + \text{H}_2\text{O} = \text{Fe}^{3+} + 3\text{OH}^- \qquad \text{(Eq. 3)}$$
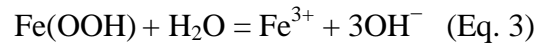
Analysis of the linear portion of each curve at pH of 6.8, 7.5 and 8.2 showed two important features. First, the rate expressed by k_3 for FeDES formation remained independent of DES concentration with pH variation. Second, the rate of iron release decreased by a factor of 5 between pH 6.8 and 8.2. The invariance of rate with DES concentration and the decrease in rate with increasing pH suggests that the iron core dissolution reaction represented by Equation 3

represents the iron release reaction in Figure 3–2. As the pH increases, the increase in OH^- concentration shifts the equilibrium to the left and causes the FeOOH core to become more stable,[25] causing the rate of iron release to decrease.

The rate dependence for the zero-order linear reaction shown in Figure 3–2 was investigated at 5 ^oC intervals from 10–50 ^oC at pH 7.5 with a 100-fold excess of DES. The rate varied uniformly with temperature and Figure 3–3 shows the Arrhenius plot for the temperature dependence of the zero-order rate constant (k_3). From Figure 3–3, an activation energy of 62.4 ± 2.1 kJ/mol was calculated. Additional activation parameters for this zero order process are shown in Table 3–1.
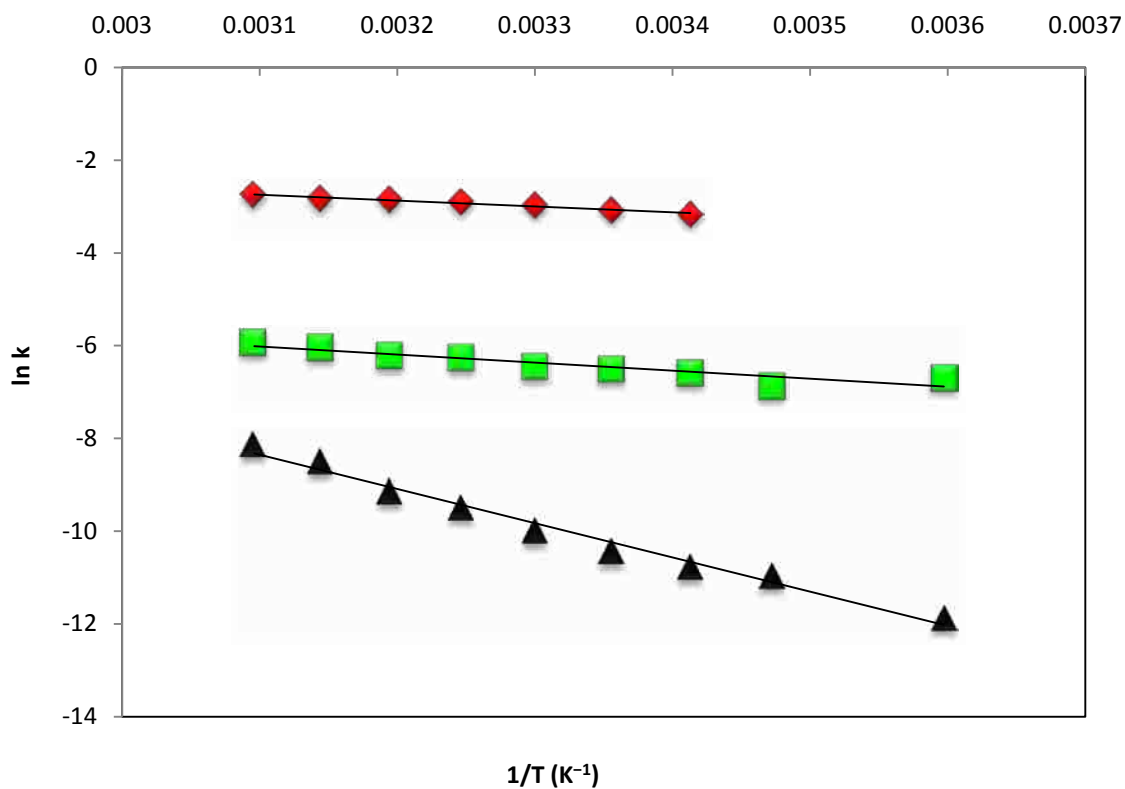
Figure 3-3. Calculated activation parameters derived from measurements of Fe release from native HoSF as a function of temperature for reactions corresponding to ($\blacklozenge$) k_1, ($\blacksquare$) k_2, and ($\blacktriangle$) k_3. Measurements were performed as described in the Materials and Methods section.

Table 3–1. Activation parameters derived from the reactions shown in Figure 3–3.

Rate constant	Ea (kJ/mol)	ΔS (J/mol K)	ΔH (kJ/mol)
k_1	10.5	151	7.95
k_2	13.5	134	11.0
k_3	62.4	266	60.0

The rate of formation of FeDES from 0–500 s is represented by a curved line and shows that Fe^{3+} chelation is initially rapid, but slows with time, indicating the chelatable iron atoms may be close to the surface of the protein and available for reaction with DES. Extrapolating the linear section of Figure 3–2 to zero time gives the absorbance change due to the rapidly reacting iron atoms and shows that 8–9 Fe^{3+}/HoSF are rapidly lost. This corresponds to ~1.0 Fe^{3+}/three-fold channel. These kinetic and stoichiometric results also suggest that the protein-bound Fe^{3+} ions are in equilibrium with the iron atoms in the FeOOH core. To test this possibility, additional kinetic studies were conducted.

In order to corroborate the conclusions derived from fitting the kinetic results by Equation 2, two additional sets of experiments were conducted: one kinetic and the second stoichiometric. The kinetic approach required reacting HoSF with excess DES as shown in Figure 3–2 for more than 500 s until the linear reaction is fully established. The HoSF-DES mixture was then separated by Sephadex G-25 chromatography at 25 $^{\circ}$C to isolate holo HoSF from excess DES and the FeDES produced in the rapid, initial phase of reaction. This holo HoSF, with only a small part of its iron core removed by the k_1 and k_2 reaction steps (fast component of Figure 3–2) was loaded into the stopped-flow after a 1-h delay and reacted with excess DES under the conditions of Figure 3–2. An identical two-phase reaction as in Figure 3–2 was observed, which yielded identical k_1, k_2, and k_3 values as the native HoSF. These results show that in the absence of DES, and with an appropriate incubation time, Fe^{3+} ions become

reestablished in the 3-fold channel and can react with DES in the identical reaction that occurs with native HoSF. This means that the burst is due to repopulation of the channels and not due to non-specifically bound iron. The repopulation of the rapidly reacting iron atoms from the HoSF FeOOH core is quite slow. This is consistent with the rate-limiting step (k_3) of the iron release process being the transfer of Fe^{3+} from the FeOOH core to the protein binding sites.

The stoichiometric experiments investigated the number of iron atoms involved in the rapid reaction shown in Figure 3–2. By extrapolating the linear reaction back to zero, the number of Fe^{3+} ions released in the burst was calculated to be 9.0 Fe^{3+}/HoSF or 1.1 rapidly reacting Fe^{3+} ions per 3-fold channel at 25 $^{\circ}$C. The two exponential reactions obtained from curve fitting the data in Figure 3–2 were evaluated using Equation 2. Values for the two amplitudes associated with k_1 and k_2 in Equation 2 were obtained. The kinetic results suggest that there are two binding sites with different affinities for iron. This result is consistent with electrostatic potential calculations showing that two divalent metal binding sites exist in the 3-fold channels of ferritin.[20] Assuming that Fe^{3+} transfer occurs through the 3-fold channel, it is concluded that more than one Fe^{3+} binding site exists in each of the eight channels and that the population in each channel site was resolved by the kinetic analysis.

To determine whether there are any errors in the fitting procedure caused by additional reactions not accounted for in Equation 2, the non-linear iron-release reaction was investigated at 5 $^{\circ}$C intervals between 10 and 50 $^{\circ}$C at a DES:HoSF ratio of 50:1. Each progress curve at each temperature was fitted using Equation 2 as outlined above. Table 3–1 summarizes the activation parameters obtained. The strict linear response of k_1, k_2, and k_3 with temperature seen in Figure 3–3 confirms that Equation 2 is a consistent representation of the Fe^{3+} loss reaction. Secondary reactions would likely have different activation energies and contribute to a change in rate with

temperature. A reaction that is unaccounted for by Equation 2 would cause the calculated values of k_1, k_2, and k_3 to vary in an irregular way with temperature instead of the linear response observed in Figure 3–3.

To confirm the binding sites are in the 3-fold channels, identical iron release experiments were performed with homopolymers of H and L human ferritin. This was done because an alternative location for monomeric Fe^{3+} ions might be the two iron binding sites of the ferroxidase center. HoSF consists of 10% H subunits or ~3 H subunits/ferritin. Potentially 6 Fe^{3+} could come from the H subunits of HoSF. Homopolymers of H ferritin contain 24-subunits, each with a ferroxidase center that can bind up to 2 Fe^{3+} ions. Therefore, a homopolymer of H ferritin could bind up to 48 Fe^{3+}/ferritin if the iron had not migrated to the interior. In contrast, L ferritin would have zero monomeric Fe^{3+} binding sites associated with the ferroxidase center. Therefore, if the Fe^{3+} was coming from the ferroxidase centers and not the 3-fold channels, we would expect a burst of 48 Fe^{3+}/ferritin from H ferritin and no burst from L ferritin. If the Fe^{3+} comes from the 3-fold channels, the burst would be ~9. We expressed and purified homopolymers of H and L chain ferritins, and loaded each sample with an equal number of iron atoms (~600 Fe/ferritin). We then performed iron chelating experiments with DES in triplicate, as described above. Our results showed a burst of 6.86 ± 0.27 for H chain ferritin and 6.40 ± 0.10 for L chain ferritin at 25 $^{\circ}$C, consistent with our proposal that the Fe^{3+} comes from the 3-fold channels.

EPR measurements were conducted to further examine the nature of the rapidly reacting iron atoms in HoSF. Monomeric Fe^{3+} in a low symmetry environment is known to exhibit an EPR signal at $g = 4.3$. The EPR studies were performed to determine if the rapidly reacting Fe^{3+} ions observed by DES release are related to the monomeric Fe^{3+} EPR signal.

HoSF was reacted with DES until the fast reaction was complete and the zero-order reaction was well established and then the DES and FeDES were separated from HoSF on a Sephadex G-25 column at 4 $^{\circ}$C. The ferritin fraction was collected and divided into two samples. The first sample was placed in an EPR tube and frozen in liquid nitrogen. This sample should have minimal population of Fe^{3+} in the protein binding sites at this low temperature because of the large activation energy for the zero-order reaction required to free Fe^{3+} from the mineral core (Table 3–1). The second sample was placed in an identical EPR tube and equilibrated at 30 $^{\circ}$C for 1.0 h to allow repopulation of Fe^{3+} into the protein binding sites. After one hour, this sample was frozen in liquid nitrogen. The kinetic results described above suggest that Site 1 and Site 2 would become populated by incubation at room temperature for one hour.

Figure 3–4 shows that the immediately frozen HoSF sample had only a small g = 4.3 signal (blue spectrum), whereas the sample that was allowed to incubate at room temperature had ~4-fold larger amplitude at g = 4.3 (black spectrum). The spectrum of native ferritin not treated with DES is identical to the black spectrum (data not shown). These results suggest that the g = 4.3 signal corresponds to monomeric Fe^{3+} ions in the 3-fold channels. The DES treated sample followed by immediate freezing was unable to repopulate the Fe^{3+} ions due to the high energy of activation of k_3. However, after incubation at room temperature for one hour, Fe^{3+} anions mobilized from the core and repopulated the binding sites in the 3-fold channels. This equilibration restored Fe^{3+} ions associated with the burst that is seen in Figure 3–2.
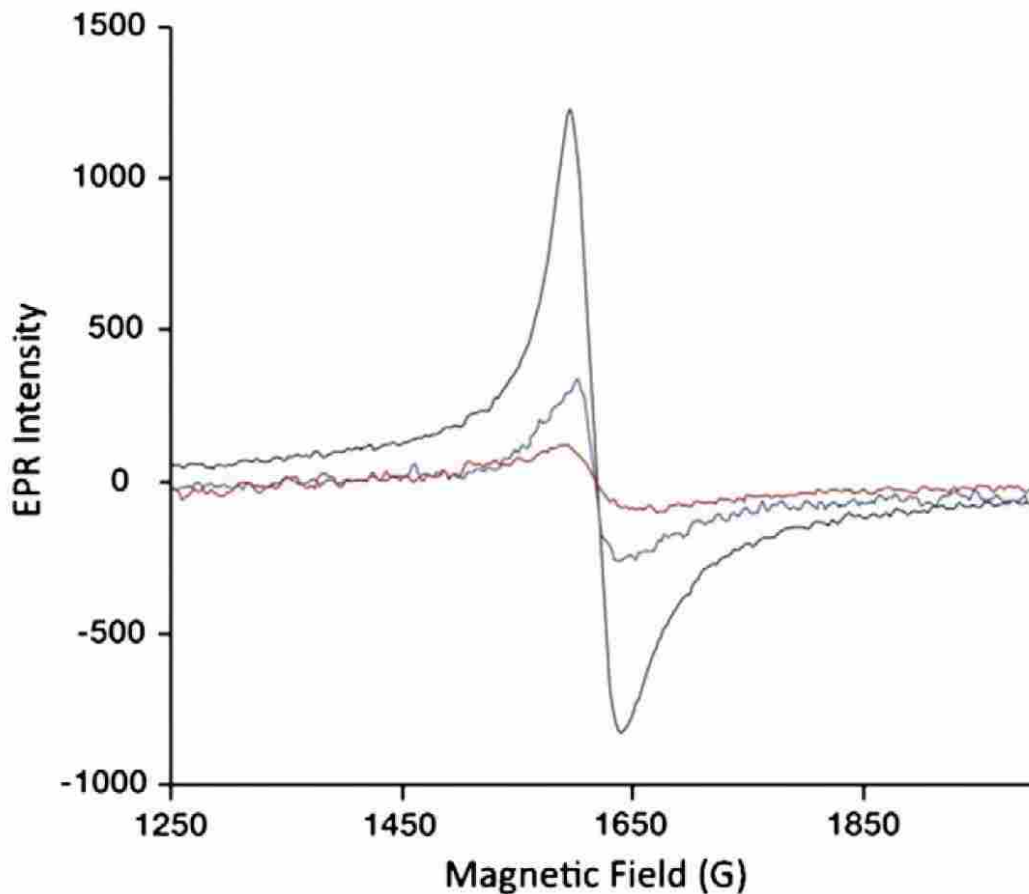
Figure 3-4. EPR spectra of ferritin samples. The **red** EPR signal is of apoferritin and is shown as the negative control. A slight peak is observed due to residual iron in apoferritin. The **blue** is from native HoSF from which Fe^{3+} was removed by DES chelation at 4 °C and passed down a Sephadex G-25 column at 4 °C to separate ferritin from unbound DES and FeDES followed by freezing immediately after elution from the column. The **black** is from native HoSF from which Fe^{3+} was removed by DES chelation at 4 °C and passed down a Sephadex G-25 column to separate ferritin from unbound DES and FeDES followed by a one hour incubation at 30 °C followed by freezing in liquid N_2. Native ferritin not treated with DES has an EPR spectrum essentially identical to the black spectrum.

In Chapter 2, we discussed how the iron core of ferritin becomes more crystalline as the core size increases and as the iron core ages. In order to determine whether the iron was accessible to varying degrees, we reconstituted iron into ferritin with target core sizes of 8, 16, 24, 50, 100, 200, 500, 1,000, and 2,000 Fe/ferritin. The first question was how well the

reconstituted HoSF compared to native HoSF. Kinetic traces of reconstituted HoSF are compared to native HoSF (Figure 3–5). Reconstituted HoSF showed a greater burst of iron, followed by a steeper linear phase. This suggests that when iron is reconstituted in ferritin in vitro, the iron core forms a different mineral than it does in vivo, and that this iron core is more accessible for non-reductive iron chelation. This data is consistent with the data found in Chapter 2, suggesting that the environment in which iron is loaded into ferritin can have a significant effect on the resulting iron core formation.
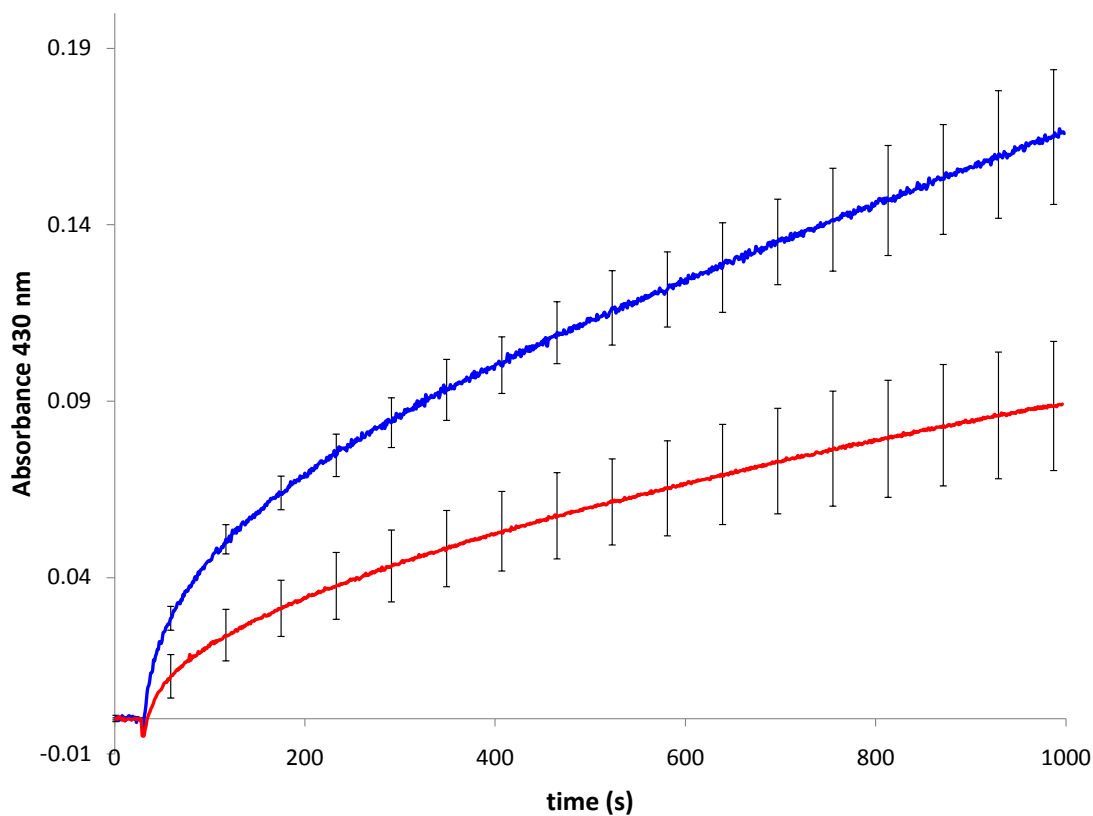
Figure 3-5. Kinetics of Fe^{3+} release from native vs. reconstituted HoSF. Each sample was run in triplicate, and the error bars represent the standard deviation for each run. The **red** curve is native ferritin and the **blue** curve is reconstituted ferritin. Each sample was done with 1 μM ferritin, ~2,000 Fe/ferritin, in 25 mM TES, 50 mM NaCl, pH 7.5, with the addition of 2.5 mM DES.

As the size of the iron core increases in reconstituted ferritin, a greater number of iron atoms are able to be chelated by DES during the burst phase. However, the burst does reach a limiting value of around 20 iron atoms, despite the increase in the core size (Figure 3–6). Similarly, as the iron core ages, the core becomes more stable, and less iron is readily chelatable by DES. These data suggest that both the size and the age of the iron core are important factors for the non-reductive release of iron from ferritin.

Fe Atoms Loaded	# Fe Released Immediately	# Fe Released After Overnight Incubation	# Fe Released After 10 Day Incubation
8	5.41 ± 0.14	2.32 ± 0.71	1.38 ± 1.04
16	6.98 ± 0.27	4.30 ± 1.82	2.07 ± 0.28
24	10.88 ± 0.10	6.52 ± 0.27	2.97 ± 0.23
50	18.79 ± 0.79	9.08 ± 0.03	4.58 ± 0.36
100	26.06 ± 1.76	15.13 ± 1.70	6.98 ± 0.17
200	43.16 ± 0.53	20.36 ± 1.07	11.46 ± 0.50
500	68.30 ± 4.89	39.91 ± 1.79	18.15 ± 0.70
1,000	317.63 ± 12.58	50.26 ± 1.85	19.20 ± 5.24
2,000	842.35 ± 45.55	609.66 ± 5.33	539.27 ± 2.47
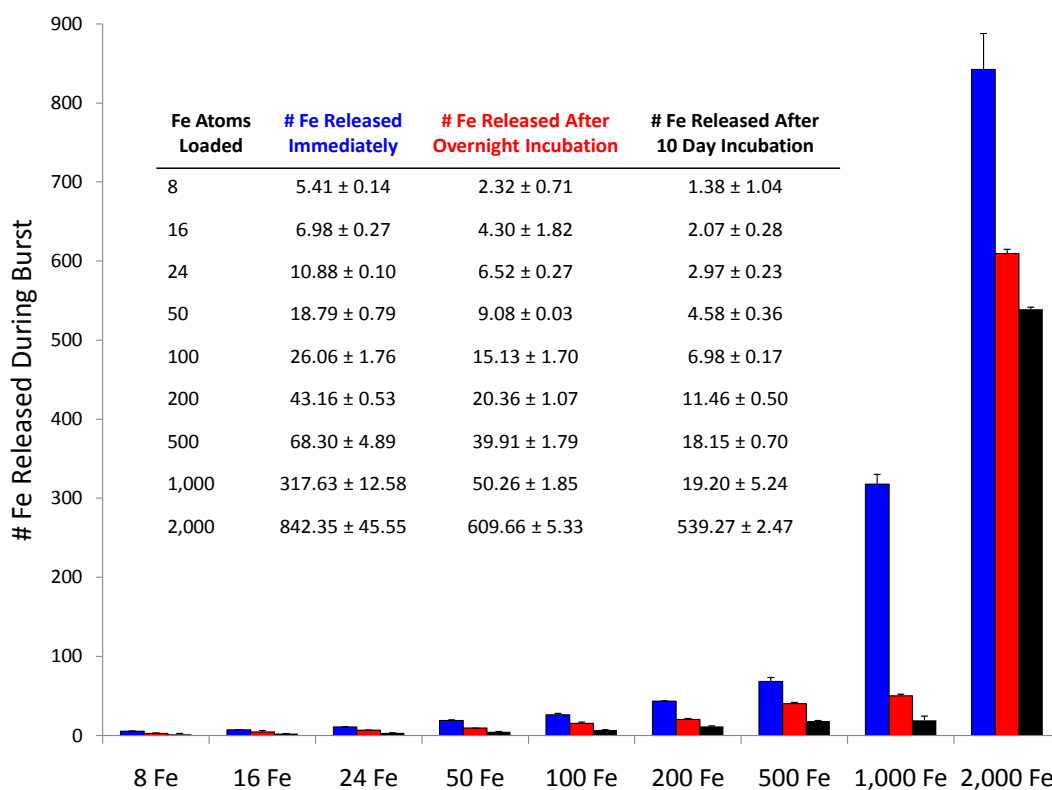
Figure 3-6. Fe^{3+} release from ferritin using DES with different core sizes and ages. The **blue** bars represent iron that is chelated from ferritin immediately following iron loading, the **red** bars represent the chelation of iron following an overnight incubation of iron into ferritin, and the **black** bars represent chelation of iron after the core was allowed to incubate for 10 days. The exact numbers represented in the bar chart are shown in the corresponding table. All runs were repeated in triplicate, and the standard deviations are reported. These runs were all performed in 25 mM TES buffer, 50 mM NaCl, pH 7.5. Iron was loaded from a 10 mM ferrous ammonium sulfate stock, in 1 mM HCl. The protein concentration was 1 μM ferritin.

The kinetic traces of iron loading and iron chelation displayed an interesting trend. Iron loading into ferritin can be observed by monitoring a shoulder at 330 nm, which represents the oxidized iron inside of ferritin, specifically the FeOOH mineral. On the other hand, the iron(III)-DES complex has a peak at 430 nm. Thus, by observing the deposition of iron into ferritin (330 nm) followed by the chelation of iron by DES (430 nm), we observed an interesting kinetic interaction. Iron loads into ferritin as normally observed, with a small tailing out to 430 nm. After the iron loading plateaus off, DES is added to the reaction, and a peak at 430 nm grows in, whereas the absorbance at 330 nm decreases, indicating that the source of the iron being chelated by DES is from the iron core of ferritin (Figure 3–7).
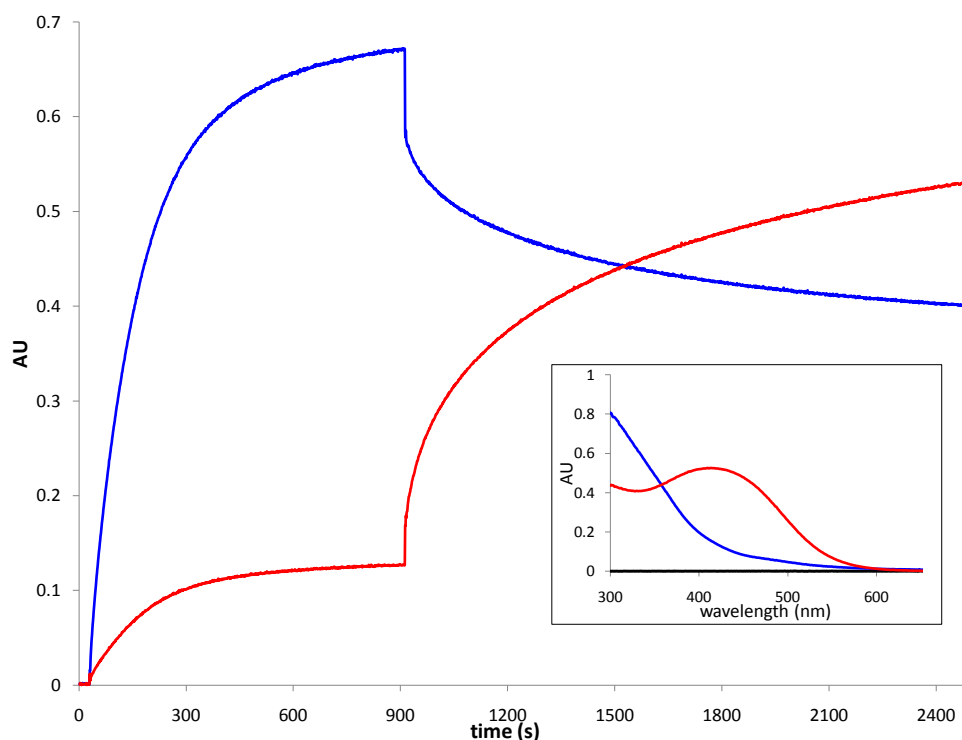
Figure 3-7. Kinetics of iron loading and chelation. The **blue** kinetic curve is the absorbance at 330 nm, and represents the loading and unloading of iron into ferritin. The **red** curve is the absorbance at 430 nm, and is the chelation of iron using DES. The inset shows the full spectra from 300 nm to 650 nm at three distinct time points. **Black** is the spectrum at time = 0 s. **Blue** is the spectrum at time = 900 s (fully loaded ferritin core). **Red** is the spectrum at time = 2,400 s (depleted iron core, and formation of FeDES).

Galvez et al. showed that both aceto- and benzo-hydroxamic acids are able to enter the ferritin interior to pull iron out of ferritin. Because of the sizes of acetohydroxamic acid (3 Å) and benzohydroxamic acid (6 Å), they are able to enter the 3-fold channels (4 Å), bind iron, and then leave the 3-fold channels because of the flexibility and dynamic breathing of ferritin. However, they also showed that in the presence of urea, the 3-fold channels increase in size, and more iron is able to be chelated. In like manner, we wondered whether DES would be able to chelate more iron in the presence of urea or other small molecules. Figure 3–8 shows the effect of these molecules. The molecules were mixed with ferritin and DES chelation experiments were performed either immediately or following an overnight incubation of ferritin with the molecules. Essentially, the only molecules that allow an increased amount of iron release and chelation by DES are citrate and pyrophosphate, and only when these are incubated overnight with ferritin. Each small molecule was also combined with urea to see if we could observe any enhanced effect. However, in this study, the presence of urea made no difference upon DES chelation.
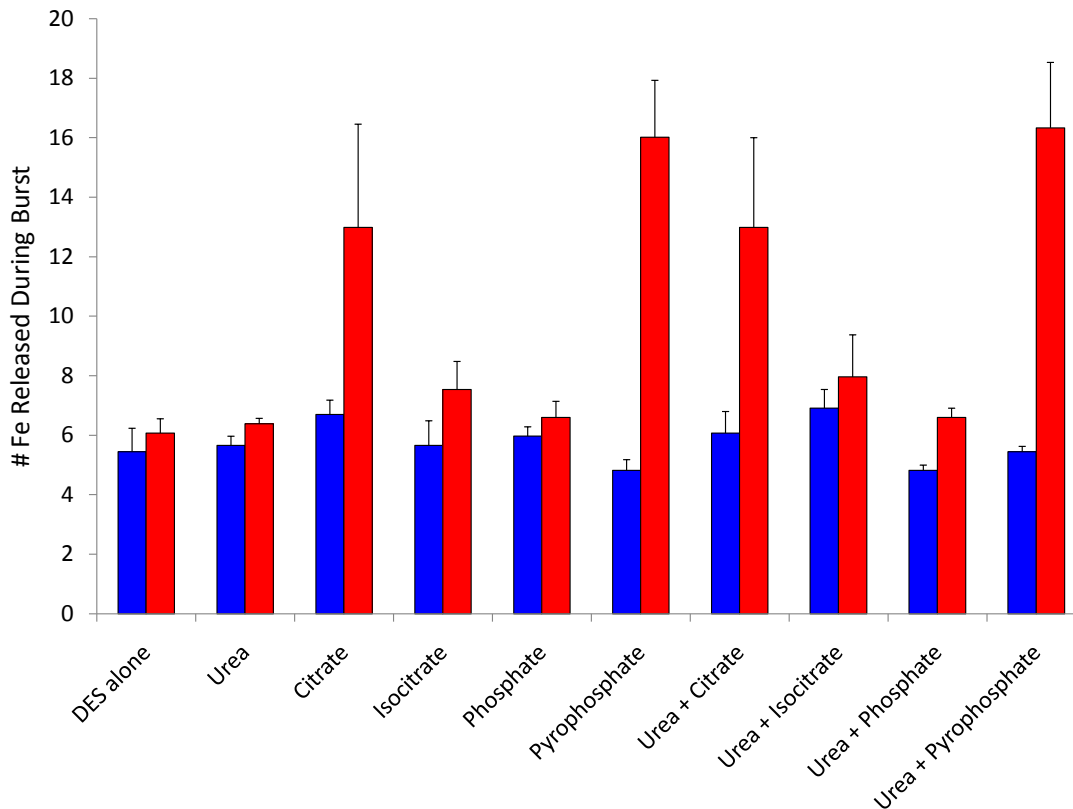
Figure 3-8. Small molecule effect on iron release. Each run was performed in triplicate, and the standard deviation is shown as error bars. The **blue** bars represent runs performed immediately following the mixture of ferritin with the small molecules, whereas the **red** bars represent the runs where the small molecules were incubated with ferritin overnight and then the samples were treated with DES.

Discussion

Numerous studies using siderophores and siderophore analogs evaluated the release of Fe^{3+} from free FeOOH, and the FeOOH-containing biominerals hemosiderin and ferritin to determine their efficacy in treatment of iron overload diseases.[22, 23, 26-30] These studies demonstrated the favorable thermodynamics of iron transfer from polynuclear iron sources to form mononuclear chelates, but the rates of chelate formation are relatively slow (on the order of hours and days) and in the order: FeOOH>hemosiderin>ferritin. The slow iron-release rates from these polynuclear sources are consistent with the ability of the chelator to gain access to the

59

surface of the iron mineral. The slow reaction for ferritin was attributed to restriction of iron transfer from the protected ferritin mineral through the protein shell to the chelator on the ferritin exterior. These results show that the ferritin protein shell is performing the exact role that it evolved to perform—to sequester iron and prevent it from reacting with other biological molecules.

Because of the slow rate of iron release from ferritin, most measurements using siderophores followed iron release at one-hour intervals or longer and did not examine iron-release reactions that occurred at the early time points. However, one report noted that iron release with DES and rhodotorulic acid was more rapid in the first hour compared to subsequent time intervals, suggesting important information was present in the early stages of iron chelation.[3] Our interest in determining the rates of iron transfer through the protein shell has led us to investigate the initial steps of iron release from HoSF using DES chelation.

Figure 3–2 shows that DES can remove Fe^{3+} from the HoSF iron core in a non-reductive process. Figure 3–1 shows the model built from the kinetic data. This model comes from evaluations of Equation 2 where the entire kinetic progress curve for the overall iron-release reaction shown in Figure 3–2 was resolved into two first-order reactions in HoSF (one rapid and a second ~4 times slower) and a third even slower reaction that is zero-order in HoSF. Figure 3–1 shows that DES removes iron from the HoSF mineral core by binding Fe^{3+} ions that are present in the 3-fold channels of the HoSF protein shell. Control reactions with H and L ferritin confirmed that the Fe^{3+} comes from the 3-fold channels and not the ferroxidase center. The kinetic results mimic those often referred to as burst kinetics. The burst comes from protein associated Fe^{3+} intermediates, which are readily chelated by DES but are slowly repopulated by a slower step.

DES is too large to enter the HoSF interior through the 3-fold channels,[23, 31-33] so it must react with Fe^{3+} bound at or near the protein surface of HoSF. The lack of DES dependence on the kinetics after this initial burst reaction suggests that DES cannot interact with Fe^{3+} bound at the mineral core surface, but that this iron is separated from DES by the protein shell. The curve fitting procedure based on Equation 2 suggests that DES chelates ~9 Fe^{3+} ions/ferritin at 25 $^{\circ}$C. Because these Fe^{3+} ions are bound in the 3-fold channels, the average population is 1.1 Fe^{3+}/channel, suggesting that two partially occupied iron-binding sites are present. A population of 1–2 Fe^{3+}/channel is consistent with results from electrostatic potential calculations suggesting that two Fe^{2+} binding sites are present in the three-fold channels.[20] Therefore, the first conclusion from this study is that the non-linear steps represent the burst of iron release from these two binding sites in the 3-fold channels.

The Fe^{3+} in Site 1 is more tightly bound, but is in equilibrium with the weaker binding Site 2 (Figure 3–1). The removal of Fe^{3+} from Site 2 by DES chelation shifts the equilibrium and the channel-bound Fe^{3+} at Site 1 moves closer to the surface and bind at Site 2. The transfer rate from Site 1 to Site 2 is slower than release from Site 2 and is reflected by the slower value of k_2.

Our results show the Fe^{3+} egress pathway consisting of two intermediate Fe^{3+} binding sites contained within the 3-fold channel. An Fe^{3+} entry pathway was previously reported that transports Fe^{3+} from the external solution to the ferritin interior.[21] For the entry pathway, only a single kinetic step was observed and not the two kinetic events observed for the egress pathway. This is consistent with Figure 3–1 because if Site 1 binds Fe^{3+} more strongly than Site 2, then the entering Fe^{3+} would rapidly pass from Site 2 to Site 1 in an apparent single kinetic event.

Once the Fe^{3+} binding sites have been depleted by DES chelation, an equilibrium state is established between DES and the FeOOH mineral core with the protein shell as a barrier

between the chelator and the iron mineral. With an equilibrium in favor of FeDES formation, the FeOOH core transfers Fe^{3+} through the channels to the external solution. Essentially, the small amount of free Fe^{3+} that exists in the ferritin interior binds to Site 1 in the 3-fold channel and is transferred to Site 2 where it can be accessed by DES. Figure 3–4 supports this view by showing that Fe^{3+} bound in the channels can be initially removed by DES and that the vacated sites can be slowly replenished by transfer from the Fe(III) stored in the core. The EPR results indicate that the majority of the Fe^{3+} observed in the g = 4.3 signal of holo HoSF is channel bound Fe^{3+} but smaller levels of additional Fe^{3+} ions may also be present. The transfer of iron from the mineral core to these channel iron-binding sites controls the overall rate of release of Fe^{3+} from the HoSF core to DES because it is the rate-limiting step. The FeOOH mineral core is in equilibrium with the channel binding sites and a small amount of Fe^{3+} is released to repopulate the binding sites in the protein channels. The reaction is driven because FeDES forms a more stable complex than the FeOOH found in the core or Fe^{3+} bound in the channels. Ultimately, the FeOOH core slowly supplies Fe^{3+} to the channels and the channels transfer Fe^{3+} to DES.

We also show that a reconstituted iron core in ferritin is more accessible for DES chelation than is native ferritin. Figure 3–5 shows that both the burst and the linear phase vary from reconstituted to native ferritins. This indicates that the iron core in the two ferritin types varies, and thus the kinetics are different. Reconstituted ferritin differs from native ferritin in that native ferritin contains a phosphate layer on the iron core, and in our reconstituted samples, no phosphate is present. Additionally, the uptake and deposition of iron inside ferritin likely varies in vitro compared to in vivo deposition and mineralization. Future work in this area would be to determine the rate constants for the release of iron from reconstituted ferritin. One precaution

would be that the reconstitution of the iron mineral can vary significantly depending on the environmental stimuli.[19]

We also observed that both the size and the age of the iron core contributed to the iron burst and the release rates with reconstituted ferritin (Figure 3–6). In general, the larger cores are able to hold on to a greater percentage of the total iron, especially when the iron core has been given enough time to rearrange. In the body, the half life of ferritin is only about 12 hours, with complete turnover being near 36 hours.[34] This would indicate that the iron core inside of ferritin is at most two days old. Therefore, the aging of the iron mineral would only be relevant in a biological system for time points less than two days. Our data indicate that when the iron mineral is youngest, it is most accessible for chelation. Thus in the body, non-reductive iron chelation may be possible given the proper environment. Furthermore, native HoSF that was used in this study was purified by Sigma-Aldrich one year prior to the study (Product # F4503-1G, lot # 040M7004). The actual moment that the iron core was formed in horse spleen was some date prior to that, but the overall conclusion is that the native ferritin used underwent a much longer aging process than would actually be relevant on a biological time scale, and thus the in vivo implications based on our results would indicate that the kinetic events that take place in vivo would be increased compared to the reported values included here. In conclusion, the aging data we report here indicates that Fe^{3+} is likely accessible from ferritin in vivo.

We also show the effects of small molecules on the release of iron from ferritin (Figure 3–7). Urea has previously been reported to open the 3-fold channels of ferritin.[22, 35] We used urea in combination with small molecules to determine whether we could chelate more iron. In this study, the presence of urea made no difference on the non-reductive release of iron from ferritin. The only significant difference that we observed was when citrate or pyrophosphate was

incubated with ferritin overnight, in the absence or presence of urea. In these cases, a significantly greater number of iron atoms were released during the burst phase. This is interesting in two arenas. First, the ability of citrate to enable us to chelate more iron may play a role in materials chemistry, and this is discussed in detail in Chapters 7 and 8. Second, in the context of chronic kidney disease (CKD), serum phosphate levels are significantly elevated. Although phosphate does not allow increased non-reductive iron release from ferritin, we wondered whether elevated levels of phosphate could somehow disrupt the ability of ferritin (or other proteins involved in iron metabolism) to bind and sequester iron. Chapters 4 and 5 investigate the role of phosphate in iron metabolism in greater detail.

Finally, although the pathway described here is for Fe^{3+}, it may also be relevant to the Fe^{2+} transfer process, with some expected differences. For example, protein Sites 1 and 2 are proposed to be composed of carboxylate side chains. Such binding sites will accommodate both Fe^{2+} and Fe^{3+}, but the latter ion will likely be more strongly bound due to electrostatic interactions. The consequence would be that Fe^{3+} transfer out from the HoSF interior should be slower than Fe^{2+}. The extent of this binding difference was demonstrated by modeling of the iron binding capabilities of the three-fold channel for both Fe^{2+} and Fe^{3+} ions.[20] This previous study showed that Fe^{3+} is bound 1.3 times stronger than Fe^{2+}. Although the present study did not measure the rate of Fe^{2+} egress for comparison, Zhang et al. reported the rate for the opposite reaction of Fe^{2+} and Fe^{3+} transfer into HoSF interior.[21] The rate of Fe^{3+} entry was twice as rapid as that for Fe^{2+}, consistent with overall stronger binding of Fe^{3+} to channel sites compared to Fe^{2+}.

This work was published in part in the Journal of Inorganic Biochemistry.[36]

References

1.   Chasteen, N. D.; Harrison, P. M. Mineralization in Ferritin: An Efficient Means of Iron Storage. *J Struct Biol* **1999,** *126* (3), 182–194.

2.   Arosio, P.; Ingrassia, R.; Cavadini, P. Ferritins: A Family of Molecules for Iron Storage, Antioxidation and More. *BBA* **2009,** *1790* (7), 589–599.

3.   Crichton, R. R.; Roman, F.; Roland, F. Iron Mobilization from Ferritin by Chelating Agents. *J Inorg Biochem* **1980,** *13* (4), 305–316.

4.   Double, K. L.; Maywald, M.; Schmittel, M.; Riederer, P.; Gerlach, M. In Vitro Studies of Ferritin Iron Release and Neurotoxicity. *J Neurochem* **1998,** *70* (6), 2492–2499.

5.   Jacobs, D. L.; Watt, G. D.; Frankel, R. B.; Papaefthymiou, G. C. Redox Reactions Associated with Iron Release from Mammalian Ferritin. *Biochemistry* **1989,** *28* (4), 1650–1655.

6.   Jones, T.; Spencer, R.; Walsh, C. Mechanism and Kinetics of Iron Telease from Ferritin by Dihydroflavins and Dihydroflavin Analogues. *Biochemistry* **1978,** *17* (19), 4011–4017.

7.   Richards, T. D.; Pitts, K. R.; Watt, G. D. A Kinetic Study of Iron Release from Azotobacter Vinelandii Bacterial Ferritin. *J Inorg Biochem* **1996,** *61* (1), 1–13.

8.   Le Brun, N. E.; Wilson, M. T.; Andrews, S. C.; Guest, J. R.; Harrison, P. M.; Thomson, A. J.; Moore, G. R. Kinetic and Structural Characterization of an Intermediate in the Biomineralization of Bacterioferritin. *FEBS Lett* **1993,** *333* (1–2), 197–202.

9.   Le Brun, N. E.; Andrews, S. C.; Harrison, P. M.; Moore, G. R.; Thomson, A. J. Identification of the Ferroxidase Centre of Escherichia Coli Bacterioferritin. *Biochem J* **1995,** *312*, 385–392.

10.   Yang, X.; Chen-Barrett, Y.; Arosio, P.; Chasteen, N. D. Reaction Paths of Iron Oxidation and Hydrolysis in Horse Spleen and Recombinant Human Ferritins. *Biochemistry* **1998,** *37* (27), 9743–9750.

11.   Xu, B.; Chasteen, N. D. Iron Oxidation Chemistry in Ferritin. Increasing Fe/O2 Stoichiometry During Core Formation. *J Biol Chem* **1991,** *266* (30), 19965–19970.

12.   Bou-Abdallah, F.; Papaefthymiou, G. C.; Stanga, S. D.; Arosio, P.; Chasteen, N. D. mu-1,2-Peroxobridged Di-Iron(III) Dimer Formation in Human H-Chain Ferritin. *Biochem J* **2002,** *364*, 57–63.

13.   Le Brun, N. E.; Crow, A.; Murphy, M. E.; Mauk, A. G.; Moore, G. R. Iron Core Mineralisation in Prokaryotic Ferritins. *BBA 1800* (8), 732–744.

14.   Arosio, P.; Drysdale, J. W. On Ferritin Heterogeneity. *J Biol Chem* **1978,** *253* (12), 4451–4458.

15.   Hanna, P. M.; Chen, Y.; Chasteen, N. D. Initial Iron Oxidation in Horse Spleen Apoferritin. Characterization of a Mixed-Valence Iron(II)-Iron(III) Complex. *J Biol Chem* **1991,** *266* (2), 886–893.

16.   Zhao, G.; Bou-Abdallah, F.; Arosio, P.; Levi, S.; Chasteen, N. D. Multiple Pathways for Mineral Core Formation in Mammalian Apoferritin. *Biochemistry* **2003,** *42* (10), 3142–3150.

17.   Zhao, G.; Su, M.; Chasteen, N. D. mu-1,2-Peroxo Diferric Complex Formation in Horse Spleen Ferritin. A Mixed H/L-Subunit Heteropolymer. *J Mol Biol* **2005,** *352* (2), 467–477.

18.   Bou-Abdallah, F.; Zhao, G. H.; Mayne, H. R.; Arosio, P.; Chasteen, N. D. Origin of the Unusual Kinetics of Iron Deposition in Human H-Chain Ferritin. *JACS* **2005,** *127* (11), 3885–3893.

19.   Snow, C. L.; Martineau, L. N.; Hilton, R. J.; Brown, S.; Farrer, J.; Boerio-Goates, J.; Woodfield, B. F.; Watt, R. K. Ferritin Iron Mineralization Proceeds by Different Mechanisms in MOPS and Imidazole Buffers. *J Inorg Biochem* **2011,** *105*, 972–977.

20.   Takahashi, T.; Kuyucak, S. Functional Properties of Threefold and Fourfold Channels in Ferritin Deduced from Electrostatic Calculations. *Biophys J* **2003,** *84* (4), 2256–2263.

21.   Zhang, B.; Watt, R. K.; Galvez, N.; Dominguez-Vera, J. M.; Watt, G. D. Rate of Iron Transfer Through the Horse Spleen Ferritin Shell Determined by the Rate of Formation of Prussian Blue and Fe-Desferrioxamine Within the Ferritin Cavity. *Biophys Chem* **2006,** *120* (2), 96–105.

22.   Galvez, N.; Ruiz, B.; Cuesta, R.; Colacio, E.; Dominguez-Vera, J. M. Release of Iron From Ferritin by Aceto- and Benzohydroxamic Acids. *Inorg Chem* **2005,** *44* (8), 2706–2709.

23.   Dominguez-Vera, J. M. Iron(III) Complexation of Desferrioxamine B Encapsulated in Apoferritin. *J Inorg Biochem* **2004,** *98* (3), 469–472.

24.   Santambrogio, P.; Levi, S.; Cozzi, A.; Arosio, P. Production and Characterization of Recombinant Heteropolymers of Human Ferritin H and L Chains. *J Biol Chem* **1993,** *268*, 12744–12748.

25.   Heqing, H.; Watt, R. K.; Frankel, R. B.; Watt, G. D. Role of Phosphate in Fe^{2+} Binding to Horse Spleen Holoferritin. *Biochemistry* **1993,** *32* (6), 1681–1687.

26.   Crichton, R. R.; Roman, F.; Roland, F. Iron Mobilization From Ferriting by Chelating Agents. *J Inorg Biochem* **1980,** *13* (4), 305–316.

27.   Kontoghiorghes, G. J.; Chambers, S.; Hoffbrand, A. V. Comparative Study of Iron Mobilization from Haemosiderin, Ferritin and Iron(III) Precipitates by Chelators. *Biochem J* **1987,** *241* (1), 87–92.

28.   Kontoghiorghes, G. J. New Concepts of Iron and Aluminium Chelation Therapy with Oral L1 (Deferiprone) and Other Chelators. A review. *Analyst* **1995,** *120* (3), 845–851.

29.   O'Connell, M. J.; Ward, R. J.; Baum, H.; Peters, T. J. Iron Release from Haemosiderin and Ferritin by Therapeutic and Physiological Chelators. *Biochem J* **1989,** *260* (3), 903–907.

30.   Tufano, T. P.; Pecoraro, V. L.; Raymond, K. N. Ferric Ion Sequestering Agents: Kinetics of Iron Release from Ferritin to Catechoylamides. *BBA* **1981,** *668* (3), 420–428.

31.   Yang, D.; Nagayama, K. Permeation of Small Molecules into the Cavity of Ferritin as Revealed by Proton Nuclear Magnetic Resonance Relaxation. *Biochem J* **1995,** *307 (Pt 1)*, 253–256.

32.   Yang, X.; Chasteen, N. D. Molecular Diffusion into Horse Spleen Ferritin: A Nitroxide Radical Spin Probe Study. *Biophys J* **1996,** *71* (3), 1587–1595.

33.   Webb, B.; Frame, J.; Zhao, Z.; Lee, M. L.; Watt, G. D. Molecular Entrapment of Small Molecules Within the Interior of Horse Spleen Ferritin. *Arch Biochem Biophys* **1994,** *309* (1), 178–183.

34.   Goralska, M.; Nagar, S.; Fleisher, L. N.; McGahan, M. C. Differential Degradation of Ferritin H- and L-Chains. *Invest Ophthal Vis Science* **2005,** *46* (10), 3521–3529.

35.   Theil, E. C.; Liu, X. S.; Tosha, T. Gated Pores in the Ferritin Protein Nanocage. *Inorg Chim Acta* **2008,** *361* (4), 868–874.

36.   Johnson, J.; Kenealey, J.; Hilton, R. J.; Brosnahan, D.; Watt, R. K.; Watt, G. D. Non-Reductive Iron Release from Horse Spleen Ferritin Using Desferoxamine Chelation. *J Inorg Biochem* **2011,** *105* (2), 202–207.

CHAPTER 4: THE ROLE OF TRANSFERRIN IN CHRONIC KIDNEY DISEASE

Abstract

Many diseases of inflammation and oxidative damage are marked by a disruption in normal iron metabolism. A common occurrence of iron disruption is the build-up of what is referred to as non-transferrin bound iron (NTBI). NTBI is harmful because when iron is not bound by the transport protein transferrin, nor stored safely within ferritin, it is capable of catalyzing the production of harmful reactive oxygen species (ROS). This can result in oxidative damage and inflammation. In order to better understand NTBI in the context of iron transport, we performed in vitro assays that mimicked chronic kidney disease (CKD). We tested the hypothesis that elevated levels of serum phosphate interrupted normal Fe^{3+} binding by transferrin. We show that phosphate competes with apotransferrin for Fe^{3+} by reacting with free Fe^{3+} ions in solution to form a polymeric iron(III)-phosphate complex. The formation of the iron(III)-phosphate complex depletes Fe^{3+} from solution and minimizes the total Fe^{3+} available for binding to apotransferrin. Once formed, the iron(III)-phosphate complex is unable to donate Fe^{3+} to apotransferrin. However, complexed forms of Fe^{3+}, such as Fe^{3+}-nitrilotriacetic acid (NTA), are not susceptible to this phosphate complexation reaction and are a better source of Fe^{3+} for delivery to apotransferrin. The formation of the iron(III)-phosphate complex may contribute to the increased levels of NTBI that is observed in patients with CKD. These in vitro data suggest that elevated phosphate concentrations significantly influence the ability of apotransferrin to bind iron, depending on the oxidation state of the iron.

Introduction

Chronic kidney disease (CKD) effects 26 million Americans and several million more are at high risk for developing the disease. CKD is manifest by a progressive loss of kidney function,

most commonly as a result of diabetes mellitus or from metabolite imbalance. This results in a general loss of wellness. Patient markers of CKD include anemia, increased non-transferrin bound iron (NTBI), decreased transferrin saturation, severe oxidative stress, 5–10 fold increase in serum ferritin, and elevated phosphate levels.[1-4] The disease progresses from a mild stage 1 to the severe kidney failure of stage 5. By stage 3, patients are generally recommended for dialysis, a time-intensive and costly treatment that is designed to replace kidney function. At this stage of treatment, the risk of death also increases.[5] Fortunately, during the past decade, two significant improvements in the management of CKD have taken place. First, the National Kidney Foundation developed guidelines and a systematic definition of CKD and its stages to increase awareness of the symptoms and treatments of the disease.[6] Second, improved medications have directly alleviated the symptoms of CKD, with more continually coming down the pipeline.[7-9]

Despite these efforts, the role that iron plays in the disease is poorly understood, although based on the serum markers of CKD (e.g., NTBI, anemia, altered iron metabolism protein concentrations), the role of iron is clearly significant. In order to fully appreciate these serum markers, one must understand the basic principles of iron metabolism in humans.

Iron is an essential element required to sustain life, but if not properly bound and directed to the correct locations in the body, it can catalyze the formation of reactive oxygen species (ROS).[10] To minimize ROS formation, nature has evolved mechanisms to transport, sequester, and escort iron to specific locations within the body. These mechanisms include membrane transport proteins, iron binding and storage proteins, hormones that regulate iron uptake and release, and iron chaperones.[11-20] In order to maintain healthy iron homeostasis, all of these mechanisms must be synchronized and functioning properly.

The average individual consumes 10–20 mg of iron each day. About 10% of this is absorbed in the small intestines where it is eventually chelated by transferrin. Transferrin is an approximate 80 kDa iron transport protein that can hold up to two iron atoms at a time.[21] The two iron binding sites are situated on separate lobes of the protein, which are very similar in structure, although not identical (Figure 4–1).
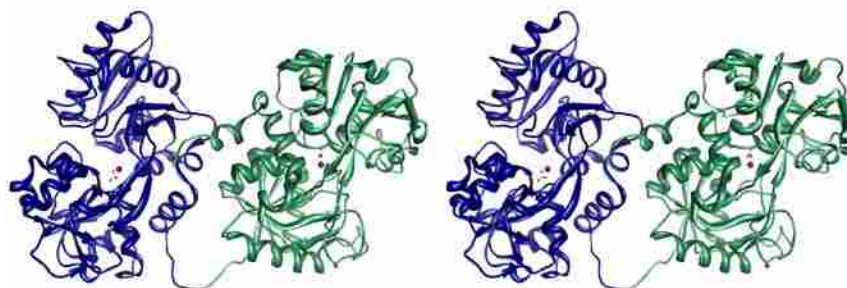
Figure 4-1. Stereo diagram of human transferrin. The N-lobe is depicted in blue and the C-lobe is depicted in green. Also shown is an iron atom in each lobe, coordinated with a corresponding synergistic anion (CO_3^{2-}). PDB code 1JNF.[22] Molecular graphics images were produced using the UCSF Chimera package from the Resource for Biocomputing, Visualization, and Informatics at the University of California, San Francisco (supported by NIH P41 RR-01081).[23]

Transferrin has a high affinity for iron(III) ($\sim10^{22}$ M^{-1}) at physiological pH.[21, 24, 25] Thus, transferrin readily binds any iron that enters the bloodstream, protecting the body from radical damage that can occur from iron-generated ROS. Iron bound to transferrin represents a small percentage of the total iron stores, only about 0.1%. However, this iron pool is a very significant indication of the health of iron metabolism in the body. The amount of iron that is actually bound to transferrin compared to the amount of transferrin that is available to bind iron is referred to as transferrin saturation (TSAT). In healthy individuals, TSAT is generally >20%. However, in patients with CKD, TSAT consistently falls below 20%.[26] Generally, such low TSAT levels is an indication of iron deficient anemia. However, although these patients do exhibit anemia (low red

blood cell levels), they have elevated iron levels in the form of NTBI, which is an inaccessible form of iron.

Free iron, also known as NTBI, represents a state where the normal iron processing mechanisms are not functioning properly and iron is found free in biological fluids.[1, 27-30] The presence of NTBI is dangerous because iron in this form is not protected by transport or storage proteins, and is capable of leading to severe oxidative damage via free radical oxidation.[31] Hemochromatosis and thalassemia patients have NTBI because the iron concentrations in the bloodstream exceed that of the iron binding capacity of serum iron binding proteins.[32, 33] Another source of NTBI is from iron supplements that are given to patients who are iron deficient.[26, 33, 34] In this case, NTBI occurs when the iron supplement dose exceeds the iron binding capacity of serum iron binding proteins.

Patients with CKD also show elevated levels of NTBI. Recent reports show the presence of NTBI in CKD patients independent of whether they received iron supplementation.[1, 32, 33, 35] This observation is puzzling because of the strong affinity that transferrin has to bind iron. The existence of NTBI in the presence of unsaturated transferrin suggests the presence of an inhibitor to transferrin iron binding or indicates the formation of an iron complex in serum that is not biologically available to transferrin.

In vitro studies with transferrin have shown that polymeric salts of iron are poor substrates for transferrin and that in vitro transferrin loading requires a chelated form of iron or a low pH treatment for efficient loading.[36, 37] In fact, many of the iron supplements currently used only transfer a small part of the iron to transferrin, while the rest of the iron is absorbed by cells lining the bloodstream. This iron can be exported back to the bloodstream through the iron export protein, ferroportin, for proper loading into transferrin.[33, 38, 39]

Unfortunately, these patients also have an inflammatory response. Hepcidin, an iron hormone, is expressed as part of the inflammatory response.[15-19] Hepcidin binds to ferroportin, causing its endocytosis and degradation, resulting in a block of iron export into the bloodstream.[40] Hepcidin is from a family of antimicrobial peptides and its function is consistent with stopping microbial growth by limiting iron in the serum.[41] The hepcidin block on ferroportin iron export helps explain the decreased TSAT levels that lead to anemia in CKD patients. Thus, the hepcidin effect may make iron supplementation less effective than hoped because iron export into the bloodstream is blocked.

With the hypothesis that a biologically unavailable iron species forms in vivo in the serum of CKD patients, we sought to identify conditions that would produce such species. We postulated that the inability of the failing kidneys to properly filter the blood leads to an increase in a metabolic species that was capable of binding iron to form species that are not biologically available to transferrin. The CKD literature shows that phosphate concentrations in the serum of CKD patients are significantly elevated.[42] Patients with CKD have phosphate concentrations more than double that of healthy individuals (~3.5 mM and 1.0 mM, respectively).[43-45] Examination of solubility product tables showed that phosphate reacts with iron to produce insoluble complexes (Equations 1 and 2).

$$3 \ Fe^{2+} + 2 \ PO_4^{3-} \leftrightarrow Fe_3(PO_4)_2 \ (s) \quad K_{sp} = 1.0 \times 10^{-36} \qquad \text{(Eq. 1)}$$

$$Fe^{3+} + PO_4^{3-} \leftrightarrow FePO_4 \ (s) \qquad K_{sp} = 1.3 \times 10^{-22} \qquad \text{(Eq. 2)}$$

The insolubility of iron-phosphate species suggests that iron may precipitate in the bloodstream as the phosphate concentrations increase. Furthermore, for proper iron binding by transferrin, a synergistic anion is required. Carbonate functions in this role in vivo; however, other anions have been able to function in this role in vitro (Scheme 4–1A). Phosphate has

previously been shown not to function as a synergistic anion, except in bacterial transferrin.[46-48] Although phosphate does not function as the synergistic anion in transferrin, we wondered whether elevated phosphate levels could nonetheless compete with carbonate for the anion binding site (Scheme 4–1B). If this is the case, then elevated phosphate would cause decreased TSAT levels, because transferrin would be unable to bind iron. Another possibility is that phosphate competes with transferrin for the binding of iron (Scheme 4–1C). In this case, iron is not taken up by transferrin because elevated phosphate levels out-compete transferrin for iron. Overall, we postulated that the elevated phosphate levels observed in the serum of CKD patients disrupts iron loading into transferrin, decreasing TSAT and producing NTBI. Furthermore, once formed, the resultant NTBI is not a substrate for binding to transferrin. This model is depicted in Scheme 4–1.

A. Transferrin Fe^{3+} Binding

$Fe^{3+} + CO_3^{2-} +$ Apo-transferrin   →   Holo-transferrin

B. Phosphate Competing with Carbonate

PO_4^{3-}

$Fe^{3+} + CO_3^{2-} +$ Apo-transferrin   → CO_3^{2-} Partially saturated Holo-transferrin

C. Phosphate Complexing or Precipitating Fe^{3+}

$Fe^{3+} + CO_3^{2-} +$
$+$
PO_4^{3-} Apo-transferrin   →   Partially saturated Holo-transferrin

NTBI
$Fe(PO_4)_x$
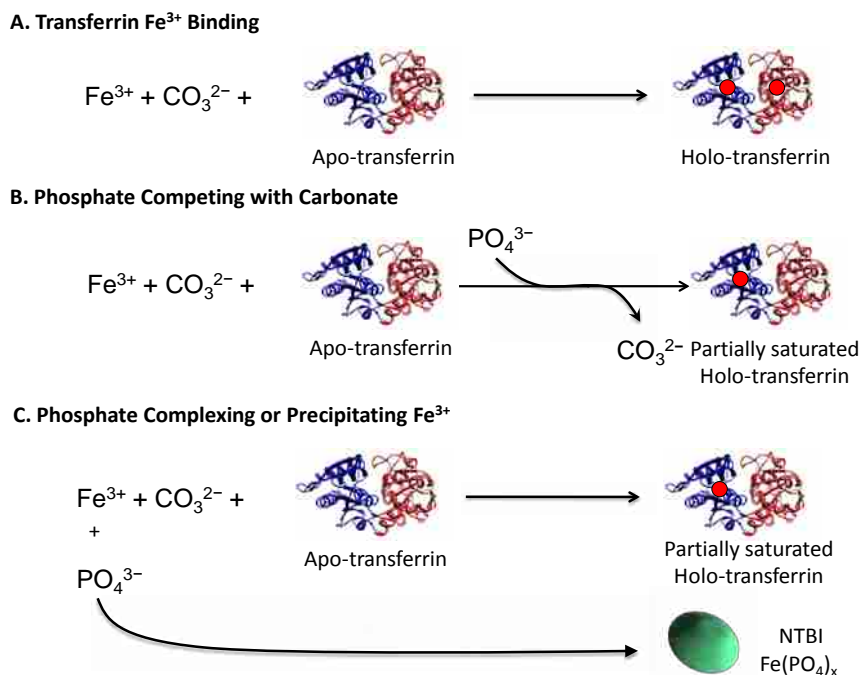
Scheme 4-1. Model of Fe^{3+} binding by transferrin. A) Model of ferric iron loading into transferrin. A synergistic anion (usually carbonate) is required for efficient iron loading to take place. B) Reactions were performed to determine whether phosphate competes with carbonate to prevent binding. C) An alternative model for phosphate

disruption of iron loading into transferrin. Here, phosphate competes with ferric iron to form a polymeric iron-phosphate species. The iron in this complex is inaccessible to transferrin, and forms NTBI.

In this work, we examined the ability of transferrin to bind iron from iron(III) salts and iron(III) complexes and evaluated the effect of phosphate on these binding reactions. We also examined conditions similar to those used by cells to export iron(II) by ferroportin where iron(II) must be oxidized to enter the bloodstream and bind to transferrin.[49, 50] To do this, we used assays that monitored the ability of transferrin to recognize iron(III) immediately after it was oxidized, but before it hydrolyzed water to form aggregates of iron.

We report that phosphate does not act as a synergistic anion under the conditions tested, but that phosphate competes with apotransferrin by reacting with free Fe^{3+} ions in solution to form an iron-phosphate complex. The formation of the iron-phosphate complex depletes Fe^{3+} from solution and minimizes the total Fe^{3+} available for binding to apotransferrin. Once formed, the iron-phosphate complex is not a substrate for donating Fe^{3+} to apotransferrin. Complexed forms of Fe^{3+} such as Fe^{3+}-nitrilotriacetic acid (NTA) are not susceptible to this phosphate complexation reaction and are a better source of Fe^{3+} for delivery to apotransferrin. Recombinant H-chain ferritin is a catalyst for oxidizing Fe^{2+} for incorporation into apotransferrin, and phosphate stimulates this reaction. Additionally, phosphate alone can coordinate Fe^{2+} in solution and facilitate oxidation to Fe^{3+}. If apotransferrin is present when this iron(II)-phosphate complex is oxidized, the Fe^{3+} is rapidly bound by transferrin. The efficiency of this reaction for donating Fe^{3+} to apotransferrin decreases as the phosphate complex increases because phosphate begins to compete for the Fe^{3+} ions formed to form the polymeric iron(III)-phosphate complex.

Materials and Methods

Materials. Human apotransferrin was purchased from Sigma. The powder was dissolved into a solution of 25 mM MOPS, pH 7.4. Recombinant human H-chain ferritin (rHuHF) (plasmid pET12b HF) was over-expressed in *E. coli* (strain BL21-DE3) and purified in our lab, as described in Chapter 3.[51, 52] $Fe(NH_4)_2(SO_4)_2 \cdot H_2O$ (Fe^{2+}), $FeCl_3$ (Fe^{3+}), Na_2HPO_4, and $NaHCO_3$, were all purchased from Fisher. Fe^{2+} and Fe^{3+} solutions were made by dissolving the solid into 0.001 M HCl. NTA was purchased from Sigma. The Fe-NTA complex was made by combining NTA with a stoichiometric amount of Fe^{3+}.[37] All solutions were prepared the day they were used.

UV-Vis Spectrophotometry. An Agilent 8453 UV-Visible spectrophotometer was used to monitor the binding of iron to transferrin. Final concentrations of protein and solutions were: 5 mg/mL transferrin, 0.2 mg/mL rHuHF (when used), 25 mM MOPS pH 7.4, 10 mM CO_3^{2-}, varying concentrations of phosphate, and 0.18 mM Fe^{3+} (for an excess amount of Fe/transferrin, ~3.5 Fe/transferrin) or 0.18 mM Fe^{2+} for the ferroxidase work. The final volume was 2 mL. The kinetic run was setup to monitor the change in absorbance at 460 nm over a time span of 1,800 s. Transferrin was combined with carbonate with or without phosphate and allowed to stir to equilibrate. The kinetic run was initiated and recorded, and the appropriate volume of Fe^{3+} was added. Runs were collected in triplicate.

Results

Transferrin specifically binds two Fe^{3+} ions, one in each lobe.[53-58] Carbonate also binds in each of the two separate lobes of the protein and acts as the synergistic anion to anchor the iron into the binding cavity.[36, 53] The proposed mechanism is that carbonate binds in the cleft of either lobe of transferrin to positively charged residues (Arg124) and also to peptide-chain nitrogens of residues (Ala126 and Gly127) on the N-terminus of transferrin to neutralize the positive charge

of these residues.[59] After neutralizing the repulsive positive charge, carbonate provides the final two ligands for coordinating the incoming Fe^{3+} ion (Figure 4–2).
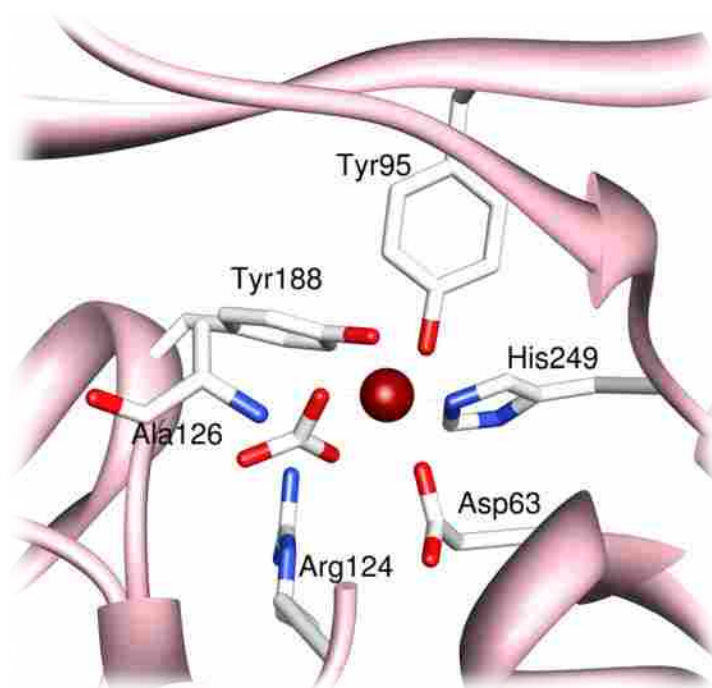
Figure 4-2. Iron binding site within the N-lobe of transferrin. Four residues (Asp63, Tyr95, Tyr188, and His249) plus carbonate bind iron. Two residues (Arg124 and Ala126) stabilize carbonate. PDB code 1JNF.[22] Molecular graphics images were produced using the UCSF Chimera package from the Resource for Biocomputing, Visualization, and Informatics at the University of California, San Francisco (supported by NIH P41 RR-01081).[23]

Our proposal that phosphate inhibits iron binding to apotransferrin might occur by two different pathways (Scheme 4–1). The first pathway requires phosphate to compete with carbonate as the synergistic anion. The second pathway involves phosphate reacting with Fe^{3+} in solution prior to binding to apotransferrin and forming a complex that is not available to bind to transferrin.

Our first goal was to confirm previous studies showing that phosphate does not act as a synergistic anion for iron binding to transferrin.[47] One indicator of iron binding to transferrin is the characteristic absorbance peak at 460 nm that forms when iron is bound to transferrin. Figure

4–3 shows that when Fe^{3+} is added to apotransferrin in the presence of carbonate, the iron loads into transferrin, forming holotransferrin, indicated by the increased absorbance at 460 nm. The control reactions show the spectrum of apotransferrin alone, apotransferrin reacted with Fe^{3+} in the absence of carbonate, and apotransferrin reacted with Fe^{3+} in the presence of phosphate but in the absence of carbonate. Each of these controls failed to produce the characteristic absorbance peak at 460 nm that is indicative of Fe^{3+} binding by transferrin.
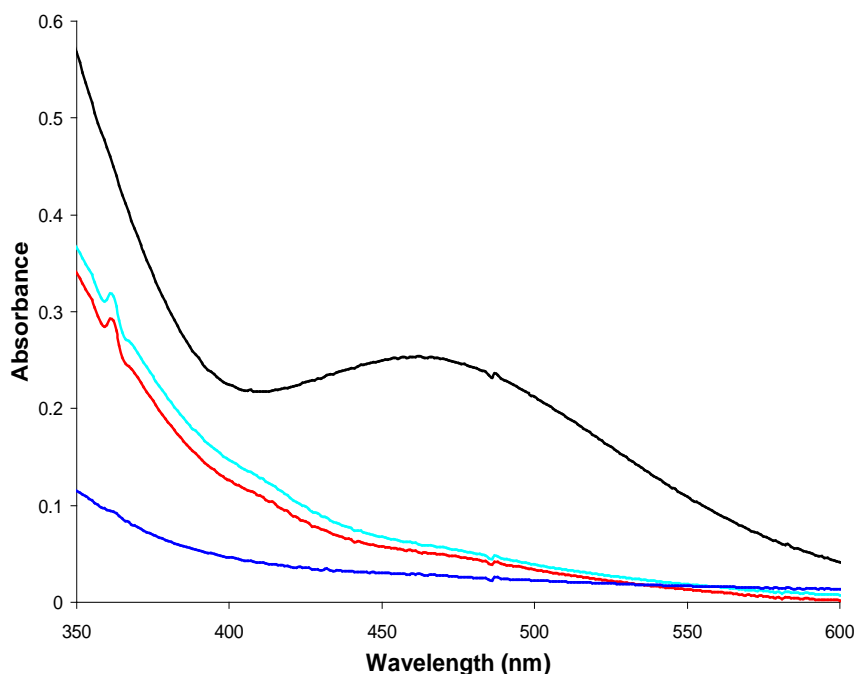
Figure 4-3. UV-Vis spectrophotometry spectra of iron binding by transferrin. Iron binding can be monitored by observing the peak that forms at 460 nm. The **blue** trace is apotransferrin alone. The **black** trace is transferrin + Fe^{3+} + CO_3^{2-}. The **cyan** trace is transferrin + Fe^{3+} without CO_3^{2-}. The **red** trace is transferrin + Fe^{3+} + PO_4^{3-}. Iron binding by transferrin only takes place in the presence of a synergistic anion, such as carbonate. In the absence of carbonate, transferrin does not bind iron. Phosphate is unable to substitute for carbonate in this capacity.

The results in Figure 4–3 confirm that phosphate does not substitute for carbonate for iron binding by transferrin. Therefore, using similar conditions, the effect of phosphate on the rate of iron loading into transferrin with carbonate present was measured. Our goal was to

determine if the presence of phosphate decreased the ability of apotransferrin to bind Fe^{3+}. Fe^{3+} was added to apotransferrin in the absence or presence of increasing phosphate concentrations. Carbonate was always present in the reaction mixtures to provide the synergistic anion. The source of Fe^{3+} in these reactions was $FeCl_3$ or Fe^{3+}-NTA. Previous work showed that $FeCl_3$ was not as efficient for binding by apotransferrin as Fe^{3+} from a complexed source.[36] Indeed, the rate of formation of the 460 nm peak was faster when the Fe^{3+} was supplied from the Fe^{3+}-NTA stock solution, but the same final absorbance was achieved by both Fe^{3+} sources.
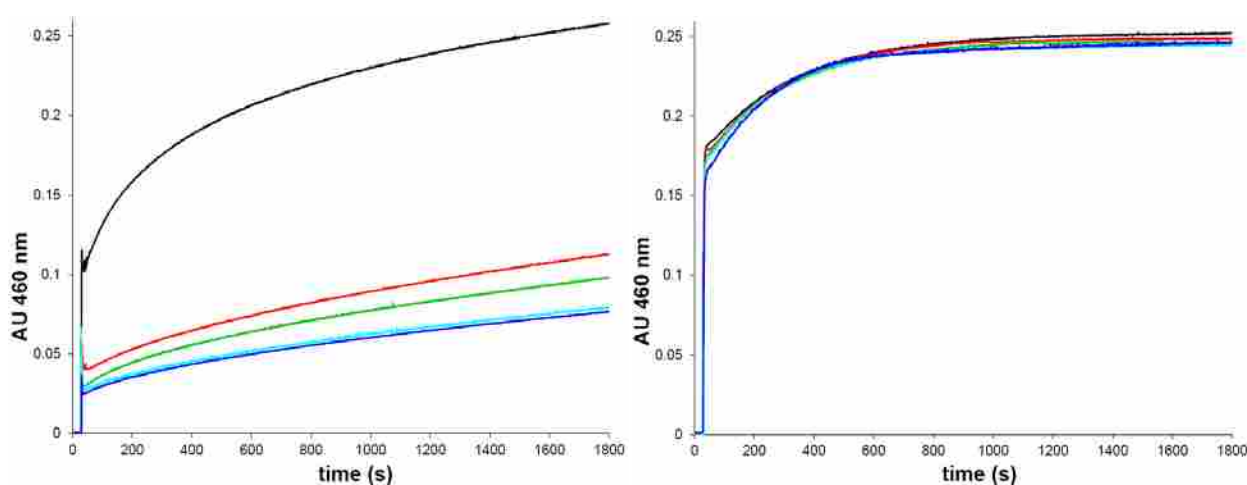
Figure 4-4. UV-Vis spectrophotometry kinetics monitoring the loading of Fe^{3+} into apotransferrin (460 nm). Left is iron loading in the form of FeCl3, whereas right is the loading of iron as the Fe^{3+}-NTA complex. Various concentrations of phosphate were used in the assays to monitor the effects of phosphate. **Black** is no phosphate, **red** is 1 mM, **green** is 2.5 mM, **cyan** is 5 mM, and **blue** is 10 mM.

When phosphate was present prior to the addition of Fe^{3+}, a significant difference in the Fe^{3+} loading kinetics into apotransferrin was observed. When the Fe^{3+} source was $FeCl_3$, the presence of phosphate produced samples with significantly less absorbance at 460 nm, indicating a significant decrease in the total Fe^{3+} that bound to apotransferrin. In contrast, when the Fe^{3+} source was Fe^{3+}-NTA, phosphate showed no inhibitory effect on Fe^{3+} binding by apotransferrin.

The Fe^{3+} complexing ability of NTA allowed Fe^{3+} to be coordinated in solution and prevented phosphate from reacting with Fe^{3+} to coordinate or precipitate Fe^{3+} from the solution.

The specificity of Fe^{3+} binding to the Fe^{3+} pocket of transferrin was examined in order to confirm that the above results were not due to non-specific binding of iron to transferrin.[37] Two of the ligands to Fe^{3+} are tyrosine residues that are deprotonated upon Fe^{3+} binding and provide evidence of specific Fe^{3+} coordination to transferrin. The deprotonation of these tyrosine residues confirms the specific binding of Fe^{3+} to transferrin.[60] Figure 4–5 shows the spectrum of $FeCl_3$ added to apotransferrin in the presence of carbonate. The peaks at 241 nm and 290 nm correspond to the deprotonation of tyrosine.[60] Titrations of 0.5 equivalents of Fe^{3+} were added until the absorbance at 241 and 290 nm ceased to increase with increasing concentration of Fe^{3+}.
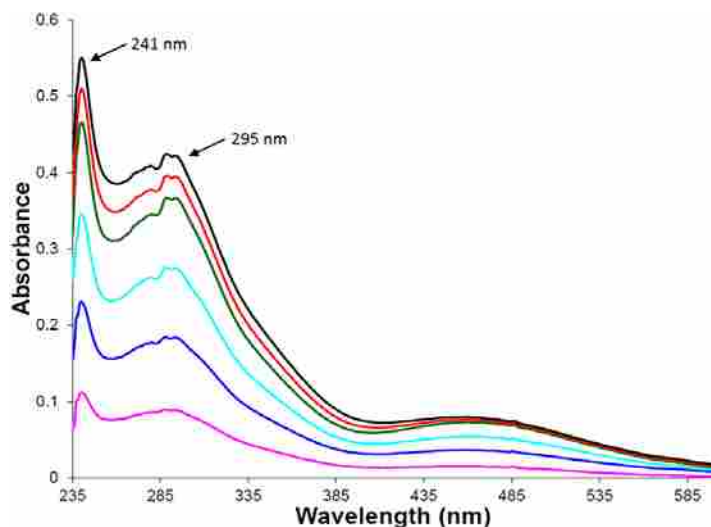
Figure 4-5. Deprotonation of tyrosine residues. Spectra show an increase in absorbance at 460 nm, indicative of iron loading into transferrin. In addition, peaks at 241 nm and 295 nm also increase with increasing iron concentration, which corresponds to the deprotonation of tyrosine residues. Ratios of Fe^{3+} to transferrin are as follows: **pink** is 0.5, **blue** is 1.0, **cyan** is 1.5, **green** is 2.0, **red** is 2.5, and **black** is 3.0.

Figure 4–6 shows a plot where the change in absorbance at 241 nm versus equivalents of Fe^{3+}/transferrin is represented. A break point is observed where the tyrosine residues are

completely deprotonated and the addition of more iron no longer leads to an increased change in the tyrosine absorbance at 241 nm. The small increase in absorbance that is observed is from additional iron added, but this does not significantly change the tyrosine absorbance. The break point occurs at 2 Fe^{3+} ions per transferrin, consistent with the two-transferrin binding sites. Figure 4–6 also shows the same experiment performed under identical conditions, but with 1mM phosphate present in solution (red). At 1 mM phosphate, 12 equivalents of iron were required to maximize the tyrosine deprotonation signal. Reactions with 2.5 mM phosphate required 14 equivalents of Fe^{3+} to completely deprotonate the tyrosine residues (green). When 5 mM phosphate was present, no break point was observed, indicating that complete tyrosine deprotonation was not achieved under the assay conditions (black). The increasing ratios of Fe^{3+} to transferrin as phosphate concentrations increase indicate that higher ratios of iron are required to saturate transferrin. This suggests that phosphate decreases the available iron from solution.
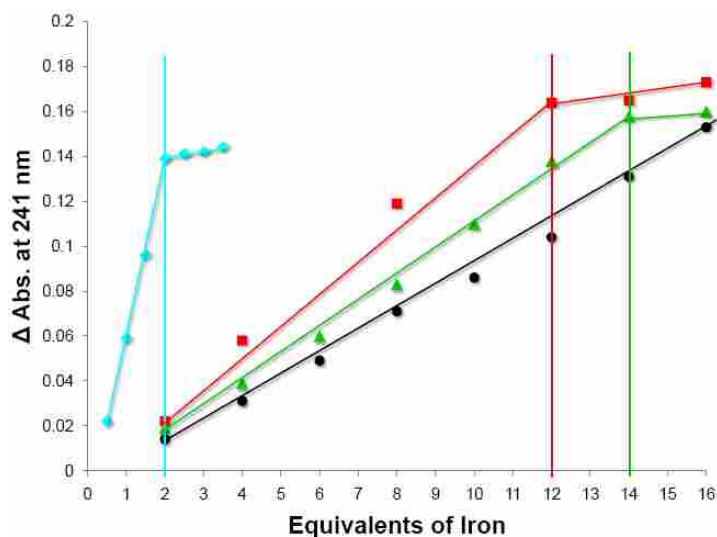
Figure 4-6. Change in absorbance at 241 nm vs. equivalents of iron to demonstrate transferrin saturation. In the absence of phosphate, transferrin saturation occurs at two iron atoms per transferrin (cyan). In 1 mM phosphate, transferrin saturation occurs at 12 irons per transferrin (red). In 2.5 mM phosphate, transferrin saturation occurs at 14 irons per transferrin (green). In 5 mM phosphate, saturation was not observed under experimental conditions (black).

We observed that no precipitate formed in these reactions, which was contradictory to what was predicted from Equations 1 and 2. In these equations, iron reacts with phosphate to form a solid and insoluble iron-phosphate precipitate. However, when phosphate is present in excess (> 10-fold), a soluble polymeric species forms.[61] Control experiments, using identical conditions but without apotransferrin, also produced solutions without any precipitate. Observing this solution spectrophotometrically revealed an identical spectrum as the red spectrum we observed in Figure 4–3. The detailed findings of this polymeric iron(III)-phosphate complex are spelled out in Chapter 5. For the purpose of this chapter, a polymeric iron(III)-phosphate complex forms under our assay conditions and this species is not a substrate for binding by transferrin. Indeed, previous work has shown that polymeric iron(III) species cannot act as substrates for binding to transferrin.[36] We prepared the iron(III)-phosphate complex and then incubated it with apotransferrin in the presence of carbonate. No evidence of Fe^{3+} binding by apotransferrin was observed as judged by monitoring the absorbance at 460 nm (data not shown). This suggests that if soluble iron(III)-phosphate complex exists in vivo as NTBI, it would not be a substrate for binding to apotransferrin.

Although the evidence presented so far suggests that an iron(III)-phosphate complex forms and competes with apotransferrin for Fe^{3+}, another potential mechanism would be that phosphate strips the Fe^{3+} from transferrin after it had bound. This type of Fe^{3+} chelation from transferrin has been previously observed for pyrophosphate.[62] Previous work has shown that holotransferrin treated with pyrophosphate loses Fe^{3+} by observing the decrease in absorbance at 460 nm with time. Identical experiments using phosphate failed to change the 460 nm peak during the same time interval, indicating that phosphate was not able to strip Fe^{3+} from transferrin (data not shown). The results confirmed that phosphate does not chelate Fe^{3+} from

transferrin and also confirm the hypothesis that phosphate prevents Fe^{3+} loading into apotransferrin by forming a polymeric iron-phosphate complex that is inaccessible for transferrin binding.

Normal Fe^{3+} loading into apotransferrin in vivo occurs when Fe^{2+} is pumped out of cells by ferroportin. When Fe^{2+} leaves ferroportin, it is oxidized to Fe^{3+} by either ceruloplasmin or hephaestin, copper oxidase enzymes.[63-65] In the absence of ceruloplasmin or hephaestin, Fe^{2+} remains in the ferroportin export channel and is not exported from cells and into the bloodstream.[64] As Fe^{2+} exits ferroportin, it might be exposed to phosphate prior to oxidation by ceruloplasmin or hephaestin. Because the K_{sp} for $Fe_3(PO_4)_2$ ($K_{sp} = 1 \times 10^{-36}$) is 10^{14} times smaller than $FePO_4$ ($K_{sp} = 1 \times 10^{-22}$) we postulated that elevated phosphate concentrations might decrease iron loading into apotransferrin because Fe^{2+} might react with phosphate before it could be oxidized by ceruloplasmin or hephaestin. Transferrin iron loading reactions were performed by adding Fe^{2+} to apotransferrin using conditions previously described for Fe^{3+} loading into transferrin. However, in this assay, iron loading required Fe^{2+} oxidation prior to binding by apotransferrin because apotransferrin has very low intrinsic ferroxidase activity.[36] We postulated that the presence of phosphate would complex or precipitate the Fe^{2+} and inhibit iron loading into transferrin.

Surprisingly, Figure 4–7 shows results that are the opposite of what was predicted using a solubility product argument. The presence of phosphate increased the rate of Fe^{3+} loading into apotransferrin when Fe^{2+} is added. As the phosphate concentration was increased through the range of 0, 1, 2.5, 5 and 10 mM phosphate, the initial rate of Fe^{3+} binding to apotransferrin increased. Interestingly, the final absorbance steadily decreased as the phosphate concentration increased. Several factors contribute to the reactions shown in Figure 4–7. First, excess

phosphate is present (at least 10-fold) compared to Fe^{2+} and instead of precipitation of $Fe_3(PO_4)_2$ (s), a soluble Fe(II)-phosphate complex forms (see Chapter 5). The precipitation reactions only occur when Fe^{2+} and phosphate are present in approximately 1:1 ratios, but excess phosphate produces a soluble Fe(II)-phosphate complex. Second, phosphate promotes oxidation of Fe^{2+} to Fe^{3+} by coordinating to the Fe^{2+}, and according to hard-soft acid base theory, increases the ability of Fe^{2+} to be more easily oxidized to Fe^{3+}.[66] Once oxidation occurs, Fe^{3+} is transferred to apotransferrin. The decrease in final absorbance is due to the formation of the iron(III)-phosphate complex that was responsible for the inhibition shown previously. Apparently the redox change from Fe^{2+} to Fe^{3+} allows apotransferrin to favorably compete for Fe^{3+} before the iron(III)-phosphate polymeric species forms. This could represent the kinetics of ligand exchange or it may simply be a better mimic of the natural reaction that occurs when Fe^{2+} passes through ferroportin and is oxidized by ceruloplasmin prior to transferrin binding. These results suggest that the redox change from Fe^{2+} to Fe^{3+} may be an important recognition system for transferrin to bind iron.
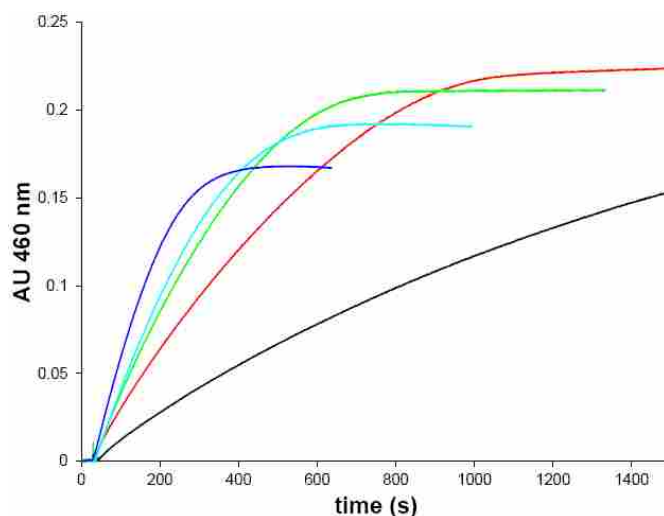

Figure 4-7. UV-Visible spectrophotometry kinetics monitoring the oxidation of Fe^{2+} and subsequent loading of Fe^{3+} into apotransferrin (460 nm). Various concentrations of phosphate were used in the assay to monitor the effects of phosphate. **Black** is no phosphate, **red** is 1 mM, **green** is 2.5 mM, **cyan** is 5 mM, and **blue** is 10 mM.

These results led us to investigate the ability of ferritin to oxidize Fe^{2+} in the presence of phosphate. Ferritin possesses ferroxidase activity and has been used as an oxidase for in vitro assays to load transferrin.[67, 68] We used this assay to determine how increasing phosphate concentrations influence Fe^{3+} loading into apotransferrin when the iron is presented as Fe^{2+}. Figure 4–8 shows that recombinant human H-chain ferritin (rHuHF) significantly stimulates the rate of Fe^{3+} loading into apotransferrin compared to the control that lacks rHuHF. Additionally, when both rHuHF and 1 mM phosphate are present, the initial rate of Fe^{3+} loading into apotransferrin is further stimulated. When higher concentrations of phosphate are present in this reaction, the initial rate of iron loading into apotransferrin continues to increase. This is consistent with reports that phosphate stimulates the rate at which the ferritin ferroxidase center functions.[69-72] Again, however, we observed that as the phosphate concentration increases, the final absorbance decreases. This suggests that at high phosphate concentrations, the formation of the iron(III)-phosphate complex begins to compete with apotransferrin for binding Fe^{3+}.
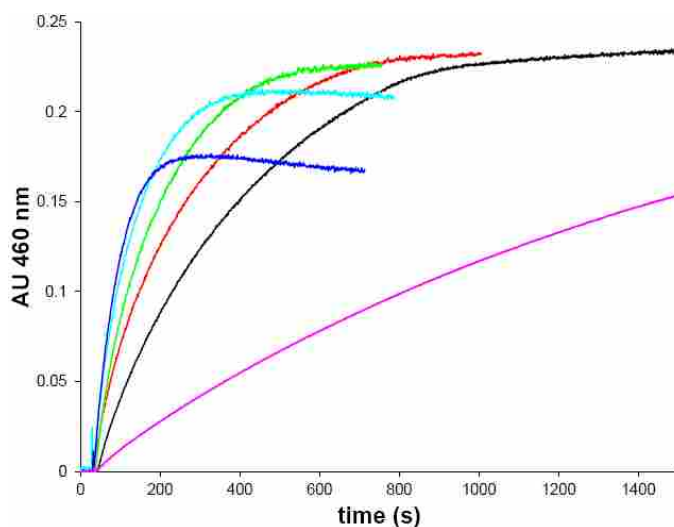

Figure 4-8. UV-Visible spectrophotometry kinetics monitoring the oxidation of Fe^{2+} using ferritin as a ferroxidase. Various concentrations of phosphate were used in the assay to monitor the effects of phosphate. **Black** is no phosphate, **red** is 1 mM, **green** is 2.5 mM, **cyan** is 5 mM, and **blue** is 10 mM. **Pink** is a control without ferritin and without phosphate.

84

To better visualize how rHuHF influences the apotransferrin loading reaction, the relative initial rates from Figures 4–7 and 4–8 are plotted together (with and without rHuHF at identical phosphate concentrations) (Figure 4–9). In the absence of phosphate, rHuHF significantly increases the Fe^{3+} loading into apotransferrin. The combination of both rHuHF and phosphate is significantly faster than the rHuHF without phosphate, suggesting that phosphate has a stimulatory effect on the ferroxidase center of ferritin.[69-72] The decrease in final absorbance is observed in the curves with 5 mM phosphate. Note that the sample without ferritin has a larger decrease than the sample with ferritin, indicating that when rHuHF is present, there is a greater efficiency of Fe^{3+} loading into apotransferrin. In fact, Figure 4–8 shows that the sample with rHuHF and 2.5 mM phosphate achieved the same final absorbance as the 1 mM phosphate sample and the sample without phosphate, which represents complete Fe^{3+} loading. These results suggest that in the presence of a protein with ferroxidase activity, iron loading is not inhibited by phosphate until the phosphate concentration reaches a value between 2.5 mM and 5 mM phosphate. Near 5 mM phosphate and above, the formation of the iron phosphate complex becomes more favorable and even in the presence of rHuHF, possessing ferroxidase activity is not sufficient to completely prevent the formation of the iron(III)-phosphate complex.
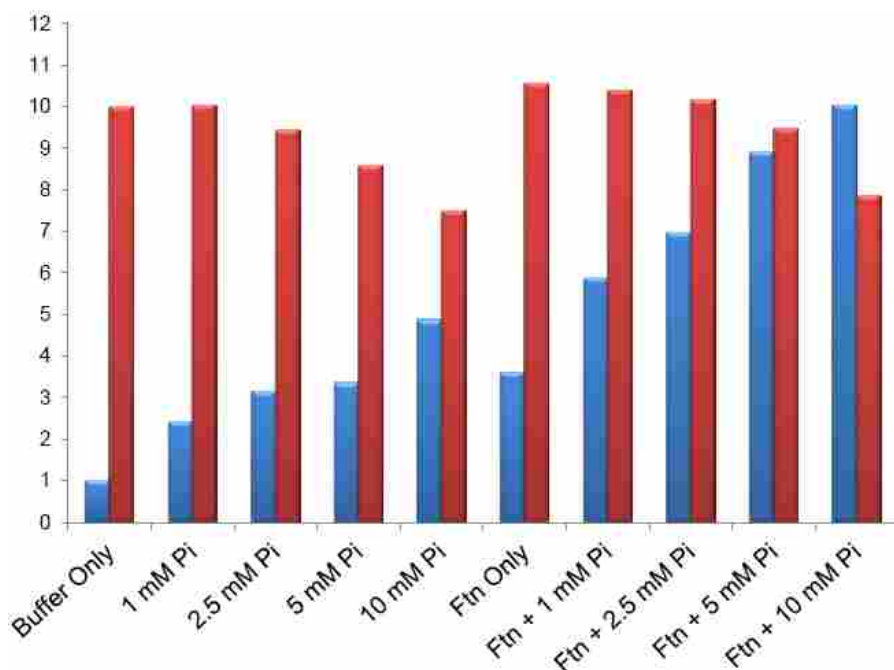
Figure 4-9. Relative rates of iron loading into transferrin. Blue bars are the relative initial rates (ΔAbs/sec) over the first 60 seconds of the reaction. Red bars are the relative final absorbance values, where a value of ten represents complete iron loading into transferrin.

The stimulation of Fe^{2+} loading into apotransferrin occurs because phosphate coordinates to Fe^{2+} and creates an environment that favors oxidation.[66] Interestingly, the iron(II)-phosphate complex appears to be a good substrate for donating Fe^{3+} to apotransferrin in contrast to the iron(III)-phosphate complex, which does not donate Fe^{3+} to apotransferrin.

Discussion

Elevated phosphate concentrations inhibit Fe^{3+} loading into apotransferrin. Because phosphate does not compete with carbonate as a synergistic anion (Figure 4–3), we propose that the inhibition must occur by another pathway. Our results show that phosphate blocks Fe^{3+} loading into apotransferrin by coordinating to Fe^{3+} and forming an iron(III)-complex that is biologically unavailable to bind to apotransferrin. When Fe^{3+} is coordinated by NTA prior to

incubation with phosphate, normal Fe^{3+} loading into apotransferrin is observed. This suggests that maintaining Fe^{3+} in a monomeric form is an essential step in apotransferrin loading.

The specificity of Fe^{3+} binding to apotransferrin was tested by monitoring the deprotonation of the tyrosine residues in transferrin that coordinate the Fe^{3+} ions. In the absence of phosphate, the expected stoichiometry of 2 Fe^{3+}/transferrin was observed. In the presence of phosphate, much higher stoichiometries of Fe^{3+} were required to completely saturate the binding sites of apotransferrin. This is consistent with the hypothesis that phosphate competes for the Fe^{3+} ions and depletes them from solution by forming an iron(III)-phosphate complex that is not a substrate for binding by apotransferrin. This is significant for CKD patients because NTBI may be forming in the serum of these patients as the phosphate levels rise as a result of the failing kidneys.

The in vivo mechanism of Fe^{3+} delivery to transferrin occurs by export of Fe^{2+} from cells by ferroportin. The release of Fe^{2+} requires an oxidase, ceruloplasmin or hephaestin, to oxidize the Fe^{2+} to Fe^{3+}. The ferroxidase activity of rHuHF was used to mimic this reaction in vitro. In the presence of rHuHF, phosphate has a less inhibitory effect on iron loading and actually stimulates the ferroxidase activity of ferritin. In the absence of rHuHF, phosphate also stimulates the oxidation of Fe^{2+}, but as the phosphate concentration increases, the formation of the iron(III)-phosphate complex begins to compete with apotransferrin for the Fe^{3+} ions in solution.

In summary, patients with CKD have serum markers of decreased TSAT, increased serum phosphate levels, elevated NTBI, elevated serum ferritin, anemia, and severe oxidative damage. The decreased levels of TSAT can be explained because transferrin is unable to bind iron. Instead, the elevated phosphate levels compete for the iron, effectively inhibiting transferrin binding and uptake. As a result, a soluble iron-phosphate complex forms, contributing to the

elevated NTBI. This makes the iron inaccessible, and anemia results. However, iron in the form of NTBI is still capable of causing oxidative damage. Another interesting feature of CKD is the presence of elevated serum ferritin levels. Considerable work has gone into understanding the role of serum ferritin in CKD, and the results from that work will be expounded upon in Chapter 5.

This work was accepted in part for publication in Biometals.

This work was presented as a poster at the International BioIron Society 2011 in Vancouver, BC Canada.

References

1.   Prakash, M.; Upadhya, S.; Prabhu, R. Serum Non-Transferrin Bound Iron in Hemodialysis Patients not Receiving Intravenous Iron. *Clin Chim Acta* **2005,** *360* (1–2), 194–198.

2.   Samouilidou, E.; Grapsa, E.; Karpouza, A.; Lagouranis, A. Reactive Oxygen Metabolites: A Link Between Oxidative Stress and Inflammation in Patients on Hemodialysis. *Blood Purif* **2007,** *25*, 175–178.

3.   Stenvinkel, P.; Barany, P. Anemia, rHuEPO Resistance, and Cardiovascular Disease in End-Stage Renal Failure; Links to Inflammation and Oxidative Stress. *Nephrol Dial Transplant* **2002,** *17*, 32–37.

4.   Lee, D.-H.; Zacharski, L.; Jacobs, J. Comparison of the Serum Ferritin and Percentage of Transferrin Saturation as Exposure Markers of Iron-Driven Oxidative Stress-Related Disease Outcomes. *Am Heart J* **2006,** *151* (6), 12471–12477.

5.   Regidor, D.; Kopple, J.; Kovesdy, P.; Kilpatrick, R.; McAllister, C. J.; Aronovitz, J.; Greenland, S.; Kalantar, K. Associations between Changes in Hemoglobin and Administered Erythropoiesis-Stimulating Agent and Survival in Hemodialysis Patients. *J Am Soc Nephrol* **2006,** *17*, 1181–1191.

6.   National Kidney Foundation: K/DOQI Clinical Practice Guidelines for Chronic Kidney Disease: Evaluation, Classification, and Stratification. *Am J Kidney Dis* **2002,** *39* (2 Suppl 1), S1-266.

7.   Fishbane, S. Erythropoiesis-Stimulating Agent Treatment with Full Anemia Correction: A New Perspective. *Kidney Int* **2008,** *75* (4), 358–365.

8.   Egrie, J. C.; Browne, J. K. Development and Characterization of Novel Erythropoiesis Stimulating Protein (NESP). *Nephrol Dialysis Transplant* **2001,** *16*, 3–13.

9.   Macdougall, I. C. CERA (Continuous Erythropoietin Receptor Activator): A New Erythropoiesis-Stimulating Agent for the Treatment of Anemia. *Curr Hematol Rep* **2005,** *4* (6), 436–440.

10.   Arosio, P.; Levi, S. Ferritin and Oxidative Damage. *Free Radical Biol Med* **2002,** *33*, 457–463.

11.   Sigel, A.; Sigel, H. Metal Ions in Biological Systems, Volume 35: Iron Transport and Storage Microorganisms, Plants, and Animals. *Met Based Drugs* **1998,** *5* (5), 262.

12.   Nemeth, E.; Ganz, T. Hepcidin Iron Metabolism. *Annu Rev Nutrition* **2006,** *26*, 323–342.

13.   Roy, C.; Andrews, N. Anemia of Inflammation. *Curr Opin Hematol* **2005,** *12*, 107–111.

14.   Goodnough, L.; Skikne, B.; Brugnara, C. Iron and Erythropoiesis. *Blood* **2000,** *96*, 823–833.

15.   Andrews, N. Anemia of Inflammation. *J Clin Invest* **2004,** *113*, 1251–1253.

16.   Kalantar-Zadeh, K.; Rodriguez, R.; Humphreys, M. Association Between Serum Ferritin and Measures of Inflammation, Nutrition and Iron in Haemodialysis Patients. *Nephrol Dial Transplant* **2004,** *19* (1), 141–149.

17.   Campbell, C. H.; Solgonick, R. M.; Linder, M. C. Translational Regulation of Ferritin Synthesis in Rat Spleen: Effects of Iron and Inflammation. *Biochem Biophys Res Commun* **1989,** *160* (2), 453–459.

18.   Tran, T.; Eubanks, S.; Schaffer, K.; Zhou, C.; Linder, M. Secretion of Ferritin by Rat Hepatoma Cells and Its Regulation by Inflammatory Cytokines and Iron. *Blood* **1997,** *90* (12), 4979–4986.

19.   Cairo, G.; Tacchini, L.; Pogliaghi, G.; Anzon, E.; Tomasi, A.; Bernelli-Zazzera, A. Induction of Ferritin Synthesis by Oxidative Stress. *J Biol Chem* **1995,** *270* (2), 700–703.

20.   Shi, H.; Bencze, K. Z.; Stemmler, T. L.; Philpott, C. C. A Cytosolic Iron Chaperone That Delivers Iron to Ferritin. *Science* **2008,** *320* (5880), 1207–1210.

21.   Aisen, P.; Listowsky, I. Iron Transport and Storage Proteins. *Annu Rev Biochem* **1980,** *49*, 357–393.

22.   Hall, D. R.; Hadden, J. M.; Leonard, G. A.; Bailey, S.; Neu, M.; Winn, M.; Lindley, P. F. The Crystal and Molecular Structures of Diferric Porcine and Rabbit Serum Transferrins at Resolutions of 2.15 and 2.60 Angstrom, Respectively. *Acta Crystallogr, Sect D* **2002,** *58*, 70–80.

23.   Pettersen, E.; Goddard, T.; Huang, C.; Couch, G.; Greenblatt, D.; Meng, E.; Ferrin, T. A Visualization System for Exploratory Research and Analysis. *J Comput Chem* **2004,** *25*, 1605–1612.

24.   Harris, W. R. Estimation of the Ferrous--Transferrin Binding Constants Based on Thermodynamic Studies of Nickel(II)--Transferrin. *J Inorg Biochem* **1986,** *27* (1), 41–52.

25.   Baker, H. M.; Anderson, B. F.; Baker, E. N. Dealing with Iron: Common Structural Principles in Proteins that Transport Iron and Heme. *PNAS* **2003,** *100* (7), 3579–3583.

26.   Jairam, A.; Das, R.; Aggarwal, P.; Kohli, H.; Gupta, K.; Sakhuja, V.; Jha, V. *Iron Status, Inflammation and Hepcidin in ESRD Patients: The Confounding Role of Intravenous Iron Therapy*. 2010; Vol. 20, p 125–131.

27.   Breuer, W.; Hershko, C.; Cabantchik, Z. I. The Importance of Non-Transferrin Bound Iron in Disorders of Iron Metabolism. *Transfus Sci* **2000,** *23* (3), 185–192.

28.   Cabantchik, Z. I.; Glickstein, H.; Milgram, P.; Breuer, W. A Fluorescence Assay for Assessing Chelation of Intracellular Iron in a Membrane Model System and in Mammalian Cells. *Anal Biochem* **1996,** *233* (2), 221–227.

29.   Espósito, B. P.; Epsztejn, S.; Breuer, W.; Cabantchik, Z. I. A Review of Fluorescence Methods for Assessing Labile Iron in Cells and Biological Fluids. *Anal Biochem* **2002,** *304* (1), 1–18.

30.   Cabantchik, Z. I.; Breuer, W.; Zanninelli, G.; Cianciulli, P. LPI-Labile Plasma Iron in Iron Overload. *Best Pract Res Clin Haematol* **2005,** *18* (2), 277–287.

31.   Prezelj, M.; Knap, B. Automated Assay for Non-Transferrin-Bound Iron in Serum Samples. *Clin Chem Lab Med* **2010,** *48* (10), 1427–1432.

32.   Kooistra, M. P.; Kersting, S.; Gosriwatana, I.; Lu, S.; Nijhoff-Schutte, J.; Hider, R. C.; Marx, J. J. M. Nontransferrin-Bound Iron in the Plasma of Haemodialysis Patients after Intravenous Iron Saccharate Infusion. *Eur J Clin Invest* **2002,** *32*, 36–41.

33. Espósito, B. P.; Breuer, W.; Slotki, I.; Cabantchik, Z. I. Labile Iron in Parenteral Iron Formulations and its Potential for Generating Plasma Nontransferrin-Bound Iron in Dialysis Patients. *Eur J Clin Invest* **2002,** *32*, 42–49.

34. Kletzmayr, J.; Sunder‑Plassmann, G.; Hörl, W. H. High Dose Intravenous Iron: A Note of Caution. *Nephrol Dial Transplant* **2002,** *17* (6), 962–965.

35. Besarab, A.; Coyne, D. W. Iron Supplementation to Treat Anemia in Patients with Chronic Kidney Disease. *Nature Rev Nephrol* **2010,** *6* (12), 699–710.

36. Bates, G. W.; Schlabach, M. R. The Reaction of Ferric Salts with Transferrin. *J Biol Chem* **1973,** *248* (9), 3228–3232.

37. Bates, G. W.; Schlabach, M. R. The Nonspecific Binding of Fe3+ to Transferrin in the Absence of Synergistic Anions. *J Biol Chem* **1975,** *250* (6), 2177–2181.

38. Agarwal, R. Transferrin Saturation with Intravenous Irons: An In Vitro Study. *Kidney Int* **2004,** *66* (3), 1139–1144.

39. Van Wyck, D.; Anderson, J.; Johnson, K. Labile Iron in Parenteral Iron Formulations: A Quantitative and Comparative Study. *Nephrol Dial Transplant* **2004,** *19* (3), 561–565.

40. Nemeth, E.; Tuttle, M. S.; Powelson, J.; Vaughn, M. B.; Donovan, A.; Ward, D. M.; Ganz, T.; Kaplan, J. Hepcidin Regulates Cellular Iron Efflux by Binding to Ferroportin and Inducing Its Internalization. *Science* **2004,** *306* (5704), 2090–2093.

41. Verga Falzacappa, M. V.; Muckenthaler, M. U. Hepcidin: Iron-Hormone and Anti-Microbial Peptide. *Gene* **2005,** *364*, 37–44.

42. Malluche, H. H.; Mawad, H. Management of Hyperphosphataemia of Chronic Kidney Disease: Lessons from the Past and Future Directions. *Nephrol Dial Transplant* **2002,** *17* (7), 1170–1175.

43. Di Marco, G. S.; Hausberg, M.; Hillebrand, U.; Rustemeyer, P.; Wittkowski, W.; Lang, D.; Pavenstadt, H. Increased Inorganic Phosphate Induces Human Endothelial Cell Apoptosis In Vitro. *Am J Phys* **2008,** *294* (6), F1381–F1387.

44.   Friedman, E. A. Consequences and Management of Hyperphosphatemia in Patients with Renal Insufficiency. In *Kidney International Supplement*, Nature Publishing Group: 2005; pp s1–s7.

45.   Tonelli, M.; Pannu, N.; Manns, B. Drug Therapy: Oral Phosphate Binders in Patients with Kidney Failure. *N Engl J Med* **2010,** *362* (14), 1312–1324.

46.   Boukhalfa, H.; Anderson, D.; Mietzner, T.; Crumbliss, A. Kinetics and Mechanism of Iron Release from the Bacterial Ferric Binding Protein *n*Fbp: Exogenous Anion Influence and Comparison with Mammalian Transferrin. *J Biol Inorg Chem* **2003,** *8* (8), 881–892.

47.   Schlabach, M. R.; Bates, G. W. Synergistic Binding of Anions and Fe^{3+} by Transferrin - Implications for Interlocking Sites Hypothesis. *J Biol Chem* **1975,** *250* (6), 2182–2188.

48.   Dhungana, S.; Taboy, C. l. H.; Anderson, D. S.; Vaughan, K. G.; Aisen, P.; Mietzner, T. A.; Crumbliss, A. L. The Influence of the Synergistic Anion on Iron Chelation by Ferric Binding Protein, a Bacterial Transferrin. *PNAS* **2003,** *100* (7), 3659–3664.

49.   Anderson, G.; Vulpe, C. Mammalian Iron Transport. *Cell Mol Life Sci* **2009,** *66* (20), 3241–3261.

50.   De Domenico, I.; Ward, D. M.; di Patti, M. C. B.; Jeong, S. Y.; David, S.; Musci, G.; Kaplan, J. Ferroxidase Activity is Required for the Stability of Cell Surface Ferroportin in Cells Expressing GPI-Ceruloplasmin. *EMBO J* **2007,** *26* (12), 2823–2831.

51.   Johnson, J.; Kenealey, J.; Hilton, R. J.; Brosnahan, D.; Watt, R. K.; Watt, G. D. Non-Reductive Iron Release from Horse Spleen Ferritin Using Desferoxamine Chelation. *J Inorg Biochem* **2011,** *105*, 202–207.

52.   Santambrogio, P.; Levi, S.; Cozzi, A.; Rovida, E.; Arosio, P. Production and Characterization of Recombinant Heteropolymers of Human Ferritin H and L Chains. *J Biol Chem* **1993,** *268*, 12744–12748.

53.   Hirose, M. The Structural Mechanism for Iron Uptake and Release by Transferrins. *Biosci Biotechnol Biochem* **2000,** *64* (7), 1328–1336.

54.   Williams, J.; Elleman, T. C.; Kingston, I. B.; Wilkins, A. G.; Kuhn, K. A. The Primary Structure of Hen Ovotransferrin. *Eur J Biochem* **1982,** *122* (2), 297–303.

55.   Anderson, B. F.; Baker, H. M.; Dodson, E. J.; Norris, G. E.; Rumball, S. V.; Waters, J. M.; Baker, E. N. Structure of Human Lactoferrin at 3.2-A Resolution. *PNAS* **1987,** *84* (7), 1769–1773.

56.   Anderson, B.; Baker, H.; Norris, G.; Rice, D.; Baker, E. Structure of Human Lactoferrin - Crystallographic Structure-Analysis and Refinement at 2.8-A Resolution. *J Mol Biol* **1989,** *209*, 711–734.

57.   Hall, D. R.; Hadden, J. M.; Leonard, G. A.; Bailey, S.; Neu, M.; Winn, M.; Lindley, P. F. The Crystal and Molecular Structures of Diferric Porcine and Rabbit Serum Transferrins at Resolutions of 2.15 and 2.60 Angstrom, Respectively. *Acta Crystallogr, Sect D* **2002,** *58*, 70–80.

58.   Lambert, L.; Perri, H.; Halbrooks, P.; Mason, A. Evolution of the Transferrin Family: Conservation of Residues Associated with Iron and Anion Binding. *Comp Biochem Physiol* **2005,** *142*, 129–141.

59.   Aisen, P. Transferrin, the Transferrin Receptor, and the Uptake of Iron by Cells. *Metal Ions in Biol Syst* **1998,** *35*, 585–631.

60.   Gelb, M. H.; Harris, D. C. Correlation of Protein Release and Ultraviolet Difference Spectra Associated with Metal-Binding by Transferrin. *Arch Biochem Biophys* **1980,** *200* (1), 93–98.

61.   Suber, L.; Foglia, S.; Fiorani, D.; Romero, H.; Montone, A.; Roig, A.; Casas, L. Synthesis, Morphological-Structural Characterization and Magnetic Properties of Amorphous Iron (III)-Oxyhydroxy-Phosphate Nanoparticles. *J Solid State Chem* **2004,** *177* (7), 2440–2448.

62.   Pollack, S.; Vanderhoff, G.; Lasky, F. Iron Removal from Transferrin - Experimental Study. *BBA* **1977,** *497* (2), 481–487.

63.   Yeh, K. Y.; Yeh, M.; Ma, Y. X.; Glass, J. Cooperation of Ferroportin 1 and Hephaestin on Iron Export from the Intestinal Epithelium to Systemic Circulation. *Gastroenterology* **2005,** *128*, A678–A678.

64.   De Domenico, I.; Ward, D. M.; Bonaccorsi di Patt, M. C.; Jeong, S. Y.; David, S.; Musci, G.; Kaplan, J. Hepcidin-Independent Regulation of Ferroportin: A Novel Role for Ceruloplasmin in Iron Export. *Am J Hematol* **2007,** *82* (6), 511–511.

65.   Eisenstein, R. S. Discovery of the Ceruloplasmin Homologue Hephaestin: New Insight into the Copper/Iron Connection. *Nutr Rev* **2000,** *58* (1), 22–26.

66.   Harris, D. C.; Aisen, P. Facilitation of Fe(II) Autoxidation by Fe(3) Complexing Agents. *BBA* **1973,** *329* (1), 156–158.

67.   Bakker, G. R.; Boyer, R. F. Iron Incorporation into Apoferritin - The Role of Apoferritin as a Ferroxidase. *J Biol Chem* **1986,** *261* (28), 3182–3185.

68.   Levi, S.; Santambrogio, P.; Albertini, A.; Arosio, P. Human Ferritin H-Chains can be Obtained in Nonassembled Stable Forms Which Have Ferroxidase Activity. *Febs Letters* **1993,** *336* (2), 309–312.

69.   Cheng, Y. G.; Chasteen, N. D. Role of Phosphate in Initial Iron Deposition in Apoferritin. *Biochemistry* **1991,** *30* (11), 2947–2953.

70.   Aitken-Rogers, H.; Singleton, C.; Lewin, A.; Taylor-Gee, A.; Moore, G. R.; Le Brun, N. E. Effect of Phosphate on Bacterioferritin-Catalysed Iron(II) Oxidation. *J Biol Inorg Chem* **2004,** *9* (2), 161–170.

71.   Polanams, J.; Ray, A.; Watt, R. Nanophase Iron Phosphate, Iron Arsenate, Iron Vanadate, and Iron Molybdate Minerals Synthesized within the Protein Cage of Ferritin. *Inorg Chem* **2005,** *44*, 3203–3209.

72.   Orino, K.; Kamura, S.; Natsuhori, M.; Yamamoto, S.; Watanabe, K. Two Pathways of Iron Uptake in Bovine Spleen Apoferritin Dependent on Iron Concentration. *Biometals* **2002,** *15* (1), 59–63.

CHAPTER 5: THE ROLE OF FERRITIN IN CHRONIC KIDNEY DISEASE

Abstract

Iron loading into ferritin was studied in the presence of physiological serum phosphate concentrations (1 mM), elevated serum concentrations (2.5–5 mM), and intracellular concentrations of phosphate (10 mM). Experiments used horse spleen ferritin to represent cytosolic ferritin and also as a serum ferritin mimic because of the high L ferritin content. Results show that both ferritin and phosphate are capable of stimulating the oxidation of Fe^{2+}, as detected by both oximetry and spectrophotometric assays. A competing side reaction was identified where a soluble iron(III)-phosphate complex forms outside ferritin. The iron(III)-phosphate complex was characterized by electron microscopy (EM) and atomic force microscopy (AFM), which revealed spherical nanoparticles between 20–200 nm. The iron(III)-phosphate complex is difficult to separate from ferritin and a new purification method was devised to separate this complex from ferritin. Elemental analysis on ferritin samples separated from the iron(III)-phosphate complex shows that as the phosphate concentration increases, iron loading into ferritin decreases. The composition of the mineral that forms in ferritin has a higher iron/phosphate ratio (~1:1) than ferritin purified from tissue (~10:1). Similar iron loading experiments were performed using homopolymers of H or L ferritin. H ferritin showed significantly better iron loading in the presence of elevated phosphate. The ferroxidase center efficiently competes with phosphate for the binding and oxidation of Fe^{2+}. Phosphate significantly inhibited iron loading into L ferritin, due to the lack of the ferroxidase center in this homopolymer.

Introduction

In the previous chapter, we showed that phosphate disrupts the ability of transferrin to bind iron. For patients with chronic kidney disease (CKD) this can have serious implications. Remember that the markers associated with CKD are increased serum phosphate levels, increased non-transferrin bound iron (NTBI), decreased transferrin saturation (TSAT), increased oxidative damage and inflammation, and increased serum ferritin levels. The increased serum phosphate levels may result in a cascade of events that ultimately lead to kidney failure. The one marker listed above that may seem somewhat out of place is the rise in serum ferritin levels. This chapter shows our efforts to understand why serum ferritin levels may be increased in patients with CKD. Because an extensive introduction was presented in the previous chapter, the reader is referred there for an understanding of iron metabolism and specifics of CKD.

Serum ferritin concentrations increase during inflammation as part of the acute-phase response.[1, 2] Hepcidin is also an inflammatory response protein that is expressed in order to limit iron export from cells. Considering that hepcidin functions to inhibit microbial growth by decreasing the serum iron concentration, it is logical that ferritin might be expressed in the serum to bind and sequester iron inside its 24-subunit protein shell to prevent the formation of ROS.[3-5] Another interesting observation is that for CKD patients with elevated serum phosphate concentrations and low TSAT, ferritin has been shown to have increased rates of iron binding in the presence of phosphate.[6] Based on these observations, we propose that serum ferritin is expressed to bind iron during symptoms of CKD in order to bind and remove NTBI that results from the inhibition of iron loading into transferrin by phosphate.

Unfortunately, this hypothesis immediately faces challenges because the effectiveness of iron binding by ferritin in the serum has been questioned. Early studies evaluating the iron

content of serum ferritin from patients with thalassemia and hemochromatosis showed a very low iron content in serum ferritin (185–540 Fe/ferritin).[7-10] Because of the elevated iron levels in these patients, it was concluded that ferritin does not bind or carry iron in the serum.

Recently, the iron content of serum ferritin was measured in healthy individuals (~1,100–1,200 Fe/ferritin) and patients with inflammation (~800 Fe/ferritin).[11, 12] The iron content of ferritin from these individuals is significantly higher than from patients with hemochromatosis and thalassemia. Furthermore, serum ferritin levels increase 4–10-fold in patients with inflammation.[2, 13] The increase in serum ferritin concentration also means an increase in total iron carried by serum ferritin, which in several studies increased approximately four-fold (normal individuals 110–140 ng ferritin/mL vs. inflammation patients 450–500 ng ferritin/mL).[11, 12] The significant increase in total serum iron in the form of serum ferritin might represent a previously unknown role for ferritin in iron transport during inflammation. This observation challenges the paradigm that serum ferritin carries very little iron under all conditions. Instead, the previous assertions that serum ferritin carries very little iron may only apply specifically to conditions of hemochromatosis and thalassemia.

In fact, the role of serum ferritin may be more significant than previously understood. A recent study shows that serum ferritin, rather than transferrin, delivers iron to kidney cells during development.[14] A recently discovered ferritin receptor Scara5[15] was identified and was shown to use serum ferritin as a source of iron for the cells. Because little is understood about how ferritin binds iron in the serum, the present study was undertaken to evaluate iron loading into ferritin under conditions found in the serum.

This work examines the ability of ferritin to bind iron under various phosphate concentrations. Ferritin iron-loading experiments were conducted in the presence of

physiological phosphate concentrations (1 mM) and elevated phosphate concentrations similar to those found in CKD patients (2.5–5 mM). For completeness, iron loading in the presence of intracellular phosphate concentrations (10 mM) was also performed. Phosphate stimulates the rate of iron oxidation both in the presence and absence of ferritin. Iron loading in the presence of phosphate produces a mineral core that has a higher phosphate content (~1–2 $Fe:PO_4^{3-}$) than ferritin isolated from healthy tissue (~10 $Fe:PO_4^{3-}$). High phosphate concentrations prevent efficient loading of iron into ferritin because a side reaction leads to the formation of a large soluble iron-phosphate complex that forms outside of ferritin. H ferritin can compete effectively with the side reaction because the ferroxidase center allows H ferritin to rapidly bind and oxidize the ferritin. Iron loading into L ferritin is significantly inhibited by phosphate because the iron-phosphate complex oxidizes the iron faster than L ferritin and once the iron-phosphate complex is formed it is inaccessible to ferritin. This complex may form in vivo at elevated phosphate concentrations and contribute to the formation of NTBI and oxidative damage observed in CKD patients.

Materials and Methods

Materials. Horse spleen apoferritin was purchased from Sigma. Recombinant human heavy chain ferritin (rHuHF) and human light chain ferritin (rHuLF) were expressed and purified as described in Chapter 3.[16, 17]

Iron Loading. Ferritin samples were reconstituted with iron alone or were reconstituted with iron in the presence of phosphate, using the following procedure. An apoferritin solution (1 μM) was prepared in 0.05 M MOPS buffer, pH 7.4, 0.05 M NaCl. Phosphate was added to the apoferritin solution to achieve the desired concentration. This solution was stirred aerobically in a cuvette in an Agilent 8453 UV-Visible spectrophotometer and Fe^{2+} ions were added from an

anaerobic 0.010 M FeSO$_4$ stock solution to attain the desired iron loading. Iron loading was monitored spectrophotometrically at 310 nm versus time.[18, 19] Control samples with no phosphate or no ferritin were prepared using the identical procedure. Ferritin with higher iron loadings were prepared by adding 100 iron/ferritin in a stirred vial and allowing the iron to incubate with the ferritin for 30 minutes. This process was repeated until the desired iron/ferritin load was achieved. The same procedure was followed for the oxygen electrode assays. The spectrum of the resulting samples and control reactions were recorded on the spectrophotometer. To remove unbound ions, samples and controls were passed over a GE-Healthcare PD-10 Sephadex G-25 column and the elution profile of these samples and controls were recorded by monitoring the elution peaks at 310 nm.

Elemental Analysis. The following procedure was used to prepare ferritin samples for elemental analysis. After the addition of iron and phosphate, the samples were centrifuged (3,200 x g for 10 minutes) to remove any precipitated protein or small insoluble complexes. The supernatant (2.0 mL) was treated with 0.5 mL of Bio-Rad Bio-Gel P-10 gel slurry (75 g in 100 mL total volume) and agitated for 30 minutes. The samples were then centrifuged at (3,200 x g for 10 minutes) and the supernatant collected. The supernatant was centrifuged through Amicon Ultra–4 centrifugal filters with a 100,000 molecular weight cut-off for 5 minutes at 3,200 x g. After the first centrifugation step, the concentrated retentate was diluted with 3 mL of 0.05 M MOPS buffer at pH 7.5 with 0.05 M NaCl and centrifuged again. The concentration and dilution steps were repeated two additional times to remove any remaining phosphate in the sample. Finally, the concentrated retentate was resuspended in 1.0 mL of 0.05 M MOPS buffer at pH 7.5 with 0.05 M NaCl.

The iron content of the samples was analyzed by inductively coupled plasma emission (ICP) on a PerkinElmer Optima 2000 DV or by formation of the $[Fe(2,2'\text{-bipiridyl})_3]^{2+}$ complex ($\varepsilon_{520} = 8,400\ M^{-1}\ cm^{-1}$) after chemical reduction of the iron with sodium dithionite. Protein concentrations were determined using the Lowry Method.[20] The phosphate content was measured using a modified phospho-molybdate assay[21] that required the addition of 2% SDS to keep the ferritin protein solubilized. Without the addition of SDS, a blue flocculent precipitate formed that was presumably denatured ferritin as this precipitate did not occur in the absence of ferritin. SDS was shown to solubilize the ferritin precipitate and to have no effect on the standard curve of the assay.

Electron Microscopy. Samples were prepared and placed on charged ultrathin carbon film supported by a lacey carbon film on a 400 mesh copper grid (Ted Pella, Inc.). The grids were charged using a discharge tube designed in the laboratory of Dr. David Belnap. A 3.5 µL sample was incubated on the grid for 30–60 seconds to allow adherence of the protein or particles to the grid. The liquid was then wicked off, and the grid was rinsed in water. The samples with ferritin were then negative stained by adding 3.5 µL of a 1% solution of uranyl acetate to allow visualization of the protein. Iron-phosphate samples were not stained, as the samples lack protein and are electron dense (iron-containing). The grids were rinsed one more time in water and allowed to dry. The grids were then analyzed using a Tecnai F30 TEM, 140 kV.

Results

Previous studies of iron loading into ferritin in the presence of phosphate concluded that phosphate stimulates the rate of iron loading into ferritin.[22-25] Phosphate is a natural constituent of ferritin isolated from tissue[26] and alters the mineral core properties of ferritin.[27] The current study was conducted to examine the effect of phosphate on iron loading into ferritin. In this way,

we desired to determine whether ferritin expression can help minimize the inhibitory effect that phosphate has on transferrin (see Chapter 4). Experiments were conducted to mimic phosphate concentrations in serum from healthy individuals (1.0 mM), CKD patients (>2.5 mM), and at intracellular phosphate concentrations (10 mM). Iron loading was monitored by spectrophotometry, oximetry, and elemental analysis of the purified samples.

Spectrophotometry. The absorbance change at 310 nm is a common assay to monitor iron loading into ferritin.[18, 28, 29] These results are shown in Figure 5–1. To simplify the graph, only the data for 1 mM and 10 mM phosphate are shown to represent the extremes of the range used in this work. The open symbols represent the control reactions performed in the absence of ferritin. The first control (open square) shows the slow oxidation of Fe^{2+} to Fe^{3+} in 0.05 M MOPS buffer pH 7.5 in the absence of phosphate or ferritin. The formation of an orange precipitate, $Fe(OH)_3$, confirmed the oxidation of Fe^{2+} to Fe^{3+} in this reaction. When 1 mM or 10 mM phosphate was present (open circle and open triangle), the initial rate of the reaction was dramatically increased 3.5-fold or 30-fold respectively, compared to the rate of iron oxidation in buffer alone (Table 5–1). In the presence of phosphate, no visible precipitate was observed, which was surprising considering the K_{sp} values presented in Equations 1 and 2. The lack of a precipitate and the change in absorbance at 310 nm implied that a soluble iron-phosphate complex formed.
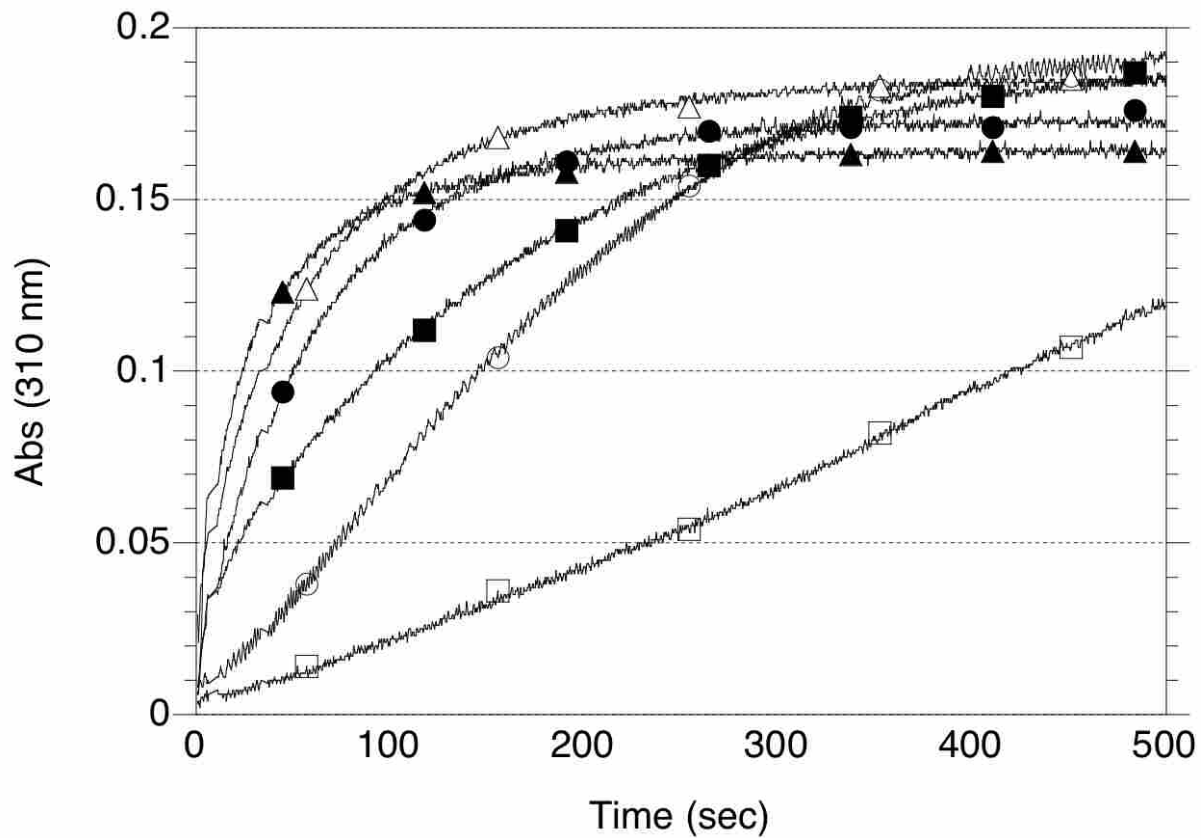
Figure 5-1. Spectrophotometric assay. Each reaction was performed in 0.05 M Mops buffer pH 7.5 and contain either no phosphate or the indicated phosphate concentration. Fe^{2+} ions (anaerobic 0.01 M $FeSO_4$) were added with a Hamilton syringe to start the reaction. Open symbols represent controls without ferritin and closed symbols represent reactions with ferritin. Samples are □-no phosphate, ■-no phosphate + ferritin, ○-1mM phosphate, ●-1 mM phosphate + ferritin, △-10 mM phosphate, ▲-10 mM phosphate + ferritin.

Table 5-1. Initial rates of iron loading.

	Sample	Initial Rate (ΔAbs/sec)	Fold increase
	UV/Vis*		
1	Iron added to MOPS buffer	0.0002	0
2	1 mM phosphate control	0.0007	3.5
3	10 mM phosphate control	0.0061	30.5
4	Ferritin	0.0012	6
5	Ferritin in 1 mM phosphate	0.0057	28.5
6	Ferritin in 10 mM phosphate	0.0136	68
	Oxygen electrode[+]	**Initial Rate (nmole O_2 consumed/min)**	**Fold Increase**
1	Iron added to MOPS buffer	0.14	0
2	1 mM phosphate control	1.04	7.2
3	10 mM phosphate control	4.33	30.2
4	Ferritin	1.03	7.2
5	Ferritin in 1 mM phosphate	2.99	20.9
6	Ferritin in 10 mM phosphate	6.31	44.1

*An apoferritin solution (1 μM) was prepared in 0.05 M MOPS buffer pH 7.4, 0.05 M NaCl. Phosphate was added to the apoferritin solution to achieve the desired concentration. This solution was stirred aerobically in a cuvette in an Ocean Optics Chem 2000 UV-Visible spectrophotometer and Fe^{2+} ions were added from an anaerobic 0.010 M $FeSO_4$ stock solution to attain the desired iron loading. Iron loading was monitored spectrophotometrically at 310 nm versus time. Control samples with no phosphate or no ferritin were prepared using the identical procedure. Initial rates were calculated from the first 15 seconds of the reaction.

[+]Identical experimental procedures were used for the oxygen electrode assays.

These results suggest a potential side-reaction might be occurring during the ferritin iron loading reactions. To test this, more controls were performed to understand the solution chemistry of iron and phosphate under these conditions. The iron and phosphate concentrations were varied to determine when soluble complexes and solid, insoluble iron-phosphate complexes form. A bluish-green precipitate was observed with a 1:1 iron to phosphate ratio, but as the phosphate concentration was increased, less precipitate was observed. When the phosphate

concentration was greater than 3-fold, the amount of precipitate decreased significantly and a 10-fold excess of phosphate produced very little precipitate. The phosphate to iron ratios in the assay shown in Figure 5–1 are in the range from ~20 to ~200 phosphate/iron, consistent with the formation of a soluble complex rather than a precipitate.

The spectrum of ferritin, apoferritin, and the iron-phosphate complex were recorded and are shown in Figure 5–2. Apoferritin shows the typical protein absorbance at 280 nm. Ferritin loaded with iron or iron and phosphate has a peak at 280 nm as well as a shoulder trailing into the visible region between 300–450 nm, characteristic of iron mineralization inside ferritin. The iron-phosphate complex has a peak near 280 nm that trails off into the visible region in a similar fashion as ferritin containing iron. The spectra show that holoferritin and the iron-phosphate complex both have significant absorbance at 310 nm. Because this is the wavelength used to monitor the formation of iron in ferritin, the kinetics reported here and in previous works may be monitoring not only the deposition of iron into ferritin, but also the formation of the soluble iron-phosphate complex.
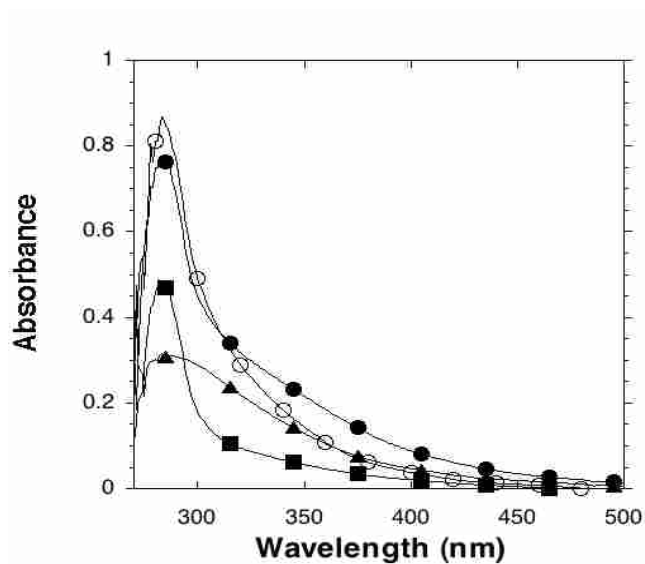

Figure 5-2. Spectra of ferritin and iron-phosphate complex samples. ■-apoferritin, ●-holoferritin, ○-ferritin reconstituted by adding Fe^{2+} in the presence of 1 mM phosphate, and ▲-the iron-phosphate complex prepared by

adding Fe^{2+} to a 1.0 mM phosphate solution. Samples were prepared to have identical ferritin concentrations. Spectra were recorded after samples were prepared and without any centrifugation steps or separation of unbound ions. This mimics the conditions observed in the kinetic trials.

Because an iron-phosphate complex may form outside of ferritin, and because the absorbance peak overlays the absorbance of holoferritin, the spectrophotometric assay does not confirm that the iron is loading into ferritin. To determine if iron and phosphate were actually loaded into ferritin, we developed a method to separate ferritin from the iron-phosphate complex and performed elemental analysis on the purified ferritin to determine the iron and phosphate content of the samples.

Separating the Iron–Phosphate Complex from Ferritin. To determine whether the iron-phosphate complex forms outside of ferritin during iron loading, the following procedure was developed. Ferritin samples and controls were prepared as described for the spectrophotometric assay (Figure 5–1) and were centrifuged to remove insoluble material. The supernatant was loaded onto a GE Healthcare PD-10 desalting column. The iron control without ferritin or phosphate present precipitated as an orange solid of $Fe(OH)_3$ during the centrifugation step and the supernatant was colorless. When the supernatant of this sample was passed over a GE Healthcare PD-10 desalting column, no elution peak was observed, consistent with all of the iron precipitating prior to chromatography (Figure 5–3). The ferritin sample prepared in the absence of phosphate had no precipitate after the centrifugation step and eluted in the void volume of the GE Healthcare PD-10 desalting column. Both the 1 mM and 5 mM phosphate controls with iron but no ferritin (representing the iron-phosphate complex) had very small greenish-white pellets. When the supernatant of these samples was passed over the GE Healthcare PD-10 desalting column, elution peaks were observed near the void volume indicating the presence of large

molecular weight species (Figure 5–3). Ferritin, with a molecular mass of ~450,000 Da, should clearly separate from Fe^{2+}, Fe^{3+}, or phosphate if they exist as ions or as small complexes. The results from the PD-10 column suggest that a large molecular mass iron-phosphate complex is formed. This also demonstrates that using a column to separate ferritin from the iron-phosphate complex is not achievable, because they co-elute.
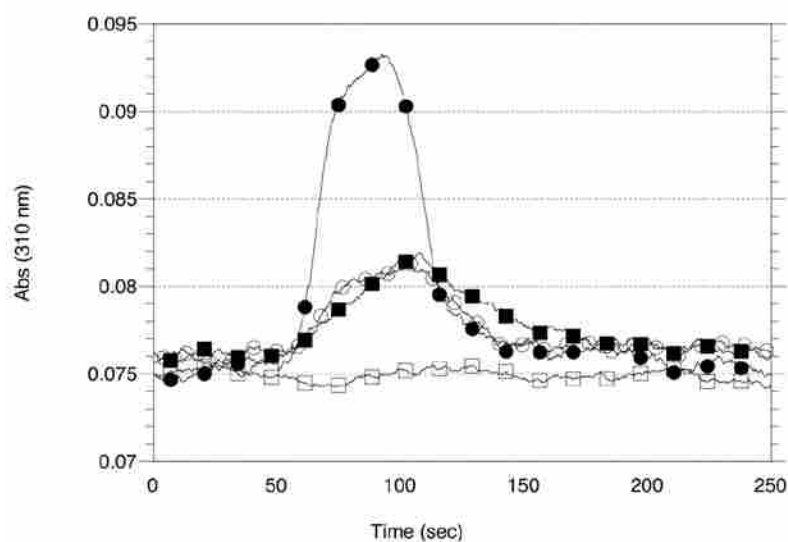

Figure 5-3. Gel filtration of ferritin or Fe-phosphate complexes on a GE Healthcare PD-10, G-25 column. ●-Fe(II) added to apoferritin, ○-Fe(II) added to 1 mM phosphate, ■-Fe(II) added to 5 mM phosphate, □-Fe(II) added to 0.05 M MOPS buffer, pH 7.5 as a negative control. The samples were centrifuged after iron was added to remove insoluble iron precipitates. After centrifugation, the supernatant was loaded onto a GE Healthcare PD-10 column and the eluting species detected as they eluted at 310 nm.

Centrifugal ultrafiltration devices were also used to confirm that the iron-phosphate controls formed large molecular weight species. Control samples were prepared by adding Fe^{2+} to solutions containing 1 mM or 5 mM phosphate. These samples were incubated for the appropriate amount of time to allow iron oxidation and complex formation. The solutions were loaded onto Amicon Ultra centrifugal filter devices with a molecular weight cut-off of 100 kDa.

106

After centrifugation, the retentate and the flow-through were analyzed for iron by the addition of 2,2'-bipyridyl, which specifically binds to Fe^{2+}. Neither the flow-thru nor retentate changed color upon 2,2'-bipyridyl addition, indicating that the Fe^{2+} ions had been oxidized to Fe^{3+}. When sodium dithionite was added to both chambers, the flow-through remained colorless but the retentate turned red, indicating that the filter retained the iron-phosphate complex. These data are consistent with the results from the GE healthcare PD-10 column (Figure 5–3) and indicate that the iron-phosphate complex is a large, soluble species. The results also show that iron is in the iron(III) oxidation state.

The iron-phosphate complex was separated from ferritin using a Bio-Rad P-10 Gel. A 2.5 cm x 15 cm column of Bio-Rad P-10 was prepared and equilibrated with 0.05 M MOPS buffer, pH 7.5 with 0.05 M NaCl. Ferritin passed through the column, whereas the iron-phosphate complex bound tightly to the column. Any remaining free phosphate could be removed from the ferritin samples by passing the sample over a GE Healthcare PD-10 column or by repeated concentration and dilution using an Amicon Ultra centrifugal filter system as described in Materials and Methods. The bound iron-phosphate complex could be decomposed and released from the Bio-Rad P-10 resin by passing an anaerobic solution of 1 mM sodium dithionite and 0.5 mM 2,2'-bipyridyl over the column, which chemically reduced and chelated the iron. Subsequent experiments showed that the addition of 0.5 mL of 70% Bio-Rad P-10 slurry in water to 2.0 mL samples specifically and quantitatively bound the iron-phosphate complex. This procedure provided a convenient method to rapidly remove iron-phosphate complexes from solution and permitted elemental analysis to be performed on ferritin samples. Samples prepared by removing the iron-phosphate complex using the Bio-Rad P-10 column or by using the batch Bio-Rad P-10

precipitation method gave the same results by elemental analysis, confirming the effectiveness of the latter method.

Preliminary characterization of this complex shows a polynuclear complex with a ratio of about two irons to three phosphates. Gel filtration and Amicon filtration experiments show the complex to be large. Electron microscopy or atomic force microscopy of the sample shows particles ranging from 20–200 nm (Figure 5–4). Because the phosphate protonation at pH 7.5 is a mixture of HPO_4^{2-} and $H_2PO_4^{-}$, changes in pH will be important in how much of this complex forms. A careful characterization of the stoichiometry, pH of formation, and size of this complex as well as reactivity toward catalyzing the formation of reactive oxygen species is underway in our laboratory.
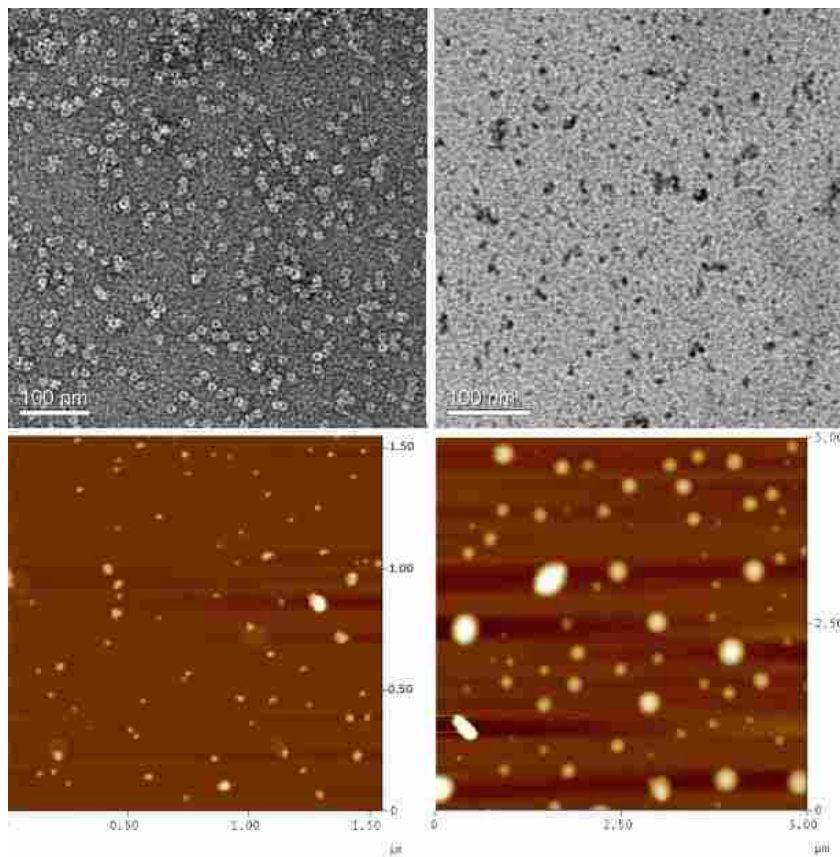
Figure 5-4. Electron micrographs of negative stained (uranyl acetate) ferritin (top left), compared to non-stained iron-phosphate complex (top right). Comparative atomic force micrographs are shown of ferritin (bottom left) and of

108

the iron-phosphate complex (bottom right). The iron-phosphate complex was formed as described and the supernatant was placed on an EM or AFM grid. The particles are around 20–200 nm in diameter.

Iron Loading into Ferritin. Once conditions were established to separate the iron-phosphate complex from ferritin, elemental analysis was performed. A combined analysis of the initial rates of the reactions (Figure 5–1 and Table 5–1) and the actual iron loading of ferritin (Table 5–2) provides valuable insight into the iron loading process in the presence of phosphate.

Table 5-2. Elemental analysis of ferritin samples loaded in the absence or presence of phosphate.

Theoretical Loading	Iron/Ferritin	Phosphate/Ferritin	Iron/Phosphate
100 Iron/Ferritin			
No phosphate	119 ±7	5.3 ± 0.4	24 ± 2
1 mM phosphate	67 ± 6	35.1 ± 1.2	2.0 ± 0.2
2.5 mM phosphate	54 ± 2	51.1 ± 0.6	1.1 ± 0.04
5 mM phosphate	33 ± 3	25.1 ± 1.4	1.4 ± 0.14
10 mM phosphate	25 ± 3	3.85 ± 0.5	6.6 ± 1.7
1,000 Iron/Ferritin			
No phosphate	1,069 ± 26	5.1 ± 0.4	210 ± 17
1 mM phosphate	752 ± 38	582 ± 24	1.3 ± 0.08
2.5 mM phosphate	692 ± 13	318 ± 19	2.1 ± 0.13
5 mM phosphate	232 ± 36	356 ± 67	0.7 ± 0.17
10 mM phosphate	84 ± 11	83 ± 20	1.01 ± 0.28

The initial rate of the reaction of Fe^{2+} with ferritin in the presence of physiological concentrations of phosphate (1 mM) is more than 4 times faster than ferritin iron loading without phosphate and is ~8 times faster than the control of 1 mM phosphate without ferritin (Figure 5–5). These data show that with normal serum phosphate concentrations, ferritin appears to load faster than without phosphate. Table 5–2 shows the actual deposition of the iron in ferritin and

shows that 67% and 75% of the iron was incorporated when 100 and 1,000 iron atoms were added to ferritin with 1 mM phosphate, respectively. The higher percentage of iron loading in the larger core is consistent with data showing that phosphate on the mineral core surface assists iron binding and oxidation.[30]
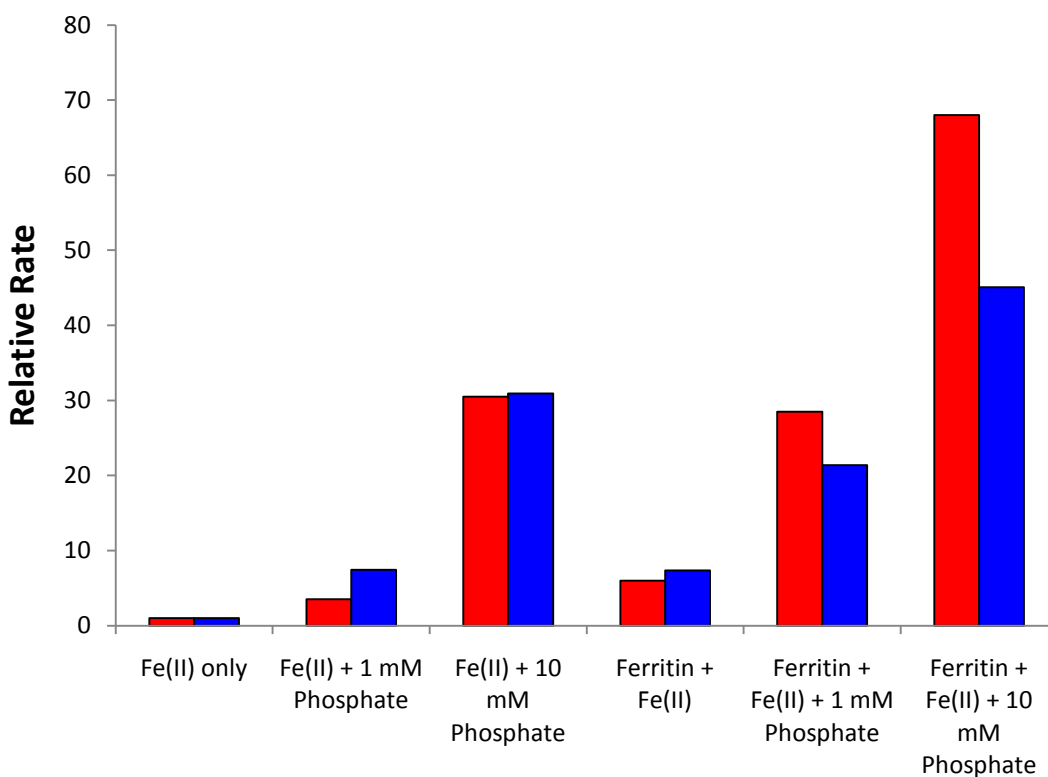

Figure 5-5. Relative rates of either iron oxidation (**red**) or oxygen consumption (**blue**). The oxygen consumption was determined as a secondary means to support the iron oxidation data, and shows a similar trend. Samples are the same as those shown in Table 5–1.

Figure 5–5 also shows that the reaction of ferritin in 10 mM phosphate displays the fastest initial rate and is ~2.4-times faster than the 1 mM phosphate reaction with ferritin present, and is ~2 times faster than the 10 mM phosphate control without ferritin. The elevated phosphate concentration improves the collision frequency of phosphate with iron in solution and competes with the ferritin for iron binding. This is confirmed in Table 5–2 where iron loading into ferritin

is significantly inhibited by the presence of 10 mM phosphate. This could be anticipated by comparing the reaction profile curves for 10 mM phosphate versus 10 mM phosphate and ferritin in Figure 5–1. The curves almost overlap, indicating that the iron-phosphate complex formation is very favorable under these conditions.

Previously, the addition of phosphate was shown to alter the absorbance properties of the iron core of ferritin.[24, 25] Figure 5–1 shows a decrease in final absorbance as phosphate concentration increases. This complicates the interpretation of the kinetic data because reactions with two different extinction coefficients are being compared. The combination of a changing extinction coefficient and a competing side-reaction (Figures 5–2 and 5–3) complicates the interpretation of the kinetic data. For this reason, Table 5–1 reports spectrophotometric data as change in absorbance versus time instead of change in molar concentration of product. Furthermore, the spectrophotometric assay may be measuring multiple steps in the iron loading process: the binding of iron to ferritin, the oxidation of iron at the ferroxidase center, and migration of the iron to the nucleation sites in the core. In an attempt to analyze the kinetics of iron loading by a more direct assay that would avoid these complications, we used oximetry to monitor the consumption of the reactant oxygen in the reaction.

Oximetry. Samples were prepared exactly as in Figure 5–1 and analyzed in a Hansatech Oxygraph oxygen electrode. Figure 5–6 shows the oximetry results. Controls prepared in the absence of ferritin are shown by open symbols and samples with ferritin are closed symbols. The control sample without ferritin or phosphate (open squares) shows that oxygen consumption (and therefore, iron oxidation) is slow. As the phosphate concentration is increased to 1 mM and 10 mM, the rate and extent of oxygen consumption increases. The initial rates from these experiments are summarized in Table 5–1. In the absence of ferritin, 1 mM and 10 mM

phosphate stimulate the rate of iron oxidation ~7-fold and ~30-fold, respectively compared to the reaction without phosphate (Figure 5–5). This is comparable to the ~4- and ~30-fold change in rate observed in the spectrophotometric assay for these controls. These results also demonstrate that phosphate significantly stimulates the rate of oxygen consumption and thus, iron oxidation, even in the absence of ferritin.
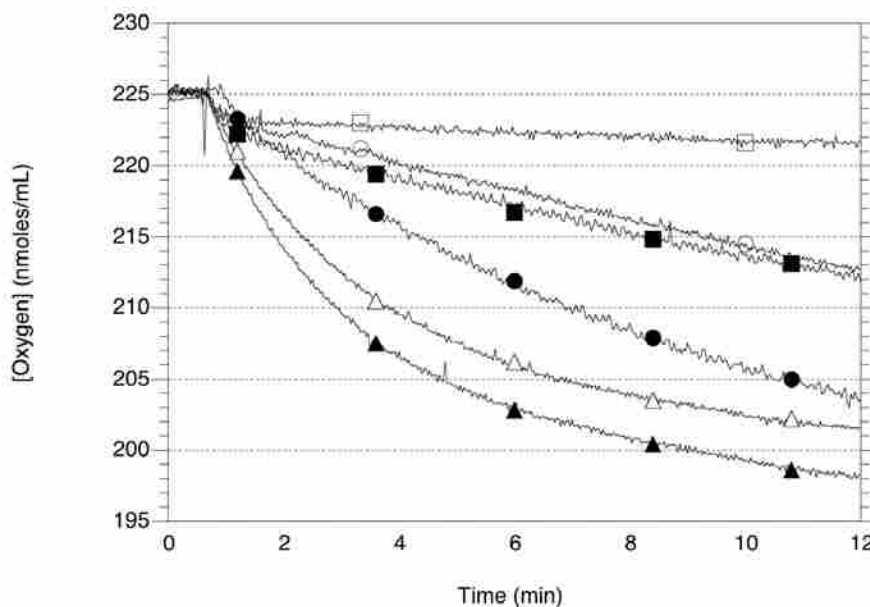

Figure 5-6. Oximetry assay. All reactions were performed in 0.05 M MOPS buffer, pH 7.5 and contain either no phosphate or the indicated phosphate concentration. Fe^{2+} ions (anaerobic 0.01 M $FeSO_4$) were added with a Hamilton syringe to start the reaction. Open symbols represent controls without ferritin and closed symbols represent reactions with ferritin. Samples are □-buffer only, ■-buffer + ferritin, O-1mM phosphate, ●-1 mM phosphate + ferritin, △-10 mM phosphate, ▲-10 mM phosphate + ferritin.

When the oximetry is performed with both ferritin and phosphate, the rate of oxygen consumption is faster than the comparable controls without ferritin (Figures 5–5 and 5–6 and Table 5–1). When ferritin and phosphate are present, the initial rate increases ~3- and ~6-fold for 1 mM and 10 mM phosphate, respectively versus the sample with ferritin and no phosphate. The

spectrophotometric assay showed ~4- and ~10-fold increase under the same conditions. Therefore, the general trends from these data show that both phosphate and ferritin stimulate the rate of iron oxidation. It appears that these data are consistent with the spectrophotometric data suggesting that the oxidation of the Fe^{2+} is the rate-limiting step for both iron loading into ferritin and the formation of the iron(III)-phosphate complex reactions. Because this is the case, both assays give the same results and the assays cannot distinguish a difference in kinetics between the ferritin iron loading and the formation of the iron-phosphate complex.

The iron(III)-phosphate complex is not a substrate for loading iron into ferritin. All attempts to use the pre-formed iron(III)-phosphate complex as a substrate for iron loading into apoferritin, including various reaction times and the presence of reducing agents,[31] were unsuccessful. Even with a large excess of iron, no more than a few iron atoms (~10/ferritin) could be loaded into ferritin. We conclude that under the conditions used, the iron(III)-phosphate complex is not a substrate for loading iron into ferritin.

Iron-Phosphate Mineralization in Ferritin. As discussed above, elemental analysis was performed to determine the extent of iron and phosphate loading into the ferritin interior (Table 5–2). Samples were prepared at two levels of iron loading: 100 iron/ferritin and 1,000 iron/ferritin. The phosphate concentrations present during iron loading were 1, 2.5, 5, and 10 mM. Table 5–2 shows that when iron was added in the absence of phosphate, essentially all of the iron was incorporated into ferritin at both low (100 iron/ferritin) and high (1,000 iron/ferritin) quantities. When the physiological concentration of serum phosphate (1 mM) was used, the efficiency of iron loading into ferritin decreased and only 67–75% of the iron was incorporated into ferritin. At 2.5 mM phosphate, approximately 50% of the iron deposited in the 100 Fe/ferritin sample and ~70% for the 1,000 iron/ferritin sample. When 5 mM phosphate was

present, iron loading was very poor, with approximately 20–30% of the iron loaded into ferritin, leaving 70–80% of the iron unbound by ferritin. Finally, 10 mM phosphate showed ~90% inhibition of iron loading into ferritin. At the lower phosphate concentrations, it appears that as the core gets larger, the efficiency of ferritin to bind and sequester iron improves (Figure 5–7). This effect is probably due to the autocatalytic iron binding and oxidation properties of the iron mineral core.[32] As the phosphate concentration increases, the larger amount of iron added to ferritin is less efficiently bound by ferritin. This suggests that at higher phosphate concentrations, the formation of the iron(III)-phosphate complex dominates the binding of iron. Thus, the early steps in core formation are critical for efficient iron loading into ferritin in the presence of phosphate. Consistent with this hypothesis is that H-chain ferritin containing the ferroxidase center may provide an important advantage in iron loading when phosphate is present.
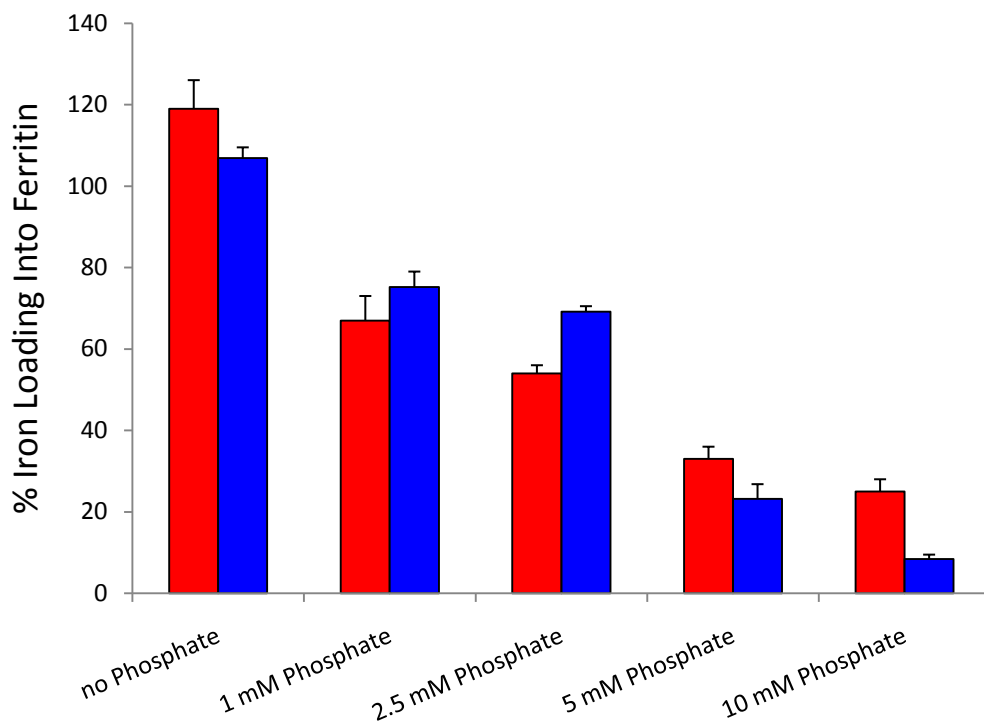
Figure 5-7. Comparative loading of iron into ferritin. Theoretical loadings of 100 Fe/ferritin (**red**) and 1,000 Fe/ferritin (**blue**), as described in Table 5–2. The general trend is that with increasing concentrations of phosphate there is a decreased level of iron loading into ferritin.

rHuHF and rHuLF. In order to better understand the effects of H and L chain ferritins, we used rHuHF and rHuLF, compared to iron loading in the presence of phosphate with horse spleen ferritin (90% L chain). Two subunits have evolved to create functional ferritin, the human heavy (H) and light (L) chain ferritins (see Chapter 1 for a discussion on the roles of the different ferritin isoforms).

Figure 5–8 shows loadings of iron into H and L chain ferritins in the presence and absence of phosphate. With rHuHF, the absence or presence of phosphate did not seem to affect the rate of iron oxidation and loading into ferritin. This suggests that the ferroxidase center of H chain ferritin is capable of oxidizing and sequestering iron faster than the iron(II)-phosphate complex can form and oxidize the iron. However, with rHuLF, the rate of iron oxidation increases significantly as the concentration of phosphate increases. This is consistent with the lack of a ferroxidase center in L chain ferritin, suggesting that phosphate out-competes L ferritin for Fe^{2+} to form the iron(II)-phosphate complex and oxidize the Fe^{2+}. As a control, the same studies were repeated in the absence of ferritin (data not shown). As the concentration of phosphate increases, the oxidation of iron increases, similar to the increases seen with the L chain ferritin. In the absence of both ferritin and phosphate, ferrous iron predictably oxidizes to ferric iron and precipitates out of solution. However, when phosphate is present, the oxidized iron does not precipitate out, again confirming that a soluble iron-phosphate complex forms. The other interesting observation is that we observe an increase at 310 nm, consistent with the oxidation of iron, even in the absence of ferritin. Thus, the formation of the iron-phosphate complex cannot easily be discerned from the oxidation and deposition of iron into ferritin.
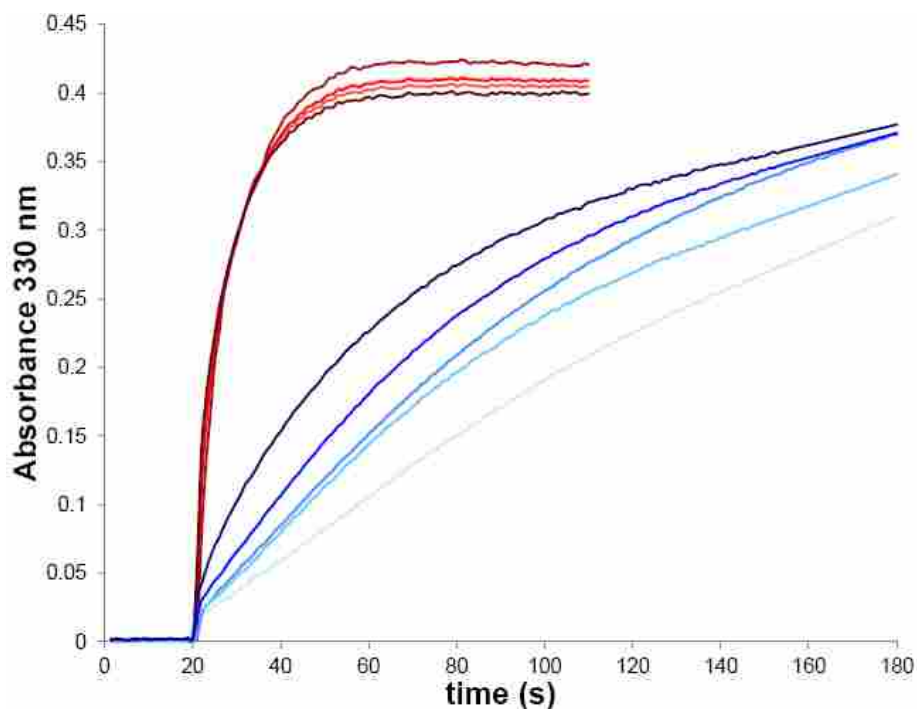
Figure 5-8. Kinetics of iron loading into H (**red**) or L (**blue**) ferritin with increasing concentrations of phosphate (0, 1, 2.5, 5, and 10, progressing from lighter to darker colors).

To determine whether the iron oxidized and loaded into ferritin or instead complexed with phosphate, we performed an elemental analysis on the samples, following purification, as previously described. The results of this analysis are summarized in Table 5–3. The data show that rHuHF does a better job of sequestering iron in the presence of phosphate than does rHuLF. However, rHuHF is unable to completely sequester iron in the presence of phosphate, and is capable of sequestering only ~54% in the presence of high phosphate concentrations. Nevertheless, this is significantly higher than loading by both rHuLF (only about 11%) and horse spleen ferritin (only about 21–27%, depending on core size) with similar phosphate concentrations. Unfortunately, it was difficult to observe this trend for varied core sizes because rHuHF is only capable of forming small iron cores, presumably because it lacks nucleation sites. Thus, only core sizes of around 500 iron atoms/ferritin were investigated in this study.

116

Table 5-3. Elemental analysis of rHuHF and rHuLF samples loaded in the absence or presence of phosphate.

Sample	Iron/Ferritin	Phosphate/Ferritin	Iron/Phosphate	Relative % Iron Loaded
rHuHF no Pi	391.63*	10.86	36.06	100
rHuHF 1mM Pi	239.14	27.69	8.64	61.06
rHuHF 2.5mM Pi	231.43	31.23	7.41	59.09
rHuHF 5mM Pi	212.88	40.18	5.30	54.36
rHuLF no Pi	471.15*	9.59	49.13	100
rHuLF 1mM Pi	97.95	16.77	5.84	20.79
rHuLF 2.5mM Pi	71.21	13.44	5.30	15.11
rHuLF 5mM Pi	53.12	5.46	9.73	11.27

*Theoretical loading of 500 iron atoms/ferritin were performed, and these numbers reflect experimental loading values as obtained from elemental analysis.

Discussion

Chronic kidney disease is characterized by severe oxidative damage, increased levels of NTBI, decreased TSAT levels, and elevated serum ferritin and serum phosphate levels. The work described in this chapter combined with the work in Chapter 4 may help to explain the interactions between these disrupted markers. Our proposed model is that elevated phosphate levels compete with transferrin for iron binding. The result is a build-up of NTBI in the form of iron(III)-phosphate. Iron in this form is capable of forming ROS that lead to oxidative damage. Our evidence shows that iron in the form of iron(III)-phosphate cannot be bound by transferrin, and we suggest that the body recognizes the elevated iron levels, and signals for ferritin expression. Ferritin is released into the serum in an attempt to bind iron and mitigate the effects of NTBI (Scheme 5–1).
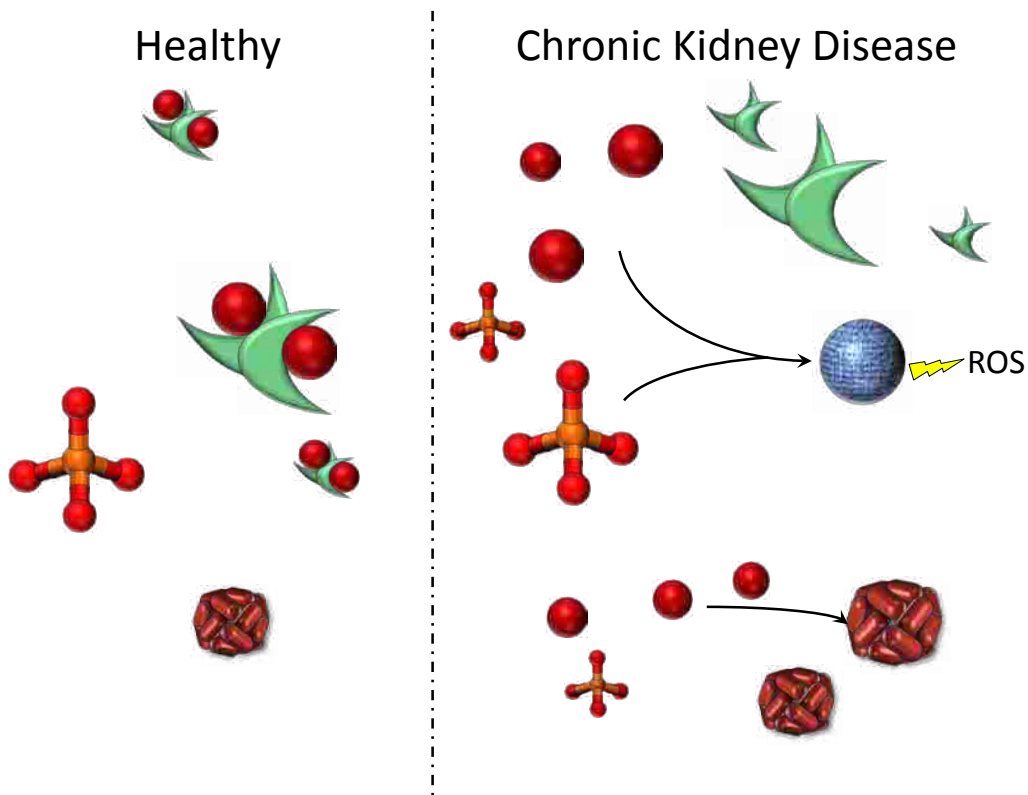
Scheme 5-1. Model of serum in healthy (left) and CKD patients (right). Transferrin is represented by the green half-moons, with TSAT levels decreasing in the diseased state. Iron is represented by the red spheres, and NTBI is represented by the blue sphere, with NTBI showing up in the diseased state, leading to oxidative damage through the generation of ROS. Phosphate is represented in ball and stick form, with phosphate levels rising in CKD. Serum ferritin levels also rise in the diseased state.

Our work highlights the fact that ferritin is only able to compete with phosphate for iron oxidation and sequestration if the ferritin is the H chain isoform. Ferritin from horse spleen, which is only 10% H chain (and has been estimated to be even lower), shows a very poor ability to sequester iron in the presence of phosphate. However, rHuHF homopolymer, consisting entirely of H chain ferritin, is able to better sequester iron, although not completely. Furthermore, studies performed in our lab show that ferritin is unable to sequester iron that is already complexed by phosphate in an iron(III)-phosphate complex (data not shown). Thus, the secretion of H chain ferritin during inflammation in CKD may be a response to bind the iron present in

serum. In this sense, ferritin expression can help slow the effects of elevated phosphate levels, but is unable to reverse the effects or to stop the formation of NTBI completely. Consistent with these ideas, H chain ferritin is expressed and secreted from cells into the serum during times of inflammation, such as would occur with CKD. The expression and secretion of H-ferritin during inflammation may be a response to provide the appropriate catalytic ferritin subunit to bind and oxidize Fe(II) in the presence of elevated phosphate.

The results of this in vitro study can now be tested in vivo to determine if elevated phosphate concentrations block normal iron transport in the serum resulting in NTBI. The iron(III)-phosphate complex could be added to an animal to determine if serum ferritin or transferrin is capable of removing such a complex from the serum. Furthermore, the animals could be injected with elevated phosphate levels, similar to those seen in CKD patients to elucidate whether H chain ferritin is secreted.

Elemental analysis on the purified ferritin samples revealed that total iron loading into ferritin was lower when the samples were prepared in the presence of phosphate and that phosphate concentrations equal to those observed in CKD patients (>2.5 mM phosphate) blocked 30–50% of the iron from entering ferritin (Table 5–2). If this occurs in vivo, a change from healthy phosphate levels (1.0 mM phosphate) to levels measured in CKD patients could cause a doubling in the amount of free iron in serum. These results confirmed our hypothesis that at least in vitro, elevated phosphate levels in serum can disrupt iron loading into ferritin.

Native ferritin is commonly reported to contain approximately 10 iron atoms per phosphate. Several groups have shown that iron release is more favorable from ferritin prepared in the presence of phosphate (1:1 Fe/phosphate) than from native ferritin.[33, 34] If ferritin in CKD patients contains phosphate rich mineral cores, these cores may be less stable under

physiological conditions and iron may be released more easily from ferritin, resulting in NTBI observed in these patients. Future work will focus on obtaining ferritin from CKD patients to determine if ferritin does in fact contain cores with high concentrations of phosphate as predicted here.

The ability of ferritin to sequester not only iron but also phosphate in large quantities in vivo is an intriguing occurrence. Ferritin is also capable of sequestering and storing other types of anions and oxoanions, and this capability of ferritin may have interesting in vitro possibilities. The ability of ferritin to bind a variety of anions in vitro was studied in our lab, and that work is discussed in detail in Chapter 6.

The discovery that a soluble iron (III)-phosphate complex forms as a competing side reaction during iron loading into ferritin has significant implications toward how iron loads into ferritin in vivo. For healthy individuals the impact of normal serum phosphate levels (1.0 mM) may not be significant because the majority of the iron enters ferritin under these conditions. Other serum components not present in our assay may compensate for any free iron and prevent the formation of the iron phosphate complex. At 2.5 mM phosphate, ~50% of the iron does not enter ferritin but forms the iron(III)-phosphate complex. The iron(III)-phosphate complex may contribute to the NTBI found in CKD patients. Perhaps a more significant discovery is the almost complete inhibition of iron loading into ferritin under intracellular phosphate concentrations (10 mM phosphate). These data infer that for ferritin to obtain iron under these conditions, a mechanism other than ferritin interacting with free Fe^{2+} ions in the cytosol is required.

References

1.   Balla, J.; Jeney, V.; Varga, Z.; Komodi, E.; Nagy, E.; Balla, G. Iron Homeostasis in Chronic Inflammation. *Acta Physiol Hungarica* **2007,** *94* (1–2), 95–106.

2.   Kalantar-Zadeh, K.; Lee, G. H. The Fascinating but Deceptive Ferritin: To Measure it or not to Measure it in Chronic Kidney Disease? *Clin J Am Soc Nephrol* **2006,** *1*, 9–18.

3.   Picard, V.; Epsztejn, S.; Santambrogio, P.; Cabantchik, Z. I.; Beaumont, C. Role of Ferritin in the Control of the Labile Iron Pool in Murine Erythroleukemia Cells. *J Biol Chem* **1998,** *273*, 15382–15386.

4.   Epsztejn, S.; Glickstein, H.; Picard, V.; Slotki, I. N.; Breuer, W.; Beaumont, C.; Cabantchik, Z. I. H-ferritin Subunit Overexpression in Erythroid Cells Reduces the Oxidative Stress Response and Induces Multidrug Resistance Properties. *Blood* **1999,** *94* (10), 3593–3603.

5.   Arosio, P.; Levi, S. Ferritin, Iron, and Oxidative Damage. *Free Rad Biol Med* **2002,** *33*, 457–463.

6.   Cheng, Y. G.; Chasteen, N. D. Role of Phosphate in Initial Iron Deposition in Apoferritin. *Biochemistry* **1991,** *30* (11), 2947–2753.

7.   Worwood, M.; Dawkins, S.; Wagstaff, M.; Jacobs, A. The Purification and Properties of Ferritin from Human Serum. *Biochem J* **1976,** *157* (1), 97–103.

8.   Arosio, P.; Yokota, M.; Drysdale, J. W. Characterization of Serum Ferritin in Iron Overload: Possible Identity to Natural Apoferritin. *Br J Haematol* **1977,** *36* (2), 199–207.

9.   Nielsen, P.; Fischer, R.; Dillmann, J. Serum Ferritin Iron in Iron Overload and Liver Damage: Correlation to Body Iron Stores and Diagnostic Relevance. *J Lab Clin Med* **2000,** *135* (5), 413–418.

10.   Yamanishi, H.; Iyama, S.; Yamaguchi, Y.; Kanakura, Y.; Iwatani, Y. Relation Between Iron Content of Serum Ferritin and Clinical Status Factors Extracted by Factor Analysis in Patients with Hyperferritinemia. *Clin Biochem* **2002,** *35* (7), 523–529.

11.   ten Kate, J.; Wolthuis, A.; Westerhuis, B.; van Deursen, C. The Iron Content of Serum Ferritin: Physiological Importance and Diagnostic Value. *Eur J Clin Chem Clin Biochem* **1997,** *35* (1), 53–56.

12.   Herbert, V.; Jayatilleke, E.; Shaw, S.; Rosman, A. S.; Giardina, P.; Grady, R. W.; Bowman, B.; Gunter, E. W. Serum Ferritin Iron, a New Test, Measures Human Body Iron Stores Unconfounded by Inflammation. *Stem Cells* **1997,** *15* (4), 291–296.

13.   Kalantar, K.; Humphreys, M. Association Between Serum Ferritin and Measures of Inflammation, Nutrition and Iron in Haemodialysis Patients. *Nephrol Dial Transplant* **2004,** *19*, 141–149.

14.   Li, J.; Paragas, N.; Ned, R.; Qiu, A.; Viltard, M.; Leete, T.; Drexler, I.; Chen, X.; Sanna-Cherchi, S.; Mohammed, F.; Williams, D.; Lin, C. S.; Schmidt-Ott, K. M.; Andrews, N. C.; Barasch, J. Scara5 Is a Ferritin Receptor Mediating Non-Transferrin Iron Delivery. *Dev Cell* **2009,** *16*, 35–46.

15.   Jiang, Y.; Oliver, P.; Davies, K. E.; Platt, N. Identification and Characterization of Murine SCARA5, a Novel Class A Scavenger Receptor That Is Expressed by Populations of Epithelial Cells. *J Biol Chem* **2006,** *281* (17), 11834–11845.

16.   Johnson, J.; Kenealey, J.; Hilton, R.; Brosnahan, D.; Watt, R.; Watt, G. Non-Reductive Iron Release from Horse Spleen Ferritin Using DES Chelation. *J Inorg Biochem* **2011,** *105*, 202–207.

17.   Santambrogio, P.; Levi, S.; Cozzi, A.; Arosio, P. Production and Characterization of Recombinant Heteropolymers of Human Ferritin H and L Chains. *J Biol Chem* **1993,** *268*, 12744–12748.

18.   Paques, E.; Paques, A.; Crichton, R. A Study of the Mechanism of Ferritin Formation - the Effect of pH, Ionic-Strength and Temperature, Inhibition by Imidazole and Kinetic-Analysis. *Eur J Biochem* **1980,** *107*, 447–453.

19.   Santambrogio, P.; Levi, S.; Cozzi, A.; Corsi, B.; Arosio, P. Evidence that the Specificity of Iron Incorporation into Homopolymers of Human Ferritin L- and H-Chains is Conferred by the Nucleation and Ferroxidase Centres. *Biochem J* **1996,** *314*, 139–144.

20.   Lowry, O. H.; Rosebrough, N. J.; Farr, A. L.; Randall, R. J. Protein Measurement with the Folin Phenol Reagent. *J Biol Chem* **1951,** *193*, 265–275.

21.   Fiske, C.; Subbarow, Y. The Determination of Phosphorus. *J Biol Chem* **1925,** *66*, 375–400.

22.   Cheng, Y. G.; Chasteen, N. D. Role of Phosphate in Initial Iron Deposition in Apoferritin. *Biochemistry* **1991,** *30* (11), 2947–2953.

23.   Orino, K.; Kamura, S.; Natsuhori, M.; Yamamoto, S.; Watanabe, K. Two Pathways of Iron Uptake in Bovine Spleen Apoferritin Dependent on Iron Concentration. *Biometals* **2002,** *15* (1), 59–63.

24.   Aitken-Rogers, H.; Singleton, C.; Lewin, A.; Taylor-Gee, A.; Moore, G. R.; Le Brun, N. E. Effect of Phosphate on Bacterioferritin-Catalysed Iron(II) Oxidation. *J Biol Inorg Chem* **2004,** *9* (2), 161–170.

25.   Polanams, J.; Ray, A.; Watt, R. Nanophase Iron Phosphate, Iron Arsenate, Iron Vanadate, and Iron Molybdate Minerals Synthesized within the Protein Cage of Ferritin. *Inorg Chem* **2005,** *44*, 3203–3209.

26.   Granick, S.; Hahn, P. F. Speed of Uptake of Iron by the Liver and its Conversion to Ferritin Iron. *J Biol Chem* **1944,** *155* (2), 661–669.

27.   Rohrer, J. S.; Islam, Q. T.; Watt, G. D.; Sayers, D. E.; Theil, E. C. Iron Environment in Ferritin with Large Amounts of Phosphate from Azotobacter-Vinelandii and Horse Spleen Analyzed Using Extended X-Ray Absorption Fine Structure Exafs. *Biochemistry* **1990,** *29* (1), 259–264.

28.   Watt, G.; Frankel, R.; Papaefthymiou, G. Reduction of Mammalian Ferritin. *PNAS* **1985,** *82*, 3640–3643.

29.   Hilty, S.; Webb, B.; Frankel, R. B.; Watt, G. D. Iron Core Formation in Horse Spleen Ferritin: Magnetic Susceptibility, pH, and Compositional Studies. *J Inorg Biochem* **1994,** *56* (3), 173–185.

30.   Xu, B.; Chasteen, N. D. Iron Oxidation Chemistry in Ferritin Increases Iron Oxygen Stoichiometry During Core Formation. *J Biol Chem* **1991,** *266* (30), 19965–19970.

31.   Levi, S.; Cozzi, A.; Arosio, P. Evidence that Residues Exposed on the Three-Fold Channels have Active Roles in the Mechanism of Ferritin Iron Incorporation. *Biochem J* **1996,** *317*, 467–473.

32.   Sun, S.; Chasteen, N. Ferroxidase Kinetics of Horse Spleen Apoferritin. *J Biol Chem* **1992,** *267*, 25160–25166.

33.   Treffry, A.; Harrison, P. M. Incorporation and Release of Inorganic-Phosphate in Horse Spleen Ferritin. *Biochem J* **1978,** *171* (2), 313–320.

34.   de Silva, D.; Guo, J. H.; Aust, S. D. Relationship Between Iron and Phosphate in Mammalian Ferritins. *Arch Biochem Biophys* **1993,** *303* (2), 451–455.

CHAPTER 6: ANION DEPOSITION IN FERRITIN

Abstract

Anion sequestration during ferritin core reduction was monitored using ion selective electrodes, elemental analysis, and energy-dispersive X-ray spectroscopy. When the core of horse spleen ferritin is fully reduced using formamidine sulfinic acid, a variety of anions, including halides and oxoanions, cross the protein shell and enter the ferritin interior. Reduction of the iron core of the ferritin nanocage initiates the release of two OH^- ions per iron and sequesters one halide ion per iron inside ferritin in a charge balancing reaction. In general, smaller anions, such as F^-, accumulate in greater abundance than do the larger oxoanions, such as MoO_4^{2-}, presumably because the protein channels restrict the transfer of the larger anionic species. Fe(II) remains stably sequestered inside ferritin as shown by electron micrograph imaging. Upon oxidation of the iron core, the halides are expelled from ferritin, returning the iron to the original Fe(O)OH mineral. The reaction shows that halides and hydroxide ions exhibit anti-port movement across the ferritin protein shell in response to reduction or oxidation. This finding is significant for three specific reasons: 1) the ability of ferritin to take up and store negatively charged species represents a new mechanistic function of ferritin, 2) because negatively charged species can be accumulated in ferritin in a controlled nano-environment, novel material synthesis can now be undertaken in a specific and controlled manner, and 3) we have the ability to develop stimuli-triggered release or uptake nano-systems to release reactants from a nanocage for the initiation of chemical reactions. In summary, redox events trigger the release of anions from ferritin, providing a redox-initiated anion release switch that is capable of changing the pH or ionic strength of solutions.

Introduction

Protein nanocages are potential delivery vehicles for the stimuli triggered release of molecules trapped within the interior of the nanocage.[1] The nanocage shell functions to separate the entrapped molecules in a non-reactive form until triggered release initiates a reaction with molecules in the external environment. However, this concept is dependent on a method to trigger the release of the sequestered reactant from the nanocage. Previous work examining the triggered disassembly of structures to release encapsulated molecules has used light, enzymes, or chemical reduction to trigger disassembly.[2, 3] These systems most often use lipid vesicles[4] or polymers[5, 6], but not protein cages. This work describes the use of the ferritin nanocage for stimuli-triggered release of OH^- or halide ions.

Ferritin is a nanocage that functions as an iron storage protein in essentially all organisms.[7] Ferritin is one of the more extensively studied bio-nanocages because of its ability to sequester iron and other metals as ~8 nm nanoparticles.[8] It is composed of 24 subunits that form a hollow sphere capable of storing up to 4,500 iron atoms as $Fe(O)OH$ (as described in previous chapters).[9] Ferritin crystallizes in 2-dimensional arrays allowing the sequestered materials to be deposited in ordered arrays on surfaces.[10, 11] Ferritin is pH stable, thermo stable[1] and is easily functionalized[12, 13] for attachment to surfaces such as electrodes for electrochemical material applications.[14-16] All of these properties make ferritin a useful bio-molecule for materials applications.

The majority of studies using ferritin in material applications have focused on metal sequestration and release from ferritin but few studies have examined anion incorporation into ferritin. The counter anion for physiological mineral formation with iron is OH^-, but the core also contains ~10% phosphate in mammalian ferritin and significantly more phosphate if the

ferritin comes from bacterial sources.[17] Other oxoanions can substitute for OH^- or phosphate during iron loading in ferritin.[18]

Upon reduction of the FeOOH mineral core, the iron mineral remains sequestered inside ferritin unless an Fe(II) chelator is present to remove the iron.[19] The addition of electrons to the ferritin interior produces a charge imbalance that is compensated for by expelling two OH^- ions per iron from the ferritin interior (Eq. 1).[20] However, this equation fails to provide charge balance inside ferritin. Subsequent studies established that chloride present in the reaction buffer entered the ferritin interior to provide charge balance (Eq. 2).[20] In the absence of halides in the buffer, only one hydroxide ion is expelled from ferritin, forming $Fe(OH)_2$ as the mineral phase inside ferritin. The large number of iron atoms present in native ferritin (typically 1,500–2,500/ferritin) allows a large number of halides or hydroxides to cross the protein shell in response to redox changes in the iron mineral core. Scheme 6–1 represents the reactions pictorially.

$$Fe(O)OH + H_2O + e^- \rightarrow Fe(OH)^+ + 2\ OH^- \qquad \text{(Eq. 1)}$$

Notice on the right that the iron-hydroxide species has a net charge of +1. However, this species remains inside the ferritin shell, and with approximately 2,000 iron atoms, this represents a net positive charge of +2,000; an impossibly high negative charge. To balance that charge, negatively charged species, often Cl^- (represented here as X^-) is transfered into the core:

$$Fe(O)OH + X^- + H_2O + e^- \rightarrow Fe(X)OH + 2\ OH^- \qquad \text{(Eq. 2)}$$

Net Rxn: $FeOOH + H_2O + e^- + Cl^- \rightarrow FeClOH + 2OH^-$
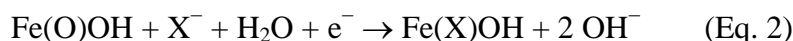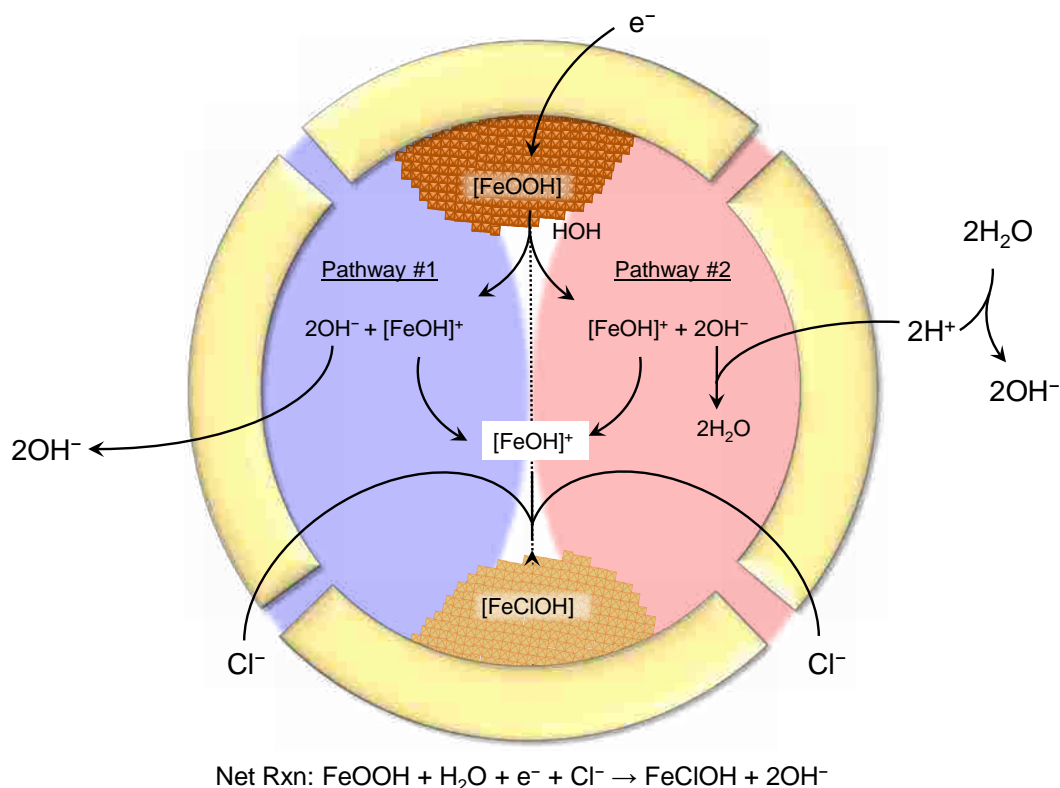
Scheme 6-1. A graphical depiction of the mechanism of anion entry, demonstrating chloride accumulation within ferritin upon reduction with OH^- ions being expelled. These reactions are reversed upon oxidation of the iron core.

Materials and Methods

Horse spleen ferritin (HoSF) was purchased from Sigma. The solution was dialyzed into buffer (0.025 M MOPS, pH 7.4) to eliminate the 0.15 M NaCl present in the stock buffer. The dialysis allowed the preparation of a defined amount and type of halide present in solution. The iron content of ferritin was 1,500 Fe/ferritin, as determined by reducing the iron using sodium hydrosulfite followed by chelation with 2,2′-bipyridine (bipy). The Fe-bipy complex has a peak maximum at 520 nm, with an extinction coefficient of 8,400 M^{-1} cm^{-1}. Protein concentrations were determined using the Lowry protein method.[21] Anion salts, including NaF, NaCl, NaBr, NaI, NaClO$_4$, Na$_2$MoO$_4$, NaH$_2$PO$_4$, NaNO$_3$, NaVO$_3$, Na$_2$WO$_4$, were obtained from Fisher

Scientific or Sigma-Aldrich, and stock solutions of 1.00 M were prepared. Formamidine sulfinic acid (FSA) was obtained from Sigma, and fresh stock solutions of 0.1 M were prepared anaerobically immediately prior to use. Ferritin was combined with an equimolar amount of anion (~1 anion per Fe atom) and then de-oxygenated and placed in an oxygen free glove box. FSA was added to the ferritin samples in an excess amount (2 FSA:1 Fe) to ensure complete reduction of the entire iron core. The reaction was allowed to stir over night. For samples treated with FSA, the Lowry method could not be used to determine protein concentrations due to FSA interference. In these instances, the Bradford method[22] was used instead, with no interference.

Ion Selective Electrodes. Ion selective electrodes (ISEs) specific for several anions were purchased from Oakton Instruments, Vernon Hills, IL. A standard curve was generated directly prior to use (Figure 6–1), and the concentration of anion prior to reduction was determined. The concentration of anion following reduction by FSA was then determined. In this case, the concentration of anion as measured using the ISE corresponds to the concentration of anion that is free in solution, or anion that is not sequestered within the interior of ferritin. Thus, the concentration inside ferritin was determined by subtracting the final concentration from the initial concentration. The samples were then exposed to oxygen, and the concentration of anion was again determined. The re-oxidized samples had anion concentrations identical to the starting concentrations. Controls were designed to determine whether FSA interfered with the ISEs readings. The reason that we use FSA as the reductant is because unlike a handful of other reductants that we tested, FSA does not interfere with the ISE.
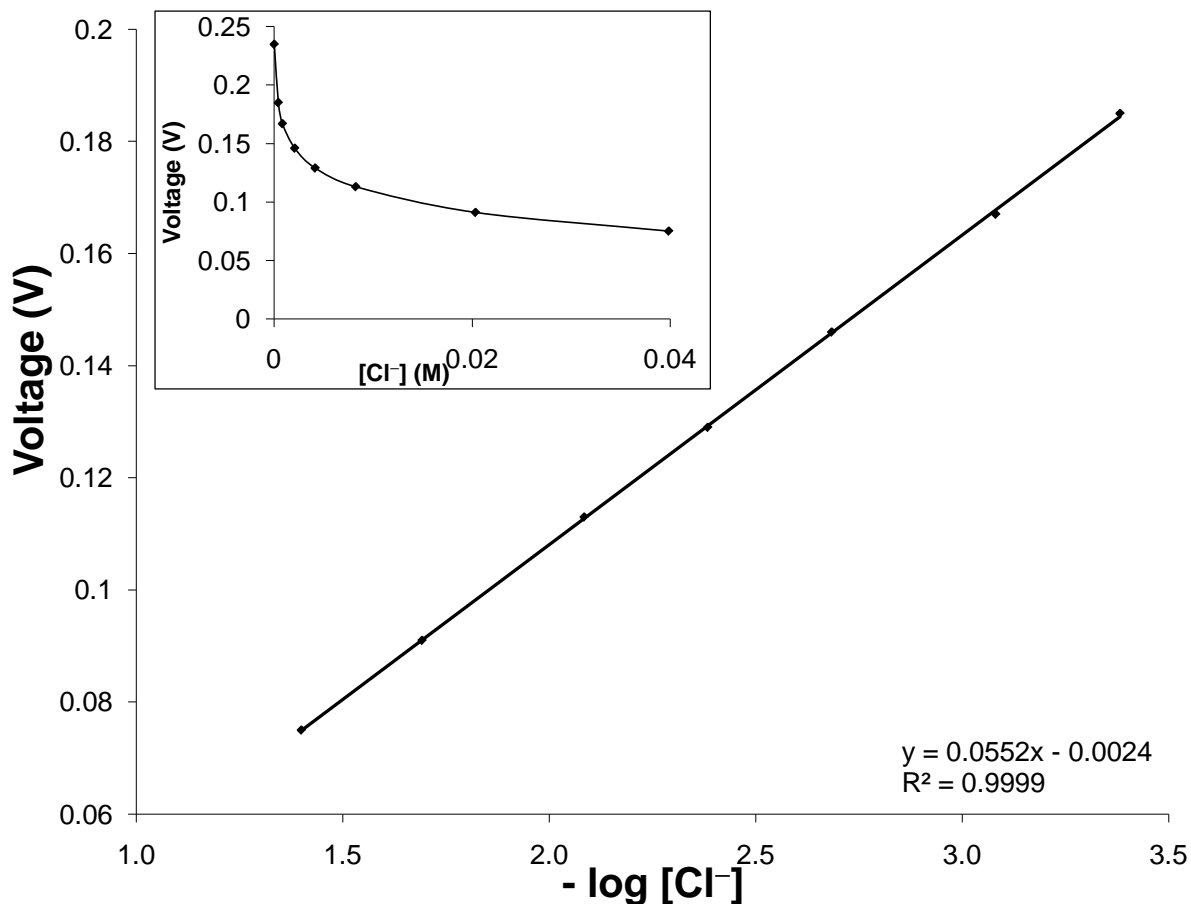
Figure 6-1. Representative standard curve for the ISE work. This particular curve is for the determination of Cl^- concentration. The concentration is plotted vs. the electrode readout (voltage, V), and is shown in the inset. To obtain the standard curve, the −log [ ] is plotted vs. voltage. Also shown is the R^2 value and the line equation. Sample concentrations are determined by measuring the voltage (y-value) and calculating for the –log [ ] (x-value). The concentration is determined by taking $10^{-\log [\,]}$.

Inductively Couple Plasma. ISEs have not been developed for each type of anion that we desired to test. In these cases, we analyzed the samples by inductively coupled plasma spectroscopy (ICP) on a PerkinElmer Optima 2000 DV. On the other hand, many of the anions that were tested with the ISEs are unable to be effectively measured using ICP. Thus, both types of analyses were needed in order to make measurements for a wide variety of anions. For ICP, it was necessary to run the reduced samples over a column to separate the anions sequestered

within ferritin from any excess anions free in solution. To do this, we used a GE-Healthcare PD-10 Sephadex G-25 column that we packed and placed in an oxygen free glove box. De-aerated buffer was passed over the column prior to the addition of the anaerobic reduced sample to equilibrate the column. The chromatography and fractionation was all performed in the oxygen free environment of the glove box. One mL fractions were collected, and each fraction was tested for protein content using the Bradford method, and also for elemental content using ICP. All samples were compared against a standard curve. Appropriate controls were treated identically.

UV-Vis Spectrophotometry. A spectrophotometer was placed in an oxygen free glove box. Samples were prepared as above, and the spectra prior to reduction and following reduction were determined. Controls without ferritin were also collected to show that the FSA peak is not responsible for the significant peaks shown.

Electron Microscopy (EM). EM samples were prepared in the glove box to eliminate oxidization in the solution prior to placement on a grid. Grids were prepared by placing 4 μL of sample on a charged lacey carbon film, 400 mesh copper grids (Ted Pella, Inc.). Following 30 to 60 seconds on the grid, the solution was wicked off the grid, and the grid was rinsed in water to remove any salts or buffers. The grids were not stained in order to avoid contamination from the uranyl acetate. The grid was allowed to dry prior to removal from the glove box. Control samples were also prepared that contained no ferritin in order to determine the degree of unspecific binding by salts and buffers. The grids were then analyzed using a Tecnai F30 TEM, 140 kV. Energy dispersive x-ray spectroscopy (EDX) was used on the various samples.

Results

To determine the extent that chloride could enter the ferritin interior and to determine if other halides or anions could substitute for chloride, ISEs for the respective anions were used to monitor anion accumulation inside the ferritin nanocage in response to reduction of the ferritin iron core. Ferritin containing 1,500 Fe/ferritin (5 mM total iron in the reaction solution) was incubated with a 5 mM concentration of the indicated anion. When the anions were transported across the ferritin protein shell and sequestered inside ferritin, they could not be detected by the ISE. The results of these reactions are summarized in Table 6–1. The general trend shows that smaller anions traverse the ferritin shell more efficiently than the larger anions. Control reactions using apoferritin showed that anions were unable to accumulate inside ferritin in the absence of the iron mineral. In addition, ferrihydrite nanoparticles that are 8 nm in diameter, but lack a protein shell, were subjected to the same reductive conditions in the presence of anions. Using these ferrihydrite nanoparticle controls, we were unable to detect a change in the anion concentration. Thus, neither the protein alone nor the ferrihydrite mineral alone can account for the change in anion concentration, supporting the model that the iron mineral inside of ferritin must be reduced, at which time the protein shell is able to sequester anionic species.

The pathway for anion influx into ferritin is unknown, but the most likely route is through channels that penetrate the ferritin nanocage at the 3-fold or 4-fold symmetry axes. However, the properties of these channels are not favorable for anion migration into the interior. The 3-fold channels are negatively charged and hydrophilic and the 4-fold channels are hydrophobic. In addition, both channels have a 4 Å diameter (2 Å radius), which is the approximate size of, if not smaller than, most of the anions, even without taking into account the size of the anions when hydrated (Table 6–1). Based on the properties of these channels it is remarkable that anions,

especially the larger anions, are capable of entering the ferritin interior. In order for anions to efficiently enter ferritin, it would require a breathing mode of ferritin that would allow an enlargement of the channels. The decreased loading of ferritin with larger halides is consistent with size and charge repulsion slowing the entry of these halides.

Table 6-1. ISE and ICP determinations of anion transfer into ferritin, listed according to size.

Anion	Ionic radius, Å	% of anion that enters ferritin	# of anions that enter ferritin	Fe/anion inside ferritin
F^-	1.36	100 ± 12	$1{,}585 \pm 165$	1.0 ± 0.1
NO_3^-	1.45	26.2 ± 10.0	393 ± 151	3.81 ± 0.35
Cl^-	1.81	94.2 ± 7.8	$1{,}278 \pm 114$	1.17 ± 0.08
Br^-	1.95	72.9 ± 2.9	$1{,}078 \pm 84$	1.39 ± 0.04
PO_4^{3-}	2.10	12.1 ± 4.4	181 ± 124	$1.32 \pm 0.23*$
I^-	2.16	80.7 ± 2.3	$1{,}210 \pm 53$	1.24 ± 0.04
ClO_4^-	2.20	57.6 ± 6.6	854 ± 303	1.76 ± 0.20
VO_4^{3-}	2.58	79.4 ± 5.5	$1{,}190 \pm 108$	1.26 ± 0.16
MoO_4^{2-}	2.64	92.0 ± 4.5	$1{,}380 \pm 158$	1.09 ± 0.24
WO_4^{2-}	2.68	14.5 ± 2.3	217 ± 22	6.91 ± 0.28

[ferritin]=1.5 mg/ml, [Fe]=5 mM, Fe/ferritin=1,500, initial [anion] in solution=5 mM, [FSA]=10 mM.

*The phosphate sample chelated iron from ferritin. Thus, the Fe:anion ratio is an artifact; although it appears close to one, it is the result of very little iron remaining inside of ferritin. In other samples, the iron content remained very close to the original amount (~1,500 Fe/Ftn). The error is the standard deviation of three separate experiments.

The reactions were all initiated with a 1:1 iron to anion ratio. In the case of the halides, following reduction of the iron core, essentially all of the halide ions present in solution entered

the ferritin interior. The 1:1 association of halides with iron is evidence that upon reduction, the iron core must change properties from a crystalline mineral to an amorphous, porous state so that the halides can intercalate in the mineral phase and interact with each individual iron atom. This reduced ferritin mineral has not yet been characterized but should provide a very interesting mineral phase to study. The percentage of oxoanion incorporation into the ferritin core is not as high as that for the halides. Nevertheless, it represents the greatest number of oxoanion incorporation into ferritin that we are aware of in the current literature. The significant input of oxoanion into ferritin provides strong support for the effectiveness of this method for creating novel anion-iron minerals within ferritin. For anions that were determined using ICP, a separation technique was required wherein we ran the samples anaerobically over a size-exclusion column and collected the fractions. Each fraction was analyzed for protein, iron, and the element of interest (such as Mo, V, and etc.) using techniques described in Materials and Methods. Representative elution profiles of these separations are shown in Figure 6–2 for MoO_4^{2-} and WO_4^-. We observe a nearly 100% incorporation of MoO_4^{2-} into the ferritin interior, as evidenced by the Mo peak shift from fraction 7 to fraction 3. On the other hand, WO_4^- only incorporates about 15% into ferritin, as shown by the minimal peak shift, and the remaining 85% remains soluble outside of ferritin.
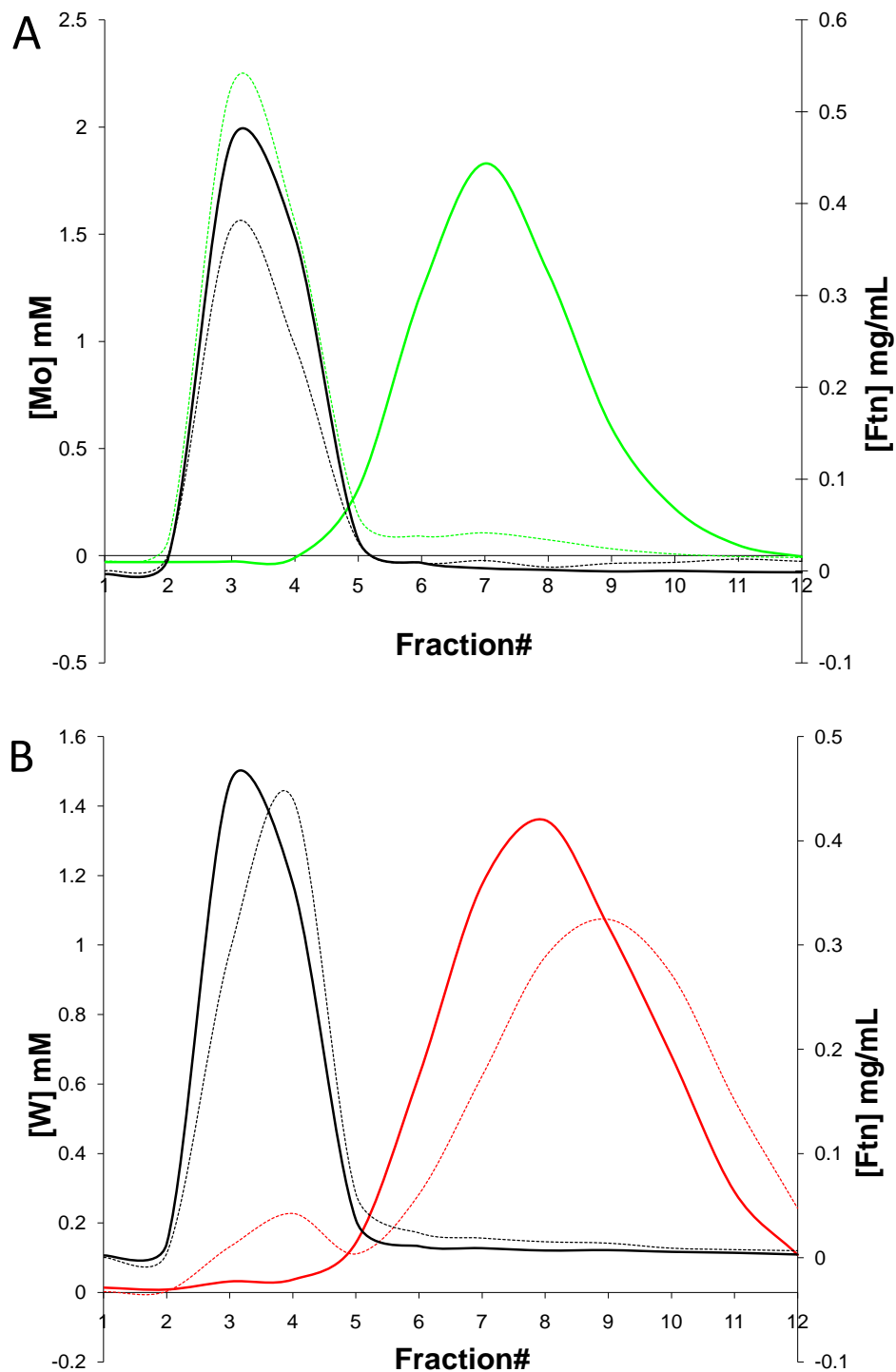
Figure 6-2. Elution profiles of samples run over a G-25 column. A) Molybdate elution profile. B) Tungstate elution profile. The **black** traces represent the protein elution profiles, whereas the colored traces are the oxoanions. The lighter lines are the samples prior to reduction, and the darker lines are the samples following FSA reduction.

In the previous chapter, we showed that phosphate can be incorporated into ferritin in a nearly 1:1 ratio of phosphate to iron, with iron cores up to about 1,000 iron atoms per ferritin. This represents a significant number of phosphate molecules that are able to be incorporated into ferritin. Interestingly, using this method, we are unable to incorporate any phosphate into ferritin. The reason we propose, is that at a 1:1 ratio of iron to phosphate in the system, upon reduction of the iron core, phosphate efficiently chelates and pulls all of the iron from ferritin. This finding is confirmed when the sample supernatant is purified in the absence of oxygen by running it over an oxygen free G-25 column and collecting fractions. The fractions are analyzed for protein, iron, and phosphate content. The protein elutes in the same fraction as normal, but both iron and phosphate are completely absent from the sample. Some iron and phosphate elute together in a later fraction. However, most of the iron and phosphate is found in the insoluble material that forms as the result of this reaction. Thus, the ability to form novel materials inside ferritin using this technique requires that the iron remain inside ferritin and directs the anion into ferritin without causing competing precipitation reactions.

The molar concentration of the anion inside ferritin can be calculated using the moles of halide and dividing by the calculated internal volume of ferritin. Ferritin, with an internal diameter of ~8 nm, has an interior volume of 2.68×10^{-22} L. The halide concentration approaches 10 M for fluoride ion incorporation inside ferritin, which is a 2,000-fold increase over the original 5 mM fluoride concentration in solution. Because the movement of anion is against a concentration gradient, the driving force for the reaction must come from the charge imbalance that occurs when two OH^- ions are expelled from the ferritin interior for each Fe(III) reduced in the iron core (Eq. 1 and Eq. 2).

Upon oxidation, the reverse reaction occurs and anions are expelled from ferritin. OH^- ions either traverse the ferritin protein shell to return to the interior, or water present on the inside of ferritin is hydrolyzed to form the iron oxyhydroxide mineral core. The exact mechanism of OH^- ion movement or proton movement across the protein shell has not yet been established, but the net yield is that two OH^- ions traverse the shell in response to reduction or oxidation of the iron core.

Several additional studies were used to confirm anion entry into ferritin. Native ferritin possesses a characteristic spectrophotometric signature. The peak at 280 nm represents the protein, and the broad shoulder tailing into the visible region (from 300–500 nm) represents the Fe(O)OH mineral sequestered inside ferritin. The oxidized ferritin solution appears reddish-brown (Figure 6–3, left inset). Upon reduction, the reddish-brown color is replaced with a very faint yellow to colorless appearance (Figure 6–3, right inset), and the broad visible shoulder from 300–500 nm decreases significantly (This is true in most cases. One exception is the formation of the iron-molybdate core, where the solution changes from reddish-brown to greenish-brown.). Reduction of ferritin in the presence of anion produces a similar spectrum to reduced ferritin but with slight variations, particularly around 320 nm, due to anion interactions with Fe(II). Reduction of ferritin in the presence of chloride shows the most significant spectral changes around 320 nm, compared to the other halides (Figure 6–3). The slight spectral variation around 320 nm when different halides are present supports the view that upon reduction, the halides accumulate inside ferritin and interact with Fe(II). Upon oxidation, the solution returns to the original reddish-brown color, and the spectrum returns to the oxidized ferritin spectrum. ISE data confirm that upon oxidation, the anions are expelled from ferritin to form the native Fe(O)OH mineral.
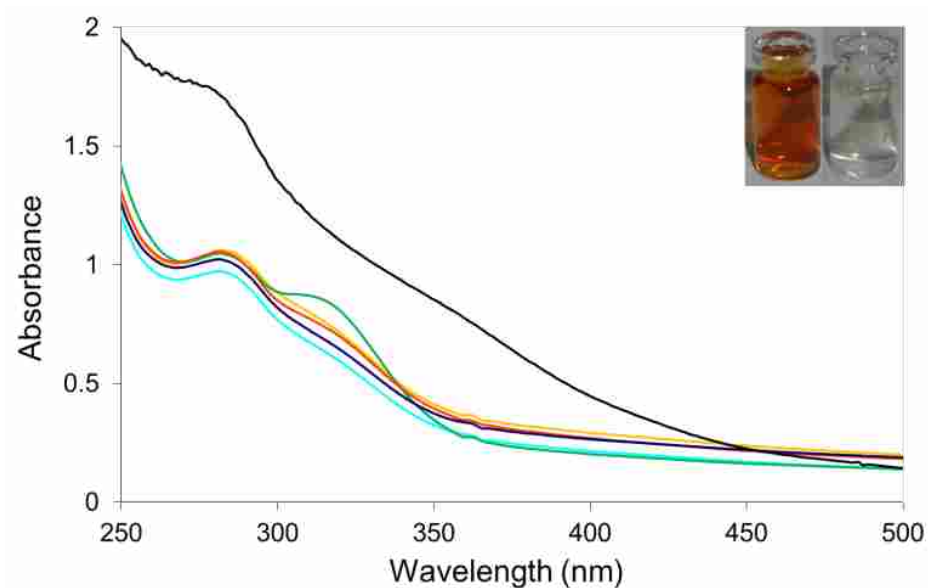
Figure 6-3. Spectra of the oxidized native ferritin core (**black**) compared to ferritin cores reduced in the presence of halides. Fe(X)OH cores (**cyan**, OH$^-$; **yellow**, F$^-$; **green**, Cl$^-$; **orange**, Br$^-$; and **blue**, I$^-$). Inset depicts the solution color prior to (left) and following (right) reduction with formamidine sulfinic acid (FSA). Following oxidation, the anions are expelled, the solution turns reddish-brown, and the spectra return to the spectrum represented by the **black** trace.

To further verify that the anions were sequestered inside the ferritin protein shell, ferritin samples were reduced in the presence of anions in an anaerobic glove box, placed on electron microscope grids, and washed extensively followed by EM analysis. Figure 6–4 shows a representative EM image of ferritin before and after being reduced in the presence of anion. Figure 6–4 also shows that Fe(II) remains sequestered inside the 8 nm interior of ferritin upon reduction.
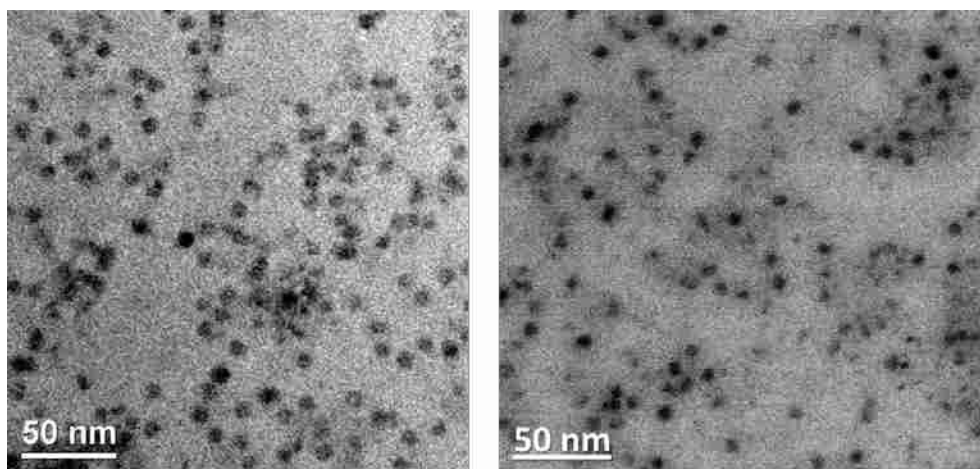
Figure 6-4. Scanning transmission electron micrographs of ferritin before reduction (left), and after reduction (right) of the mineral core reduced in the presence of anions (representative micrographs). The sample is not negatively stained, thus the density represents the iron core within ferritin and not the protein.

In addition, the halide samples were studied using energy-dispersive X-ray spectroscopy (EDX) to determine the elemental composition inside ferritin (Figure 6–5). The samples were prepared as described above in an anaerobic glove box. Identical washing procedures were used for ferritin samples and control samples of apoferritin and no ferritin. The scanning area was half a micron squared. This area samples an average of 1,500 ferritin molecules. The spectra show the expected peaks corresponding to each individual halogen element, except for F, because the Kα peak of F (0.677 keV) is buried in the Lα peak of Fe (0.705 keV). In all other spectra, each respective halogen peak is identifiable. Controls with apoferritin reduced in the presence of halides did not show halogen peaks with EDX analysis, nor did controls coating grids with the holoferritin and the individual halides without reduction where the identical washing procedure was performed prior to EDX analysis. To confirm the presence of these halides within the protein shell, STEM was used to selectively scan a ~12 nanometer square region that contained a single ferritin molecule. The combined data support the claim that the respective halides accumulate inside the nanocage of ferritin.

138
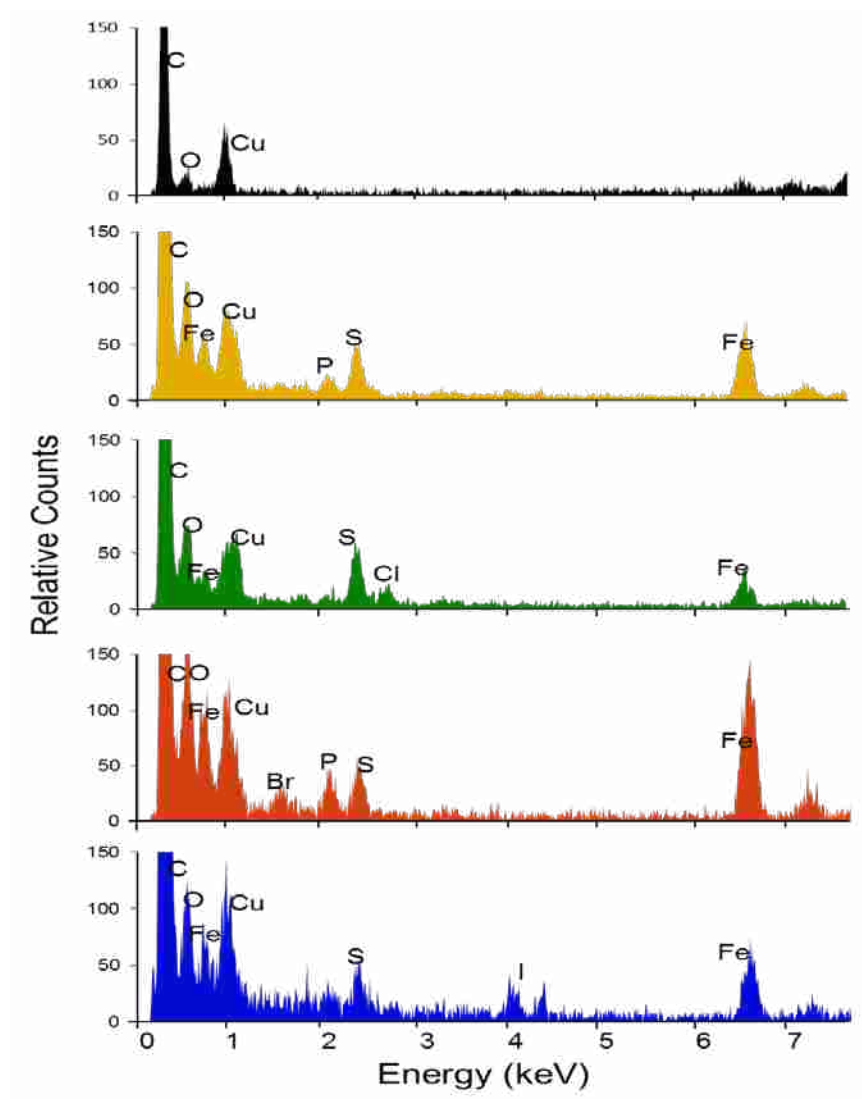
Figure 6-5. EDX shows unique spectra for the various Fe(X)OH cores, where X is a halide. **Black** is the control with no ferritin placed on the grid. The remaining spectra are of Fe(F)OH, **yellow**; Fe(Cl)OH, **green**; Fe(Br)OH, **orange**; and Fe(I)OH, **blue**.

Discussion

The role of ferritin in biological systems is to store iron, protecting the organism from iron-catalyzed oxidative damage. The structure of ferritin makes it very effective for the uptake of iron; eight 3-fold channels are negatively charged, and act as a funnel for cation sequestration. In this work, we show that ferritin is also capable of accumulating a significant number of

anions. Thus, our perspective on the ability of ferritin to take up ions has been expanded beyond only cations. This has significant applications in materials chemistry, where previously, we have been limited to the uptake of cations, but new anionic species can be sequestered and used for materials synthesis within ferritin. In addition, stimuli-triggered uptake and release can be controlled in this nano-environment in a controlled manner. This may have significant applications in the fields of nano-actuators and nano-devices.

In Chapter 5, we showed that phosphate competes with ferritin for the uptake of iron. In this work, we also highlight that under conditions used in this work, phosphate coordinates iron, forming an insoluble $Fe_3(PO4)_2$ precipitate. Thus it is noteworthy to emphasize that the environmental conditions surrounding ferritin has a significant impact in the ability of ferritin to retain iron and other materials. This is important not only for general ferritin function, but also in diseased states and in materials applications as well. In fact, Chapters 7 and 8 will show that the presence of iron-coordinating molecules has a significant impact on our ability to control nanoparticle synthesis.

The results presented in this chapter bring up an interesting biochemical question relating to the evolution of ferritin. If ferritin expels only one OH^- ion/iron it would remain charge balanced. Why then, does ferritin expel two OH^- ions/iron upon reduction and produce a state that requires anion import to maintain charge balance? Below, we outline a mechanism suggesting that the expulsion of two OH^- ions/iron may have evolved as a protective mechanism to prevent protein denaturation from elevated pH.

The reactions driving OH^- ion efflux from ferritin may be better understood by evaluating the concentrations of species that form inside ferritin. Upon reduction of the iron, halides accumulate inside ferritin at concentrations approaching 10 M (based on the number of

iron atoms in the volume of ferritin, and comparing the ratio of iron to anion inside ferritin, Table 6–1). Even higher concentrations of OH^- ions are liberated by the reduction of the ferritin iron core. The reduction of the FeOOH mineral of ferritin produces $Fe(OH)^+$ and releases two OH^- ions into the ferritin interior (Eq. 1). If these reactions happened instantaneously, the resulting OH^- concentration inside ferritin would approach ~20 M. Ferritin is stable up to ~pH 10 but the concentration of OH^- ions inside ferritin under these conditions would be ~pH 15, which would denature the protein. To maintain protein structural integrity, ferritin must rapidly expel the OH^- ions. If all of the OH^- ions were released simultaneously, the concentration gradient driving this reaction would be powerful with an internal OH^- ion concentration of ~20 M and an external OH^- ion concentration of 10^{-7} M at pH 7.0. To avoid OH^- denaturation, ferritin must efficiently efflux OH^- ions to maintain protein integrity. The elimination of only one OH^- ion/iron would be insufficient to protect the protein from pH denaturation.

In a simplistic stepwise view, after reduction of the iron core, ferritin expels all of the free OH^- ions in an attempt to lower the OH^- ion concentration to a safe level and in the process becomes charge imbalanced. Ferritin now requires anions to compensate for the positive charge build-up inside ferritin. The available anions for charge balance are halides (the 5 mM concentration was chosen to mimic the in vivo chloride concentration) and OH^- ions, present at 10^{-7} M at pH 7.0. Because the halides are present at a 50,000 times greater concentration, halides enter ferritin to balance the charge. In reality, such a stepwise reaction cannot occur, thus the efflux of OH^- ions must be simultaneously matched by an influx of halide ions. Understanding these reactions and taking into account the properties of ferritin will allow ferritin to be used as a redox-switch nanocage actuator for the storage and redox-controlled release of OH^- and halide ions.

Finally, these findings may have in vivo implications. In healthy humans, the average chloride concentration within a cell is ~5 mM. The inside of a cell is a reducing environment, and iron release from ferritin is proposed to occur by a reductive mechanism. Because iron chlorides are more soluble than iron hydroxides, the accumulation of chloride ions inside ferritin upon reduction of the iron may be a specific biological mechanism to facilitate the solubility and release of iron from ferritin. This is in contrast to the view that ferritin would need to be degraded in the lysosome in order to release iron.[23] The association of iron with chloride inside ferritin is an attractive model for iron release from ferritin that allows iron to remain available for iron binding.[24]

This work was accepted in part by the Journal of Inorganic Biochemistry.

This work was presented as a poster at BioMetals 2010 in Tucson, AZ and as a talk and poster at nanoUtah 2010 in SLC, UT.

References

1.   Uchida, M.; Klem, M. T.; Allen, M.; Suci, P.; Flenniken, M.; Gillitzer, E.; Varpness, Z.; Liepold, L. O.; Young, M.; Douglas, T. Biological Containers: Protein Cages as Multifunctional Nanoplatforms. *Adv Mater* **2007,** *19* (8), 1025–1042.

2.   Johnston, A. P. R.; Such, G. K.; Caruso, F. Triggering Release of Encapsulated Cargo. *Angew Chem, Int Ed Eng,* **2010,** *49,* 2664–2666.

3.   Pastine, S. J.; Okawa, D.; Zettl, A.; Frechet, J. M. J. Chemicals On Demand with Phototriggerable Microcapsules. *JACS* **2009,** *131* (38), 13586–13587.

4.   Westhaus, E.; Messersmith, P. Triggered Release of Calcium from Lipid Vesicles: A Bioinspired Strategy for Rapid Gelation of Polysaccharide and Protein Hydrogels. *Biomaterials* **2001,** *22*, 453–462.

5.   Esser-Kahn, A. P.; Sottos, N. R.; White, S. R.; Moore, J. S. Programmable Microcapsules from Self-Immolative Polymers. *JACS 132* (30), 10266–10268.

6.   Yaroslavov, A. A.; Melik-Nubarov, N. S.; Menger, F. M. Polymer-Induced Flip-Flop in Biomembranes. *Acc Chem Res* **2006,** *39* (10), 702–710.

7.   Arosio, P.; Ingrassia, R.; Cavadini, P. Ferritins: A Family of Molecules for Iron Storage, Antioxidation and More. *BBA* **2009,** *1790* (7), 589–599.

8.   Yamashita, I.; Iwahori, K.; Kumagai, S. Ferritin in the Field of Nanodevices. *BBA* **2010,** *1800*, 846–857.

9.   Harrison, P. M.; Arosio, P. The Ferritins: Molecular Properties, Iron Storage Function and Cellular Regulation. *BBA* **1996,** *1275* (3), 161–203.

10.   Matsumoto, M. Spread Monolayers of a Water-Soluble Protein (Ferritin) and its 2-Dimensional and 3-Dimensional Arrays. *Langmuir* **1994,** *10* (11), 3922–3925.

11.   Yamashita, I. Fabrication of a Two-Dimensional Array of Nano-Particles Using Ferritin Molecule. *Thin Solid Films* **2001,** *393* (1–2), 12–18.

12.   Fernandez, B.; Galvez, N.; Sanchez, P.; Cuesta, R.; Bermejo, R.; Dominguez-Vera, J. M. Fluorescence Resonance Energy Transfer in Ferritin Labeled with Multiple Fluorescent Dyes. *J Biol Inorg Chem* **2008,** *13* (3), 349–355.

13.   Wong, K. K. W.; Colfen, H.; Whilton, N. T.; Douglas, T.; Mann, S. Synthesis and Characterization of Hydrophobic Ferritin Proteins. *J Inorg Biochem* **1999,** *76* (3-4), 187–195.

14.   Cherry, R. J.; Bjornsen, A. J.; Zapien, D. C. Direct Electron Transfer of Ferritin Adsorbed at Tin-Doped Indium Oxide Electrodes. *Langmuir* **1998,** *14* (8), 1971–1973.

15.   Tominaga, M.; Ohira, A.; Yamaguchi, Y.; Kunitake, M. Electrochemical, AFM and QCM Studies on Ferritin Immobilized onto a Self-Assembled Monolayer-Modified Gold Electrode. *J Electroanal Chem* **2004,** *566* (2), 323–329.

16.   Kim, J. W.; Choi, S. H.; Lillehei, P. T.; Chu, S. H.; King, G. C.; Watt, G. D. Electrochemically Controlled Reconstitution of Immobilized Ferritins for Bioelectronic Applications. *J Electroanal Chem* **2007,** *601* (1-2), 8–16.

17.   Rohrer, J. S.; Islam, Q. T.; Watt, G. D.; Sayers, D. E.; Theil, E. C. Iron Environment in Ferritin with Large Amounts of Phosphate from Azotobacter-Vinelandii and Horse Spleen Analyzed Using Extended X-Ray Absorption Fine Structure Exafs. *Biochemistry* **1990,** *29* (1), 259–264.

18.   Polanams, J.; Ray, A.; Watt, R. Nanophase Iron Phosphate, Iron Arsenate, Iron Vanadate, and Iron Molybdate Minerals Synthesized within the Protein Cage of Ferritin. *Inorg Chem* **2005,** *44*, 3203–3209.

19.   Watt, R. K.; Frankel, R. B.; Watt, G. D. Redox Reactions of Apo Mammalian Ferritin. *Biochemistry* **1992,** *31* (40), 9673–9679.

20.   Hilty, S.; Webb, B.; Frankel, R. B.; Watt, G. D. Iron Core Formation in Horse Spleen Ferritin: Magnetic Susceptibility, pH, and Compositional Studies. *J Inorg Biochem* **1994,** *56* (3), 173–185.

21.   Lowry, O. H.; Rosebrough, N. J.; Farr, A. L.; Randall, R. J. Protein Measurement with the Folin Phenol Reagent. *J Biol Chem* **1951,** *193* (1), 265–275.

22.   Bradford, M. M. Rapid and Sensitive Method for Quantitation of Microgram Quantities of Protein Utilizing Principle of Protein-Dye Binding. *Anal Biochem* **1976,** *72* (1–2), 248–254.

23.   Kidane, T. Z.; Sauble, E.; Linder, M. C. Release of Iron from Ferritin Requires Lysosomal Activity. *Am J Physiol Cell Physiol* **2006,** *291* (3), 445–455.

24.   De Domenico, I.; Ward, D. M.; Kaplan, J. Specific Iron Chelators Determine the Route of Ferritin Degradation. *Blood* **2009,** *114* (20), 4546–4551.

CHAPTER 7: FERRITIN AS A PHOTOCATALYST FOR GOLD NANOPARTICLE FORMATION

Abstract

The ferrihydrite mineral core of ferritin is a semi-conductor capable of catalyzing oxidation/reduction reactions. This chapter shows that light can photo-reduce $AuCl_4^-$ to form gold nanoparticles (AuNPs) with ferritin as a photocatalyst. An important goal of this work was to identify innocent reaction conditions that prevented formation of AuNPs unless the sample was illuminated in the presence of ferritin. Tris buffer satisfied this requirement and produced AuNPs with spherical morphology with diameters of 5.7 ± 1.6 nm and a surface plasmon resonance (SPR) peak at 530 nm. Size-exclusion chromatography of the AuNP-ferritin reaction mixture produced two peaks containing both ferritin and AuNPs. TEM analysis of the peak close to where native ferritin normally elutes showed that AuNPs form inside ferritin. The other peak eluted at a volume indicating a particle size much larger than ferritin. TEM analysis revealed AuNPs adjacent to ferritin molecules, suggesting that a dimeric ferritin-AuNP species forms. We propose that the ferritin protein shell acts as a nucleation site for AuNP formation leading to the AuNP-ferritin dimeric species. Ferrihydrite nanoparticles (~10 nm diameter) were unable to produce soluble AuNPs under identical conditions unless apoferritin was present, indicating that the ferritin protein shell was essential for stabilizing AuNPs in aqueous solution.

Introduction

Nanoparticle synthesis can be guided by using templates to control the size and morphology of the resulting nanoparticles.[1-4] The iron storage protein ferritin provides a template for size-constrained nanoparticle synthesis because it is composed of 24 polypeptide subunits that assemble into a hollow sphere with a 12-nm exterior diameter and an 8-nm interior diameter

145

cavity.[5] Ferritin can accommodate up to 4,500 iron atoms as crystalline ferrihydrite. The iron can be removed by reduction and chelation, resulting in an empty apoferritin protein shell.[6] Other metallic materials have been prepared inside ferritin using a variety of synthetic methods. Synthetic ferritin minerals include: metal oxides of chromium, manganese, iron, cobalt, nickel, titanium, europium, and uranium;[7-13] sulfides (and in some instances selenides) of iron, cadmium, gold, lead, and zinc.[14-19] In addition, metal ions have been reduced to their elemental form to produce metallic palladium, copper, cobalt, nickel, gold, and silver nanoparticles (AgNPs).[18, 20-25]

In addition to being a nano-reactor to sequester metallic materials, ferritin has been used as a photocatalyst for performing redox reactions in solution. Exposure to light generates an electron-hole pair in the ferrihydrite mineral core that is sufficiently long-lived to react with other components in solution, including sacrificial electron donors and electron acceptors.[26] Photochemical studies include the photo-reduction of Cr(VI) to Cr(III),[27] Cu(II) to Cu(0),[28] and the photo-reduction of cytochrome c and viologens.[26] In addition, metal loading into ferritin occurs photochemically by reducing metal-citrate complexes of Fe(III), Eu(III), and Ti(IV) and allowing the reduced form of the metal to be oxidized by the ferroxidase center of the ferritin H-chain leading to incorporation of the metal into ferritin.[13]

Recently, several studies describing the preparation of AuNPs or AgNPs using ferritin as a template were reported. Two of the studies prepared gold on the exterior surface of ferritin,[18, 29, 30] whereas others produced AuS, Au, Ag, or AgAu alloy nanoparticles inside ferritin.[18, 24, 25, 31, 32] Some of these studies relied on diffusion of Au or Ag ions into the interior of ferritin followed by reduction by $NaBH_4$. Other studies used protein engineering to incorporate thiolate and

histidine ligands inside ferritin to attract and bind the Au and Ag. In addition, less powerful reductants (MOPS buffer) were required and light was used for the reduction of Ag^+ to $Ag(0)$.

AuNPs have been used in a variety of applications including colorimetric assays,[33-38] immuno-detection assays,[39, 40] treatment of cancer[41] and amyloid fiber related diseases,[42] carbon nanotube synthesis,[43] and selective oxidation catalysts.[44] Because AuNPs have different characteristics depending on their size and the passivity of the surface, it is important to develop controlled synthetic routes to create particles with different morphologies, sizes, and surface passivation.[45] In addition, if the AuNPs are to be used in biological systems, capping agents and buffers used must be compatible for biology.[46] The solubility, reactivity, and photonic properties of ferritin AuNPs are sensitive to the size of the particle and the local environment of the gold surface. For instance, the use of different reducing agents to prepare AuNPs with ferritin influences the catalytic properties of the AuNPs.[29] Therefore, the deposition of AuNPs on the exterior or interior of ferritin will influence the potential applications of the nanoparticles.

Several photochemical methods to form AuNPs have been published.[47-52] However, these methods require "gold seeds" or the use of detergents or other chemical stabilizers, reducing agents, or capping agents that are not biologically compatible.[40] One advantage of photochemical methods is that chemical reductants are not required and this minimizes contaminants, by-products, and other potential reactants that can affect studies in biological systems. This study was undertaken to use ferritin and a minimal reaction system to photo-reduce $AuCl_4^-$ to form AuNPs without requiring gold seeds, non-biological reducing agents, or chemical stabilizers. Potentially the AuNPs might form inside the ferritin cavity, as was observed for Cu(II) photo-reduction,[28] providing an encapsulation method for AuNP delivery. Alternatively, the AuNPs may form on the exterior of ferritin and provide a potential catalyst as was observed for chemical

147

reduction of AuNPs in the presence of ferritin.[29] If ferritin sequesters the AuNPs or acts as a capping agent for the AuNPs, the products would be a useful medium for introducing AuNPs into biological systems. To establish the importance of the protein shell, we tested ferrihydrite nanoparticles to determine if the ferrihydrite catalyst was sufficient to form AuNPs or if the ferritin protein shell was required for the formation of AuNPs. We report that ferritin can catalyze the formation of AuNPs and that the protein shell is required for gold nanoparticle formation and solubilization. We observed that AuNPs form both on the exterior and interior of ferritin. Furthermore, we observed that buffers significantly influence both the size of the particles and the absorbance maximum of the SPR peak of the AuNP products.

Materials and Methods

Horse spleen ferritin was obtained from Sigma. Ferritin was prepared in the desired buffer by performing buffer exchanges using Amicon Ultra centrifuge tubes with a molecular weight cutoff of 100,000 Da to concentrate the solution and exchange the buffer to 2-amino-2-hydroxymethyl-propane-1,3-diol (Tris) buffer (100 mM Tris, 25 mM NaCl, pH 7.5) or 3-morpholinopropane-1-sulfonic acid (MOPS) buffer (25 mM MOPS, 25 mM NaCl, pH 7.5). The protein concentration was measured using the Lowry method.[53] The iron concentration was measured after treatment with dithionite to reduce the iron followed by chelation by 2,2'-bipyridine to form the $Fe(bipy)_3^{2+}$ complex. The absorbance at 520nm ($\varepsilon_{520} = 8,400$ M^{-1} cm^{-1}) was measured to determine iron content.[54]

AuNPs were prepared by mixing the ferritin catalyst, the sacrificial electron donor citrate, and $AuCl_4^-$ in a quartz cuvette followed by illumination with an ultra violet Oriel Hg lamp (model 66056). The wavelength of light required for photocatalysis was from 290–310 nm. Sample temperature was maintained at 25 °C using a water-circulating cuvette holder connected

to a water bath. The final volume of each sample was 1.25 mL. The final concentrations of MOPS containing samples were: 0.155 mg/mL protein, 0.44 mM iron, 4 mM MOPS, 125 mM NaCl, 32 mM citrate, and 0.8 mM $AuCl_4^-$. This corresponds to 2,300 Au atoms per ferritin molecule. Final concentrations of Tris containing samples were: 0.15 mg/mL protein, 0.42 mM iron, 20 mM Tris, 125 mM NaCl, 32 mM citrate, and 0.8 mM $AuCl_4^-$. This corresponds to 2,400 Au atoms per ferritin molecule with 1,000 Fe atoms within each ferritin molecule. Control reactions were performed without citrate to determine if the buffers could act as electron donors. Reactions in MOPS buffer still produced AuNPs, showing that MOPS could substitute for citrate as an electron donor in the absence of citrate. However, reactions in Tris or in water did not produce AuNPs, indicating that Tris could not be oxidized under these conditions to donate electrons to $AuCl_4^-$.

UV-visible absorption spectra were measured using an Agilent 8453 spectrophotometer. Transmission electron microscopy (TEM), scanning TEM (STEM), and energy-dispersive X-ray spectroscopy (EDX) were performed on a Tecnai F20 Analytical STEM operating at 200 keV. Samples were deposited on copper TEM grids (Ted Pella lacey carbon film grids) by placing a 5 µL sample onto the grid for 20 seconds and then washing the grid with deionized water for 3 seconds. For samples that were stained to visualize the protein, a 5 µL addition of 1% uranyl acetate was placed on the grid for 10 seconds after the water wash. The grid was then allowed to air dry. In between each step the grid was blotted with filter paper. Fast protein liquid chromatography was performed on a GE Healthcare ÄKTApurifier. A Superdex ^{TM} 200 10/300 GL size-exclusion column was used to determine the particle size. The sample was eluted in 0.02 M Tris with 0.125 M NaCl at pH 7.4.

The reactions in each figure were prepared as described above. The time that each sample was exposed to light depended on the buffer used to prepare the sample. Figure 7–1 shows that some reactions occurred more rapidly than others. For each sample, the reaction was prepared as in Figure 7–1 and when the plateau was reached, the reaction was stopped by turning off the light. All other analyses were performed on samples after the reaction had reached a plateau in the spectrophotometric assay.

Results and Discussion

The photocatalytic formation of AuNPs can be detected by observing the surface plasmon resonance (SPR) band that forms around 530 nm. Samples containing ferritin, $AuCl_4^-$, and citrate with the indicated buffer were placed in a spectrophotometer and illuminated with a mercury lamp perpendicular to the spectrophotometer light path and the rate of AuNP formation was monitored at 530 nm under a variety of reactions conditions (Scheme 7–1). It was essential to find conditions that did not permit AuNP formation in the absence of ferritin so that any AuNP formation observed was catalyzed by the illumination of ferritin.
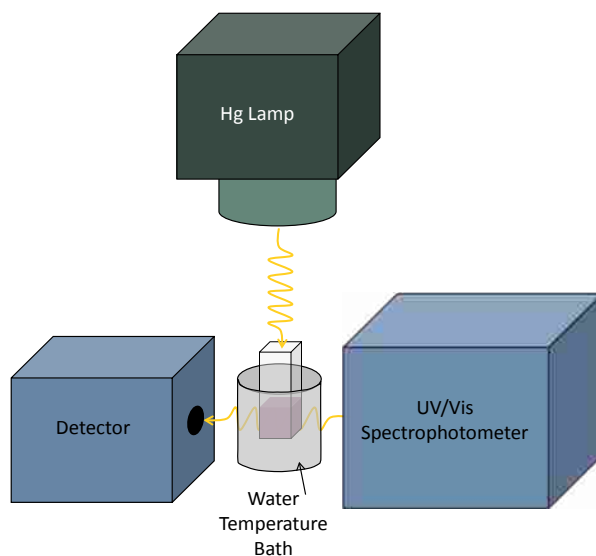
Scheme 7-1. A diagram of the photo-illumination equipment used to prepare AuNPs.

150

Results shown in Figure 7–1A follow the formation of the AuNPs kinetically at 530 nm and Figure 7–1B shows the spectrum of the resulting samples. Insets show photographs of the initial solution and the product solutions. Figure 7–1A shows that in the absence of light, samples prepared in Tris buffer do not form AuNPs as evidenced by the absence of the SPR absorbance peak at 530 nm. Similar results were observed for samples prepared in water (data not shown). Upon illumination in Tris (or water), ferritin catalyzes the oxidation of citrate and the reduction of $AuCl_4^-$ to produce a red solution containing AuNPs with an absorbance maximum at 530 nm.
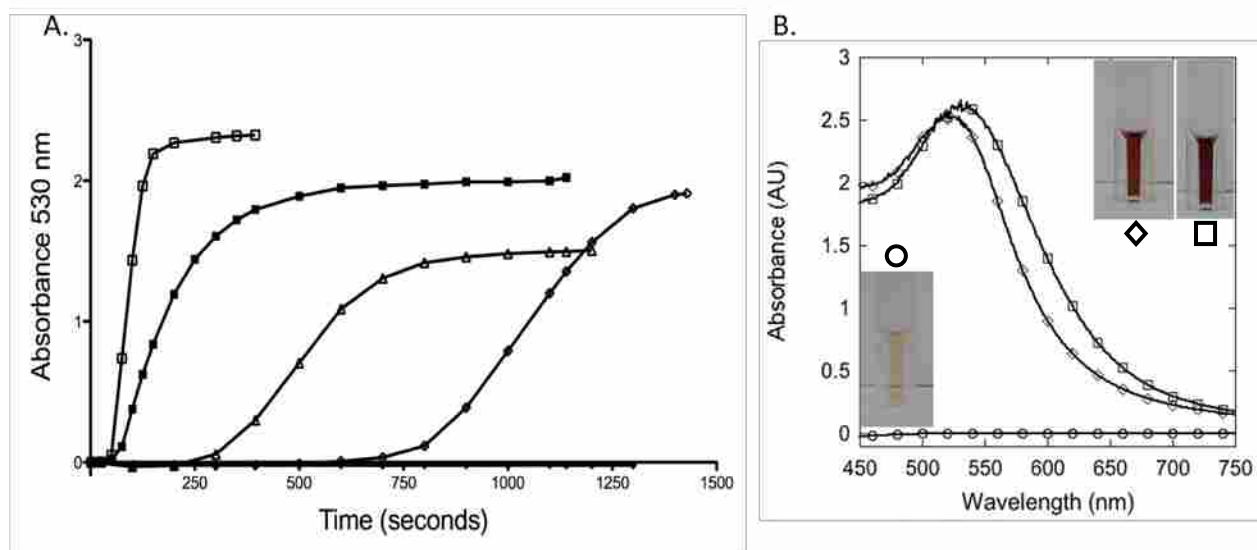
Figure 7-1. Spectrophotometric analysis of AuNPs. A) Solutions were prepared with ferritin, citrate, and $AuCl_4^-$ in the following buffers and illumination conditions and the formation of AuNPs was monitored by following the change in absorbance at 530 nm with time. (□) MOPS with illumination; (■) MOPS dark; (Δ) water with illumination; (◊) Tris with illumination; (♦) Tris and water dark (identical curves). B) The spectrum of AuNPs from the Tris illuminated (◊) and MOPS illuminated (□) reactions. (○) represents the spectrum of the samples prior to illumination. Insets show photos of the solutions before and after illumination.

In contrast, MOPS has previously been shown to chemically reduce $AuCl_4^-$ to AuNPs both in the absence and presence of ferritin.[29, 55, 56] The results in Figure 7–1A show that AuNPs form more rapidly when illuminated in MOPS, but that they also rapidly form in the dark. Interestingly, both of the reactions in MOPS produce purple solutions and not the red solution observe for the Tris reaction (Figure 7–1B inset) and have a broader, red-shifted SPR maximum of 550 nm (Figure 7–1B).

To confirm that AuNPs formed under the conditions shown in Figure 7–1, the samples were characterized by TEM (Figure 7–2). Electron micrographs of the illuminated Tris sample (Figure 7–2A) show the formation of spherical gold nanoparticles with diameters of 5.7 ± 1.6 nm. In comparison, the illuminated MOPS sample shows larger, more irregularly shaped particles that are 15–30 nm in diameter along with many smaller, spherically shaped particles (Figure 7–2B). We wondered why this sample contained both small and large particles, and so we performed the MOPS reaction in the dark, focusing on the chemical reduction of AuNPs. In this sample, we observed only the larger, more irregularly shaped particles in the 15-30 nm diameter size range (Figure 7–2C). These results suggest that the MOPS illuminated sample represents a mixture of light and dark reactions, where light reactions form smaller ~6-nm diameter particles and chemical reduction (dark reactions) form larger 15–30-nm diameter particles.

This led us to determine whether ferritin was necessary during the chemically reducing reactions (MOPS reactions). In the absence of ferritin, the solution initially turned purple, but then aggregates formed. Observing this sample with electron microscopy, we see large gold aggregates (Figure 7–2D). This demonstrates that ferritin acts as a nano-architecture structure to guide the size and shape of the chemically reduced AuNPs.[29]
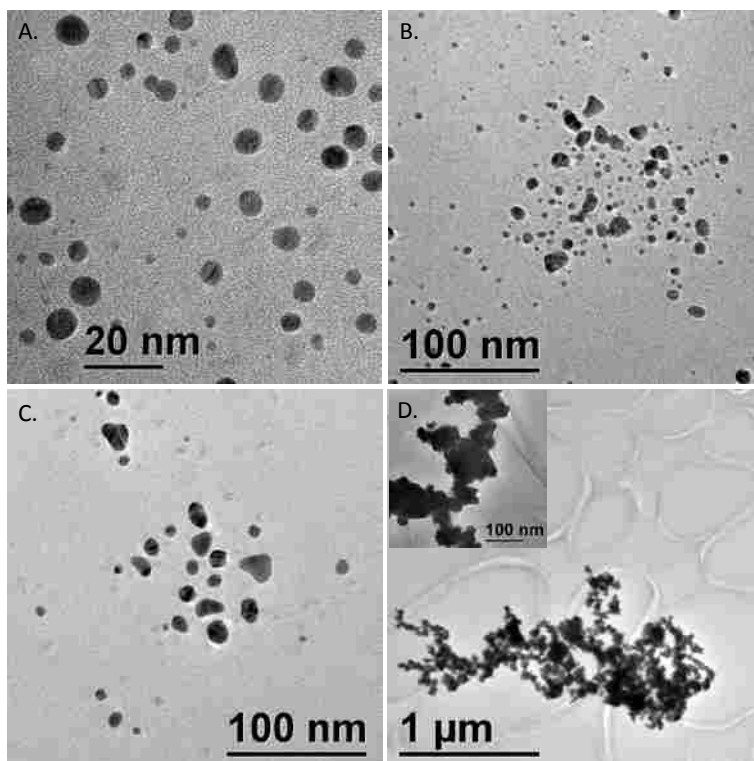
Figure 7-2. TEM of AuNPs formed under different conditions. TEM of AuNPs formed by A) illuminating ferritin in Tris, B) illuminating ferritin in MOPS, C) chemical reduction by MOPS in the presence of ferritin, D) chemical reduction by MOPS in the absence of ferritin.

The illuminated MOPS reaction produced both large and small AuNPs (Figure 7–2B) and is proposed to be a mixture of both the light catalyzed reaction (small particles) and dark chemical reduction reaction (larger, irregularly-shaped particles). Because the light reaction proceeds at a faster rate, we hypothesized that the AuNP particle size can be controlled in MOPS buffer depending on the timing of when $AuCl_4^-$ is added to the reaction. A MOPS sample was prepared by mixing all of the components of the reaction mixture except for the $AuCl_4^-$ and the sample was placed in the spectrophotometer and the mercury light was focused on the sample. The absence of gold prevented the chemical reduction (dark reaction) from beginning prior to illumination. We refer to this reaction as the pre-illuminated MOPS reaction. While the solution

153

was illuminated, AuCl$_4^-$ was added and the reaction proceeded as detected by SPR band formation at 530 nm. The product that formed in this reaction was red and not purple as seen previously for MOPS reactions. Figure 7–3 compares the spectrum of the product of the MOPS pre-illuminated reaction with a sample illuminated in Tris. Both show spectra for the SPR maxima at 530 nm with nearly identical peak width. Furthermore, the TEM images show similarly sized, spherically-shaped particles with a diameter of 5.7 ± 1.6 nm for reactions in Tris compared to diameters of 5.5 ± 1.8 nm for the reaction in MOPS. These data indicate that illumination prior to the addition of AuCl$_4^-$ to MOPS drives product formation by the photo-reduction reaction.
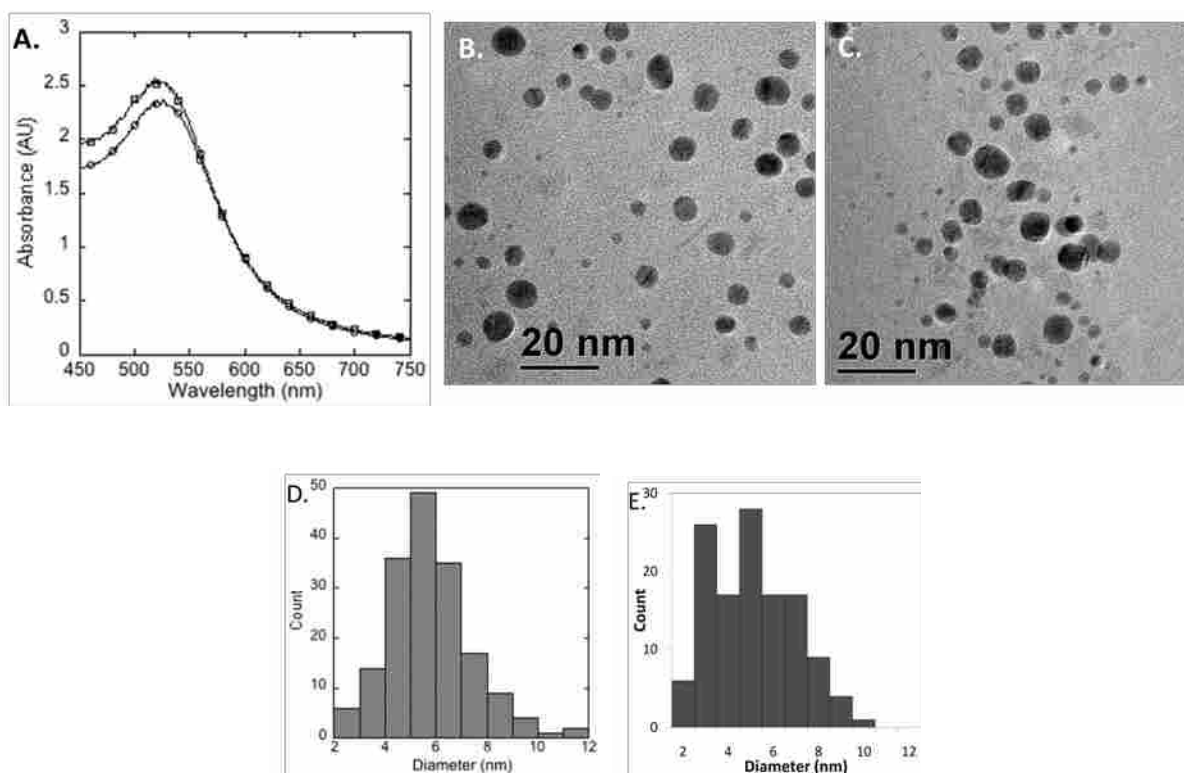
Figure 7-3. MOPS reactions pre-illuminated before AuCl$_4^-$ addition. A) Comparison of the spectrum of (○) Tris illuminated AuNPs with pre-illuminated (□) MOPS AuNPs. B) TEM of Tris illuminated AuNPs, C) TEM of MOPS pre-illuminated AuNPs. D) Size distribution of the AuNP diameters from B), whereas E) shows the size distribution of the particles from C).

154

Control reactions in Tris in the absence of ferritin but with citrate and $AuCl_4^-$ failed to produce AuNPs upon illumination. Similar reactions adding apoferritin to citrate and $AuCl_4^-$ in Tris failed to produce AuNPs under illumination, indicating that the ferrihydrite mineral inside ferritin is the photocatalyst. To determine if ferrihydrite alone (without ferritin) could catalyze the formation of AuNPs, we repeated the reaction using a colloidal suspension of ferrihydrite nanoparticles (ferrihydrite nanoparticle powder shown in Figure 7–4A) with an average size of 10 nm (a kind gift from Brian Woodfield).[57] The product of this reaction was a gray precipitate (Figure 7–4B shows the dried product) and not the red or purple solution that is indicative of soluble AuNP formation. TEM of the gray precipitate (Figure 7–4C) shows large aggregates and not discrete nanoparticles. These controls confirm that the protein shell is essential for the formation and solubility of the AuNPs. We propose that the protein shell; 1) separates the ferrihydrite photocatalyst from the nucleating gold particles and prevents interactions between the iron and gold that lead to precipitation reactions between these metals; 2) provides amino acid residues on the protein exterior surface that act as nucleation sites for gold deposition; and 3) acts as a capping agent for the AuNPs to maintain solubility.
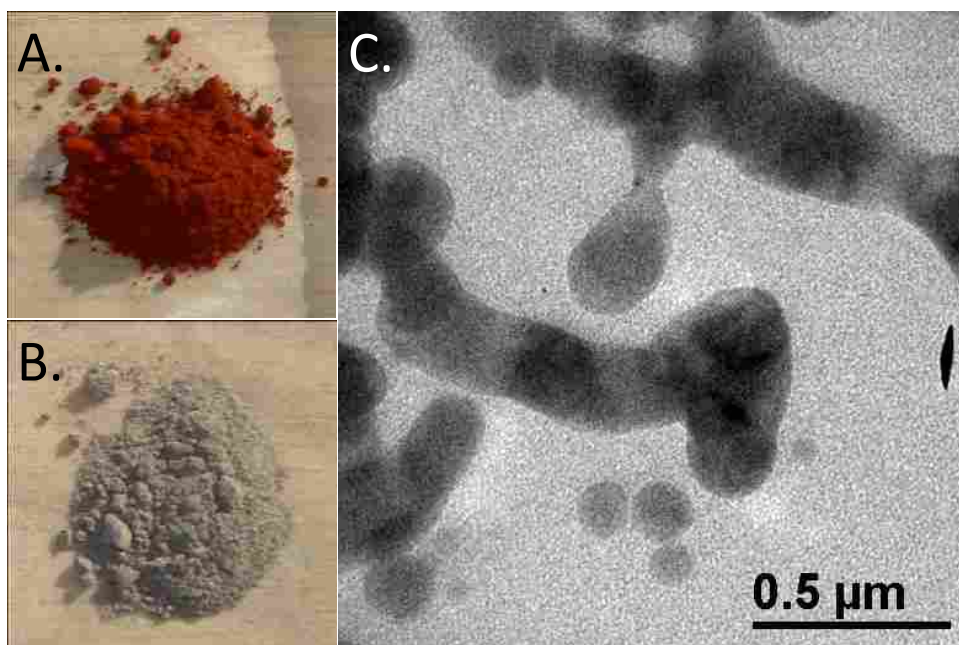
Figure 7-4. Control reactions to form AuNPs using ferrihydrite nanoparticles. Using identical conditions to the previous studies, ferrihydrite nanoparticles were substitute for ferritin in the reactions. A) Photograph of the 10 nm diameter ferrihydrite powder used to prepare a colloidal suspension to act as a photocatalyst for AuNP synthesis. B) Photograph of the dried product that formed when ferrihydrite nanoparticles were illuminated with citrate and $AuCl_4^-$. C) TEM of the sample shown in B.

Understanding the elemental composition of the AuNPs is important in determining whether the AuNPs form inside ferritin or on the outside surface. One potential mechanism for AuNP formation is that Au^{3+} ions enter ferritin and that the iron mineral surface acts as a nucleation site for the photo-reduction and deposition of AuNPs inside ferritin.[28] This is a particularly appealing proposal because the illuminated Tris samples produced ~6 nm diameter sized nanoparticles, which compares favorably to the inner dimension of the ferritin interior with a ~8 nm diameter interior. If the ferritin iron core is the site of reduction and nucleation of the nascent AuNPs, the new particles should be a mixture of both gold and iron. Therefore, the elemental composition of the resulting particles was analyzed by EDX for gold and iron. Figure

7–5A shows two highlighted nanoparticles, a bright particle that obviously contains gold due to the electron scattering in box 1, and a faint particle corresponding to what is presumably ferritin with an iron core in box 2. The elemental composition of the nanoparticles is shown in Figure 7–5B for box 1 and Figure 7–5C for box 2. Figure 7–5B confirms that box 1 is a gold nanoparticle but shows evidence of a small iron peak. Box 2, which is the less intense and smaller nanoparticle, shows an iron EDX signal in addition to a gold signal. These results are consistent with gold nucleating on the iron core surface followed by growth of the gold nanoparticle.
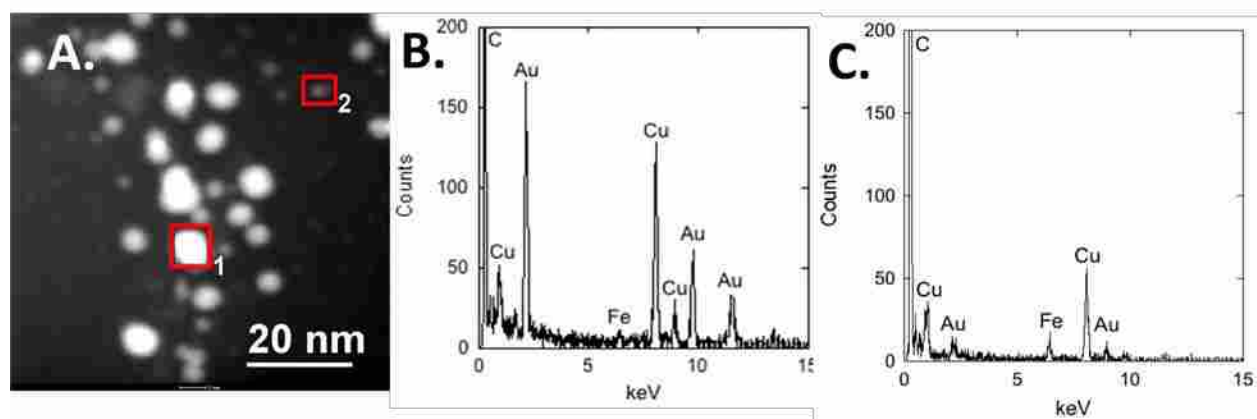
Figure 7-5. STEM and EDX of particles formed in Tris. A) STEM image of gold particles formed by illumination of ferritin and $AuCl_4^-$ in Tris. Box 1 and box 2 correspond to the EDX graphs in panel B and C, respectively. B) Spectrum from EDX on box 1, presumably a gold particle. Gold peaks are observed at characteristic locations of 2.12, 9.712, and 11.919 keV. In addition, a characteristic peak for iron is observed at 6.403 keV. This indicates that iron is nearby or within the gold particle. C) This smaller, less dense particle (box 2) is confirmed to be iron by EDX and also shows a small gold peak.

Size-exclusion chromatography was used as another method to determine if AuNPs were forming inside ferritin. The presence of AuNPs (530 nm) or ferritin (280 nm) in the fractions was detected by monitoring the absorbance of fractions eluted from a Superdex[TM] 200 10/300 GL size-exclusion column. The first peak eluted at ~8 mL and showed absorbance at both 530 and 280 nm, representing AuNPs and ferritin, respectively (Figure 7–6). A second peak eluted at 10–

157

11 mL, where purified ferritin normally elutes from this column. This peak was predominantly a protein peak (280 nm absorbance) with smaller amounts of AuNPs (530 nm absorbance).
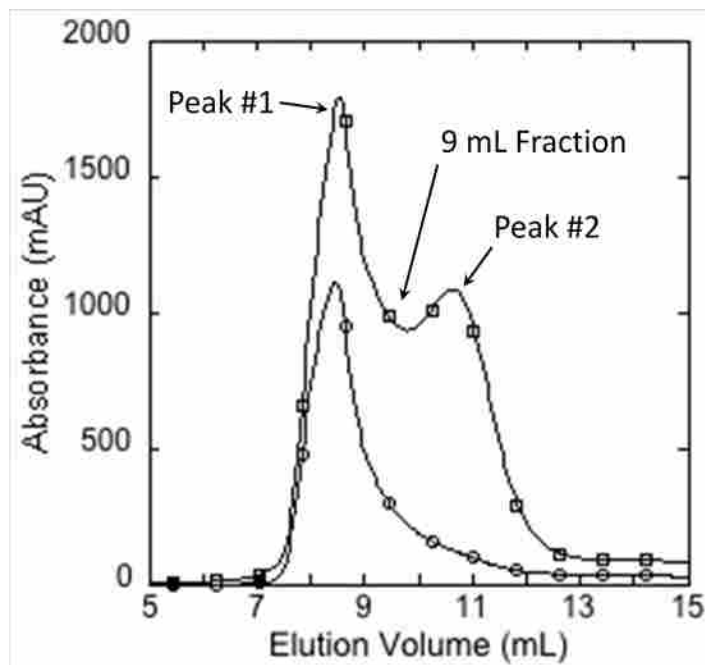
Figure 7-6. Size-exclusion chromatography of samples prepared in Tris. The size-exclusion elution profile of a sample prepared by illumination in Tris. Wavelengths of 280 nm (○) and 530 nm (□) detect ferritin and AuNPs, respectively.

The major elution peak of the chromatograph is at ~8 mL. This fraction elutes much earlier than native ferritin (peak #2, ~10 mL). Fraction 8 has two intense peaks, one for the protein (280 nm), and one for the AuNPs (530 nm). Inductively coupled plasma (ICP) analysis of this fraction showed the highest concentration of gold in any of the fractions (data not shown). TEM analysis using uranyl acetate to stain for the ferritin protein shell showed both AuNPs and ferritin in this fraction, even though purified ferritin normally elutes at a later volume (Figure 7–7). The elution of this fraction prior to the expected elution volume of ferritin suggests a large hydrodynamic radius for the eluting particles. Because ferritin is observed in this fraction, it suggests that ferritin is attached to AuNPs and that these two particles are co-migrating. The

arrows point to ferritin molecules adjacent to AuNPs. The ferritin is the lighter halo that surrounds the slightly darker iron cores. The thickness of the white halos is consistent with the 2 nm thickness of the ferritin protein shell. The TEM image confirms that ferritin is found adjacent or attached to AuNPs and explains why ferritin eluted much earlier than expected. This suggests that AuNPs form on the external surface of ferritin. Because this fraction contains the majority of the AuNPs (greatest absorbance at 530 nm), it appears this is the predominant reaction forming AuNPs under the conditions tested.
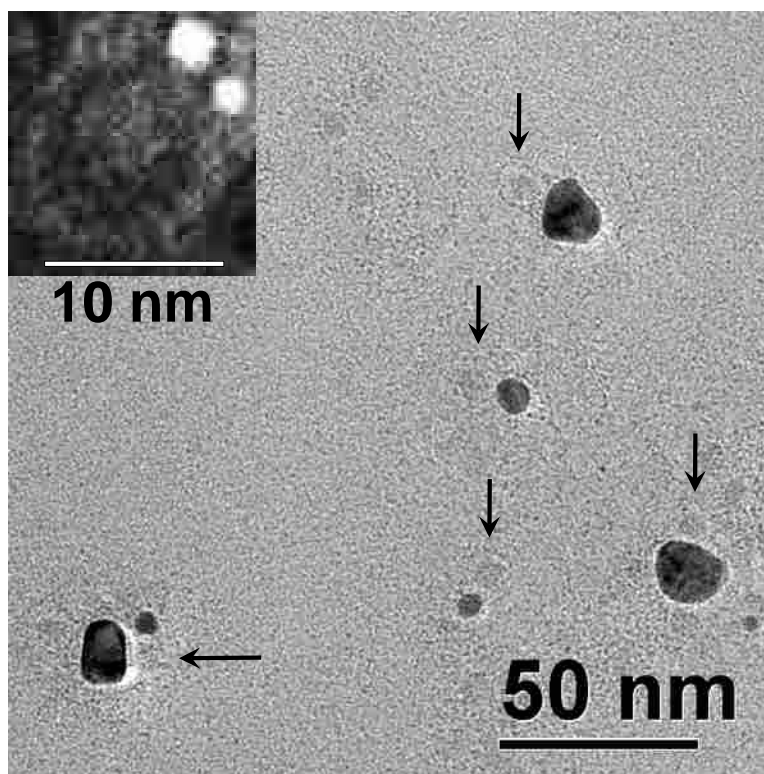
Figure 7-7. AuNP formation on the exterior surface of ferritin. Representative electron micrograph of the sample that eluted at 8 mL from the size-exclusion column. The sample was prepared and stained with uranyl acetate on TEM grids, as describe in the Materials and Methods section. The arrows identify ferritin molecules that are adjacent to AuNPs. The presence of ferritin in this elution fraction suggests that ferritin is attached to these AuNPs. Inset shows a STEM image from the 9 mL fraction. This image shows small AuNP seeds attached to the external surface of ferritin.

159

The inset in Figure 7–7 shows a STEM image of a representative ferritin observed in fraction 9, and shows two very small 1–2-nm AuNPs attached to the protein surface. The presence of small gold seeds attached to ferritin is consistent with the hypothesis that gold ions nucleate on the external surface of ferritin, followed by growth of the AuNP. Scheme 7–2 shows a model of how this reaction may proceed.
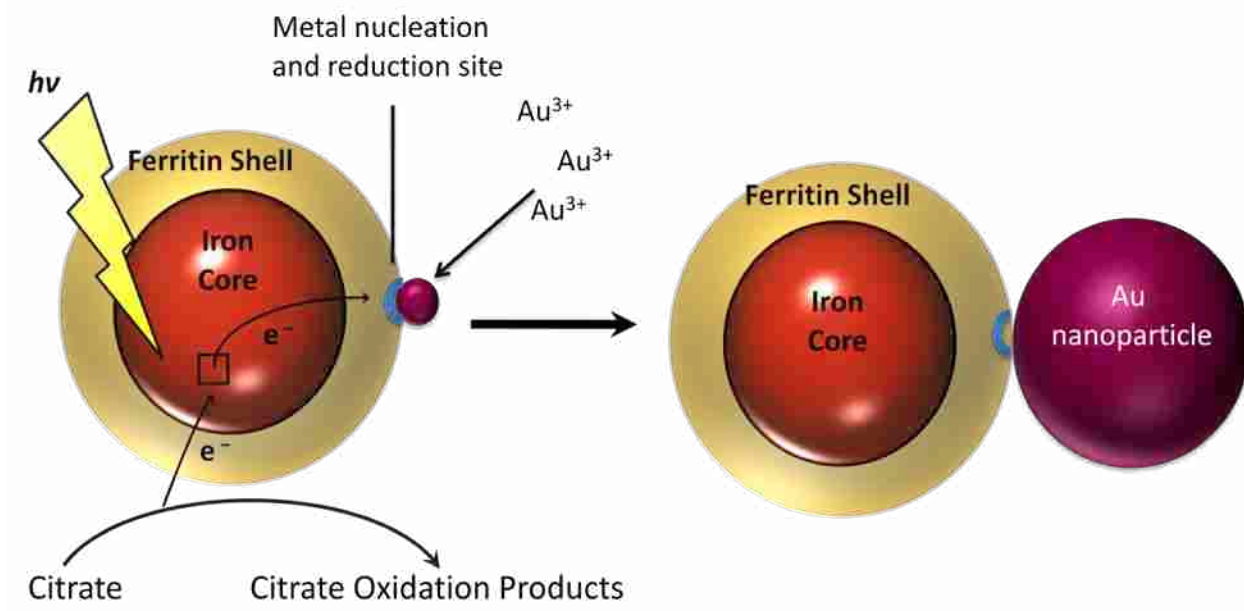
Scheme 7-2. Mechanism of AuNP formation by ferritin illumination. Ferritin possesses a putative nucleation site that attracts Au^{3+} ions. Photochemical excitation of the iron core transfers electrons across the ferritin protein shell to reduce the Au^{3+} ions. The electron holes created by this photochemistry are replenished from the sacrificial electron donor citrate. The initial gold particle seed acts as a nucleation site that attracts more Au^{3+}, which in turn are reduced and deposited on the growing gold particle.

Scheme 7–2 suggests that there is a metal nucleation site near the exterior surface of ferritin. A likely location might be the threefold channel of ferritin, which contains cysteine amino acid residues that have high affinity for binding gold. Kim et al. demonstrated that small AuNPs were able to bind at the threefold channel sites.[30] Once gold has nucleated on ferritin,

electrons can be transferred to this site as a method of reduction and nanoparticle growth. Electron transfer through the 2-nm protein shell has been previously demonstrated by several methods.[58, 59]

Unfortunately, the model proposed in Scheme 7–2 conflicts with the proposed model for chromate reduction by ferritin as the authors suggested that reduction occurred inside ferritin rather than on the outside surface.[27] This model was based on the observation that some of the Cr(III) product was observed inside ferritin despite the fact that Cr(III) does not diffuse into ferritin. In contrast, an alternate model showed that the majority of Cr(III) produced was found in the exterior solution but not attached to ferritin. This might be rationalized by the fact that gold has a much higher affinity for thiolate ligands than Cr(III) and may stay attached to ferritin, whereas the formation of Cr(III) on the exterior surface would more easily dissociate into solution. Therefore, our results suggest that the model showing AuNP reduction on the exterior surface of ferritin and the chromate reduction on the exterior surface of ferritin are consistent. The fact that both studies show smaller amounts of product on the interior of ferritin suggests that another mechanism also exists for metal reduction on the interior of ferritin, but the mechanism is not yet established for how this occurs.

Although the majority of the AuNPs form on the outside of ferritin, we do observe a significant fraction of AuNPs that form on the inside of ferritin. Fraction 9 from the size-exclusion column contained the majority of the gold-containing ferritin particles. TEM analysis of fraction 9 produced images that show AuNPs surrounded by ferritin (Figure 7–8). The ferritin is visualized by staining with uranyl acetate, and the protein is identified with white halos in the micrographs. The arrows in Figure 7–8 identify gold-containing ferritin nanoparticles and compare them to iron-containing ferritin molecules (white halos with less intensity due to iron).

STEM analysis shows ferritin stained with uranyl acetate with a very faint mineral core signal due to iron in the core (top), ferritin with a much brighter core, indicating a mixture of gold and iron (middle), and a gold core inside ferritin (bottom). This is consistent with the EDX analysis shown in Figure 7–5. These three images suggest that there might be a progression from an iron core to a gold core as the gold nucleates and grows within the ferritin protein shell. Another explanation for this observation is that the ferritin sample has different iron loadings based on the inhomogeneity of the native ferritin sample. Perhaps different iron contents leads to different gold loading on the interior of ferritin molecules.
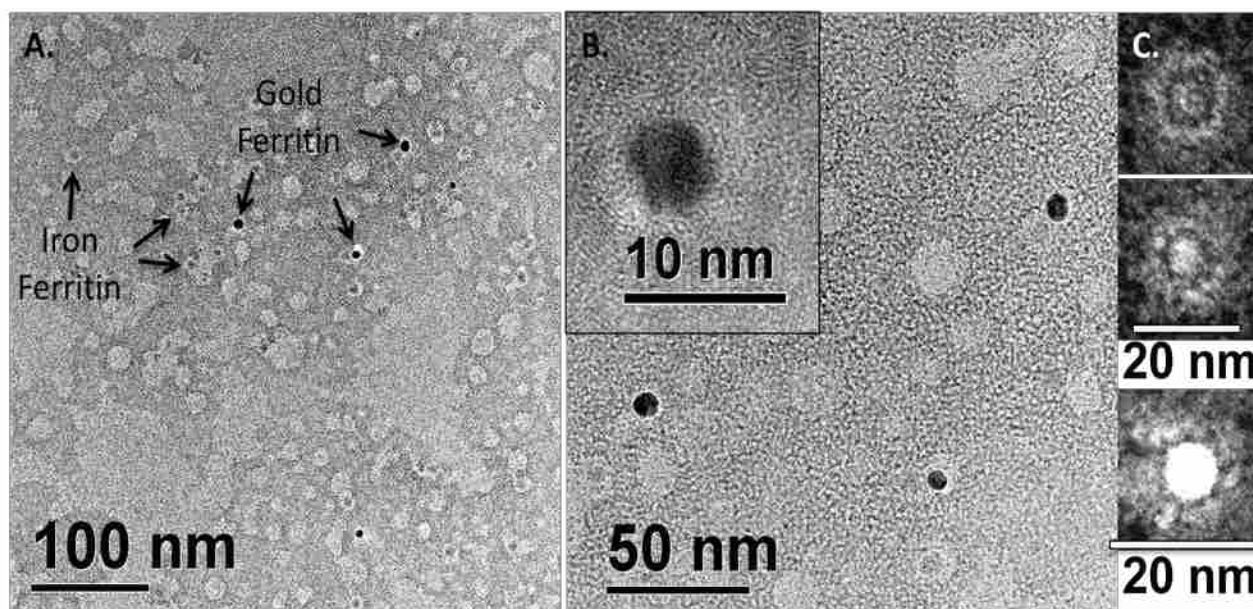
Figure 7-8. AuNP formation on the interior of ferritin. Fraction 9 from the size-exclusion column shows AuNPs surrounded by a white halo. These TEM images were stained with uranyl acetate, to allow visualization of the protein shell (white halos). A) Compares iron-containing ferritin with gold-containing ferritin. B) Shows greater magnifications of the gold containing-ferritin. C) STEM analysis of iron and gold containing ferritin. Top is a ferritin containing iron. Middle is a ferritin with a brighter mineral core suggesting a mixture of gold and iron. Bottom is a ferritin with a very bright interior, indicative of gold inside ferritin.

Conclusions

In summary, we have presented a photochemical method to prepare protein stabilized ~6-nm diameter spherically shaped AuNPs using ferritin as a photocatalyst. Our results are consistent with two pathways for AuNP formation. One pathway is an external AuNP growth pathway, observed in Figure 7–7. The second is gold deposition on the inside of ferritin, where gold is proposed to nucleate in the iron core of ferritin, as seen in Figure 7–8. We are currently exploring conditions to control whether the AuNPs form only on the surface or only on the interior of ferritin.

The work presented here highlights that the formation of AuNPs can be controlled by using ferritin as a photocatalyst. In Chapter 3, the role of citrate was discussed for the non-reductive release of iron from ferritin. In this work, citrate is used as an electron donor, but we also wondered about the possibility of citrate acting as an iron chelator. Chapter 8 discusses progress we have made in better understanding the role of citrate in this reaction.

This work was published in part in the Journal of Nanoparticle Research[60] *and in* Proceedings of SPIE[61, 62].

This work was presented as a poster at nanoUtah 2009 in SLC, UT and as a poster and talk at SPIE 2010 in San Diego, CA.

References

1.   Uchida, M.; Klem, M. T.; Allen, M.; Suci, P.; Flenniken, M.; Gillitzer, E.; Varpness, Z.; Liepold, L. O.; Young, M.; Douglas, T. Biological Containers: Protein Cages as Multifunctional Nanoplatforms. *Adv Mater* **2007,** *19* (8), 1025–1042.

2.   Whaley, S. R.; English, D. S.; Hu, E. L.; Barbara, P. F.; Belcher, A. M. Selection of Peptides with Semiconductor Binding Specificity for Directed Nanocrystal Assembly. *Nature* **2000,** *405*, 665–668.

3.   Niemeyer, C. M. Nanoparticles, Proteins, and Nucleic Acids: Biotechnology Meets Materials Science. *Angew Chem, Int Ed Eng* **2001,** *40* (22), 4128–4158.

4.   Katz, E.; Willner, I. Integrated Nanoparticle-Biomolecule Hybrid Systems: Synthesis, Properties, and Applications. *Angew Chem, Int Ed Eng* **2004,** *43* (45), 6042–6108.

5.   Harrison, P. M.; Arosio, P. Ferritins: Molecular Properties, Iron Storage Function and Cellular Regulation. *BBA* **1996,** *1275* (3), 161–203.

6.   Arosio, P.; Ingrassia, R.; Cavadini, P. Ferritins: A Family of Molecules for Iron Storage, Antioxidation and More. *BBA* **2009,** *1790* (7), 589–599.

7.   Meldrum, F. C.; Wade, V. J.; Nimmo, D. L.; Heywood, B. R.; Mann, S. Synthesis of Inorganic Nanophase Materials in Supramolecular Protein Cages. *Nature* **1991,** *349* (6311), 684–687.

8.   Okuda, M.; Iwahori, K.; Yamashita, I.; Yoshimura, H. Fabrication of Nickel and Chromium Nanoparticles Using the Protein Cage of Apoferritin. *Biotech and Bioeng* **2003,** *84* (2), 187–194.

9.   Zhang, B.; Harb, J. N.; Davis, R. C.; Kim, J. W.; Chu, S. H.; Choi, S.; Miller, T.; Watt, G. D. Kinetic and Thermodynamic Characterization of the Cobalt and Manganese Oxyhydroxide Cores Formed in Horse Spleen Ferritin. *Inorg Chem* **2005,** *44* (10), 3738–3745.

10.   Douglas, T.; Stark, V. T. Nanophase Cobalt Oxyhydroxide Mineral Synthesized within the Protein Cage of Ferritin. *Inorg Chem* **2000,** *39* (8), 1828–1830.

11.   Meldrum, F. C.; Douglas, T.; Levi, S.; Arosio, P.; Mann, S. Reconstitution of Manganese Oxide Cores in Horse Spleen and Recombinant Ferritins. *J Inorg Biochem* **1995,** *58* (1), 59–68.

12.   Hainfeld, J. F. Uranium-Loaded Apoferritin with Antibodies Attached - Molecular Design Uranium Neutron-Capture Therapy. *PNAS* **1992,** *89* (22), 11064–11068.

13.   Klem, M.; Mosolf, J.; Young, M.; Douglas, T. Photochemical Mineralization of Europium, Titanium, and Iron Oxyhydroxide Nanoparticles in Ferritin. *Inorg Chem* **2008,** *47*, 2237–2239.

14.   Douglas, T.; Dickson, D. P. E.; Betteridge, S.; Charnock, J.; Garner, C. D.; Mann, S. Synthesis and Structure of an Iron (III) Sulfide-Ferritin Bioinorganic Nanocomposite. *Science* **1995,** *269*, 54–57.

15.   Wong, K. K. W.; Mann, S. Biomimetic Synthesis of Cadmium Sulfide-Ferritin Nanocomposites. *Adv Mater* **1996,** *8* (11), 928–932.

16.   Yamashita, I.; Hayashi, J.; Hara, M. Bio-Template Synthesis of Uniform CdSe Nanoparticles Using Cage-Shaped Protein, Apoferritin. *Chem Lett* **2004,** *33* (9), 1158–1159.

17.   Iwahori, K.; Yoshizawa, K.; Muraoka, M.; Yamashita, I. Fabrication of ZnSe Nanoparticles in the Apoferritin Cavity by Designing a Slow Chemical Reaction System. *Inorg Chem* **2005,** *44*, 6393–6400.

18.   Yoshizawa, K.; Iwahori, K.; Sugimoto, K.; Yamashita, I. Fabrication of Gold Sulfide Nanoparticles Using the Protein Cage of Apoferritin. *Chem Lett* **2006,** *35* (10), 1192–1193.

19.   Turyanska, L.; Bradshaw, T. D.; Sharpe, J.; Li, M.; Mann, S.; Thomas, N. R.; Patane, A. The Biocompatibility of Apoferritin-Encapsulated PbS Quantum Dots. *Small* **2009,** *5* (15), 1738–1741.

20.   Kasyutich, O.; Ilari, A.; Fiorillo, A.; Tatchev, D.; Hoell, A.; Ceci, P. Silver Ion Incorporation and Nanoparticle Formation inside the Cavity of Pyrococcus furiosus Ferritin: Structural and Size-Distribution Analyses. *JACS* **2010,** *132* (10), 3621–3627.

21.   Ueno, T.; Suzuki, M.; Goto, T.; Matsumoto, T.; Nagayama, K.; Watanabe, Y. Size-Selective Olefin Hydrogenation by a Pd Nanocluster Provided in an Apo-Ferritin Cage. *Angew Chem, Int Ed Eng* **2004,** *43* (19), 2527–2530.

22.   Galvez, N.; Sanchez, P.; Dominguez-Vera, J. Preparation of Cu and CuFe Prussian Blue Derivative Nanoparticles Using the Apoferritin Cavity as Nanoreactor. *Dalt Transact* **2005,** *15*, 2492–2494.

23.   Galvez, N.; Sanchez, P.; Dominguez-Vera, J. M.; Soriano-Portillo, A.; Clemente-Leon, M.; Coronado, E. Apoferritin-Encapsulated Ni and Co Superparamagnetic Nanoparticles. *J Mater Chem* **2006,** *16* (26), 2757–2761.

24.   Shin, Y. S.; Dohnalkova, A.; Lin, Y. H. Preparation of Homogeneous Gold-Silver Alloy Nanoparticles Using the Apoferritin Cavity As a Nanoreactor. *J Phys Chem C* **2010,** *114*, 5985–5989.

25.   Butts, C. A.; Swift, J.; Kang, S. G.; Di Costanzo, L.; Christianson, D. W.; Saven, J. G.; Dmochowski, I. J. Directing Noble Metal Ion Chemistry within a Designed Ferritin Protein. *Biochemistry* **2008,** *47* (48), 12729–12739.

26.   Nikandrov, V. V.; Grätzel, C. K.; Moser, J. E.; Grätzel, M. Light Induced Redox Reactions Involving Mammalian Ferritin as Photocatalyst. *J Photochem Photobiol B* **1997,** *41* (1–2), 83–89.

27.   Kim, I.; Hosein, H.-A.; Strongin, D. R.; Douglas, T. Photochemical Reactivity of Ferritin for Cr(VI) Reduction. *Chem Mater* **2002,** *14* (11), 4874–4879.

28.   Ensign, D.; Young, M.; Douglas, T. Photocatalytic Synthesis of Copper Colloids from Cu(II) by the Ferrihydrite Core of Ferritin. *Inorg Chem* **2004,** *43* (11), 3441–3446.

29.   Zhang, L.; Swift, J.; Butts, C. A.; Yerubandi, V.; Dmochowski, I. J. Structure and Activity of Apoferritin-Stabilized Gold Nanoparticles. *J Inorg Biochem* **2007,** *101* (11-12), 1719–1729.

30.   Kim, J. W.; Posey, A. E.; Watt, G. D.; Choi, S. H.; Lillehei, P. T. Gold Nanoshell Assembly on a Ferritin Protein Employed as a Bio-Template. *J Nanosci Nanotech* **2010,** *10* (3), 1771–1777.

31.   Fan, R. L.; Chew, S. W.; Cheong, V. V.; Orner, B. P. Fabrication of Gold Nanoparticles Inside Unmodified Horse Spleen Apoferritin. *Small* **2010,** *6* (14), 1483–1487.

32.   Dominguez-Vera, J. M.; Galvez, N.; Sanchez, P.; Mota, A. J.; Trasobares, S.; Hernandez, J. C.; Calvino, J. J. Size-Controlled Water-Soluble Ag Nanoparticles. *Eur J Inorg Chem* **2007**, *30,* 4823–4826.

33.   Liu, J. W.; Lu, Y. A Colorimetric Lead Biosensor Using DNAzyme-Directed Assembly of Gold Nanoparticles. *JACS* **2003,** *125* (22), 6642–6643.

34.   Liu, J. W.; Lu, Y. Fast Colorimetric Sensing of Adenosine and Cocaine Based on a General Sensor Design Involving Aptamers and Nanoparticles. *Angew Chem, Int Ed Eng* **2006,** *45* (1), 90–94.

35.   Kuong, C.; Chen, W.; Chen, Y. Semi-Quantitative Determination of Cationic Surfactants in Aqueous Solutions Using Gold Nanoparticles as Reporter Probes. *Anal Bioanal Chem* **2007,** *387*, 2091–2099.

36.   Cao, Y. W. C.; Jin, R. C.; Mirkin, C. A. Nanoparticles with Raman Spectroscopic Fingerprints for DNA and RNA Detection. *Science* **2002,** *297* (5586), 1536–1540.

37.   Lee, J. S.; Ulmann, P. A.; Han, M. S.; Mirkin, C. A. A DNA-Gold Nanoparticle-Based Colorimetric Competition Assay for the Detection of Cysteine. *Nano Lett* **2008,** *8* (2), 529–533.

38.   Taton, T. A.; Mirkin, C. A.; Letsinger, R. L. Scanometric DNA Array Detection with Nanoparticle Probes. *Science* **2000,** *289* (5485), 1757–1760.

39.   Yang, M. H.; Kostov, Y.; Bruck, H. A.; Rasooly, A. Gold Nanoparticle-Based Enhanced Chemiluminescence Immunosensor for Detection of Staphylococcal Enterotoxin B (SEB) in Food. *Int J Food Microbiol* **2009,** *133* (3), 265–271.

40.   Yeh, C. H.; Hung, C. Y.; Chang, T. C.; Lin, H. P.; Lin, Y. C. An Immunoassay Using Antibody-Gold Nanoparticle Conjugate, Silver Enhancement and Flatbed Scanner. *Microfluid Nanofluid* **2009,** *6* (1), 85–91.

41.   Skrabalak, S. E.; Chen, J.; Au, L.; Lu, X.; Li, X.; Xia, Y. Gold Nanocages for Biomedical Applications. *Adv Mater* **2007,** *19*, 3177–3184.

42.   Chikae, M.; Fukuda, T.; Kerman, K.; Idegami, K.; Miura, Y.; Tamiya, E. Amyloid-Beta Detection with Saccharide Immobilized Gold Nanoparticle on Carbon Electrode. *Bioelectrochem* **2008,** *74* (1), 118–123.

43.   Bhaviripudi, S.; Mile, E.; Steiner, S. A.; Zare, A. T.; Dresselhaus, M. S.; Belcher, A. M.; Kong, J. CVD Synthesis of Single-Walled Carbon Nanotubes from Gold Nanoparticle Catalysts. *JACS* **2007,** *129* (6), 1516–1517.

44.   Turner, M.; Golovko, V. B.; Vaughan, O. P. H.; Abdulkin, P.; Berenguer-Murcia, A.; Tikhov, M. S.; Johnson, B. F. G.; Lambert, R. M. Selective Oxidation with Dioxygen by Gold Nanoparticle Catalysts Derived from 55-Atom Clusters. *Nature* **2008,** *454* (7207), 981–983.

45.   Daniel, M. C.; Astruc, D. Gold Nanoparticles: Assembly, Supramolecular Chemistry, Quantum-Size-Related Properties, and Applications Toward Biology, Catalysis, and Nanotechnology. *Chem Rev* **2004,** *104* (1), 293–346.

46.   Huang, W. C.; Chen, Y. C. Photochemical Synthesis of Polygonal Gold Nanoparticles. *J Nanopart Res* **2008,** *10* (4), 697–702.

47. Mallick, K.; Witcomb, M. J.; Scurrell, M. S. Polymer-Stabilized Colloidal Gold: A Convenient Method for the Synthesis of Nanoparticles by a UV-Irradiation Approach. *Appl Phys A* **2005,** *80*, 395–398.

48. Shankar, S. S.; Rai, A.; Ankamwar, B.; Singh, A.; Ahmad, A.; Sastry, M. Biological Synthesis of Triangular Gold Nanoprisms. *Nature Mater* **2004,** *3* (7), 482–488.

49. Eustis, S.; Hsu, H. Y.; El-Sayed, M. A. Gold Nanoparticle Formation from Photochemical Reduction of Au3+ by Continuous Excitation in Colloidal Solutions. A Proposed Molecular Mechanism. *J Phys Chem* **2005,** *109* (11), 4811–4815.

50. Esumi, K.; Matsuhisa, K.; Torigoe, K. Preparation of Rodlike Gold Nanoparticles by UV Irradiation Using Cationic Micelles as a Template. *Langmuir* **1995,** *11* (9), 3285–3287.

51. Sau, T. K.; Pal, A.; Jana, N. R.; Wang, Z. L.; Pal, T. Size Controlled Synthesis of Gold Nanoparticles Using Photochemically Prepared Seed Particles. *J Nanopart Res* **2001,** *3* (4), 257–261.

52. Zhou, Y.; Wang, C. Y.; Zhu, Y. R.; Chen, Z. Y. A Novel Ultraviolet Irradiation Technique for Shape-Controlled Synthesis of Gold Nanoparticles at Room Temperature. *Chem Mater* **1999,** *11* (9), 2310–2311.

53. Lowry, O. H.; Rosebrough, N. J.; Farr, A. L.; Randall, R. J. Protein Measurement with the Folin Phenol Reagent. *J Biol Chem* **1951,** *193* (1), 265–75.

54. Watt, R. K.; Frankel, R. B.; Watt, G. D. Redox Reactions of Apo Mammalian Ferritin. *Biochemistry* **1992,** *31* (40), 9673–9679.

55. Habib, A.; Tabata, M.; Wu, Y. G. Formation of Gold Nanoparticles by Good's buffers. *Bull Chem Soc Jpn* **2005,** *78* (2), 262–269.

56. Xie, J. P.; Lee, J. Y.; Wang, D. I. C. Seedless, Surfactantless, High-Yield Synthesis of Branched Gold Nanocrystals in HEPES Buffer Solution. *Chem Mater* **2007,** *19* (11), 2823–2830.

57. Liu, S. F.; Liu, Q. Y.; Boerio-Goates, J.; Woodfield, B. F. Preparation of a Wide Array of Ultra-High Purity Metals, Metal Oxides, and Mixed Metal Oxides with Uniform Particle Sizes from 2 nm to Bulk. *J Adv Mater* **2007,** *39*, 18–23.

58.   Zhang, B.; Watt, G. D. Anaerobic Iron Deposition into Horse Spleen, Recombinant Human Heavy and Light and Bacteria Ferritins by Large Oxidants. *J Inorg Biochem* **2007,** *101*, 1676–1685.

59.   Watt, G. D.; Jacobs, D.; Frankel, R. B. Redox Reactivity of Bacterial and Mammalian Ferritin: Is Reductant Entry into the Ferritin Interior a Necessary Step for Iron Release? *PNAS* **1988,** *85*, 7457–7461.

60.   Keyes, J.; Hilton, R.; Farrer, J.; Watt, R. Ferritin as a Photocatalyst and Scaffold for Gold Nanoparticle Synthesis. *J Nanopart Res* **2011,** *13* (6), 2563–2575.

61.   Hilton, R. J.; Keyes, J. D.; Watt, R. K. In *Maximizing the Efficiency of Ferritin as a Photocatalyst for Applications in an Artificial Photosynthesis System*, Nanosensors, Biosensors, and Info-Tech Sensors and Systems 2010, San Diego, CA, USA, SPIE: San Diego, CA, USA, 2010; pp 76460–76468.

62.   Hilton, R. J.; Keyes, J. D.; Watt, R. K. In *Photoreduction of Au(III) to Form Au(0) Nanoparticles Using Ferritin as a Photocatalyst*, Nanosensors, Biosensors, and Info-Tech Sensors and Systems 2010, San Diego, CA, USA, SPIE: San Diego, CA, USA, 2010; pp 764607–764610.

CHAPTER 8: FERRITIN PHOTOCATALYST; INTERMEDIATES AND MECHANISM

Abstract

The mechanism of gold nanoparticle (AuNP) formation using ferritin as a photocatalyst was examined. The purpose of this study was to determine the effectiveness of using ferritin as a photocatalyst for use in an artificial photosynthesis system. AuNPs were used because it is easy to monitor the rate and efficiency of the reaction, based upon the readily observable surface plasmon resonance of AuNPs. We investigated each component of the reaction (buffer, salt, citrate, gold, protein) to determine the effect that each one plays in the growth of these particles. We show that Tris buffer is the only buffer that increases the length of the lag phase in the reaction. Tris inhibits the autocatalytic formation of AuNPs, and so in an effort to understand the intermediates in the lag phase, the majority of the studies were undertaken using Tris buffer. We propose that the iron core of ferritin becomes photo-reduced, so that the ferrihydrite mineral dissolves into a soluble iron(II) mineral. The iron(II) then re-oxidizes, and a new mineral forms that appears to be the new photocatalyst, as the lag phase is significantly decreased with this new mineral form of ferritin. We show that ferritin is required in order to form a tight distribution of size-constrained AuNPs.

Introduction

AuNPs have been increasingly simple to synthesize in a size-constrained manner using a variety of techniques.[1-5] Interest in AuNP synthesis revolves around the properties of AuNPs, including optical and electrical properties, and is also based upon the potential applications in biomedical research,[6-8] as was discussed in the previous chapter. The optical properties of AuNPs are especially useful for us because it renders a simple colorimetric assay for determining the rate and efficiency of the transfer of electrons using ferritin. Essentially, we are able to

readily monitor the reaction using ferritin as a photocatalyst by the observance of the localized surface plasmon resonance (SPR) peak of AuNPs at 530 nm. SPR is an electromagnetic wave that propagates along the surface of metal nanoparticles. This wave emits an intense red color for AuNPs, so that a relatively small amount of reactant can be detected and monitored. Shifts in the SPR peak are attributed to the properties of the surface, namely the diameter of the particles or the adsorption of other molecules on the surface. In our studies, the shift in the SPR peak has been observed to relate strictly to the size and distribution of the particles, as observed using electron microscopy. A tight peak at 530 nm indicates a tight distribution of nanoparticles in the ~6 nm range, with a red solution color. As the peak broadens, the distribution becomes broader. Likewise, when the peak red-shifts, the particle size increases and the solution becomes blue.

Materials and Methods

Horse spleen ferritin was purchased from Sigma-Aldrich. The ferritin was dialyzed into pure water, to eliminate the high salt concentration that is present in Sigma ferritin. Protein concentration was determined using the Lowry method[9] and iron concentrations were determined using the reduction/chelation method by treating with dithionite and 2,2'-bipyridine.[10]

Reaction conditions were 0.1 mg/mL (2.2 x 10^{-4} mM) ferritin, 20 mM 2-amino-2-hydroxymethyl-propane-1,3-diol (Tris) buffer, pH 7.4, 50 mM NaCl, 0.4 mM $AuCl_4^-$, 20 mM citrate to a final volume of 1 mL. In addition, a wide array of buffers was used in this study. All buffers were prepared identical to the Tris buffer solution, to maintain consistency across experiments.

UV-Visible spectrophotometry was performed using an Agilent 8453 spectrophotometer. The cuvette holder was coupled to a water-circulated stirring mechanism and also a water-

circulated temperature bath to maintain constant temperature at 23 °C. Photochemistry was performed using a Sun Ray 400 UV flood lamp (Integrated Dispensing).

Transmission electron microscopy was performed using a Tecnai F30 EM, operating at 140 keV. Samples were deposited on copper TEM grids (Ted Pella lacey carbon film grids) by placing a 3.5 µL sample onto the grid, followed by a short incubation and a rinse with deionized water. The grid was allowed to air dry.

Results

To study the mechanism of AuNP growth using ferritin, and thereby maximize the efficiency of ferritin as a photocatalyst, we performed all reactions using Tris buffer. Tris buffer lengthens the time of the lag phase, and it also limits any side reactions that take place. To monitor the efficiency of the electron transfer reactions initiated by light over a variety of conditions, we used the colorimetric properties of AuNPs. As discussed in the previous chapter, the growth of AuNPs can be observed by monitoring the absorbance peak at 530 nm (Figure 8–1).
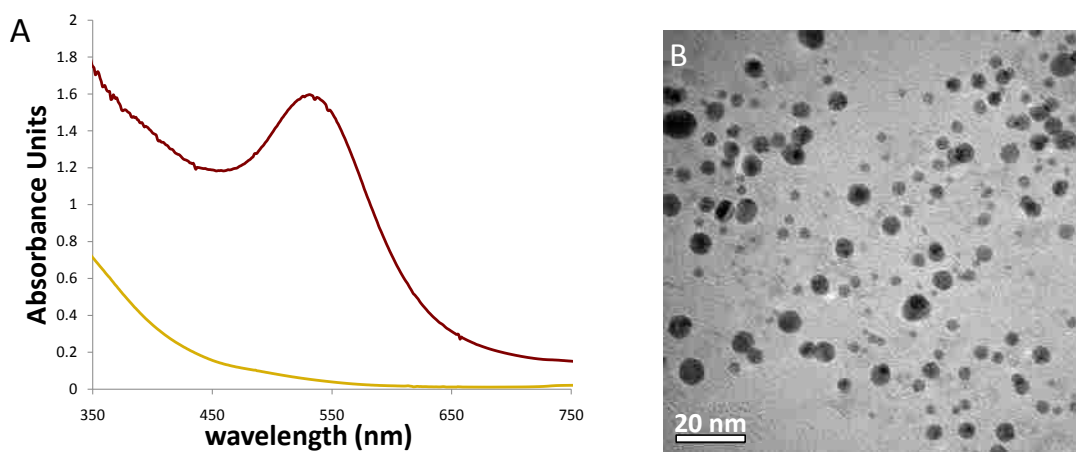
Figure 8-1. Spectrophotometric analysis of AuNPs. A) The absorbance of AuNPs can be observed spectrophotometrically by monitoring the peak at 530 nm. **Yellow** is the absorbance prior to illumination, and **red** is the absorbance following formation of AuNPs. B) The AuNPs were observed using EM, and we observe particles with an average diameter of approximately 6 nm.

We observed previously that MOPS buffer stimulates the rate of the reaction compared to water and that Tris buffer inhibits the rate of the reaction compared to water.[11] Because buffers have a significant effect on the reaction, we sought to characterize a wide array of commonly used buffers, to determine how they affect the rate and final product. Generally, we observe that buffers containing a morpholino group significantly enhance the rate of the reaction (Figure 8–2). Most other buffers have no stimulatory effect, compared to water. Tris buffer is the only buffer that significantly decreases the rate of the reaction. The stimulatory buffers, EPPS, HEPES, MOPS, MES, and PIPES, stimulate the rate of the reaction from ~6–14-fold. The structures of these buffers are similar, with each containing a morpholino group. Previous work has shown that some Good's buffers are able to auto-reduce gold ions, forming AuNPs.[12] This is confirmed in this study, where we observe broad, red-shifted peaks, indicating the formation of a broad distribution of particle sizes, generally of a larger nature. The particles also tend to be less spherical. These results indicate that neither ferritin nor light are necessary for the formation of AuNPs using these buffers, and thus the use of these buffers should be avoided when trying to understand the mechanism of ferritin photocatalysis of AuNPs.

On the other hand, buffers that do not dramatically affect the rate of the reaction often seem to play a role in the final product of the reaction. This was concluded by observing that the peak was broader and red-shifted, and the solution appears blue, rather than red. From this information, we conclude that side reactions may be occurring that lead to multiple products in the reaction. Furthermore, in an effort to study the mechanism of the reaction, it is desirable to extend the lag phase, which effectively extends the formation of intermediates that may be playing a role as the catalyst for AuNP formation. As a result, we chose to work with Tris buffer, which did not shift the peak in any way, and which is the only buffer that considerably extends the lag phase.
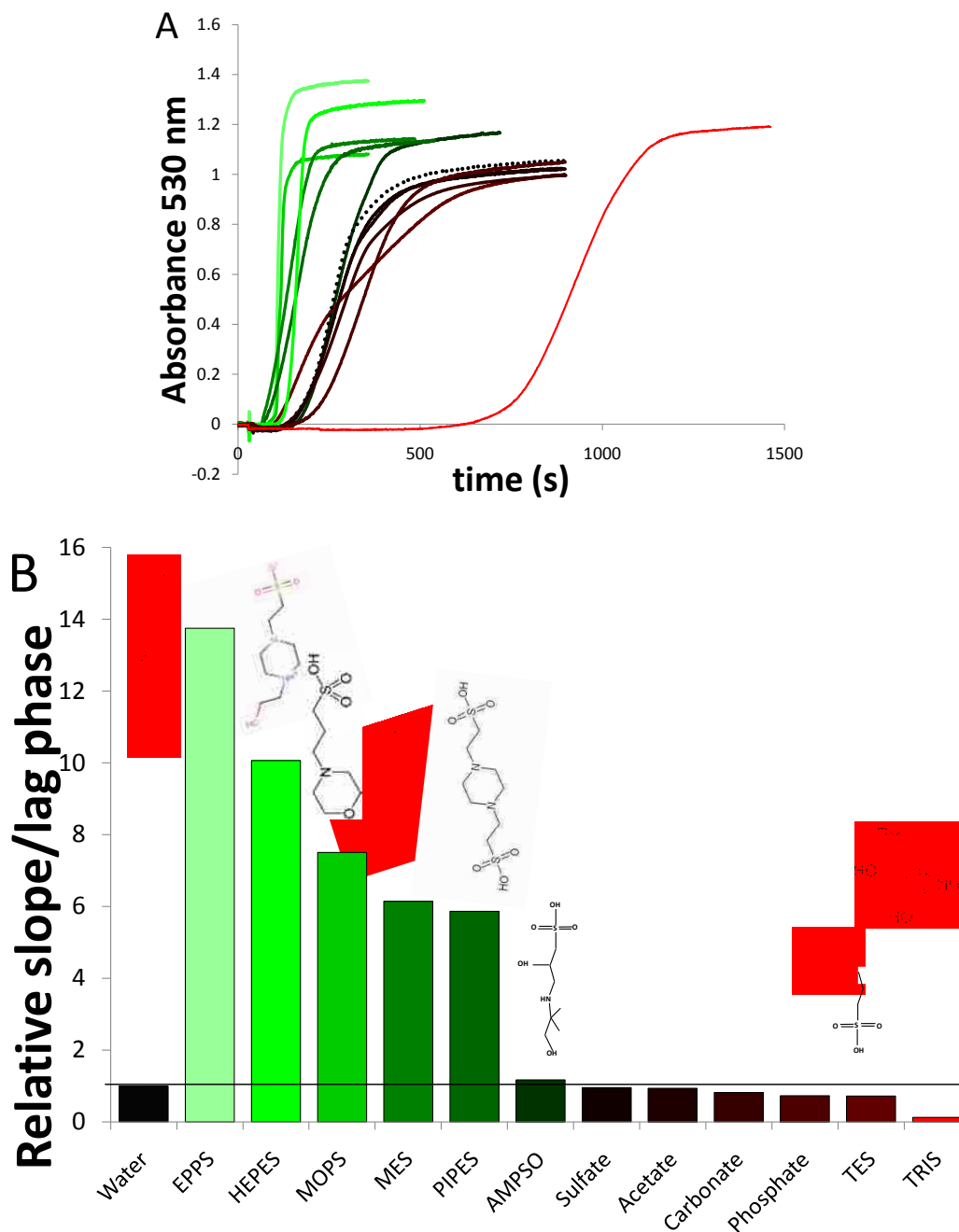
Figure 8-2. Buffers significantly influence the rate of reaction. A) The rate of AuNP formation was monitored at 530 nm in a variety of buffers. We observed that buffers containing N-morpholino groups stimulate (**green**) the rate of the reaction up to 14-fold (for EPPS buffer). Several other buffer types have rates very similar to water (**black dots**). Tris buffer is the only buffer that we tested that strongly inhibits (**red**) the rate of formation of AuNPs. B) The relative rates (compared to water) are shown as a chart for comparison, where the rate is the slope of formation divided by the lag phase. Also shown are the less well-known structures of the buffers.

In addition to buffers, we also wanted to break down the reaction by looking at ideal concentrations for each component in the reaction. By keeping all components constant and by varying only one, we were able to determine the appropriate concentrations and relevance of each variable in the system (buffer, NaCl, citrate, $AuCl_4^-$, protein) (data not shown). Based on these studies, there are a few interesting observations. First, limited concentrations of Tris buffer (< 2 mM) tend to stimulate the reaction slightly, but at concentrations above 2 mM, we observe that Tris inhibits the auto-reduction of gold ions to AuNPs. The ideal concentration for preventing auto-reduction side reactions and only allowing the photo-reduction reaction is 20 mM Tris. The presence of salt tends to stimulate the rate of the reaction, to a point. Once we reach 50 mM salt, the rate of the reaction reaches a maximum. We also observe that the ideal ratio of citrate to gold is 50:1. Finally, we determined that approximately 2,000 gold ions for every ferritin molecule is ideal (~1:1 ratio of gold to iron). Together, these studies help elucidate ideal conditions for the synthesis of AuNPs, which can be extended to the synthesis of other metal nanoparticles. These studies may also help shed light on the exact molecular interactions that may be taking place.

After having determined the appropriate buffer to use for this study, including the ideal concentration of each variable in the reaction, we sought to determine what changes were taking place to the ferritin core upon illumination. Previous work has shown that light photo-reduces the iron core of ferritin.[13] Thus, upon photo-reduction, one should be able to detect Fe(II). We set up the identical reaction conditions, but instead of adding gold ions to the reaction, we added an excess of 2,2′-bipyridine (greater than 3:1 ratio of 2,2′-bipyridine to iron). Figure 8–3 shows the results of this experiment.
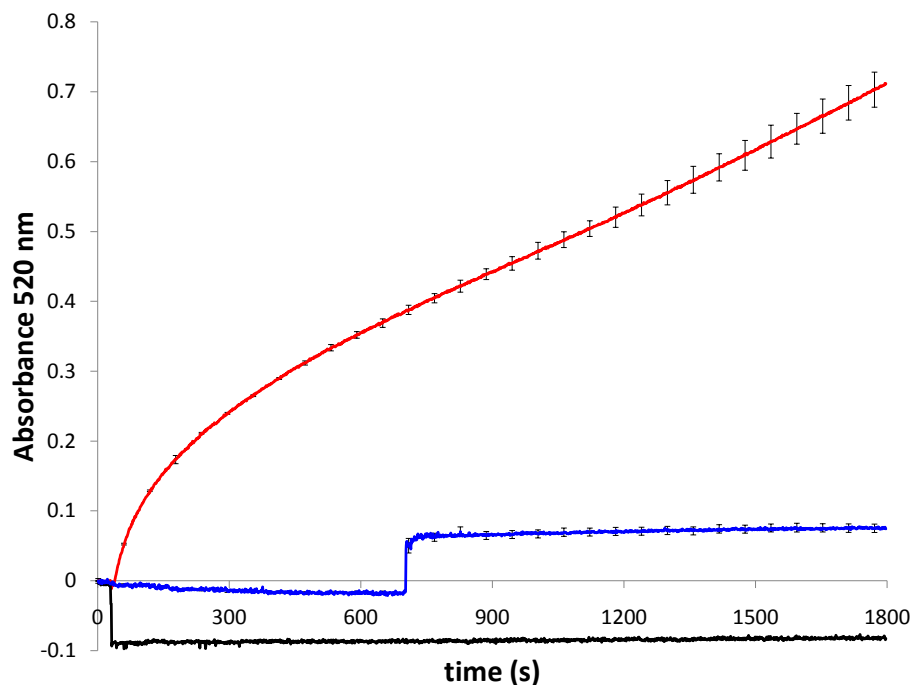
Figure 8-3. Photochemical reduction of the iron core inside ferritin. The reaction is placed under illumination, and 2,2'-bipyridine is added after 30 seconds. **Black** is the addition of 2,2'-bipyridine, but in the absence of illumination. **Red** is the addition of 2,2'-bipyridine with illumination. **Blue** is illumination at 30 seconds, but 2,2'-bipyridine is not added until 700 seconds (after the lag phase), at which time the illumination is cut off. These data show that the iron core of ferritin is reduced to Fe^{2+} with illumination. When light is not present or when it is removed, no increase in Fe^{2+} concentration is observed. Each reaction was performed in triplicate.

When 2,2'-bipyridine is added with concomitant illumination, a burst of Fe^{2+} is observed, followed by a steady state release of Fe^{2+} from ferritin, as observed by the formation of a red $[Fe(2,2'\text{-bipyridyl})_3]^{2+}$ complex at 520 nm. This indicates that the illumination of ferritin results in a reduction of ferric iron to ferrous iron. The black line shows that the addition of 2,2'-bipyridine to ferritin in the absence of light does not chelate iron, consistent with a ferric iron core. The observed decrease in absorbance that we see is the result of dilution from the addition of the 2,2'-bipyridine. The formation of AuNPs from Figure 8–2 does not start until about 700 s with Tris buffer. Thus, we illuminated ferritin through the 700 s time period, at which point we

turned off the lamp and added 2,2'-bipyridine. The blue line in Figure 8–3 shows that when we add 2,2'-bipyridine after illuminating through the lag phase of 700 s, Fe^{2+} is present, even though the illumination is stopped upon addition of 2,2'-bipyridine. Initially, we anticipated that the increase in absorbance at 520 nm with the blue trace would equal the absorbance in the red trace at the same time point. However, the absorbance of the blue tends to be about one-fourth that of the red curve. This can be explained in two ways: 1) with illumination in the absence of 2,2'-bipyridine, the iron core of ferritin is reduced but the Fe^{2+} re-oxidizes, and 2) in the presence of 2,2'-bipyridine, Fe^{2+} is immediately complexed upon formation, driving the equilibrium of Fe^{3+} to Fe^{2+}.

Based on these data, we propose that the photo illumination of ferritin causes the reduction of the ferritin iron core from a ferric mineral to ferrous iron. The ferrous iron re-oxidizes and forms a new mineral. We propose that this newly formed mineral is the photocatalyst for the formation of AuNPs. We observe that Fe^{2+} forms upon illumination of ferritin. However, ferrous iron is rapidly oxidized back to Fe^{3+}. To test our hypothesis that this newly formed mineral is the photocatalyst, we ran the identical reaction in the absence of gold ions and also in the absence of 2,2'-bipyridine. Following the reaction, the sample was incubated in the fridge for 3 hours or overnight. Following this incubation period, all of the iron oxidized back to Fe^{3+}, as observed when upon the addition of 2,2 -bipyridine, there was no formation of $[Fe(2,2'-bipyridyl)_3]^{2+}$. We then repeated the photo-reduction of the gold ions using these previously illuminated ferritin samples. The rate of AuNP formation was characterized using UV-Visible spectrophotometry. Figure 8–4 shows the results of these studies. The previously illuminated samples were treated as normal, with the addition of $AuCl_4^-$ at 30 seconds. We observe a dramatic decrease in the lag phase compared to the control reaction. This suggests that

the native core is not a photocatalyst in this reaction, but that the photocatalyst can be generated by illumination of ferritin. Once the photocatalyst is generated, the reaction proceeds more rapidly.
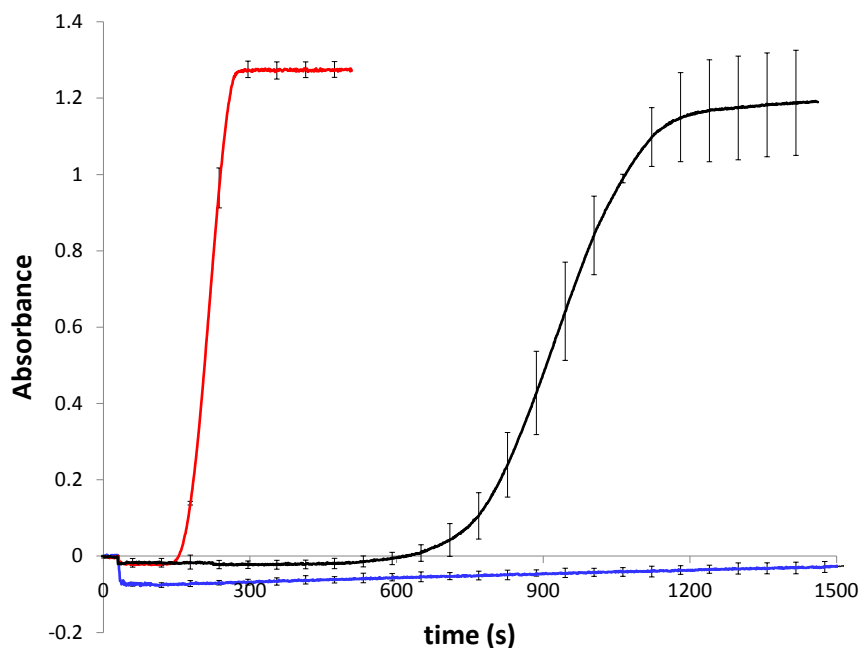
Figure 8-4. AuNP formation with native vs. photo-reduced ferritin. **Black** is the control sample and shows the normal rate of AuNP formation using Tris buffer (AU 530 nm). **Red** shows the rate of the same reaction that was initially illuminated through the 700 s lag phase, but then removed from illumination and incubated for a period of 3 hours or overnight. The reaction was then initiated as normal, but the lag phase is considerably shorter (AU 530 nm). **Blue** is the addition of 2,2'-bipyridine to the photo-reduced ferritin sample after the incubation period to show that oxidation of the core occurred and that no Fe^{2+} is present (AU at 520 nm). All runs were performed in triplicate.

These results indicate that illumination reduces the ferric core of ferritin to a ferrous state. The ferrous iron then oxidizes and arranges into the photocatalyst that is capable of reducing gold ions. This leads to two plausible possibilities. First, the ferrous iron can be oxidized by ferritin and deposited back into ferritin to create a newly arranged iron core. Second, the ferrous iron could be chelated by citrate, and over time, the ferrous iron oxidizes to ferric, forming a ferric-citrate complex. To test these models, we photo-reduced the iron core of ferritin, and then

178

incubated the samples to allow the reduced iron to oxidize. We then ran the column over a GE-Healthcare PD-10 Sephadex G-25 column to separate ferritin from citrate or ferric-citrate. We analyzed each fraction for protein and iron content. Figure 8–5 shows the results of this separation technique.
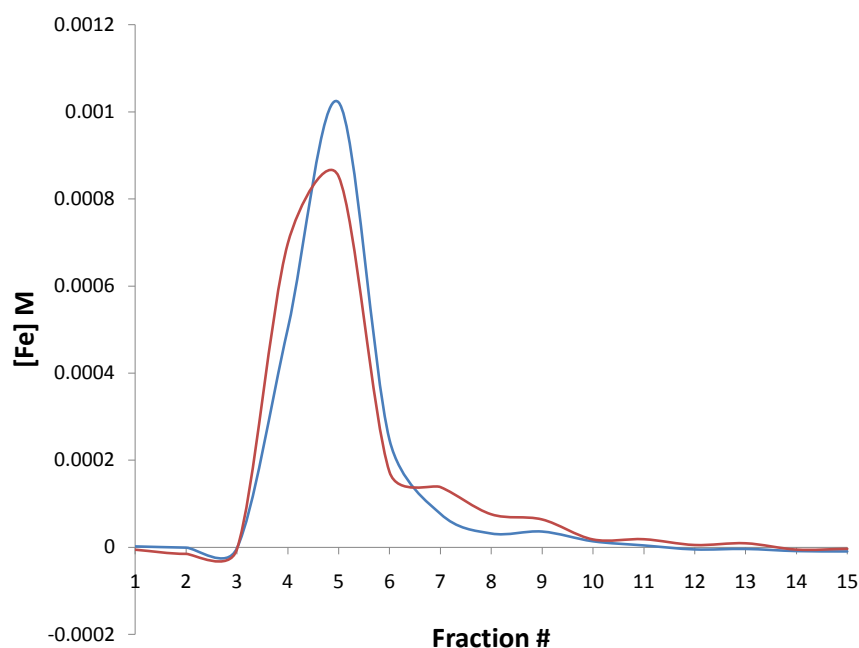
Figure 8-5. Size-exclusion chromatography of illuminated ferritin following an incubation period. The **blue** trace is the control of ferritin and citrate run over the column without illumination (identical to the control of ferritin illuminated in the absence of ferritin). The **red** trace is the sample of ferritin and citrate with illumination, following an oxidation incubation. The peaks show the molar concentration of iron in each fraction.

The size-exclusion data show nearly identical elution profiles. Indeed, the total amount of iron in each profile is identical. Small deviations are observed in fractions six and seven, where a shoulder is observed in the ferritin sample that was illuminated in the presence of citrate. This shoulder likely represents a small ferric-citrate complex that elutes at a later fraction than where ferritin elutes. Consistent with this is the results of a protein analysis for each fraction, which shows that the protein elutes in the first large peak that is observed in Figure 8–5 (data not

179

shown). This suggests that most of the iron is retained by ferritin, but that a small amount forms a smaller ferric-citrate complex outside of ferritin.

To test whether ferric-citrate is the catalyst for this reaction, we performed this reaction with ferric-citrate in the absence of ferritin, or in the presence of proteins of various types. The results of these kinetic reactions are shown in Figure 8–6.
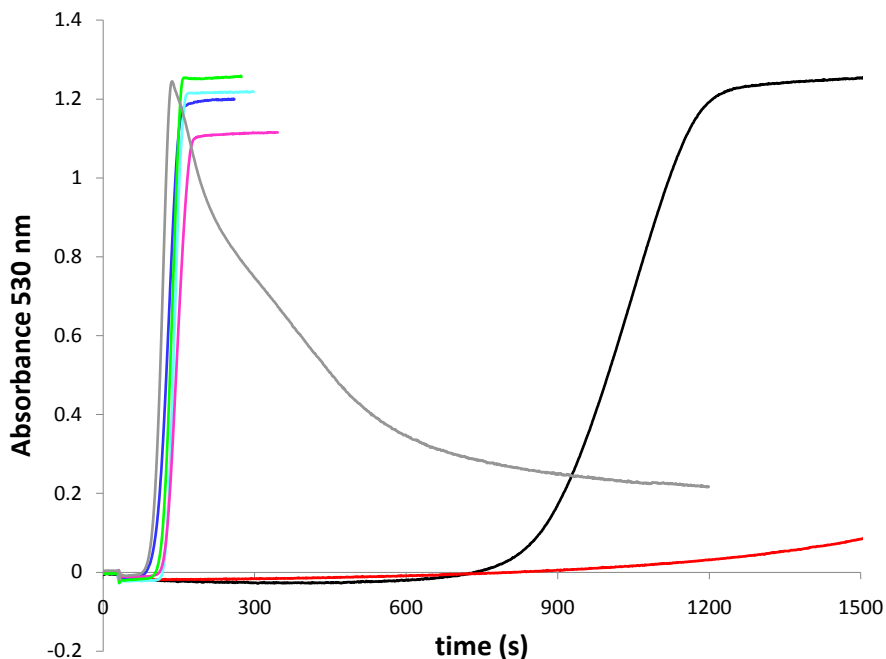
Figure 8-6. Kinetic runs using ferric-citrate as a catalyst. Ferric-citrate was added to the reaction buffer with concentrations of iron identical to what we would have if holoferritin were present (~0.4 mM). The **gray** trace is ferric-citrate without protein. **Red** is a control of apoferritin without ferric-citrate. **Black** is the control reaction as performed above. The other traces are the presence of ferric-citrate with various proteins: **green**, transferrin; **cyan**, apoferritin; **blue**, holoferritin; and **pink**, BSA.

The kinetic data show that using ferric-citrate alone, without any protein allows the formation of AuNPs initially, but the particles quickly aggregate and precipitate out of solution. With all other proteins, the rate of AuNP formation is significantly faster when ferric-citrate is present, than in the absence of ferric-citrate. This would indicate that ferric-citrate is the

important photocatalyst for the formation of AuNPs, and that protein of any kind is required to help passivate the particles, allowing them to remain soluble and distinct in solution. Upon further investigation, we noticed that the final products for each protein that we used varied significantly in color, indicating that we were obtaining different sized AuNPs. This was initially characterized by UV-Visible spectrophotometry (Figure 8–7).
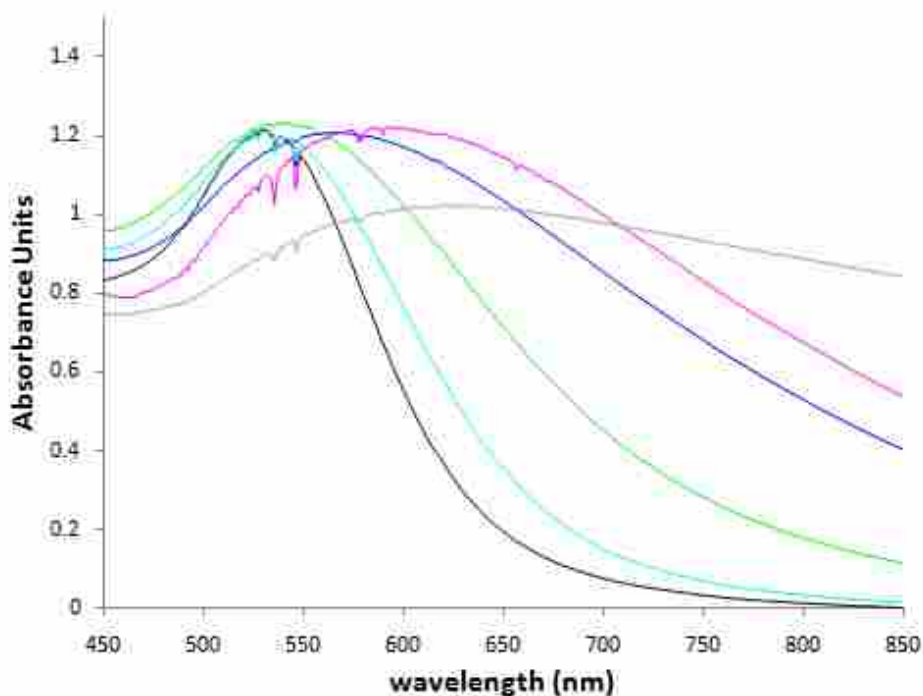
Figure 8-7. Spectra of AuNPs catalyzed with ferric citrate with various proteins present. Color scheme is identical to that in Figure 8–6. **Black** is the control with the original conditions (holoferritin without ferric-citrate). **Gray** is ferric-citrate without protein present. The rest are ferric-citrate with different proteins: **cyan**, apoferritin; **green**, transferrin; **blue**, holoferritin; **pink**, BSA.

These spectra show that all samples compared to the control are broader and more red-shifted to varying degrees. Indeed, the solutions with spectra that are broader and more red-shifted appear much bluer than the sharp peak at 530 nm for the control reaction. Using EM, these particles were analyzed, and consistent with the spectral information, the samples were

181

composed of a variety of sizes of nanoparticles that were generally not spherical in shape (data not shown).

Discussion

A large number of variables influence the ferritin photocatalyzed formation of AuNPs. When the reaction is performed in Tris buffer, the auto-catalyzed reduction of gold ions to AuNPs is inhibited. Thus, the reaction can be carried out in a controlled manner, and the result is a size-controlled distribution of AuNPs. How does Tris buffer inhibit the auto photo-reduction of AuNPs, thereby lengthening the lag phase of the reaction? Tris buffer has previously been shown to complex with Cu^{2+} and Ni^{2+} species.[14] Additionally, Tris has been shown to be a poor buffer of choice for iron loading into ferritin.[15, 16] When reconstituting iron into ferritin in vitro, ferrous iron is used. The ferrous iron then migrates to the ferroxidase center, where it is oxidized to ferric iron and subsequently deposited into ferritin, forming a crystalline ferrihydrite mineral (see Chapter 1). Generally, this is carried out in Good's buffers, such as MOPS or MES. However, when using Tris buffer, precipitation occurs and the efficiency of iron loading is poor. Taken together, a likely mechanism for this action is that Tris buffer can coordinate Fe^{2+}, inhibiting the iron from migrating to the ferroxidase center. The iron eventually oxidizes and forms insoluble rust, precipitating out of solution. The coordination of Tris to iron likely has relevance in this reaction as well. When the iron core is photo-reduced, Tris competes with citrate for the iron. Eventually, either citrate or ferritin oxidize the iron, and are able to out-compete Tris. Nonetheless, Tris is able to slow the reaction down. This is shown with an overall mechanism in Scheme 8–1.
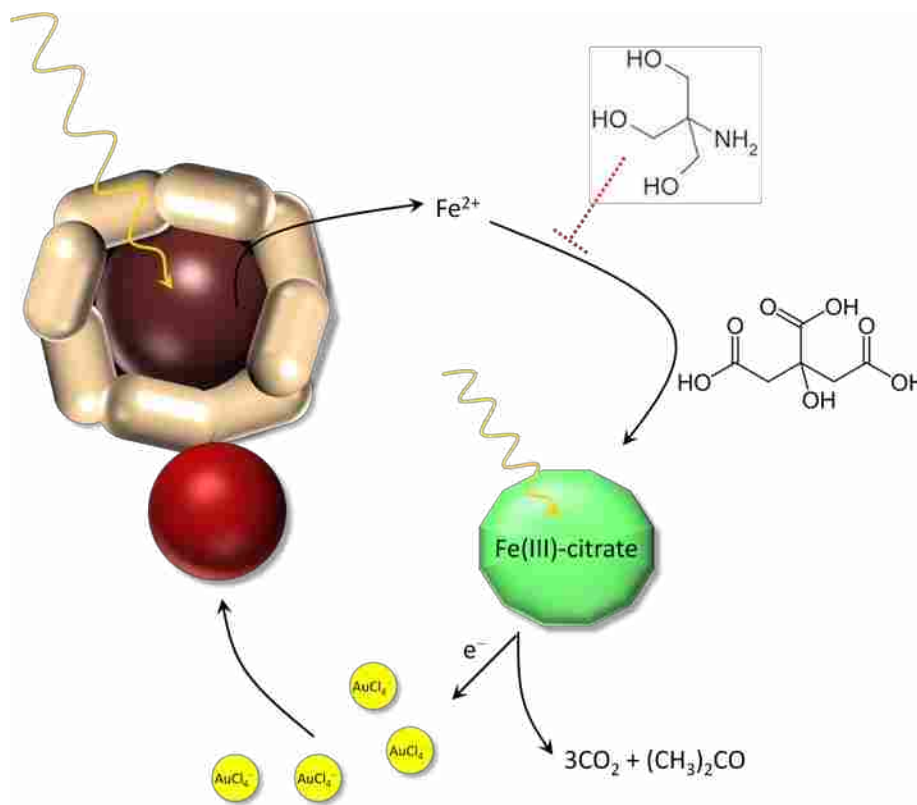
Scheme 8-1. A model depicting the photocatalysis of AuNPs. Light reduces iron within ferritin, forming ferrous iron. Ferrous iron is coordinated by citrate. The ferrous-citrate oxidizes to ferric-citrate, and the formation of AuNPs takes place on nucleation sites on ferritin.

When ferritin is illuminated, the core photo-reduces. Citrate has previously been shown to be able to bind both ferrous and ferric iron, though it binds ferric iron more tightly.[17-19] Our data indicate that ferrous iron oxidizes to ferric iron. A small amount of ferric-citrate forms, but most of the iron is retained in ferritin. We attempted electron diffraction on the ferritin cores prior to illumination and after illumination to determine the diffraction pattern. This would tell us whether a new mineral forms following illumination. Unfortunately, these attempts were unsuccessful. Indeed, it is difficult to obtain adequate diffraction patterns on nano-particles within ferritin. However, it may be possible to optimize conditions so that diffraction patterns can be obtained.

It is currently not known whether the ferric-citrate that forms outside ferritin, a newly formed mineral inside ferritin, or both contribute to the formation of the AuNPs. Ferric-citrate alone can form AuNPs, but these are unstable. On the other hand, holoferritin without citrate is also able to form AuNPs. In this case, electron donors such as oxalate or tartrate are used. Thus, it is difficult to separate the ferritin catalyzed reaction from the ferric-citrate catalyzed reactions. Most likely, both catalysts contribute to the formation of the AuNPs, and the use of both of them together creates a more efficient system for the photocatalysis of AuNPs. Future work on this project should be focused on determining the roles that each catalyst plays in the reaction mechanism.

References

1.   Martin, M. N.; Basham, J. I.; Chando, P.; Eah, S. K. Charged Gold Nanoparticles in Non-Polar Solvents: 10-min Synthesis and 2D Self-Assembly. *Langmuir* **2010,** *26* (10), 7410–7417.

2.   Grabar, K. C.; Freeman, R. G.; Hommer, M. B.; Natan, M. J. Preparation and Characterization of Au Colloid Monolayers. *Anal Chem* **1995,** *67* (4), 735–743.

3.   Manna, A.; Chen, P.-L.; Wei, T.-X.; Tamada, K.; Knoll, W. Optimized Photoisomerization on Gold Nanoparticles Capped by Unsymmetrical Azobenzene Disulfides. *Chem Mater* **2002,** *15*, 20–28.

4.   Brust, M.; Walker, M.; Bethell, D.; Schiffrin, D. J.; Whyman, R. Synthesis of Thiol-Derivatised Gold Nanoparticles in a Two-Phase Liquid-Liquid System. *J Chem Soc, Chem Commun* **1994,** 801–802.

5.   Liu, X.-Y.; Cheng, F.; Liu, Y.; Li, W.-G.; Chen, Y.; Pan, H.; Liu, H.-J. Thermoresponsive Gold Nanoparticles with Adjustable Lower Critical Solution Temperature as Colorimetric Sensors for Temperature, pH and Salt Concentration. *J Mater Chem* **2010,** *20* (2), 278–284.

6.   Yang, M. H.; Kostov, Y.; Bruck, H. A.; Rasooly, A. Gold Nanoparticle-Based Enhanced Chemiluminescence Immunosensor for Detection of Staphylococcal Enterotoxin B (SEB) in Food. *Int J Food Microbiol* **2009,** *133* (3), 265–271.

7.   Skrabalak, S. E.; Chen, J.; Au, L.; Lu, X.; Li, X.; Xia, Y. Gold Nanocages for Biomedical Applications. *Adv Mater* **2007,** *19*, 3177–3184.

8.   Chikae, M.; Fukuda, T.; Idegami, K.; Miura, Y.; Tamiya, E. Amyloid-Beta Detection with Saccharide Immobilized Gold Nanoparticle on Carbon Electrode. *Bioelectrochem* **2008,** *74*, 118–123.

9.   Lowry, O. H.; Rosebrough, N. J.; Farr, A. L.; Randall, R. J. Protein Measurement with the Folin Phenol Reagent. *J Biol Chem* **1951,** *193* (1), 265–75.

10.   Jacobs, D. L.; Watt, G. D.; Frankel, R. B.; Papaefthymiou, G. C. Redox Reactions Associated with Iron Release from Mammalian Ferritin. *Biochemistry* **1989,** *28* (4), 1650–1655.

11.   Keyes, J.; Hilton, R.; Farrer, J.; Watt, R. Ferritin as a Photocatalyst and Scaffold for Gold Nanoparticle Synthesis. *J Nanopart Res* **2011,** *13* (6), 2563–2575.

12.   Habib, A.; Tabata, M.; Wu, Y. G. Formation of Gold Nanoparticles by Good's Buffers. *Bull Chem Soc Jpn* **2005,** *78* (2), 262–269.

13.   Nikandrov, V. V.; Grätzel, C. K.; Moser, J. E.; Grätzel, M. Light Induced Redox Reactions Involving Mammalian Ferritin as Photocatalyst. *J Photochem Photobiol B* **1997,** *41* (1–2), 83–89.

14.   Hall, J. L.; Swisher, J. A.; Brannon, D. G.; Liden, T. M. Copper(II) Ion and Nickel(II) Ion Complexes with Tris. Reactions with Sodium Hydroxide. *Inorg Chem* **1962,** *1* (2), 409–413.

15.   Clegg, G. A.; Fitton, J. E.; Harrison, P. M.; Treffry, A. Ferritin - Molecular-Structure and Iron-Storage Mechanisms. *Progr Biophys Mol Biol* **1980,** *36* (2–3), 53–86.

16.   Yang, X.; Chasteen, N. D. Ferroxidase Activity of Ferritin: Effects of pH, Buffer and Fe(II) and Fe(III) Concentrations on Fe(II) Autoxidation and Ferroxidation. *Biochem J* **1999,** *338* (3), 615–618.

17.   Pierre, J. L.; Gautier-Luneau, I. Iron and Citric Acid: A Fuzzy Chemistry of Ubiquitous Biological Relevance. *Biometals* **2000,** *13* (1), 91–96.

18.   Gautier-luneau, I.; Bertet, P.; Jeunet, A.; Pierre, J.-L. Iron-Citrate Complexes and Free Radicals Generation: Is Citric Acid an Innocent Additive in Foods and Drinks? *Biometals* **2007,** *20*, 793–796.

19.   Orino, K.; Kamura, S.; Natsuhori, M.; Yamamoto, S.; Watanabe, K. Two Pathways of Iron Uptake in Bovine Spleen Apoferritin Dependent on Iron Concentration. *Biometals* **2002,** *15* (1), 59–63.

CHAPTER 9: EVALUATION AND OUTLOOK

Although ferritin was discovered nearly 75 years ago, we are continuing to learn a great deal about iron mineralization and release from ferritin, the role ferritin may play in diseases, and the role of ferritin as a scaffold or catalyst for materials chemistry. Our work has extended the field in these three areas, and has also opened up many doors for future work and investigation. The purpose of this chapter is to evaluate the work contained in this dissertation and to suggest future studies that may be undertaken based upon the findings in this work.

Mechanisms of Iron Core Formation and Iron Release

Many studies have been undertaken to understand the pathway of iron deposition into ferritin.[1] These studies have resulted in a general consensus of iron uptake, oxidation, and deposition into ferritin. Nevertheless, there remains uncertainty in the field as to the mineralization of iron in ferritin. This study begins to elucidate the nature of the mineral core formation under various conditions in vitro. The ferrihydrite core of ferritin appears to exhibit a variety of properties depending largely upon the environmental conditions. Notably, the age and size of the iron core tend to be significant factors in the crystalline property of ferritin. Given that ferritin has a turnover rate on the order of days in the human body,[2] the normally studied core properties of ferritin cores using months-old horse spleen ferritin may not completely represent in vivo properties of ferritin. Likely, the storage of iron in ferritin is a dynamic function, where the iron is constantly coming in and out of ferritin. In this scenario, of necessity is the careful regulation of these events by transport proteins, chaperones, and other regulators that carefully monitor the iron levels within the cell. Such a dynamic and living system seems appropriate given the important nature of iron in biology.

The greatest weakness of this study from a biological standpoint is that it was performed in vitro. To truly obtain an idea of the core formation in ferritin on a biologically relevant level,

these studies would need to be performed in vivo. The general idea would be to perform several mouse trials. One would be on a low iron diet, one with a normal iron diet, and one on a high iron diet. The iron cores of ferritin could be analyzed by taking the livers of the mice, purifying the ferritin, and determining the crystallinity of the iron cores within ferritin. One would need to take into account the high turnover of ferritin. In addition, one should take care during the ferritin purification process so as not to disrupt the potential oxidation states of the core. Remember, within the cell is a reducing environment. During the purification process, one should attempt to maintain this environment; otherwise the core structure may change during the process. The cores should be quickly examined for crystallinity using the techniques described in Chapter 2. The study of iron core formation in vivo is a difficult prospect because the age, size, and oxidation can significantly modify the crystalline structure, and these factors are difficult to control during purification and analysis.

On the other hand, from a materials chemistry standpoint, this work has significant applications. It is often desirable to form cores within ferritin as large as possible, thus forming iron nanoparticles of maximum size. These particles have a number of uses, including quantum dots, superparamagnetic nanocomposites, nano seeds for carbon nanotube growth, nanobatteries, and targeted treatment of cancer and diseases.[3-12] Understanding optimal conditions to maximize iron loading and also to predict core formation will give the researcher the benefit of targeted materials synthesis. Future work in this area includes the use of other transition metals, including the use of multiple metals for the synthesis of alloy materials, which would be useful in the fields of nanomagnetics for high-density storage memory media, and photochemistry for high-density and maximized semi-conductor properties.

The release of iron from ferritin is also an intriguing area of research, based on current models of iron release from ferritin. In the most extreme camp, ferritin is thought of as a dead-end trap for iron, similar to how metallothioneins are for copper.[13] This pathway seems unlikely, however, considering that when cells are iron deficient, iron has clearly been shown to be recycled from ferritin.[14, 15] In another camp, the argument is that ferritin is directed to the lysosome for lysosomal degradation and subsequent release of free iron. This iron is then directed to the appropriate locations for use.[16-18] The evidence presented for this pathway is compelling, and likely represents one pathway for iron release from ferritin. In the final camp, iron is released directly from ferritin in the presence of biological iron chelators or possibly through ferritin binding iron chaperone proteins.[19-22] Together, these two pathways of extracting iron from ferritin may help to explain the dynamic role ferritin plays in iron homeostasis. Thus, iron can be extracted as needed under a variety of conditions (Scheme 9–1). Our work from Chapter 3 shows how iron can be released from ferritin in a non-reductive manner using small molecules.[23] This work has significance in both showing the pathway of iron exit as well as in giving further credence to the non-degradation extraction of iron from ferritin.
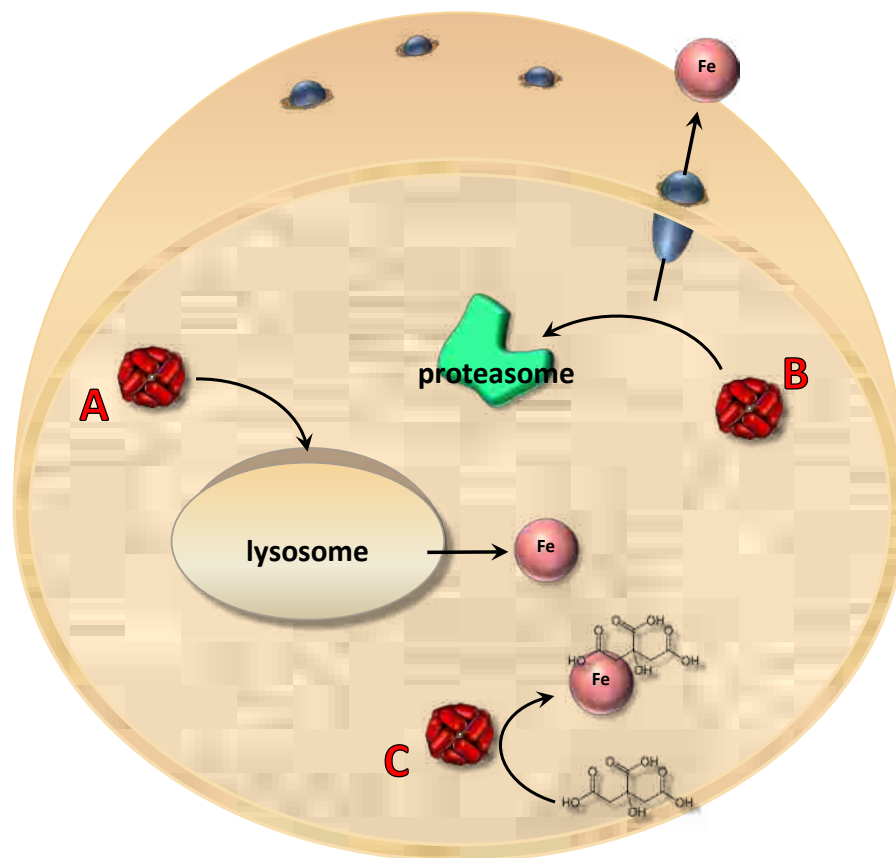
Scheme 9-1. Model of iron recycling from ferritin. A) Ferritin is directed to the lysosome for lysosomal degradation and subsequent iron release. B) Iron is chelated from ferritin and exported through ferroportin, and then directed to the proteasome for degradation. C) Small cytosolic molecules, such as citrate, chelate iron from ferritin. Figure adapted from Theil et al.[24]

Role of Transferrin and Ferritin in CKD

Ferritin has recently been implicated as being a key player in a number of diseases and biological functions. These range from a number of iron-related diseases, such as Alzheimer's and Parkinson's diseases,[25-30] as well as other surprising conditions and functions, such as attention-deficit hyperactivity disorder,[31] and the normal function of the circadian clock.[32]

189

Our in vitro work shows that ferritin is likely important in chronic kidney disease (CKD). We showed that elevated serum phosphate levels, like those shown in CKD, is a likely culprit for many of the markers found in patients with CKD (increased NTBI, decreased transferrin saturation, increased oxidative damage and inflammation, increased serum ferritin). Elevated phosphate levels mean that transferrin must compete with phosphate for binding of iron. Once an iron(III)-phosphate complex forms (in the form of NTBI), transferrin cannot effectively take up the iron, and the result is decreased transferrin saturation (TSAT). The iron(III)-phosphate complex is proposed to form reactive oxygen species (ROS), and the result is oxidative damage and inflammation. The inflammatory response is known to trigger H ferritin expression and secretion from cells. We showed that H ferritin is effective in competing with phosphate for iron. As highlighted in Chapter 5, a series of tests can be performed to determine whether our in vitro model is consistent in vivo.

Other future works can be directed at determining the structure of the iron(III)-phosphate complex. From our studies, we know that it is a large molecular weight species, as determine with size-exclusion chromatography, EM, AFM, and Amicon Ultra-centrifugation studies. We also determined that the complex has an iron to phosphate ratio of 2:3. Studies using ^{31}P NMR may help to reveal the structure of this polymeric species.

Materials Chemistry

Using ferritin as a template for materials chemistry has yielded important information in our lab. Our work showing the ability of ferritin to take up a significant number of anions showed surprising results. Ferritin, which evolved to sequester positively charged ions, specifically iron, has been shown to efficiently take up negatively charged species. Figure 9–1 shows a close up of the 4-fold hydrophobic channel of ferritin and the 3-fold negatively charged

channel of ferritin. Based on the crystal structure of ferritin, the most likely entry point for these anions is through one or both of these two channels, based on the size of these anions. However, the likelihood of anions entering either channel based on hydrophobicity (4-fold channel) or on negative charge repulsion (3-fold channel) appears slim. Contrary to these observations, we observe a high through-put of anions into ferritin. The explanation can only be the driving force of the enormous charge imbalance that takes place upon reduction of the iron core. Current work in our laboratory involves the use of metals that block the 3-fold channels (such as zinc, terbium, or cadmium) to determine whether the anions enter through this channel.[33-35] Blockage of these channels followed by the reductive reaction that pumps anions should help us understand whether anions enter through the 3-fold channels.
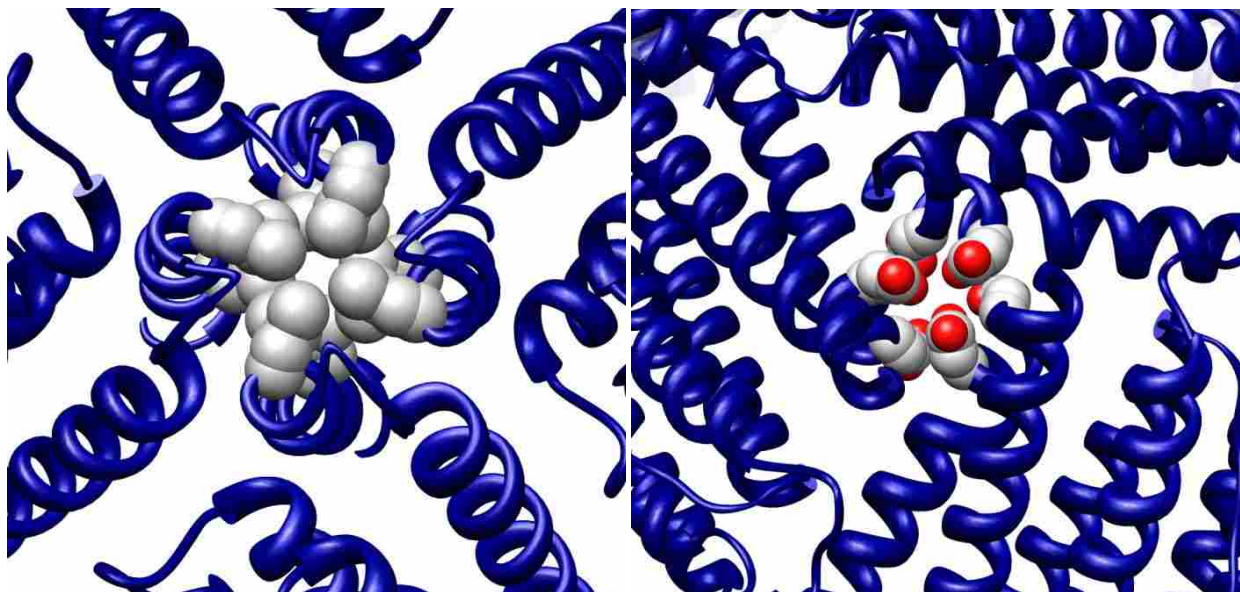
Figure 9-1. Detailed view of the ferritin channels. Left, 4-fold channel with the hydrophobic residues in gray. Right, 3-fold channel with the negatively charged residues highlighted.

In addition to using this method for the synthesis of novel materials in ferritin, there is potential to use this as a redox actuated device. Ferritin could be attached to electrodes in a closed system. One could pass a current through the electrode, reducing the iron core of ferritin.

Anions in solution would be taken up into ferritin until the current is shut off, at which time the ferritin core would oxidize, and anions would be expelled. In this way, anion influx and efflux can be specifically controlled by using ferritin as a gated anion storage container. Applications with such a device range from artificial muscles[36] to bioremediation of anionic contaminants.[37]

In Chapters 7 and 8 we discussed the progress we made using ferritin as a photocatalyst. This was worked out using gold nanoparticles (AuNPs), in part because Au^{3+} is readily reduced to Au^0, and also because AuNPs have an intense surface plasmon resonance band that makes the formation of AuNPs easily detectable. But how general is this method for making a variety of nanoparticles? Recently, we have investigated this question and have obtained a considerable amount of preliminary data that shows that we are capable of forming metal nanoparticles of copper, platinum, silver, and palladium, as well as metal alloy nanoparticles of gold and silver (Figures 9–2 and 9–3). Although electron micrographs are not shown here, preliminary studies using the microscope reveal that in each case, we are forming metal nanoparticles, with some having a tighter size distribution than others. Thus, the photocatalytic ability of ferritin to make AuNPs is a broad principle that can be applied to a variety of materials, depending on the goals and potential applications that the researcher has in mind.
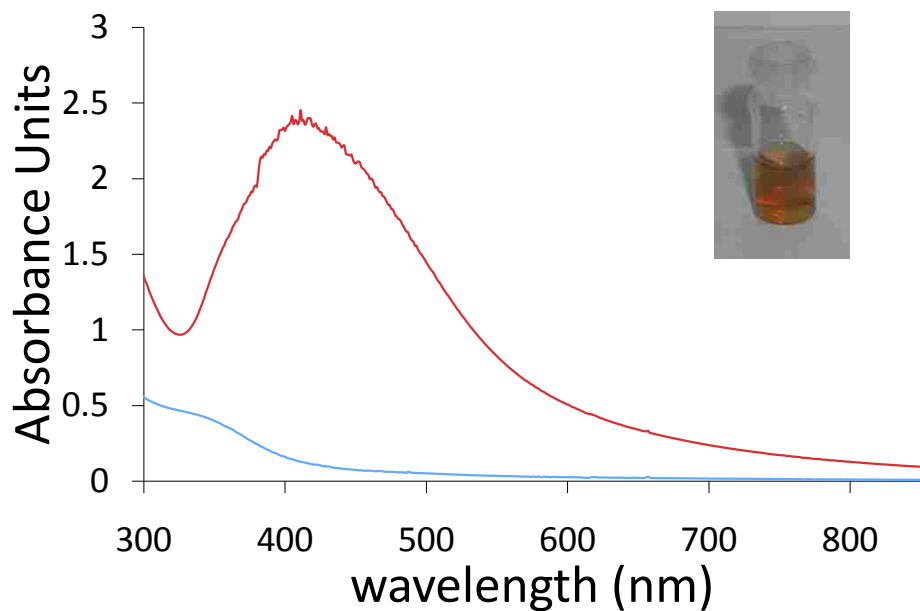
Figure 9-2. Silver nanoparticles. UV-Visible spectra show the sample prior to illumination (**blue**) and after illumination (**red**). The peak at 415 is characteristic of silver nanoparticles. The inset shows characteristic yellow solution of silver nanoparticles.
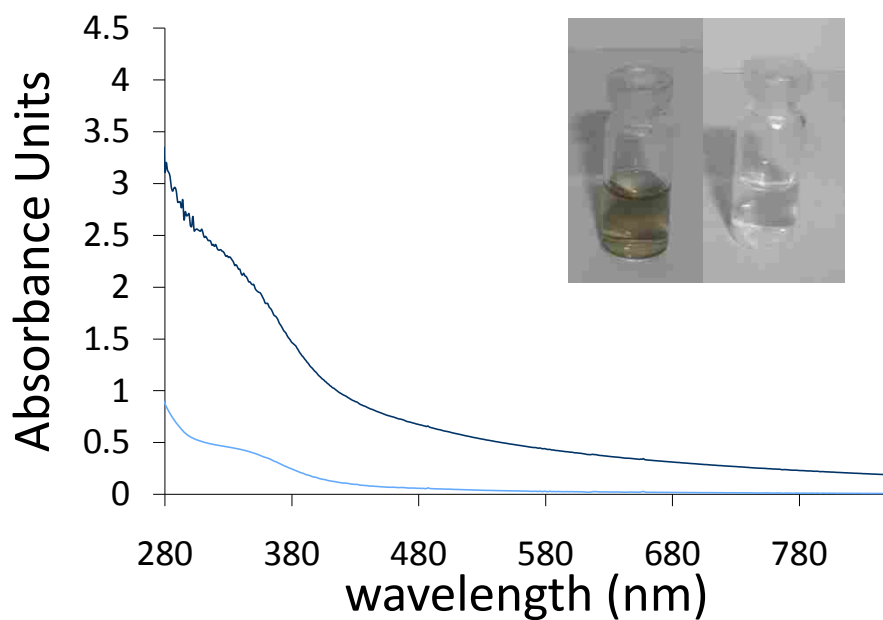
Figure 9-3. Palladium and platinum nanoparticles. The UV-Visible spectra show the reaction prior to illumination (**light blue**) and following illumination (**dark blue**). Following illumination with either palladium or platinum results in identical spectra. The products are shown in the inset, with palladium nanoparticles on the left, and platinum nanoparticles on the right.

The ability of ferritin to catalyze the photo-reduction of gold ions prompted us to attempt site-directed deposition of AuNPs, referred to as surface photo deposition (SPD). By depositing a small volume of ferritin onto a surface (this can be done in arrays or in any design that the researcher deems useful), the photochemical reaction can be carried out (Scheme 9–2). Initial studies showed promise in our ability to guide the deposition of AuNPs to locations only where ferritin is present (Figure 9–4). Initial attempts were successful both for spot blotting of ferritin and also in native gels of ferritin, where the AuNPs only nucleate and form on ferritin, producing distinct purple bands.
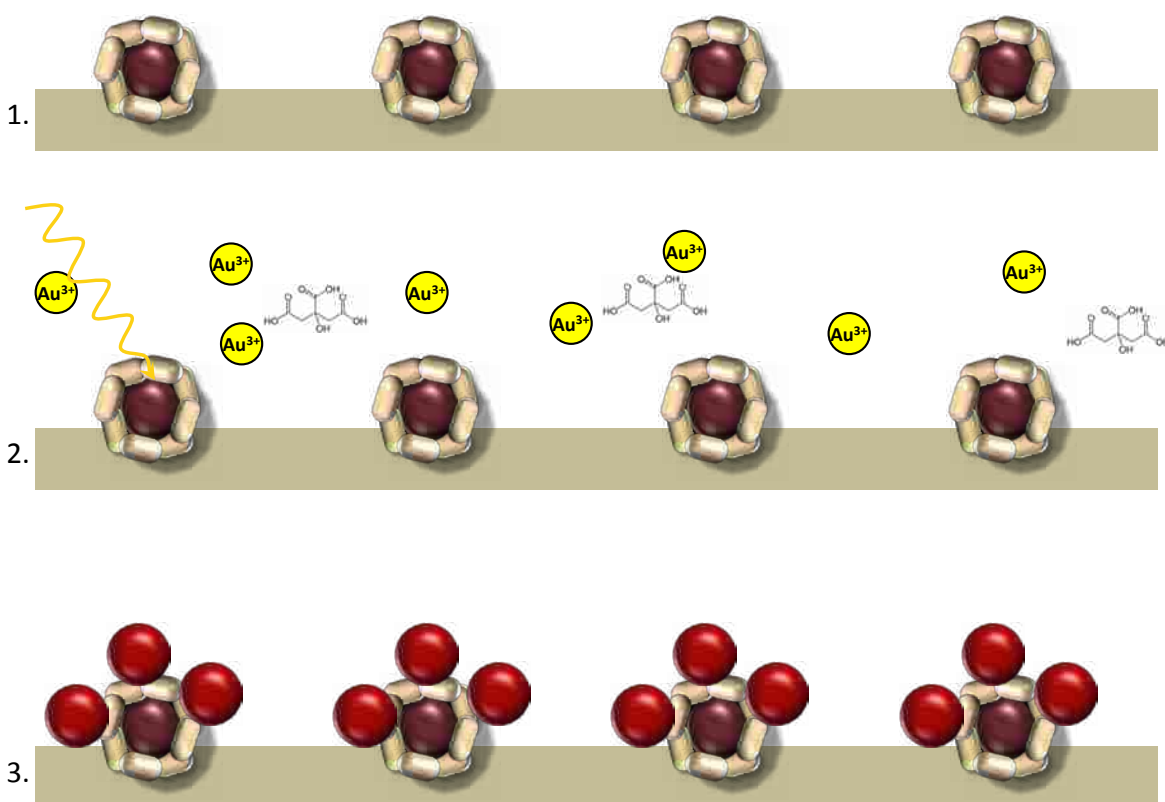
Scheme 9-2. Principle of surface photo deposition. Step 1, deposit ferritin onto a surface in precise locations in an array or pattern. Step 2, introduce gold ions, an electron donor, and a light source. Step 3, gold deposits only where ferritin is located.

194
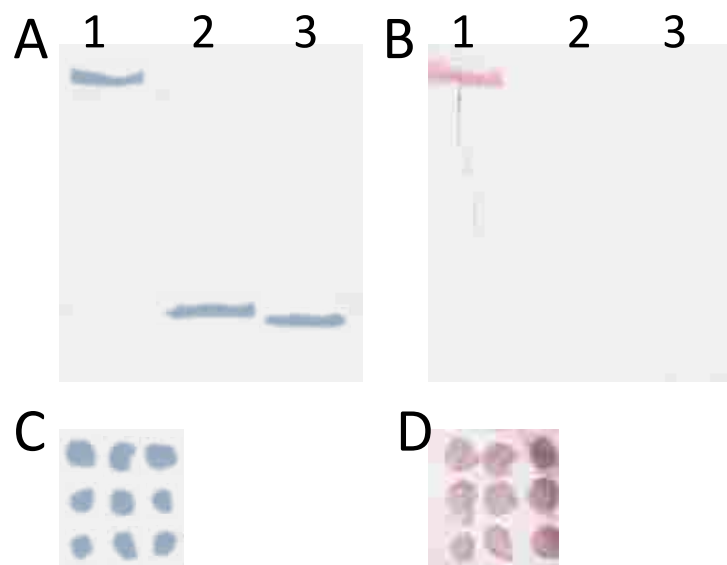
Figure 9-4. Blots of surface photo deposition. A) Native gel of ferritin (lane 1, 450 kDa), transferrin (lane 2, 80 kDa), and bovine serum albumin (lane 3, 70 kDa) stained with GelCode Blue for protein detection. B) Same blot as in A, but instead of staining the membrane, we illuminate with gold ions present. C) Spot blot of ferritin onto a membrane in an array (each spot is ~1 mm in diameter), stained for protein with GelCode Blue. D) Same spot blot as in C, but with surface photo deposition of AuNPs.

Future work can be designed to spot ferritin into microarrays using the method developed by Zhang et al., in the labs of Matthew Linford and Matthew Asplund.[38] In this way, arrays can be specifically and accurately designed. In addition, ferritin can be printed onto surfaces using printing technologies that are being refined in the laboratory of Greg Nordin. Using this technology, an endless possibility of nano gold deposition patterning can be achieved. Collectively, these techniques can be used for a precise deposition of ferritin to create nucleation locations for gold nanoparticles. These can then be used for junctions for applications in nano-circuits and other nano-devices.

References

1.   Bou-Abdallah, F.; Zhao, G.; Biasiotto, G.; Poli, M.; Arosio, P.; Chasteen, N. Facilitated Diffusion of Iron(II) and Dioxygen Substrates into Human H-Chain Ferritin. A Fluorescence and Absorbance Study Employing the Ferroxidase Center Substitution Y34W. *JACS* **2008,** *130*, 17801–17811.

2.   Goralska, M.; Nagar, S.; Fleisher, L. N.; McGahan, M. C. Differential Degradation of Ferritin H- and L-Chains: Accumulation of L-Chain-Rich Ferritin in Lens Epithelial Cells. *Invest Ophthal Vis Sci* **2005,** *46* (10), 3521–3529.

3.   Desai, J. D.; Pathan, H. M.; Min, S.-K.; Jung, K.-D.; Joo, O.-S. Formamtion of Self-Assembled Quantum Dots of Iron Oxide Thin Films by Spray Pyrolysis from Non-Aqueous edium. *Appl Surf Sci* **2006,** *252* (23), 8039–8042.

4.   Haikarainen, T.; Paturi, P.; Linden, J.; Haataja, S.; Meyer-Klaucke, W.; Finne, J.; Papageorgiou, A. C. Magnetic Properties and Structural Characterization of Iron Oxide Nanoparticles Formed by Streptococcus Suis Dpr and Four Mutants. *J Biol Inorg Chem* **2011,** *16* (5), 799–807.

5.   Jung, J. H.; Hyun, Y. H.; Park, S. Y.; Lee, Y. P.; Shin, M. K.; Kim, S. J. Giant Superparamagnetic Nanocomposites Using Ferritin. *J Korean Phys Soc* **2011,** *58* (4), 797–800.

6.   Papadopoulos, G.; Anetakis, C.; Gravalidis, C.; Kassavetis, S.; Vouroutzis, N.; Frangis, N.; Logothetidis, S. Simple Method for Coating Si (100) Surfaces with Ferritin Monolayers-Iron Oxide Quantum Dots. *Mater Sci Engin B* **2011,** *176* (6), 500–503.

7.   Valero, E.; Tambalo, S.; Marzola, P.; Ortega-Munoz, M.; Lopez-Jaramillo, F. J.; Santoyo-Gonzalez, F.; Lopez, J. D.; Delgado, J. J.; Calvino, J. J.; Cuesta, R.; Dominguez-Vera, J. M.; Galvez, N. Magnetic Nanoparticles-Templated Assembly of Protein Subunits: A New Platform for Carbohydrate-Based MRI Nanoprobes. *JACS* **2011,** *133* (13), 4889–4895.

8.   Uchida, M.; Flenniken, M. L.; Allen, M.; Willits, D. A.; Crowley, B. E.; Brumfield, S.; Willis, A. F.; Jackiw, L.; Jutila, M.; Young, M. J.; Douglas, T. Targeting of Cancer Cells with Ferrimagnetic Ferritin Cage Nanoparticles. *JACS* **2006,** *128* (51), 16626–16633.

9.   Dominguez-Vera, J. M.; Colacio, E. Nanoparticles of Prussian Blue Ferritin: A New Route for Obtaining Nanomaterials. *Inorg Chem* **2003,** *42* (22), 6983–6985.

10.   Choi, H. C.; Kim, W.; Wang, D. W.; Dai, H. J. Delivery of Catalytic Metal Species onto Surfaces with Dendrimer Carriers for the Synthesis of Carbon Nanotubes with Narrow Diameter Distribution. *J Phys Chem* **2002,** *106* (48), 12361–12365.

11.   Allen, M.; Willits, D.; Mosolf, J.; Young, M.; Douglas, T. Protein Cage Constrained Synthesis of Ferrimagnetic Iron Oxide Nanoparticles. *Adv Mater* **2002,** *14* (21), 1562–1563.

12.   Zhang, B.; Harb, J. N.; Davis, R. C.; Choi, S.; Kim, J.-W.; Miller, T.; Chu, S.-H.; Watt, G. D. Electron Exchange between Fe(II)-Horse Spleen Ferritin and Co(III)/Mn(III) Reconstituted Horse Spleen and Azotobacter Vinelandii Ferritins. *Biochemistry* **2006,** *45* (18), 5766–5774.

13.   Rae, T. D.; Schmidt, P. J.; Pufahl, R. A.; Culotta, V. C.; V. O'Halloran, T. Undetectable Intracellular Free Copper: The Requirement of a Copper Chaperone for Superoxide Dismutase. *Science* **1999,** *284* (5415), 805–808.

14.   Arosio, P.; Levi, S. Ferritin, Iron Homeostasis, and Oxidative Damage. *Free Radical Biol Med* **2002,** *33* (4), 457–463.

15.   Andrews, S. C.; Harrison, P. M.; Yewdall, S. J.; Arosio, P.; Levi, S.; Bottke, W.; von Darl, M.; Briat, J.-F.; Laulhère, J.-P.; Lobreaux, S. Structure, Function, and Evolution of Ferritins. *J Inorg Biochem* **1992,** *47* (1), 161–174.

16.   Radisky, D. C.; Kaplan, J. Iron in Cytosolic Ferritin can be Recycled Through Lysosomal Degradation in Human Fibroblasts. *Biochem J* **1998,** *336*, 201–205.

17.   Roberts, S.; Bomford, A. Ferritin Iron Kinetics and Protein-Turnover in K562 Cells. *J Biol Chem* **1988,** *263* (35), 19181–19187.

18.   Kidane, T. Z.; Sauble, E.; Linder, M. C. Release of Iron from Ferritin Requires Lysosomal Activity. *Am J Physiol* **2006,** *291* (3), C445–C455.

19.   Cassanelli, S.; Moulis, J.-M. Sulfide is an Efficient Iron Releasing Agent for Mammalian Ferritins. *BBA* **2001,** *1547* (1), 174–182.

20. Liu, X. S.; Patterson, L. D.; Miller, M. J.; Theil, E. C. Peptides Selected for the Protein Nanocage Pores Change the Rate of Iron Recovery from the Ferritin Mineral. *J Biol Chem* **2007,** *282* (44), 31821–31825.

21. De Domenico, I.; Ward, D. M.; Kaplan, J. Specific Iron Chelators Determine the Route of Ferritin Degradation. *Blood* **2009,** *114* (20), 4546–4551.

22. De Domenico, I.; Vaughn, M. B.; Li, L.; Bagley, D.; Musci, G.; Ward, D. M.; Kaplan, J. Ferroportin-Mediated Mobilization of Ferritin Iron Precedes Ferritin Degradation by the Proteasome. *EMBO J* **2006,** *25* (22), 5396–5404.

23. Johnson, J.; Kenealey, J.; Hilton, R. J.; Brosnahan, D.; Watt, R. K.; Watt, G. D. Non-Reductive Iron Release from Horse Spleen Ferritin Using Desferoxamine Chelation. *J Inorg Biochem* **2011,** *105* (2), 202–207.

24. Theil, E. C. Mining Ferritin Iron: 2 Pathways. *Blood* **2009,** *114* (20), 4325–4326.

25. Liu, G.; Men, P.; Perry, G.; Smith, M. A. Nanoparticle and Iron Chelators as a Potential Novel Alzheimer Therapy. *Methods Mol Biol* **2010,** *610*, 123–44.

26. Lavados, M.; Guillon, M.; Mujica, M. C.; Rojo, L. E.; Fuentes, P.; Maccioni, R. B. Mild Cognitive Impairment and Alzheimer Patients Display Different Levels of Redox-Active CSF Iron. *J Alzheimers Dis* **2008,** *13* (2), 225–32.

27. Gerlach, M.; Ben-Shachar, D.; Riederer, P.; Youdim, M. B. Altered Brain Metabolism of Iron as a Cause of Neurodegenerative Diseases? *J Neurochem* **1994,** *63* (3), 793–807.

28. Connor, J. R.; Boeshore, K. L.; Benkovic, S. A.; Menzies, S. L. Isoforms of Ferritin have a Specific Cellular Distribution in the Brain. *J Neurosci Res* **1994,** *37* (4), 461–465.

29. Choi, Y. G.; Park, J. H.; Lim, S. Acupuncture Inhibits Ferric Iron Deposition and Ferritin-Heavy Chain Reduction in an MPTP-Induced Parkinsonism Model. *Neurosci Lett* **2009,** *450* (2), 92–96.

30. Kaur, D.; Rajagopalan, S.; Andersen, J. K. Chronic Expression of H-Ferritin in Dopaminergic Midbrain Neurons Results in an Age-Related Expansion of the Labile Iron Pool and Subsequent Neurodegeneration: Implications for Parkinson's Disease. *Brain Res* **2009,** *1297*, 17–22.

31.   Millichap, J. G.; Yee, M. M.; Davidson, S. I. Serum Ferritin in Children with Attention-Deficit Hyperactivity Disorder. *Ped Neurol* **2006,** *34* (3), 200–203.

32.   Kosmidis, S.; Botella, J. A.; Mandilaras, K.; Schneuwly, S.; Skoulakis, E. M. C.; Rouault, T. A.; Missirlis, F. Ferritin Overexpression in Drosophila Glia Leads to Iron Deposition in the Optic Lobes and Late-Onset Behavioral Defects. *Neurobiol Dis* **2011,** *43* (1), 213–219.

33.   Harrison, P. M.; Lilley, T. H. Ferritin. *Loehr, T. M. (Ed.). Physical Bioinorganic Chemistry Series, Vol. 5. Iron Carriers and Iron Proteins. Xvii+533p. Vch Publishers, Inc.: New York, New York, USA; Vch Verlagsgesellschaft Mbh: Weinheim, West Germany. Illus* **1989**, 123–238.

34.   Levi, S.; Santambrogio, P.; Corsi, B.; Cozzi, A.; Arosio, P. Evidence that Residues Exposed on the Three-Fold Channels have Active Roles in the Mechanism of Ferritin Iron Incorporation. *Biochem J* **1996,** *317*, 467–473.

35.   Bou-Abdallah, F.; Arosio, P.; Levi, S.; Janus-Chandler, C.; Chasteen, N. D. Defining Metal Ion Inhibitor Interactions with Recombinant Human H- and L-Chain Ferritins and Site-Directed Variants: An Isothermal Titration Calorimetry Study. *J Biol Inorg Chem* **2003,** *8* (4), 489–497.

36.   Otero, T. F. Soft, Wet, and Reactive Polymers. Sensing Artificial Muscles and Conformational Energy. *J Mater Chem* **2009,** *19* (6), 681–689.

37.   Tripp, A. R.; Clifford, D. A. Ion Exchange for the Remediation of Perchlorate-Contaminated Drinking Water. *J Am Water Works Assoc* **2006,** *98* (4), 105–114.

38.   Zhang, F.; Gates, R. J.; Smentkowski, V. S.; Natarajan, S.; Gale, B. K.; Watt, R. K.; Asplund, M. C.; Linford, M. R. Direct Adsorption and Detection of Proteins, Including Ferritin, onto Microlens Array Patterned Bioarrays. *JACS* **2007,** *129* (30), 9252–9252.

APPENDIX: ARTICLES AND POSTERS

Articles

- Watt, R. K.; Hilton, R. J.; Graff, D. M. Oxido-reduction is not the only mechanism allowing ions to traverse the ferritin protein shell. *BBA*, **2010**, *1800 (8)*, 745–759.
- Snow, C. L.; Martineau, L. N.; Hilton, R. J.; Brown, S.; Farrer, J.; Boerio-Goates, J.; Woodfield, B. F.; Watt, R. K. Ferritin Iron Mineralization Proceeds by Different Mechanisms in MOPS and Imidazole Buffers. *J. Inorg. Biochem.* **2011**, *105 (7)*, 972–977.
- Johnson, J.; Kenealey, J.; Hilton, R. J.; Brosnahan, D.; Watt, R. K.; Watt, G. D. Non-reductive Iron Release from Horse Spleen Ferritin using Desferoxamine Chelation. *J. Inorg. Biochem.* **2011**, *105*, 202–207.
- Keyes, J.; Hilton, R.; Farrer, J.; Watt, R. Ferritin as a Photocatalyst and Scaffold for Gold Nanoparticle Synthesis. *J. Nanopart. Res.* Published online, Nov. 21, 2010.
- Hilton, R. J.; Keyes, J. D.; Watt, R. K. Maximizing the efficiency of ferritin as a photocatalyst for applications in an artificial photosynthesis system. *Proc. SPIE,* **2010**, *7646*, 76460J–8.
- Hilton, R. J.; Keyes, J. D.; Watt, R. K. Photoreduction of Au(III) to form Au(0) nanoparticles using ferritin as a photocatalyst. *Proc. SPIE,* **2010**, 7646, 764607–10**.**

The papers are shown below.

In addition, the following papers have been accepted for publication, but are not shown below because they are still in press.

- Hilton, R. J.; Andros, N. D.; Kenealey, Z.; Watt, R. K. The Ferroxidase Center is Essential for Ferritin Iron Loading in the Presence of Phosphate and Minimizes Side Reactions Forming Fe(III)-Phosphate Colloids. *Biometals*, in press.
- Hilton, R. J.; Seare, M. C.; Kenealey, Z.; Andros, N. D.; Watt, R. K. Phosphate Inhibits In Vitro Fe^{3+} Loading into Transferrin by Forming a Soluble Fe(III)-Phosphate Complex; A Potential Non-Transferrin Bound Iron Species. *Biometals*, in press.
- Hilton, R. J.; Zhang, B.; Watt, G. D.; Watt, R. K. Anion Transfer into Ferritin. *J. Inorg. Biochem.*, in press.

Talks and Posters

- Poster, *Phosphate Inhibits Fe^{3+} Binding by Transferrin.* International BioIron Society, Vancouver, BC, Canada, May 2011.

- Talk, *The Controlled Accumulation, Storage, and Release of Anions from Ferritin*. Intermountain Graduate Research Symposium, Logan, UT, March 2011.

- Talk, *The Controlled Accumulation, Storage, and Release of Anions from Ferritin*. BYU Spring Research Conference, Provo, UT, March 2011.

- Talk and Poster, *A Negative Role for the Ferritin Nano-Cage: Anion Transport*. nanoUtah Conference, Salt Lake City, UT, October 2010.

- Poster, *The Negative Aspect of Ferritin: Anion Transport.* International BioMetals Symposium, Tucson, AZ, July 2010.

- Poster, *Maximizing the Efficiency of Ferritin as a Photocatalyst for Applications in an Artificial Photosynthesis System*. LDS Life Sciences Symposium, Park City, UT, July 2010.

- Talk, *Ferritin as a Photocatalyst for Nano Devices and Sensors.* Intermountain Graduate Research Symposium, Logan, UT, March 2010. Received 3rd place speaking award.

- Talk, *Ferritin as a Photocatalyst in an Artificial Photosynthesis System*. BYU Spring Research Conference, Provo, UT, March 2010. Received 1st place speaking award.

- Talk and Poster, *Maximizing the Efficiency of Ferritin as a Photocatalyst for Applications in an Artificial Photosynthesis System*. International Society for Optics and Photonics (SPIE), San Diego, CA, March 2010.

- Poster, *Ferritin as a Photocatalyst in an Artificial Photosynthesis System*. nanoUtah Conference, Salt Lake City, UT, October 2009. Received 3rd place poster award.

- Talk, *Iron-Phosphate Complex: A Possible Source of Oxidative Stress.* BYU Spring Research Conference, Provo, UT, March 2009.

- Poster, *Understanding the Mechanism of Iron-Catalyzed Oxidative Damage in Chronic Kidney Disease.* National Student Research Forum, Galveston, TX, April 2008.

The posters are shown below, from the earliest to the most recent.

BYU

BRIGHAM YOUNG
UNIVERSITY

UNDERSTANDING THE MECHANISM OF IRON-CATALYZED OXIDATIVE DAMAGE IN CHRONIC KIDNEY DISEASE

Hilton, Robert J. and Watt, Richard K. — Department of Chemistry and Biochemistry, Brigham Young University, Provo, Utah 84602

OVERVIEW

Oxidative damage is a prevalent symptom in several diseases, including cardiovascular disease, diabetes, Parkinson's disease, Alzheimer's disease, and chronic kidney disease (CKD). Here we introduce preliminary data suggesting that metabolites that exist in CKD patients at high levels inhibit iron loading into ferritin. This leads to free iron, which is then capable of catalyzing oxidative damage in patients with CKD.

INTRODUCTION

In addition to filtering impurities from the bloodstream, the kidneys are responsible for sensing oxygen concentrations and, under hypoxic conditions, for excreting the hormone erythropoietin (EPO) into the bloodstream. Because the iron containing protein hemoglobin is the major component of red blood cells, and the EPO signal stimulates the bone marrow to increase red blood cell expression, the availability of iron is critical for proper oxygen delivery. With the onset of kidney disease, EPO expression decreases leading to anemia. The disruption of red blood cell synthesis appears to have a secondary effect on the overall ability of the body to regulate iron. Overall symptoms of CKD include:

- Severe increase in oxidative damage
- Increase in serum ferritin levels
- Decrease in transferrin saturation levels
- Increase in serum phosphate levels☐

These symptoms all further complicate the effect of decreased EPO levels. Inflammation increases in CKD and this leads to the expression of another hormone, hepcidin. Hepcidin binds to the iron export protein ferroportin and blocks iron export into the bloodstream further limiting the available iron for red blood cell production. Once a patient starts down this path it is very difficult to recover from these symptoms.

Figure 1*: Iron cycle in the body. 75% of total body iron is bound by hemoglobin and 20% is stored in ferritin. In CKD, this cycle is disrupted, ferritin levels increase, transferrin levels decrease, and erythropoietin production decreases.
*Figure obtained from www.cdc.gov

OBJECTIVES

- Present the mechanism of iron release by phosphate
- Present evidence for the formation of iron-phosphate complexes
- Discuss the ability of these complexes to catalyze oxidative damage
- Discuss potential treatments to prevent iron release

Figure 2*: Ferritin, the iron-storage protein.
A) Ferritin is a 450,000 Da protein that can hold up to 4500 iron atoms. It is composed of 24 subunits assembled into a hollow spherical structure.
B) 3D imaging of ferritin showing the hollow interior where iron is stored.
*Figure created using UCSF Chimera

Phosphate naturally occurs inside the ferritin core with iron in a 1:10 ratio. Normal physiological phosphate levels are 1 mM. However, in CKD patients, phosphate levels are commonly 5 mM.

Hypothesis

- Elevated phosphate concentration alters iron loading of ferritin.

Iron loading into ferritin in the presence of phosphate:

$Fe^{2+} + PO_4^{3-} + O_2 + Ferritin \rightarrow FeOOH (PO_4)_x$

1.0 mM	
2.5 mM	What happens with higher phosphate
5.0 mM	concentrations?
10.0 mM	

RESULTS

Figure 3. Iron loading into ferritin in the presence or absence of phosphate.
A) Spectrophotometric assay. The reaction is performed in a spectrophotometer with a stirred cuvette sample holder. The buffer is 0.025 M Mops buffer at pH 7.4 with 0.05 M NaCl present. The sample is prepared with the appropriate components and is stirred - represented by the horizontal line at the beginning of each plot. The reaction is initiated by injecting iron (50 Fe/ferritin) using a Hamilton syringe. Control reactions with no ferritin are represented by the open symbols and are ☐ - no phosphate, O - 1.0 mM phosphate and △ - 10 mM phosphate. Samples with ferritin present (1 µM) are filled symbols and are represented by ■ - no phosphate, ● - 1.0 mM phosphate and ◆ - 10 mM phosphate.

B) Oxygen consumption. Reaction conditions and symbols are identical to those in part A. The reactions are performed in a closed Hansatech oxygen electrode to monitor the consumption of oxygen.

- PO_4^{3-} stimulates the rate of iron loading into ferritin
- PO_4^{3-} stimulates the rate of oxygen consumption suggesting an interaction at the ferroxidase site.
- Physiological phosphate concentrations and ferritin without iron have almost identical ferroxidase activity.

$Fe(II) + PO_4^{3-} + O_2 \rightarrow Fe(III) - PO_4^{3-} (aq)$

- The iron is oxidized
- The complex is soluble
- Does the formation of the $Fe(III) - PO_4^{3-}(aq)$ complex compete with ferritin iron loading?

$Ferritin + Fe(II) + PO_4^{3-} + O_2 \rightarrow Fe(III) - PO_4^{3-} (aq)$

$\rightarrow Ferritin - Fe(III)$

Absorbance Spectra: Apoferritin and Holoferritin

Figure 4. Spectra obtained showing the formation of an iron-phosphate complex at wavelength 280-300nm.

Table 1 Elemental Analysis.

Theoretical Loading	Iron/Ferritin	Phosphate/Ferritin	Iron/Phosphate
100 Iron/Ferritin			
No phosphate	119 ± 7	53 ± 0.4	2.0 ± 0.1
1 mM phosphate	67 ± 6	33 ± 1.2	1.4 ± 0.3
5 mM phosphate	33 ± 3	24.2 ± 0.6	
1000 Iron/Ferritin			
No phosphate	1069 ± 26	5.1 ± 0.4	
1 mM phosphate	752 ± 38	581.8 ± 23.9	1.3 ± 0.1
5 mM phosphate	232 ± 56	556.2 ± 67.1	0.7 ± 0.1

CONCLUSIONS

In this poster, we examine potential causes for the oxidative damage with the hope that stopping oxidative damage will allow us to minimize the expression of hepcidin. If hepcidin expression can be minimized then potentially normal iron saturation of transferrin can be maintained and red blood cell synthesis can be continued.

We therefore conclude that

- Phosphate stimulates the rate of iron oxidation *in vivo*
- Phosphate inhibits iron loading into ferritin by forming an iron-phosphate complex in solution
- High phosphate concentrations produced a new iron-phosphate mineral inside ferritin

Significance

- High phosphate shifts the redox potential in blood serum causing the oxidation of Fe(II) to Fe(III)
- The iron-phosphate complex that forms is not bound by ferritin
- Physiological levels of phosphate (1 mM) inhibited ~30% of iron and 5 mM inhibited ~70% loading into ferritin

REFERENCES

1. Aruoja, P. and S. Lewis, *Ferritin, iron homeostasis, and oxidative damage.* Free Radical Biology and Medicine, 2002. 33(4): p. 457-463.
2. Sizaret, W., et al. *Oxidative stress in chronic renal failure as a cardiovascular risk factor.* Clinical Nephrology, 2002. 58(1): p. S12-S19
3. Malhotra, R.H. and H. Menrad, *Management of hyperphosphatemia of chronic kidney disease: lessons from the past and future directions.* Nephrology, Dialysis, Transplantation. Official Publication Of The European Dialysis And Transplant Association - European Renal Association. 2002. 17(7): p. 1170
4. Martin, C.J. and Gauldie-Meadad, C.M., *Oxidative Damage in Chronic Kidney Disease. Issues in Renal Nutrition, 2005. 32(6): p. 683-685.*

Ferritin as a Photocatalyst in an Artificial Photosynthesis System

BYU

BRIGHAM YOUNG UNIVERSITY

Robert J. Hilton ++, Jeremiah D. Keyes +, Richard K. Watt

Department of Chemistry and Biochemistry, Brigham Young University, Provo, Utah 84602

Introduction

We describe a bio-photocatalyst based on the iron storage protein ferritin. This method is a mimic of the natural process of photosynthesis. In photosynthesis, photosystem II uses photons of light to energize electrons. These electrons are channeled into the photosynthesis pathway, where they are used for energy. The source of the electrons in photosynthesis is water (Figure 1).

Ferritin is a 12 nm spherical protein that naturally sequesters iron as ferrihydrite. Ferrihydrite is a semi-conductor material. An assay has been established where ferritin can photocatalytically oxidize citrate and channel the liberated electrons to Cu(II), which is reduced to Cu(0) nanoparticles (10–30 nm). This process mimics the photosystem II pathway, in that the protein mediates the transfer of electrons to an electron acceptor (Figure 2). We describe efforts to maximize the efficiency of this system.

Photosystem II: electron transfer pathway
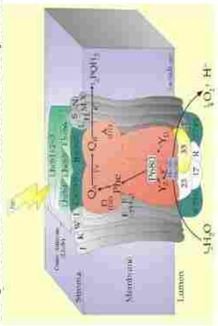
Figure 1. Photons of light energize electrons, which are then channeled through photosystem II to an electron acceptor. The resulting P680 is a powerful oxidant that can oxidize electron donor molecules.

Ferritin Mimic: electron transfer pathway
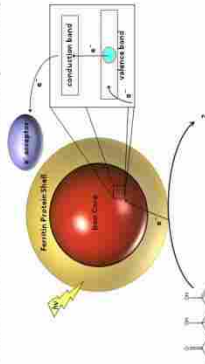
Figure 2. Photons of light excite electrons from the valence band to the conduction band of the ferrihydrite semi-conductor. A sacrificial electron donor fills the electron hole and an electron acceptor captures the excited electron.

Methods

Apo-Ferritin is reconstituted with an iron core (ferrihydrite) of about 800 iron atoms per ferritin. A reaction vial containing a final concentration of 0.15 mg/ml ferritin is stirred with 40 mM NaCl citrate (or other electron donor), 100 mM NaCl, and 4 mM copper, gold, or other electron acceptor. This solution is introduced to a light source and simultaneously monitored by UV-visible spectrophotometry (Figure 3). The light excites electrons from the semi-conductor ferrihydrite core of ferritin from the valence band to the conduction band. This electron then passes to an electron acceptor, in this case a metal ion. The metal ion is reduced and forms a metal nanoparticle of tightly distributed size and shape. The ferrihydrite core is replenished with electrons from an electron donor source, such as citrate.

Figure 3. A light source illuminates ferritin in solution. This initiates a photocatalytic process that causes electrons to be excited and captured by an electron acceptor. The result is a metal nanoparticle with an intense color change.

Table 1: Ferritin Photocatalyst Conditions

Donors	Acceptors	Enhancers	Catalysts
Sulfite	Cr(VI)	Salt - NaCl	Horse spleen ferritin
Thiol compounds	Cu(II)	Sulfur containing buffers	Recombinant human H-ferritin
Citrate	Cytochrome c	Ferric Citrate	Recombinant human L-ferritin
Tartrate	Ag(I)	Reductant	Ferrihydrite
Glycerol/glycol/Glycerol	Pt(II)		Iron Phosphate/Iron Arsenate
Formaldehyde/Methanol	Au(III)		Bacterial Ferritin Heme Groups
Ethanolamine	Ru(I)		Cobalt
Glucose	Vanadate		Manganese
	Pt/Au Electrodes		Titanium
	Perchlorate		

Black - Previous work   Red - Successfully tested   Green - Future plans or studies

Results

Gold Nanoparticle Formation with or without Preincubation

— Addition Without Preincubation
— Addition with Preincubation

Figure 4. A preincubation or lag phase is necessary for formation of an intermediate. This intermediate plays a key role in nanoparticle formation and electron channeling. The blue trace represents the reaction performed under normal conditions. Next, we illuminated a sample through the lag phase, or until just prior to an increase in absorbance. We stopped illumination and incubated the sample in the dark for 24 hours and the sample was again illuminated. The lag phase was thus bypassed, and the rate of gold nanoparticle formation was significantly increased (red trace). This suggests that an intermediate forms that is required for nanoparticle formation. Furthermore, this intermediate is stable.

Copper Nanoparticle Formation in the Presence or Absence of Iron Citrate

— Holo-ferritin Without Iron Citrate
— Holo-ferritin with Iron Citrate
— Apo-ferritin Without Iron Citrate
— Apo-ferritin with Iron Citrate

Figure 5. To determine what the intermediate in the reaction is, we incubated holo-ferritin (ferritin with an iron core) or apo-ferritin (ferritin lacking any iron core) with or without Fe(III)-citrate. The black trace represents a control of holo-ferritin under normal conditions. With the addition of Fe(III)-citrate to holo-ferritin, the rate of the reaction increases considerably (red trace). As expected, apo-ferritin under normal conditions shows no change in absorbance due to a lack of any iron present (green trace). Surprisingly, when Fe(III)-citrate was added to an apo-ferritin solution, we observed a significant increase in the rate of nanoparticle formation (blue trace). As controls, Fe(III)-citrate or ferrihydrite without the protein present was unable to catalyze copper nanoparticle formation (data not shown), however black magnetic precipitate does form under these conditions. These results suggest that the formation of Fe(III)-citrate in solution plays a key role in mediating an altered iron core in ferritin that is necessary for the reaction to occur.

Conclusions

Using ferritin as a model system, we are able to effectively funnel electrons to electron acceptors. Our current research has investigated metal ions as electron acceptors, however other acceptors, such as electrodes, have the potential to harvest the electrons for use in fuel cells and bio-battery applications.

To maximize the efficiency of this system, we sought to better understand the mechanism of the reaction. We determined that a stable intermediate forms and plays a key role in the reactions. This intermediate forms quickly when Fe(III)-citrate is in solution. We have developed a scheme to illustrate our hypothesis of the reaction (Figure 6).

Figure 6. Mechanism of Intermediate Formation

To form the intermediate, iron is chelated from the ferrihydrite core of ferritin with an iron chelator, such as citrate. The chelation and subsequent formation of an Fe(III)-citrate complex is the slow step in this reaction. Once Fe(III)-citrate forms, light reduces the iron, releasing it from citrate. Fe(II) is then bound by ferritin. We have not yet established if the iron that re-enters ferritin exists as Fe(II) or Fe(III). However, a mixed valent core of Fe(II) and Fe(III) is a potential intermediate since light is known to reduce iron in the ferrihydrite mineral. Ferritin is known to stabilize reduced forms of iron. For the apo-ferritin reaction, it has been shown that in the presence of oxygen that Fe(III) citrate can be photoreduced and the liberated Fe(II) can bind to ferritin and be oxidized and incorporated into the ferritin core. Perhaps the mineral that forms in the early stages of core development is the actual catalyst for photochemistry. Dominguez-Vera has shown that ferritin is made up of magnetite, hematite, and ferrihydrite and as the core is smaller the composition is mostly magnetite (JACS, 2008, 8062-8068). Future studies will examine this hypothesis.

Future Direction

- Investigate electron donors that are waste products of other reactions to break them down into environmentally friendly products
- Determine the structure and composition of the intermediate that acts as the photocatalyst
- Can we prepare other minerals in ferritin with different band gaps? This may allow us to tune the potential of the photocatalyst
- Use an electrode as an electron acceptor to harvest the energy for bio-battery or fuel cell use.

Maximizing the Efficiency of Ferritin as a Photocatalyst for Applications in an Artificial Photosynthesis System

Robert J. Hilton, Jeremiah D. Keyes, Richard K. Watt

Department of Chemistry and Biochemistry, Brigham Young University, Provo, Utah 84602

BYU
BRIGHAM YOUNG UNIVERSITY

Introduction

As the reserves of fossil fuels decrease, there is a growing need to investigate renewable energies. One of the most promising renewable energy sources is the sun. We describe a bio-photocatalyst based on the iron storage protein ferritin. This method is a mimic of the natural process of photosynthesis. In photosynthesis, photosystem II (PSII) uses photons of light to excite electrons. These electrons are channeled into the photosynthesis pathway, where they are used for energy (Fig 1).

Ferritin is a 12 nm spherical protein that naturally sequesters iron as ferrihydrite, a semi-conductor material. We are able to mimic PSII using ferritin (Fig 2). We describe efforts to maximize the efficiency of this system.

Figure 1. PSII electron transfer pathway. Photons cause a charge separation at P680 that initiates electron transfer reactions. Excited electrons are transferred to electron acceptors and electrons are extracted from electron donors. Ultimately, the water oxidizing complex (WOC) extracts electrons from water.

Figure 2. Ferritin PSII mimic: electron transfer pathway. Photons cause charge separation in the ferrihydrite semi-conductor. Excited electrons are transferred to electron donors such as $AuCl_4^-$. A sacrificial electron donor provides electrons to fill the electron hole caused by the charge separation reaction.

Methods

Ferritin with 1000 iron atoms (0.15 mg/ml) is stirred with 40 mM citrate, 100 mM NaCl, and 4 mM $AuCl_4^-$. This solution is illuminated and simultaneously monitored by UV-visible spectrophotometry (Fig. 3). Excited electrons are transferred to $AuCl_4^-$, forming Au nanoparticles (NPs). This method was used as an assay to evaluate reaction conditions that maximize the efficiency of this photochemical reaction. Early studies showed that buffers significantly influenced the rate of AuNP formation. We designed experiments with minimal reagents to test the effect of any additive, such as buffers, for stimulatory or inhibitory effects on the reaction.

Figure 3. Method of AuNP formation. A) A light source illuminates ferritin, citrate, and $AuCl_4^-$ in solution. This initiates a photocatalytic process whereby the excited electrons reduce Au ions. The result is AuNPs with an intense color change. B) This color change can be observed spectrophotometrically, monitoring peak growth at 530 nm, based on the surface plasmon resonance of AuNPs. C) Electron micrograph of the AuNP product (Tecnai F30 TEM, 140 kV).

Figure 4. Ferritin is required to maintain AuNP solubility. A) $AuCl_4^-$, citrate, and ferrihydrite NPs (ruby-red inset) were mixed in solution and illuminated. A grey-purple precipitate formed (grey inset). Electron micrograph shows an aggregated material, as compared to B) reaction performed with the ferrihydrite inside of ferritin.

Results

The role of ferritin was examined by using 10 nm ferrihydrite NPs as photocatalysts (Fig. 4). Ferritin is required for AuNP formation. Studies show that buffers significantly influenced the rate of AuNP formation. We designed experiments with minimal reagents to test the effect of any additive such as buffers for stimulatory or inhibitory effects on the reaction (Figs. 5 and 6)

Figure 5. Buffer effects on AuNP formation. The absorbance at 530 nm was monitored over time with the addition of varied concentrations of buffers. Increasing the concentrations of both MES buffer (A) and MOPS buffer (B) enhance the reaction. However, increasing concentrations of TRIS buffer (C) inhibit the reaction. D) Direct comparison of 25 mM of each buffer. E) Carbonate and phosphate buffers do not affect the reaction compared to the control in water. F) Arrows indicate peak maxima near 530 nm. Different buffers in the reaction lead to different peaks, and different colored product of AuNPs (G). All data was performed in triplicate, with error bars representing the standard deviation.
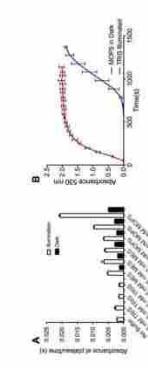
Figure 6. AuNP formation with or without illumination. A) Bar graph representing the final absorbance divided by the time it took to reach that absorbance for varied buffers and concentrations. MES and MOPS both have anti-oxidative properties in the dark, but the rates are significantly increased with illumination. B) Compared time traces of 50 mM MOPS performed in the dark and 50 mM TRIS performed in the light. The lag phase in the TRIS reaction represents the formation of the active photocatalyst.

Conclusions

Using ferritin as a model system, we are able to photocatalytically funnel electrons to electron acceptors. Our current research has investigated metal ions as electron acceptors, however other acceptors, such as electrodes, have the potential to harvest the electrons for use in fuel cells and bio-battery applications (Fig 7).

To maximize the efficiency of this system, we sought to better understand the mechanism of the reaction. We established a minimal reaction system with ferritin in water, citrate, and $AuCl_4^-$. Tests with ferrihydrite without ferritin did not catalyze the reaction. MES and MOPS buffers stimulated the reaction and TRIS buffer inhibited the reaction. Controls without citrate demonstrated that MOPS and MES acted as electron donors to stimulate the reaction. We determined that light causes the formation of an intermediate that plays a key role in the reactions (Fig. 6B). Studies are underway to characterize this intermediate.

Future Direction

- Study the effectiveness of other electron donors (besides citrate) in this system
- Test other ferritin mineral cores as photocatalysts, such as $MnOOH$, $CoOOH$, or TiO_2.
- Couple liberated electrons to electrodes for applications in fuel cells (Fig. 7).

Figure 7. Ferritin fuel cell. Proposed model of a ferritin catalyzed fuel cell. Upon illumination, citrate donates electrons, which flow through the electrode, generating a current. Photons flow through the membrane, reacting with oxygen to form water.

Contact Information

Robert J. Hilton: rbrt.hilton@gmail.com
Richard K. Watt: rwatt@chem.byu.edu
http://people.chem.byu.edu/rwatt

International Society for Optics and Photonics (SPIE), San Diego, CA, 2010.

International BioMetals Symposium, Tucson, AZ, 2010.

BYU A Negative Role for the Ferritin Nano-cage: Anion Transport

Robert J. Hilton, William M. Anderson, Richard K. Watt
Department of Chemistry and Biochemistry, Brigham Young University, Provo, Utah 84602
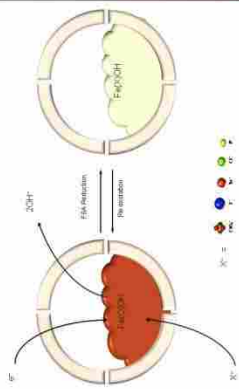
Introduction

Ferritin is an iron storage protein that can hold up to 4500 iron atoms. The structure of ferritin is advantageous for materials chemistry because the protein forms a 12 nm hollow sphere, wherein materials can be deposited. In this way, the ferritin "nano-cage" has been used in a variety of nanoparticle syntheses.[1-4]

Here, we describe a novel use of ferritin as an anion pump. In this application, anions are guided into the ferritin interior upon reduction of the native iron core. We have successfully incorporated a variety of anions into the interior of ferritin.

Methods

The iron core of ferritin is reduced using formamadine sulfinic acid (FSA), according to this equation:

$$Fe(O)OH + H_2O + e^- \rightarrow FeOH^+ + 2OH^- \quad (eq.\ 1)$$

This leaves a charge imbalance within ferritin. When this reaction is performed anaerobically in the presence of anions, the anions are pumped into ferritin to compensate for the charge imbalance (Scheme 1):

$$Fe(O)OH + X^- + H_2O + e^- \rightarrow Fe(X)OH + 2OH^- \quad (eq.\ 2)$$

Scheme 1. Proposed mechanism of anion entry into ferritin upon anaerobic reduction with FSA.

Samples are analyzed using ion selective electrodes (ISEs), UV-Visible spectrophotometry, and electron microscopy

Results

Table 1. Determination of Anion Transfer into Ferritin using ISEs.

Anion	Ionic radius (pm)	% of anion that enters ftn*	Anion atoms that enter ftn	Fe/anion inside ftn	[Anion] inside ftn
F⁻	136	99.8 ± 11.6	1585 ± 165	0.95 ± 0.11	9.82 ± 1.02
Cl⁻	181	94.2 ± 7.8	1278 ± 114	1.17 ± 0.08	7.92 ± 0.71
Br⁻	195	72.9 ± 2.9	1078 ± 84	1.39 ± 0.04	6.68 ± 0.52
I⁻	216	80.7 ± 2.3	1210 ± 53	1.24 ± 0.04	7.49 ± 0.33
ClO₄⁻	220	57.6 ± 6.6	854 ± 303	1.76 ± 0.20	5.29 ± 1.88

*Fe=ferritin
[ftn]=12 mg/mL, [Fe]=1.2 mM, Fe/ftn=1500, [anion] in solution=5 mM, [FSA]=10 mM

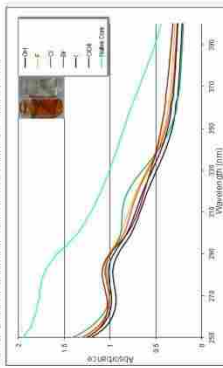
Figure 1. Representative UV-Visible spectra of reduced ferritin in the presence of various anions. Each spectrum is very similar to the next in the reduced form, indicating that there is little difference in the way that iron associates with the anion. Inset shows the color of solution prior to reduction (orange solution) and during reduction (colorless solution). Upon oxidation, the colorless solution returns to the original orange color.

Figure 2. UV-Visible time course of oxidation of the reduced core, representative of any anion present. Reaction was performed in an anaerobic environment in the glovebox. The sample was removed and stirred in air to allow for oxidation. Upon oxidation, the anion is expelled from ferritin, and the spectrum returns to the native state.
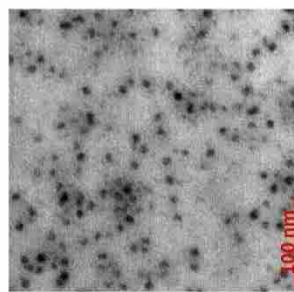

Figure 3. Scanning transmission electron microscopy image of ferritin loaded with anion (representative image). EM grids were prepared anaerobically. Fe(II) remains in ferritin when the core is reduced.
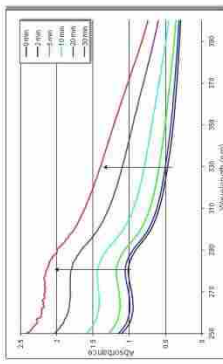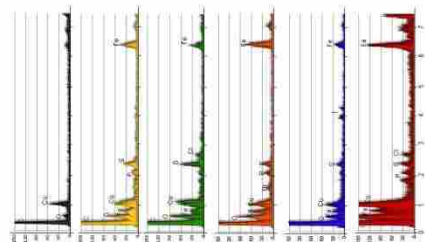

Figure 4. Representative energy dispersive X-ray spectroscopy (EDX) of various ferritin anion cores. The black scan is a control scan lacking ferritin, but with identical buffers, salts, and washing procedures. Yellow is the F loaded ferritin. The F peak is buried in the Fe peak at 0.7 keV. Green is the Cl scan with a Cl peak at 2.6 keV. Orange is the Br scan, with a Br peak at 1.5 keV. Blue is the I scan, with I peaks at 4.0 and 4.2 keV. Finally, red is the ClO₄⁻ scan, with a Cl peak at 2.6 keV.

Conclusions

Anions are shown to enter ferritin, and this is significant because:
- Possible in vivo relevance for iron release from ferritin, because anion incorporation lends to a more accessible store of iron.
- Ferritin can be used to store anions.
  - We are able to concentrate anions from millimolar concentrations up to ~10 M concentrations within the protein.
- Ferritin is a selective transport membrane.

Smaller anions enter ferritin more readily than do the larger anions.

Upon re-oxidation in air, the anions are expelled from ferritin, and the core returns to the native Fe(O)OH.

Future Direction

- Anion of pH titrator:
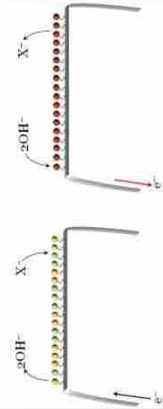 - Link ferritin to an electrode, and use the current to adjust the pH or anion concentrations.
- Sensors

Figure 5. Linking ferritin to an electrode, we can control the pH of a solution or the salt concentration of a solution with a current.

References

(1) Klem, M. T.; Mosolf, J.; Young, M.; Douglas, T. Inorganic Chemistry 2008, 47, 2237–2239.
(2) Ensign, D.; Young, M.; Douglas, T. Inorganic Chemistry 2004, 43, 3441–3446.
(3) Kasyutich, O.; Ilari, A.; Fiorillo, A.; Tatchev, D.; Hoell, A.; Ceci, P. Journal of the American Chemical Society. 432, 3621-3627.
(4) Kim, I.; Hosein, H.-A.; Strongin, D. R.; Douglas, T. Chemistry of Materials 2002, 14, 4874-4879.

Contact information: Richard K. Watt, rwatt@chem.byu.edu

Phosphate Inhibits Fe^{3+} Binding by Transferrin

Robert J. Hilton, M. Curtis Seare, Zachary Kenealey, N. David Andros, and Richard K. Watt

Brigham Young University, Provo, Utah

Introduction

Non-transferrin bound iron (NTBI) is present in many diseases that have inflammation and oxidative damage. Chronic kidney disease (CKD), in particular, has increased oxidative damage and NTBI. In addition, phosphate levels are elevated in CKD. We tested the hypothesis that elevated levels of serum phosphate interrupted normal Fe^{3+} binding by transferrin (Tf).
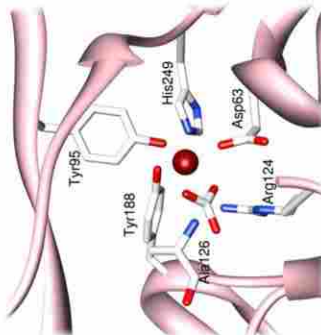

Figure 1. Crystal structure of transferrin, highlighting the site of iron binding within the N-lobe. Four residues (Asp63, Tyr95, Tyr188, and His249) act in concert with carbonate to coordinate iron. Two residues (Arg124 and Ala126) stabilize carbonate PDB code 1JNF.

Methods

Spectrophotometric assays were employed to monitor iron loading into Tf. Phosphate was added to the assays in amounts that mimic healthy levels (1 mM), diseased levels (2.5–5 mM), and intracellular levels (10 mM).
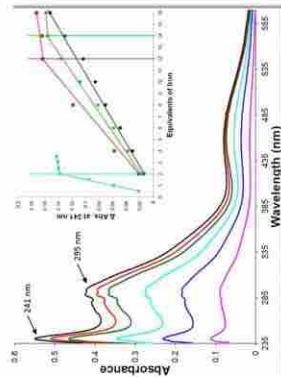
Results

Figure 2. The first question we addressed was whether phosphate can act as a synergistic anion to bind iron in the iron binding pocket. We confirm previous reports that phosphate is unable to function in this way. Apotransferrin (**blue**), apotransferrin + Fe^{2+} (**red**), apotransferrin + Fe^{2+} and PO$_4^{3-}$ (**cyan**), and apotransferrin + Fe^{2+} + CO$_3^{2-}$ (**black**).
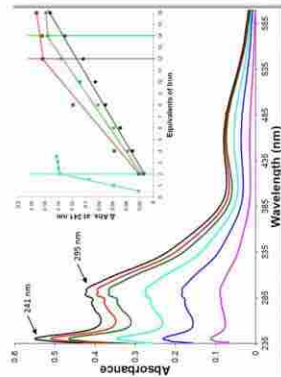

Figure 3. Spectra show an increase in absorbance at 460 nm, indicative of iron loading into Tf. In addition, peaks at 241 nm and 295 nm also increase, corresponding to the deprotonation of tyrosine residues. Ratios of Fe^{3+}:Tf are as follows: **pink** is 0.5, **blue** is 1.0, **cyan** is 1.5, **green** is 2.0, **red** is 2.5, and **black** is 3.0. *Inset.* Change in absorbance at 241 nm from Figure 3 vs. equivalents of iron to demonstrate Tf saturation. **Cyan** — in the absence of phosphate, Tf is saturated at 2 iron atoms. In 1 mM and 2.5 mM phosphate, Tf saturation occurs at 12 iron atoms (**red**), and 14 iron atoms (**green**), respectively. In 5 mM phosphate, Tf saturation was not observed (**black**).

Figure 4. Fe^{3+} loading into Tf with (A) FeCl$_3$ or (B) Fe(III)-NTA. Tf binding of Fe^{3+} is more efficient from a complexed iron source, especially with increased [PO$_4^{3-}$]. (C) is Fe^{2+} loading into transferrin in MES buffer at pH 6.0. Increased [PO$_4^{3-}$] enhances the rate of iron oxidation and subsequent binding by Tf, although the total binding decreases. All graphs represent various concentrations of phosphate: no phosphate (**black**), 1 mM (**red**), 2.5 mM (**green**), 5 mM (**cyan**), and 10 mM (**blue**).

Conclusions

- Iron loading into Tf is inhibited with increasing levels of phosphate.
- Iron loading can be improved, if iron is in a complexed form, such as Fe(III)-NTA.
- Phosphate can oxidize Fe^{2+} and lead to subsequent binding by Tf.

A. Transferrin Fe^{3+} Binding

Fe^{3+} + CO$_3^{2-}$ +

B. Phosphate Competing with Carbonate

Fe^{3+} + CO$_3^{2-}$ +

C. Phosphate Complexing or Precipitating Fe^{3+}

Fe^{3+} + CO$_3^{2-}$ +
PO$_4^{3-}$

Scheme 1. Model of phosphate inhibition of iron binding by Tf. A. Normal iron binding mechanism of Tf requires carbonate as a synergistic anion. B. Phosphate does not replace carbonate as the synergistic anion, and thus model B is incorrect. C. Phosphate competes with Tf for binding to iron by forming an Fe(III)-phosphate complex, which may represent NTBI in diseases such as CKD.

Acknowledgements

The Ferroxidase Center Facilitates Iron Loading into Ferritin in the Presence of Phosphate

Richard K. Watt, Robert J. Hilton, N. David Andros, Zachary Kenealey

Brigham Young University, Provo, Utah

Introduction

Patients with chronic kidney disease suffer from inflammation and oxidative damage. The oxidative damage is proposed to be associated with the elevated levels of non-transferrin bound iron (NTBI). In addition, patients with chronic kidney disease have elevated levels of serum phosphate. This work examines the hypothesis that elevated phosphate concentrations disrupt iron loading by ferritin, resulting in the formation of NTBI.

Methods

Iron loading into ferritin was monitored using a spectrophotometric assay. The reactions monitored iron loading in the presence of physiological serum phosphate concentrations (1 mM), elevated serum phosphate concentrations (2-5 mM), and intracellular phosphate concentrations (10 mM). Experiments used horse spleen ferritin to represent cytosolic ferritin and also as a serum ferritin mimic because of the high L ferritin content. In addition, studies were performed with H and L homopolymers of ferritin.

Results

Experiments show that both ferritin and phosphate are capable of stimulating the oxidation of Fe^{2+} (Figure 1). We identified a competing side reaction to ferritin iron loading where phosphate forms a soluble FeIII-phosphate complex. The formation of that product is difficult to analyze spectrophotometrically because the absorbance of the complex overlaps the typical absorbance peak (310 nm) used for iron loading into ferritin (Figure 2).
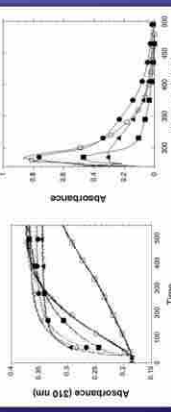
Figure 1. The rate of iron loading into ferritin increases as the concentration of phosphate increases. Concentration of phosphate are □ - 0 but no ferritin, ○ - ferritin 0 mM, ■ - 1 mM, ◆ - 2.5 mM, ▲ - 5 mM, and ▲ - 10 mM.

Figure 2. Spectra of ■ - apoferritin, □ - iron-phosphate complex, ○ - + ferritin reconstituted with phosphate, ● - holoferritin.

Results

The FeIII-phosphate complex was characterized by electron microscopy (EM) and atomic force microscopy (AFM), which show spherical nanoparticles between 20–200 nm (Figure 3). Elemental analysis of purified ferritin samples shows that as the phosphate concentration increases, iron loading into ferritin decreases (Table 1). The composition of the mineral that does form in ferritin has a higher iron phosphate ratio (~1:1) than ferritin purified from tissue (~10:1). Similar iron loading experiments were performed using homopolymers of H or L ferritin (Figure 4 and Table 1). H ferritin showed significantly better iron loading in the presence of phosphate due to the ferroxidase center that allows ferritin to rapidly bind and oxidize Fe^{2+}. Iron loading into L ferritin, lacking the ferroxidase center, was significantly inhibited by phosphate Figure 5 shows that H ferritin ferroxidase activity can load Fe^{2+} into transferrin, even in the presence of up to 5 mM phosphate.

Table 1. Iron loading into small or large core ferritin and into recombinant human heavy (rHuH) or light (rHuL) ferritin

Sample	Iron Ferritin		Relative % Iron Loading	
	Small Core	Large Core	Small Core	Large Core
No phosphate	119 ± 7	1,069 ± 26	100	100
1 mM phosphate	67 ± 6	752 ± 38	56	70
2.5 mM phosphate	54 ± 2	692 ± 13	45	65
5 mM phosphate	33 ± 3	232 ± 36	28	22
	rHuH	rHuL	rHuH	rHuL
No phosphate	391.63	47.15	100	100
1 mM phosphate	239.14	97.93	61.06	20.79
2.5 mM phosphate	231.43	71.21	59.09	15.11
5 mM phosphate	212.88	53.12	54.36	11.27

Figure 3. Electron micrographs and atomic force microscopy of ferritin and FeIII-phosphate complexes. (A) EM images of ferritin that were negative stained with uranyl acetate to show the ferritin shell, compared to (B) non-stained iron-phosphate complexes. (C) Atomic force micrographs are shown of (C) ferritin and (D) the iron-phosphate complex.

Figure 4. Kinetics of iron loading into H (red) or L (blue) ferritin with increasing concentrations of phosphate (0, 1, 2.5, 5, and 10, progressing from lightest to darker colors).

Figure 5. Eight schematic representation of the assay for ferritin ferroxidase activity oxidizing iron for deposition into transferrin. Left, iron loading into transferrin was monitored kinetically with H ferritin oxidizing the iron. △ - no H ferritin, ○ - H ferritin. H ferritin plus phosphate. □ - 1mM, ▲ - 2.5 mM, ● - 5 mM, and ■ - 10 mM. Ferroxidase activity minimizes the formation of NTBI until phosphate reaches ~5 mM.

Conclusions

Physiologically relevant concentrations of serum phosphate (~1.0 mM) inhibit iron loading into L-ferritin (serum ferritin) unless ferroxidase activity is present to rapidly oxidize the Fe^{2+} for deposition into ferritin (Scheme 1). This study supports the requirement for the ferroxidase activity of ceruloplasmin to load iron into apo transferrin by oxidizing Fe^{2+} as it passes through ferroportin to transferrin (Figure 5). In a similar fashion, cytosolic phosphate concentrations (10 mM) require ferroxidase activity of the H ferritin subunit for proper loading of Fe^{2+} into ferritin to prevent the formation of FeIII-phosphate complexes in the cytosol.

Scheme 1. Iron incorporation into ferritin is inhibited with increasing concentrations of phosphate.

Acknowledgement

ISSN 0304-4165
Volume 1800, Issue 8, August 2010

Biochimica et Biophysica Acta

BBA
General
Subjects

**Special Issue:
Ferritin: Structures,
Properties and
Applications**

Guest Editor
F. Bou-Abdallah

ELSEVIER
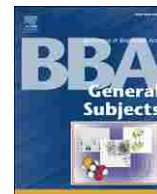
Review

Oxido-reduction is not the only mechanism allowing ions to traverse the ferritin protein shell

Richard K. Watt *, Robert J. Hilton, D. Matthew Graff

Department of Chemistry and Biochemistry, C-100 Benson Building, Brigham Young University, Provo, UT 84602, USA

ARTICLE INFO

ABSTRACT

Background: Most models for ferritin iron release are based on reduction and chelation of iron. However, newer models showing direct Fe(III) chelation from ferritin have been proposed. Fe(III) chelation reactions are facilitated by gated pores that regulate the opening and closing of the channels.
Scope of review: Results suggest that iron core reduction releases hydroxide and phosphate ions that exit the ferritin interior to compensate for the negative charge of the incoming electrons. Additionally, chloride ions are pumped into ferritin during the reduction process as part of a charge balance reaction. The mechanism of anion import or export is not known but is a natural process because phosphate is a native component of the iron mineral core and non-native anions have been incorporated into ferritin *in vitro*. Anion transfer across the ferritin protein shell conflicts with spin probe studies showing that anions are not easily incorporated into ferritin. To accommodate both of these observations, ferritin must possess a mechanism that selects specific anions for transport into or out of ferritin. Recently, a gated pore mechanism to open the 3-fold channels was proposed and might explain how anions and chelators can penetrate the protein shell for binding or for direct chelation of iron.
Conclusions and general significance: These proposed mechanisms are used to evaluate three *in vivo* iron release models based on (1) equilibrium between ferritin iron and cytosolic iron, (2) iron release by degradation of ferritin in the lysosome, and (3) metallo-chaperone mediated iron release from ferritin.

© 2010 Elsevier B.V. All rights reserved.

1. Background and scope of the review

The discovery and initial characterization of ferritin [1–3] ushered in an era of active investigation of this unusual metal encapsulating bio molecule by biochemists, chemists, physicists, and material scientists. Biochemists and cell biologists seek to determine the biochemical role of ferritin in iron metabolism as it functions to protect the cell against the deleterious effects of unbound iron and oxidative damage [4,5]. More recent studies show that ferritin is involved in inflammation [6–10] and angiogenesis [11–13] (in this issue, Torti). Chemists investigating the mechanism of iron deposition and release study the nature of the unique ferrihydrite-phosphate mineral core and ask why this unusual mineral forms and not other iron oxyhydroxy minerals (in this issue, LeBrun and Moore and Bou-Abdallah). Physicists and chemists study the magnetism [14,15], photochemical [16–18], and semiconducting properties [19,20] of the

mineral core [15,21] (in this issue, Papaefthymiou). Material scientists use the unique architecture of apo ferritin to create new non-biological minerals and nano-material compounds within the hollow ferritin interior for technological applications (in this issue, Douglas) [22,23]. These latter efforts produced mineral cores of magnetite [24,25], quantum dots [26,27], and even a ferritin-based nano battery [28]. These efforts continue to produce new nano materials encapsulated within the protein interior with the promise of continued success.

It is the purpose of this review to summarize some of the unique chemical, redox, and mineral formation properties of ferritin in relation to ion transport (both cations and anions) across the ferritin protein shell to form both native and non-native minerals in ferritin. Understanding how ions are transported in and out of ferritin, especially with respect to the transfer of electrons, will provide important information about how the cell controls iron concentrations. These results will also provide insight toward developing synthetic procedures to prepare non-biological compounds inside ferritin for materials applications.

2. Mechanism of ferritin iron loading

Iron loading into ferritin has been studied extensively, and Bou-Abdallah and LeBrun cover this topic in this issue. A brief discussion of

the ferritin structure, subunit function, mineral core composition, and iron loading as they relate to anion incorporation and how ions traverse the protein shell is presented below, but we refer to reviews in this issue by Crichton, Andrews, Papaefthymiou, and LeBrun for a more extensive coverage of these topics.

2.1. Ferritin structure

The structures of many ferritins isolated from a wide range of biological tissues have been determined as well as structures of recombinant proteins containing only H and L subunits (in this issue, Crichton). A common architecture has been conserved throughout biological species and consists of a spherical molecule composed of 24 subunits arranged in 4, 3, 2 symmetry with an outside diameter of 12 nm and a hollow internal cavity 8 nm in diameter. Six channels lined with hydrophobic residues ~0.4 nm in diameter pass through the 2 nm protein shell at the 4-fold axes. Eight channels, ~0.4 nm in diameter, lined with carboxylate groups are formed at the 3-fold axes [29,30]. Molecular traffic passing from the surrounding exterior solution into the ferritin hollow interior is proposed to occur through the 3-fold channels [31]. Calculations of the electrostatic surface potential of ferritin identified a funnel of negative charge that would attract the Fe^{2+} ions toward the 3-fold channel and into the ferritin interior [32,33]. Ferritin is remarkably stable to temperature and pH changes, as evidenced by its stability up to >70 °C and over pH extremes of 3–10 [34]. At pH less than 3, the 24 subunits dissociate but reversibly reassemble at pH greater than 3 [34].

Mammalian ferritin is composed of two different but very similar peptide subunits known as H-chain and L-chain ferritin, which share 55% amino acid sequence identity and are structurally homologous (RMSD = 0.461 Å) [35]. The H-chain is so named because it is ~21 kDa (182 amino acids) compared to ~19 kDa (174 amino acids) for the L-chain. The H-chain/L-chain ratios differ depending on the tissue from which the ferritin is isolated [36]. Ferritin isolated from liver, a very iron-rich organ, is predominantly L-chain ferritin. The L-chain ferritin possesses protein residues (Glu-57 amd Glu-60) on the inside surface of the protein that are involved in iron binding and nucleation and aid in the formation of a stable iron mineral core [32,37]. H-chain ferritin is predominant in heart tissue and possesses the ferroxidase center that is required for rapid Fe^{2+} oxidation and is important in rapid iron loading into ferritin [15].

2.2. Ferritin mineral core

The prevailing mechanism for iron loading suggests that Fe^{2+} binds to the ferritin protein and migrates to an enzyme site, named the ferroxidase center where oxidation to Fe^{3+} occurs. After oxidation, the iron migrates from the ferroxidase center to the protein interior where it forms the iron mineral. The nature of the iron mineral core of ferritin has been the focus of numerous studies utilizing a wide variety of physical and chemical techniques [38–44]. Initial compositional studies of the ferritin iron core proposed a composition of $(FeOOH)_8(FeO:OPO_3H_2)$ [45]. X-ray diffraction studies revealed two and six line diffraction patterns indicative of a ferrihydrite mineral composition [15]. Magnetic measurements of the iron core confirm that the iron is Fe(III) and reveal a super paramagnetic iron core [46]. Early transmission electron microscopy reveals a core size of 7–8 nm, consistent with the internal size of the protein shell [39]. However, more recent HAADF-STEM studies show smaller 2 nm clusters indicative of multiple smaller nanoparticles forming inside the ferritin cavity [47]. Small inorganic clusters of copper were observed in the synthesis of copper and palladium nanoparticles inside ferritin [48,49]. These observations are consistent with multiple metal nucleation sites inside ferritin and relates well with the 4, 3, 2 symmetry of the ferritin molecule that would suggest multiple sites for nucleation. Furthermore, these studies demonstrate

that the true nature of crystal growth and core formation is still an active area of study. Ferritins with mixed iron and phosphate cores have also been studied extensively [40,50–56]. These cores are more amorphous than the crystalline cores without phosphate present.

A recent study has examined the iron mineral core of ferritin by transmission electron microscopy (TEM), X-ray absorption Near Edge Spectroscopy (XANES), Electron Energy-Loss Spectroscopy (EELS), Small-Angle X-ray Scattering (SAXS), and SQUID magnetic studies [57]. The core was gradually removed with thioglycolic acid, and the mineral properties and composition were observed to change as the total iron in the core decreased. Three different mineral phases were observed in this study: ferrihydrite, magnetite, and hematite (Fig. 1). The model proposes that all three of these minerals are present and occur at different locations in relation to the protein shell of ferritin depending on core size. In support of this model, previous work in bacterial ferritin reported two populations of Fe atoms, which consisted of mostly bulk iron and a small group of iron atoms bound to the heme [58] (Section 3.4). The existence and function of ferritin multi-phase iron minerals and any *in vivo* significance have yet to be established.

2.3. Iron oxidation in ferritin

The process of iron oxidation for iron loading is reviewed in this issue by Bou-Abdallah. Our purpose here is to briefly discuss how iron oxidation is involved in ion movement through the protein shell. Early experiments showed that adding Fe^{2+} to apo ferritin in the presence of an oxidizing agent was essential for iron to be incorporated into the ferritin interior to form the mineral core [1]. Bakker et al. found that ferritin was capable of oxidizing iron under lower pH conditions
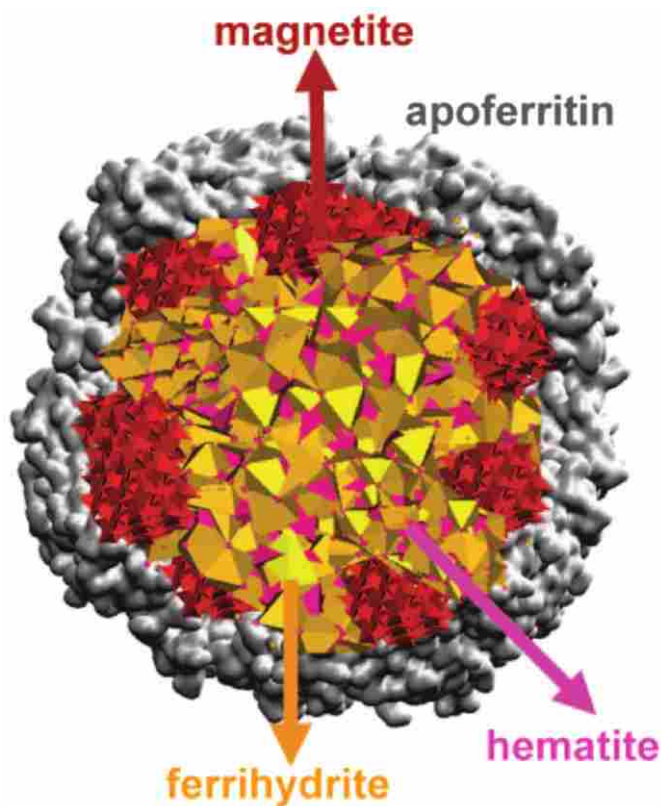
Fig. 1. Composition of the ferritin mineral core. Spectroscopic analysis suggests that ferritin is composed of a mixture of iron minerals located in different regions within the ferritin protein cavity. Magnetite appears to form along the inner surface of the protein shell, while hematite and ferrihydrite are more prevalent closer to the center of the mineral [57]. (Reproduced with permission from the *Journal of the American Chemical Society*).

(pH = 6.0) where Fe^{2+} was stable against oxidation by O_2 and that transferrin could be used in this reaction to bind the resulting Fe^{3+} to monitor iron oxidation [59]. The ferritin enzyme activity associated with iron oxidation is called ferroxidase activity. Lawson identified the ferroxidase center active site as a di-iron cofactor found inside the 4-helix bundle of the H-chain ferritin subunit [60]. Two Fe^{2+} ions bind to the ferroxidase center and, in the presence of oxygen, are oxidized to Fe^{3+}. After oxidation, the Fe^{3+} ions migrate from the ferroxidase center to the interior of ferritin where mineral core formation occurs at the nucleation sites of the L-chain ferritin. This process is essential for the early stages of core formation when no iron is present in ferritin. After a mineral core is formed, iron is proposed to migrate through the 3-fold channels and become oxidized directly on the mineral core surface [32]. Iron oxidation on the core surface is faster than at the ferroxidase center, and although studies show that the ferroxidase center still functions after a core is established, its contribution to Fe^{2+} oxidation is less significant than the oxidation on the mineral core surface [15].

2.4. Fe^{2+} binding and oxidation of iron on the core surface phosphate layer

The work of Treffry began to disclose the true nature of the native ferritin mineral core and the role of phosphate associated with ferritin. This work suggested that a phosphate layer "caps" the crystalline ferrihydrite mineral [50]. Treffry demonstrated that ferritin, reconstituted in the presence of phosphate, was very different than a native core. However, if ferritin was reconstituted with iron and later incubated with phosphate, a phosphate layer formed on the mineral core surface (Fig. 2A) and possessed similar properties to a native mineral core. This provided evidence that anions could diffuse through the ferritin protein shell and become associated with the iron mineral of ferritin by binding to the surface and stacking faults in the iron mineral crystal.

Further studies showed that a phosphate layer could be formed on a reconstituted ferritin core by adding Fe^{2+} in the presence of at least a 3-fold excess of phosphate under anaerobic conditions [61]. A phosphate layer consisting of one iron for three phosphates formed under these conditions (Fig. 2B). Additional reactivity studies of native or reconstituted ferritins containing phosphate on the mineral surface demonstrated that Fe^{2+} readily binds to the phosphate layer under anaerobic conditions (Fig. 2C) [62]. Furthermore, once the incoming Fe^{2+} binds to the core, it is in redox equilibrium with the existing Fe(III) core such that the incoming Fe^{2+} is oxidized to Fe^{3+}

and the electrons are transferred to the internal iron atoms where they are delocalized within the mineral core (Fig. 2D) [54,62]. Once oxidized, the resulting Fe^{3+} becomes buried under the phosphate layer (Fig. 2E). This was shown by adding more Fe^{2+} to ferritin that had been through a cycle of Fe^{2+} binding and oxidation and the incoming Fe^{2+} ions bound indicating that the phosphate was still on the surface and available to bind more incoming iron (Fig. 2F) [54]. The movement of iron through the phosphate layer during cycles of oxidation and iron removal was clearly established by removing Fe^{3+} by DFO chelation [54]. During this process, the phosphate layer only decreased in size by one phosphate for every six Fe^{3+} removed and continued to cap the decreasing size of the mineral core [54].

Similar to animal ferritin, bacterial ferritins also contain phosphate-iron mineral cores. However, in contrast to mammalian ferritin, the bacterial cores are amorphous and contain a homogeneous phosphate/iron distribution with a ratio of ~1.0 [63]. The phosphate-containing bacterial ferritin mineral core avidly binds Fe^{2+} under anaerobic conditions and the incoming Fe^{2+} is oxidized to Fe^{3+} upon binding to the phosphate similar to mammalian ferritin [63].

2.5. Iron loading in the presence of phosphate

The difference in mineral core composition and properties between bacterial and animal ferritins led to a series of synthetic and spectroscopic studies in which animal ferritin was reconstituted in the presence of phosphate [40]. Furthermore, it has been reported that phosphate stimulates the rate of iron loading into ferritin [51,56,64,65]. Iron loading kinetics on bacterial ferritin showed that phosphate stimulated the rate of iron oxidation and the authors proposed that phosphate binds at or near the ferroxidase center [65]. Similar results have been observed for mammalian ferritin where phosphate caused 2-fold acceleration and appeared to alter the reaction mechanism from two potential iron-loading pathways to a single pathway [64]. Cheng et al. reported iron deposition at 12 Fe(II)/ ferritin with 0.5–1.0 mM phosphate [56] and observed increased oxidation rates resulting from phosphate shifting the redox potential of Fe^{2+} to a more negative potential.

Phosphate appears to play an important role in later steps of iron loading as well. Cheng et al. observed that phosphate stimulated the decay of an EPR signal representing an iron(III) species that formed after oxidation at the ferroxidase site. They reported a stimulated decay of this signal in the presence of phosphate, suggesting that phosphate aids migration of iron from the ferroxidase center to the core [56]. Orino et al. suggest that the prompt iron uptake may be due
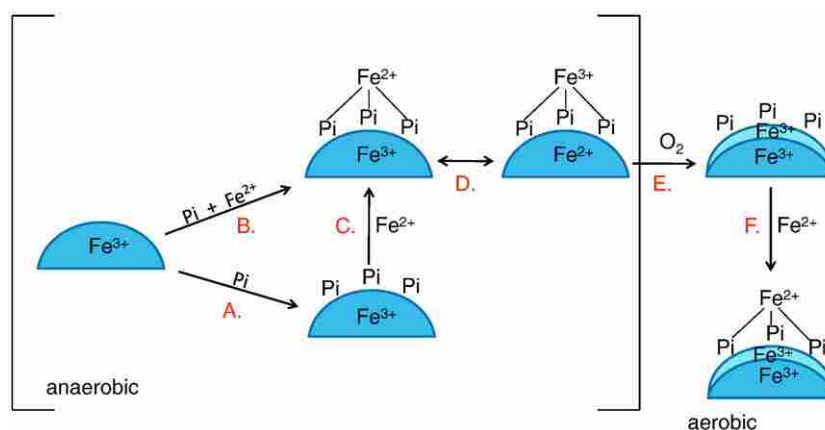
Fig. 2. Formation of the phosphate layer on the ferritin iron mineral. (A) A phosphate layer can be formed on the surface of a reconstituted mineral core by incubating the sample with phosphate. (B) The addition of phosphate and Fe^{2+} ions under anaerobic conditions to a reconstituted iron core will allow Fe^{2+} and phosphate to be deposited onto the mineral surface. (C) Fe^{2+} added anaerobically to a ferritin core with phosphate will bind to the mineral surface. (D) Upon binding anaerobically, the incoming Fe^{2+} is in redox equilibrium with the existing Fe^{3+} core such that the incoming Fe^{2+} is oxidized to Fe^{3+} and the electrons are transferred to the internal iron atoms where they are delocalized within the semiconducting ferrihydrite mineral core. (E) The resulting Fe^{3+} is transferred under the phosphate layer upon oxidation because, (F) the anaerobic addition of more Fe^{2+} ions permits more binding to the core surface, indicating that the phosphate was still on the surface and available to bind more incoming Fe^{2+} ions.

to phosphate facilitating iron core growth rather than helping at the ferroxidase center. This is consistent with previous work where phosphate was shown to provide binding sites for incoming iron atoms [54,61,62]. The iron phosphate mineral core has a decreased UV/Vis absorbance compared to ferritin prepared in the absence of phosphate [51]. The charge transfer band from iron interacting with hydroxide is much more intense than iron interacting with phosphate [64,65].

2.6. Iron loading with oxoanions

An extension of the studies of iron loading in the presence of phosphate was done using phosphate analogs. Tetrahedral oxoanions of arsenate, vanadate, and molybdate were reacted with apo ferritin and Fe^{2+} in the presence of oxygen to load iron into ferritin. In each case, the oxoanion was co-deposited with iron in an approximate 1:1 iron to oxoanion ratio [51]. This work further substantiated the transport of anions across the protein shell *in vitro*.

To further clarify the process of anion transport, additional studies were performed with sulfate, nitrate, and carbonate [66]. Iron loading into ferritin was slightly inhibited under these conditions, but the inhibition was due to the counter cations (sodium or potassium) of sulfate, nitrate, and carbonate, which competed with Fe^{2+} for the negative charges of the 3-fold channel [32]. Sulfate, carbonate, and nitrate were not incorporated into ferritin and did not show an inhibitory effect on iron loading. The question arises as to why most tetrahedral oxoanions were incorporated into ferritin and sulfate was not. Furthermore, the trigonal planar oxoanions were not incorporated into ferritin. It was concluded that deposition into ferritin was based on solubility. If the anion formed an insoluble complex with iron, a complex formed inside ferritin. If the iron and anion complex was relatively soluble, then iron hydroxide formed instead [66].

A role for *in vivo* incorporation of molybdate or vanadate is unclear. These metals are used in the active sites of enzymes [67,68] and may use ferritin as a storage site as these metals have been found as native component of ferritin [51,69]. Little is known about ferritin oxoanion import or export, but it is a well-documented process that occurs as a native and artificial process across the protein shell of ferritin. Further discussion of ion transport through the protein shell is covered in Section 4.

3. Iron release from ferritin—reduction and chelation models

Typical *in vitro* methods to remove iron from ferritin require chemical reduction of the iron(III) mineral in the presence of Fe^{2+} chelating agents. This process has been performed with many chemical reductants and chelators. Eq. (1) represents this reaction with the chelator bipyridyl (bipy). This overall process can be viewed as a two-step process consisting of reduction followed by chelation of Fe^{2+} from the mineral core.

$$\text{Holo}-\text{ferritin}+\text{reductant}+3\text{bipy}\rightarrow[\text{Fe(bipy)3}]2^{+}+\text{apoferritin} \qquad (1)$$
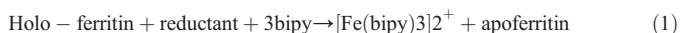
Four specific iron release models have been proposed and tested and will be reviewed below because they provide unique insights into possible iron release mechanisms and how ions are transported across the ferritin protein shell. The models are quite varied and not mutually exclusive. Therefore, under *in vivo* conditions, each model may be functioning depending on conditions that exist in the cell.

3.1. Subunit displacement

In 1993, Massover summarized evidence that large reagents gained access to the core by direct reagent-core particle contact [70]. Electron microscopy images supported this view by showing ferritin shell alterations consistent with subunit removal. However,

the strong stability of the ferritin subunits to high temperatures, denaturants such as urea, and pH extremes argue against facile subunit displacement. Furthermore, no studies since this proposal have supported this view and its present status has declined in view of alternate proposals. However, this idea is interesting due to the formation of hemosiderin, which appears to be a damaged form of ferritin with missing subunits. It may be that certain signals or cellular conditions promote subunit displacement leading to the formation of hemosiderin [71].

3.2. Diffusion of molecules through the 3-fold channels

The unique architecture of ferritin derived from its X-ray crystal structure suggested that the 3- and 4-fold channels, 0.4 nm in nominal diameter, provided access to the ferritin interior from external reagents [29]. The 3-fold channels are a currently accepted route for iron entry and exit through the protein shell [31] with the ferroxidase site an entry pathway when ferritin iron content is low. Initial proposals suggested that reducing agents and chelators diffused through the ferritin channels and reduced and chelated iron by direct contact. This view was supported by using free reduced FMN and reduced FMN attached to polymers. The former readily released iron, presumably by diffusing into the ferritin interior to directly reduce the iron core. However, the latter did not mobilize iron because attachment to a polymer was thought to prevent FMN from diffusing into the ferritin interior [72]. However, the requirement for diffusion became problematic when redox reagents and iron chelators with a larger diameter than the channel size successfully reduced and chelated iron from ferritin [73] (see Section 3.4).

Diffusion of molecules through the 3-fold channel was elegantly established through a series of studies using EPR active nitroxide radical spin probes [74,75] with negative, neutral, and positive charges. The basis of this procedure relies on the attenuation of the EPR signal when the nitroxide free radicals enter the ferritin interior. The EPR signal is attenuated because of the slow tumbling of the N-oxide-ferritin complex. The positively charged spin probe successfully penetrated the ferritin shell, but the negatively charged spin probe was repelled by the negative charge of the 3-fold channel and did not enter ferritin. The neutral spin probe bound to ferritin shell but did not enter the interior. Increased temperature increased the rate of diffusion of these spin probes into ferritin. Interestingly, the dimensions of the spin probes were ~0.7–0.9 nm in diameter, which is approximately twice the size of the 3-fold channel. Since the diameter of the 3-fold channel was determined crystallographically, it is possible that in solution, ferritin has breathing modes that allow molecules of larger diameter to enter the ferritin cavity. In this study, the charge of the molecules appears to be a more important attribute than the size for traversing the protein shell. These studies are consistent with electrostatic calculations based on the surface charge and channel charge of ferritin where positively charged ions would be attracted into the 3-fold channels by the negatively charged amino acids and negatively charged ions would be repelled [32,33]. It is interesting that the electrostatic calculations and the nitroxide spin probe studies both indicate that anions such as phosphate, chloride, and hydroxide would not readily traverse the ferritin protein shell. Their presence inside ferritin is anomalous in relation to these studies and requires that anions enter the interior by some other process. One explanation suggests that anions are accompanied by a flow of positive ions in the same direction.

The importance of charge was further investigated using the natural substrates Fe^{2+} and Fe^{3+} by measuring the rates of transfer of these ions across the protein shell from the exterior solution to the ferritin interior [76]. The procedure consisted of reacting apo ferritin containing encapsulated $[Fe(CN)_6]^{3-}$ with Fe^{2+} or $[Fe(CN)_6]^{4-}$ with Fe^{3+} and measuring the rate of Prussian blue (PB) formation within the ferritin interior [76]. When compared to control reactions with [Fe

$(CN)_6]^{3-}$ added to Fe^{2+} or $[Fe(CN)_6]^{4-}$ added to Fe^{3+} in solution with no ferritin, the reactions with $[Fe(CN)_6]^{3-}$ or $[Fe(CN)_6]^{4-}$ encapsulated inside ferritin had a 15- to 20-s lag phase before PB was formed. This indicated that the lag phase was due to iron traversing the protein shell. Similar results were obtained when DFO was encapsulated inside ferritin and Fe^{3+} traversed the protein shell. An unexpected observation was that Fe^{3+} ions crossed the protein shell much faster than Fe^{2+} indicating that the inability of ferritin to bind and sequester Fe^{3+} in most reaction assays is probably due to the rapid hydrolysis and insolubility of the $Fe(OH)_3$. Another explanation is that the gated pores of ferritin (see Section 3.3) may be selective for Fe^{2+} or Fe^{3+} under different conditions. The simplest explanation for this behavior is that the $Fe^{2+,3+}$ ions migrated through the 3-fold channels and once inside the ferritin interior rapidly react with DFO or $[Fe(CN)_6]^{3-,4-}$ to form products.

Additionally, ferritins have been prepared with anions such as $[PdCl]_4^{2-}$ and $[PtCl]_4^{2-}$ and after chemical reduction, the elemental form of these metals has been obtained [77,78]. This synthesis would require these anions to shed the chloride ligands or to diffuse through the channels as large anions. Since these anions are slightly larger than the dimensions of the channels and have negative charges, these anions should not traverse the 3-fold channels of ferritin. The mechanism of how these metals enter ferritin is still not established.

3.3. Gated pores

Ion transport across membranes requires mechanisms allowing ions to traverse the hydrophobic barrier of the membranes. This process occurs in both the exterior membranes of cells and is also required for ions to enter and leave organelles. Transmembrane proteins mediate this process by forming channels or pores that allow ions to pass through the membrane. These pores have mechanisms to regulate ion flow by opening or closing, depending on cellular requirements. Pores that can be opened or closed are called gated pores. Some channels function to allow ions to flow from a high concentration to a low concentration and are called ion channels. Other proteins transport ions against a concentration gradient (from low to high concentrations) and are called ion pumps or ion transporters. Ion pumps require the input of energy to move the ions against a concentration gradient.

The protein shell of ferritin has a similar function as cellular membranes in that it separates the cytosol from the stored iron. This is a protective barrier that prevents radical chemistry initiated by iron. Recently, Theil et al. explained how the 3-fold channels of ferritin act as gated pores and the newly elucidated mechanism explains how molecules larger than 0.4 nm can traverse the ferritin protein shell [79]. Increased temperature and physiological concentrations of urea (2–7 mM in plasma and in cells) were shown to open the channels and significantly increase the rate of iron release as monitored by an iron release assay of $FMNH_2$ as a reductant and bipy as chelator [80]. A creative amino acid search was performed using three criteria to identify amino acids responsible for forming the gated pore. These criteria included (1) amino acids conserved in all ferritins, (2) proximity to the 3-fold channel, and (3) "orphan residues" with no other known function [79]. Three residues fit the search and were identified as Leu-110, Arg-72, and Asp-122. Assays on proteins mutated at these residues confirmed that changing these residues significantly increased the ability of iron to migrate out of the ferritin interior during reductive iron release studies [81]. Structural analysis shows that Arg-72 and Asp-122 form an ion pair at the opening of the 3-fold channel that gates the pore. Furthermore, it was shown that Leu-110 interacts with conserved Leu-134 [82] by hydrophobic interactions. In combination, these four residues have a significant impact on the formation and stability of the 3-fold channel.

The conformation representing the closed 3-fold channels of ferritin is shown in Fig. 3A. The electrostatic gating interaction between Asp-122 and Arg-72 is shown. A proline substitution [82] at the conserved residue Leu-134 disrupts the hydrophobic interaction between Leu-134 and Leu-110 weakening the hydrophobic stabilization between helices C and D (Fig. 3C). Proline is a helix breaker, and the structure of the Leu134Pro mutation shows a significantly shorter D helix (compare Fig. 3A to B). This mutation also disrupts the loop that connects the C and D helices and alters a flexible region from residues 114–133, near the 3-fold channel. This change is critical because it prevents the formation of the electrostatic interaction between Asp-122 and Arg-72 (Fig. 3B and C) that act as the gated pair to stabilize the 3-fold channel. As a result, a much larger 3-fold pore is observed in the crystal structure of the mutant that is approximately 3 nm in diameter, compared to a ~0.4-nm diameter pore in wild-type ferritin (Fig. 3B). In actuality, the pore may not be 3 nm in diameter, but this mutation has such a destabilizing effect on ferritin that structural analysis does not show crystallographically defined order in the area surrounding the 3-fold channel. Therefore, that ability of the protein to regulate what ions pass through the 3-fold channel is significantly altered by this mutation.

In addition, this mutation causes a disruption in the gated pore, by destabilizing the hydrophobic interaction between Leu-134 and Leu-110 that normally stabilizes the protein tertiary structure. The additive effect of the Pro substitution on all 24 subunits of the nanocage results in disruptions to both interhelical and intersubunit interactions. Ultimately, these four residues significantly affect the structure and size of the 3-fold gated pore. Studies with circular dichroism (CD) spectroscopy, temperature [83], chaotropic compounds, iron release [80,82], and mutant proteins [81] all point to the conclusion that localized melting of these residues increases the rate of iron release from ferritin.

Peptides from a combinatorial library were created, which bound to the ferritin subunits and presumably altered their flexibility, which in turn regulated iron release by opening or closing the pores [83]. It is proposed that the opened or closed state of the 3-fold channel is regulated by binding of substrate [80] or by regulatory proteins binding to ferritin *in vivo* [79,83].

3.4. Electron transfer through the protein shell

A clear compositional distinction between animal and bacterial ferritins is the presence of protoporphyrin IX in bacterial ferritins. The reduction potential of the 12-heme groups in apo *Azotobacter* bacterial ferritin is −205 mV but becomes more negative (−430 mV) in the presence of the mineral core [84]. This property suggests that the mineral and the heme groups are in close proximity, and this contact could facilitate electron transfer from external reagents directly to the mineral core facilitating reduction of the latter for iron release. In fact, two populations [58] of Fe atoms were found in bacterial ferritin, which consisted of mostly bulk iron and a small group of iron atoms bound to the heme. In contrast to animal ferritin, which have a pH-dependent reduction potential of −190, −310, −416 mV at pH 7.0, 8.0, and 9.0, respectively, the reduction potential of holo bacterial ferritin iron core is more negative (−430 mV) and is independent of pH.

For bacterial ferritin, direct electron transfer from large exterior reductants through the heme to the mineral core is mediated by the heme [58,85]. This process eliminates the requirement for reductants to diffuse through the channels to reduce the iron mineral core directly. For mammalian ferritin, there is no obvious pathway for long-range electron transfer through the 2 nm protein shell of ferritin; however, studies have shown that large reductants and oxidants, too large to enter the ferritin interior, can transfer electrons through the animal ferritin protein shell to the mineral core [73,86]. These studies suggest that a specific electron transfer pathway exists within the ferritin protein shell. Although an electron transfer pathway through the protein shell has not been identified in mammalian ferritin, the
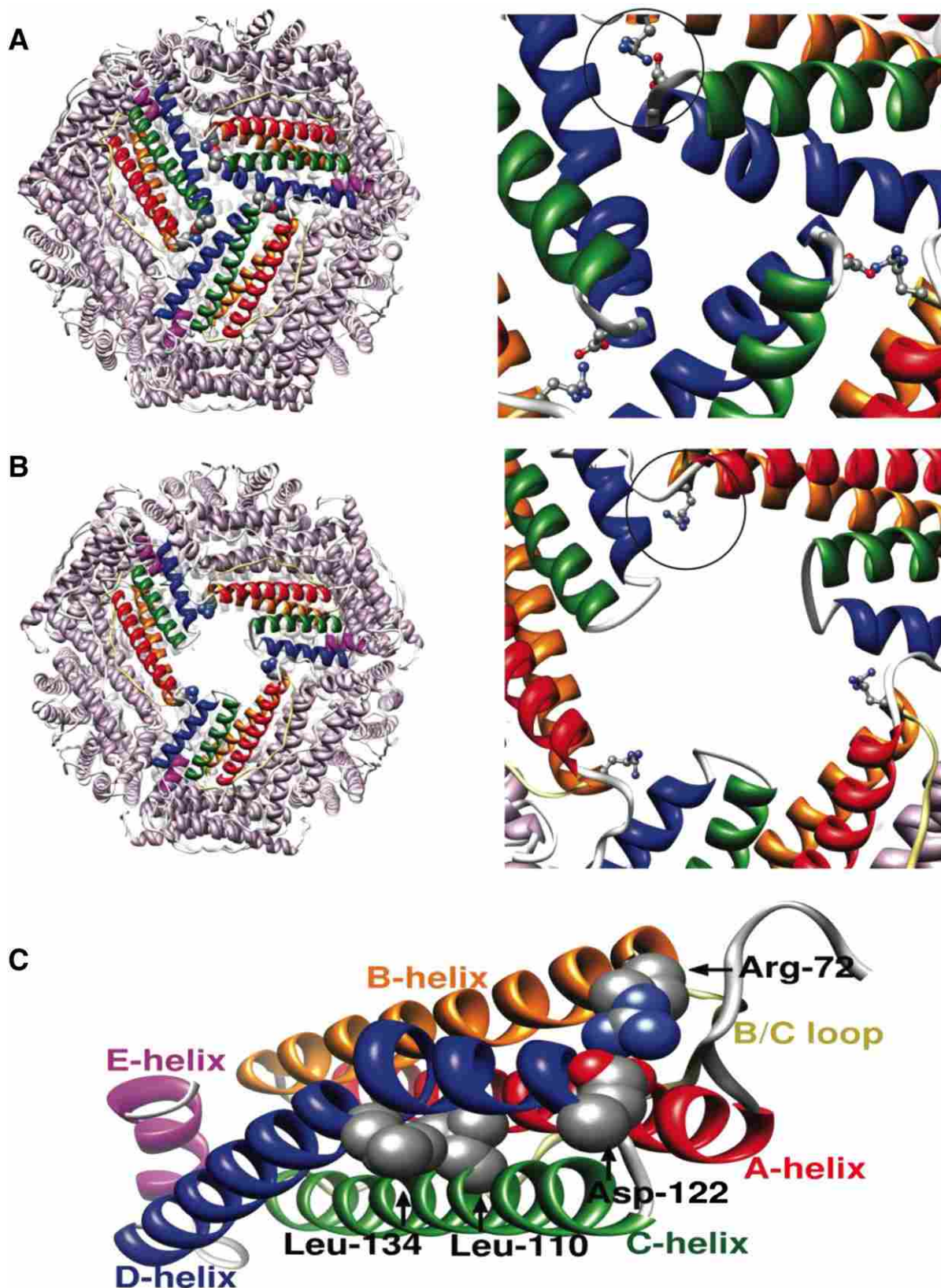
Fig. 3. The gated pores of the 3-fold channel. (A) The structure of the H-chain ferritin 3-fold channel showing the ionic interaction of Arg-72 and Asp-122 (represented by ball and stick models in the circled region). (B) The structure of the Leu110Pro mutant with a significantly larger 3-fold channel with shorter C and D helices and the lack of Asp-122 to form the gated pair with Arg-72. (C) Ribbon diagram of the individual H-chain ferritin subunit showing the hydrophobic interaction between Leu-110 and Leu-134. Also present is the Arg-72–Asp-122 ionic interaction at the mouth of the 3-fold channel.

presence of heme groups in bacterial ferritin suggests that such a system might be required, especially since the thickness of the ferritin protein shell (2 nm) is near the maximum distance for electron

tunneling [87]. An electron transfer pathway to mediate electrons across the protein shell of animal ferritin has been proposed and is currently being evaluated [88]. This pathway for the H-chain ferritin is

predicted to use, from the exterior to the interior of ferritin, Cys-90, Trp-93, Met 37, Phe-55, Tyr-54, and Lys-53. A similar pathway for L-chain ferritin was identified and consists of, from exterior to interior (using the equivalent numbering as for H-chain ferritin) Gln-90, Trp-93, Leu-37, Phe-55, Phe-54 [88].

Support of this hypothesis was suggested when the apo protein shell of ferritin was shown to possess redox properties in the absence of cofactors such as heme [89]. When treated with oxygen or chemical oxidants, the apo ferritin shell becomes oxidized. Microcoulometry of oxidized apo horse spleen ferritin showed that the shell is capable of accepting six electrons per 24 subunits consisting of 6 H-chain ferritin subunits and 18 L-chain ferritin subunits. The reduction potential was −310 mV at pH 6.0–8.5. The reduced apo ferritin was able to donate electrons to cytochrome c and an Fe(III)-ATP complex under anaerobic conditions. Oxidized apo ferritin was able to oxidize Fe^{2+} under anaerobic conditions showing functionality of the redox center in ferritin. Oxidized ferritin has a yellow color with increased absorbance at wavelengths from 300 to 600 nm compared to an identical concentration of apo ferritin reduced with dithionite. The ferritin was dissociated by low pH and dialyzed to remove any potential cofactors. After dialysis, the yellow color remained with the ferritin protein after it was reassembled and oxidized. Al-Massad et al. identified quinones in both animal and bacterioferritin [90]. The fact that the quinone was not released by low pH treatment and dialysis suggests that the quinone is formed from an amino acid such as tyrosine or phenylalanine within the protein shell [91].

Horse spleen apo ferritin and rat apo ferritin with different H- and L-chain compositions accepted different numbers of electrons when chemically oxidized and analyzed by microcoulometry. Heteropolymers of recombinant human H- and L-chains were prepared by combining apo H- and L-chain ferritin subunits in various ratios at pH 2.0 followed by reassembly of the subunits at pH 7.0. These heteropolymers were tested for redox activity by microcoulometry [92] and compared to homopolymers of H- and L-chain ferritin. The redox reactions were only observed when both H- and L-subunits were present. H- and L-homopolymers of ferritin were not redox-reactive. The maximum number of twelve redox centers was observed with an equal mixture of twelve H-subunits and twelve L-subunits. Studies with mutant H-chain subunits showed that Trp-93 from H-chain ferritin subunits is an important component of the redox center that forms in apo ferritin [92].

4. Redox reactions require ion transport for charge balance

Based upon the iron loading and iron release results discussed above, redox reactions play a significant role in iron entry and release from ferritin. Several facets of this complex process have been actively investigated including the ferroxidase center (Section 2.3), the nucleation sites (Section 2.3), the redox properties of the mineral core (Section 2.4), the redox reactivity of the associated phosphate layer (Section 2.4), and the redox reactivity of the protein shell itself (Section 3.4). However, while insights into these aspects of ferritin function have been and are being actively investigated, processes associated with ion transfer across the protein shell, particularly anions required for charge balance, have been largely ignored. Ion transfer is an inherent property of electrochemistry and redox reactions. In any electrochemical cell, a salt bridge is an essential component because ion migration must occur to prevent charge build-up on either side of the half-cells. An identical process occurs in ferritin in which the protein shell acts as an ion permeable membrane. As iron is reduced in the mineral core, due to incoming electrons, a concomitant release of negative charge from the core must occur to balance the incoming negative charge. Experiments related to redox reactions that involve ion transfer across the protein shell of ferritin clearly highlight this important process.

4.1. Chloride and hydroxide ions traversing the ferritin protein shell

Electrochemical measurements show a pH-dependent process with a reduction potential of −190 mV at pH 7.0 that shifts −120 mV/pH unit more negative as the pH changes to pH 8.0 (−310 mV) and to pH 9.0 (−430 mV). Studies monitoring pH confirmed that two hydroxide ions are released during $Fe(OH)_3$ reduction, as shown by Eq. (2) [93]. However, this stoichiometry is not consistent with the expected result shown in Eq. (3), which suggests that only one hydroxide ion should be released upon iron reduction. This behavior demonstrates a more complex core reduction process than was originally anticipated.

$$Fe(OH)_3 + e^- = Fe(OH)^+ + 2OH^- \qquad (2)$$

$$Fe(OH)_3 + e^- = Fe(OH)_2 + OH^- \qquad (3)$$

Eq. (2) is not charge balanced and implies that an impossibly large charge build-up should occur if greater than 2000 $Fe(OH)_3$ are reduced forming 2000 $Fe(OH)^+$ ions within the ferritin interior. This dilemma was resolved when chemical analysis of the resulting reduced ferritin mineral core showed that charge compensation occurred when chloride ions from the buffer were incorporated into the ferritin core (Fig. 4) [14]. In the absence of chloride ions, hydroxide ions were the preferred anion to complex the iron atoms and Eq. (3) was observed. The nature of this new core has not yet been studied nor has its relationship to physiological processes been established. One hypothesis is that the $Fe(OH)_2$ mineral core is less soluble than the core of FeClOH. The presence of chloride may improve the solubility of the Fe^{2+} ion and facilitate iron release.

4.2. Phosphate release by reduction

The presence of phosphate as a surface layer in animal ferritins and its presence as a 1:1 homogeneous mineral in bacterial ferritin demonstrated that phosphate is naturally occurring and possibly is an essential component in ferritin function [40,50]. One role was suggested when reduction of the mineral core by 10% mobilized the majority of the phosphate layer [61]. It appears that the surface iron atoms are the first to be reduced and results in the release of the associated phosphate layer. The release of the negatively charged phosphate ions from the ferritin surface in response to the incoming electrons may be a rapid response for charge balance. However, if each entering electron causes the release of one phosphate as $H_2PO_4^-$/HPO_4^{2-} at pH 7– 8, a large instantaneous negative charge build-up will occur inside ferritin. The magnitude of this effect is seen by calculating the concentration of released phosphate ($\sim$400 phosphate groups per mineral core of 2000 iron atoms) as $H_2PO_4^-$/$H_2PO_4^{2-}$ within the half filled ferritin interior (1.3×10^{-19} cm^3), giving an instantaneous phosphate concentration of >5 M. Such a high concentration would
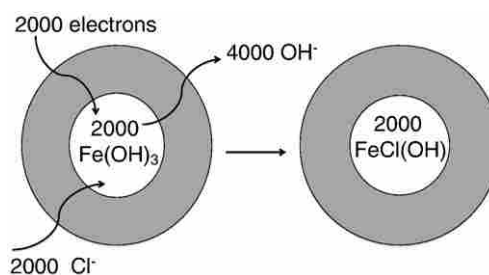

Fig. 4. Chloride ion pumping during chemical reduction of the iron core. Eq. (3) shows that upon chemical reduction of the iron mineral core of ferritin, two hydroxide ions are released for each iron reduced. To compensate for charge, one chloride ion is pumped into ferritin for each iron reduced. The resulting core has a composition of FeClOH.

certainly drive a diffusional process to decrease the phosphate concentration within the ferritin interior. An additional possibility is that the elevated phosphate concentration acts as a trigger to open the gated pores (Section 3.3) and allow ions to flow through the 3-fold channels. An alternate possibility for the presence of phosphate is that the release of phosphate may provide a local complexing agent to maintain solubility of the iron as it moves out from ferritin.

Section 4.1 discussed the observation that chloride enters ferritin during iron reduction in order to provide charge balance to compensate for the expulsion of hydroxide ions from the ferritin interior. These arguments were based on the hydroxide ion release (Eq. (2)), but the release of phosphate must also enter into arguments related to charge compensation because of the phosphate species that form ($H_2PO_4^-$, HPO_4^{2-}, or PO_4^{3-}) and pH changes because of the weak acid and weak base properties of these species. Phosphate is associated with the first 10% of the iron released. As mentioned above, its release may trigger pore opening that facilitates hydroxide ion release from the ferritin interior.

However, an alternate possibility is that protons are transferred from the exterior of the ferritin shell to the interior to neutralize the hydroxide ions that are released. H_2O could be easily eliminated through the protein channels. If protons traverse the protein shell to compensate for the increased negative charge caused by hydroxide release from the mineral core, the interior of ferritin remains charge balanced. However, the release of the negatively charged phosphate is not compensated for by this mechanism. We propose that an alternate reason for chloride to enter the ferritin interior is to compensate for the removal of the negatively charged phosphate species that are liberated upon chemical reduction of the ferritin mineral core. The actual charge of the phosphate anion ($H_2PO_4^-$, HPO_4^{2-}, or PO_4^{3-}) that leaves ferritin would determine the number of chloride ions that are required to enter the ferritin cavity to balance the charge. The results presented here clearly demonstrate the need for further studies on the mechanism of maintaining charge balance in ferritin during redox reactions associated with iron deposition and release.

From a materials synthesis perspective, it will be interesting to study what other anions can substitute for chloride in this reaction. Such a mechanism might allow for the synthesis of new materials by chemically reducing the mineral core of ferritin in the presence of the anion one desired to incorporate into the ferritin core.

The driving force for anion transfer across the ferritin protein shell is an interesting question that requires further study. When phosphate is released by reduction the concentration inside ferritin would exceeds 5 M facilitating phosphate release by charge and concentration arguments. The opposite argument would be made for chloride ion diffusion into ferritin. The chloride ion concentration is approximately 4 mM inside the cell but would be 24 M inside ferritin if 2000 chloride ions entered the interior of a half-filled ferritin cavity. To transfer 2000 chloride ions into the ferritin interior would require energy and would be appropriately classified as pumping as defined for membrane ion pumps discussed previously (Section 3.3). The mechanism allowing chloride ions to be pumped into ferritin has not yet been elucidated but must be driven by charge compensation and possibly by a port–antiport mechanism associated with phosphate diffusion out of the ferritin interior. Further studies on this mechanism are required to completely understand this system.

5. Iron release from ferritin—non-reductive processes

The removal of iron from the ferritin core by Fe^{3+} chelators is more difficult and much slower than the reductive processes discussed above [94,95]. Therefore, the treatment of human iron overload diseases requires chelation therapy, which consists of administering very powerful chelator drugs such as DFO, which is a bacterial siderophore from *Streptomyces pilosus* that has a binding affinity for iron of greater than 10^{30} [96]. The goal is to find Fe(III) chelators that

are capable of removing excess iron from the natural and overloaded cellular locations that include ferritin and hemosiderin [97]. The resulting iron-chelate is then excreted from the body. DFO is not lipid soluble and is not effective for crossing membranes or penetrating organelles but is effectively excreted. The use of the orally administered and membrane permeable chelators deferiprone and deferasirox has given a great advance to chelation therapy since these chelators cross cell membranes and permeate organelles [98,99]. Current treatments use a combination of lipid soluble chelators such as deferiprone or deferasirox to diffuse into iron loaded cells or organelles, followed by diffusion back to the bloodstream where DFO is capable of removing iron from lipid soluble chelators [100–102]. Once the iron is sequestered in DFO, the DFO–iron complex is excreted.

During the evaluation phases of chelate selection, tests showed a general trend for iron removal of freshly precipitated FeO(OH)>> hemosiderin>ferritin. The slowness of iron release from ferritin was attributed to the inability of chelators to directly access the mineral core, which is sequestered within the hollow interior and only accessible through the 3-fold channels of ferritin. As chelators are usually larger than the channel openings, the slow transfer of iron from the sequestered ferritin core through the protein shell to the chelators at the ferritin exterior limits the rate of chelation therapy. Numerous kinetic studies have monitored iron release from ferritin [97,103,104] over time increments of hours or days and showed that iron loss was zero order in ferritin due to the rate limiting release of iron from the stored mineral core. However, some studies noted that iron release occurred more rapidly in the initial time interval than later in the reaction [105]. This was an important observation because it suggests that early events in the iron loss process had been overlooked and were potentially relevant to the overall iron loss process. Additionally, newer studies have identified more rapid chelation processes that rely upon diffusion of the chelator through the 3-fold channel or use the gated pores discussed in Section 3.3 [106]. With new data supporting mechanisms for Fe(III) chelation from the ferritin mineral core, alternate mechanisms for *in vitro* and *in vivo* iron release must be considered.

5.1. Direct Fe^{3+} chelation from ferritin

Iron chelation from ferritin using the Fe(III) chelators, aceto- and benzo-hydroxamates, demonstrated that 30–60% of the iron core could be removed from the $Fe(OH)_3$ mineral core. In the presence of physiological concentrations of urea to open the gated pores (Section 3.3), complete removal of iron from ferritin was achieved at pH 7.4 in one hour [106]. The authors concluded that the chelating molecules had entered the ferritin interior via the 3-fold channels and directly interacted with the iron mineral core. This view stands in contrast with other chelating agents such as DFO that remove iron without entering the ferritin interior [107]. However, the dimensions of the benzo-hydroxamate chelator (~0.6 nm) would require breathing modes or opening of the gated pores (Section 3.3) to allow it to pass through the 3-fold channels of ferritin. Additionally, the negative charge of these molecules would impede the progress of these chelators to pass through the 3-fold channels. However, the authors suggest that it is the neutral species that diffuses into ferritin. To explain how the large iron–chelate complex could leave ferritin, the authors proposed that first, a mono(hydroxamate) complex formed inside ferritin and the Fe(III)-mono(hydroxamate) diffused out of the ferritin channel. After exiting ferritin, higher coordination complexes of the iron–chelate complex formed.

In another study, release of iron by catechols was examined. Traditionally catechols were thought to reduce iron in ferritin by a redox rearrangement to form Fe^{2+} and a quinone, followed by chelation of the Fe^{2+} [108–110]. Sanchez et al. showed that the iron was directly chelated from ferritin without redox reactions occurring

[111]. This reaction presumably followed the same mechanism as the aceto- and benzo-hydroxamates.

5.2. Proposed model for Fe(III) chelation from ferritin

In all considerations involving equilibrium transfer of iron, it must be considered that the $Fe(OH)_3$ mineral core in ferritin is a slow responding sink of iron with a K_{sp} of 1.6×10^{-39}. Therefore, proposals involving equilibrium transfer of iron out of ferritin must be constrained by this limit or the chelators receiving iron from ferritin must have very large binding constants. For models that prevent direct chelator access to the iron mineral core, the protein shell must perform a role in iron mobilization. A potential role for ferritin in Fe^{3+} release is suggested by electrostatic calculations of the channels [33]. In this study, two metal binding sites in the 3-fold channel were observed. Although these calculations were performed for Fe^{2+}, the carboxylate residues also have affinity for Fe^{3+}, and in fact, Fe^{3+} binds in these channels [112,113]. A model that might explain Fe^{3+} removal from ferritin is outlined in Fig. 5. The model represents how Fe^{3+} might pass through the 3-fold channel but a similar model could be used for the two metal binding sites of the ferroxidase center. This model shows the iron core and the two binding sites within the 3-fold channel. The unloading sequence suggested by Fig. 5 indicates that Fe^{3+} dissociates (k_1) from the mineral core and binds at site 1. Although the amount of free Fe^{3+} is small, a tiny amount of iron does dissociate from the iron mineral core. Once bound at site 1, the Fe^{3+} can migrate to site 2 (k_2), which is in equilibrium with site 1. Site 2 has a lower affinity for Fe^{2+} than site 1 according to iron loading studies [76], but the affinities for Fe^{3+} are unknown. In the absence of chelators, Fe^{3+} partially populates sites 1 and 2 but when a strong iron chelator is present, the equilibrium would pull Fe^{3+} outward from the iron mineral core through the 3-fold channel to chelators at the ferritin exterior.

The existence of iron in the channels is supported by two studies. First, EPR studies commonly show a $g = 4.3$ EPR signal for holo ferritin. The $g = 4.3$ EPR signal is due to isolated Fe^{3+} ions in a rhombic environment [114]. This signal is also observed in the early stages of iron oxidation when Fe^{2+} is oxidized to Fe^{3+} [115]. Since a $g = 4.3$ signal is always present in holo ferritin, this supports the existence of

monomeric Fe^{3+} that may be accessible for chelation. Bauminger et al. further substantiated surface bound Fe^{3+} by showing the transfer of Fe^{3+} between ferritin molecules [116]. This work reported that once oxidized, $^{57}Fe^{3+}$ could be transferred to other ferritin molecules containing cores of differing sizes as measured by Mossbauer spectroscopy. This study shows that a small population of Fe^{3+} appears to remain surface bound and available for exchange. Such studies support the model that a minor population of Fe^{3+} is available for slow chelation from ferritin. This small population of Fe^{3+} explains the rapid iron release that occurred in the initial time interval in the kinetic studies by Crichton et al. [105].

While Fe^{3+} release by this process is much less rapid than iron release from a reduced mineral core, a significant Fe^{3+} flux is still available from all ferritin molecules in the cell if a suitable chelator is present. An important question to evaluate is the role of phosphate and other anions, such as chloride and citrate in modulating the release of iron from the mineral core. For instance, the K_{sp} of $FePO_4$ (s) is 4×10^{-27} so such a layer on the surface of the ferritin core would allow Fe^{3+} to be over 12 orders of magnitude more soluble than $Fe(OH)_3$ (s) with a K_{sp} of 1.6×10^{-39}. $Fe(OH)_2$ has a K_{sp} of 7.9×10^{-16}, and it is known that chloride salts of metals are more soluble than the hydroxides or phosphates. Even the mineral ferrihydrite is more available for biological processes than other iron oxides [117]. Therefore, alterations to the mineral core composition will significantly increase the ability of the cell to obtain iron from the ferritin mineral core.

Considering the solubility product data listed above, the total amount of Fe^{3+} available for release by such a mechanism would still be very small but may meet the demands of the cell. By invoking the gated pore model where substrate or proteins bind to the ferritin exterior, one could envision alterations in the affinity of site 1 and site 2 for Fe^{3+} in a way that would allow iron release. Measurements of Fe^{3+} under these conditions are still required to realistically consider the Fe^{3+} release models from a thermodynamic standpoint.

6. Biochemical models for *in vivo* iron release

The mechanism of iron release from ferritin *in vivo* is unknown, but several studies shed light on potential mechanisms. Three distinct
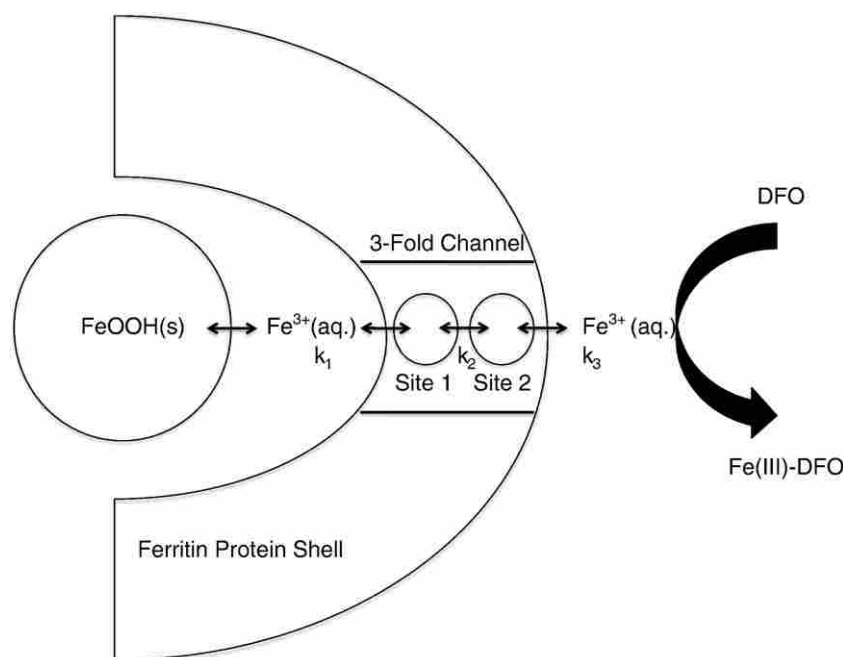

Fig. 5. Chelation of Fe^{3+} from ferritin. In the presence of DFO, iron is removed from the 3-fold channels (site 1 and site 2). In the absence of DFO, sites 1 and 2 are repopulated as Fe^{3+} ions slowly dissociate from the FeOOH mineral core and populate these sites. The reactions representing the rate constants k_1, k_2, and k_3 are represented.

models have been proposed and include (1) a model based on simple equilibrium between cytosolic iron and iron sequestered in ferritin, (2) ferritin degradation in the lysosome for iron release, and (3) a chaperone protein that docks with ferritin to reduce and removes iron from ferritin.

6.1. Intracellular equilibrium of cytosolic and ferritin iron

A model suggesting ferritin iron is in equilibrium with cytosolic iron was proposed by De Domenico and Kaplan [118] and was based upon studies where the intracellular iron concentration of cells was depleted by expressing proteins that transports iron out of the cytosol. The model suggests that iron is released by ferritin when the iron concentration in the cytosol decreases. For these studies, the depletion of iron in the cytosol was caused by the expression of ferroportin, which acts as an iron export transporter, or by Ccc1p, a yeast protein that transports iron into the vacuole [118]. These studies showed that as the intracellular iron concentration decreased, the iron levels in ferritin also decreased. Once the ferritin shell was depleted of iron, it was mono-ubiquitinated and disassembled to monomers followed by degradation in the proteasome. When similar studies were performed in yeast, an organism that does not naturally possess ferritin, iron release was observed from ferritin. The authors concluded that no ferritin-specific biochemical machinery was required to release iron from ferritin since yeast does not naturally possess ferritin. This conclusion would be correct unless there is an evolutionarily retained system that was conserved for another purpose but still functions to release iron from ferritin.

Based on the difficulty of releasing Fe^{3+} from ferritin (Section 5.2), an equilibrium model where Fe^{3+} is in equilibrium with the cytosol is challenging to believe. Fortunately, for this model, the intracellular compartment has a reducing environment and the iron core of ferritin may exist in a mixed valent state with sufficient Fe^{2+} to be in equilibrium with iron in the cytosol. Perhaps signals for iron release also include the accumulation of reduced species that donate electrons to ferritin to reduce iron prior to chelation. More extensive studies need to be performed to understand the mechanism of this iron release process.

6.2. Ferritin iron release by lysosomal degradation

The results of De Domenico and Kaplan, showing that cytosolic iron is in equilibrium with ferritin iron, is in conflict with previous studies. Truty et al. grew rat hepatoma cells in the absence or presence of ferric ammonium citrate (FAC) with ferritin labeled with [^{35}C]Met and ^{59}Fe [119]. In the absence of FAC, ferritin was degraded and iron was released to the cells. This result was unexpected because of the substantial *in vitro* work (Sections 3 and 5), suggesting that iron diffuses through the 3-fold channels of ferritin for release. In a follow-up study, using the chelator DFO to deplete cells of iron, it was shown that independent of cell type (using hepatoma cells, Caco2 and K562 cells) ferritin was degraded in the lysosome to supply the depleted cells with iron. The lysosomal protease inhibitors, leupeptin and chymostatin, prevented ferritin degradation during iron limitation caused by DFO treatment, consistent with the model that ferritin is degraded in the lysosome as a mechanism for iron release. This model suggests that iron is irreversibly trapped inside the ferritin protein shell and can only be released by degradation of the ferritin protein shell.

This model is appealing based on the solubility arguments presented previously. Degradation of the ferritin shell would allow access of chelators to the iron core. Furthermore, the lysosome is at lower pH where iron is more soluble and reducing agents are present in this compartment. However, iron in the lysosome is also dangerous as iron and peroxide react to initiate radical chemistry that is damaging to the lysosome and the cell [120].

6.3. Two pathways for in vivo ferritin iron release by chelators

To resolve the conflict between these two iron-release models (lysosomal degradation model Section 6.2 and the intracellular equilibrium model Section 6.1), De Domenico and Kaplan studied how several chelators depleted cells of iron [118,121]. In these studies, the effect of DFO, which is not absorbed after oral administration and is not membrane permeable, was compared to the orally administered and membrane permeable chelators deferiprone and deferasirox. The method of cellular entry appears to have a significant effect on the way iron is released and how and when ferritin is degraded. DFO enters cells by endocytosis and is targeted to the lysosome and endosome. The presence of DFO in the lysosome induced autophagy leading to the transfer of ferritin from the cytosol to the lysosome. The presence of DFO in the lysosome correlated with the cytosolic accumulation of LC2B, a protein that is essential for autophagy. The DFO effect could be blocked by treating cells with a plasmid expressing the dominant negative mutant (K44A) of dynamin that blocks the clathrin mediated endocytosis process. By excluding DFO from the lysosome, ferritin degradation in the lysosome was inhibited. These results confirmed that the presence of DFO in the lysosome induces autophagy and leads to ferritin degradation in the lysosome.

In contrast to DFO, deferiprone and deferasirox traverse the membrane and upon entering the cytosol bind iron from the intracellular iron pool. Depletion of the intracellular iron pool triggers the release of iron from ferritin [121]. The resulting empty ferritin nanocages are ubiquitinated and degraded by the proteasome in a similar fashion as when iron is depleted by ferroportin. Thus, two independent chelator pathways exist *in vivo*: (1) a depletion of cytosolic iron leading to proteasomal degradation of the empty ferritin nano cage and (2) iron depletion in the lysosome, leading to autophagy where ferritin is moved from the cytosol into the lysosome for degradation and iron release.

In another study, cationized ferritin was endocytosed by cells and degraded in the lysosome [122]. The released iron was transported to the cytosol and induced the synthesis of ferritin. These studies indicate that the iron concentrations in the cytosol and lysosome are in equilibrium through membrane transporters that can transport iron in both directions. Disturbances in iron concentrations in either the cytosol or lysosome trigger signals that allow iron to be moved from one location to the other. These studies further confirm the presence of a cytosolic iron pool and demonstrate that ferritin iron is released to replenish this pool when it decreases. Further studies are required to better understand this relationship between cytosolic iron and ferritin iron.

6.4. Iron delivery and/or release by iron chaperones

Recently, an intracellular iron chaperone protein was discovered [123]. The iron chaperone protein is PCBP1, from a family of RNA-binding proteins belonging to the heterogeneous nuclear ribonucleo-protein K-homology domain superfamily [124]. Previous studies showed that when ferritin is expressed in yeast, an organism that does not naturally express ferritin, the iron loading of ferritin is very low [123]. The co-expression of PCBP1 and ferritin in yeast allowed iron loading to occur in ferritin [123]. A complimentary experiment was to deplete PCBP1 in human cells and observe the inhibition of ferritin iron loading. *In vitro* iron loading studies also confirmed that PCBP1 loads iron into ferritin. PCBP1 binds to ferritin in the presence of Fe^{2+} as detected by co-immunoprecipitation. PCBP1 binds 3 Fe(II) with a $K_d = 0.9\ \mu M$ for the first binding site and a $K_d = 5.8\ \mu M$ as an average for the second and third binding sites. The presence of an iron metallo-chaperone is very appealing because a cytosolic iron-binding chaperone could potentially minimize the formation of reactive oxygen radical chemistry catalyzed by free iron and oxygen. Studies

need to be done to determine if PCBP1 is the mediator that senses and releases iron from ferritin when cytosolic iron concentrations decrease. Metallo-chaperones have been identified for other transition metal ions such as copper, manganese, and nickel [125–129].

6.5. Ferritin binding proteins

Several ferredoxin-like proteins have been identified in DNA regions close to ferritin in bacteria *Escherichia coli* [130] and *Pseudomonas aeruginosa* [131]. These ferredoxin proteins have been purified and characterized as electron transfer proteins containing 2Fe-2S clusters [131–133]. The fact that these proteins bind to ferritin suggests that they may have a role in redox chemistry associated with iron loading or iron release. Additionally, similarity to the NifU and IscU proteins that are involved in iron sulfur cluster assembly strengthens this hypothesis [134–136]. Investigations of global transcriptional response of iron-starved cultures of *P. aeruginosa* provide valuable insight into the role of this bacterial ferritin-related protein. The bacterioferritin is expressed under high iron conditions, whereas the ferredoxin protein called Bfd is upregulated 200-fold under low iron conditions. This regulation suggested that Bfd might be expressed for mobilizing iron from ferritin during iron deprivation. Weeratunga et al. [85] established a system where NADP reductase (FPR) and NADPH were used as a reducing system to reduce iron in bacterioferritin and bipy was used to chelate the resulting Fe^{2+} [85]. This *in vitro* system failed to reduce the heme of the bacterial ferritin and was sluggish in removing iron from ferritin. However, when the same system was used and Bfd ferredoxin was added, the heme was rapidly reduced and iron release was significantly stimulated. Interestingly, the iron-deficient form of the ferredoxin was also capable of stimulating heme reduction. The ferredoxin acts to make the heme "conductive" and allows electrons to pass through the protein shell. This system supports the model discussed in Section 3.4, proposing that electrons are transferred through the protein shell followed by Fe(II) chelation as model for iron release.

Finally, a series of studies have reported other proteins that bind to ferritin. These proteins include serum proteins involved in clearing proteins from the blood such as alpha-2-macroglobulin [137]. Apolipoprotein B has a role in heme binding in serum and was also found to bind ferritin [138]. The apolipoprotein B/ferritin complex may play a role in the recovery of iron from senescent red blood cells. Recently a feline serum binding protein was reported that altered the ability of antibodies to recognize ferritin [139]. Bovine alpha-casein is a protein from milk that binds ferritin [140]. Currently any physiological roles for these proteins binding to ferritin have not yet been established. However, based upon the mechanisms discussed in this review, such interactions with ferritin may indicate (1) roles for degrading ferritin to release iron, (2) directing ferritin to receptors for binding and endocytosis, and (3) proteins that dock with ferritin to open or close the 3-fold channels of ferritin to regulate iron storage or iron release.

7. Major conclusions

A major goal in studying ferritin is to understand the mechanism of iron loading and iron release so treatments can be devised to alleviate iron overload or iron deficiency diseases. This includes understanding disease states with elevated levels of free iron that acts as a catalyst for oxidative damage and why this free iron is not sequestered in ferritin. From a material science perspective, understanding how ions are transferred across the protein shell and coupling this understanding with the natural metal binding and mineralization capacity of ferritin makes this protein a unique reaction vessel for size constrained nanoparticle synthesis. In this review, we have discussed the mechanisms of iron loading and iron release in the context of how

iron and other ions traverse the protein shell of ferritin, with the goal of understanding ways to maximize iron sequestration or iron release.

In vitro studies show that the most efficient method to remove iron from ferritin is by reduction and chelation. The use of low potential reductants and chelators with high affinity for Fe^{2+} rapidly remove iron from the ferritin interior to make apoferritin [72]. Bi-functional molecules, such as thioglycolic acid, act as both a reducing agent and a chelating agent to remove iron from ferritin [50,141]. Direct evidence to support the reduction and chelation model *in vivo* has been lacking but has been implied because (1) Fe(II) chelation from ferritin is fast and complete and (2) early studies on the removal of Fe(III) from ferritin by Fe(III) chelators [97,103,104] or transferrin [95] was significantly slower and required chelators with very strong binding constants. Furthermore, the intracellular environment is reducing and molecules such as glutathione and ascorbic acid are capable of reducing the iron core of ferritin [142,143]. Additionally, electron transfer proteins are capable of reducing the iron core of ferritin [73], suggesting a docking site and an electron transfer pathway through the protein shell of animal ferritin [88]. This evidence suggests that there may be a specific mechanism to reduce the iron in ferritin when iron release is required. The discovery of a ferredoxin that specifically binds to the heme of bacterial ferritin and opens electron transfer through the protein shell supports the reductive release model [85]. A potential problem with the reduction model is that Fe^{2+} reacts with oxygen to produce the toxic reactive oxygen species (ROS) superoxide, peroxide, and the hydroxyl radical. To prevent the formation of ROS from Fe^{2+}, a reductive iron release model would be strengthened by the existence of a metallo-chaperone or Fe^{2+} chelating molecule that rapidly binds Fe^{2+} ions in a protective environment where it is not reactive with O_2. The discovery of PCBP1, a metallo-chaperone that docks to ferritin and binds Fe^{2+}, is powerful evidence supporting the reduction and chelation model [123].

The presence of an intracellular iron pool or labile iron pool (LIP) under cellular reducing conditions seems contradictory to the iron-scavenging role of ferritin. If the role of ferritin were to sequester and store iron to protect the cell against free iron, one would expect a very low level of free iron in the cell. The LIP is estimated to be around 1–5 μM [144]. In contrast, free Cu concentration is estimated to be 6 fM or essentially 1 free Cu^{2+} ion per cell [145]. The discrepancy between the concentration of the free Cu^{2+} pool and that of iron has two distinct explanations. The first is that the methods used to measure free iron are disturbing the iron pool resulting in the mobilization of iron from ferritin and other iron proteins and these assays give an artificially high result. The second possibility indicates that cytosolic iron availability is essential for critical reactions.

The LIP is proposed to be both Fe(II) and Fe(III) bound by small organic acid ligands, phosphate, pyrophosphate, ATP, ADP, polypeptides, and membrane components [144]. The existence of the LIP supports the model proposed by De Domenico and Kaplan (Section 6.1), suggesting that cytosolic iron is in equilibrium with ferritin iron. When ferroportin was over-expressed, the cytosolic iron concentration decreased in the cells. This shift in iron equilibrium caused iron to be released from ferritin, eventually resulting in apo ferritin that was degraded. An equilibrium between iron in the cytosol and ferritin also suggests that changes in the concentrations of organic acids capable of complexing Fe(II) or Fe(III) *in vivo* could significantly increase the LIP and decrease the iron contained in ferritin [106,111].

The gated pores model may open a new field of study and make a significant contribution towards understanding how iron loading and release reactions occur in ferritin [79]. Perhaps a change in the intracellular concentration of certain organic acids is a trigger for the ferritin channels to open and release iron. One potential mechanism involves the known iron chelator citrate. Cytosolic citrate concentrations are related to the cytosolic enzyme aconitase. Cytosolic aconitase (c-acon) is a bi-functional enzyme that switches activities based on the available iron concentration [146–149]. When iron is

present, c-acon has a functioning 4Fe-4S cluster and converts citrate to isocitrate. When cytosolic iron levels drop, the 4Fe-4S cluster is disassembled and c-acon is converted in the iron-responsive protein-1 (IRP-1), which binds to mRNA and blocks ferritin synthesis and stabilizes the mRNA of the transferrin receptor, increasing the flow of iron into the cell. During iron limitation, citrate concentrations in the cytosol increase due to the lack of active c-acon. Does the increase in citrate concentration open the gated pores releasing iron for use by other enzymes? Does citrate traverse the protein shell and chelate Fe(III) from ferritin? Perhaps citrate concentrations increase to prepare for incoming iron that is triggered by the increased synthesis of transferrin receptors as a result of IRP-1 activation.

An alternate hypothesis suggests that substrate binding to ferritin increases the affinity of the iron binding sites in the channels and shifts the equilibrium from internalized iron to surface iron where chelators can gain access to the iron (Fig. 5). Iron in the channel may be more accessible to the small organic chelators and facilitate iron release to the LIP. Potential experiments to test this hypothesis could involve growing cells on an increased concentration of citrate and test to determine if the LIP increases and if ferritin iron levels drop resulting in ubiquitination of ferritin. Such studies would support both the Theil gated pore model (Section 3.3) and the iron equilibrium model of De Dominico and Kaplan (Section 6.1).

The transport of anions across the ferritin protein shell has been much less studied but, in light of data presented above (Section 4), appears to play an important role in overall iron sequestration process. Phosphate binding to the ferritin mineral core and its release from the core upon reduction of the iron has been studied, but its physiological function was not evident [50,62,63]. The new discovery of gated pores and the ability to open these pores by small molecules and proteins is an interesting new model to test in order to determine if the release of phosphate is involved in opening these gated pores (Section 4.2). Furthermore, the significance of chloride being pumped into ferritin was initially proposed to be a mechanism to compensate for charge balance [14]. However, as discussed above, comparing the solubilities of $Fe(OH)_3$, $Fe(OH)_2$ or the chloride salts of iron clearly shows that chloride may function to convert the stable and insoluble iron hydroxides to iron chloride salts as a mechanism for iron mobilization *in vivo*. The pumping of chloride into the ferritin core upon reduction produces the iron mineral FeClOH, which is more soluble [14]. The pumping of chloride into ferritin during reduction may be by evolutionary design to form a mineral core that is more soluble for the mobilization and release of iron from ferritin.

Another interesting observation is that the iron concentration of the cytosol and the lysosome are in equilibrium and that depletion of iron in one compartment draws upon iron in the other compartment [121]. That there are two different pathways to replenish the iron between these compartments indicates the importance of maintaining a LIP for enzymes to access iron. This suggests an important role in maintaining a free iron pool for some as yet undiscovered purpose.

The presence of ferritin binding proteins may also play a significant role in iron binding or release. Liu et al. reported that a combinatorial library identified peptides that open or close the gated pores of ferritin [83]. Whether proteins known to bind to ferritin such as alpha-macrogolobulin [137], α-casein [140], feline serum ferritin binding protein [139], apolipoprotein [138], or other proteins yet to be identified influence iron regulation by opening or closing the gated pores of the 3-fold channels has not been studied. These or other proteins may play an important role in iron regulation.

Clearly, many mechanisms are involved in iron release from ferritin *in vivo*. Perhaps each of the mechanisms discussed in this review functions under different metabolic conditions. Reductive release may occur during hypoxic conditions when oxygen levels are low and the formation of ROS is less likely. During times of elevated respiration and ample oxygen concentrations, Fe(III) mobilization by chelation or by opening of the gated pores may be the safest

mechanism to prevent ROS formation. In relation to oxidative damage diseases, conditions may exist where the safety mechanisms designed to prevent free iron are failing. It is vital to gain an understanding of iron metabolic processes in order to develop treatments to prevent the damage caused by free iron.

References

[1] S. Granick, L. Michaelis, Ferritin and apoferritin, Science 95 (1942) 439–440.
[2] N. Kresge, R.D. Simoni, R.L. Hill, The characterization of ferritin and apoferritin by Leonor Michaelis and Sam Granick, J. Biol. Chem. 279 (2004) e9–e11.
[3] V. Laufberger, Sur la Cristallisation de la Ferritine, Bull. Soc. Chim. Biol. 19 (1937) 1575–1582.
[4] P. Arosio, S. Levi, Ferritin, iron homeostasis, and oxidative damage, Free Radic. Biol. Med. 33 (2002) 457–463.
[5] P. Arosio, R. Ingrassia, P. Cavadini, Ferritins: a family of molecules for iron storage, antioxidation and more, Biochim. Biophys. Acta 1790 (2009) 589–599.
[6] C.H. Campbell, R.M. Solgonick, M.C. Linder, Translational regulation of ferritin synthesis in rat spleen effects of iron and inflammation, Biochem. Biophys. Res. Commun. 160 (1989) 453–459.
[7] A.M. Konijn, N. Carmel, R. Levy, C. Hershko, Ferritin synthesis in inflammation 2. Mechanism of increased ferritin synthesis, Br. J. Haematol. 49 (1981) 361–370.
[8] B.A. Leggett, L.M. Fletcher, G.A. Ramm, L.W. Powell, J.W. Halliday, Differential regulation of ferritin H and L subunit mRNA during inflammation and long-term iron overload, J. Gastroenterol. Hepatol. 8 (1993) 21–27.
[9] N. Madani, M.C. Linder, Differential effects of iron and inflammation on ferritin synthesis on free and membrane-bound polyribosomes of rat liver, Arch. Biochem. Biophys. 299 (1992) 206–213.
[10] S.V. Torti, F.M. Torti, Iron and ferritin in inflammation and cancer, Adv. Inorg. Biochem. 10 (1994) 119–137.
[11] L.G. Coffman, J.C. Brown, D.A. Johnson, N. Parthasarathy, R.B. D'Agostino Jr., M.O. Lively, X. Hua, S.L. Tilley, W. Muller-Esterl, M.C. Willingham, F.M. Torti, S.V. Torti, Cleavage of high-molecular-weight kininogen by elastase and tryptase is inhibited by ferritin, Am. J. Physiol. Lung Cell. Mol. Physiol. 294 (2008) L505–L515.
[12] I. De Domenico, D.M. Ward, J. Kaplan, Serum ferritin regulates blood vessel formation: a role beyond iron storage, Proc. Natl. Acad. Sci. U. S. A. 106 (2009) 1683–1684.
[13] L.G. Coffman, J.C. Brown, D.A. Johnson, N. Parthasarathy, R.B. D'Agostino Jr., M.O. Lively, X. Hua, S.L. Tilley, W. Muller-Esterl, M.C. Willingham, F.M. Torti, S.V. Torti, Cleavage of high-molecular-weight kininogen by elastase and tryptase is inhibited by ferritin, Am. J. Physiol. Lung Cell. Mol. Physiol. 294 (2008) L505–L515.
[14] S. Hilty, B. Webb, R.B. Frankel, G.D. Watt, Iron core formation in horse spleen ferritin: magnetic susceptibility, pH, and compositional studies, J. Inorg. Biochem. 56 (1994) 173–185.
[15] N.D. Chasteen, P.M. Harrison, Mineralization in ferritin: an efficient means of iron storage, J. Struct. Biol. 126 (1999) 182–194.
[16] I. Kim, H.A. Hosein, D.R. Strongin, T. Douglas, Photochemical reactivity of ferritin for Cr(VI) reduction, Chem. Mater. 14 (2002) 4874–4879.
[17] D. Ensign, M. Young, T. Douglas, Photocatalytic synthesis of copper colloids from Cu(II) by the ferrihydrite core of ferritin, Inorg. Chem. 43 (2004) 3441–3446.
[18] M.T. Klem, J. Mosolf, M. Young, T. Douglas, Photochemical mineralization of europium, titanium, and iron oxyhydroxide nanoparticles in the ferritin protein cage, Inorg. Chem. 47 (2008) 2237–2239.
[19] V.V. Nikandrov, Inorganic semiconductors as photosensitizers of biochemical redox reactions, Biol. Membrany (Moscow) 15 (1998) 598–609.
[20] V.V. Nikandrov, C.K. Gratzel, J.E. Moser, M. Gratzel, Light induced redox reactions involving mammalian ferritin as photocatalyst, J. Photochem. Photobiol. B 41 (1997) 83–89.
[21] A. Lewin, G.R. Moore, N.E. Le Brun, Formation of protein-coated iron minerals, Dalton Trans. (2005) 3597–3610.
[22] M.T.K.M. Uchida, M. Allen, P. Suci, M. Flenniken, E. Gillitzer, Z. Varpness, L.O. Liepold, M. Young, T. Douglas, Biological containers: protein cages as multifunctional nanoplatforms, Adv. Mater. 19 (2007) 1025–1042.
[23] L. Zhang, J. Swift, C.A. Butts, V. Yerubandi, I.J. Dmochowski, Structure and activity of apoferritin-stabilized gold nanoparticles, J. Inorg. Biochem. 101 (2007) 1719–1729.
[24] F.C. Meldrum, B.R. Heywood, S. Mann, Magnetoferritin: in vitro synthesis of a novel magnetic protein, Science 257 (1992) 522–523.
[25] J.W. Bulte, T. Douglas, S. Mann, R.B. Frankel, B.M. Moskowitz, R.A. Brooks, C.D. Baumgarner, J. Vymazal, M.P. Strub, J.A. Frank, Magnetoferritin: characterization of a novel superparamagnetic MR contrast agent, J. Magn. Reson. Imaging 4 (1994) 497–505.
[26] L. Turyanska, T.D. Bradshaw, J. Sharpe, M. Li, S. Mann, N.R. Thomas, A. Patane, The biocompatibility of apoferritin-encapsulated PbS quantum dots, Small 5 (2009) 1738–1741.

[27] R. Xing, X. Wang, L. Yan, C. Zhang, Z. Yang, Z. Guo, Fabrication of water soluble and biocompatible CdSe nanoparticles in apoferritin with the aid of EDTA, Dalton Trans. (2009) 1710–1713.

[28] B. Zhang, J.N. Harb, R.C. Davis, S. Choi, J.W. Kim, T. Miller, S.H. Chu, G.D. Watt, Electron exchange between Fe(II)-horse spleen ferritin and Co(III)/Mn(III) reconstituted horse spleen and *Azotobacter vinelandii* ferritins, Biochemistry 45 (2006) 5766–5774.

[29] G.C. Ford, P.M. Harrison, D.W. Rice, J.M. Smith, A. Treffry, J.L. White, J. Yariv, Ferritin: design and formation of an iron-storage molecule, Philos. Trans. R. Soc. Lond. B Biol. Sci. 304 (1984) 551–565.

[30] P.M. Harrison, P. Arosio, The ferritins: molecular properties, iron storage function and cellular regulation, Biochim. Biophys. Acta 1275 (1996) 161–203.

[31] J.G. Wardeska, B. Viglione, N.D. Chasteen, Metal ion complexes of apoferritin. Evidence for initial binding in the hydrophilic channels, J. Biol. Chem. 261 (1986) 6677–6683.

[32] T. Douglas, D.R. Ripoll, Calculated electrostatic gradients in recombinant human H-chain ferritin, Protein Sci. 7 (1998) 1083–1091.

[33] T. Takahashi, S. Kuyucak, Functional properties of threefold and fourfold channels in ferritin deduced from electrostatic calculations, Biophys. J. 84 (2003) 2256–2263.

[34] S.P. Martsev, A.P. Vlasov, P. Arosio, Distinct stability of recombinant L and H subunits of human ferritin: calorimetric and ANS binding studies, Protein Eng. 11 (1998) 377–381.

[35] S. Levi, S.J. Yewdall, P.M. Harrison, P. Santambrogio, A. Cozzi, E. Rovida, A. Albertini, P. Arosio, Evidence of H- and L-chains have co-operative roles in the iron-uptake mechanism of human ferritin, Biochem. J. 288 (Pt 2) (1992) 591–596.

[36] M. Wagstaff, M. Worwood, A. Jacobs, Properties of human tissue isoferritins, Biochem. J. 173 (1978) 969–977.

[37] P. Santambrogio, S. Levi, A. Cozzi, B. Corsi, P. Arosio, Evidence that the specificity of iron incorporation into homopolymers of human ferritin L- and H-chains is conferred by the nucleation and ferroxidase centres, Biochem. J. 314 (Pt 1) (1996) 139–144.

[38] T.G. St. Pierre, N.T. Gorham, P.D. Allen, J.L. Costa-Kramer, K.V. Rao, Apparent magnetic energy-barrier distribution in horse-spleen ferritin: evidence for multiple interacting magnetic entities per ferrihydrite nanoparticle, Phys. Rev. B 65 (2001) 024436.

[39] T.G. St, P. Chan Pierre, K.R. Bauchspiess, J. Webb, S. Betteridge, S. Walton, D.P.E. Dickson, Synthesis, structure and magnetic properties of ferritin cores with varying composition and degrees of structural order: models for iron oxide deposits in iron-overload diseases, Coord. Chem. Rev. 151 (1996) 125–143.

[40] J.S. Rohrer, Q.T. Islam, G.D. Watt, D.E. Sayers, E.C. Theil, Iron environment in ferritin with large amounts of phosphate from *Azotobacter-vinelandii* and horse spleen analyzed using extended X-ray absorption fine structure exafs, Biochemistry 29 (1990) 259–264.

[41] S. Mann, J.V. Bannister, R.J. Williams, Structure and composition of ferritin cores isolated from human spleen, limpet (*Patella vulgata*) hemolymph and bacterial (*Pseudomonas aeruginosa*) cells, J. Mol. Biol. 188 (1986) 225–232.

[42] S. Mann, J.M. Williams, A. Treffry, P.M. Harrison, Reconstituted and native iron-cores of bacterioferritin and ferritin, J. Mol. Biol. 198 (1987) 405–416.

[43] A. Treffry, P.M. Harrison, M.I. Cleton, W.C. de Bruijn, S. Mann, A note on the composition and properties of ferritin iron cores, J. Inorg. Biochem. 31 (1987) 1–6.

[44] V.J. Wade, A. Treffry, J.P. Laulhere, E.R. Bauminger, M.I. Cleton, S. Mann, J.F. Briat, P.M. Harrison, Structure and composition of ferritin cores from pea seed (*Pisum sativum*), Biochim. Biophys. Acta 1161 (1993) 91–96.

[45] S.H. Banyard, D.K. Stammers, P.M. Harrison, Electron density map of apoferritin at 2.8 Å resolution, Nature 271 (1978) 282–284.

[46] A.K. Powell, Ferritin. Its mineralization, Met. Ions Biol. Syst. 35 (1998) 515–561.

[47] Y.H. Pan, K. Sader, J.J. Powell, A. Bleloch, M. Gass, J. Trinick, A. Warley, A. Li, R. Brydson, A. Brown, 3D morphology of the human hepatic ferritin mineral core: new evidence for a subunit structure revealed by single particle analysis of HAADF-STEM images, J. Struct. Biol. 166 (2009) 22–31.

[48] M. Ceolín, N. Gálvez, P. Sánchez, B. Fernández, J.M. Domínguez-Vera, Structural aspects of the growth mechanism of copper nanoparticles inside apoferritin, Eur. J. Inorg. Chem. 2008 (2008) 795–801.

[49] T. Ueno, M. Abe, K. Hirata, S. Abe, M. Suzuki, N. Shimizu, M. Yamamoto, M. Takata, Y. Watanabe, Process of accumulation of metal ions on the interior surface of apo-Ferritin: crystal structures of a series of apo-ferritins containing variable quantities of Pd(II) ions, J. Am. Chem. Soc. 131 (2009) 5094–5100.

[50] A. Treffry, P.M. Harrison, Incorporation and release of inorganic-phosphate in horse spleen ferritin, Biochem. J. 171 (1978) 313–320.

[51] J. Polanams, A.D. Ray, R.K. Watt, Nanophase iron phosphate, iron arsenate, iron vanadate, and iron molybdate minerals synthesized within the protein cage of ferritin, Inorg. Chem. 44 (2005) 3203–3209.

[52] A.N. Mansour, C. Thompson, E.C. Theil, N.D. Chasteen, D.E. Sayers, Fe(III).ATP complexes. Models for ferritin and other polynuclear iron complexes with phosphate, J. Biol. Chem. 260 (1985) 7975–7979.

[53] S.H. Juan, S.D. Aust, Iron and phosphate content of rat ferritin heteropolymers, Arch. Biochem. Biophys. 357 (1998) 293–298.

[54] J.L. Johnson, M. Cannon, R.K. Watt, R.B. Frankel, G.D. Watt, Forming the phosphate layer in reconstituted horse spleen ferritin and the role of phosphate in promoting core surface redox reactions, Biochemistry 38 (1999) 6706–6713.

[55] D. de Silva, J.H. Guo, S.D. Aust, Relationship between iron and phosphate in mammalian ferritins, Arch. Biochem. Biophys. 303 (1993) 451–455.

[56] Y.G. Cheng, N.D. Chasteen, Role of phosphate in initial iron deposition in apoferritin, Biochemistry 30 (1991) 2947.

[57] N. Galvez, B. Fernandez, P. Sanchez, R. Cuesta, M. Ceolin, M. Clemente-Leon, S. Trasobares, M. Lopez-Haro, J.J. Calvino, O. Stephan, J.M. Dominguez-Vera, Comparative structural and chemical studies of ferritin cores with gradual removal of their iron contents, J. Am. Chem. Soc. 130 (2008) 8062–8068.

[58] T.D. Richards, K.R. Pitts, G.D. Watt, A kinetic study of iron release from *Azotobacter vinelandii* bacterial ferritin, J. Inorg. Biochem. 61 (1996) 1–13.

[59] G.R. Bakker, R.F. Boyer, Iron incorporation into apoferritin the role of apoferritin as a ferroxidase, J. Biol. Chem. 261 (1986) 13182–13185.

[60] D.M. Lawson, A. Treffry, P.J. Artymiuk, P.M. Harrison, S.J. Yewdall, A. Luzzago, G. Cesareni, S. Levi, P. Arosio, Identification of the ferroxidase centre in ferritin, FEBS Lett. 254 (1989) 207–210.

[61] H. Heqing, R.K. Watt, R.B. Frankel, G.D. Watt, Role of phosphate in Fe^{2+} binding to horse spleen holoferritin, Biochemistry 32 (1993) 1681–1687.

[62] D. Jacobs, G.D. Watt, R.B. Frankel, G.C. Papaefthymiou, Fe2+ binding to apo and holo mammalian ferritin, Biochemistry 28 (1989) 9216–9221.

[63] G.D. Watt, R.B. Frankel, D. Jacobs, H. Huang, G.C. Papaefthymiou, Fe^{2+} and phosphate interactions in bacterial ferritin from *Azotobacter vinelandii*, Biochemistry 31 (1992) 5672–5679.

[64] K. Orino, S. Kamura, M. Natsuhori, S. Yamamoto, K. Watanabe, Two pathways of iron uptake in bovine spleen apoferritin dependent on iron concentration, Biometals 15 (2002) 59–63.

[65] H. Aitken-Rogers, C. Singleton, A. Lewin, A. Taylor-Gee, G.R. Moore, N.E. Le Brun, Effect of phosphate on bacterioferritin-catalysed iron(II) oxidation, JBIC J. Biol. Inorg. Chem. 9 (2004) 161–170.

[66] C. Cutler, A. Bravo, A.D. Ray, R.K. Watt, Iron loading into ferritin can be stimulated or inhibited by the presence of cations and anions: a specific role for phosphate, J. Inorg. Biochem. 99 (2005) 2270–2275.

[67] N.D. Chasteen, Vanadium and its role in life, in: H.S. Sigel, A. (Eds.), Metal ions in Biological Systems, vol. 31, Marcel Dekker, New York, 1995.

[68] R. Hille, The mononuclear molybdenum enzymes, Chem. Rev. 96 (1996) 2757–2816.

[69] J.K. Grady, J. Shao, P. Arosio, P. Santambrogio, N.D. Chasteen, Vanadyl(IV) binding to mammalian ferritins. An EPR study aided by site-directed mutagenesis, J. Inorg. Biochem. 80 (2000) 107–113.

[70] W.H. Massover, Ultrastructure of ferritin and apoferritin: a review, Micron 24 (1993) 389–437.

[71] S.C. Andrews, A. Treffry, P.M. Harrison, Siderosomal ferritin. The missing link between ferritin and haemosiderin? Biochem. J. 245 (1987) 439–446.

[72] T. Jones, R. Spencer, C. Walsh, Mechanism and kinetics of iron release from ferritin by dihydroflavins and dihydroflavin analogues, Biochemistry 17 (1978) 4011–4017.

[73] G.D. Watt, D. Jacobs, R.B. Frankel, Redox reactivity of bacterial and mammalian ferritin: is reductant entry into the ferritin interior a necessary step for iron release? Proc. Natl. Acad. Sci. U. S. A. 85 (1988) 7457–7461.

[74] X. Yang, N.D. Chasteen, Molecular diffusion into horse spleen ferritin: a nitroxide radical spin probe study, Biophys. J. 71 (1996) 1587–1595.

[75] X. Yang, P. Arosio, N.D. Chasteen, Molecular diffusion into ferritin: pathways, temperature dependence, incubation time, and concentration effects, Biophys. J. 78 (2000) 2049–2059.

[76] B. Zhang, R.K. Watt, N. Galvez, J.M. Dominguez-Vera, G.D. Watt, Rate of iron transfer through the horse spleen ferritin shell determined by the rate of formation of Prussian Blue and Fe-desferrioxamine within the ferritin cavity, Biophys. Chem. 120 (2006) 96–105.

[77] T. Ueno, M. Suzuki, T. Goto, T. Matsumoto, K. Nagayama, Y. Watanabe, Size-selective olefin hydrogenation by a Pd nanocluster provided in an Apo-ferritin cage, Angew. Chem. Int. Ed. 43 (2004) 2527–2530.

[78] Q.Y. Deng, B. Yang, J.F. Wang, C.G. Whiteley, X.N. Wang, Biological synthesis of platinum nanoparticles with apoferritin, Biotechnol Lett. 31 (2009) 1505–1509.

[79] E.C. Theil, X.S. Liu, T. Tosha, Gated pores in the ferritin protein nanocage, Inorg. Chim. Acta 361 (2008) 868–874.

[80] X. Liu, W. Jin, E.C. Theil, Opening protein pores with chaotropes enhances Fe reduction and chelation of Fe from the ferritin biomineral, Proc. Natl. Acad. Sci. U. S. A. 100 (2003) 3653–3658.

[81] W. Jin, H. Takagi, B. Pancorbo, E.C. Theil, "Opening" the ferritin pore for iron release by mutation of conserved amino acids at interhelix and loop sites, Biochemistry 40 (2001) 7525–7532.

[82] H. Takagi, D. Shi, Y. Ha, N.M. Allewell, E.C. Theil, Localized unfolding at the junction of three ferritin subunits. A mechanism for iron release? J. Biol. Chem. 273 (1998) 18685–18688.

[83] X.S. Liu, L.D. Patterson, M.J. Miller, E.C. Theil, Peptides selected for the protein nanocage pores change the rate of iron recovery from the ferritin mineral, J. Biol. Chem. 282 (2007) 31821–31825.

[84] G.D. Watt, J.W. McDonald, C.H. Chiu, K.R. Reddy, Further characterization of the redox and spectroscopic properties of *Azotobacter vinelandii* ferritin, J. Inorg. Biochem. 51 (1993) 745–758.

[85] S.K. Weeratunga, C.E. Gee, S. Lovell, Y. Zeng, C.L. Woodin, M. Rivera, Binding of *Pseudomonas aeruginosa* apobacterioferritin-associated ferredoxin to bacterioferritin B promotes heme mediation of electron delivery and mobilization of core mineral iron, Biochemistry 48 (2009) 7420–7431.

[86] B. Zhang, G.D. Watt, Anaerobic iron deposition into horse spleen, recombinant human heavy and light and bacteria ferritins by large oxidants, J. Inorg. Biochem. 101 (2007) 1676–1685.

[87] H.B. Gray, J.R. Winkler, Electron transfer in proteins, Annu. Rev. Biochem. 65 (1996) 537–561.

[88] C.H. Lee, Evaluation and Application of Molecular Modeling to Peptides and Proteins, Department of Chemistry and Biochemistry, vol. PhD, Brigham Young University, Provo, 1997, p. 157.

[89] R.K. Watt, R.B. Frankel, G.D. Watt, Redox reactions of apo mammalian ferritin, Biochemistry 31 (1992) 9673–9679.

[90] F.K. al-Massad, F.H. Kadir, G.R. Moore, Animal ferritin and bacterioferritin contain quinones, Biochem. J. 283 (Pt 1) (1992) 177–180.

[91] J.P. Klinman, Redox-Active Amino Acids in Biology, Academic Press, New York, 1995.

[92] J.L. Johnson, D.C. Norcross, P. Arosio, R.B. Frankel, G.D. Watt, Redox reactivity of animal apoferritins and apoheteropolymers assembled from recombinant heavy and light human chain ferritins, Biochemistry 38 (1999) 4089–4096.

[93] G.D. Watt, R.B. Frankel, G.C. Papaefthymiou, Reduction of mammalian ferritin, Proc. Natl. Acad. Sci. U. S. A. 82 (1985) 3640–3643.

[94] W. Linert, G.N. Jameson, Redox reactions of neurotransmitters possibly involved in the progression of Parkinson's disease, J. Inorg. Biochem. 79 (2000) 319–326.

[95] D.C. Harris, Iron exchange between ferritin and transferrin in vitro, Biochemistry 17 (1978) 3071–3078.

[96] J.B. Neilands, Microbial iron compounds, Annu. Rev. Biochem. 50 (1981) 715–731.

[97] G.J. Kontoghiorghes, S. Chambers, A.V. Hoffbrand, Comparative study of iron mobilization from haemosiderin, ferritin and iron(III) precipitates by chelators, Biochem. J. 241 (1987) 87–92.

[98] G.J. Kontoghiorghes, New concepts of iron and aluminium chelation therapy with oral L1 (deferiprone) and other chelators. A review, Analyst 120 (1995) 845–851.

[99] F. Imran, P. Phatak, Pharmacoeconomic benefits of deferasirox in the management of iron overload syndromes, Expert Rev. Pharmacoecon. Outcomes Res. 9 (2009) 297–304.

[100] G. Zanninelli, H. Glickstein, W. Breuer, P. Milgram, P. Brissot, R.C. Hider, A.M. Konijn, J. Libman, A. Shanzer, Z.I. Cabantchik, Chelation and mobilization of cellular iron by different classes of chelators, Mol. Pharmacol. 51 (1997) 842–852.

[101] W. Breuer, M.J.J. Ermers, P. Pootrakul, A. Abramov, C. Hershko, Z.I. Cabantchik, Desferrioxamine-chelatable iron, a component of serum non-transferrin-bound iron, used for assessing chelation therapy, Blood 97 (2001) 792–798.

[102] Y.-S. Sohn, W. Breuer, A. Munnich, Z.I. Cabantchik, Redistribution of accumulated cell iron: a modality of chelation with therapeutic implications, Blood 111 (2008) 1690–1699.

[103] M.J. O'Connell, R.J. Ward, H. Baum, T.J. Peters, Iron release from haemosiderin and ferritin by therapeutic and physiological chelators, Biochem. J. 260 (1989) 903–907.

[104] T.P. Tufano, V.L. Pecoraro, K.N. Raymond, Ferric ion sequestering agents: kinetics of iron release from ferritin to catechoylamides, Biochim. Biophys. Acta 668 (1981) 420–428.

[105] R.R. Crichton, F. Roman, F. Roland, Iron mobilization from ferritin by chelating agents, J. Inorg. Biochem. 13 (1980) 305–316.

[106] N. Galvez, B. Ruiz, R. Cuesta, E. Colacio, J.M. Dominguez-Vera, Release of iron from ferritin by aceto- and benzohydroxamic acids, Inorg. Chem. 44 (2005) 2706–2709.

[107] J.M. Dominguez-Vera, Iron(III) complexation of Desferrioxamine B encapsulated in apoferritin, J. Inorg. Biochem. 98 (2004) 469–472.

[108] K.L. Double, M. Maywald, M. Schmittel, P. Riederer, M. Gerlach, In vitro studies of ferritin iron release and neurotoxicity, J. Neurochem. 70 (1998) 2492–2499.

[109] R.F. Boyer, H.M. Clark, A.P. LaRoche, Reduction and release of ferritin iron by plant phenolics, J. Inorg. Biochem. 32 (1988) 171–181.

[110] G.N. Jameson, R.F. Jameson, W. Linert, New insights into iron release from ferritin: direct observation of the neurotoxin 6-hydroxydopamine entering ferritin and reaching redox equilibrium with the iron core, Org. Biomol. Chem. 2 (2004) 2346–2351.

[111] P. Sanchez, N. Galvez, E. Colacio, E. Minones, J.M. Dominguez-Vera, Catechol releases iron(III) from ferritin by direct chelation without iron(II) production, Dalton Trans. (2005) 811–813.

[112] A. Treffry, E.R. Bauminger, D. Hechel, N.W. Hodson, I. Nowik, S.J. Yewdall, P.M. Harrison, Defining the roles of the threefold channels in iron uptake, iron oxidation and iron-core formation in ferritin: a study aided by site-directed mutagenesis, Biochem. J. 296 (Pt 3) (1993) 721–728.

[113] D.M. Lawson, P.J. Artymiuk, S.J. Yewdall, J.M. Smith, J.C. Livingstone, A. Treffry, A. Luzzago, S. Levi, P. Arosio, G. Cesareni, et al., Solving the structure of human H ferritin by genetically engineering intermolecular crystal contacts, Nature 349 (1991) 541–544.

[114] S.L. Baader, E. Bill, A.X. Trautwein, G. Bruchelt, B.F. Matzanke, Mobilization of iron from cellular ferritin by ascorbic acid in neuroblastoma SK-N-SH cells: an EPR study, FEBS Lett. 381 (1996) 131–134.

[115] S. Sun, N.D. Chasteen, Rapid kinetics of the EPR-active species formed during initial iron uptake in horse spleen apoferritin, Biochemistry 33 (1994) 15095.

[116] E.R. Bauminger, A. Treffry, A.J. Hudson, D. Hechel, N.W. Hodson, S.C. Andrews, S. Levi, I. Nowik, P. Arosio, J.R. Guest, et al., Iron incorporation into ferritins: evidence for the transfer of monomeric Fe(III) between ferritin molecules and for the formation of an unusual mineral in the ferritin of *Escherichia coli*, Biochem. J. 302 (Pt 3) (1994) 813–820.

[117] U. Schwertmann, Solubility and dissolution of iron oxides, Plant Soil 130 (1991) 1–25.

[118] I. De Domenico, M.B. Vaughn, L. Li, D. Bagley, G. Musci, D.M. Ward, J. Kaplan, Ferroportin-mediated mobilization of ferritin iron precedes ferritin degradation by the proteasome, EMBO J. 25 (2006) 5396–5404.

[119] J. Truty, R. Malpe, M.C. Linder, Iron prevents ferritin turnover in hepatic cells, J. Biol. Chem. 276 (2001) 48775–48780.

[120] T. Kurz, Can lipofuscin accumulation be prevented? Rejuvenation Res. 11 (2008) 441–443.

[121] I. De Domenico, D.M. Ward, J. Kaplan, Specific iron chelators determine the route of ferritin degradation, Blood (2009).

[122] D.C. Radisky, J. Kaplan, Iron in cytosolic ferritin can be recycled through lysosomal degradation in human fibroblasts, Biochem. J. 336 (Pt 1) (1998) 201–205.

[123] H. Shi, K.Z. Bencze, T.L. Stemmler, C.C. Philpott, A cytosolic iron chaperone that delivers iron to ferritin, Science 320 (2008) 1207–1210.

[124] A.V. Makeyev, S.A. Liebhaber, The poly(C)-binding proteins: a multiplicity of functions and a search for mechanisms, RNA 8 (2002) 265–278.

[125] R.K. Watt, P.W. Ludden, Nickel-binding proteins, CMLS Cell. Mol. Life Sci. 56 (1999) 604–625.

[126] J. Kuchar, R.P. Hausinger, Biosynthesis of metal sites, Chem. Rev. 104 (2004) 509–525.

[127] V.C. Culotta, M. Yang, T.V. O'Halloran, Activation of superoxide dismutases: putting the metal to the pedal, Biochim. Biophys. Acta 1763 (2006) 747–758.

[128] T.V. O'Halloran, V.C. Culotta, Metallochaperones, an intracellular shuttle service for metal ions, J. Biol. Chem. 275 (2000) 25057–25060.

[129] P.A. Cobine, F. Pierrel, D.R. Winge, Copper trafficking to the mitochondrion and assembly of copper metalloenzymes, BBA - Mol. Cell Res. 1763 (2006) 759–772.

[130] S.C. Andrews, P.M. Harrison, J.R. Guest, Cloning, sequencing, and mapping of the bacterioferritin gene (bfr) of *Escherichia coli* K-12, J. Bacteriol. 171 (1989) 3940–3947.

[131] A. Wang, Y. Zeng, H. Han, S. Weeratunga, B.N. Morgan, P. Moenne-Loccoz, E. Schonbrunn, M. Rivera, Biochemical and structural characterization of *Pseudomonas aeruginosa* Bfd and FPR: ferredoxin NADP+ reductase and not ferredoxin is the redox partner of heme oxygenase under iron-starvation conditions, Biochemistry 46 (2007) 12198–12211.

[132] R.P. Garg, C.J. Vargo, X. Cui, D.M. Kurtz Jr., A [2Fe-2S] protein encoded by an open reading frame upstream of the *Escherichia coli* bacterioferritin gene, Biochemistry 35 (1996) 6297–6301.

[133] M.A. Quail, P. Jordan, J.M. Grogan, J.N. Butt, M. Lutz, A.J. Thomson, S.C. Andrews, J.R. Guest, Spectroscopic and voltammetric characterisation of the bacterioferritin-associated ferredoxin of *Escherichia coli*, Biochem. Biophys. Res. Commun. 229 (1996) 635–642.

[134] W. Fu, R.F. Jack, T.V. Morgan, D.R. Dean, M.K. Johnson, *nifU* gene product from *Azotobacter vinelandii* is a homodimer that contains two identical [2Fe-2S] clusters, Biochemistry 33 (1994) 13455–13463.

[135] S. Bandyopadhyay, K. Chandramouli, M.K. Johnson, Iron-sulfur cluster biosynthesis, Biochem. Soc. Trans. 36 (2008) 1112–1119.

[136] X.M. Xu, S.G. Moller, Iron-sulfur cluster biogenesis systems and their crosstalk, Chembiochem 9 (2008) 2355–2362.

[137] P. Santambrogio, W.H. Massover, Rabbit serum alpha-2-macroglobulin binds to liver ferritin: association causes a heterogeneity of ferritin molecules, Br. J. Haematol. 71 (1989) 281–290.

[138] T. Seki, T. Kunichika, K. Watanabe, K. Orino, Apolipoprotein B binds ferritin by hemin-mediated binding: evidence of direct binding of apolipoprotein B and ferritin to hemin, Biometals 21 (2008) 61–69.

[139] H. Sakamoto, T. Kuboi, T. Nagakura, S. Hayashi, F. Hoshi, K. Mutoh, K. Watanabe, K. Orino, Characterization of feline serum ferritin-binding proteins: the presence of a novel ferritin-binding protein as an inhibitory factor in feline ferritin immunoassay, Biometals 22 (2009) 793–802.

[140] G. Sugawara, R. Inoue, K. Watanabe, H. Ohtsuka, K. Orino, Short communication: bovine alpha-casein is a ferritin-binding protein and inhibitory factor of milk ferritin immunoassay, J. Dairy Sci. 92 (2009) 3810–3814.

[141] M.S. Joo, G. Tourillon, D.E. Sayers, E.C. Theil, Rapid reduction of iron in horse spleen ferritin by thioglycolic acid measured by dispersive X-ray absorption spectroscopy, Biol. Met. 3 (1990) 171–175.

[142] S. Sirivech, E. Frieden, S. Osaki, The release of iron from horse spleen ferritin by reduced flavins, Biochem. J. 143 (1974) 311–315.

[143] S. Levi, P. Santambrogio, B. Corsi, A. Cozzi, P. Arosio, Evidence that residues exposed on the three-fold channels have active roles in the mechanism of ferritin iron incorporation, Biochem. J. 317 (Pt 2) (1996) 467–473.

[144] O. Kakhlon, Z.I. Cabantchik, The labile iron pool: characterization, measurement, and participation in cellular processes(1), Free Radic. Biol. Med. 33 (2002) 1037–1046.

[145] T.D. Rae, P.J. Schmidt, R.A. Pufahl, V.C. Culotta, T.V. O'Halloran, Undetectable intracellular free copper: the requirement of a copper chaperone for superoxide dismutase, Science 284 (1999) 805–808.

[146] R. Leipuviene, E.C. Theil, The family of iron responsive RNA structures regulated by changes in cellular iron and oxygen, Cell. Mol. Life Sci. 64 (2007) 2945–2955.

[147] E.C. Theil, Regulation of ferritin and transferrin receptor mRNAs, J. Biol. Chem. 265 (1990) 4771–4774.

[148] E.C. Theil, Coordinating responses to iron and oxygen stress with DNA and mRNA promoters: the ferritin story, Biometals 20 (2007) 513–521.

[149] K.J. Hintze, E.C. Theil, Cellular regulation and molecular interactions of the ferritins, Cell. Mol. Life Sci. 63 (2006) 591–600.

Richard K. Watt obtained a PhD in biochemistry from the University of Wisconsin-Madison, USA, in 1998 under the direction of Prof. Paul W. Ludden. Following 2 years of postdoctoral studies on photosynthesis at Princeton University with Prof. G. Charles Dismukes, he joined the Chemistry Department at the University of New Mexico. In 2006, he moved to his Alma Mater, Brigham Young University, where he joined the Department of Chemistry and Biochemistry.

Robert J. Hilton earned his bachelor's degree in biochemistry from Brigham Young University, Provo, UT, in 2006. He worked for a year with a retinal surgeon as an ophthalmic assistant, gaining experience and knowledge in the medical field. He started his PhD in biochemistry at Brigham Young University in 2008. Robert enjoys spending time in the outdoors with his wife and two boys.

D. Matthew Graff earned his bachelor's degree in biochemistry in neuroscience from Brigham Young University, Provo, UT, in 2008. He is currently in the Master's degree program in the Chemistry and Biochemistry Department at Brigham Young University. His future goals include medical school to specialize in podiatry.
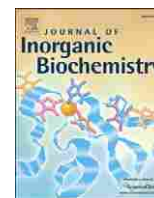
Ferritin iron mineralization proceeds by different mechanisms in MOPS and imidazole buffers

Claine L. Snow [a], L. Naomi Martineau [a], Robert J. Hilton [a], Spencer Brown [a], Jeffrey Farrer [b], Juliana Boerio-Goates [a], Brian F. Woodfield [a], Richard K. Watt [a,*]

[a] Department of Chemistry and Biochemistry, C-210 Benson Building, Brigham Young University, Provo, UT 84602, United States
[b] Department of Physics and Astronomy, N283 ESC Building, Brigham Young University, Provo, UT 84602, United States

ARTICLE INFO

ABSTRACT

The buffer used during horse spleen ferritin iron loading significantly influences the mineralization process and the quantity of iron deposited in ferritin. Ferritin iron loading in imidazole shows a rapid hyperbolic curve in contrast to iron loading in 3-(N-morpholino)propanesulfonic acid (MOPS), which displays a slower sigmoidal curve. Ferritin iron loading in an equimolar mixture of imidazole and MOPS produces an iron-loading curve that is intermediate between the imidazole and MOPS curves indicating that one buffer does not dominate the reaction mechanism. The UV–visible spectrum of the ferritin mineral has a higher absorbance from 250 to 450 nm when prepared in imidazole buffer than in MOPS buffer. These results suggest that different mineral phases form in ferritin by different loading mechanisms in imidazole and MOPS buffered reactions. Samples of 1500 Fe/ferritin were prepared in MOPS or imidazole buffer and were analyzed for crystallinity and using the electron diffraction capabilities of the electron microscope. The sample prepared in imidazole was significantly more crystalline than the sample prepared in MOPS. X-ray powder diffraction studies showed that small cores (~500 Fe/ferritin) prepared in MOPS or imidazole possess a 2-line ferrihydrite spectrum. As the core size increases the mineral phase begins to change from 2-line to 6-line ferrihydrite with the imidazole sample favoring the 6-line ferrihydrite phase. Taken together, these results suggest that the iron deposition mechanism in ferritin can be controlled by properties of the buffer with samples prepared in imidazole forming a larger, more ordered crystalline mineral than samples prepared in MOPS.

1. Introduction

The use of proteins as a template for the production of nanomaterials is an emerging and promising area of biochemical engineering [1,2]. Research in materials science has assimilated the concepts of biology on a basic level, and it now faces the challenge of carrying this knowledge over to applied materials. Establishing the fundamental principles of protein metal interactions for this discipline is essential for many reasons. For example, protein cages are among just a few nano platforms capable of simultaneous control over size, shape, and biocompatibility [3]. Studies have shown that protein interactions are capable of guiding the nucleation of inorganic materials and can control the crystal type, face, and size, even of metastable forms of the minerals. In addition, proteins can perform these reactions in aqueous solutions and under ambient conditions [1,3]. Furthermore, protein cages yield products that are dispersed in solution and avoid the problems of solubility and agglomeration common with other nanomaterial production methods.

Proteins are also attractive because they are amenable to alterations in functionality through both chemical and genetic means.

Ferritin, the biological protein for iron storage [4], has been studied extensively as a nano platform for nanoparticle synthesis. A variety of non-native materials have been prepared in ferritin and include: Mn(O)OH, Mn_3O_4, Co(O)OH, Co_3O_4, $Cr(OH)_3$, $Ni(OH)_3$, In_2O_3, FeS, CdS, CdSe, and ZnSe [1,2,5–10]. Metallic nanoparticles such as Pd, Ag, and CoPt have also been synthesized within ferritin by pre-incubation of the protein with a metal salt and subsequent chemical reduction by a strong reducing agent [3]. Compounds formed in ferritin have shown promise in catalysis, electrochemistry, targeted drug delivery, and bio imaging [1,3,5,10].

Ferritin is composed of 24 subunits that self-assemble into a spherical protein cage with an outer diameter of 12 nm and an interior cavity diameter of 8 nm [4]. Molecules enter and leave ferritin through channels of 0.4 nm in diameter, eight of which are hydrophilic and six are hydrophobic. Inside ferritin, the iron atoms crystallize to form a ferric oxyhydroxide core in the center of the ferritin cavity that most resembles ferrihydrite [11–13]. The solid iron core can be removed through chemical reduction followed by chelation and dialysis [14,15].

Ferritin can theoretically sequester 4500 iron atoms, although in nature the average is closer to 2000. It has been proposed that oxidative

* Corresponding author. Tel.: +1 801 422 1923; fax: +1 801 422 0153.
E-mail address: rwatt@chem.byu.edu (R.K. Watt).

damage to apoferritin results in the termination of core formation and presents a serious problem when trying to maximize the number of iron atoms loaded into the protein for materials purposes [4,16]. In the natural process of core formation, Fe^{2+} is oxidized at the ferroxidase center or oxidized on the mineral core surface where it crystallizes in the central cavity [17]. If the Fe^{2+} is oxidized at other protein sites, hydroxyl radicals are produced through the well-known Fenton reaction. The production of these radicals damages the ferritin protein and inhibits iron core formation [18]. An alternative hypothesis for the much lower iron loading in vitro may simply be based on solubility arguments.

For materials applications, a fully loaded ferritin with a densely packed mineral in the 8 nm diameter core is desired. Previous studies show that buffers can greatly affect iron uptake in ferritin during in vitro iron loading [19–21]. In addition, salt concentrations influence the rate of iron loading into ferritin. Studies by Cutler et al.[22] concluded that, in general, cations slow the rate of iron loading into ferritin by competing with Fe^{2+} for negatively charged amino acids near the 3-fold channels. Specific anions such as halides and sulfate had no effect. However, phosphate and its tetrahedral oxo-anion analogs have been shown to stimulate the rate of iron loading into ferritin and produce a different mineral phase with the oxo-anions incorporated into the mineral [16,23–25].

This study examines the effects of buffers on iron loading in ferritin with the goal of maximizing iron content in ferritin. We reasoned that maximal iron loading into ferritin might be enhanced by using buffers that stabilized Fe^{2+} in solution by slowing oxidation, minimizing the formation of radicals that might damage ferritin, and minimizing side reactions that lead to precipitation of $Fe(OH)_3$ (s) outside ferritin. Ferritin iron-loading reactions were performed in imidazole buffer that can coordinate Fe^{2+} and its oxidation product Fe^{3+}. These reactions were compared to iron loading reactions performed in MOPS buffer, which is commonly used for iron loading reactions with ferritin. MOPS buffer can coordinate to Fe^{2+}, but only poorly. We observed that the iron loading kinetics were very different in imidazole than in MOPS. Ferritin prepared in imidazole loaded to a greater extent and formed a mineral that was more crystalline and possessed different physical properties than ferritin prepared in MOPS.

2. Experimental

2.1. Materials

All aqueous solutions in this study were made using Milli-Q water having a resistance of 18 MΩ. Chemical reagents were obtained commercially and used without further purification. Horse spleen ferritin (HoSF) was acquired from Sigma-Aldrich in a 0.15 M NaCl solution. Thioglycolic acid was also purchased from Sigma-Aldrich as a 98% solution, and 3-(N-morpholino)propanesulfonic acid (MOPS) from Fisher Bioreagents with purity greater than 97%. All other reagents had a purity of at least 97%.

2.2. Preparation of apoferritin

Native HoSF obtained from Sigma-Aldrich was treated according to established methods to make apoferritin [26]. As obtained, HoSF in saline solution was dialyzed for 24 h against 1% thioglycolic acid and 0.25 M sodium acetate ($NaC_2H_3O_2$) at 4 °C. This process was repeated with an addition of 100 mg·L^{-1} of 2,2′ bipyridyl (bipy) which chelates Fe^{2+} forming the red $[Fe(bipy)_3]^{2+}$ complex. The HoSF was then dialyzed twice with 5 g·L^{-1} sodium bicarbonate ($NaHCO_3$) at 4 °C. The apoferritin solution was then dialyzed several times with H_2O at 4 °C to remove ionic species from the solution. Dialysis with H_2O was terminated when Na, S, C, Cl^-, and Fe could not be detected in the water outside the dialysis tubing. The Na was analyzed by atomic absorption spectrometry, while S, C, and Fe were analyzed using inductively coupled plasma optical emission spectrometry, and the Cl^- was quantified using ion chromatography.

2.3. Kinetics of iron core formation in MOPS and imidazole buffers

Kinetic studies of iron loading in ferritin were carried out on an Agilent 8453 UV–Vis spectrometer equipped with a magnetic stirring motor. Imidazole ($C_3H_4N_2$) and MOPS solutions (0.05 M) were prepared and the pH adjusted to 7.5 by the addition of NaOH for MOPS and HNO_3 for imidazole. A 0.010 M Fe^{2+} solution was prepared by dissolving Fe$(NH_4)_2(SO_4)_2$·$6H_2O$ in a 1 mM HCl solution. Iron loading reactions were carried out in a cuvette by adding apoferritin (0.3 μM) and a Teflon stir bar into 2.0 mL of the indicated buffer. The spectrophotometer was blanked on the buffer prior to the addition of ferritin. The reaction was initiated by the addition of 25 μL of 0.010 M Fe^{2+} (~400 Fe^{2+}/ferritin) and the absorbance at 310 nm was measured over time to monitor ferritin iron mineralization. The absorbance measurements were continued until the reaction reached a plateau, and in some instances multiple additions of Fe^{2+} were added to the same solution.

2.4. Transmission electron microscopy (TEM)

Samples were prepared by adding 1.0 ml apo ferritin (5.4 mg/ml) into 10 mL 0.050 M MOPS, 0.1 M NaCl pH 7.5 or 0.050 M imidazole buffer, 0.1 M NaCl pH 7.5. The samples were stirred in air and 0.60 mL of 0.010 M ferrous ammonium sulfate was added to deliver 500 Fe/ferritin. The sample was stirred for 30 min in air to allow the Fe^{2+} to oxidize. For the 1500 Fe/ferritin sample, two additional aliquots of 500 Fe^{2+} were added following the identical procedure. The samples were centrifuged to remove any unbound iron or precipitated protein and an iron and protein analysis was performed to confirm that the samples contained 1500 Fe/ferritin. The samples were deposited on charged grids (lacey carbon fiber, 400 mesh copper grids, Ted Pella, Inc.). Following 30 to 60 s on the grid, the solution was wicked off of the grid, and the grid was rinsed in water to remove salts or buffers. The grid was then dried. Two independent samples of both the MOPS and imidazole samples were prepared and analyzed and both studies gave similar EM data. The grids were analyzed using a FEI Tecnai F30 TEM (FEI Company, the Netherlands), operating at 140 keV. The concentric rings verify crystalline pattern.

2.5. Preparation and characterization of reconstituted ferritin mineral cores in MOPS and imidazole

Ferritin was reconstituted in the presence of imidazole or MOPS buffer by adding apoferritin to the imidazole or MOPS buffer followed by slowly titrating with a 0.010 M Fe^{2+} solution at room temperature under constant stirring. Various imidazole and MOPS concentrations were tested and reactions were performed in the presence and absence of various concentrations of NaCl. Some samples were loaded with iron by slowly adding Fe^{2+} from a peristaltic pump that delivered a very dilute Fe^{2+} concentration at a very slow delivery speed. The pH of the solutions was monitored and maintained at 7.5 by the addition of NaOH (aq). As the titration progressed the solution turned to a dark brownish-red. When the solution began to appear cloudy the addition of iron was stopped and the sample was centrifuged to remove any solid material. The ferritin solution was then transferred to a dialysis bag and dialyzed at 4 °C with repeated changes of water to remove all salts and impurities. The water removed from each round of dialysis was analyzed for S, Na, C, and Cl^-. Once the levels of these species were below detection limits (using the methods described in Section 2.2), the dialysis was stopped. Samples used for X-ray powder diffraction (XRD) were lyophilized. The crystallinity of the ferritin cores was characterized by XRD using a Scintag Diffractometer (Cu-Kα radiation, λ = 1.54176 nm) at a scanning rate of 0.1 2θ·min^{-1} and a power of 15 kW over the range 10 to 85°. The XRD data for the ferritin samples were smoothed using a boxcar calculation of 25 points on either side of a given point. While the signal intensity is slightly decreased as a result of the smoothing, the noise in the spectrum is dramatically reduced and the XRD reflections are much more evident.

Qualitatively, higher buffer concentrations helped for higher ferritin iron loadings by maintaining a constant pH. The presence of NaCl favored core growth in both buffers. The addition of iron after the solution appeared cloudy caused further protein precipitation and did not lead to improved iron loading into ferritin. We observed that the lower doses of iron/ferritin were more favorable for reaching higher iron loadings of ferritin, presumably because excess iron initiated more radicals that caused damage to the ferritin protein. The peristaltic pump method, allowing a very slow exposure of Fe^{2+} to ferritin, produced the samples with the highest loaded mineral cores.

3. Results and discussion

3.1. Kinetic traces of iron loading in the presence of MOPS and imidazole

Since iron mineralization in ferritin corresponds with a strong absorbance at 310 nm, the absorbance change at this wavelength versus time was measured [21]. The reactions were performed in both MOPS and imidazole to compare the iron loading kinetics for each buffer (Fig. 1). The MOPS reaction is characterized by a sigmoidal shape, which Xu and Chasteen [17,27] described previously as the result of two different iron-loading reactions. The first reaction occurs when no iron is present in ferritin and Fe^{2+} is oxidized at a ferroxidase center. As a core begins to form inside ferritin, Fe^{2+} can be oxidized on the surface of the growing mineral. As the surface area of the core increases, the rate of iron oxidation increases, and the sigmoidal shape is a result of these two reactions. In contrast, the curve for the imidazole reaction is hyperbolic (Fig. 1). This behavior suggests that the mechanism of iron loading in imidazole is different than the MOPS reaction although the mechanism has yet to be characterized. The final absorbance of the imidazole sample was higher than the MOPS sample suggesting that the imidazole sample forms a mineral with slightly different properties than the MOPS sample.

3.2. The effects of combining buffers

The observation that imidazole appeared to load by a different mechanism than MOPS lead us to test an equal mixture of the two buffers to determine if one of them was dominant in controlling the reaction mechanism and the resulting iron mineral that formed. Fig. 2 shows kinetic traces of iron loading in ferritin for solutions of 0.050 M MOPS, 0.050 M imidazole, or an equal mixture of 0.025 M MOPS and 0.025 M imidazole. The equimolar mixture of MOPS and imidazole produces an iron-loading curve that is intermediate between that of the individual buffers. As additional iron is added, the curves begin to approach the same kinetic rates, suggesting that oxidation of iron on the core surface begins to be the dominant mechanism for iron deposition into ferritin [17].

The easiest explanation for the higher final absorbance of the imidazole sample after the first addition of iron (Fig. 1) is that a different mineral phase forms with a higher extinction coefficient than the mineral formed using MOPS. Fig. 3 shows spectra of ferritin samples of identical protein concentration (1.0 μM) that were treated with identical concentrations of iron (200 μM) and stirred in air for 30 min. No obvious distinguishing features are apparent in either of the curves except for the small peak at 280 nm attributed to the protein absorbance, yet a comparison of the two curves shows that the imidazole sample has a more intense absorbance from 250 to 450 nm and therefore has different properties in the mineral core.

The differences in extinction coefficients between the imidazole and MOPS samples intensities might be due to the iron distribution within ferritin. Using X-ray crystallography of cobalt loaded ferritin, Theil et al. recently observed metal ions lining the pathway from the ferroxidase center to the nucleation sites [28,29]. The diffuse organization of iron atoms would have a different extinction coefficient than iron atoms clustered in an ordered mineral phase. In contrast to the disperse ions lining the protein interior, other studies have shown that the iron mineral core forms in discrete clusters initiated from the nucleation sites on the interior of ferritin. The crystallinity and number of these individual sites may influence the absorbance maxima of the mineral formed inside ferritin [30,31].

Since no precipitation was observed during iron loading in our studies, it is assumed that all of the iron is bound to ferritin in both reactions. The different buffers may influence the distribution of iron between the mineral core, the ferroxidase center, the channels, and the outside surface of ferritin. For instance, a higher extinction coefficient may be expected from strong iron oxygen interactions associated with an organized and ordered iron mineral core. Our results suggest that imidazole drives all of the iron to the nucleation sites forming a larger more organized crystalline mineral. In contrast, individual iron atoms lining the interior of the protein shell might have less intense charge transfer interactions. Therefore, MOPS appears to favor iron bound to
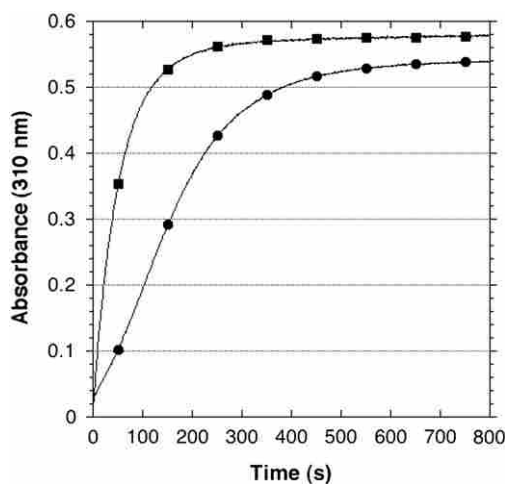

Fig. 1. Kinetics of iron loading into ferritin in MOPS or imidazole buffer. The absorbance at 310 nm versus time was monitored to follow iron core formation. The reaction was initiated by adding 50 μL of 0.010 M Fe^{2+} to 0.3 μM apo ferritin for an ~800 Fe/ferritin ratio. Each buffer was 0.050 M at pH 7.5. The reaction was stirred constantly with a magnetic stirrer. ■) Represents the sample prepared in imidazole and ●) represents the sample prepared in MOPS. The curves are the average of 2–3 runs. For simplicity, the size of the symbols was chosen to represent the largest error bars in the data.
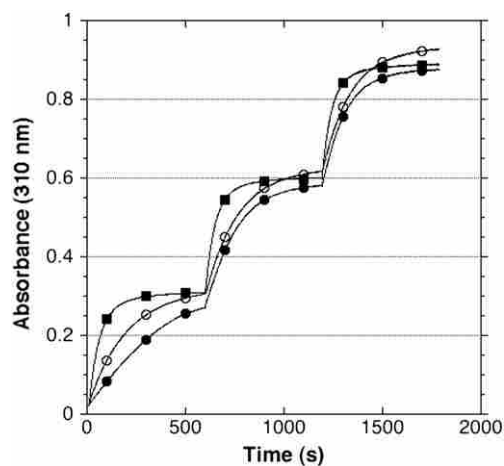

Fig. 2. Comparison of iron loading kinetics in MOPS, imidazole and an equimolar mixture of MOPS/imidazole. Kinetic traces of Fe^{2+} (25 μL 0.010 M Fe^{2+}) added to ferritin (0.3 μM). The different reactions are done in ■) 0.050 M imidazole buffer pH 7.5, ●) 0.050 M MOPS buffer pH 7.5, and ○) 0.025 M MOPS, 0.025 M imidazole mixture pH 7.5. 400 Fe^{2+} were added in each addition for 1200 Fe/ferritin at the end of the reaction. The data represents the average of 2–3 samples and the sizes of the symbols were chosen to represent the maximum error bars between duplicate or triplicate samples prepared for each run.
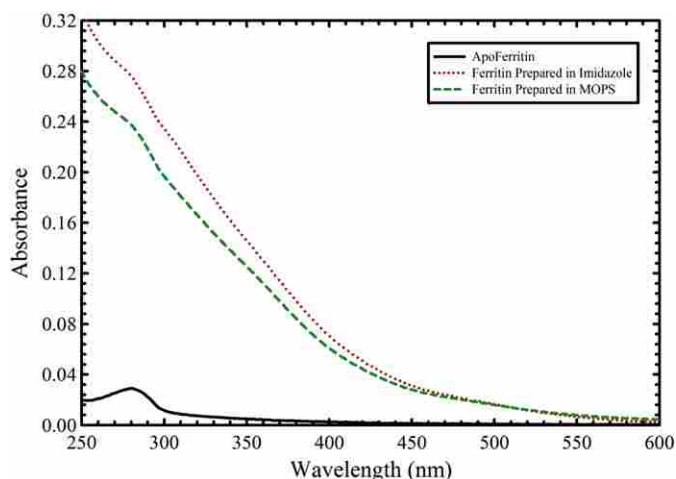
Fig. 3. Spectra of ferritin samples prepared in MOPS or imidazole buffer. (Black) apo ferritin, (red) 200 Fe/ferritin loaded in 0.050 M imidazole buffer pH 7.5, and (green) 200 Fe/ferritin loaded in 0.050 M MOPS buffer pH 7.5. (For interpretation of the references to color in this figure legend, the reader is referred to the web version of this article.)

the surface, the channels, the ferroxidase centers, and the pathway to the nucleation site, with a smaller more disorganized mineral phase.

Another possibility is that MOPS or imidazole is incorporated into the iron mineral and the presence of the buffer trapped inside the iron mineral phase influences the final absorbance of the core. The incorporation of other molecules in the mineral core was observed in previous studies where oxo-anions substituted for hydroxide ions in the iron mineral phase [25]. Ultimately, the spectrophotometric results are not sufficient to confirm that the increased absorbance for the imidazole sample correlates with a different mineral phase forming inside ferritin. To confirm the minerals that formed inside ferritin in MOPS and imidazole had different physical properties we studied the samples with electron microscopy and X-ray powder diffraction.

3.3. Structural characterization of the iron core

To test the hypothesis that MOPS and imidazole form minerals with different properties, the ferritin cores were studied using transmission electron microscopy (TEM). Ferritin samples containing 1500 Fe/ferritin were prepared in either MOPS or imidazole buffer and placed on EM grids. Iron analysis and protein analysis demonstrated that each sample contained 1500 Fe/ferritin and that the samples contained the same amount of protein. The results of the TEM analysis of the 1500 Fe/ferritin sample are shown in Fig. 4. The ferritin samples appear similar in size (Fig. 4A and B) and are dispersed on the EM grid in similar densities. However, the crystallinity of the two samples was very different when studied by electron diffraction. The MOPS sample (Fig. 4C) did not diffract as well as the imidazole sample (Fig. 4D) indicative of a less crystalline mineral phase produced in MOPS. In contrast, the imidazole sample (Fig. 4D) had a strong diffraction pattern indicative of a more crystalline mineral phase. Ferrihydrite is the mineral generally reported to form in ferritin. The d-spacing of the electron diffraction data was analyzed and the MOPS sample showed only two d-spacing rings (Fig. 4C) where the imidazole sample showed 4 defined rings (Fig. 4D). The rings of the d-spacing gave similar results to those published previously for ferrihydrite in ferritin [11–13].

To further characterize these ferritin samples, the ferritin was lyophilized and analyzed by XRD. An XRD spectrum in the range of 5° to 85° for a lyophilized sample of apoferritin (control sample) can be found
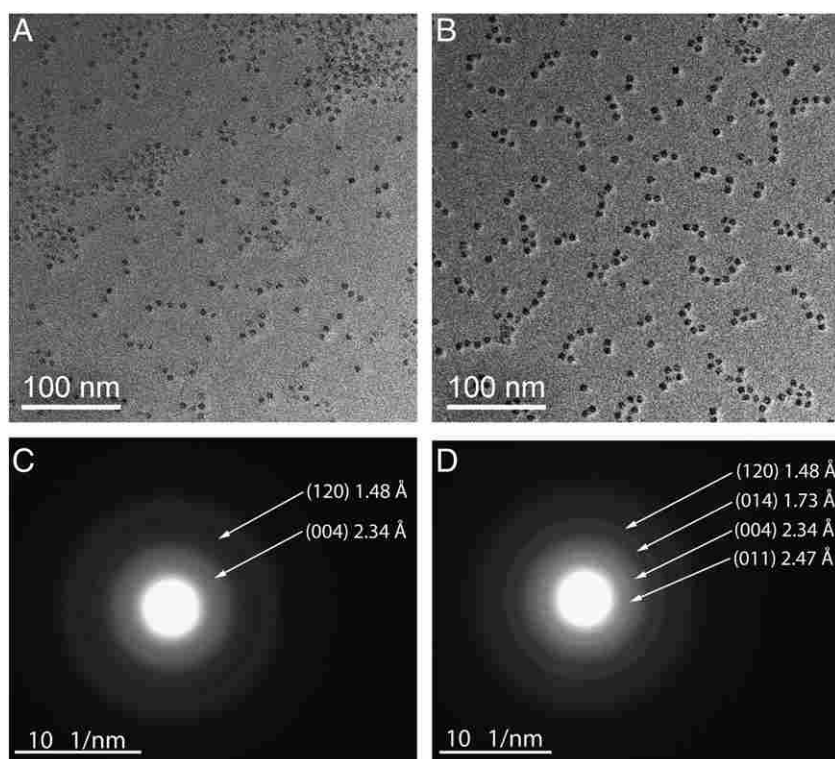

Fig. 4. Electron microscopy of ferritin samples prepared in MOPS or imidazole buffers. Ferritin samples were prepared with 1500 Fe/ferritin in A) MOPS or B) imidazole and analyzed by EM to visualize the ferritin particles. Iron minerals of approximately 8 nm diameters were observed in both samples. The distribution of ferritin was similar on both grids. Using the electron diffraction capabilities of the electron microscope the samples were analyzed for crystallinity. Both samples showed electron diffraction and crystallinity but the sample prepared C) MOPS showed less electron diffraction compared to the sample prepared in D) imidazole which had a more crystalline mineral phase within the ferritin protein. The d-spacing of the rings is shown for each sample and these data correspond to d-spacing for ferrihydrite. The numbers in parentheses show the planes of the lattice fringes. The grids were analyzed using a FEI Tecnai F30 TEM (FEI Company, the Netherlands), operating at 140 keV. The concentric rings verify crystalline pattern.
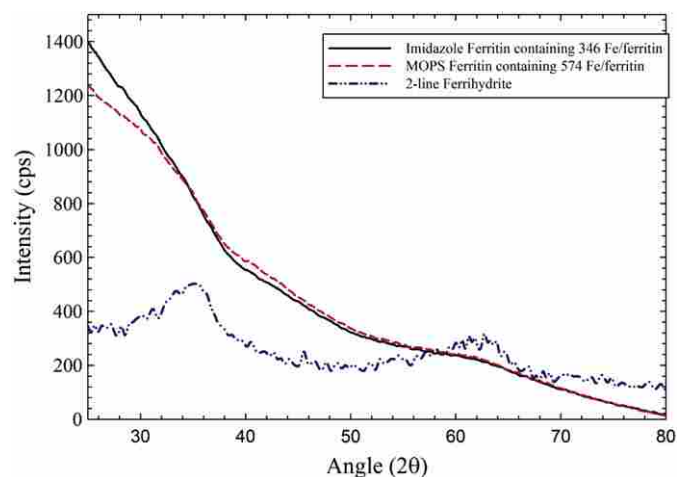
Fig. 5. XRD spectra of ~500 Fe/ferritin samples reconstituted in MOPS or imidazole. Imidazole with 346 Fe/ferritin is shown in black and MOPS with 574 Fe/ferritin is shown in red. A control of 2-line ferrihydrite is shown with peaks at 35° and 63°. In both the MOPS and imidazole samples, an absorption peak is observed at 63° and a shoulder is observed at 35°. The Fe/ferritin rations were chosen to give spectra with similar intensities. (For interpretation of the references to color in this figure legend, the reader is referred to the web version of this article.)

in Supplemental Fig. S1. Two reflections are observed at 2θ values of 9.72°, and 19.80°. After the second peak the spectrum decays with no other features. This spectrum can be seen as the background in the XRD spectra of the imidazole and MOPS reconstituted ferritin powders (Figs. 5 and 6).

Ferrihydrite is known to exist as the 2-line polymorph in small particles and shifts to the 6-line structure as the particle grows and becomes more ordered [32]. To determine if a similar process occurred in ferritin, samples were prepared with a small iron core ~500 Fe/ferritin to compare the XRD spectra of ferritin of low iron contents. Fig. 5 shows the XRD patterns for ferritin samples prepared with ~500 Fe/ferritin in imidazole and MOPS. These patterns are almost identical and mainly resemble the pattern for apoferritin (Fig. S1). However, focusing on the region where the 2-line ferrihydrite sample is observed, a reflection at 64° for 2-line ferrihydrite is visible and a shoulder around 35° is observed. This indicates that low iron loading into ferritin in both MOPS
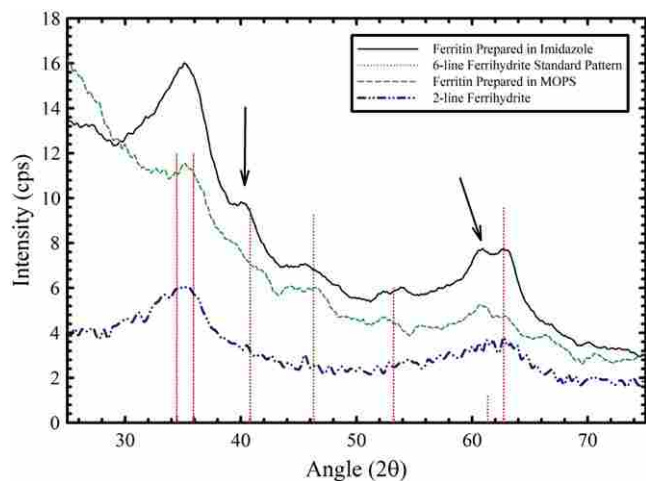
Fig. 6. XRD spectrum of heavily loaded ferritin samples reconstituted in MOPS and imidazole. The red lines represent the standard pattern for 6-line ferrihydrite. The blue trace represents a 2-line ferrihydrite standard. The green line represents ferritin loaded in MOPS with ~2000 Fe/ferritin. The black line represents ferritin loaded in imidazole (3300 Fe/ferritin). The data suggest that as the iron cores of ferritin become larger, there is a transition from 2-line ferrihydrite to 6-line ferrihydrite. (For interpretation of the references to color in this figure legend, the reader is referred to the web version of this article.)

and imidazole produces a 2-line ferrihydrite mineral phase. It is interesting to note that to find similar XRD intensities between the MOPS and imidazole samples, we had to prepare an imidazole sample that had approximately 60% of the iron of the MOPS sample. In all samples studied, the intensity of the ferrihydrite spectrum from imidazole samples was more intense based on an Fe/ferritin basis (data not shown) suggesting that the imidazole samples were more crystalline than the MOPS samples.

The ferrihydrite mineral phase is known to shift to the 6-line polymorph structure as the ferrihydrite mineral increases in size. To determine if the 6-line mineral can form in ferritin in either MOPS or imidazole buffer, samples were prepared with the highest iron content we could obtain. An interesting observation was that imidazole allows a much higher iron loading into ferritin than MOPS. The imidazole sample allowed us to study a much larger core to determine if 6-line ferrihydrite can form in ferritin as imidazole samples (3300 Fe/ferritin) began to approach the theoretical maximal capacity of ferritin (4500 Fe/ferritin).

Fig. 6 shows the XRD spectrum from two samples, one loaded in MOPS (~2000 Fe/ferritin) and one loaded in imidazole (~3300 Fe/ferritin). These samples represented the maximal iron loading we could achieve without protein precipitation occurring. Fig. 6 also shows the reference peaks for the reflections of six-line ferrihydrite found in JCPDS card 00-029-0712 [31] and the spectrum for a 2-line ferrihydrite sample synthesized in our lab and acquired on the same instrument. The spectrum of the 2-line ferrihydrite pattern matches that for 2-line ferrihydrite as originally published by Drits et al. [33]. An inspection of this figure yields some useful information regarding the relationship between the iron content and crystal structure of the core. The MOPS sample shows an overall lower intensity and properties that mostly corresponds to 2-line ferrihydrite. There is a small indication of reflections at 46° and 53°, suggesting that cores of this size have some 6-line character. These reflections are seen with much more intensity in the spectrum of the imidazole sample that has a much larger core. As indicated by the arrows in this figure, there are two prominent features, which are not observed in the spectrum of the MOPS sample. First is an additional peak at 41°, and the second is the bifurcation of the peak centered at 62°. Both of these features indicate a greater 6-line character in the imidazole sample than observed in the spectrum of the MOPS sample.

The evidence provided in this figure suggests that while both buffers direct the formation of ferrihydrite, the higher iron loading allowed by imidazole allows imidazole ferritin to form larger particles that are capable of producing the 6-line ferrihydrite product inside ferritin. The fact that imidazole produces a more crystalline core (Fig. 4) may also contribute to the 6-line spectrum because 6-line ferrihydrite is more ordered than 2-line ferrihydrite [34]. At present, it is unclear if the more ordered core observed in the imidazole samples leads to the production of the 6-line ferrihydrite mineral or if the increased core size is simply large enough to cross the threshold that transitions the mineral from 2-line to 6-line ferrihydrite. The reason that MOPS cannot achieve the higher iron content achieved by imidazole is also puzzling. Does imidazole influence the stability of ferritin by preventing the formation of radicals and favor more extensive iron loading, or does the more ordered mineral allow more efficient iron mineralization inside ferritin. Future work will examine these possibilities.

4. Conclusion

The use of different buffers during ferritin iron loading significantly influences the mechanism of iron uptake, the total amount of iron deposited in ferritin, and the crystallinity of the iron mineral that forms within the ferritin interior. Iron loading kinetics showed that iron uptake in imidazole was hyperbolic while reactions in MOPS were slower and had a sigmoidal character. These results indicate that the mineral formation occurs by different mechanisms. UV–Vis spectra show that the imidazole samples produce a mineral with a higher absorbance from 250 nm to 450 nm. TEM studies confirmed that the mineral formed in

imidazole was crystalline and the mineral formed in MOPS was less crystalline. XRD studies showed that ferritin samples prepared in imidazole and MOPS both favor the formation of ferrihydrite, but that imidazole allows more iron deposition producing a larger core capable of producing 6-line ferrihydrite. These results are consistent with our hypothesis that coordinate buffers may improve iron loading into ferritin by stabilizing Fe^{2+} in solution and preventing oxidative damage to the ferritin protein. These results also suggest that buffers can affect the mechanism of iron loading and the final size and crystallinity of the iron core in ferritin.

Supplementary materials related to this article can be foundonline at doi:10.1016/j.jinorgbio.2011.04.003.

Abbreviations

MOPS	3-(N-morpholino)propanesulfonic acid
HoSF	Horse spleen ferritin
XRD	X-ray powder diffraction
EM	Electron Microscopy
TEM	Transmission electron microscopy

Acknowledgements

References

[1] E. Katz, I. Willner, Angew. Chem. Int. Ed. 43 (2004) 6042–6108.
[2] K. Iwahori, I. Yamashita, Rec. Res. Dev. Biotech. Bioeng. 7 (2005) 41–68.
[3] M. Uchida, M.T. Klem, M. Allen, P. Suci, M. Flenniken, E. Gillitzer, Z. Varpness, L.O. Liepold, M. Young, T. Douglas, Adv. Mater. 19 (2007) 1025–1042.
[4] P. Arosio, R. Ingrassia, P. Cavadini, Biochim. Biophys. Acta 1790 (2009) 589–599.
[5] J.W. Bulte, T. Douglas, S. Mann, R.B. Frankel, B.M. Moskowitz, R.A. Brooks, C.D. Baumgarner, J. Vymazal, M.P. Strub, J.A. Frank, J. Magn. Reson. Imaging 4 (1994) 497–505.
[6] J.M. Dominguez-Vera, E. Colacio, Inorg. Chem. 42 (2003) 6983–6985.
[7] T. Douglas, D.P.E. Dickson, S. Betteridge, J. Charnock, C.D. Garner, S. Mann, Science 269 (1995) 54–57.
[8] F.C. Meldrum, T. Douglas, S. Levi, P. Arosio, S. Mann, J. Inorg. Biochem. 58 (1995) 59–68.
[9] I. Yamashita, J. Hayashi, M. Hara, Chem. Lett. 33 (2004) 1158–1159.
[10] P. Sanchez, N. Galvez, E. Colacio, E. Minones, J.M. Dominguez-Vera, Dalton Trans. 4 (2005) 811–813.
[11] M. Allen, T. Douglas, D. Nest, M. Schoonen, D. Strongin, ACS Symp. Ser. 890 (2005) 226–229.
[12] N.T. Gorham, T.G.S. Pierre, W. Chua-Anusorn, G.M. Parkinson, J. Appl. Physiol. 103 (2008) 054302.
[13] S.-W. Kim, H.-Y. Seo, Y.-B. Lee, Y.S. Park, K.-S. Kim, Bull. Korean Chem. Soc. 29 (2008) 1969–1972.
[14] M.S. Tourillon, G. Tourillon, D.E. Sayers, E.C. Theil, Biol. Met. 3 (1990) 171–175.
[15] S. Granick, L. Michaelis, Science 95 (1942) 439–440.
[16] K. Orino, S. Kamura, M. Natsuhori, S. Yamamoto, K. Watanabe, Biometals 15 (2002) 59–63.
[17] B. Xu, N.D. Chasteen, J. Biol. Chem. 266 (1991) 19965–19970.
[18] M.C. Linder, H.R. Kakavandi, P. Miller, P.L. Wirth, G.M. Nagel, Arch. Biochem. Biophys. 269 (1989) 485–496.
[19] X. Yang, N.D. Chasteen, Biochem. J. 338 (1999) 615–618.
[20] X. Yang, N.D. Chasteen, Biochem. J. 338 (1999) 615–618.
[21] E.P. Paques, A. Paques, R.R. Crichton, Eur. J. Biochem. 107 (1980) 447–453.
[22] C. Cutler, A. Bravo, A.D. Ray, R.K. Watt, J. Inorg. Biochem. 99 (2005) 2270–2275.
[23] Y.G. Cheng, N.D. Chasteen, Biochemistry 30 (1991) 2947.
[24] H. Aitken-Rogers, C. Singleton, A. Lewin, A. Taylor-Gee, G.R. Moore, N.E. Le Brun, J. Biol. Inorg. Chem. 9 (2004) 161–170.
[25] J. Polanams, A.D. Ray, R.K. Watt, Inorg. Chem. 44 (2005) 3203–3209.
[26] A. Treffry, P.M. Harrison, Biochem. J. 171 (1978) 313–320.
[27] P.M. Hanna, Y. Chen, N.D. Chasteen, J. Biol. Chem. 266 (1991) 886–893.
[28] T. Tosha, H.-L. Ng, O. Bhattasali, T. Alber, E.C. Theil, J. Am. Chem. Soc. 132 (2010) 14562–14569.
[29] P. Turano, D. Lalli, I.C. Felli, E.C. Theil, I. Bertini, Proc. Natl. Acad. Sci. U.S.A. 107 (2010) 545–550.
[30] W.H. Massover, Micron 24 (1993) 389–437.
[31] Y.H. Pan, K. Sader, J.J. Powell, A. Bleloch, M. Gass, J. Trinick, A. Warley, A. Li, R. Brydson, A. Brown, J. Struct. Biol. 166 (2009) 22–31.
[32] D. Carta, M.F. Casula, A. Corrias, A. Falqui, G. Navarra, G. Pinna, Mater. Chem. Phys. 113 (2009) 349–355.
[33] V.A. Drits, B.A. Sakharov, A.L. Salyn, A. Manceau, Clay Miner. 28 (1993) 185–207.
[34] D. Carta, M.F. Casula, A. Corrias, A. Falqui, G. Navarra, G. Pinna, Mater. Chem. Phys. 113 (2009) 349–355.
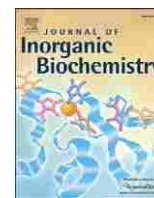
Non-reductive iron release from horse spleen ferritin using desferoxamine chelation

Joseph Johnson, Jason Kenealey [1], Robert J. Hilton, David Brosnahan [1], Richard. K. Watt *, Gerald D. Watt *

Department of Chemistry and Biochemistry, Brigham Young University, Provo, UT, 84602, United States

ARTICLE INFO

ABSTRACT

The rate of Fe^{3+} release from horse spleen ferritin (HoSF) was measured using the Fe^{3+}-specific chelator desferoxamine (DES). The reaction consists of two kinetic phases. The first is a rapid non-linear reaction followed by a slower linear reaction. The overall two-phase reaction was resolved into three kinetic events: 1) a rapid first-order reaction in HoSF (k_1); 2) a second slower first-order reaction in HoSF (k_2); and 3) a zero-order slow reaction in HoSF (k_3). The zero-order reaction was independent of DES concentration. The two first-order reactions had a near zero-order dependence on DES concentration and were independent of pH from 6.8 to 8.2. The two first-order reactions accounted for 6–9 rapidly reacting Fe^{3+} ions. Activation energies of 10.5 ± 0.8, 13.5 ± 2.0 and 62.4 ± 2.1 kJ/mol were calculated for the kinetic events associated with k_1, k_2, and k_3, respectively. Iron release occurs by: 1) a slow zero-order rate-limiting reaction governed by k_3 and corresponding to the dissociation of Fe^{3+} ions from the FeOOH core that bind to an Fe^{3+} binding site designated as site 1 (proposed to be within the 3-fold channel); 2) transfer of Fe^{3+} from site 1 to site 2 (a second binding site in the 3-fold channel) (k_2); and 3) rapid iron loss from site 2 to DES (k_1).

© 2010 Elsevier Inc. All rights reserved.

1. Introduction

Ferritins are hollow, multi-subunit, spherical proteins widely distributed in nature that are involved in iron storage for living systems [1–7]. The ability of ferritins to dynamically control iron within an organism is determined by two distinct biochemical redox reactions. The first is the binding and oxidation of free Fe^{2+} with subsequent deposition as FeOOH within the hollow ferritin interior during periods of abundant cellular iron [8]. This iron deposition process not only stores iron within the hollow interior for later metabolic uses but also decreases the likelihood of cellular damage arising from the formation of oxygen radicals [7]. The second redox process is the reductive release of Fe^{2+} from the FeOOH mineral core stored within the ferritin interior [9–13]. Both processes are readily conducted in vitro using various types of ferritins ranging from native animal and bacterial ferritins to a variety of recombinant ferritins [14–18].

The reactions conducted by native animal ferritins are of particular interest because, in contrast to the bacterial ferritins which only have one subunit type [19], the animal ferritins are heteropolymers consisting of two different subunit types, heavy (H) and light (L) [20]. The presence of H and L subunits in animal ferritins suggests specialized roles for each of these subunits. The fact that these subunits are found in different ratios in different tissues indicates that these subunits function in an important catalytic role relating to iron metabolism. The H and L subunits have high amino acid sequence homology, similar structures and similar relative molecular mass (Mr) values near 20,000 and 19,000, respectively. Studies with the H subunit have established the presence of a ferroxidase center that efficiently conducts Fe^{2+} oxidation by O_2 for in vitro iron deposition reactions [21,22]. The L subunit possesses iron-binding residues (Glu-57, Glu-60, Glu-62, Glu-64, Glu-67) that form a nucleation center that assists in Fe^{3+} hydrolysis and the formation of the FeOOH mineral core [23]. The L subunit lacks a ferroxidase center, whereas the H ferritin lacks the nucleation center. Although extensive studies of iron deposition within various ferritin types have been conducted [16–18,24–27], the complete loading process remains poorly understood because it is difficult to separately study the redox reactions from the non-redox processes of migration and hydrolysis of Fe^{3+} to form the mineral core.

Initial iron loading requires the ferroxidase center to catalyze the oxidation of Fe^{2+} to Fe^{3+} followed by migration of the Fe^{3+} to the interior of ferritin for nucleation and mineralization. Once a mineral core begins to form, Fe^{2+} can pass through the 3-fold channels and become oxidized on the mineral core surface without passing through the ferroxidase center [17]. Electrostatic potential calculations for divalent metals entering the ferritin 3-fold channel showed that there are two divalent metal binding sites in each 3-fold channel [28]. From
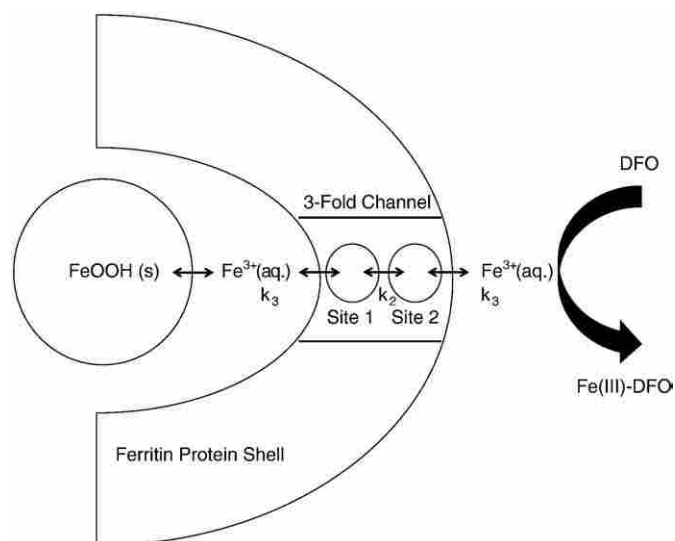
Scheme 1. A model for the release of Fe^{3+} from ferritin by DES. DES rapidly chelates Fe^{3+} bound in site 1 and site 2 of the 3-fold channels. The kinetics for this reaction shows a rapid burst and represents k_1 and k_2. Once the channel-bound Fe^{3+} has been removed, iron release is dependent on the rate-limiting step, which is the equilibrium of Fe^{3+} dissociating from the iron mineral core inside ferritin represented by k_3.

these calculations, there are two potential metal ion-binding sites in each of the 3-fold channels of ferritin. A model showing these channel binding sites is represented in Scheme 1.

In a previous study, we attempted to separate the non-redox reactions from the redox reactions [29]. We investigated the rates of Fe^{3+} and Fe^{2+} transfer into HoSF interior by trapping ferrocyanide or ferricyanide inside ferritin. As Fe^{3+} or Fe^{2+} traversed the protein shell and entered the ferritin interior, a color change was observed by forming Prussian blue. The rate of Fe^{3+} entering ferritin was also measured by trapping the Fe^{3+}-specific chelator desferoxamine (DES) inside ferritin by pH disassembly of ferritin followed by reassembly of ferritin in the presence of DES. These studies showed that Fe^{3+} entered ferritin at a slightly faster rate than Fe^{2+} with rate constants of $0.4 \, s^{-1}$ for Fe^{2+} and $0.76 \, s^{-1}$ for Fe^{3+} [29]. Unfortunately, attempts to measure the rate of transfer of these two iron species out of the HoSF interior were not successful.

In a recent study the non-redox release of Fe^{3+} from the mineral core of HoSF was studied by using the small iron chelating agents, aceto- and benzo-hydroxamic acids [30]. The results suggested that these small chelators entered the ferritin interior and directly removed iron from the mineral core. In contrast, in the current work we examined the non-redox release of Fe^{3+} from the mineral core in HoSF using DES. DES is larger than aceto- and benzo-hydroxamic acids and is restricted from entering the ferritin interior. As a consequence, iron must transfer through the protein shell to DES at the ferritin exterior [31]. During redox mediated iron release, Fe^{2+} is the dominant form of iron transferred through the ferritin protein shell to the external chelating reagents. However, the information gained by studying Fe^{3+} transfer was deemed a useful approximation to Fe^{2+} transfer because, both Fe^{2+} and Fe^{3+} enter ferritin at comparable rates [29]. Here we describe the reactions for Fe^{3+} release from native HoSF using DES chelation and identify several steps involved in the Fe^{3+} export system. From these reactions, we propose an overall mechanism for iron transport from the mineral core through binding sites within the 3-fold channels to the chelator on the exterior of ferritin.

2. Materials and methods

HoSF containing 2050 iron atoms and 375 phosphate groups was obtained from Sigma. Stock HoSF solutions at 0.5 and 7.0 mg/mL (1.1 and 16 μM) were prepared in 0.025 M (N-tris(hydroxymethyl)methyl-2-aminoethanesulfonic acid (TES), 0.05 M NaCl at pH values of 6.8, 7.5 and 8.2. Medicinal grade desferoxamine (DES) was obtained from Ciba-

Geigy Limited, Basel, Switzerland and stock solutions were prepared in 0.025 M TES at pH values of 6.8, 7.5 and 8.2. A molar absorptivity of $2865 \, M^{-1} \, cm^{-1}$ at 430 nm for FeDES was used to quantitate iron release from HoSF. Ferritin samples were incubated with EDTA and passed down a Sephadex G-25 column to remove adventitiously bound iron. Iron-release reactions were compared with samples treated with or without EDTA and no differences were observed between these samples.

2.1. Stopped-flow measurements

A DX.17MV Sequential Stopped flow Spectrofluorimeter from Applied Photophysics with optical path lengths of 10.0 and 2.0 mm was used for the acquisition of stopped-flow kinetic data. The stopped-flow instrument was connected to a variable temperature circulator-water bath that controlled the temperature of the optical cell and the sample syringes to $\pm 0.10 \, °C$. Kinetic traces were typically obtained by mixing ~0.01 M DES with 1.0–5.0 μM native holo HoSF (DES/HoSF = 2000, DES/Fe = 1.0) at 5 °C intervals using computer programmed temperature variation from 10 to 50 °C. Multiple kinetic reactions (5–8) were recorded and averaged at each temperature to correct for random error. When the reaction sequence was finished at 50 °C, the temperature was returned to 20 °C for the final reaction. This final 20 °C reaction was compared with the 20 °C reaction measured during the initial 10–50 °C temperature sequence to be certain that no modification of the protein occurred while at 50 °C. Stopped-flow curves were analyzed using a user-derived equation consisting of two exponential terms and a linear zero-order term.

The reaction of DES with native holo HoSF produced a two-phase kinetic curve, which indicated a rapid non-linear release of iron lasting ~500 s followed by a slower nearly linear release of iron. Another set of stopped-flow measurements were conducted after holo HoSF was first equilibrated with DES for >500 s to eliminate the rapid kinetic phase. For this sequence of reactions, 1.0 mL of ~5.0 μM holo HoSF was reacted with a 100-fold excess of DES for 500 s to remove the rapidly reacting iron atoms and the reacted holo HoSF was separated from unreacted DES and FeDES on a 1.0×10 cm Sephadex G-25 column equilibrated in 0.05 M TES, 0.05 M NaCl pH 7.5. This DES-free HoSF was then loaded into the stopped-flow instrument ~1–2 h later and reacted with a second portion of DES as outlined above to determine if the rapidly reacting iron atoms had been restored.

2.2. EPR measurements

HoSF was reacted with DES until the fast reaction was complete and the zero-order reaction was well established. The reaction mixture was cooled and passed through a Sephadex G-25 column equilibrated at 4 °C to separate holo HoSF from FeDES and unreacted DES. A portion of the separated HoSF at 4 °C was then placed in an EPR tube and frozen in liquid nitrogen. A second portion was placed in an identical EPR tube and equilibrated at 30 °C for 1.0 h, to allow repopulation of the rapidly reacting sites from the FeOOH mineral core, and then frozen in liquid nitrogen. The EPR spectra of these samples were collected at a temperature of 4 K on a Bruker EMX spectrometer with the following settings: power 1.997 mW, modulation frequency 100 kHz, modulation amplitude 9.99 G.

3. Results

Fig. 1 shows the rate of FeDES formation at 25 °C. Eq. (1) represents the reaction of holo HoSF with a ten-fold excess of H_4DES ($H_4DES/HoSF$) at pH 7.5.

$$FeOOH + H_4DES = FeDES + 2H_2O + H^+ \qquad (1)$$

FeOOH represents the native mineral core sequestered within the hollow interior of HoSF and H_4DES is the protonated form of DES
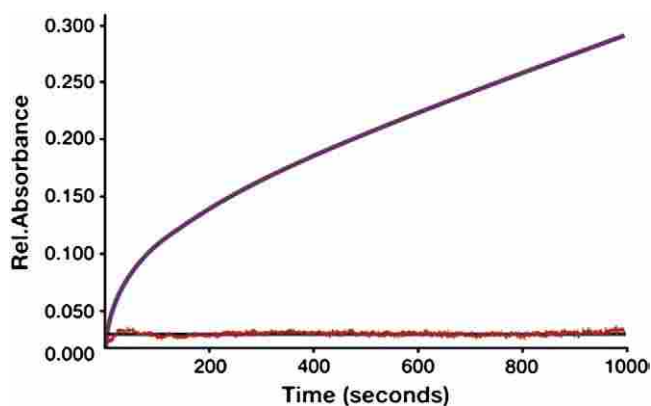
Fig. 1. The release of Fe^{3+} from the HoSF mineral core using DES chelation. The change of absorbance at 430 nm during the release of Fe^{3+} from HoSF was monitored by stopped-flow spectrophotometry (solid blue line). The fit to the experimental data using Eq. (2) is shown as the red dashed line that overlays the blue line. The lower curve is the deviation of the fit from the experimental measurement. The relative standard deviation is less than 1% for each rate constant and the variance of the overall fit is less than 10^{-6} for all 4000 data points. Only a slight deviation is observed during the first 10 s of the reaction for which Eq. (2) was unable to account. The kinetic traces were obtained by mixing 0.01 M DES with 5.0 μM native holo HoSF (2050 Fe/ferritin) in the following ratios (DES/HoSF = 2000, DES/Fe = 1.0) in TES buffer pH 7.5 at 25 °C. (For interpretation of the references to color in this figure legend, the reader is referred to the web version of this article.)

occurring at pH 7.5 prior to Fe^{3+} chelation. The reaction was monitored at 430 nm, where FeDES has a maximum absorbance. Fitting analysis of this iron-release curve shows two distinct kinetic phases for the formation of FeDES. The first is a non-linear reaction occurring from about 0 to 500 s followed by a slower, nearly linear reaction occurring from about 500 s until the reaction was terminated at 1000 s. The shape of the curve is typical of "burst" kinetics, indicating that intermediates were quickly lost but the reaction slowly attains a steady state replenishment of these intermediates. The analysis of each of these distinct kinetic regions provides information about the movement of iron from the mineral core through the protein shell to the DES chelator.

Various rate laws were tested but the best-fit line in Fig. 1 was calculated using Eq. (2).

$$\text{rate} = ae_1^{-k}t + be_2^{-k}t + k_3t + c \tag{2}$$

The overall reaction sequence given by Eq. (2) and consists of two sequential first-order iron-release reactions followed by a zero-order iron-release reaction. The rate constants, k_1 (6.2×10^{-2} s^{-1}) and k_2 (5.7×10^{-3} s^{-1}) are first-order rate constants in HoSF accounting for the rapid release ("burst") of iron, k_3 is a zero-order rate constant, t is time in s and a, b and c are representative amplitudes ($a = 4.4 \times 10^{-2}$, $b = 6.6 \times 10^{-2}$, and $c = 0.13$) associated with k_1, k_2 and k_3, respectively. Eq. (2) gives good fits to the absorbance vs. time data in Fig. 1, as seen by the calculated residuals shown in Fig. 1.

3.1. The zero-order iron-release reaction, k_3

The linear rate for iron chelation was truncated for convenience of presentation after 1000 s in Fig. 1 but remains linear for much longer time intervals. This linear portion suggests a zero-order reaction for Fe^{3+} release. The zero-order rate constant for k_3 was determined to be 1.6×10^{-4} M s^{-1}. To more fully describe the rate law for this linear iron-release process, identical reactions were conducted with a 10-, 50- and a 100-fold excess of DES under identical conditions. In all cases, linear curves were obtained with k_3 values nearly identical to that in Fig. 1, showing that the reaction was independent of DES

concentration. The DES independence of k_3 suggests iron release from the HoSF core is the rate-limiting step and corresponds to Eq. (3).

$$Fe(OOH) + H_2O = Fe^{3+} + 3OH^- \tag{3}$$

To further explore this possibility, identical reactions to those shown in Fig. 1 were conducted at pH values of 6.8, 7.5 and 8.2. Biphasic curves similar to Fig. 1 were obtained as a function of pH showing that two distinct kinetic phases were still present for the iron-release reaction (data not shown).

Analysis of the linear portion of each curve at each pH showed two important features. First, the rate expressed by k_3 for FeDES formation remained independent of DES concentration with pH variation and secondly, the rate of iron release decreased by a factor of 5 between pH 6.8 and 8.2. The invariance of rate with DES concentration and the decrease in rate with increasing pH suggests the iron core dissolution reaction represented by Eq. (3) represents the iron-release reaction in Fig. 1. As the pH increases, the increase in OH^- concentration shifts the equilibrium to the left and causes the FeOOH core to become more stable [32], causing the rate of iron release to decrease.

The rate dependence for the zero-order linear reaction shown in Fig. 1 was investigated at 5 °C intervals from 10 to 50 °C at pH 7.5 with a 100-fold excess of DES. The rate varied uniformly with temperature and Fig. 2 shows the Arrhenius plot for the temperature dependence of the zero-order rate constant (k_3). From Fig. 2, an activation energy of 62.4 ± 2.1 kJ/mol was calculated. Additional activation parameters for this zero-order process are shown in Table 1.

3.2. The initial, non-linear iron-release reaction

The rate of formation of FeDES from 0 to 500 s is represented by a curved line and shows that Fe^{3+} chelation is initially rapid, but slows with time, indicating the chelatable iron atoms may be close to the surface of the protein and available for reaction with DES. Extrapolating the linear section of Fig. 1 to zero time gives the absorbance change due
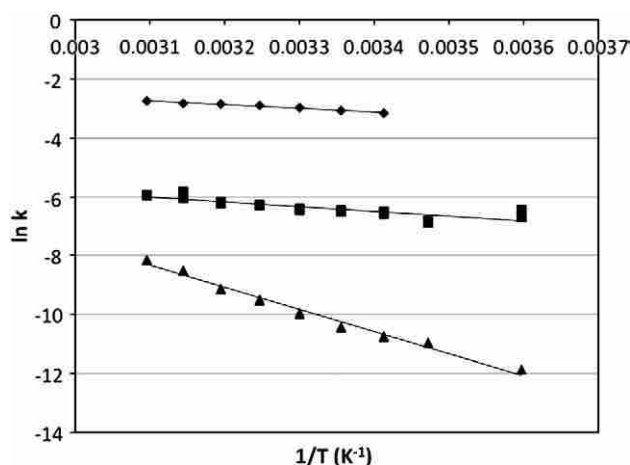

Fig. 2. Activation parameters. Calculated activation parameters derived from measurements of FeDES release from native HoSF as a function of temperature for reactions corresponding to (◆) k_1, (■) k_2, and (▲) k_3. Measurements were performed in a DX.17MV Sequential Stopped Flow Spectrofluorimeter from Applied Photophysics with optical path lengths of 10.0 and 2.0 mm used for the acquisition of stopped-flow kinetic data. The temperature was controlled within ± 0.10 °C of the desired temperature with a water bath. Kinetic traces were obtained by mixing 0.01 M DES with 5.0 μM native holo HoSF (DES/HoSF = 2000, DES/Fe = 1.0) in TES buffer at pH 7.5. Values were collected at 5 °C intervals using computer programmed temperature variation from 10 to 50 °C. Multiple kinetic reactions (5–8) were recorded and averaged at each temperature to correct for random error. When the reaction sequence was finished at 50 °C, the temperature was returned to 20 °C for the final reaction. This final 20 °C reaction was compared with the 20 °C reaction measured during the initial 10–50 °C temperature sequence to be certain that no modification of the protein occurred while at 50 °C.

Table 1
Activation parameters derived from the reactions shown in Fig. 2.

Rate constant	Ea (kJ/mol)	ΔS (J/mol K)	ΔH (kJ/mol)
k_1	10.5	151	7.95
k_2	13.5	134	11.0
k_3	62.4	266	60.0

to the rapidly reacting iron atoms and shows that 8–9 Fe^{3+}/HoSF are rapidly lost. This corresponds to ~1.0 Fe^{3+}/3-fold channel. These kinetic and stoichiometric results also suggest that the protein-bound Fe^{3+} ions are in equilibrium with the iron atoms in the FeOOH core. To test this possibility, additional kinetic studies were conducted.

3.3. Determining if the reactions are sequential

In order to corroborate the conclusions derived from fitting the kinetic results by Eq. (2), two additional sets of experiments were conducted: one kinetic and the second stoichiometric. The kinetic approach required reacting HoSF with excess DES as shown in Fig. 1 for more than 500 s until the linear reaction is fully established. The HoSF–DES mixture was then separated by Sephadex G-25 chromatography at 25 °C to isolate holo HoSF from excess DES and the FeDES produced in the rapid, initial phase of reaction. This holo HoSF, with only a small part of its iron core removed by the k_1 and k_2 reaction steps (fast component of Fig. 1) was loaded into the stopped-flow after a 1-h delay and reacted with excess DES under the conditions of Fig. 1. An identical two-phase reaction as in Fig. 1 was observed, which yielded identical k_1, k_2 and k_3 values as the native HoSF. These results show that in the absence of DES, and with an appropriate incubation time, Fe^{3+} ions can become reestablished in the 3-fold channel and can react with DES in the identical reaction that occurs with native HoSF. This means that the burst is due to repopulation of the channels and not due to non-specifically bound iron. The repopulation of the rapidly reacting iron atoms from the HoSF FeOOH core is quite slow. This is consistent with the rate-limiting step (k_3) of the iron-release process being the transfer of Fe^{3+} from the FeOOH core to the protein binding sites.

The stoichiometric experiments investigated the number of iron atoms involved in the rapid reaction shown in Fig. 1. By extrapolating the linear reaction back to zero the number of Fe^{3+} ions released in the burst was calculated to be 9.0 Fe^{3+}/HoSF or 1.1 rapidly reacting Fe^{3+} ions per 3-fold channel at 25 °C. The two exponential reactions obtained from curve fitting the data in Fig. 1 were evaluated using Eq. (2). Values for the two amplitudes associated with k_1 and k_2 in Eq. (2) were obtained. The kinetic results suggest that there are two binding sites with different affinities for iron. This result is consistent with electrostatic potential calculations showing that two divalent metal binding sites exist in the 3-fold channels of ferritin [28]. Temperature dependence studies were performed to evaluate how iron release changed with temperature. By fitting each curve at each temperature using Eq. (2), the total number of iron atoms per ferritin and the number associated with each of the individual binding sites was calculated and is shown in Table 2. As the temperature increases, the overall number of rapidly reacting Fe^{3+} per HoSF increases from

Table 2
Temperature dependence on 3-fold channel Fe^{3+} binding sites.

Temperature °C	Fe^{3+} in site 2 (k_1)	Fe^{3+} in site 1 (k_2)	Fe^{3+} total
15.0	2.3	4.7	7.0
20.0	2.6	5.0	7.6
25.0	3.1	5.9	9.0
30.0	3.3	6.7	10.0
35.0	4.1	7.3	11.4
45.0	4.5	7.8	12.3

7.0 Fe^{3+} at 15 °C to 12.3 at 45 °C. The amplitudes were used to calculate the population of Fe^{3+} in each site as the temperature increased (Table 2). These results suggest that a temperature sensitive equilibrium is operating within HoSF that shifts Fe^{3+} from the mineral core into protein sites where DES chelation can occur. Assuming that Fe^{3+} transfer occurs through the 3-fold channel, it is concluded that more than one Fe^{3+} binding site exists in each of the eight channels and that the population in each channel site was resolved by the kinetic analysis (Table 2).

To confirm the binding sites are in the 3-fold channels, identical iron-release experiments were performed with homopolymers of H and L human ferritin. This was done because an alternative location for monomeric Fe^{3+} ions might be the two iron-binding sites of the ferroxidase center. HoSF has 10% H subunits or ~3H subunits/ferritin. Potentially 6 Fe^{3+} could come from the H subunits of HoSF. Homopolymers of H ferritin contain 24-subunits, each with a ferroxidase center that can bind up to 2 Fe^{3+} ions. Therefore a homopolymers of H ferritin could bind up to 48 Fe^{3+}/ferritin if the iron had not migrated to the interior. In contrast, L ferritin would have zero monomeric Fe^{3+} binding sites associated with the ferroxidase center. Therefore, if the Fe^{3+} was coming from the ferroxidase centers and not the 3-fold channels we would expect a burst of 48 Fe^{3+}/ferritin from H ferritin and no burst from L ferritin. If the Fe^{3+} comes from the 3-fold channels, the burst would be ~8 for either homopolymers of ferritin. Our results showed a burst between 6 and 8 Fe^{3+} for H and L ferritin at 25 °C consistent with our proposal that the Fe^{3+} comes from the 3-fold channels (data not shown).

3.4. EPR measurements with native HoSF

EPR measurements were conducted to further examine the nature of the rapidly reacting Fe^{3+} ions in HoSF. Monomeric Fe^{3+} in a low symmetry environment is known to exhibit an EPR signal at $g = 4.3$. The EPR studies were performed to determine if the rapidly reaction Fe^{3+} ions observed by DES release are related to the monomeric Fe^{3+} EPR signal.

HoSF was reacted with DES until the fast reaction was complete and the zero-order reaction was well established and then the DES and FeDES were separated from HoSF on a Sephadex G-25 column at 4 °C. The ferritin fraction was collected and divided into two samples. The first sample was placed in an EPR tube and frozen in liquid nitrogen. This sample should have minimal population of Fe^{3+} in the protein binding sites at this low temperature because of the large activation energy for the zero-order reaction required to free Fe^{3+} from the mineral core (Table 1). The second sample was placed in an identical EPR tube and equilibrated at 30 °C for 1.0 h, to allow repopulation of Fe^{3+} into the protein binding sites. After 1 h, this sample was frozen in liquid nitrogen. The kinetic results shown in Table 2 suggest that site 1 and site 2 would become populated by incubation at room temperature for 1 h.

Fig. 3 shows that the HoSF sample maintained at 4 °C had only a small $g = 4.3$ signal (blue spectrum), whereas the sample equilibrated at 30 °C for 1 h had ~4-fold larger amplitude at $g = 4.3$ (black spectrum). The spectrum of native ferritin not treated with DES is identical to the black spectrum (data not shown). These results suggest that the $g = 4.3$ signal corresponds to monomeric Fe^{3+} ions in the 3-fold channels. The DES treated sample at 4 °C was unable to repopulate the Fe^{3+} ions due to the high energy of activation of k_3. After incubation at 30 °C for 1 h, Fe^{3+} ions could be mobilized from the core and repopulate the binding sites in the 3-fold channels. This equilibration restored Fe^{3+} ions associated with the "burst" that is seen in Fig. 1.

3.5. DES dependence of k_1 and k_2

Further experiments were conducted to determine the DES dependence for the two reactions that constitute the rapid iron-release reactions in Fig. 1. The overall rate of iron release from HoSF at
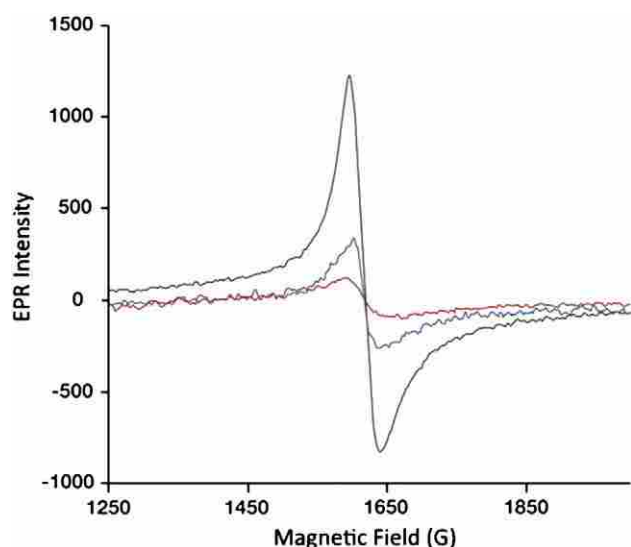
Fig. 3. EPR spectra of ferritin samples. The red (bottom spectrum) EPR signal is of apo ferritin and is shown as the negative control. A slight peak is observed due to residual iron in apo ferritin. The blue (middle spectrum) is from native HoSF from which Fe^{3+} was removed by DES chelation at 4 °C and passed down a Sephadex G-25 column at 4 °C to separate ferritin from unbound DES and Fe(III)DES followed by freezing immediately after elution from the column. The black (top spectrum) is from native HoSF from which Fe^{3+} was removed by DES chelation at 4 °C and passed down a Sephadex G-25 column to separate ferritin from unbound DES and Fe(III)DES followed by a 1-h incubation at 30 °C followed by freezing in liquid N_2. Native ferritin not treated with DES has an EPR spectrum essentially identical to the black (top) spectrum that was incubated at 30 °C for 1 h (data not shown). The EPR spectra were obtained at 4 K at 5 mg/ml ferritin in 0.025 M TES pH 7.5 as described in Materials and methods. (For interpretation of the references to color in this figure legend, the reader is referred to the web version of this article.)

10-, 100- and 1000-fold excess of DES per HoSF is only slightly increased in comparison to the large increase in [DES] (data not shown). This indicates that the reaction is essentially independent of DES concentration and that the reactions are first order in HoSF and zero order in DES.

3.6. Temperature variation of k_1 and k_2

To determine if there are any errors in the fitting procedure caused by additional reactions not accounted for in Eq. (2), the non-linear iron-release reaction was investigated at 5 °C intervals between 10 and 50 °C at a DES:HoSF ratio of 50:1. Each progress curve at each temperature was fit using Eq. (2) as outlined above. Table 1 summarizes the activation parameters obtained. The strict linear response of k_1, k_2, and k_3 with temperature seen in Fig. 2 confirms that Eq. (2) is a consistent representation of the Fe^{3+} loss reaction. Secondary reactions would likely have different activation energies and contribute to a change in rate with temperature. A reaction that is unaccounted for by Eq. (2) would cause the calculated values of k_1, k_2 and k_3 to vary in an irregular way with temperature instead of the linear response observed in Fig. 2.

4. Discussion

Numerous studies using siderophores and siderophore analogs evaluated the release of Fe^{3+} from free Fe(O)OH, and the Fe(O)OH-containing biominerals hemosiderin and ferritin to determine their efficacy in treatment of iron overload diseases [9,30,31,33–36]. These studies demonstrated the favorable thermodynamics of iron transfer from polynuclear iron sources to form mononuclear chelates but the rates of chelate formation are relative slow (on the order of h and days) and in the order: Fe(O)OH>hemosiderin>ferritin. The slow iron-release rate from these polynuclear sources is consistent with the ability of the chelator to gain access to the surface of the iron mineral.

The slow reaction for ferritin was attributed to restriction of iron transfer from the protected ferritin mineral through the protein shell to the chelator on the ferritin exterior. These results show that the ferritin protein shell is performing the exact role that it evolved to perform, that is, to sequester iron and prevent it from reacting with other biological molecules.

Because of the slow rate of iron release from ferritin, most measurements using siderophores followed iron release at 1-h intervals or longer and did not examine iron-release reactions that occurred at the early time points. However, one report noted that iron release with DES and rhodotorulic acid was more rapid in the first h compared to subsequent time intervals, suggesting important information was present in the early stages of iron loss [9]. Our interest in determining the rates of iron transfer through the protein shell has led us to investigate the initial steps of iron release from HoSF using DES chelation.

Fig. 1 shows that DES can remove Fe^{3+} from the HoSF iron core in a non-reductive process. Scheme 1 shows the model built from the kinetic data. The scheme comes from evaluations of Eq. (2) where the entire kinetic progress curve for the overall iron-release reaction shown in Fig. 1 was resolved into two first-order reactions in HoSF (one rapid and a second ~4 times slower) and a third even slower reaction that is zero order in HoSF. Scheme 1 shows that DES removes iron from the HoSF mineral core by binding Fe^{3+} ions that are present in the 3-fold channels of the HoSF protein shell. Control reactions with H and L ferritin confirmed that the Fe^{3+} comes from the 3-fold channels and not the ferroxidase center. The kinetic results mimic those often referred to as burst kinetics. The burst comes from protein associated Fe^{3+} intermediates, which are readily chelated by DES but are slowly repopulated by a slower step.

DES is too large to enter the HoSF interior through the 3-fold channels [31,37–39], so it must react with Fe^{3+} bound at or near the protein surface of HoSF. The lack of DES dependence on the kinetics after this initial burst reaction suggests that DES cannot interact with Fe^{3+} bound at the mineral core surface, but that this iron is separated from DES by the protein shell. The curve fitting procedure based on Eq. (2) suggests that DES chelates 9 Fe^{3+} ions/ferritin at 25 °C. Since these Fe^{3+} ions are bound in the 3-fold channels, the average population is 1.1 Fe^{3+}/channel, suggesting that two partially occupied iron-binding sites are present. This behavior is more apparent in Table 2 where at higher temperatures up to 1.4 Fe^{3+}/channel was observed. A population of 1–2 Fe^{3+} ions/channel is consistent with results from electrostatic potential calculations suggesting that two Fe^{2+} binding sites are present in the three-fold channels [28]. Therefore, the first conclusion from this study is that the non-linear steps represent the "burst" of iron release from these two binding sites in the 3-fold channels.

At 45 °C, 12.3 Fe^{3+} ions were bound in the channels and accessible for DES chelation. The Fe^{3+} occupation per site was determined (Table 2) using the amplitudes of the rate constants for k_1 and k_2. The Fe^{3+} in site 1 is more tightly bound, as the calculated distribution indicates, but is in equilibrium with the weaker binding site 2 (Scheme 1). The removal of Fe^{3+} from site 2 by DES chelation shifts the equilibrium and the channel-bound Fe^{3+} at site 1 moves closer to the surface and binds at site 2. The transfer rate from site 1 to site 2 is slower than release from site 2 and is reflected by the slower value of k_2.

Our results show the Fe^{3+} egress pathway consisting of two intermediate Fe^{3+} binding sites contained within the 3-fold channel. An Fe^{3+} entry pathway was previously reported which transports Fe^{3+} from the external solution to the ferritin interior [29]. For the entry pathway, only a single kinetic step was observed and not the two kinetic events observed for the egress pathway. This is consistent with Scheme 1 because if site 1 binds Fe^{3+} more strongly than site 2, then the entering Fe^{3+} would rapidly pass from site 2 to site 1 in an apparent single kinetic event.

Once the Fe^{3+} binding sites have been depleted by DES chelation, an equilibrium state is established between DES and the FeOOH

mineral core with the protein shell as a barrier between the chelator and the iron mineral. With an equilibrium in favor of FeDES formation, the FeOOH core transfers Fe^{3+} through the channels to the external solution. Essentially the small amount of free Fe^{3+} that exists in the ferritin interior binds to site 1 in the 3-fold channel and is transferred to site 2 where it can be accessed by DES. Fig. 3 supports this view by showing that Fe^{3+} bound in the channels can be initially removed by DES and that the vacated sites can be slowly replenished by transfer from the Fe(III) stored in the core. The EPR results indicate that the majority of the Fe^{3+} observed in the $g = 4.3$ signal of holo HoSF is channel-bound Fe^{3+} but smaller levels of additional Fe^{3+} ions also may be present. The transfer of iron from the mineral core to these channel iron-binding sites controls the overall rate of release of Fe^{3+} from the HoSF core to DES because it is the rate-limiting step. The FeOOH mineral core is in equilibrium with the channel binding sites and a small amount of Fe^{3+} is released to repopulate the binding sites in the protein channels. The reaction is driven because FeDES forms a more stable complex than the FeOOH found in the core or Fe^{3+} bound in the channels. Ultimately, the FeOOH core slowly supplies Fe^{3+} to the channels and the channels transfer Fe^{3+} to DES.

Although the pathway described here is for Fe^{3+}, it may also be relevant to the Fe^{2+} transfer process, with some expected differences. For example, protein sites 1 and 2 are proposed to be composed of carboxylate side chains. Such binding sites will accommodate both Fe^{2+} and Fe^{3+}, but the latter ion will likely be more strongly bound due to electrostatic interaction. The consequence would be that Fe^{3+} transfer out from the HoSF interior should be slower than Fe^{2+}. The extent of this binding difference was demonstrated by modeling of the iron-binding capabilities of the three-fold channel for both Fe^{2+} and Fe^{3+} ions [28]. This previous study showed that Fe^{3+} is bound 1.3 times stronger than Fe^{2+}. While the present study did not measure the rate of Fe^{2+} egress for comparison, Zhang et al. reported the rate for the opposite reaction of Fe^{2+} and Fe^{3+} transfer into HoSF interior [29]. The rate of Fe^{3+} entry was twice as rapid as that for Fe^{2+}, consistent with overall stronger binding of Fe^{3+} to channel sites compared to Fe^{2+}.

This work is also consistent with recently proposed *in vitro* and *in vivo* models for iron release. Theil proposed a gated pore model and identified amino acid residues involved in opening and closing of the 3-fold channels of ferritin [40]. This model suggests that the 3-fold channels regulate the flow of iron in and out of ferritin [41–43]. Non-reductive iron(III) release based on gated pore model was demonstrated by using chelators normally too large to penetrate the 3-fold channels [30]. In the presence of urea, a reagent that opens the gated pores, rapid iron release was observed. This model suggests that interaction of ferritin with small molecules or other proteins may regulate opening and closing of the 3-fold channels for iron release or iron storage functions [40].

De Domenico and Kaplan have made *in vivo* observations that suggest that cytosolic iron and ferritin iron are in equilibrium and that depletion of the cytosolic iron pool triggers iron release from ferritin [44]. The over-expression of the iron export protein ferroportin caused a decrease in cytosolic iron levels and the depletion of cytosolic iron eventually depleted iron stores in ferritin [44]. Studies with Fe^{3+} chelators that bind cytosolic iron also depleted ferritin stores [45]. Finally, studies in yeast, that naturally lack ferritin, but had ferritin over-expressed for the studies showed that depletion of cellular iron caused ferritin to release its iron [44]. This study suggested that specific iron-release machinery does not exist and that iron release from ferritin in yeast was an equilibrium driven process. Our results support these two new models and provide evidence that a slow, controlled release of Fe^{3+} from ferritin is a viable iron-release model for ferritin. Future work will examine the ability of other chelators to perform the same reaction and tests will be performed on ferritins from other sources to determine how broad this effect is across the ferritin family.

Abbreviations

HoSF	horse spleen ferritin
DES	desferoxamine
H_4DES	the protonated form of DES
FeDES	the Fe^{3+} complex with DES
H ferritin	heavy chain ferritin
L ferritin	light chain ferritin
TES	(N-tris(hydroxymethyl)methyl-2-aminoethanesulfonic acid
Mr	relative molecular mass

References

[1] E.C. Theil, Annu. Rev. Biochem. 56 (1987) 289–315.
[2] R.R. Crichton, M. Charloteaux-Wauters, Eur. J. Biochem. 164 (1987) 485–506.
[3] G.C. Ford, P.M. Harrison, D.W. Rice, J.M. Smith, A. Treffry, J.L. White, J. Yariv, Philos. Trans. R. Soc. Lond. B Biol. Sci. 304 (1984) 551–565.
[4] P.M. Proulxcurry, N.D. Chasteen, Coord. Chem. Rev. 144 (1995) 347–368.
[5] W.H. Massover, Micron 24 (1993) 389–437.
[6] P.M. Harrison, P. Arosio, Biochim. Biophys. Acta 1275 (1996) 161–203.
[7] P. Arosio, R. Ingrassia, P. Cavadini, Biochim. Biophys. Acta 1790 (2009) 589–599.
[8] N.D. Chasteen, P.M. Harrison, J. Struct. Biol. 126 (1999) 182–194.
[9] R.R. Crichton, F. Roman, F. Roland, J. Inorg. Biochem. 13 (1980) 305–316.
[10] K.L. Double, M. Maywald, M. Schmittel, P. Riederer, M. Gerlach, J. Neurochem. 70 (1998) 2492–2499.
[11] D.L. Jacobs, G.D. Watt, R.B. Frankel, G.C. Papaefthymiou, Biochemistry 28 (1989) 1650–1655.
[12] T. Jones, R. Spencer, C. Walsh, Biochemistry 17 (1978) 4011–4017.
[13] T.D. Richards, K.R. Pitts, G.D. Watt, J. Inorg. Biochem. 61 (1996) 1–13.
[14] N.E. Le Brun, M.T. Wilson, S.C. Andrews, J.R. Guest, P.M. Harrison, A.J. Thomson, G.R. Moore, FEBS Lett. 333 (1993) 197–202.
[15] N.E. Le Brun, S.C. Andrews, J.R. Guest, P.M. Harrison, G.R. Moore, A.J. Thomson, Biochem. J. 312 (Pt 2) (1995) 385–392.
[16] X. Yang, Y. Chen-Barrett, P. Arosio, N.D. Chasteen, Biochemistry 37 (1998) 9743.
[17] B. Xu, N.D. Chasteen, J. Biol. Chem. 266 (1991) 19965.
[18] F. Bou-Abdallah, G.C. Papaefthymiou, D.M. Scheswohl, S.D. Stanga, P. Arosio, N.D. Chasteen, Biochem. J. 364 (2002) 57.
[19] N.E. Le Brun, A. Crow, M.E. Murphy, A.G. Mauk, G.R. Moore, Biochim. Biophys. Acta 1800 (2010) 732–744.
[20] P. Arosio, T.G. Adelman, J.W. Drysdale, J. Biol. Chem. 253 (1978) 4451–4458.
[21] D.M. Lawson, P.J. Artymiuk, S.J. Yewdall, J.M. Smith, J.C. Livingstone, A. Treffry, A. Luzzago, S. Levi, P. Arosio, G. Cesareni, et al., Nature 349 (1991) 541–544.
[22] P.M. Harrison, S.C. Andrews, P.J. Artymiuk, G.C. Ford, J.R. Guest, J. Hirzmann, D.M. Lawson, J.C. Livingstone, J.M.A. Smith, A. Treffry, S.J. Yewdall, Adv. Inorg. Chem. 36 (1991) 449–486.
[23] P. Santambrogio, S. Levi, CozziA., B. Corsi, P. Arosio, Biochem. J. 314 (Pt 1) (1996) 139–144.
[24] P.M. Hanna, Y. Chen, N.D. Chasteen, J. Biol. Chem. 266 (1991) 886.
[25] G. Zhao, F. Bou-Abdallah, P. Arosio, S. Levi, C. Janus-Chandler, N.D. Chasteen, Biochemistry 42 (2003) 3142.
[26] ZhaoG., SuM., ChasteenN.D., J. Mol. Biol. 352 (2005) 467.
[27] F. Bou-Abdallah, G.H. Zhao, H.R. Mayne, P. Arosio, N.D. Chasteen, J. Am. Chem. Soc. 127 (2005) 3885–3893.
[28] T. Takahashi, S. Kuyucak, Biophys. J. 84 (2003) 2256–2263.
[29] B. Zhang, R.K. Watt, N. Galvez, J.M. Dominguez-Vera, G.D. Watt, Biophys. Chem. 120 (2006) 96–105.
[30] N. Galvez, B. Ruiz, R. Cuesta, E. Colacio, J.M. Dominguez-Vera, Inorg. Chem. 44 (2005) 2706–2709.
[31] J.M. Dominguez-Vera, J. Inorg. Biochem. 98 (2004) 469–472.
[32] H. Heqing, R.K. Watt, R.B. Frankel, G.D. Watt, Biochemistry 32 (1993) 1681–1687.
[33] G.J. Kontoghiorghes, S. Chambers, A.V. Hoffbrand, Biochem. J. 241 (1987) 87–92.
[34] G.J. Kontoghiorghes, Analyst 120 (1995) 845–851.
[35] M.J. O'Connell, R.J. Ward, H. Baum, T.J. Peters, Biochem. J. 260 (1989) 903–907.
[36] T.P. Tufano, V.L. Pecoraro, K.N. Raymond, Biochim. Biophys. Acta 668 (1981) 420–428.
[37] D. Yang, K. Nagayama, Biochem. J. 307 (Pt 1) (1995) 253–256.
[38] X. Yang, N.D. Chasteen, Biophys. J. 71 (1996) 1587–1595.
[39] B. Webb, J. Frame, Z. Zhao, M.L. Lee, G.D. Watt, Arch. Biochem. Biophys. 309 (1994) 178–183.
[40] E.C. Theil, X.S. Liu, T. Tosha, Inorg. Chim. Acta 361 (2008) 868–874.
[41] X. Liu, E.C. Theil, Ann. NY Acad. Sci. 1054 (2005) 136–140.
[42] X. Liu, E.C. Theil, Acc. Chem. Res. 38 (2005) 167–175.
[43] X.S. Liu, L.D. Patterson, M.J. Miller, E.C. Theil, J. Biol. Chem. 282 (2007) 31821–31825.
[44] I. De Domenico, M.B. Vaughn, L. Li, D. Bagley, G. Musci, D.M. Ward, J. Kaplan, EMBO J. 25 (2006) 5396–5404.
[45] I. De Domenico, D.M. Ward, J. Kaplan, Blood 114 (2009) 4546–4551.

RESEARCH PAPER

Ferritin as a photocatalyst and scaffold for gold nanoparticle synthesis

Jeremiah D. Keyes · Robert J. Hilton ·
Jeffrey Farrer · Richard K. Watt

Abstract The ferrihydrite mineral core of ferritin is a semi-conductor capable of catalyzing oxidation/reduction reactions. This report shows that ferritin can photoreduce $AuCl_4^-$ to form gold nanoparticles (AuNPs). An important goal was to identify innocent reaction conditions that prevented formation of AuNPs unless the sample was illuminated in the presence of ferritin. TRIS buffer satisfied this requirement and produced AuNPs with spherical morphology with diameters of 5.7 ± 1.6 nm and a surface plasmon resonance (SPR) peak at 530 nm. Size-exclusion chromatography of the AuNP–ferritin reaction mixture produced two fractions containing both ferritin and AuNPs. TEM analysis of the fraction close to where native ferritin normally elutes showed that AuNPs form inside ferritin. The other peak eluted at a volume indicating a particle size much larger than ferritin. TEM analysis revealed AuNPs adjacent to ferritin molecules suggesting that a dimeric ferritin–AuNP species forms. We propose that the ferritin protein shell acts as a nucleation site for AuNP formation leading to the AuNP-ferritin dimeric species. Ferrihydrite nanoparticles (~ 10 nm diameter) were unable to produce soluble AuNPs under identical conditions unless apo ferritin was present indicating that the ferritin protein shell was essential for stabilizing AuNPs in aqueous solution.

Keywords Gold nanoparticles · Ferritin · Nanoparticle synthesis · Photochemistry · Photoreduction

Introduction

Nanoparticle synthesis can be guided by using templates to control the size and morphology of the resulting nanoparticles (Uchida et al. 2007; Whaley et al. 2000; Niemeyer 2001; Katz and Willner 2004). The iron storage protein ferritin provides a template for size-constrained nanoparticle synthesis because it is composed of 24-polypeptide subunits that assemble into a hollow sphere with a 12-nm exterior diameter and an 8-nm diameter cavity (Harrison and Arosio 1996). Ferritin can accommodate up to 4,500 iron atoms as crystalline ferrihydrite. The iron can be removed by reduction and chelation, resulting in an empty (apo) ferritin protein shell (Arosio et al. 2009).

J. D. Keyes · R. J. Hilton · R. K. Watt (✉)
Department of Chemistry and Biochemistry, Brigham Young University, C-210 Benson Building, Provo, UT 84602, USA
e-mail: rwatt@chem.byu.edu

J. Farrer
Department of Physics and Astronomy, Brigham Young University, N283 ESC Building, Provo, UT 84602, USA

Other metallic materials have been prepared inside ferritin using a variety of synthetic methods. Synthetic ferritin minerals include metal oxides of chromium, manganese, iron, cobalt, nickel, titanium, europium, and uranium (Meldrum et al. 1991; Okuda et al. 2003; Zhang et al. 2005; Douglas and Stark 2000; Meldrum et al. 1995; Hainfeld 1992; Klem et al. 2008); sulfides (and in some instances selenides) of iron, cadmium, gold, lead, and zinc (Douglas et al. 1995; Wong and Mann 1996; Yamashita et al. 2004; Iwahori et al. 2005; Yoshizawa et al. 2006; Turyanska et al. 2009). In addition, metal ions have been reduced to their elemental form to produce metallic palladium, copper, cobalt, nickel, gold, and silver nanoparticles (Ueno et al. 2004; Galvez et al. 2005, 2006; Kasyutich et al. 2010; Shin et al. 2010; Butts et al. 2008; Yoshizawa et al. 2006).

In addition to being a nanoreactor to sequester metallic materials, ferritin has been used as a photocatalyst for performing redox reactions in solution. Exposure to light generates an electron–hole pair in the ferrihydrite mineral core that is sufficiently long-lived to react with other components in solution, including sacrificial electron donors and electron acceptors (Nikandrov et al. 1997). Photochemical studies include the photoreduction of Cr(VI) to Cr(III) (Kim et al. 2002), Cu(II) to Cu(0) (Ensign et al. 2004) and the photoreduction of cytochrome c and viologens (Nikandrov et al. 1997). Most recently $AuCl_4^-$ has been reduced to gold nanoparticles (AuNPs) using ferritin as a photocatalyst (Hilton et al. 2010a, b). In addition, metal loading into ferritin occurs photochemically by reducing metal citrate complexes of Fe(III), Eu(III), and Ti(IV) and allowing the reduced form of the metal to be oxidized by the ferroxidase center of the ferritin H-chain leading to incorporation of the metal into ferritin (Klem et al. 2008).

Recently, several studies describing the preparation of AuNPs or silver nanoparticles (AgNPs) using ferritin as a template were reported. Two of the studies prepared gold on the exterior surface of ferritin (Zhang et al. 2007; Kim et al. 2010; Yoshizawa et al. 2006), whereas others produced AuS, Au, Ag, or AgAu alloy nanoparticles inside ferritin (Yoshizawa et al. 2006; Shin et al. 2010; Domìnguez-Vera et al. 2007; Fan et al. 2010; Butts et al. 2008). Some of these studies relied on diffusion of Au or Ag ions into the interior of ferritin followed by reduction by $NaBH_4$ (Fan et al. 2010; Shin et al. 2010). Other studies used protein engineering to incorporate thiolate and histidine ligands inside ferritin to attract and bind the Au and Ag. In addition, less powerful reductants (MOPS buffer) were required and light was used for the reduction of Ag^+ to Ag(0) (Butts et al. 2008).

AuNPs have been used in a variety of applications including colorimetric assays (Liu and Lu 2003, 2006; Lee et al. 2008; Kuong et al. 2007; Cao et al. 2002; Taton et al. 2000), immuno-detection assays (Yang et al. 2009; Yeh et al. 2009), treatment of cancer (Skrabalak et al. 2007) and amyloid-fiber-related diseases (Chikae et al. 2008), carbon nanotube synthesis (Bhaviripudi et al. 2007), and selective oxidation catalysts (Turner et al. 2008). As AuNPs have different characteristics depending on their size and the passivity of the surface, it is important to develop controlled synthetic routes to create particles with different morphologies, sizes, and surface passivation (Daniel and Astruc 2003). In addition, if the AuNPs are to be used in biological systems, capping agents, and buffers used must be compatible for biology (Huang and Chen 2008). The solubility, reactivity, and photonic properties of ferritin AuNPs are sensitive to the size of the particle and the local environment of the gold surface. For instance, the use of different reducing agents to prepare AuNPs with ferritin influenced the catalytic properties of the AuNPs (Zhang et al. 2007). Therefore, the deposition of AuNPs on the exterior or interior of ferritin will influence the potential applications of the nanoparticles.

Several photochemical methods to form AuNPs have been published (Mallick et al. 2005; Shankar et al. 2004; Eustis et al. 2005; Zhou et al. 1999; Sau et al. 2001; Esumi et al. 1995). However, these methods require "gold seeds" or use detergents or other chemical stabilizers, reducing agents or capping agents that are not biologically compatible (Yeh et al. 2009). One advantage of photochemical methods is that chemical reductants are not required and this minimizes contaminants, by-products and other potential reactants that can affect studies in biological systems. This study was undertaken to use ferritin and a minimal reaction system to photo-reduce $AuCl_4^-$ to form AuNPs without requiring "gold seeds," non-biological reducing agents or chemical stabilizers. Potentially, the AuNPs might form inside

the ferritin cavity, as was observed for Cu(II) photoreduction (Ensign et al. 2004) providing an encapsulation method for AuNP delivery. Alternatively, the AuNPs may form on the exterior of ferritin and provide a potential catalyst as was observed for chemical reduction of AuNPs in the presence of ferritin (Zhang et al. 2007). If ferritin sequesters the AuNPs or acts as a capping agent for the AuNPs, the products would be a useful medium for introducing AuNPs into biological systems. To establish the importance of the protein shell, we tested ferrihydrite nanoparticles to determine if the ferrihydrite catalyst was sufficient to form AuNPs or if the ferritin protein shell was required for the formation of AuNPs. We report that ferritin can catalyze the formation of AuNPs and that the protein shell is required for AuNP formation and solubilization. We observed that AuNPs form both on the exterior and interior of ferritin. Furthermore, we observed that buffers significantly influence both the size of the particles and the absorbance maximum of the plasmon resonance peak of the AuNP products.

Materials and methods

Horse Spleen ferritin was obtained from Sigma. Ferritin was prepared in the desired buffer by performing buffer exchanges using Amicon Ultra centrifuge tubes with a molecular weight cutoff of 100,000 Da to concentrate the solution and exchange the buffer to 2-amino-2-hyroxymethyl-propane-1,3-diol (TRIS) buffer (100 mM TRIS, 25 mM NaCl, pH 7.5) or 3-morpholinopropane-1-sulfonic acid (MOPS) buffer (25 mM MOPS, 25 mM NaCl, pH 7.5). The protein concentration was measured using the Lowry method (Lowry et al. 1951). The iron concentration was measured after treatment with dithionite to reduce the iron followed by chelation by bipyridyl to form the $Fe(bipy)_3^{2+}$ complex. The absorbance at 520 nm ($\varepsilon_{520} = 8,400$) was measured to determine iron content (Watt et al. 1992).

AuNPs were prepared by mixing the ferritin catalyst, the sacrificial electron donor citrate, and $AuCl_4^-$ in a quartz cuvette followed by illumination with an Oriel Hg lamp (model 66056). Sample temperature was maintained at 25 °C using a water-circulating cuvette holder connected to a water bath.

The final volume of each sample was 1.25 mL. The final concentrations of MOPS containing samples were 0.155 mg/mL protein, 0.44 mM iron, 4 mM MOPS, 125 mM NaCl, 32 mM citrate, and 0.8 mM $AuCl_4^-$. This corresponds to 2,300 Au atoms per ferritin molecule. Final concentrations of TRIS containing samples were 0.15 mg/mL protein, 0.42 mM iron, 20 mM TRIS, 125 mM NaCl, 32 mM citrate, and 0.8 mM $AuCl_4^-$. This corresponded to 2,400 Au atoms per ferritin molecule with $\sim$1,000 Fe atoms within each ferritin molecule. Control reactions were performed without citrate to determine if the buffers could act as electron donors. Reactions in MOPS buffer still produced AuNPs showing that MOPS could substitute for citrate as an electron donor in the absence of citrate. However, reactions in TRIS or in water did not produce AuNPs indicating that TRIS could not be oxidized under these conditions to donate electrons to $AuCl_4^-$.

UV–visible absorption spectra were measured using an Agilent 8453 spectrophotometer. Transmission electron microscopy (TEM), scanning TEM (STEM), and X-ray energy dispersive spectrometry (XEDS) were performed on a Tecnai F20 Analytical STEM operating at 200 keV. Samples were deposited on copper TEM grids (Ted Pella lacey carbon film grids) by placing a 5 μL sample onto the grid for 20 s and then washing the grid with deionized water for 3 s. For samples that were stained to visualize the protein, a 5 μL addition of 1% uranyl acetate was placed on the grid for 10 s after the water wash. The grid was then allowed to air dry. In between each step the grid was blotted with filter paper. Fast protein liquid chromatography was performed on a GE Healthcare ÄKTApurifier. A Superdex™ 200 10/300 GL size-exclusion column was used to determine the particle size. The sample was eluted in 0.02 M TRIS with 0.125 M NaCl at pH 7.4.

The reactions in each figure were prepared as described above. The time of each sample was exposed to light depended on the buffer used to prepare the sample. Figure 2 shows that some reactions occurred more rapidly than others. For each sample the reaction was prepared as in Fig. 2 and when the plateau was reached, the reaction was stopped by turning off the light. All other analyses were performed on samples after the reaction had reached a plateau in the spectrophotometric assay.

Results and discussion

The photocatalytic formation of AuNPs can be detected by observing the formation of the surface plasmon resonance (SPR) band that forms around 530 nm. Samples containing ferritin, $AuCl_4^-$, and citrate with the indicated buffer were placed in a spectrophotometer and illuminated with a mercury lamp perpendicular to the spectrophotometer light path and the rate of AuNP formation was monitored at 530 nm under a variety of reactions conditions (Fig. 1). It was essential to find conditions that did not permit AuNP formation in the absence of ferritin so that any AuNP formation observed was catalyzed by the illumination of ferritin.

Results shown in Fig. 2a follow the formation of the AuNPs kinetically at 530 nm and Fig. 2b shows the spectrum of the resulting samples. Insets show photographs of the initial solution and the product solutions. Figure 2a shows that in the absence of light, samples prepared in TRIS buffer do not form AuNPs as evidenced by the absence of the SPR absorbance peak at 530 nm. Similar results were observed for samples prepared in water (data not shown). Upon illumination in TRIS (or water), ferritin catalyzes the oxidation of citrate and the reduction of $AuCl_4^-$ to produce a red solution containing AuNPs with an absorbance maximum at 530 nm.

In contrast, MOPS has previously been shown to chemically reduce $AuCl_4^-$ to AuNPs both in the absence and presence of ferritin (Habib et al. 2005; Xie et al. 2007; Zhang et al. 2007). The results in Fig. 2a show that AuNPs form more rapidly when illuminated in MOPS but that they also form in the dark. Interestingly, both of the reactions in MOPS produce purple solutions and not the red solution observed for the TRIS reaction (Fig. 2b inset), and have a broader, blue shifted SPR maximum of 550 nm (Fig. 2b). In addition, in comparison to reactions in MOPS, both the water and the TRIS samples have a lag phase before AuNPs form. Even in comparison to the reaction in water, the TRIS sample has a longer lag phase before AuNPs begin to form. TRIS has an inhibitory effect on the photocatalysis reaction, but the origin of this inhibition has

Fig. 1 A diagram of the photo-illumination equipment used to prepare AuNPs
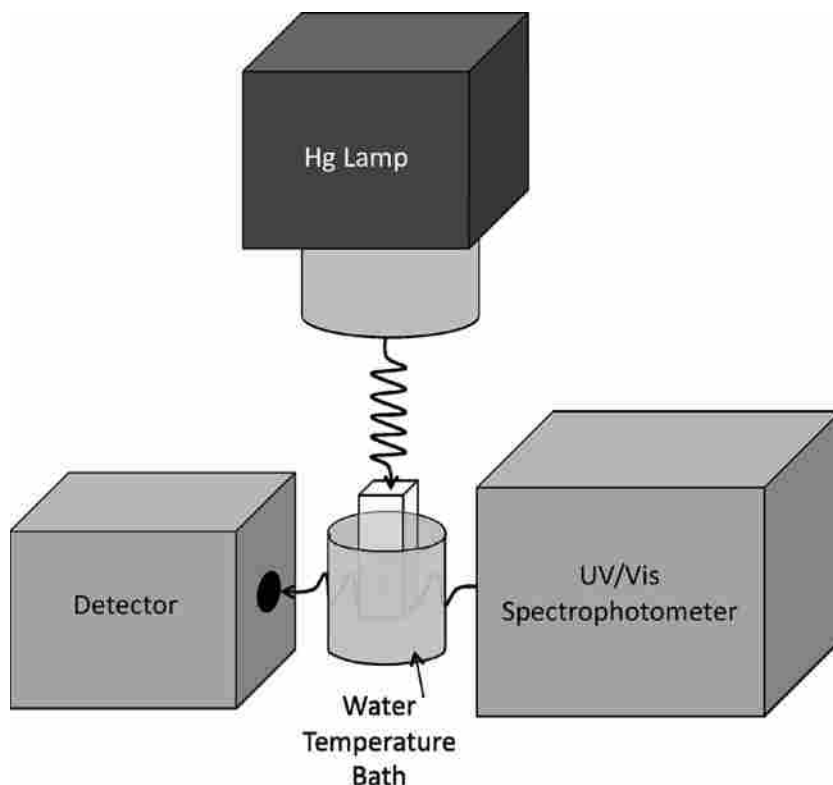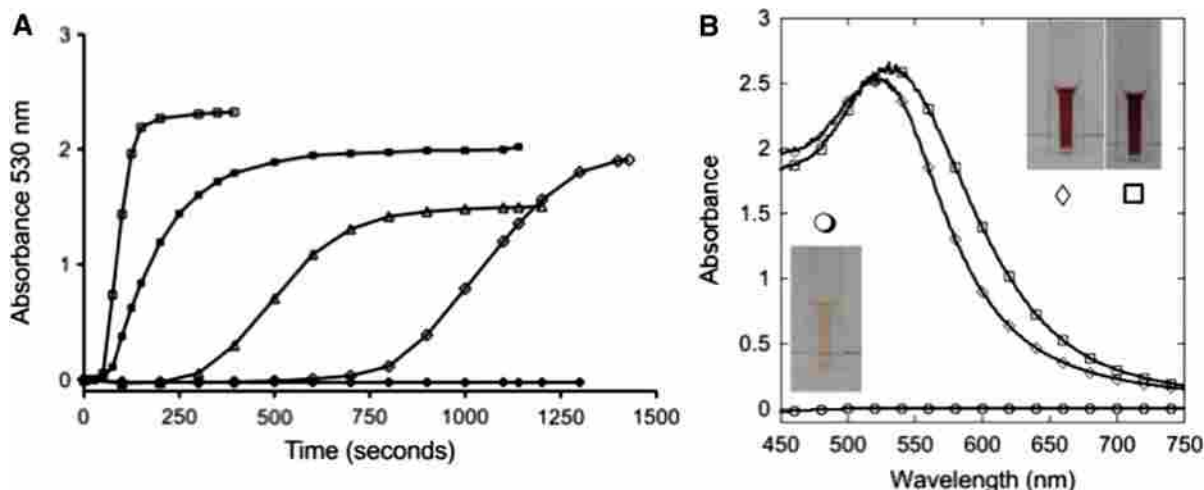
Fig. 2 Spectrophotometric analysis of AuNPs. **a** Solutions were prepared with ferritin, citrate, and $AuCl_4^-$ in the following buffers and illumination conditions and the formation of AuNPs was monitored by following the change in absorbance at 530 nm with time. *Square* MOPS with illumination, *filled square* MOPS dark, *triangle* water illuminated, *diamond* TRIS illuminated, and *filled diamond* TRIS dark. In addition, the water sample was also analyzed in the dark and was identical to TRIS in the dark. **b** The spectrum of AuNPs from the TRIS illuminated (*diamond*) and MOPS illuminated (*square*) reactions. The lower spectrum represents for spectrum of the samples prior to illumination (*circle*). Insets show photos of the solutions before and after illumination according to buffer conditions shown by symbols

not yet been elucidated. The lower final absorbance in the water sample is believed to be due to a lack of buffering as the reaction proceeds.

TEM was used to further characterize the AuNPs (Fig. 3). Electron micrographs of the illuminated TRIS sample (Fig. 3a) show the formation of spherical AuNPs with diameters of 5.7 ± 1.6 nm (size distribution is shown in Fig. S1). In comparison, the illuminated MOPS sample shows a mixture of 15–30 nm diameter particles that are more irregularly shaped and smaller, spherically shaped particles (Fig. 3b). For further clarification, a MOPS dark sample was prepared that only showed the 15–30 nm diameter irregularly shaped particles (Fig. 3c). These results suggest that the particles formed in the MOPS illuminated sample represents a mixture of light and dark reactions where light reactions form smaller ~ 6-nm diameter particles and chemical reduction (dark reactions) form larger 15–30-nm diameter particles.

Ferritin was shown to act as a nucleation site for AuNP formation by performing controls in MOPS in the absence of ferritin (Fig. 3d). In the absence of ferritin, large gold aggregates form and demonstrates that ferritin acts as a nano-architecture structure to guide the size and shape of the chemically reduced AuNPs (Zhang et al. 2007).

The illuminated MOPS reaction produced both large and small AuNPs (Fig. 3b) and is proposed to be a mixture of both the light catalyzed reaction (small particles) and dark chemical reduction reaction (larger particles). Since the light reaction proceeds at a faster rate, we hypothesized that the AuNP size could be controlled in MOPS buffer by manipulating when $AuCl_4^-$ was added to the reaction. A MOPS sample was prepared by mixing all of the components of the reaction mixture except for the $AuCl_4^-$ and the sample was placed in the spectrophotometer and the light was focused on the sample. This prevented the chemical reduction (dark reaction) from beginning prior to illumination. While the solution was illuminated, $AuCl_4^-$ was added and the reaction proceeded as detected by SPR band formation at 530 nm. We refer to this reaction as the pre-illuminated MOPS reaction. The product that formed in this reaction was red and not purple as seen previously for MOPS reactions. Figure 4 compares the spectrum of the product of the MOPS pre-illuminated reaction with a sample illuminated in TRIS. Both show spectra for the SPR maxima at 530 nm with nearly identical peak width (Fig. 4a). Furthermore, the TEM images show similar sized spherically shaped particles with a diameter of

Fig. 3 TEM of AuNPs formed under different conditions. TEM of AuNPs formed by **a** illuminating ferritin in TRIS, **b** illuminating ferritin in MOPS, **c** chemical reduction by MOPS in the presence of ferritin, and **d** chemical reduction by MOPS in the absence of ferritin
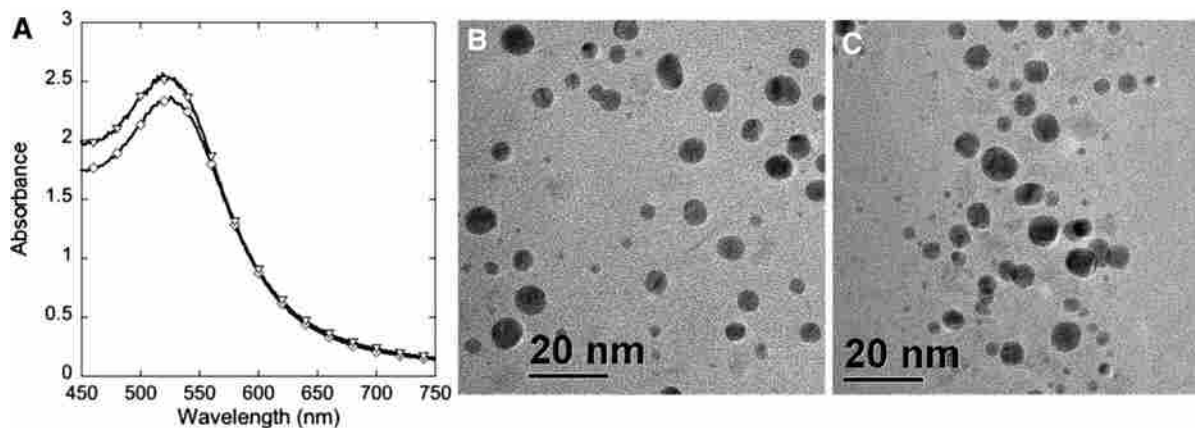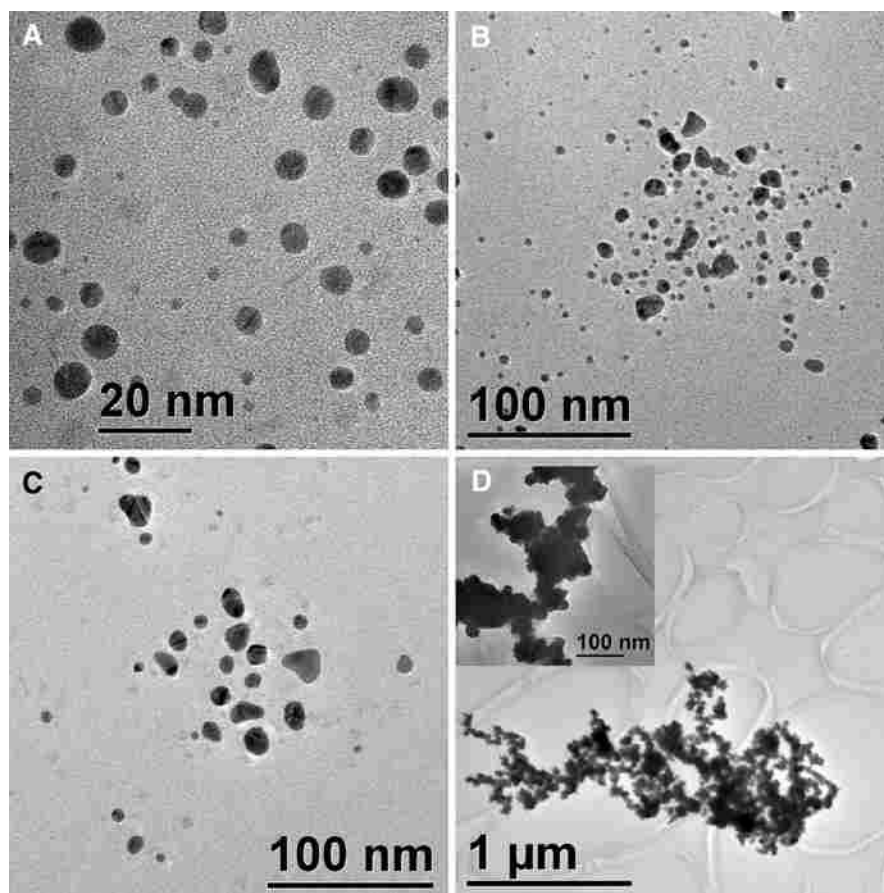
Fig. 4 MOPS reactions pre-illuminated prior to $AuCl_4^-$ addition. **a** Comparison of the spectrum of (*diamond*) TRIS illuminated AuNPs with (*downward triangle*) pre-illuminated MOPS AuNPs, **b** TEM of TRIS illuminated AuNPs, and **c** TEM of MOPS pre-illuminated AuNPs

5.7 ± 1.6 nm for reactions in TRIS (Fig. 4b, Fig. S1) compared to diameters of 5.5 ± 1.8 nm for the reaction in MOPS (Fig. 4c, Fig. S1). These data indicate that illumination prior to the addition of $AuCl_4^-$ to MOPS selectively drives product formation by the photoreduction reaction.

Control reactions in TRIS in the absence of ferritin but with citrate and $AuCl_4^-$ failed to produce AuNPs upon illumination. Similar reactions adding apo ferritin to citrate and Au(III) in TRIS failed to produce AuNPs under illumination indicating that the ferrihydrite mineral inside ferritin is the photocatalyst. To determine if ferrihydrite in the absence of ferritin could catalyze the formation of AuNPs we repeated the reaction using a colloidal suspension of ferrihydrite nanoparticles (ferrihydrite nanoparticle powder shown in Fig. 5a) with an average size of 10 nm (a kind gift from Dr. Brian Woodfield) (Liu et al. 2007). The product of this reaction was a gray precipitate (Fig. 5b shows the dried product) and not the red or purple solution that is indicative of soluble AuNP formation. TEM of the gray precipitate (Fig. 5c) shows large aggregates and not discrete nanoparticles. These controls confirm that the protein shell is essential for the formation and solubility of the AuNPs. We propose that the protein shell (1) separates the ferrihydrite photocatalyst from the nucleating gold particles and prevents interactions between the iron and gold that lead to precipitation reactions between these metals; (2) provides amino acid residues on the protein exterior surface that act as nucleation sites for gold deposition; and (3) acts as a capping agent for the AuNPs to maintain solubility.

To confirm that ferritin allows the AuNPs to remain soluble, the following control reaction was performed. Apo ferritin, $AuCl_4^-$, and ferrihydrite nanoparticles were added to a reaction with TRIS and citrate and illuminated. In this reaction, a purple solution similar to the MOPS reaction was observed indicating that the external surface of apo ferritin is able to stabilize the AuNPs that form by illumination. The purple color suggests that the products of this reaction are larger aggregates instead of smaller AuNPs that produce the red color. In a separate control reaction, the same reactants were used except apo ferritin was replaced by bovine serum albumin and a purple solution also formed indicating that ferrihydrite could catalyze the reaction if protein ligands (capping agents) were present to stabilize the AuNPs that formed.

Understanding the elemental composition of the AuNPs is important in determining if the AuNPs form inside ferritin or on the outside surface. One potential mechanism for AuNP formation is that Au^{3+} ions enter ferritin and that the iron mineral surface acts as a nucleation site for the photoreduction and deposition of AuNPs inside ferritin (Ensign et al. 2004). This is a particularly appealing proposal because the illuminated TRIS samples produced ~ 6-nm diameter sized nanoparticles which compares favorably to the inner dimension of the ferritin interior (~ 8 nm diameter interior) (see Figs. 3a, 4b and c). If the ferritin iron core is the site of reduction and nucleation of the nascent AuNPs, the new

Fig. 5 Reactions to form AuNPs with ferrihydrite nanoparticles. Using identical conditions to the previous studies, ferrihydrite nanoparticles were substitute for ferritin in the reactions. **a** Photograph of the 10-nm-diameter ferrihydrite powder used to prepare a colloidal suspension to act as a photocatalyst for AuNP synthesis. **b** Photograph of the dried product that formed when ferrihydrite nanoparticles were illuminated with citrate and $AuCl_4^-$. **c** TEM of the sample shown in **b**

particles should be a mixture of both gold and iron. Therefore, the elemental composition of the resulting particles was analyzed by XEDS for gold and iron. Figure 6a shows two highlighted nanoparticles, a bright particle that contains gold due to the electron scattering in box 1, and a faint particle corresponding to what is presumably ferritin with an iron core in box 2. The elemental composition of the nanoparticles is shown in Fig. 6b for the box 1 and Fig. 6c for box 2. Figure 6b confirms that box 1 is a AuNP but shows evidence of a small iron peak. Box 2, which is the less intense and smaller nanoparticle, shows an iron XEDS signal as well as a gold signal. These results are consistent with gold nucleating on the iron core surface followed by growth of the AuNP.

Size-exclusion chromatography was used as another method to determine if AuNPs were forming inside ferritin. The presence of AuNPs or ferritin in the fractions was detected by monitoring the absorbance of fractions eluted from this column. The first peak eluted at ∼8 mL (labeled peak #1 in Fig. 7) and showed absorbance at both 530 and 280 nm representing AuNPs and ferritin, respectively. A second peak (labeled as peak #2 in Fig. 7) eluted at 10–11 mL, where purified ferritin normally elutes from this column. This peak was predominantly a protein peak (280 nm absorbance) with smaller amounts of AuNPs (530 nm absorbance).

Figure 7 shows the major elution peak (peak #1) from the size-exclusion column at ∼8 mL. This
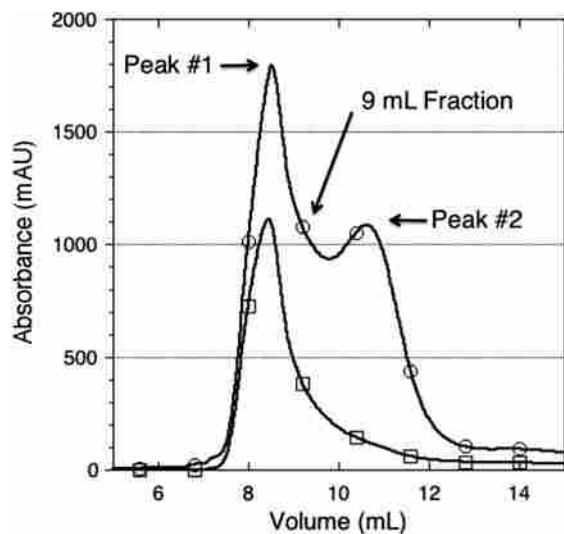
Fig. 7 Size-exclusion chromatography of samples prepared in TRIS. The size-exclusion elution profile of a sample prepared by illumination in TRIS. Wavelengths of 280 nm (*circle*) and 530 nm (*square*) detect ferritin and AuNPs, respectively

fraction elutes much earlier than native ferritin (peak #2). This peak had an intense protein peak (280 nm absorbance) and an intense AuNP peak (530 nm absorbance). Inductively coupled plasma emission spectroscopy (ICP-ES) analysis of this fraction showed the highest concentration of gold in any of the fractions (data not shown). This fraction was studied by TEM using uranyl acetate to stain for the ferritin protein shell and shows both AuNPs and
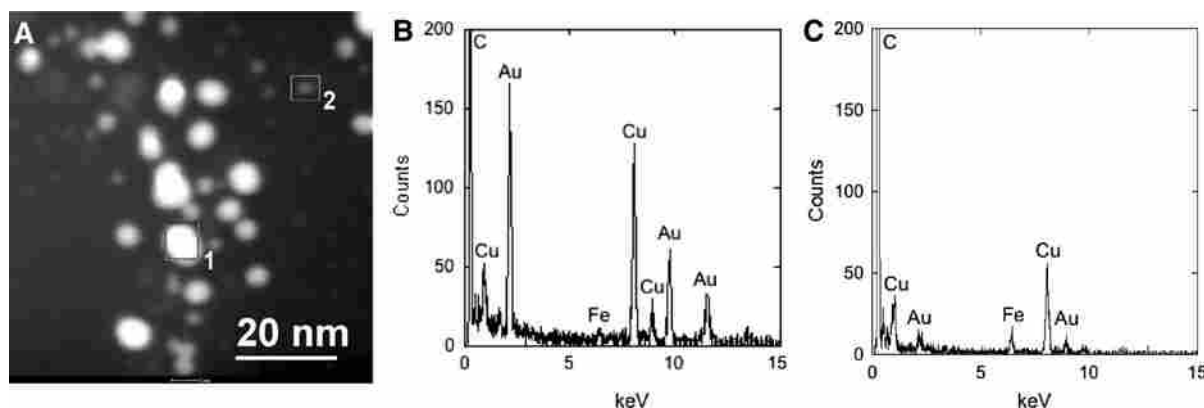
Fig. 6 STEM and XEDS of particles formed in TRIS. **a** STEM image of gold particles formed by illumination of ferritin and $AuCl_4^-$ in TRIS. *Box 1* corresponds to the XEDS graph in panel **b**. *Box 2* corresponds to XEDS spectrum in panel **c**. **b** Spectrum from XEDS on *box 1*, presumably a gold

particle. Strong gold peaks are observed at the characteristic locations. In addition, iron's characteristic peak is observed. This indicates that iron is nearby or within the gold particle. **c** This smaller, less dense particle (*box 2*) is confirmed to be iron by XEDS and shows a small gold peak

ferritin in this fraction (Fig. 8a, b). The elution of this fraction (8 mL) prior to the expected elution volume of ferritin (10–11 mL) suggests a large hydrodynamic radius for the eluting molecules. Since ferritin is observed in this fraction it suggests that ferritin is attached to AuNPs and these two particles are co-migrating. The arrows (Fig. 8) point to ferritin molecules adjacent to AuNPs. The ferritin is the lighter halo that surrounds the slightly darker iron cores. The thickness of the white halos is consistent with the 2 nm thickness of the ferritin protein shell. The TEM images confirm that ferritin is found adjacent or attached to AuNPs and explains why ferritin eluted much earlier than expected. This suggests that AuNPs form on the external surface of ferritin. Since this fraction contains the majority of the AuNPs (greatest absorbance at 530 nm) it appears this is the predominant reaction forming AuNPs under the conditions we tested.

This mechanism would require a gold nucleation site on the external surface of ferritin where the gold binds and grows. Based on this mechanism, we would expect to observe smaller "gold seeds" that are in the early process of growth. These "seeds" might be observed in later fractions of the size-exclusion column because these "seeds species" would have a smaller hydrodynamic radius than those observed in Fig. 8. To test this hypothesis, we prepared samples for TEM analysis from the fraction that eluted at 8 mL from the size-exclusion column (peak #2 in Fig. 7), but this fraction contained ferritin with very few AuNPs. Although a peak does not exist at the 9 mL fraction from the gel filtration column (9 mL fraction Fig. 7) we observed a fairly strong absorbance at both 280 and 530 nm in this fraction so it was studied for ferritin and AuNPs.

The inset in Fig. 8 shows a STEM image of a representative ferritin observed in this fraction and shows two very small 1–2 nm gold particles attached to the protein surface. The presence of small "gold seeds" attached to ferritin is consistent with the hypothesis that gold ions nucleate on the external surface of ferritin followed by growth of the AuNP. Figure 10 shows a model of how this reaction may proceed.

Figure 10 suggests there is a metal nucleation site near the exterior surface of ferritin. A likely location might be the threefold channel of ferritin, which contains cysteine amino acid residues that
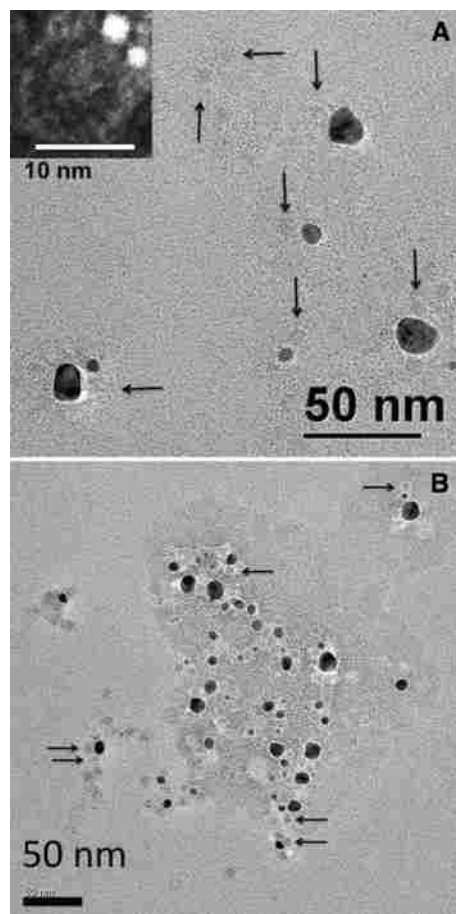
Fig. 8 AuNP formation on exterior surface of ferritin. TEM image of the sample that eluted at 8 mL from the size-exclusion column. The sample was prepared and stained with uranyl acetate on TEM grids as described in the "Materials and methods" section. The *arrows* identify ferritin molecules that are adjacent to AuNPs. The presence of ferritin in this elution fraction suggests that ferritin is attached to these AuNPs. The samples in **a** and **b** represent different images at different magnifications. *Inset* shows a STEM image from the 9 mL fraction (Fig. 7) from the size-exclusion column. This image shows small AuNPs (seeds) attached to the external surface of ferritin

have high affinity for binding gold. Kim et al. demonstrated that small AuNPs were able to bind at the threefold channel sites (Kim et al. 2010). Once gold has nucleated on ferritin, electrons can be transferred to this site as a method of reduction and nanoparticle growth. Electron transfer through the 2-nm protein shell has been previously demonstrated by several methods (Watt et al. 1988; Zhang and Watt 2007; Marken et al. 2002; Cherry et al. 1998).
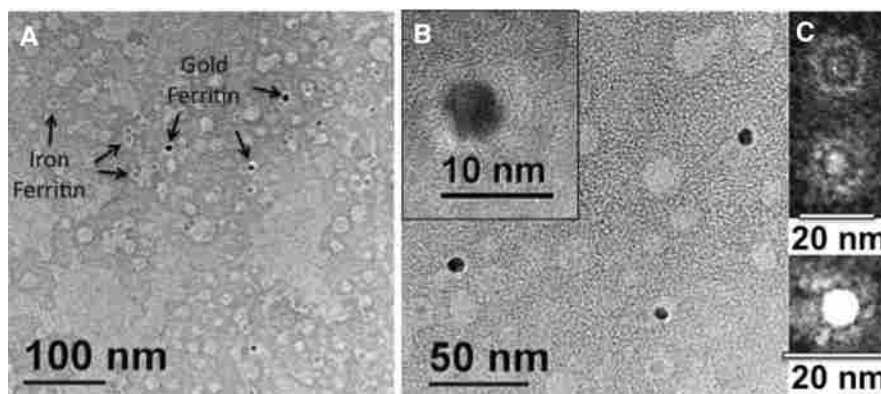
Fig. 9 AuNP formation inside ferritin. The 9 mL fraction (Fig. 7) that eluted from the size-exclusion column shows AuNPs surrounded by a white halo. These TEM images were stained by uranyl acetate, to allow visualization of the protein shell (*white halos*). **a** A comparison of ferritin with iron inside with ferritin containing gold. **b** Shows greater magnifications of the gold containing ferritin. **c** STEM analysis of iron and gold containing ferritin. Top is a ferritin containing iron. Middle is a ferritin with a brighter mineral core suggesting a mixture of gold and iron. Bottom is a ferritin with a very bright interior, indicative of gold inside ferritin. The sample is stained with uranyl acetate to visualize the ferritin
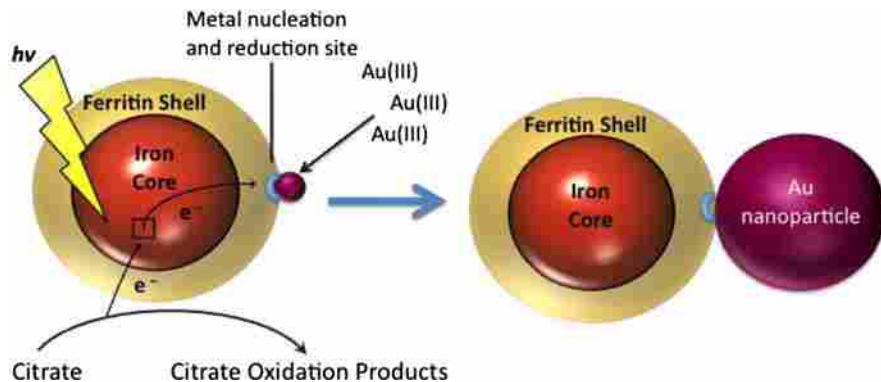
Fig. 10 Mechanism of AuNP formation by ferritin illumination. Ferritin possesses a putative nucleation site that attracts Au(III) ions. Photochemical excitation of the iron core transfers electrons across the ferritin protein shell to reduce the Au(III) ions. The electron holes created by this photochemistry are replenished from the sacrificial electron donor citrate. The initial gold particle acts as a nucleation site that attracts more Au(III), which in turn are reduced and deposited on the growing gold particle

The model shown in Fig. 10 conflicts with one of the proposed model for chromate reduction by ferritin as the authors suggested that reduction occurred inside ferritin rather than on the exterior surface (Kim et al. 2002). This model was based on the observation that some of the Cr(III) product was observed inside ferritin but that Cr(III) did not diffuse into ferritin. In contrast, an alternate model showed that the majority Cr(III) produced was found in the exterior solution but not attached to ferritin. This might be rationalized by the fact that gold has a much higher affinity for thiolate ligands than Cr(III) and may stay attached to ferritin, whereas the formation of Cr(III) on the exterior surface would more easily dissociate into solution. Therefore, our results suggest that the model showing AuNP reduction on the exterior surface of ferritin and the chromate reduction on the exterior surface of ferritin are consistent. The fact that both studies show smaller amounts of product on the interior of ferritin suggests another mechanism also exist for metal reduction on the interior of ferritin, but the mechanism is not yet established for how this occurs.

Fraction #9 from the gel filtration also showed other ferritin samples of interest. TEM analysis produced images that show AuNPs surrounded by ferritin (Fig. 9). The ferritin is visualized by staining

with uranyl acetate, which is visualized as a white halo (Fig. 9a, b). The arrows in Fig. 9a identify gold ferritin nanoparticles and compare them to iron-containing ferritin molecules (white halos with less intensity due to iron). STEM analysis (Fig. 9c) shows ferritin stained with uranyl acetate with a very faint mineral core signal due to iron in the core (top), ferritin with a much brighter core indicating a mixture of gold and iron (middle), and a gold core inside ferritin (bottom). This is consistent with the XEDS analysis shown in Fig. 6b, c. These three images suggest that there might be a progression from an iron core to a gold core as gold nucleates and grows within the ferritin protein shell. Another explanation for this observation is that the ferritin sample has different iron loadings based on the inhomogeneity of the native ferritin sample. Perhaps different iron content leads to different gold loading on the interior of ferritin molecules.

Conclusions

In summary, we have presented a photochemical method to prepare protein stabilized ~ 6 nm diameter spherically shaped AuNPs using ferritin as a photo-catalyst. Our results are consistent with two pathways for AuNP formation. One pathway is gold deposition on the inside of ferritin, where gold is proposed to nucleate in the iron core of ferritin (Fig. 9). The second is an external AuNP growth pathway observed in Fig. 8 and a model of this reaction is shown in Fig. 10. We are currently exploring synthetic pathways to control whether the AuNPs form inside ferritin or on the exterior surface.

References

Arosio P, Ingrassia R, Cavadini P (2009) Ferritins: a family of molecules for iron storage, antioxidation and more. Biochim Biophys Acta 1790(7):589–599. doi:10.1016/j.bbagen.2008.09.004

Bhaviripudi S, Mile E, Steiner SA, Zare AT, Dresselhaus MS, Belcher AM, Kong J (2007) Cvd synthesis of single-walled carbon nanotubes from gold nanoparticle catalysts. J Am Chem Soc 129(6):1516–1517. doi:10.1021/ja0673332

Butts CA, Swift J, Kang SG, Di Costanzo L, Christianson DW, Saven JG, Dmochowski IJ (2008) Directing noble metal ion chemistry within a designed ferritin protein. Biochemistry 47(48):12729–12739. doi:10.1021/bi8016735

Cao YWC, Jin RC, Mirkin CA (2002) Nanoparticles with Raman spectroscopic fingerprints for DNA and RNA detection. Science 297(5586):1536–1540

Cherry RJ, Bjornsen AJ, Zapien DC (1998) Direct electron transfer of ferritin adsorbed at tin-doped indium oxide electrodes. Langmuir 14(8):1971–1973. doi:10.1021/la970685p

Chikae M, Fukuda T, Kerman K, Idegami K, Miura Y, Tamiya E (2008) Amyloid-[beta] detection with saccharide immobilized gold nanoparticle on carbon electrode. Bioelectrochemistry 74(1):118–123

Daniel M-C, Astruc D (2003) Gold nanoparticles: assembly, supramolecular chemistry, quantum-size-related properties, and applications toward biology, catalysis, and nanotechnology. Chem Rev 104(1):293–346. doi:10.1021/cr030698+

Domìnguez-Vera JM, Gálvez N, Sánchez P, Mota AJ, Trasobares S, Hernández JC, Calvino JJ (2007) Size-controlled water-soluble Ag nanoparticles. Eur J Inorg Chem 2007(30):4823–4826

Douglas T, Stark VT (2000) Nanophase cobalt oxyhydroxide mineral synthesized within the protein cage of ferritin. Inorg Chem 39(8):1828–1830

Douglas T, Dickson DPE, Betteridge S, Charnock J, Garner CD, Mann S (1995) Synthesis and structure of an iron (iii) sulfide-ferritin bioinorganic nanocomposite. Science 269(5220): 54–57

Ensign D, Young M, Douglas T (2004) Photocatalytic synthesis of copper colloids from Cu(II) by the ferrihydrite core of ferritin. Inorg Chem 43(11):3441–3446

Esumi K, Matsuhisa K, Torigoe K (1995) Preparation of rod-like gold particles by UV irradiation using cationic micelles as a template. Langmuir 11(9):3285–3287. doi: 10.1021/la00009a002

Eustis S, Hsu H-Y, El-Sayed MA (2005) Gold nanoparticle formation from photochemical reduction of Au³⁺ by continuous excitation in colloidal solutions. A proposed molecular mechanism. J Phys Chem B 109(11):4811–4815. doi:10.1021/jp0441588

Fan RL, Chew SW, Cheong VV, Orner BP (2010) Fabrication of gold nanoparticles inside unmodified horse spleen apoferritin. Small 6(14):1483–1487. doi:10.1002/smll.201000457

Galvez N, Sanchez P, Dominguez-Vera JM (2005) Preparation of Cu and CuFe Prussian blue derivative nanoparticles using the apoferritin cavity as nanoreactor. Dalton Trans 7(15):2492–2494. doi:10.1039/b506290j

Galvez N, Sanchez P, Dominguez-Vera JM, Soriano-Portillo A, Clemente-Leon M, Coronado E (2006) Apoferritin-encapsulated Ni and Co superparamagnetic nanoparticles. J Mater Chem 16(26):2757–2761

Habib A, Tabata M, Wu YG (2005) Formation of gold nanoparticles by good's buffers. Bull Chem Soc Jpn 78:262–269

Hainfeld JF (1992) Uranium-loaded apoferritin with antibodies attached: molecular design for uranium neutron-capture therapy. Proc Natl Acad Sci USA 89(22):11064–11068

Harrison PM, Arosio P (1996) The ferritins: molecular properties, iron storage function and cellular regulation. Biochim Biophys Acta 1275(3):161–203

Hilton RJ, Keyes JD, Watt RK (2010a) Maximizing the efficiency of ferritin as a photocatalyst for applications in an

artificial photosynthesis system. In: Varadan VK (ed) SPIE smart structures/NDE 2010, San Diego, CA. SPIE nanosensors, biosensors and info-tech sensors and systems. Proc. of SPIE, p 76460J

Hilton RJ, Keyes JD, Watt RK (2010b) Photoreduction of Au(III) to form Au(0) nanoparticles using ferritin as a photocatalyst. In: Varadan VK (ed) SPIE smart structures/NDE 2010, San Diego, CA. SPIE nanosensors, biosensors and info-tech sensors and systems. Proc. of SPIE, pp 764601–764607

Huang WC, Chen YC (2008) Photochemical synthesis of polygonal gold nanoparticles. J Nanopart Res 10(4):697–702. doi: 10.1007/s11051-007-9293-8

Iwahori K, Yoshizawa K, Muraoka M, Yamashita I (2005) Fabrication of ZnSe nanoparticles in the apoferritin cavity by designing a slow chemical reaction system. Inorg Chem 44(18):6393–6400. doi:10.1021/ic0502426

Kasyutich O, Ilari A, Fiorillo A, Tatchev D, Hoell A, Ceci P (2010) Silver ion incorporation and nanoparticle formation inside the cavity of pyrococcus furiosus ferritin: structural and size-distribution analyses. J Am Chem Soc 132(10):3621–3627. doi:10.1021/ja910918b

Katz E, Willner I (2004) Integrated nanoparticle-biomolecule hybrid systems: synthesis, properties, and applications. Angew Chem Int Ed 43(45):6042–6108

Kim I, Hosein HA, Strongin DR, Douglas T (2002) Photochemical reactivity of ferritin for Cr(VI) reduction. Chem Mater 14(11):4874–4879

Kim JW, Posey AE, Watt GD, Choi SH, Lillehei PT (2010) Gold nanoshell assembly on a ferritin protein employed as a bio-template. J Nanosci Nanotechnol 10(3): 1771–1777

Klem MT, Mosolf J, Young M, Douglas T (2008) Photochemical mineralization of europium, titanium, and iron oxyhydroxide nanoparticles in the ferritin protein cage. Inorg Chem 47(7):2237–2239

Kuong C-L, Chen W-Y, Chen Y-C (2007) Semi-quantitative determination of cationic surfactants in aqueous solutions using gold nanoparticles as reporter probes. Anal Bioanal Chem 387(6):2091–2099

Lee J-S, Ulmann PA, Han MS, Mirkin CA (2008) A DNA–gold nanoparticle-based colorimetric competition assay for the detection of cysteine. Nano Lett 8(2):529–533. doi: 10.1021/nl0727563

Liu J, Lu Y (2003) A colorimetric lead biosensor using DNAzyme-directed assembly of gold nanoparticles. J Am Chem Soc 125(22):6642–6643. doi:10.1021/ja034775u

Liu J, Lu Y (2006) Fast colorimetric sensing of adenosine and cocaine based on a general sensor design involving aptamers and nanoparticles. Angew Chem Int Ed 45(1): 90–94

Liu SF, Liu QY, Boerio-Goates J, Woodfield BF (2007) Preparation of a wide array of ultra-high purity metals, metal oxides, and mixed metal oxides with uniform particle sizes from 1 nm to bulk. J Adv Mater 39(2):18–23

Lowry OH, Rosebrough NJ, Farr AL, Randall RJ (1951) Protein measurement with the folin phenol reagent. J Biol Chem 193(1):265–275

Mallick K, Witcomb MJ, Scurrell MS (2005) Polymer-stabilized colloidal gold: a convenient method for the synthesis

of nanoparticles by a UV-irradiation approach. Appl Phys A 80(2):395–398

Marken F, Patel D, Madden CE, Millward RC, Fletcher S (2002) The direct electrochemistry of ferritin compared with the direct electrochemistry of nanoparticulate hydrous ferric oxide. New J Chem 26(2):259–263

Meldrum FC, Wade VJ, Nimmo DL, Heywood BR, Mann S (1991) Synthesis of inorganic nanophase materials in supramolecular protein cages. Nature 349(6311):684–687

Meldrum FC, Douglas T, Levi S, Arosio P, Mann S (1995) Reconstitution of manganese oxide cores in horse spleen and recombinant ferritins. J Inorg Biochem 58(1):59–68

Niemeyer CM (2001) Nanoparticles, proteins, and nucleic acids: biotechnology meets materials science. Angew Chem Int Ed 40(22):4128–4158

Nikandrov VV, Gratzel CK, Moser JE, Gratzel M (1997) Light induced redox reactions involving mammalian ferritin as photocatalyst. J Photochem Photobiol B 41(1–2):83–89

Okuda M, Iwahori K, Yamashita I, Yoshimura H (2003) Fabrication of nickel and chromium nanoparticles using the protein cage of apoferritin. Biotechnol Bioeng 84(2): 187–194

Sau TK, Pal A, Jana NR, Wang ZL, Pal T (2001) Size controlled synthesis of gold nanoparticles using photochemically prepared seed particles. J Nanopart Res 3(4): 257–261

Shankar SS, Rai A, Ankamwar B, Singh A, Ahmad A, Sastry M (2004) Biological synthesis of triangular gold nanoprisms. Nat Mater 3(7):482–488

Shin Y, Dohnalkova A, Lin Y (2010) Preparation of homogeneous gold' and silver alloy nanoparticles using the apoferritin cavity as a nanoreactor. J Phys Chem C 114(13):5985–5989. doi:10.1021/jp911004a

Skrabalak SE, Chen J, Au L, Lu X, Li X, Xia Y (2007) Gold nanocages for biomedical applications. Adv Mater Deerfield 19(20):3177–3184. doi:10.1002/adma.200701972

Taton TA, Mirkin CA, Letsinger RL (2000) Scanometric DNA array detection with nanoparticle probes. Science 289(5485):1757–1760

Turner M, Golovko VB, Vaughan OPH, Abdulkin P, Berenguer-Murcia A, Tikhov MS, Johnson BFG, Lambert RM (2008) Selective oxidation with dioxygen by gold nanoparticle catalysts derived from 55-atom clusters. Nature 454(7207):981–983

Turyanska L, Bradshaw TD, Sharpe J, Li M, Mann S, Thomas NR, Patane A (2009) The biocompatibility of apoferritin-encapsulated PbS quantum dots. Small 5(15):1738–1741. doi:10.1002/smll.200900017

Uchida M, Klem MT, Allen M, Suci P, Flenniken M, Gillitzer E, Varpness Z, Liepold LO, Young M, Douglas T (2007) Biological containers: protein cages as multifunctional nanoplatforms. Adv Mater 19(8):1025–1042

Ueno T, Suzuki M, Goto T, Matsumoto T, Nagayama K, Watanabe Y (2004) Size-selective olefin hydrogenation by a Pd nanocluster provided in an apo-ferritin cage. Angew Chem Int Ed 43(19):2527–2530

Watt GD, Jacobs D, Frankel RB (1988) Redox reactivity of bacterial and mammalian ferritin: is reductant entry into the ferritin interior a necessary step for iron release? Proc Natl Acad Sci USA 85(20):7457–7461

Watt RK, Frankel RB, Watt GD (1992) Redox reactions of apo mammalian ferritin. Biochemistry 31(40):9673–9679

Whaley SR, English DS, Hu EL, Barbara PF, Belcher AM (2000) Selection of peptides with semiconductor binding specificity for directed nanocrystal assembly. Nature 405(6787):665–668

Wong KKW, Mann S (1996) Biomimetic synthesis of cadmium sulfide-ferritin nanocomposites. Adv Mater 8(11): 928–932

Xie J, Lee JY, Wang DIC (2007) Seedless, surfactantless, high-yield synthesis of branched gold nanocrystals in hepes buffer solution. Chem Mater 19(11):2823–2830. doi: 10.1021/cm0700100

Yamashita I, Hayashi J, Hara M (2004) Bio-template synthesis of uniform CdSe nanoparticles using cage-shaped protein, apoferritin. Chem Lett 33(9):1158–1159

Yang M, Kostov Y, Bruck HA, Rasooly A (2009) Gold nanoparticle-based enhanced chemiluminescence immunosensor for detection of staphylococcal enterotoxin b (SEB) in food. Int J Food Microbiol 133(3):265–271

Yeh CH, Hung CY, Chang TC, Lin HP, Lin YC (2009) An immunoassay using antibody-gold nanoparticle conjugate, silver enhancement and flatbed scanner. Microfluid Nanofluid 6(1):85–91. doi:10.1007/s10404-008-0298-0

Yoshizawa K, Iwahori K, Sugimoto K, Yamashita I (2006) Fabrication of gold sulfide nanoparticles using the protein cage of apoferritin. Chem Lett 35(10):1192–1193

Zhang B, Watt GD (2007) Anaerobic iron deposition into horse spleen, recombinant human heavy and light and bacteria ferritins by large oxidants. J Inorg Biochem 101(11–12): 1676–1685

Zhang B, Harb JN, Davis RC, Kim JW, Chu SH, Choi S, Miller T, Watt GD (2005) Kinetic and thermodynamic characterization of the cobalt and manganese oxyhydroxide cores formed in horse spleen ferritin. Inorg Chem 44(10):3738–3745. doi:10.1021/ic0490851

Zhang L, Swift J, Butts CA, Yerubandi V, Dmochowski IJ (2007) Structure and activity of apoferritin-stabilized gold nanoparticles. J Inorg Biochem 101(11–12):1719–1729. doi:10.1016/j.jinorgbio.2007.07.023

Zhou Y, Wang CY, Zhu YR, Chen ZY (1999) A novel ultraviolet irradiation technique for shape-controlled synthesis of gold nanoparticles at room temperature. Chem Mater 11(9):2310–2312. doi:10.1021/cm990315h

Maximizing the efficiency of ferritin as a photocatalyst for applications in an artificial photosynthesis system

Robert J. Hilton, Jeremiah D. Keyes, Richard K. Watt*

Brigham Young University, Provo, UT, USA 84602

ABSTRACT

Alternate fuel sources are becoming increasingly important as the reserve of fossil fuels decrease. We describe a photosynthesis mimic that is capable of extracting electrons from sacrificial electron donors. This model is based on the bio-photo-catalyst ferritin. Ferritin is an iron storage protein that naturally sequesters ferrihydrite inside a spherical 12 nm protein shell. Ferrihydrite is a semi-conductor that functions as a photo-catalyst in aqueous solvents. Ferritin has been shown to photoreduce Au^{3+} to form $Au(0)$ nanoparticles. Citrate acts as a sacrificial electron donor to supply electrons for the photoreduction. We describe studies designed to understand the mechanism of this catalyst in order to improve the efficiency of the reaction. We have developed a spectrophotometric assay to simultaneously illuminate the sample and kinetically monitor the formation of products of Au^{3+} reduction. We report that buffers containing sulfur significantly increase the rate of the reactions. Control reactions with colloidal ferrihydrite nanoparticles do not catalyze the photochemical reaction, but produce a black precipitate indicating that the protein shell has an important function in nanoparticle formation.

Keywords: ferritin, ferrihydrite, gold nanoparticles, photoreduction, artificial photosynthesis, photosystem II

1. INTRODUCTION

1.1 Alternate fuel systems

The use of fossil fuels in our society presents two fundamental problems. First, these stores are limited and are continually diminishing. Models predict that non-renewable fossil fuels stores will be extinguished by the year 2112.[1] While fossil fuels will continue to dominate as energy sources in the near future, renewable and reliable long-term energy is essential to sustain current standards of living. Second, the use of these fuels generates pollution that may have significant health and environmental effects. As a result, research into alternate, clean, and renewable energy has reached unprecedented levels. The largest source of renewable energy available comes from the sun. Unfortunately, technologies tapping into this vast energy source are inefficient, albeit promising.

1.2 Photosynthesis model

Nature has long used an efficient method of extracting the sun's energy using photosynthesis. The first stage of photosynthesis relies on light-dependent reactions. A group of proteins, collectively referred to as Photosystem II (PSII), uses photons of light to create a charge separation at the P680 reaction center (Fig. 1).[2] The source of electrons in photosynthesis is water, which is oxidized by the water-oxidizing complex (WOC) made up of a tetra-manganese cluster.[3] The electron acceptors in the photosystem II complex siphon electrons away from the P680 reaction center to prevent recombination.[4] The reductive power generated by photosynthesis is used in anabolic processes, in particular to synthesize sugars that can be stored or used for energy.

*rwatt@chem.byu.edu; phone 1 801 422-1923; fax 1 801 422-0153; http://people.chem.byu.edu/rwatt
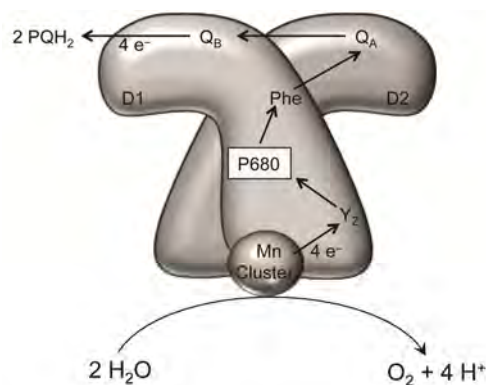
Figure 1. Reaction center of photosystem II. The electrons from water are channeled through the protein complex to an external electron acceptor.

1.3 Ferritin model

Our research goal is to mimic the P680 charge separation reaction using ferritin as a photocatalyst. The model for our system is shown in Figure 2. Ferritin is an iron storage protein found in nearly all forms of life.[5] It is a spherical nanocage of 450 kDa.[6] Iron is stored within ferritin as ferrihydrite.[7] We use ferritin as a P680 reaction center mimic because ferrihydrite is a semi-conductor with a band gap of appropriate energy to allow electron excitation in the UV/Vis light range.[8] Furthermore, the electron trapped in the conduction band is long-lived, allowing ferritin to diffuse and interact with other species in solution. Finally, ferritin can oxidize organic acids in solution as a WOC mimic.[8] In the PSII system, the abundant electron donor is water; in our system citrate is the abundant and inexpensive electron donor.
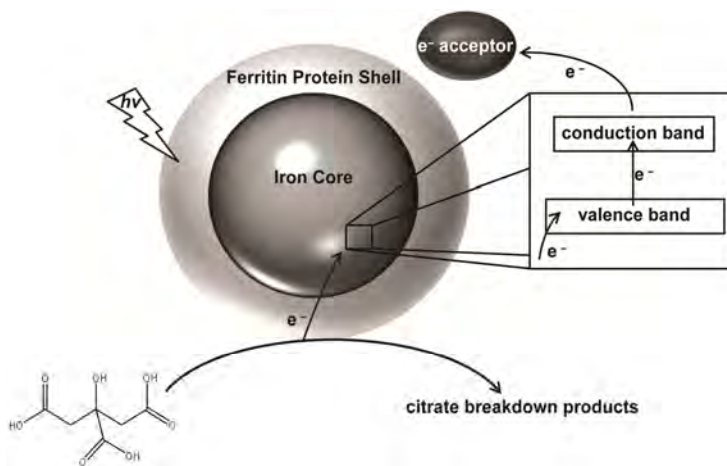
Figure 2. The ferritin P680 mimic. Upon illumination, electrons are excited from the valence band to the conduction band of the ferrihydrite semi-conductor. The valence band is filled with an electron from the sacrificial electron donor citrate. The excited electrons are transferred to an electron acceptor.

In our lab, initial studies using this model gave results that were not consistently reproducible. Our goal was to maximize the ability of ferritin to act as a photocatalyst and the irreproducibility was a stumbling block in achieving this goal. To gain a better understanding of this photocatalytic system experiments were designed that would identify the minimal requirements for photocatalysis to occur. The advantage of this system is that when Au^{3+} ions are reduced to Au(0), the gold nanoparticles that form (5–30 nm diameter particles) possess plasmon resonance properties that give a distinct color change to the solution.[9, 10] This provides an easy colorimetric assay to monitor the progress of the reaction. In this report we use this assay to test conditions that increase or decrease the reaction rate. By doing these studies, we advance our understanding of the fundamental requirements for this catalyst to function. These principles will be used to improve the reactivity of the ferritin photocatalyst to allow more efficient P680 mimics to be designed.

2. MATERIALS AND METHODS

2.1 Ferritin preparation

Holoferritin (Sigma) was dialyzed against thioglycolic acid to remove the native iron core.[11] Reconstitution of ferritin cores to desired iron loadings was performed as described previously.[12] Briefly, reconstituted ferritin was prepared by adding equivalents of 100 Fe^{2+}/ferritin to a ferritin solution that was stirred in air. Additional aliquots of Fe^{2+} were added every 10 minutes until the desired iron loading (1000 Fe/ferritin) was obtained. The protein concentration was measured using the Lowry method[13] and the iron concentration was measured after dithionite reduction, followed by addition of bipyridine to measure the $[Fe(bipyridine)_3]^{2+}$ complex at 520nm ($\varepsilon_{520} = 8400$).[14]

2.2 Metal nanoparticle formation

Au nanoparticles were prepared by mixing reconstituted ferritin, the sacrificial electron donor citrate, and $AuCl_4^-$ in a quartz cuvette followed by illumination with an Oriel Hg lamp (model 66056), similar to conditions reported by Ensign.[15] Sample temperature was maintained using a water-circulating cuvette holder connected to a 15 ℃ water bath. The final volume of each sample was 1 mL. The final concentrations were: 0.150 mg/ml protein, 0.33 mM iron, 32 mM citrate, 0.125 M NaCl, and 0.66 mM Au^{3+}. These sample conditions correspond to 1000 Fe per ferritin and 2000 Au atoms per ferritin. We used varied concentrations of tris(hydroxymethyl)aminomethane (TRIS), 3-(N-morpholino)propanesulfonic acid (MOPS), 2-(*N*-morpholino)ethanesulfonic acid (MES), phosphate, or carbonate buffers at pH 7.4 to determine the effect these buffers have on the reaction. The buffer concentrations are reported in the figure legends.

2.3 Electron microscopy

Transmission electron microscopy (TEM) was performed on a Tecnai F30 TEM, 140 kV. Samples were prepared by placing 3 μL of sample solution onto ultrathin lacey carbon film copper EM grids (Ted Pella, product number 01824). The excess solution was wicked off, and the grid was rinsed in deionized water. Prior to loading on the grids, some samples were purified by performing FPLC on a GE Healthcare AKTApurifier. A Superdex[TM] 200 10/300 GL size exclusion column was used for these separations.

3. RESULTS AND DISCUSSION

3.1 Buffers affect the rate of nanoparticle formation with illumination

After only a few minutes of illumination, a deep red colored solution begins to appear with a maximum peak at ~530 nm (Fig. 3A). This peak corresponds to the plasmon resonance band of gold nanoparticles.[9, 10] TEM studies show that the products of this reaction correspond to 5−10 nm gold nanoparticles (Fig. 3B).
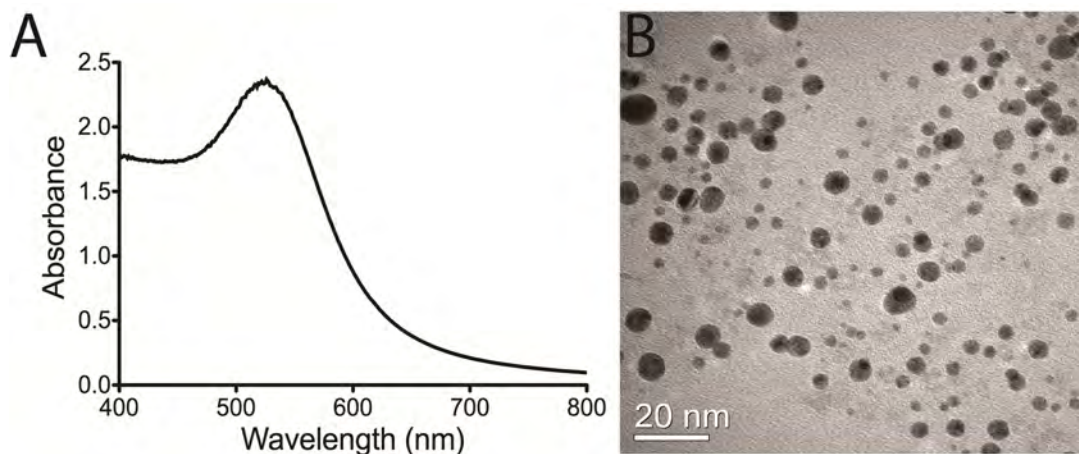
Figure 3. Gold nanoparticles formed by illumination of Ferritin. A) Upon illumination, the solution turns red and an absorbance peak is observed at 530 nm. B) Electron micrograph of the particles formed in the illumination reaction. Particles are of a relatively uniform size with spherical morphology.

Buffers play an important role in the photoreductive process. Buffers containing sulfur atoms (MOPS and MES) were shown to enhance the rates of the reactions, compared to the control in water (Fig. 4A and 4B). TRIS buffer also seemed to have a stimulatory effect on the rate of the reaction, but only at low concentrations (Fig. 4C). At higher concentrations (>5mM), TRIS appears to have an inhibitory effect on the rate. Interestingly, MOPS has a higher stimulatory effect than does MES (Fig. 4D), although these buffers differ in structure by a single carbon.
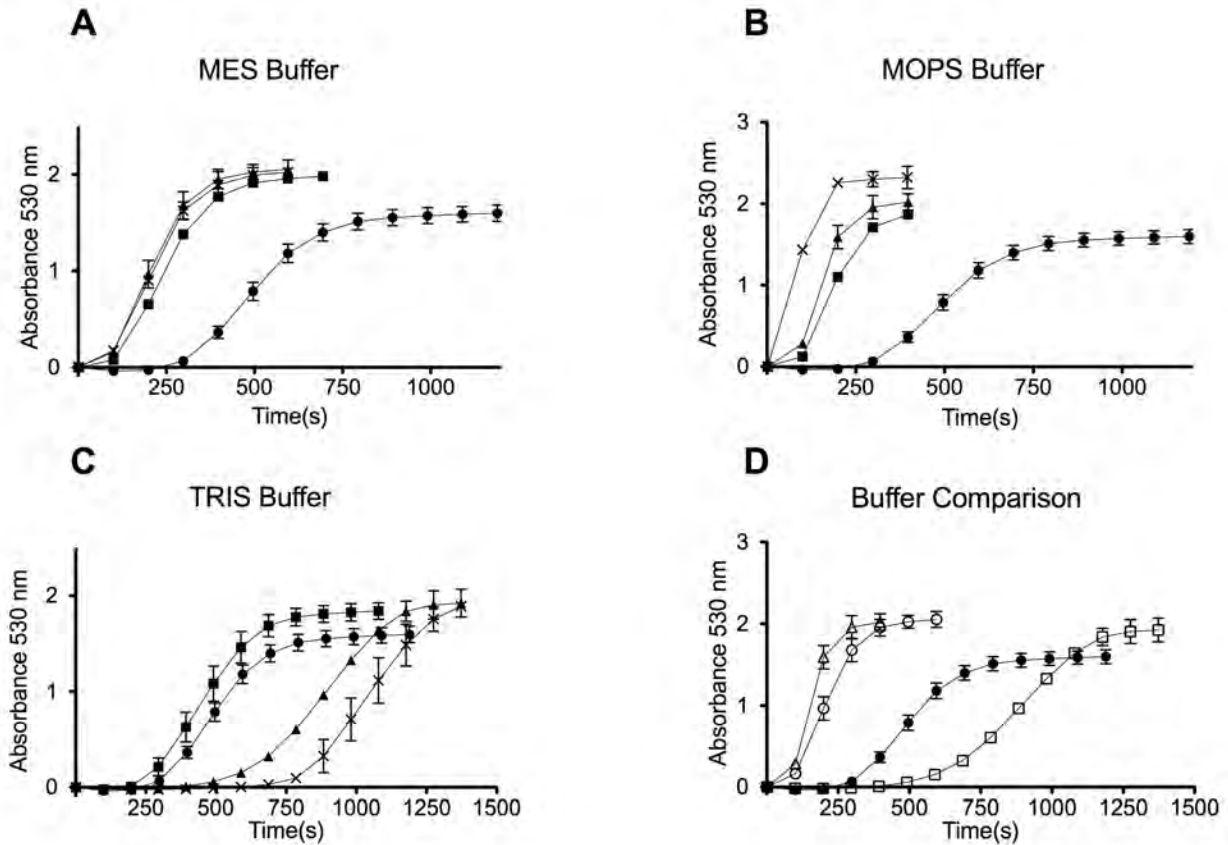
Figure 4. Buffers influence the kinetics of gold nanoparticle formation during illumination. A) MES buffer, B) MOPS buffer, and C) TRIS buffer. ● – control without buffer. ■ – 5 mM buffer. ▲ – 25 mM buffer. X – 50 mM buffer. D) Comparison of different buffers at 25 mM. ● – control without buffer, Δ – MOPS, ○ – MES, and □ – TRIS.

Phosphate and carbonate buffers had no effect on the rate of the reaction compared to a control without buffer (Fig. 5A). However, upon reaction completion, the sample solutions had slightly different red colors. Spectrophotometric analysis of the colored solutions showed that the control in water had an absorption maximum at 520 nm. The maximum peak was observed to change depending on the buffer with the following maxima observed for each of the following buffers: phosphate (515 nm), carbonate (530 nm), MOPS with illumination (530 nm), and MOPS in the dark (540 nm) (Fig. 5B). Additionally, we report peak maxima for TRIS (520 nm), MES with illumination (530 nm), and MES in the dark (540 nm) (data not shown). The plasmon resonance peak of gold nanoparticles is known to shift depending on the size of the particles that form.[9, 10] Collectively, these data suggest that buffers can influence the reactions by altering the rate of formation and the size of the resulting nanoparticles.
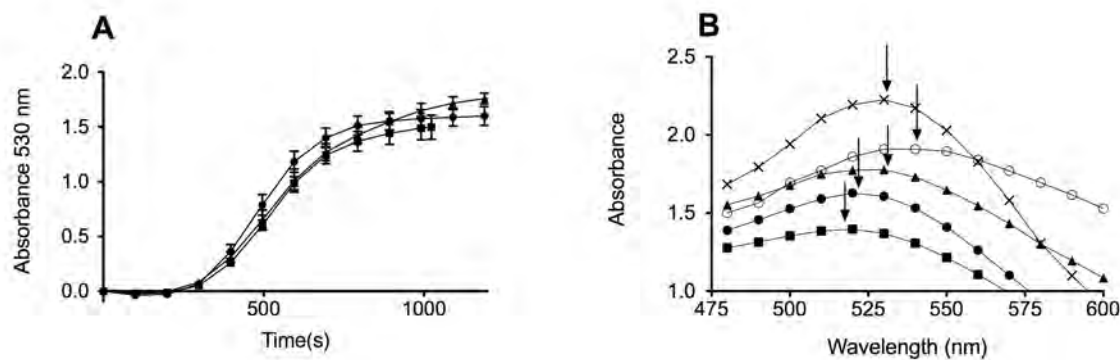
Figure 5. Product formation depends upon the buffers used in the reaction. A) Kinetic run of 10 mM phosphate and carbonate buffers compared to control. ● – control no buffer, ■ – PO_4^{3-} buffer, and ▲ – CO_3^{2-} buffer. B) Final absorbance around 530 nm with arrowheads pointing to peak maxima. ● – control no buffer (520 nm), ■ – PO_4^{3-} buffer (515 nm), ▲ – CO_3^{2-} buffer (530 nm), X – MOPS with illumination (530 nm), and ○ – MOPS in the dark (540 nm).

3.2 Buffers affect the rate of nanoparticle formation in the dark

Previous studies have shown that MOPS buffer is able to reduce Au^{3+} ions to gold nanoparticles in the presence of ferritin without illumination.[16] To confirm these results and compare the dark reactions with the illuminated reactions, the experiments were repeated in the dark. Figure 6 shows data that represent how quickly the reaction reaches completion in the light versus dark reactions. Under the conditions used, the reactions are complete when they reach a plateau near an absorbance of 1.5 to 2.0. Gold nanoparticles begin to form immediately in MOPS in the dark,[16] but the light reactions have a lag phase prior to the first observance of the plasmon resonance band near 530 nm (see Fig. 4). In order to qualitatively compare all of the reactions (because each buffer has a different lag time before the appearance of gold nanoparticles) we developed an "artificial" method of comparing the time until the reaction reached completion. We use the plateau (Abs = 1.5–2.0) and divide by the number of seconds required to reach the plateau. This should not be confused with a rate because it is not an analysis of the slope of the gold nanoparticle formation. The larger the bar in Figure 6, the faster the reaction reached completion. Both MOPS and MES are able to chemically reduce Au^{3+} ions in the dark in the presence of ferritin, but this reduction is significantly slower than the photoreduction reaction. TRIS buffer is unable to catalyze chemically reduction of Au^{3+} ions in the dark.
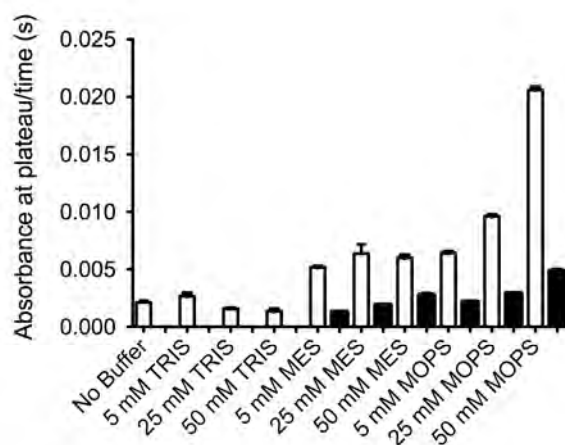
Figure 6. Effect of buffers on nanoparticles formation. MOPS and MES buffers are able to chemically reduce Au(III) in the dark (black bars), although not as rapidly as when illuminated (white bars). TRIS is unable to chemically reduce Au^{3+} ions in the dark. All data represent the mean of three independent runs, with error bars representing the standard deviation. The method of calculating the values is described in the text. The larger the bar, the faster the reaction occurred.

3.3 The ferritin protein shell is necessary for nanoparticle formation

To determine the importance of the protein shell, ferrihydrite nanoparticles[17] of uniform size (5–10 nm diameter) were illuminated in the presence of Au^{3+} ions and citrate under identical conditions as the control reactions reported above. Rather than producing the classical wine red colors that was seen with ferritin, a gray solution containing a black precipitate formed. This precipitate was analyzed using TEM and determined to be a large incongruent mass of undetermined composition (Fig. 7A). Magnetic studies using a Magnetic Susceptibility Balance (MSB) confirmed that these particles are not magnetic (data not shown). In comparison, TEM images of the gold particles formed with ferritin are spherical in shape with a relatively tight size distribution of 5–10 nm in diameter (Fig. 7B).
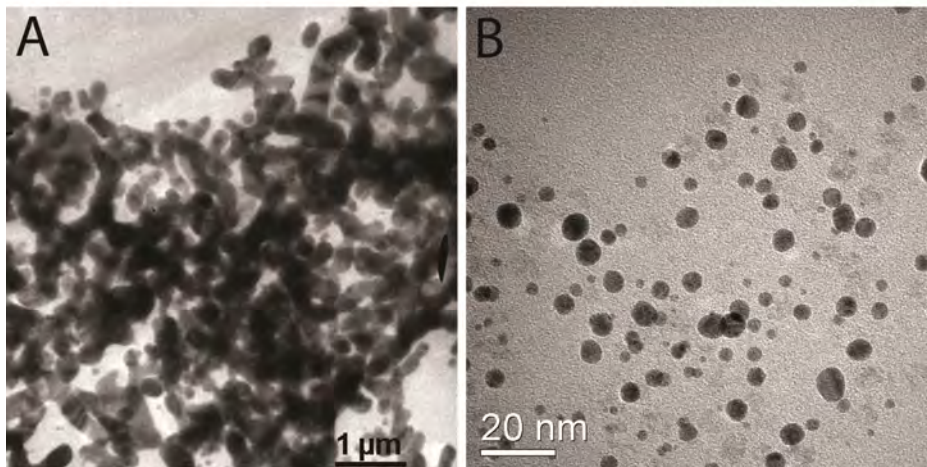
Figure 7. The protein shell of ferritin is crucial for metal nanoparticle formation. A) TEM images of the product of ferrihydrite-catalyzed nanoparticles depict large aggregated material with non-spherical morphology (scalebar 1μM). B) TEM of spherical gold nanoparticles produced in the presence of ferritin (scalebar 20 nm).

4. CONCLUSIONS

Previous studies have shown that ferritin acts as a photocatalyst to reduce various metal species, proteins and redox dyes.[15, 18, 19] In each of these studies, a sacrificial electron donor was used to fill the photo-induced electron hole in the ferrihydrite mineral core. The excited electron in the conduction band was then passed to an electron acceptor, leading to reduction of the various electron acceptors.

Our research goal is to expand the use of this system for photocatalytic reduction of other electron acceptors. However, early efforts in this arena showed very inconsistent results in achieving reproducible data. The present study has focused on determining the minimal requirements for the ferritin photocatalysis reactions to occur. We demonstrate that the choice of buffer significantly influences the rate of the reaction and alters the final products that form. These studies have provided valuable information relating to light and dark reactions that occur and which buffers to use to avoid chemical reduction in the dark.

MOPS was previously shown to reduce Au^{3+} ions to form micrometer sized gold nanoparticle aggregates.[20] Using ferritin as a scaffold for gold nanoparticle synthesis, it was shown that instead of micrometer-sized aggregates, spherical gold nanoparticles were prepared in a size similar to ferritin 15–30 nm.[16] The authors concluded that amino acids supplied from the protein shell of ferritin provided nucleation sites for Au^{3+} binding and in the presence of MOPS, reduction occurred to form gold nanoparticles that were close in size to the 12 nm exterior diameter of ferritin.

In contrast to MOPS or MES, TRIS was unable to catalyze the formation of nanoparticles in the dark and is therefore, an ineffective reductant in this assay. However, in the light reactions, TRIS formed gold nanoparticles in the 5–10 nm diameter range. Figure 5B shows that the absorbance maximum of the MOPS dark reaction has a wavelength of 540 nm and is purple in color. The TRIS reaction has an absorbance maximum at 530 and has a red color. This is consistent with TRIS forming smaller nanoparticles because of the shift in the plasmon peak.[9, 10] By understanding the nature of the

reduction, whether it is chemical or photochemical and judiciously choosing the buffers used in the reaction, the average size of the nanoparticles formed can be controlled and observed by monitoring the absorbance peak near 530 nm.

In the photochemical reaction, TRIS is the slowest buffer for the formation of gold nanoparticles and as its concentration increases, the reaction slows. At present the cause of this is not known. The sacrificial electron donor in this assay is citrate. In the absence of citrate, reactions in water or TRIS result in the precipitation of the ferritin. This has been observed previously when no electron donor was added to the solution and was attributed to the ferritin protein shell acting as the electron donor and being oxidized and denatured.[8] Because MOPS and MES can reduce Au^{3+} in the dark, we postulated that they might act as sacrificial electron donors in the photochemical reactions and substitute for citrate. Reactions confirmed that in the absence of citrate, both MOPS and MES were capable of supplying electrons to ferritin to sustain gold nanoparticle formation (data not shown). Therefore, their ability to stimulate the reactions is most likely due to an enhancement in electron donation to fill electron holes generated in the ferrihydrite mineral of ferritin.

Previous studies identified ferrihydrite as the photocatalyst in this reaction.[15, 19] We performed tests to determine if ferrihydrite nanoparticles could substitute for ferritin in this reaction. Upon illumination the solution changed color but instead of a red color a black precipitate was observed. The product was analyzed by TEM and was an aggregate of micrometer size. This experiment shows that the ferritin protein is important for 1) acting as a nucleation site for nanoparticle nucleation; and/or 2) preventing the ferrihydrite from interacting with the nascent nanoparticles. In either case, the role of ferritin in this reaction is essential for gold nanoparticle formation.

The results presented in this paper provide valuable background data allowing us to understand the minimal requirements for the photochemical reactions to occur. Armed with this information, future work will focus on understanding how citrate interacts with the ferritin protein or the iron mineral core for oxidation. Likewise, the docking site for metal reduction (or other potential electron acceptors) will be identified. Understanding these fundamental principles will lead to methods for extracting electrons for practical use in bio-batteries or bio-fuels, with the source of energy being the sun.

REFERENCES

[1]   S. Shafiee, and E. Topal, "When will fossil fuel reserves be diminished?," Energy Policy, 37(1), 181-189 (2009).

[2]   G. Renger, and T. Renger, "Photosystem II: The machinery of photosynthetic water splitting," Photosynth Res, 98(1-3), 53-80 (2008).

[3]   R. J. Debus, "The manganese and calcium ions of photosynthetic oxygen evolution," Biochim Biophys Acta, 1102(3), 269-352 (1992).

[4]   A. Ehrenberg, "Protein dynamics and reactions of photosystem II," Biochim Biophys Acta, 1655(1-3), 231-4 (2004).

[5]   P. Arosio, R. Ingrassia, and P. Cavadini, "Ferritins: a family of molecules for iron storage, antioxidation and more," Biochim Biophys Acta, 1790(7), 589-99 (2009).

[6]   P. M. Harrison, and P. Arosio, "The ferritins: molecular properties, iron storage function and cellular regulation," Biochim Biophys Acta, 1275(3), 161-203 (1996).

[7]   N. D. Chasteen, and P. M. Harrison, "Mineralization in ferritin: an efficient means of iron storage," J Struct Biol, 126(3), 182-94 (1999).

[8]   V. V. Nikandrov, C. K. Gratzel, J. E. Moser et al., "Light induced redox reactions involving mammalian ferritin as photocatalyst," J Photochem Photobiol B, 41(1-2), 83-9 (1997).

[9]   M. M. Alvarez, J. T. Khoury, T. G. Schaaff et al., "Optical Absorption Spectra of Nanocrystal Gold Molecules," The Journal of Physical Chemistry B, 101(19), 3706-3712 (1997).

[10]   S. E. Skrabalak, J. Chen, L. Au et al., "Gold Nanocages for Biomedical Applications," Adv Mater Deerfield, 19(20), 3177-3184 (2007).

[11]   A. Treffry, and P. M. Harrison, "Incorporation and Release of Inorganic-Phosphate in Horse Spleen Ferritin," Biochemical Journal, 171(2), 313-320 (1978).

[12]   H. Heqing, R. K. Watt, R. B. Frankel et al., "Role of phosphate in Fe^{2+} binding to horse spleen holoferritin," Biochemistry, 32(6), 1681-7 (1993).

[13]   O. H. Lowry, N. J. Rosebrough, A. L. Farr *et al.*, "Protein measurement with the folin phenol reagent," J. Biol. Chem.*, 193(1), 265-275 (1951).

[14]   R. K. Watt, R. B. Frankel, and G. D. Watt, "Redox reactions of apo mammalian ferritin," Biochemistry*, 31(40), 9673-9 (1992).

[15]   D. Ensign, M. Young, and T. Douglas, "Photocatalytic Synthesis of Copper Colloids from Cu(II) by the Ferrihydrite Core of Ferritin," Inorg. Chem.*, 43(11), 3441-3446 (2004).

[16]   L. Zhang, J. Swift, C. A. Butts *et al.*, "Structure and activity of apoferritin-stabilized gold nanoparticles," J Inorg Biochem*, 101(11-12), 1719-29 (2007).

[17]   S. F. Liu, Q. Y. Liu, J. Boerio-Goates *et al.*, "Preparation of a wide array of ultra-high purity metals, metal oxides, and mixed metal oxides with uniform particle sizes from 1 nm to bulk," Journal of Advanced Materials*, 39(2), 18-23 (2007).

[18]   V. V. Nikandrov, "Inorganic semiconductors as photosensitizers in biochemical redox reactions," Membr Cell Biol*, 12(5), 755-69 (1998).

[19]   I. Kim, H. A. Hosein, D. R. Strongin *et al.*, "Photochemical Reactivity of Ferritin for Cr(VI) Reduction," Chem. Mater.*, 14(11), 4874-4879 (2002).

[20]   A. Habib, M. Tabata, and Y. G. Wu, "Formation of Gold Nanoparticles by Good's Buffers," Bull. Chem. Soc. Jpn.*, 78, 262-269 (2005).

Photoreduction of Au(III) to form Au(0) nanoparticles using ferritin as a photocatalyst

Robert J. Hilton, Jeremiah D. Keyes, Richard K. Watt*
Brigham Young University, Provo, UT, USA 84602

ABSTRACT

Gold metal nanoparticles have applications in bio sensing technology, nano-tube formation, and cancer therapy. We report attempts to synthesize gold nanoparticles within the ferritin cavity (8 nm) or to use ferritin as a scaffold for coating gold on the outside surface (12 nm). The intrinsic iron oxide core of ferritin is a semi-conductor and light can excite electrons to a conduction band producing a powerful reductant when a sacrificial electron donor fills the electron hole. We present a method using ferritin to photo chemically reduce Au(III) to metallic gold nanoparticles. During initial studies we observed that the choice of buffers influenced the products that formed as evidenced by a red product formed in TRIS and a purple produce formed in MOPS. Gold nanoparticles formed in MOPS buffer in the absence of illumination have diameters of 15-30 nm whereas illumination in TRIS buffer produced 5-10 nm gold nanoparticles. Increases in temperature cause the gold nanoparticles to form more rapidly. Chemical reduction and photochemical reduction methods have very different reaction profiles with photochemical reduction possessing a lag phase prior to the formation of gold nanoparticles.

Keywords: Ferritin, photochemistry, gold nanoparticles, photoreduction, ferrihydrite, bio-materials

1. INTRODUCTION

1.1 Gold Nanoparticles

Nanoparticles have different reactivities and chemistry than the same material of identical composition existing in the bulk phase.[1] Metal nanoparticles are particularly interesting due to effects related to plasmon resonance.[2, 3] Because of these interesting properties, gold nanoparticles have uses in a variety of applications that include colorimetric assays [4-6], immuno-detection assays [7], treatment of cancer [3] and amyloid fiber related diseases [8], carbon nanotube synthesis [9], and selective oxidation catalysts [10]. The ability to control the size and morphology of gold nanoparticles is important for controlling the chemistry and reactivity of nanoparticles. Furthermore, finding mild reaction conditions with minimal waste products is important in any synthesis method because of environmental concerns.

1.2 Ferritin photochemistry

As the cellular iron storage protein, ferritin naturally contains an iron mineral core between 2000-3000 iron atoms but has a capacity of up to 4500 iron atoms.[11] The iron mineral core is ferrihydrite, a mineral with an average compositional formula of FeOOH that possesses semi-conductor properties.[12] The iron is sequestered inside a protein nanocage that is composed of 24 polypeptide subunits. The protein nanocage has a molecular weight of 450,000 and has an external diameter of 12 nm with an internal hollow cavity with a diameter of 8 nm where the iron is deposited.[13] Channels traverse the protein nanocage and allow ions to enter and leave the interior. The combination of a protein shell that encapsulates semi-conductor materials allows ferritin to disperse the semi-conductor material in solution, maximizing the exposure of the semi-conductor to light.

*rwatt@chem.byu.edu; phone 1 801 422-1923; fax 1 801 422-0153; http://people.chem.byu.edu/rwatt

The physical properties of ferritin as a metal binding protein have been used to synthesize a variety of size-constrained nanomaterials inside the 8 nm diameter cavity. These materials include metal oxides of chromium, manganese, iron, cobalt, nickel titanium, europium and uranium [14-20]; sulfides (and in some instances selenides) of iron, cadmium, gold, lead and zinc [21-26]; and metallic palladium, copper, cobalt and nickel nanoparticles.[27-29] These materials have potential uses in magnetic storage, medical imaging, battery applications and catalysis.

Recently ferritin was used in a new application as a photocatalyst.[30] The electrons generated from the photochemical reaction were used to reduce ions in solution (Figure 1). The first studies with ferritin showed reaction that reduced viologens and cytochrome c. [30] Later, ferritin was used to photochemically reduce chromate to Cr(III) [31] and Cu(II) to copper nanoparticles [32]. The goal of this paper is to use the photocatalytic properties of ferritin to photoreduce Au(III) to Au(0) and form gold nanoparticles. This should proceed at neutral pH without additional reducing agents producing gold nanoparticles under mild synthetic conditions. Figure 2 represents the experimental set-up used to illuminate the sample and detect product formation. The reaction is monitored spectrophotometrically as the products form. This system allows the reaction to be monitored and the addition of various molecules can be monitored for their stimulatory or inhibitory effects on the reaction.
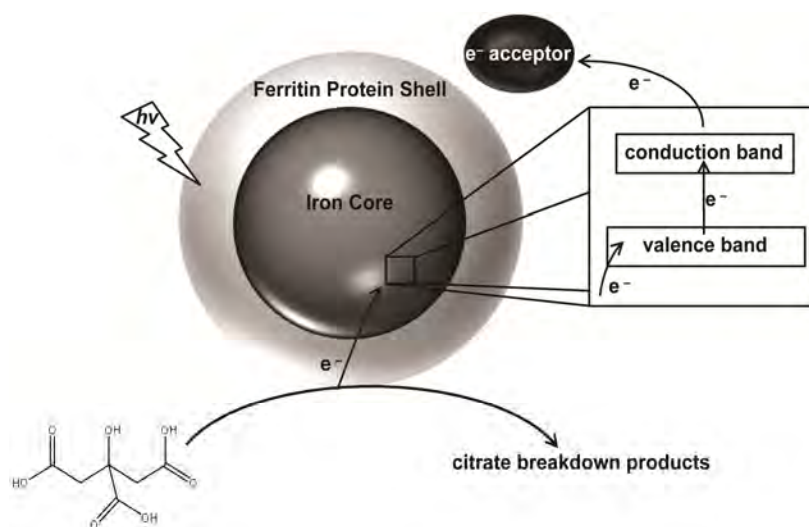
Figure 1. Model of the ferritin photocatalyst. In this system, charge separation occurs when valence electrons are excited into the conduction band of the ferrihydrite semi-conductor. Citrate is used as a sacrificial electron donor. Au(III) is used as the electron acceptor for experiments used in this paper.
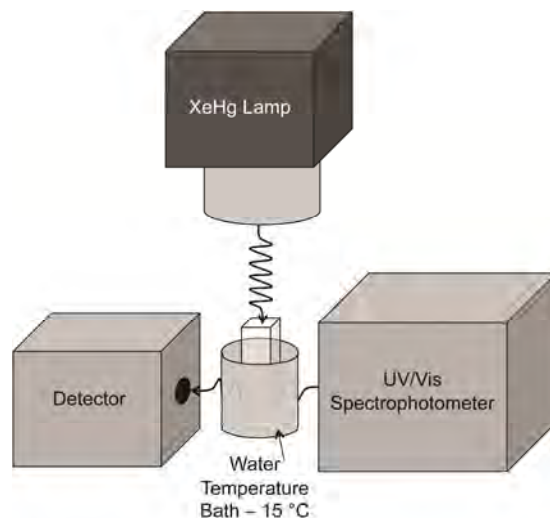
Figure 2. Schematic of experimental setup. An Oriel Hg lamp is aligned over the cuvette holder of an Agilent 8453 diode-array spectrophotometer. This allows simultaneous illumination of the sample and detection of the products that form in the reaction.

2. MATERIALS AND METHODS

2.1 Ferritin preparation

Holoferritin (Sigma) was dialyzed against thioglycolic acid to remove the native iron core.[33] Reconstitution of ferritin cores to desired iron loadings was performed as described previously.[34] Briefly, reconstituted ferritin was prepared by adding equivalents of 100 Fe^{2+}/ferritin to a ferritin solution that was stirred in air. Additional aliquots of Fe^{2+} were added every 10 minutes until the desired iron loading (1000 Fe/ferritin) was obtained. The protein concentration was measured using the Lowry method[35] and the iron concentration was measured after dithionite reduction, followed by addition of bipyridine to measure the $[Fe(bipyridine)_3]^{2+}$ complex at 520nm ($\varepsilon_{520} = 8400$).[36]

2.2 Metal nanoparticle formation

Au nanoparticles were prepared by mixing reconstituted ferritin, the sacrificial electron donor citrate, and $AuCl_4^-$ in a quartz cuvette followed by illumination with an Oriel Hg lamp (model 66056), similar to conditions reported by Ensign.[32] Sample temperature was maintained at the desired temperature using a water-circulating cuvette holder connected to a water bath. The final volume of each sample was 1 mL. The final concentrations were: 0.150 mg/ml protein, 0.33 mM iron, 32 mM citrate, 0.125 M NaCl, and 0.66 mM $AuCl_4^-$. These sample conditions correspond to 1000 Fe per ferritin and 2000 Au atoms per ferritin. Samples prepared by centrifugation were treated by taking the sample after illumination and placing the sample in an Eppendorf Model 5415C centrifuge and spinning the sample at 15,000 x g for 10 minutes. The supernatant was removed and the spectrum recorded.

2.3 Electron microscopy

Transmission electron microscopy (TEM) was performed on a Tecnai F30 TEM, 140 kV. Samples were prepared by placing 3 μL of sample solution onto ultrathin lacey carbon film copper EM grids (Ted Pella, product number 01824). The excess solution was wicked off, and the grid was rinsed in deionized water. Prior to loading on the grids, some samples were purified by performing FPLC on a GE Healthcare AKTApurifier. A Superdex[TM] 200 10/300 GL size exclusion column was used for these separations.

3. RESULTS AND DISCUSSION

3.1 Formation of gold nanoparticles

Illuminating a ferritin solution containing $AuCl_4^-$ and citrate produces gold nanoparticles. Prior to illumination the solution has a slight yellow color due to the iron core of ferritin and negligible absorbance in the visible range (see x-axis in Fig. 3). During illumination, the solution turns red and has an absorbance maximum at 530 nm (Fig. 3) due to the plasmon resonance band of gold nanoparticles.[3] Previous work demonstrated that gold nanoparticles reduced with MOPS or sodium borohydride produced purple solutions and TEM analysis showed nanoparticles with diameters of 15-30 nm.[37] Figure 3 compares the spectrum of each of these samples and shows that the illuminated sample has a narrower absorbance peak that is blue-shifted ($Abs_{max} = 530$ nm) compared to the chemically reduced gold nanoparticle sample ($Abs_{max} = 550$ nm).
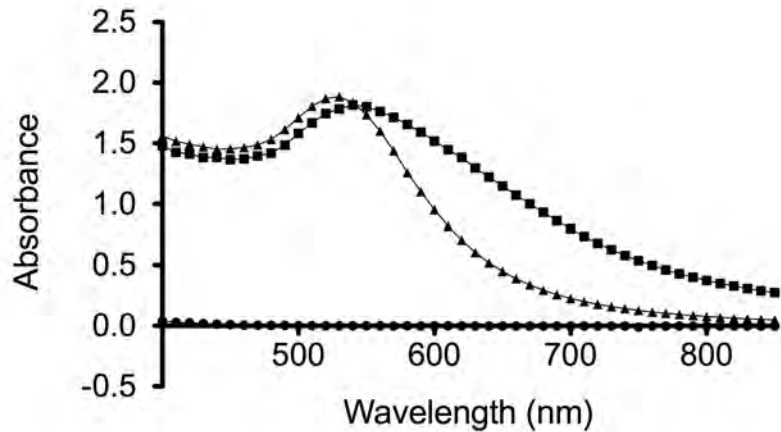
Figure 3. Spectra of gold nanoparticles formed by photochemical reduction and chemical reduction. Samples include, ▲ – ferritin in TRIS illuminated, ■ – ferritin in MOPS in the dark, ● – control spectrum recorded before illumination of the sample.

3.2 TEM characterization of gold nanoparticles

Plasmon resonance peaks are known to shift with the size of the nanoparticles and a shift to smaller wavelengths is consistent with the formation of smaller particles. To confirm this hypothesis, the samples were analyzed by TEM (Fig. 4). Images show that the gold nanoparticles formed by photochemical reduction of Au(III) form gold nanoparticles in the 5-10 nm range. Additionally, very few nanoparticles in the 15-30 nm range are observed, indicating that these two synthesis methods provide pathways to prepare 5-10 nm particles by photoreduction in TRIS or 15-30 nm particles using the MOPS reduction method.
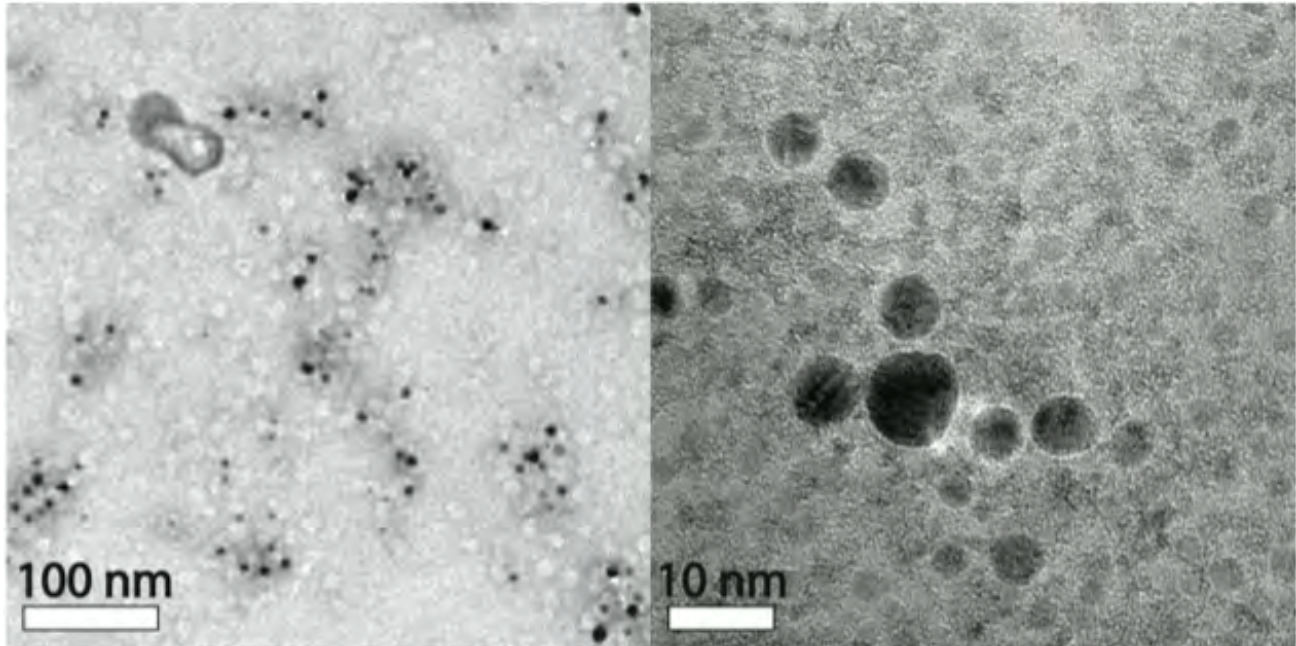
Figure 4. TEM of gold nanoparticles formed by illumination of ferritin in TRIS. A) Sample of ferritin and gold nanoparticles. The sample was stained by uranyl acetate to mark the ferritin protein shell. The darkest spheres are gold nanoparticles. The white halos are from the ferritin protein shell. Inside the white halos can be seen darker spheres representing the ferritin iron core. B) Gold nanoparticles in the 5-10 nm diameter range.

3.3 Evaluation of size distribution versus aggregation of nanoparticles

To determine if the width of the absorbance peak (Fig. 3) was due to a mixture of large and small nanoparticles or if it was an affect of aggregation of similar sized nanoparticles, the sample was centrifuged to remove larger particles. Centrifugation decreased the total amount of absorbance due to the removal of some nanoparticles, however the absorbance maximum of the centrifuged samples did not shift to a lower wavelength. This observation indicates that the particles that were removed by centrifugation in both the TRIS illuminated sample and the MOPS dark sample were aggregates instead of the removal of larger particles (Fig. 5).[37]
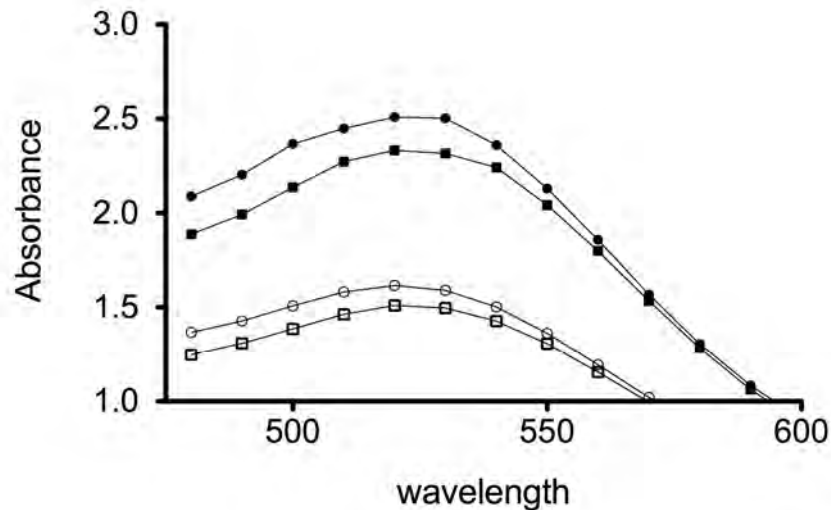
Figure 5. Aggregation versus size of particles. The absorbance maximum and width of absorbance peak is based on the nanoparticle size and distribution of various sized particles in the sample. Centrifugation will remove the larger particles. A shift in peak maxima and narrowing of the peak indicates that larger particles are removed. A general decrease in peak intensity is evaluated as the removal of aggregated particles. Samples are: ■ – MOPS no centrifugation. □ – MOPS centrifuged, ● – TRIS no centrifugation. ○ – TRIS centrifuged.

3.4 Temperature dependence on gold nanoparticle formation

Using a temperature controlled cuvette holder, the time required to reach completion for gold nanoparticle formation was studied as an effect of temperature. Figure 6A follows the formation of gold nanoparticles at the plasmon resonance band at 530 nm. As the temperature increases the time required for product formation is significantly decreased. Figure 6B shows a bar graph that represent how quickly the reaction reaches completion. Under the conditions used, the reactions are complete when they reach a plateau near an absorbance of 2.0. Unfortunately, there is a lag phase that is much longer in the colder reactions. In order to qualitatively compare all of the reactions (because each temperature has a different lag time before the appearance of gold nanoparticles) we developed an "artificial" method of comparing the time until the reaction reached completion. We divided the absorbance at the plateau (Abs = 1.5–2.0) by the number of seconds required to reach the plateau. This should not be confused with a rate because it is not an analysis of the slope of the gold nanoparticle formation. The larger the bar in Figure 6, the faster the reaction reached completion. Ferritin provides a unique protein environment for this type of analysis because ferritin is unusually stable to temperature changes compared to most proteins.[38] As shown, ferritin is stable to 80° C. The observation that gold nanoparticle formation increases with increased temperature is consistent with the requirement for Au(III) to diffuse and interact with the ferritin protein shell prior to nucleation of Au(III) on the ferritin external surface.
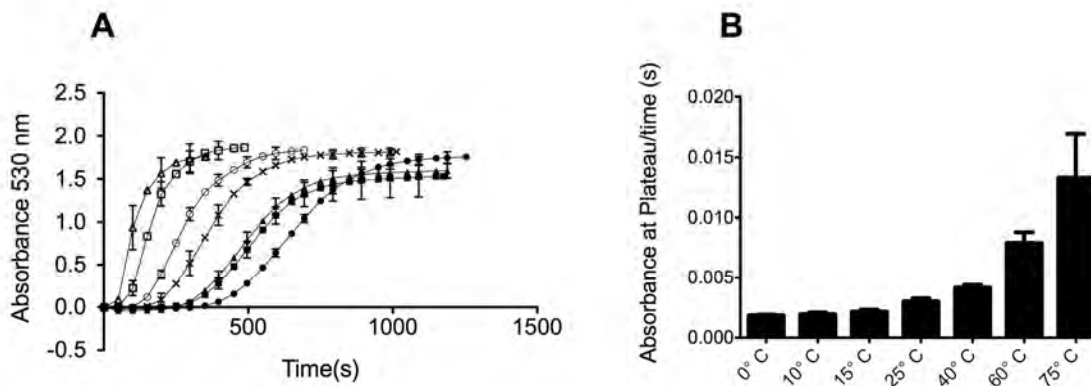
Figure 6. Temperature dependence for gold nanoparticle formation. A) Product formation versus time with product formation measured at the plasmon resonance peak at 530 nm. Conditions were: ● = 0 °C, ■ = 10 °C, ▲ = 15 °C, X = 25 °C, ○ = 40 °C, □ = 60 °C, Δ = 75 °C. B) Due to the lag phase of the reactions start at different times. A method to qualitatively evaluate the time required for samples to reach completion is plotted. Please see text for method of calculation.

3.5 Comparison of chemical reduction by MOPS and photoreduction by TRIS

The lag phase observed in Figure 6 prior to the first gold nanoparticle products being formed is particularly interesting, especially as it is lengthened with colder temperatures. In comparison, gold nanoparticle formation using chemical reduction with MOPS has a very short lag phase of less than 1 minute (Fig. 7). For the plasmon resonance effect to occur, the gold nanoparticle must achieve a minimal size before the effect can be observed. However, this minimal size is achieved rapidly when MOPS acts as the chemical reductant. For the illuminated reaction in TRIS, the lag phase is significantly longer than that observed for MOPS chemical reduction. Controls with TRIS in the dark show that no chemical reduction takes place on the timescale of these studies and after two weeks in the dark only a very faint purple color was observed. There are several potential reasons for this lag phase. The first is that a critical number of electrons must be excited into the conducting band of the ferrihydrite mineral core prior to initial reduction of Au(III) to Au(0). This may depend on how rapidly the electron holes are filled. Perhaps a certain oxidizing potential must be obtained before citrate can be oxidized. Once sufficient holes have been created, the citrate can be oxidized and the holes are filled trapping the excited electrons in the conduction band. Potentially, kinetic studies examining the concentration dependence of citrate on the formation of gold nanoparticles could test this model. A second model may require conversion of the ferrihydrite to a different mineral in ferritin. It is known that photochemistry reduces the iron and free Fe^{2+} has been observed.[30] It is possible that a mixed-valent Fe(II)-Fe(III) mineral is the active photocatalyst and that the lag phase is the rearrangement of ferrihydrite to this new mineral.
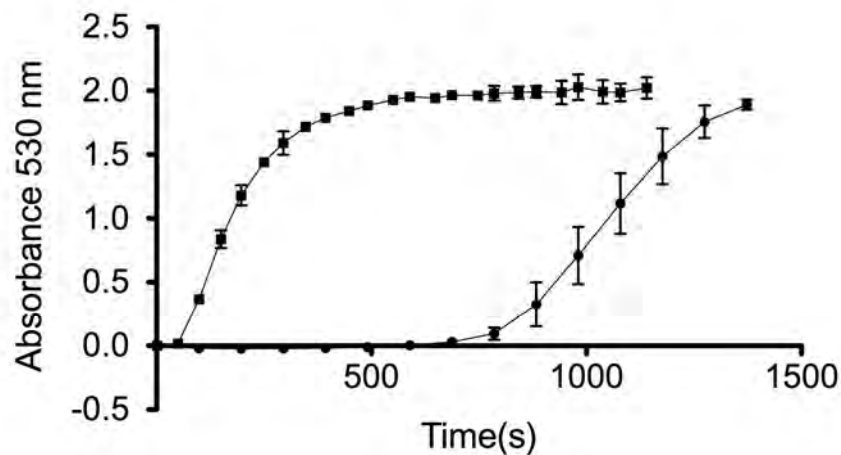
Figure 7. Chemical reduction of gold nanoparticles in MOPS compared to photochemical reduction in TRIS. MOPS reduction is rapid and begins within 1-minute ■ – MOPS in the dark. TRIS photoreduction is slower and has a lag phase prior to the first gold nanoparticles being formed ● – TRIS illuminated kinetics.

3.6 Wavelength dependence on the photochemistry of ferritin catalyzed gold nanoparticle formation

To estimate the energy required for excitation of electrons from the valence band to the conduction band of ferrihydrite, we used wavelength filters to determine wavelengths required for gold nanoparticle formation to occur. A filter that blocked wavelengths of 410 nm and below (shorter more energetic wavelengths) was used in a reaction and no gold nanoparticles formed with this filter. A second filter blocking 370 nm and below (shorter more energetic wavelengths) permitted the formation of gold nanoparticles. Therefore, the energy required to excite electrons from the valence band into the conduction band of ferrihydrite lies between 370 and 410 nm. These energies correspond to energies of 3.00 – 3.35 eV. A similar optical band gap (2.5 to 3.5 eV) was reported for the ferritin photoreduction of chromate to Cr(III).[31]

4. CONCLUSIONS

The ferrihydrite mineral core of ferritin acts as a photocatalyst for aqueous redox reactions (Fig. 1). In this study we have used this system to oxidize citrate and reduce Au(III) to gold nanoparticles. The advantage of using Au(III) as a substrate is that the plasmon resonance band of the gold nanoparticle products has a distinct color change. Using a modified spectrophotometer, the sample can be illuminated and the formation of products can be simultaneously monitored (Fig. 2). We used this system to kinetically monitor the formation of the products to determine how alterations of the reaction conditions increase or decrease the rate of product formation.

Illumination of ferritin in the presence of Au(III) produced a red solution with an absorbance maximum of 530 nm (Fig. 3) and 5-10 nm diameter gold nanoparticles as the product (Fig. 4). Previous ferritin work where Au(III) was chemically reduced by MOPS produced 15-30 nm particles.[37] The previous work proposed that amino acids on the external surface of ferritin created nucleation sites for gold deposition. In the photochemical reaction, the nanoparticles are in the same size as the internal diameter of ferritin. Although EM images did not show conclusive evidence that the gold particles are entrapped inside ferritin, the observed size distribution suggests that this is a possibility due to the apparent restricted size of the nanoparticles. If this is correct, there are two distinct synthetic pathways using ferritin as a scaffold for nanoparticle synthesis. The first is the dark chemical reduction of Au(III) in the presence of ferritin where 15-30 nm gold nanoparticles are deposited on the external surface of ferritin. The second is a photocatalytic reduction of Au(III) where 5-10 nm gold nanoparticles are deposited on the inside of ferritin.

The samples were also tested for size-distribution using a centrifugation step (Fig. 5). Centrifugation should remove the largest particles from solution. If the larger particles are removed and the smaller particles remain in solution the absorbance maximum of the solution should change to a lower wavelength due to the plasmon resonance of the smaller particles. If aggregated particles of a similar size are removed by centrifugation, the peak maximum would not change but the total absorbance would decrease. The removal of aggregated nanoparticles is what was observed indicating that the size distribution is very regular in both the TRIS photochemical preparation of gold nanoparticles and the MOPS preparation.[37]

The time the photochemical reaction required to reach completion was measured as a function of temperature (Fig. 6). Samples were tested in a temperature range from 0 to 70º C. As the temperature increased, the time to reach completion of the reaction decreased. This is consistent with more rapid diffusion of the Au(III) in solution and increased collisions for the Au(III) to find nucleation sites on the ferritin protein exterior. Additionally, the diffusion of the sacrificial electron donor citrate to interact with ferritin and be oxidized would be increase.

The optical band gap of 3.0 – 3.5 eV measured in these experiments is in a similar range to that reported previously for the ferritin photocatalyst (2.5 – 3.5 eV).[31] This corresponds to wavelengths ranging from 370 – 410 nm. Incidentally this is the range where ferritin has an absorption shoulder in the UV/Vis spectrum. As mentioned in the introduction, there are a variety of metal oxides, metal sulfides and metal selenides that have been prepared in ferritin. Future work will examine these materials for their optical band gap and the ability to catalyze photooxidation and photoreduction reactions. A future goal will be to prepare tunable photocatalysts based on the optical band gap of these ferritin materials.

REFERENCES

[1]   A. Henglein, "Small-particle research: physicochemical properties of extremely small colloidal metal and semiconductor particles," Chemical Reviews, 89(8), 1861-1873 (2002).

[2]   M. M. Alvarez, J. T. Khoury, T. G. Schaaff et al., "Optical Absorption Spectra of Nanocrystal Gold Molecules," The Journal of Physical Chemistry B, 101(19), 3706-3712 (1997).

[3]   S. E. Skrabalak, J. Chen, L. Au et al., "Gold Nanocages for Biomedical Applications," Adv Mater Deerfield, 19(20), 3177-3184 (2007).

[4]   J. Liu, and Y. Lu, "Fast Colorimetric Sensing of Adenosine and Cocaine Based on a General Sensor Design Involving Aptamers and Nanoparticles13," Angewandte Chemie International Edition, 45(1), 90-94 (2006).

[5]   J. Liu, and Y. Lu, "A Colorimetric Lead Biosensor Using DNAzyme-Directed Assembly of Gold Nanoparticles," Journal of the American Chemical Society, 125(22), 6642-6643 (2003).

[6]   J.-S. Lee, P. A. Ulmann, M. S. Han et al., "A DNA‚àíGold Nanoparticle-Based Colorimetric Competition Assay for the Detection of Cysteine," Nano Letters, 8(2), 529-533 (2008).

[7]   M. Yang, Y. Kostov, H. A. Bruck et al., "Gold nanoparticle-based enhanced chemiluminescence immunosensor for detection of Staphylococcal Enterotoxin B (SEB) in food," International Journal of Food Microbiology, 133(3), 265-271 (2009).

[8]   M. Chikae, T. Fukuda, K. Kerman et al., "Amyloid-[beta] detection with saccharide immobilized gold nanoparticle on carbon electrode," Bioelectrochemistry, 74(1), 118-123 (2008).

[9]   S. Bhaviripudi, E. Mile, S. A. Steiner et al., "CVD Synthesis of Single-Walled Carbon Nanotubes from Gold Nanoparticle Catalysts," Journal of the American Chemical Society, 129(6), 1516-1517 (2007).

[10]   M. Turner, V. B. Golovko, O. P. H. Vaughan et al., "Selective oxidation with dioxygen by gold nanoparticle catalysts derived from 55-atom clusters," Nature, 454(7207), 981-983 (2008).

[11]   N. D. Chasteen, and P. M. Harrison, "Mineralization in ferritin: an efficient means of iron storage," J Struct Biol, 126(3), 182-94 (1999).

[12]   V. V. Nikandrov, "Inorganic semiconductors as photosensitizers in biochemical redox reactions," Membr Cell Biol, 12(5), 755-69 (1998).

[13]   P. M. Harrison, and P. Arosio, "The ferritins: molecular properties, iron storage function and cellular regulation," Biochim Biophys Acta, 1275(3), 161-203 (1996).

[14]   F. C. Meldrum, V. J. Wade, D. L. Nimmo et al., "Synthesis of inorganic nanophase materials in supramolecular protein cages," Nature, 349(6311), 684-687 (1991).

[15]   M. Okuda, K. Iwahori, I. Yamashita et al., "Fabrication of nickel and chromium nanoparticles using the protein cage of apoferritin," Biotechnology and Bioengineering, 84(2), 187-194 (2003).

[16]   B. Zhang, J. N. Harb, R. C. Davis et al., "Kinetic and thermodynamic characterization of the cobalt and manganese oxyhydroxide cores formed in horse spleen ferritin," Inorg Chem, 44(10), 3738-45 (2005).

[17]   T. Douglas, and V. T. Stark, "Nanophase Cobalt Oxyhydroxide Mineral Synthesized within the Protein Cage of Ferritin," Inorg. Chem., 39(8), 1828-1830 (2000).

[18]   F. C. Meldrum, T. Douglas, S. Levi et al., "Reconstitution of manganese oxide cores in horse spleen and recombinant ferritins," Journal of Inorganic Biochemistry, 58(1), 59-68 (1995).

[19]   J. F. Hainfeld, "Uranium-loaded apoferritin with antibodies attached: molecular design for uranium neutron-capture therapy," Proceedings of the National Academy of Sciences of the United States of America, 89(22), 11064-11068 (1992).

[20]   M. T. Klem, J. Mosolf, M. Young et al., "Photochemical Mineralization of Europium, Titanium, and Iron Oxyhydroxide Nanoparticles in the Ferritin Protein Cage," Inorg. Chem., 47(7), 2237-2239 (2008).

[21]   T. Douglas, D. P. E. Dickson, S. Betteridge et al., "Synthesis and Structure of an Iron (III) Sulfide-Ferritin Bioinorganic Nanocomposite," Science, 269(5220), 54-57 (1995).

[22]   K. K. W. Wong, and S. Mann, "Biomimetic synthesis of cadmium sulfide-ferritin nanocomposites," Advanced Materials, 8(11), 928-932 (1996).

[23]   I. Yamashita, J. Hayashi, and M. Hara, "Bio-template Synthesis of Uniform CdSe Nanoparticles Using Cage-shaped Protein, Apoferritin," Chemistry Letters, 33(9), 1158-1159 (2004).

[24]   K. Iwahori, K. Yoshizawa, M. Muraoka et al., "Fabrication of ZnSe Nanoparticles in the Apoferritin Cavity by Designing a Slow Chemical Reaction System," Inorganic Chemistry, 44(18), 6393-6400 (2005).

[25]   K. Yoshizawa, K. Iwahori, K. Sugimoto et al., "Fabrication of Gold Sulfide Nanoparticles Using the Protein Cage of Apoferritin," Chemistry Letters, 35(10), 1192-1193 (2006).

[26]   L. Turyanska, T. D. Bradshaw, J. Sharpe et al., "The biocompatibility of apoferritin-encapsulated PbS quantum dots," Small, 5(15), 1738-41 (2009).

[27]   T. Ueno, M. Suzuki, T. Goto et al., "Size-Selective Olefin Hydrogenation by a Pd Nanocluster Provided in an Apo-Ferritin Cage," Angewandte Chemie International Edition, 43(19), 2527-2530 (2004).

[28]   N. Galvez, P. Sanchez, and J. M. Dominguez-Vera, "Preparation of Cu and CuFe Prussian Blue derivative nanoparticles using the apoferritin cavity as nanoreactor," Dalton Trans, 7(15), 2492-4 (2005).

[29]   N. Galvez, P. Sanchez, J. M. Dominguez-Vera et al., "Apoferritin-encapsulated Ni and Co superparamagnetic nanoparticles," Journal of Materials Chemistry, 16(26), 2757-2761 (2006).

[30]   V. V. Nikandrov, C. K. Gratzel, J. E. Moser et al., "Light induced redox reactions involving mammalian ferritin as photocatalyst," J Photochem Photobiol B, 41(1-2), 83-9 (1997).

[31]   I. Kim, H. A. Hosein, D. R. Strongin et al., "Photochemical Reactivity of Ferritin for Cr(VI) Reduction," Chem. Mater., 14(11), 4874-4879 (2002).

[32]   D. Ensign, M. Young, and T. Douglas, "Photocatalytic Synthesis of Copper Colloids from Cu(II) by the Ferrihydrite Core of Ferritin," Inorg. Chem., 43(11), 3441-3446 (2004).

[33]   A. Treffry, and P. M. Harrison, "Incorporation and Release of Inorganic-Phosphate in Horse Spleen Ferritin," Biochemical Journal, 171(2), 313-320 (1978).

[34]   H. Heqing, R. K. Watt, R. B. Frankel et al., "Role of phosphate in Fe^{2+} binding to horse spleen holoferritin," Biochemistry, 32(6), 1681-7 (1993).

[35]   O. H. Lowry, N. J. Rosebrough, A. L. Farr et al., "Protein measurement with the folin phenol reagent," J. Biol. Chem., 193(1), 265-275 (1951).

[36]   R. K. Watt, R. B. Frankel, and G. D. Watt, "Redox reactions of apo mammalian ferritin," Biochemistry, 31(40), 9673-9 (1992).

[37]   L. Zhang, J. Swift, C. A. Butts et al., "Structure and activity of apoferritin-stabilized gold nanoparticles," J Inorg Biochem, 101(11-12), 1719-29 (2007).

[38]   S. P. Martsev, A. P. Vlasov, and P. Arosio, "Distinct stability of recombinant L and H subunits of human ferritin: calorimetric and ANS binding studies," Protein Eng, 11(5), 377-81 (1998).

BYU
BRIGHAM YOUNG UNIVERSITY

UNDERSTANDING THE MECHANISM OF IRON-CATALYZED OXIDATIVE DAMAGE IN CHRONIC KIDNEY DISEASE

Hilton, Robert J. and Watt, Richard K. — Department of Chemistry and Biochemistry, Brigham Young University, Provo, Utah 84602

OVERVIEW

Oxidative damage is a prevalent symptom in several diseases, including cardiovascular disease, diabetes, Parkinson's disease, Alzheimer's disease, and chronic kidney disease (CKD). Here we introduce preliminary data suggesting that metabolites that exist in CKD patients at high levels inhibit iron loading into ferritin. This leads to free iron, which is then capable of catalyzing oxidative damage in patients with CKD.

INTRODUCTION

In addition to filtering impurities from the bloodstream, the kidneys are responsible for sensing oxygen concentrations and, under hypoxic conditions, for excreting the hormone erythropoietin (EPO) into the bloodstream. Because the iron containing protein hemoglobin is the major component of red blood cells, and the EPO signal stimulates the bone marrow to increase red blood cell expression, the availability of iron is critical for proper oxygen delivery. With the onset of kidney disease, EPO expression decreases leading to anemia. The disruption of red blood cell synthesis appears to have a secondary effect on the overall ability of the body to regulate iron. Overall symptoms of CKD include:

- Severe increase in oxidative damage
- Increase in serum ferritin levels
- Decrease in transferrin saturation levels
- Increase in serum phosphate levels

These symptoms all further complicate the effect of decreased EPO levels. Inflammation increases in CKD and this leads to the expression of another hormone, hepcidin. Hepcidin binds to the iron export protein ferroportin and blocks iron export into the bloodstream further limiting the available iron for red blood cell production. Once a patient starts down this path, it is very difficult to recover from these symptoms.

Figure 1. Iron cycle in the body. ~75% of total body iron is bound by hemoglobin and 20% is stored in ferritin. In CKD, this cycle is disrupted: ferritin levels increase, transferrin levels decrease, and erythropoietin production decreases. *Figure obtained from www.cdc.gov*

OBJECTIVES

- Present the mechanism of iron release by phosphate
- Present evidence for the formation of iron-phosphate complexes
- Discuss the ability of these complexes to catalyze oxidative damage
- Discuss potential treatments to prevent iron release

Figure 2. Ferritin, the iron-storage protein.
A) Ferritin is a 450,000 Da protein that can hold up to 4500 iron atoms. It is composed of 24 subunits assembled into a hollow spherical structure.
B) 3D imaging of ferritin showing the hollow interior where iron is stored.
Figures created using UCSF Chimera

Phosphate naturally occurs inside the ferritin core with iron in a 1:10 ratio. Normal physiological phosphate levels are 1 mM. However, in CKD patients, phosphate levels are commonly 5 mM.

Hypothesis

- Elevated phosphate concentration alters iron binding of ferritin.

Iron loading into ferritin in the presence of phosphate

$$Fe^{2+} + PO_4^{3-} + O_2 + Ferritin \rightarrow FeOOH\,(PO_4)_x$$

1.0 mM	
2.5 mM	What happens with higher phosphate
5.0 mM	incorporation?
10.0 mM	

RESULTS

Figure 3. Iron loading into ferritin in the presence or absence of phosphate
A) Spectrophotometric assay. The reaction is performed in a spectrophotometer with a stirred cuvette sample holder. The buffer is 0.025 M Mops buffer at pH 7.4 with 0.05 M NaCl present. The sample is prepared with the appropriate components and is stirred - represented by the horizontal line at the beginning of each plot. The reaction is initiated by injecting iron (50 Fe/ferritin) using a Hamilton syringe. Control reactions with no ferritin are represented by the open symbols and are □ - no phosphate, O - 1.0 mM phosphate and △ - 10 mM phosphate. Samples with ferritin present (1 μM) are filled symbols and are represented by ■ - no phosphate, ● - 1.0 mM phosphate and ▲ - 10 mM phosphate.

B) Oxygen consumption. Reaction conditions and symbols are identical to those in part A. The reactions are performed in a closed Hansatech oxygen electrode to monitor the consumption of oxygen.

- PO_4^{3-} stimulates the rate of iron loading into ferritin.
- PO_4^{3-} stimulates the rate of oxygen consumption suggesting an interaction at the ferroxidase site.
- Physiological phosphate concentrations and ferritin without iron have almost identical ferroxidase activity.

$$Fe(II) + PO_4^{3-} + O_2 \rightarrow Fe(III)\text{-}PO_4^{3-}\,(aq)$$

- The iron is oxidized
- The complex is soluble
- Does the formation of the Fe(III)- PO_4^{3-}(aq) complex compete with ferritin iron loading?

$$Ferritin + Fe(II) + PO_4^{3-} + O_2 \rightarrow Fe(III)\text{-}PO_4^{3-}\,(aq)$$
$$Ferritin\text{-}Fe(III)$$

Absorbance Spectra: Apoferritin and Holoferritin

Figure 4. Spectra obtained showing the formation of an iron-phosphate complex at wavelength 280-300 nm.

Table 1 Elemental Analysis

Theoretical Loading	Iron/Ferritin	Phosphate/Ferritin	Iron/Phosphate
100 Iron/Ferritin			
No phosphate	119 ± 7	5.9 ± 0.4	20 ± 0.1
1 mM phosphate	67 ± 6	35.1 ± 1.2	1.4 ± 0.3
5 mM phosphate	93 ± 3	24.2 ± 0.6	
1000 Iron/Ferritin			
No phosphate	1069 ± 26	5.1 ± 0.4	
1 mM phosphate	752 ± 38	581.8 ± 23.9	1.3 ± 0.1
5 mM phosphate	232 ± 36	356.2 ± 67.1	0.7 ± 0.1

CONCLUSIONS

In this poster, we examine potential causes for the oxidative damage with the hope that stopping oxidative damage will allow us to minimize the expression of hepcidin. If hepcidin expression can be minimized then potentially normal iron saturation of transferrin can be maintained and red blood cell synthesis can be continued.

We therefore conclude that:

Phosphate stimulates the rate of iron oxidation *in vitro*

Phosphate inhibits iron loading into ferritin by forming an iron-phosphate complex in solution

High phosphate concentrations produced a new iron-phosphate mineral inside ferritin

Significance

High phosphate shifts the redox potential in blood serum causing the oxidation of Fe(II) to Fe(III)

The iron-phosphate complex that forms is not bound by ferritin

Physiological levels of phosphate (1 mM) inhibited ~30% of iron and 5 mM inhibited ~70% loading into ferritin

REFERENCES

1. Aisen, P. and S. Levi, *Ferritin, iron homeostasis, and oxidative damage. Free Radical Biology and Medicine.* 2002. 33(8): p. 457-463.
2. Stuart, W. et al. *Oxidative stress in chronic renal failure as a cardiovascular risk factor. Clinical Nephrology.* 2002. 58(1): p. S12-S19
3. Malluche, H.H. and H. Mawad. *Management of hyperphosphatemia of chronic kidney disease: lessons from the past and future directions. Nephrology, Dialysis, Transplantation. Official Publication Of The European Dialysis And Transplant Association - European Renal Association.* 2002. 17(7): p. 1170
4. Martin, C.J., and Goeddeke-Merickel, C.M., *Oxidative Damage in Chronic Kidney Disease. Issues in Renal Nutrition.* 2005. 32(6): p. 683-685.
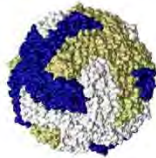
CONTACT INFORMATION

For further information, please contact the authors at:
Robert J. Hilton - robthilton@gmail.com
Richard K. Watt - rwatt@chem.byu.edu
Laboratory website: http://people.chem.byu.edu/rwatt

Ferritin as a Photocatalyst in an Artificial Photosynthesis System

Robert J. Hilton ++, Jeremiah D. Keyes +, Richard K. Watt
Department of Chemistry and Biochemistry, Brigham Young University, Provo, Utah 84602

BYU
BRIGHAM YOUNG
UNIVERSITY

Introduction

We describe a bio-photocatalyst based on the iron storage protein ferritin. This method is a mimic of the natural process of photosynthesis. In photosynthesis, photosystem II uses photons of light to energize electrons. These electrons are channeled into the photosynthesis pathway, where they are used for energy. The source of the electrons in photosynthesis is water (Figure 1).

Ferritin is a 12 nm spherical protein that naturally sequesters iron as ferrihydrite. Ferrihydrite is a semi-conductor material. An assay has been established where ferritin can photocatalytically oxidize citrate and channel the liberated electrons to Cu(II), which is reduced to Cu(0) nanoparticles (10-30 nm). This process mimics the photosystem II pathway, in that the protein mediates the transfer of electrons to an electron acceptor (Figure 2). We describe efforts to maximize the efficiency of this system.

Methods

Apo-ferritin is reconstituted with an iron core (ferrihydrite) of about 800 iron atoms per ferritin. A reaction vial containing a final concentration of 0.15 mg/ml ferritin is stirred with 40 mM citrate (or other electron donor), 100 mM NaCl, and 4 mM copper, gold, or other electron acceptor. This solution is introduced to a light source and simultaneously monitored by UV-visible spectrophotometry (Figure 3). The light excites electrons from the semi-conductor ferrihydrite core of ferritin from the valence band to the conduction band. This electron then passes to an electron acceptor, in this case a metal ion. The metal ion is reduced and forms a metal nanoparticle of tightly distributed size and shape. The ferrihydrite core is replenished with electrons from an electron donor source, such as citrate.

Photosystem II: electron transfer pathway

Figure 1. Photons of light energize electrons, which are then channeled through photosystem II to an electron acceptor. The resulting P680 is a powerful oxidant that can oxidize electron donor molecules.

Ferritin Mimic: electron transfer pathway

Figure 2. Photons of light excite electrons from the valence band to the conduction band of the ferrihydrite semi-conductor. A sacrificial electron donor fills the electron hole and an electron acceptor captures the excited electron.

Figure 3. A light source illuminates ferritin in solution. This initiates a photocatalytic process that causes electrons to be excited and captured by an electron acceptor. The result is a metal nanoparticle with an intense color change.

Table 1: Ferritin Photocatalyst Conditions

Donors	Acceptors	Enhancers	Catalysts
Sulfite	Cr(VI)	Salt - NaCl	Horse spleen ferritin
Thiol compounds	Cu(II)	Sulfate containing buffers	Recombinant Human H-ferritin
Citrate	Cytochrome c	Ferric Citrate	Recombinant Human L-ferritin
Tartrate	Ag(I)	Fe(II)	Ferrihydrite
Glycerol/Methyl glycerol	Pt(II)		Iron/Phosphate/Iron Arsenate
Formaldehyde/Methanol	Au(III)		Bacterial Ferritin Heme Group
Ethanol/mmol	Fe(III)		Cobalt
Glucose	Viologens		Manganese
	PbNi Electrodes		Titanium
	Ferrichrome		

Black = Previous work   Red = Successfully updated   Green = Future planned studies

Results

Gold Nanoparticle Formation with or without Preincubation

Figure 4. A preincubation or lag phase is necessary for formation of an intermediate. This intermediate plays a key role in nanoparticle formation and electron channeling. The blue trace represents the reaction performed under normal conditions. Next, we illuminated a sample through the lag phase, or until just prior to an increase in absorbance. We stopped illumination and incubated the sample in the dark for 24 hours and the sample was again illuminated. The lag phase was thus bypassed, and the rate of gold nanoparticle formation was significantly increased (red trace). This suggests that an intermediate forms that is required for nanoparticle formation. Furthermore, this intermediate is stable.

Copper Nanoparticle Formation in the Presence or Absence of Iron Citrate

Figure 5. To determine what the intermediate in the reaction is, we incubated holo-ferritin (ferritin with an iron core) or apo-ferritin (ferritin lacking any iron core) with or without Fe(III)-citrate. The black trace represents a control of holo-ferritin citrate to holo-ferritin, the rate of the reaction increases considerably (red trace). As expected, apo-ferritin under normal conditions shows no change in absorbance due to a lack of any iron present (green trace). Surprisingly, when Fe(III)-citrate was added to an apo-ferritin solution, we observed a significant increase in the rate of nanoparticle formation (blue trace). As controls, Fe(III)-citrate or ferrihydrite without the protein present was unable to catalyze copper nanoparticle formation (data not shown), however black magnetic precipitate does form under these conditions. These results suggest that the formation of Fe(III)-citrate in solution plays a key role in mediating an altered iron core in ferritin that is necessary for the reaction to occur.

Conclusions

Using ferritin as a model system, we are able to effectively funnel electrons to electron acceptors. Our current research has investigated metal ions as electron acceptors, however other acceptors, such as electrodes, have the potential to harvest the electrons for use in fuel cells and bio-battery applications.

To maximize the efficiency of this system, we sought to better understand the mechanism of the reaction. We determined that a stable intermediate forms and plays a key role in the reactions. This intermediate forms quickly when Fe(III)-citrate is in solution. We have developed a scheme to illustrate our hypothesis of the reaction (Figure 6).

Figure 6. Mechanism of Intermediate Formation

To form the intermediate, iron is chelated from the ferrihydrite core of ferritin with an iron chelator, such as citrate. The chelation and subsequent formation of an Fe(III)-citrate complex is the slow step in this reaction. Once Fe(III)-citrate forms, light reduces the iron, releasing it from citrate. Fe(II) is then bound by ferritin. We have not yet established if the iron that re-enters ferritin exists as Fe(II) or Fe(III). However, a mixed valent core of Fe(II) and Fe(III) is a potential intermediate since light is known to reduce iron in the ferrihydrite mineral. Ferritin is known to stabilize reduced forms of iron. For the apo-ferritin reaction, it has been shown that in the presence of oxygen that Fe(III) citrate can be photoreduced and the liberated Fe(II) can bind to ferritin and be oxidized and incorporated into the ferritin core. Perhaps the mineral that forms in the early stages of core development is the actual catalyst for photochemistry. Dominguez-Vera has shown that ferritin is made up of magnetite, hematite, and ferrihydrite and as the core is smaller the composition is mostly magnetite (*JACS*, **2008**, 8062-8068). Future studies will examine this hypothesis.

Future Direction

- Investigate electron donors that are waste products of other reactions to break them down into environmentally friendly products
- Determine the structure and composition of the intermediate that acts as the photocatalyst
- Can we prepare other minerals in ferritin with different band gaps? This may allow us to tune the potential of the photocatalyst
- Use an electrode as an electron acceptor to harvest the energy for bio-battery or fuel cell use

BYU
BRIGHAM YOUNG
UNIVERSITY

Maximizing the Efficiency of Ferritin as a Photocatalyst for Applications in an Artificial Photosynthesis System

Robert J. Hilton, Jeremiah D. Keyes, Richard K. Watt

Department of Chemistry and Biochemistry, Brigham Young University, Provo, Utah 84602

Introduction

As the reserves of fossil fuels decrease, there is a growing need to investigate renewable energies. One of the most promising renewable energy sources is the sun. We describe a bio-photocatalyst based on the iron storage protein ferritin. This method is a mimic of the natural process of photosynthesis. In photosynthesis, photosystem II (PSII) uses photons of light to excite electrons. These electrons are channeled into the photosynthesis pathway, where they are used for energy (Fig 1)

Ferritin is a 12 nm spherical protein that naturally sequesters iron as ferrihydrite, a semi-conductor material. We are able to mimic PSII using ferritin (Fig. 2). We describe efforts to maximize the efficiency of this system

Figure 1. PSII: electron transfer pathway. Photons cause a charge separation at P680 that initiates electron transfer reactions. Excited electrons are transferred to electron acceptors and electrons are extracted from electron donors. Ultimately, the water oxidizing complex (WOC) extracts electrons from water

Figure 2. Ferritin PSII mimic: electron transfer pathway. Photons cause charge separation in the ferrihydrite semi-conductor. Excited electrons are transferred to electron donors such as $AuCl_4^-$. A sacrificial electron donor provides electrons to fill the electron hole caused by the charge separation reaction.

Methods

Ferritin with 1000 iron atoms (0.15 mg/ml) is stirred with 40 mM citrate, 100 mM NaCl, and 4 mM $AuCl_4^-$. This solution is illuminated and simultaneously monitored by UV-visible spectrophotometry (Fig. 3). Excited electrons are transferred to $AuCl_4^-$ forming Au nanoparticles (NPs). This method was used as an assay to evaluate reaction conditions that maximize the efficiency of this photochemical reaction. Early studies showed that buffers significantly influenced the rate of AuNP formation. We designed experiments with minimal reagents to test the effect of any additive, such as buffers, for stimulatory or inhibitory effects on the reaction.

Figure 3. Method of AuNP formation. A) A light source illuminates ferritin, citrate, and $AuCl_4^-$ in solution. This initiates a photocatalytic process whereby the excited electrons reduce Au ions. The result is AuNPs with an intense color change. B) This color change can be observed spectrophotometrically, monitoring peak growth at 530 nm, based on the surface plasmon resonance of AuNPs. C) Electron micrograph of the AuNP product (Tecnai F30 TEM, 140 kV).

Figure 4. Ferritin is required to maintain AuNP solubility. A) $AuCl_4^-$, citrate, and ferrihydrite NPs (rusty-red inset) were mixed in solution and illuminated. A grey-purple precipitate formed (grey inset). Electron micrograph shows an aggregated material, as compared to B) reaction performed with the ferrihydrite inside of ferritin.

Results

The role of ferritin was examined by using 10 nm ferrihydrite NPs as photocatalysts (Fig. 4). Ferritin is required for AuNP formation. Studies show that buffers significantly influenced the rate of AuNP formation. We designed experiments with minimal reagents to test the effect of any additive such as buffers for stimulatory or inhibitory effects on the reaction (Figs. 5 and 6)

Figure 5. Buffer effects on AuNP formation. The absorbance at 530 nm was monitored over time with the addition of varied concentrations of buffers. Increasing the concentrations of both MES buffer (A) and MOPS buffer (B) enhance the reaction. However, increasing concentrations of TRIS buffer (C) inhibit the reaction. D) Direct comparison of 25 mM of each buffer. E) Carbonate and phosphate buffers do not affect the reaction compared to the control in water. F) Arrows indicate peak maxima near 530 nm. Different buffers in the reaction lead to different colored product of AuNPs (G). All data was performed in triplicate, with error bars representing the standard deviation.

Figure 6. AuNP formation with or without illumination. A) Bar graph representing the final absorbance divided by the time it took to reach that absorbance for varied buffers and concentrations. MES and MOPS both have anti-oxidative properties in the dark, but the rates are significantly increased with illumination. B) Coupled time traces of 50 mM and MOPS performed in the dark and 50 mM TRIS performed in the light. The lag phase in the TRIS reaction represents the formation of the active photocatalyst.

Conclusions

Using ferritin as a model system, we are able to photocatalytically funnel electrons to electron acceptors. Our current research has investigated metal ions as electron acceptors, however other acceptors, such as electrodes, have the potential to harvest the electrons for use in fuel cells and bio-battery applications (Fig 7)

To maximize the efficiency of this system, we sought to better understand the mechanism of the reaction. We established a minimal reaction system with ferritin in water, citrate, and $AuCl_4^-$. Tests with ferrihydrite without ferritin did not catalyze the reaction. MES and MOPS buffers stimulated the reaction and TRIS buffer inhibited the reaction. Controls without citrate demonstrated that MOPS and MES acted as electron donors to stimulate the reaction. We determined that light causes the formation of an intermediate that plays a key role in the reactions (Fig 6B). Studies are underway to characterize this intermediate

Future Direction

- Study the effectiveness of other electron donors (besides citrate) in this system
- Test other ferritin mineral cores as photocatalysts, such as MnOOH, CoOOH, or TiO_2
- Couple liberated electrons to electrodes for applications in fuel cells (Fig. 7).
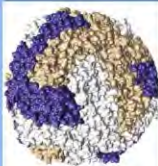

Figure 7. Ferritin fuel cell. Proposed model of a ferritin catalyzed fuel cell. Upon illumination, citrate donates electrons, which flow through the electrode, generating a current. Protons flow through the membrane, reacting with oxygen to form water.

Contact Information

Robert J Hilton rbrt.hilton@gmail.com
Richard K. Watt rwatt@chem.byu.edu
http://people.chem.byu.edu/rwatt

International Society for Optics and Photonics (SPIE), San Diego, CA, 2010.

International BioMetals Symposium, Tucson, AZ, 2010.

BYU A Negative Role for the Ferritin Nano-cage: Anion Transport

Robert J. Hilton, William M. Anderson, Richard K. Watt

Department of Chemistry and Biochemistry, Brigham Young University, Provo, Utah 84602
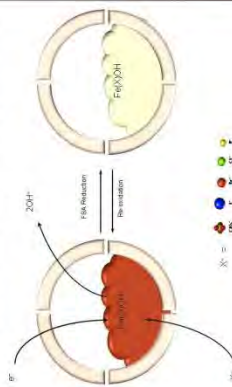
Introduction

Ferritin is an iron storage protein that can hold up to 4500 iron atoms. The structure of ferritin is advantageous for materials chemistry because the protein forms a 12 nm hollow sphere, wherein materials can be deposited. In this way, the ferritin "nano-cage" has been used in a variety of nanoparticle syntheses.[1-4]

Here, we describe a novel use of ferritin as an anion pump. In this application, anions are guided into the ferritin interior upon reduction of the native iron core. We have successfully incorporated a variety of anions into the interior of ferritin.

Methods

The iron core of ferritin is reduced using formamadine sulfinic acid (FSA), according to this equation:

$$Fe(O)OH + H_2O + e^- \rightarrow FeOH^+ + 2OH^- \quad (eq. 1)$$

This leaves a charge imbalance within ferritin. When this reaction is performed anaerobically in the presence of anions, the anions are pumped into ferritin to compensate for the charge imbalance (Scheme 1):

$$Fe(O)OH + X^- + H_2O + e^- \rightarrow Fe(X)OH + 2OH^- \quad (eq. 2)$$

Scheme 1. Proposed mechanism of anion entry into ferritin upon anaerobic reduction with FSA.

Samples are analyzed using ion selective electrodes (ISEs), UV-Visible spectrophotometry, and electron microscopy

Results

Table 1. Determination of Anion Transfer into Ferritin using ISEs.

Anion	Ionic radius (pm)	% of anion that enters ftn*	Anion atoms that enter ftn	Fe/anion inside ftn	[Anion] inside ftn
F⁻	136	99.8 ± 11.6	1585 ± 105	0.95 ± 0.11	9.82 ± 1.02
Cl⁻	181	94.2 ± 7.8	1278 ± 114	1.17 ± 0.08	7.92 ± 0.71
Br⁻	195	72.9 ± 2.9	1078 ± 84	1.39 ± 0.04	6.68 ± 0.52
I⁻	216	80.7 ± 2.3	1210 ± 53	1.24 ± 0.04	7.49 ± 0.33
ClO₄⁻	220	57.6 ± 6.6	854 ± 303	1.76 ± 0.20	5.29 ± 1.88

*ftn = ferritin
[ftn] = 0.8 mg/mL (1.8 μM); ~1 mM; Fe/ftn = 1500; [anion] in solution = 5 mM; [FSA] = 10 mM.
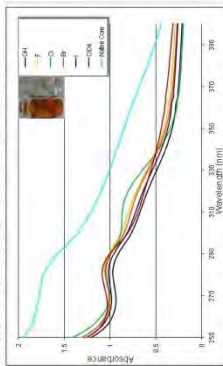
Figure 1. Representative UV-Visible spectra of reduced ferritin in the presence of various anions. Each spectrum is very similar to the next in the reduced form, indicating that there is little difference in the way that iron associates with the anion. Inset shows the color of solution prior to reduction (orange solution) and during reduction (colorless solution). Upon oxidation, the colorless solution returns to the original orange color.
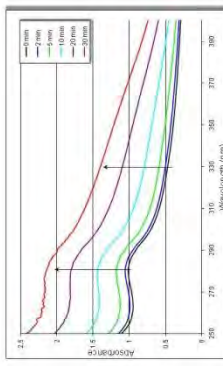
Figure 2. UV-Visible time course of oxidation of the reduced core, representative of any anion present. Reaction was performed in an anaerobic environment in the glovebox. The sample was removed and stirred in air to allow for oxidation. Upon oxidation, the anion is expelled from ferritin, and the spectrum returns to the native state.
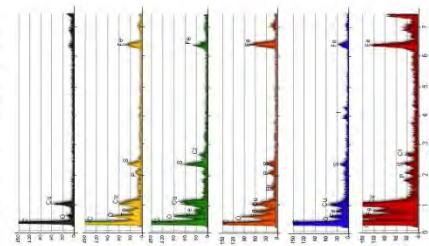
Figure 3. Scanning transmission electron microscopy image of ferritin loaded with anion (representative image). EM grids were prepared anaerobically. Fe(II) remains in ferritin when the core is reduced.

Figure 4. Representative energy dispersive X-ray spectroscopy (EDX) of various ferritin anion cores. The black scan is a control scan lacking ferritin, but with identical buffers, salts, and washing procedures. Yellow is the F loaded ferritin. The F peak is buried in the Fe peak at 0.7 keV. Green is the Cl scan, with a Cl peak at 2.6 keV. Orange is the Br scan, with a Br peak at 1.5 keV. Blue is the I scan, with I peaks at 4.0 and 4.2 keV. Finally, red is the ClO₄⁻ scan, with a Cl peak at 2.6 keV.

Conclusions

Anions are shown to enter ferritin, and this is significant because:
- Possible in vivo relevance for iron release from ferritin, because anion incorporation lends to a more accessible store of iron.
- Ferritin can be used to store anions.
  - We are able to concentrate anions from millimolar concentrations up to ~10 M concentrations within the protein.
- Ferritin is a selective transport membrane. Smaller anions enter ferritin more readily than do the larger anions.
- Upon re-oxidation in air, the anions are expelled from ferritin, and the core returns to the native Fe(O)OH.

Future Direction

- Anion of pH titrator:
  - Link ferritin to an electrode, and use the current to adjust the pH or anion concentrations.
- Sensors

Figure 5. Linking ferritin to an electrode, we can control the pH of a solution or the salt concentration of a solution with a current.

References

(1) Klem, M. T.; Mosolf, J.; Young, M.; Douglas, T. Inorganic Chemistry 2008, 47, 2237-2239.
(2) Ensign, D.; Young, M.; Douglas, T. Inorganic Chemistry 2004, 43, 3441-3446.
(3) Kasyutich, O.; Ilari, A.; Fiorillo, A.; Tatchev, D.; Hoell, A.; Ceci, P. Journal of the American Chemical Society, 432, 3621-3627.
(4) Kim, I.; Hosein, H.-A.; Strongin, D. R.; Douglas, T. Chemistry of Materials 2002, 14, 4874-4879.

Contact information: Richard K. Watt, rwatt@chem.byu.edu

nanoUtah Conference, Salt Lake City, UT, 2010.

BYU
DEPARTMENT OF CHEMISTRY AND BIOCHEMISTRY

Phosphate Inhibits Fe³⁺ Binding by Transferrin

Robert J. Hilton, M. Curtis Seare, Zachary Kenealey, N. David Andros, and Richard K. Watt

Brigham Young University, Provo, Utah

Introduction

Non-transferrin bound iron (NTBI) is present in many diseases that have inflammation and oxidative damage. Chronic kidney disease (CKD), in particular, has increased oxidative damage and NTBI. In addition, phosphate levels are elevated in CKD. We tested the hypothesis that elevated levels of serum phosphate interrupted normal Fe³⁺ binding by transferrin (Tf).
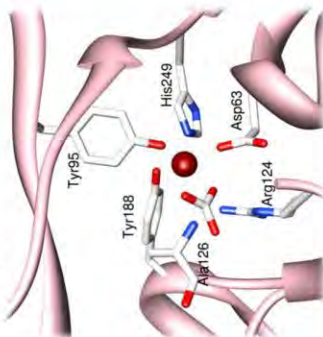
Figure 1. Crystal structure of transferrin, highlighting the site of iron binding within the N-lobe. Four residues (Asp63, Tyr95, Tyr188, and His249) act in concert with carbonate to coordinate iron. Two residues (Arg124 and Ala126) stabilize carbonate PDB code 1JNF

His249
Asp63
Tyr95
Tyr188
Arg124
Ala126

Methods

Spectrophotometric assays were employed to monitor iron loading into Tf. Phosphate was added to the assays in amounts that mimic healthy levels (1 mM), diseased levels (2.5–5 mM), and intracellular levels (10 mM).
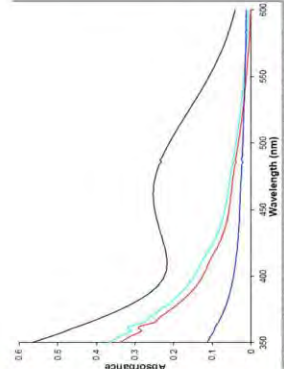
Results

Figure 2. The first question we addressed was whether phosphate can act as a synergistic anion to bind iron in the iron binding pocket. We confirm previous reports that phosphate is unable to function in this way. Apotransferrin (blue), apotransferrin + Fe³⁺ (red), apotransferrin + Fe³⁺ and PO₄³⁻ (cyan), and apotransferrin + Fe³⁺ + CO₃²⁻ (black).
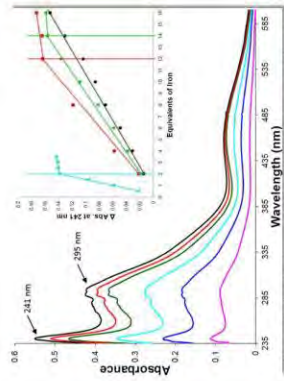
Figure 3. Spectra show an increase in absorbance at 460 nm, indicative of iron loading into Tf. In addition, peaks at 241 nm and 295 nm also increase, corresponding to the deprotonation of tyrosine residues. Ratios of Fe³⁺/Tf are as follows: pink is 0.5, blue is 1.0, cyan is 1.5, green is 2.0, red is 2.5, and black is 3.0.
Inset. Change in absorbance at 241 nm from Figure 3 vs. equivalents of iron to demonstrate Tf saturation. Cyan – in the absence of phosphate, Tf is saturated at 2 iron atoms. In 1 mM and 2.5 mM phosphate, Tf saturation occurs at 12 iron atoms (red), and 14 iron atoms (green), respectively. In 5 mM phosphate, Tf saturation was not observed (black).
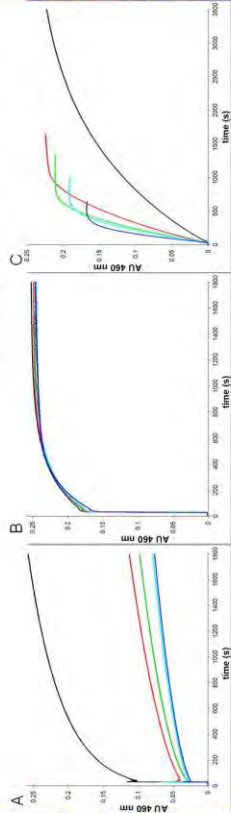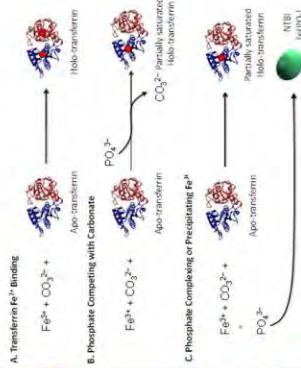
Figure 4. Fe³⁺ loading into Tf with (A) FeCl₃ or (B) Fe(III)-NTA. Tf binding of Fe³⁺ is more efficient from a complexed iron source, especially with increased [PO₄³⁻]. (C) is Fe³⁺ loading into transferrin in MES buffer at pH 6.0. Increased [PO₄³⁻] enhances the rate of iron oxidation and subsequent binding by Tf, although the total binding decreases. All graphs represent various concentrations of phosphate: no phosphate (black), 1 mM (red), 2.5 mM (green), 5 mM (cyan), and 10 mM (blue).

Conclusions

- Iron loading into Tf is inhibited with increasing levels of phosphate.
- Iron loading can be improved, if iron is in a complexed form, such as Fe(III)-NTA.
- Phosphate can oxidize Fe²⁺ and lead to subsequent binding by Tf.

A. Transferrin Fe³⁺ Binding
Fe³⁺ + CO₃²⁻ +
Apo-transferrin → Holo-transferrin

B. Phosphate Competing with Carbonate
Fe³⁺ + CO₃²⁻ +
Apo-transferrin → CO₃²⁻ Partially saturated Holo-transferrin

C. Phosphate Complexing or Precipitating Fe³⁺
Fe³⁺ + CO₃²⁻ +
Apo-transferrin → Partially saturated Holo-transferrin
PO₄³⁻ → NTBI FeIIIPO₄³⁻

Scheme 1. Model of phosphate inhibition of iron binding by Tf. A. Normal iron binding mechanism of Tf requires carbonate as a synergistic anion. B. Phosphate does not replace carbonate as the synergistic anion, and thus model B is incorrect. C. Phosphate competes with Tf for binding to iron by forming an Fe(III)-phosphate complex, which may represent NTBI in diseases such as CKD.

Acknowledgements

The Ferroxidase Center Facilitates Iron Loading into Ferritin in the Presence of Phosphate

Richard K. Watt, Robert J. Hilton, N. David Andros, Zachary Kenealey

Brigham Young University, Provo, Utah

Introduction

Patients with chronic kidney disease suffer from inflammation and oxidative damage. The oxidative damage is proposed to be associated with the elevated levels of non-transferrin bound iron (NTBI). In addition, patients with chronic kidney disease have elevated levels of serum phosphate. This work examines the hypothesis that elevated phosphate concentrations disrupt iron loading by ferritin, resulting in the formation of NTBI

Methods

Iron loading into ferritin was monitored using a spectrophotometric assay. The reactions monitored iron loading in the presence of physiological serum phosphate concentrations (1 mM), elevated serum phosphate concentrations (2-5 mM), and intracellular phosphate concentrations (10 mM). Experiments used horse spleen ferritin to represent cytosolic ferritin and also as a serum ferritin mimic because of the high L ferritin content. In addition, studies were performed with H and L homopolymers of ferritin

Results

Experiments show that both ferritin and phosphate are capable of stimulating the oxidation of Fe^{2+} (Figure 1). We identified a competing side reaction to ferritin iron loading where phosphate forms a soluble Fe(III)-phosphate complex. The formation of this product is difficult to analyze spectrophotometrically because the absorbance of the complex overlaps the typical absorbance peak (310 nm) used for iron loading into ferritin (Figure 2).
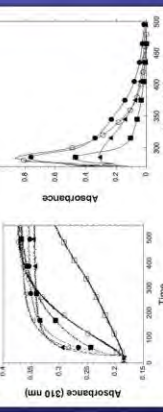
Figure 1. The rate of iron loading into ferritin increases as the concentration of phosphate increases. Concentration of phosphate are □ - 0 but no ferritin, ○ - 0 mM, ■ - 1 mM, ● - 2.5 mM, ▲ - 5 mM, and △ - 10 mM.

Figure 2. Spectra of ■ - apoferritin, ▲ - iron-phosphate complex, □ - ferritin reconstituted with phosphate, ● - holoferritin.

Results

The Fe(III)-phosphate complex was characterized by electron microscopy (EM) and atomic force microscopy (AFM), which show spherical nanoparticles between 20–200 nm (Figure 3). Elemental analysis of purified ferritin samples shows that as the phosphate concentration increases, iron loading into ferritin decreases (Table 1). The composition of the mineral that does form in ferritin has a higher iron/phosphate ratio (~ 1.1) than ferritin purified from tissue (~ 10:1). Similar iron loading experiments were performed using homopolymers of H or L ferritin (Figure 4 and Table 1). H ferritin showed significantly better iron loading in the presence of phosphate due to the the ferroxidase center that allows ferritin to rapidly bind and oxidize Fe^{2+}. Iron loading into L ferritin, lacking the ferroxidase center, was significantly inhibited by phosphate Figure 5 shows that H ferritin ferroxidase activity can load Fe^{3+} into transferrin, even in the presence of up to 5 mM phosphate.

Table 1. Iron loading into small or large core ferritin and into recombinant human heavy (rHuH) or light (rHuL) ferritin

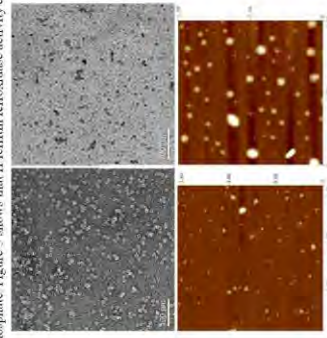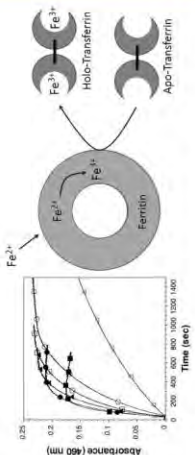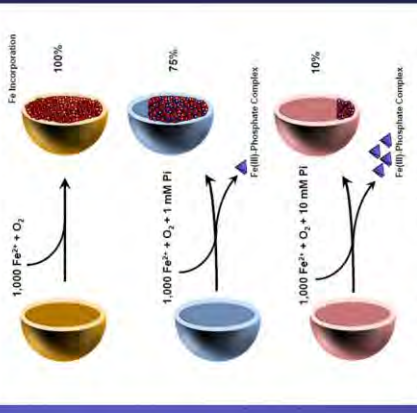| Sample	Iron Ferritin			Relative % Iron Loading		
	Small Core	Large Core		Small Core		Large Core
No phosphate	119 ± 7	1,069 ± 26		100		100
1 mM phosphate	67 ± 6	752 ± 38		56		70
2.5 mM phosphate	54 ± 2	692 ± 13		45		65
5 mM phosphate	33 ± 3	232 ± 36		28		22
	rHuH	rHuL		rHuH		rHuL
No phosphate	391.63	471.15		100		100
1 mM phosphate	239.14	97.95		61.06		20.79
2.5 mM phosphate	231.43	71.21		59.09		15.11
5 mM phosphate	212.88	53.12		54.36		11.27

Figure 3. Electron micrographs and atomic force microscopy of ferritin and Fe(III)-phosphate complexes. (A) EM images of ferritin that were negative stained with uranyl acetate to show the protein shell, compared to (B) non-stained iron-phosphate complexes. (C) Atomic force micrographs are shown of (C) ferritin and (D) the iron-phosphate complex.

Figure 4. Kinetics of iron loading into H (red) or L (blue) ferritin with increasing concentrations of phosphate (0, 1, 2.5, 5, and 10, progressing from lighter to darker colors)

Figure 5. Right, schematic representation of the assay for ferritin ferroxidase activity oxidizing iron for deposition into transferrin. Left, iron loading into transferrin was monitored kinetically, with H ferritin oxidizing the iron. △ – no H ferritin, ○ – H ferritin. H ferritin plus phosphate; □ - 1mM, ▲ - 2.5 mM, ● - 5 mM, and ■ - 10 mM. Ferroxidase activity minimizes the formation of NTBI until phosphate reaches ~5 mM

Conclusions

Physiologically relevant concentrations of serum phosphate (~1.0 mM) inhibit iron loading into L-ferritin (serum ferritin) unless ferroxidase activity is present to rapidly oxidize the Fe^{2+} for deposition into ferritin (Scheme 1). This study supports the requirement for the ferroxidase activity of ceruloplasmin to load iron into apo transferrin by oxidizing Fe^{2+} as it passes through ferroportin to transferrin (Figure 5). In a similar fashion, cytosolic phosphate concentrations (10 mM) require ferroxidase activity of the H ferritin subunit for proper loading of Fe^{2+} into ferritin to prevent the formation of Fe(III)-phosphate complexes in the cytosol

Fe Incorporation

$1,000\ Fe^{2+} + O_2$ — 100%

$1,000\ Fe^{2+} + O_2 + 1\ mM\ Pi$ — 75% Fe(III)-Phosphate Complex

$1,000\ Fe^{2+} + O_2 + 10\ mM\ Pi$ — 10% Fe(III)/Phosphate Complex

Scheme 1. Iron incorporation into ferritin is inhibited with increasing concentrations of phosphate.

Acknowledgement